

SIMULATION OF SHEAR-DRIVEN FLOWS: TRANSITION WITH A FREE SURFACE AND CONFINED TURBULENCE

THÈSE N° 3837 (2007)

PRÉSENTÉE LE 27 AOÛT 2007

À LA FACULTÉ DES SCIENCES ET TECHNIQUES DE L'INGÉNIEUR
Laboratoire d'ingénierie numérique
PROGRAMME DOCTORAL EN MÉCANIQUE DES SOLIDES ET DES FLUIDES

ÉCOLE POLYTECHNIQUE FÉDÉRALE DE LAUSANNE

POUR L'OBTENTION DU GRADE DE DOCTEUR ÈS SCIENCES

PAR

Roland BOUFFANAIS

Magistère des sciences de la matière, École Normale Supérieure de Lyon, France
et de nationalité française

acceptée sur proposition du jury:

Prof. A. Curnier, président du jury
Prof. M. Deville, Prof. E. Leriche, directeurs de thèse
Dr P. Fischer, rapporteur
Prof. L. Kleiser, rapporteur
Prof. P. Sagaut, rapporteur



ÉCOLE POLYTECHNIQUE
FÉDÉRALE DE LAUSANNE

Suisse
2007

Abstract

The research work reported in the present dissertation is aimed at the analysis of complex physical phenomena involving instabilities and nonlinearities occurring in fluids through state-of-the-art numerical modeling. Solutions of intricate fluid physics problems are devised in two particularly arduous situations: fluid domains with moving boundaries and the high-Reynolds-number regime dominated by nonlinear convective effects. Shear-driven flows of incompressible Newtonian fluids enclosed in cavities of varying geometries are thoroughly investigated in the two following frameworks: transition with a free surface and confined turbulence.

The physical system we consider is made of an incompressible Newtonian fluid filling a bounded, or partially bounded cavity. A series of shear-driven flows are easily generated by setting in motion some part of the container boundary. These driven-cavity flows are not only technologically important, they are of great scientific interest because they display almost all physical fluid phenomena that can possibly occur in incompressible flows, and this in the simplest geometrical settings. Thus corner eddies, secondary flows, longitudinal vortices, complex three-dimensional patterns, chaotic particle motions, nonuniqueness, transition, and turbulence all occur naturally and can be studied in the same geometry. This facilitates the comparison of results from experiments, analysis, and computation over the whole range of Reynolds numbers. The flows under consideration are part of a larger class of confined flows driven by linear or angular momentum gradients.

This dissertation reports a detailed study of a novel numerical method developed for the simulation of an unsteady free-surface flow in three-space-dimensions. This method relies on a moving-grid technique to solve the Navier–Stokes equations expressed in the arbitrary Lagrangian–Eulerian (ALE) kinematics and discretized by the spectral element method. A comprehensive analysis of the continuous and discretized formulations of the general problem in the ALE frame, with nonlinear, non-homogeneous and unsteady boundary conditions is presented.

In this dissertation, we first consider in the internal turbulent flow of a fluid enclosed in a bounded cubical cavity driven by the constant translation of its lid. The solution of this flow relied on large-eddy simulations, which served to improve our physical understanding of this complex flow dynamics. Subsequently, a novel subgrid model based on approximate deconvolution methods coupled with a dynamic mixed scale model was devised. The large-eddy simulation of the lid-driven cubical cavity flow based on this novel subgrid model has shown improvements over traditional subgrid-viscosity type of models. Finally a new interpretation of approximate deconvolution models when used with implicit filtering as a way to approximate the projective grid filter was given. This led to the introduction of the grid filter models.

Through the use of a newly-developed method of numerical simulation, in this dissertation we solve unsteady flows with a flat and moving free-surface in the transitional regime. These flows are the incompressible flow of a viscous fluid enclosed in a cylindrical container with an open top surface and driven by the steady rotation of the bottom wall. New flow states are investigated based on the fully three-dimensional solution of the Navier–Stokes equations for these free-surface cylindrical swirling flows, without resorting to any symmetry properties unlike all other results available in the literature. To our knowledge, this study delivers the most general available results for this free-surface problem due to its original mathematical treatment. This second part of the dissertation is a basic research task directed at increasing our understanding of the influence of the presence of a free surface on the intricate transitional flow dynamics of shear-driven flows.

Keywords: free-surface flows; confined turbulence; transitional flows; large-eddy simulations; approximate deconvolution models; driven-cavity flows; vortex breakdown bubbles; Legendre spectral element method; arbitrary Lagrangian–Eulerian kinematics; moving-grid technique.

Résumé

Le but du travail de recherche présenté dans cette thèse est l'analyse de phénomènes physiques complexes, conséquences de la présence et du développement d'instabilités et de non-linéarités au sein d'un fluide. On utilise des modélisations numériques basées sur des méthodes d'ordre élevé. Deux types de problèmes complexes issus de la physique des fluides sont considérés : écoulements de fluides avec des frontières libres et les problèmes à haut nombre de Reynolds, dominés par les effets non-linéaires convectifs. Des écoulements de cisaillement de fluides newtoniens incompressibles au sein de cavités de géométries variables sont minutieusement étudiés dans les deux cadres suivants : la transition vers la turbulence en présence d'une surface libre et la turbulence en milieu confiné.

Le système physique étudié est constitué d'un fluide newtonien incompressible emplissant une cavité fermée ou bien partiellement ouverte. Toute une famille d'écoulements de cisaillement peut être facilement engendrée par la mise en mouvement d'une partie des parois de la cavité. Ces écoulements entraînés par du cisaillement ne sont pas seulement importants d'un point de vue technologique mais présentent aussi un intérêt scientifique considérable car ils incluent presque tous les phénomènes physiques intervenant dans des écoulements incompressibles. Ainsi on y observe naturellement des écoulements de coin, des recirculations secondaires, des vortex longitudinaux, des phénomènes purement tri-dimensionnels, des mouvements particuliers chaotiques, des problèmes de non-unicité, de la transition et de la turbulence, qui peuvent être étudiés dans une seule et unique géométrie. Cela facilite grandement la comparaison entre les expériences, la théorie et les simulations numériques sur un large intervalle de nombre de Reynolds. Les écoulements ainsi considérés font partie d'une classe plus générale d'écoulements confinés entraînés par des gradients de quantité de mouvement ou de moment cinétique.

Dans cette thèse, on s'intéresse tout d'abord à l'écoulement interne et turbulent d'un fluide enfermé dans une cavité cubique et entraîné par le mouvement de translation uniforme d'une des faces. On utilise des simulations des grandes échelles afin dans un premier temps, d'accroître notre compréhension de la dynamique de cet écoulement. Ensuite, un nouveau modèle de sous-maille utilisant une technique de déconvolution approchée couplée à un modèle dynamique d'échelles mixtes est développé. La simulation des grandes échelles utilisant ce nouveau modèle a permis d'améliorer les résultats par rapport à ceux obtenus avec des modèles traditionnels de viscosité de sous-maille. Enfin, on donne une nouvelle interprétation des méthodes de déconvolution approchée lorsqu'elles sont utilisées conjointement avec des techniques de filtrage implicite, afin d'approcher l'effet projectif du filtre du maillage. Cette approche permet d'introduire une nouvelle classe de modèles, dite modèles de filtre de maillage.

Par le biais d'une méthode de simulation numérique nouvellement développée, on a simulé des écoulements instationnaires en présence d'une surface libre et en régime transitionnel. Ces écoulements incompressibles sont ceux d'un fluide visqueux au sein d'une cavité cylindrique ouverte sur le dessus, et entraîné par la rotation constante du disque de fond. De nouveaux états d'écoulement sont étudiés par le biais de solutions tri-dimensionnelles des équations de Navier–Stokes, sans avoir besoin de recourir à des propriétés de symétrie comme le font tous les travaux de recherche disponibles dans la littérature scientifique. Cette étude fournit les résultats les plus généraux à ce jour sur ces problèmes à surface libre, et ce grâce à l'originalité du traitement mathématique. Cette seconde partie de la thèse constitue un travail de recherche fondamentale ayant pour but de mieux comprendre l'influence d'une surface libre sur la dynamique des écoulements transitionnels entraînés par cisaillement.

La présente thèse contient également une présentation détaillée de la nouvelle méthode numérique développée afin de simuler les écoulements instationnaires à surface libre en trois dimensions. Cette méthode repose sur une technique de maillage mobile pour résoudre les équations de Navier–Stokes exprimées dans la cinématique arbitraire eulérienne lagrangienne (“ALE” en anglais dans le texte) et discrétisée par la méthode des éléments spectraux. Nous donnons une analyse complète des formulations discrètes et continues du problème général en formulation ALE et soumis à des conditions aux limites non-linéaires, non-homogènes et instationnaires.

Mots-clefs : écoulements à surface libre ; turbulence en milieu confiné ; écoulements transitionnels ; simulation des grandes échelles ; modèles de déconvolution approchée ; écoulements dans des cavités entraînés ; “vortex breakdown bubbles” ; méthode des éléments spectraux de Legendre ; cinématique lagrangienne–eulérienne arbitraire ; technique de maillage mobile.

Acknowledgements

I would first and foremost like to thank Prof. Michel Deville who has supervised this work. His guidance and support have been invaluable and immensely enriching. I would also like to thank Prof. Emmanuel Leriche who has co-supervised my thesis, for his constant interest and for the numerous discussions we had.

I am also extremely grateful to Prof. Lai Choy Heng from the National University of Singapore (NUS) and to Prof. Wei Guo Wei from the Michigan State University, for introducing me to the fascinating world of Scientific Computing. I am indebted to them for their advice and scientific vision all along my two-year stay at NUS.

My thanks to Professor Lian Shen from the Johns Hopkins University (JHU) for his extremely warmth welcome during my stay at JHU as a visiting scholar. I have greatly appreciated our scientific discussions and I really look forward to having new opportunities of collaborating with him in the future.

I am thankful to Dr. Christos Frouzakis and Prof. Ananias Tomboulides from ETH Zürich for initiating a collaboration with us on our LES activities. It was always a real pleasure to visit them in Zürich.

I wish also to thank Prof. Peter Monkewitz from the LMF for his support and for giving me the opportunity to assist him in his teaching activities at EPFL.

I would like to thank Dr. David Lo Jacono from Monash University and Marc-Antoine Habisreutinger with whom I had extensive and enriching scientific interactions. Both of them were also assiduous coffee-mates and conference-mates and will remain very good friends.

To everyone at the Laboratory of Computational Engineering (LIN) I express my appreciation for their time and assistance, and in particular: Dr. Ralf Gruber and Vincent Keller for the thorough parallel benchmark of our code; Heidi Francelet for a very precious assistance in all non-scientific matters; Ali Tolou for his permanent assistance related to the cluster management; Orestis Malaspinas deserves a special mention for having put up with sharing an office and a coffee-machine with me.

To my coffee-mates and friends: Emeric Grandjean, Radboud Nelissen, Richard Vonlanthen, Etienne Robert, Orestis Malaspinas and all others, I have a single word to say: “Café !”. I will certainly miss our short but numerous coffee-discussions.

I am very grateful to Dr. Paul F. Fischer, Prof. Leonhard Kleiser and Prof. Pierre Sagaut for their participation in the thesis committee and for taking the time to read through the manuscript and attend the private defense. Their comments and suggestions have been greatly appreciated. I would also like to thank Prof. Alain Curnier for presiding over the committee.

I would like to acknowledge the Swiss National Science Foundation for its financial support.

Last but certainly not least, I reserve my deepest thanks for Ariane for her support, understanding and patience during these three and a half years.

Contents

| | |
|--|-------------|
| Abstract | iii |
| Résumé | v |
| Acknowledgements | vii |
| Contents | xiii |
| Nomenclature | xv |
| | |
| I Introduction | 1 |
| 1 Introduction | 3 |
| 1.1 Motivations and objectives | 3 |
| 1.1.1 Fluid physics in driven cavities | 3 |
| 1.1.2 Moving-boundary problems and free-surface flows | 3 |
| 1.1.3 Large-eddy simulation of turbulent flows | 4 |
| 1.1.4 High-order and spectral element method developments | 6 |
| 1.1.5 Parallel and high-performance computations | 7 |
| 1.2 Contributions of the present work | 7 |
| 1.2.1 Turbulence modeling and large-eddy simulation | 7 |
| 1.2.2 Physics of shear-driven flows in cavities | 8 |
| 1.2.3 Applied numerical mathematics | 8 |
| 1.3 Organization of the dissertation | 9 |
| 1.3.1 Description | 9 |
| 1.3.2 Preliminary notes | 9 |
| | |
| II Numerical modeling | 11 |
| 2 Numerical methods for simulating shear-driven flows | 13 |
| 2.1 Introduction | 13 |
| 2.2 Space discretization methods | 14 |
| 2.2.1 Finite difference methods | 14 |
| 2.2.2 Finite volume method | 15 |
| 2.2.3 Finite element methods | 15 |
| 2.2.4 Spectral and spectral element methods | 15 |
| 2.2.5 Meshless methods | 16 |
| 2.3 Legendre spectral element method | 16 |
| 2.3.1 Weak formulation of the problem | 17 |
| 2.3.2 Galerkin approximation | 18 |
| 2.3.3 Semi-discrete Navier–Stokes formulation | 19 |
| 2.3.4 Mortar element formulation | 20 |
| 2.3.5 Time discretization | 20 |
| 2.3.6 System solving techniques | 21 |
| 2.3.7 Stabilization technique | 21 |
| 2.4 Summary | 21 |
| | |
| 3 Spectral element method for moving-boundary problems | 23 |
| 3.1 Introduction | 23 |
| 3.2 Mathematical model | 24 |
| 3.2.1 The ALE kinematic framework | 24 |
| 3.2.2 The strong ALE formulation for the Navier–Stokes equations | 25 |

| | | |
|--|--|-----------|
| 3.2.3 | The weak ALE formulation for the moving-boundary problem governed by the Navier–Stokes equations | 26 |
| 3.3 | Numerical technique and discretization | 27 |
| 3.3.1 | Spectral element discretization | 28 |
| 3.3.2 | Galerkin approximation | 28 |
| 3.3.3 | Semi-discrete Navier–Stokes moving-boundary problem in the ALE form | 29 |
| 3.3.4 | Time discretization | 30 |
| 3.3.5 | Specificities pertaining to free-surface flows and fluid-structure interaction | 30 |
| 3.4 | Moving-grid techniques | 31 |
| 3.5 | Numerical simulations and results | 32 |
| 3.5.1 | Accuracy in curved domains | 32 |
| 3.5.2 | Motion of a cylinder inside a square cavity | 34 |
| 3.5.3 | Sloshing in a three-dimensional tank | 37 |
| 3.6 | Conclusions | 39 |
| III Confined shear-driven turbulent flows | | 41 |
| 4 | Turbulent lid-driven cubical cavity flow | 43 |
| 4.1 | Introduction | 43 |
| 4.2 | The model and numerical technique | 44 |
| 4.2.1 | Mathematical modeling | 44 |
| 4.2.2 | Subgrid-scale models | 45 |
| 4.2.3 | Numerical technique | 47 |
| 4.2.4 | Filtering techniques | 48 |
| 4.3 | Physical and computational parameters | 50 |
| 4.3.1 | Statistical ensemble averaging | 51 |
| 4.3.2 | Under-resolved DNS and Smagorinsky model | 52 |
| 4.3.3 | Comparisons with available results | 55 |
| 4.3.4 | Physical parameters of the LES modeling | 61 |
| 4.4 | Characterization of turbulence in the flow | 61 |
| 4.4.1 | Inhomogeneity of turbulence | 62 |
| 4.4.2 | The turbulence production near the downstream wall | 63 |
| 4.4.3 | Small-scales turbulent structures | 67 |
| 4.4.4 | Helical properties of the cavity flow | 71 |
| 4.5 | Conclusions | 73 |
| 5 | A coupled approximate deconvolution and dynamic mixed scale model for LES | 75 |
| 5.1 | Introduction | 75 |
| 5.2 | Governing equations and numerical method | 76 |
| 5.2.1 | Governing equations | 76 |
| 5.2.2 | Space discretization | 76 |
| 5.2.3 | Time integration | 77 |
| 5.3 | Subgrid modeling | 77 |
| 5.3.1 | General considerations | 77 |
| 5.3.2 | Approximate deconvolution model | 78 |
| 5.3.3 | Coupling with a dynamic mixed scale model | 79 |
| 5.3.4 | Particular cases of ADM-DMS | 81 |
| 5.4 | Filtering | 81 |
| 5.4.1 | Description of the filter | 81 |
| 5.4.2 | Transfer function | 82 |
| 5.4.3 | Filter cutoff length | 82 |
| 5.4.4 | Filtering operators related to ADM | 83 |
| 5.5 | LES of the lid-driven cubical cavity flow | 83 |
| 5.5.1 | General considerations | 83 |
| 5.5.2 | Validation of the approximate deconvolution procedure | 86 |
| 5.5.3 | <i>A posteriori</i> validations | 87 |
| 5.5.4 | Reynolds stresses production | 91 |
| 5.5.5 | Dynamic parameter for ADM-DMS | 92 |
| 5.5.6 | Subgrid activity | 93 |

| | | |
|-----------|--|------------|
| 5.5.7 | Subgrid kinetic energy | 95 |
| 5.6 | Conclusions | 95 |
| 6 | Grid filter models for LES of shear-driven confined flows | 99 |
| 6.1 | Introduction | 99 |
| 6.2 | Different formulations of the problem | 100 |
| 6.2.1 | General considerations | 100 |
| 6.2.2 | Filtered formulation | 100 |
| 6.2.3 | Deconvoluted formulation | 101 |
| 6.2.4 | Implicit projective grid filter | 101 |
| 6.3 | Grid filter models | 102 |
| 6.3.1 | Definition | 102 |
| 6.3.2 | Interpretation | 102 |
| 6.4 | Numerical results | 103 |
| 6.4.1 | <i>A priori</i> validations | 103 |
| 6.4.2 | <i>A posteriori</i> validations | 104 |
| 6.4.3 | Evolution of total resolved kinetic energy and enstrophy of the flow | 105 |
| 6.4.4 | Assessment based on the Reynolds stress tensor | 106 |
| 6.5 | Conclusions | 108 |
| IV | Open shear-driven transitional swirling flows | 109 |
| 7 | Transitional open swirling flow | 111 |
| 7.1 | Introduction | 111 |
| 7.1.1 | General considerations | 111 |
| 7.1.2 | The lid-driven cylindrical cavity flow | 112 |
| 7.1.3 | Open swirling flow | 114 |
| 7.1.4 | Motivations and objectives | 115 |
| 7.2 | Mathematical model and problem formulation | 115 |
| 7.2.1 | Mathematical description of the problem | 115 |
| 7.2.2 | Angular velocity distribution | 116 |
| 7.2.3 | Free-surface modeling | 117 |
| 7.3 | Computational approach | 118 |
| 7.3.1 | Space discretization | 118 |
| 7.3.2 | Time integration | 119 |
| 7.3.3 | Convergence tests | 119 |
| 7.4 | Numerical simulations and results | 121 |
| 7.4.1 | General physical characteristics of the flow | 121 |
| 7.4.2 | Cases studied | 122 |
| 7.4.3 | Physical description of flow states | 124 |
| 7.4.4 | One-dimensional momentum budgets | 138 |
| 7.4.5 | Nonaxisymmetric modes in the unsteady transitional flow | 147 |
| 7.5 | Conclusions | 151 |
| 8 | Free-surface swirling flow | 153 |
| 8.1 | Introduction | 153 |
| 8.1.1 | General considerations | 153 |
| 8.1.2 | Motivations and objectives | 153 |
| 8.2 | Mathematical model and problem formulation | 154 |
| 8.2.1 | Mathematical description of the problem | 154 |
| 8.2.2 | Free-surface modeling | 155 |
| 8.2.3 | Mesh velocity problem and boundary conditions | 156 |
| 8.3 | Computational approach | 157 |
| 8.3.1 | Space discretization | 157 |
| 8.3.2 | Time integration | 157 |
| 8.3.3 | Computational parameters | 157 |
| 8.4 | Numerical simulations and results | 158 |
| 8.4.1 | Free surface profiles | 158 |
| 8.4.2 | Vortex breakdown bubbles and meridional flow fields | 160 |

| | | |
|-----------|--|------------|
| 8.4.3 | Free-surface flow fields | 165 |
| 8.4.4 | Study of some nonlinear convective terms | 165 |
| 8.5 | Conclusions | 169 |
| V | Summary and conclusions | 171 |
| 9 | Summary and conclusions | 173 |
| 9.1 | Outcomes and summary | 173 |
| 9.2 | Outlook and perspectives | 175 |
| VI | Appendices | 177 |
| A | Mesh update techniques for free-surface flow solvers | 179 |
| A.1 | Introduction | 179 |
| A.2 | Governing Equations | 179 |
| A.3 | Numerical technique and discretization | 181 |
| A.4 | Moving-grid technique | 181 |
| A.5 | Mesh-transfer operation | 182 |
| A.6 | Conclusion and future studies | 185 |
| A.7 | Annex 1 | 186 |
| A.7.1 | Parent-element point positioning algorithm | 187 |
| A.7.2 | Implementation of the field-spectral interpolation algorithm | 188 |
| A.7.3 | Performance of the Field-spectral interpolation algorithm | 189 |
| A.8 | Annex 2 | 189 |
| A.8.1 | GL polynomial bases and interpolation algorithm | 190 |
| A.8.2 | GL mesh-transfer algorithm performance tests | 191 |
| B | Closed cylindrical swirling flow | 193 |
| B.1 | Introduction | 193 |
| B.2 | Numerical results | 194 |
| B.2.1 | Vortex breakdowns with increasing Reynolds number | 194 |
| B.2.2 | Transition to unsteadiness | 197 |
| B.3 | Conclusions | 198 |
| B.4 | Annex: Closed swirling flow without recirculation bubble | 200 |
| C | Computational performance analysis of a parallelized high-order spectral and mortar element toolbox | 203 |
| C.1 | Introduction | 203 |
| C.2 | Speculoos numerical and software context | 204 |
| C.2.1 | Spectral and mortar element method | 204 |
| C.2.2 | Object-oriented programming | 204 |
| C.2.3 | Parallel implementation | 204 |
| C.2.4 | Benchmark evaluation test cases description | 205 |
| C.3 | Single-processor performance analysis | 207 |
| C.3.1 | Influence of the computer architecture | 208 |
| C.3.2 | Compiler optimization | 208 |
| C.3.3 | Linking optimization | 209 |
| C.3.4 | Profiling | 210 |
| C.4 | Parallel implementation | 210 |
| C.4.1 | Influence of processor dispatching on performance | 211 |
| C.4.2 | Scalability study and influence of the size of the problem | 211 |
| C.4.3 | Communications | 213 |
| C.5 | Advanced parallel benchmarking | 216 |
| C.5.1 | Speculoos characteristics | 217 |
| C.5.2 | Hardware and software used | 217 |
| C.5.3 | Fixed problem size | 218 |
| C.5.4 | Increase CPU performance | 218 |
| C.5.5 | Varying the number of processing element P with problem size | 218 |
| C.5.6 | CPU usage and the Γ model | 220 |

| | |
|--|------------|
| C.5.7 Modification of the number of running threads per SMP node | 222 |
| C.6 Conclusions | 223 |
| C.7 Annex: Profiling information | 223 |
| Bibliography | 225 |
| Curriculum vitae | 237 |

Nomenclature

Roman symbols

| | |
|--|--|
| A | stiffness matrix associated with the spectral element method, can be time-dependent |
| L and L_{ij} | Leonard stress tensor and its entries |
| $\mathbf{g}(t)$ | value of the prescribed velocity of the boundary $\partial\Omega_t^{\mathcal{D}}$ |
| S and S_{ij} | rate-of-strain tensor and its entries |
| T and T_{ij} | sub-test scale stress tensor and its entries |
| $\mathcal{A}(\mathbf{u}, \hat{\mathbf{v}})$ | energy bilinear form |
| \mathcal{V} | fluid domain enclosed in the cavity |
| \mathcal{A}_t | family of time-dependent mappings, which at each $t \in I$ associates a point $\mathbf{Y} \in \Omega_0$ to a point $\mathbf{x} \in \Omega_t$ |
| $\mathcal{B}(\hat{\mathbf{v}}, p)$ | bilinear form expressing the weak form of the incompressibility constraint |
| C | discrete convective operator associated with the spectral element method, can be time-dependent |
| \mathcal{C} | modified SGS cross term in the Leonard decomposition |
| $\mathcal{C}(\hat{\mathbf{v}}; \mathbf{u}, \mathbf{w}), \mathcal{C}(\mathbf{u}, \mathbf{v})$ | nonlinear weak convective form |
| C_d | dynamic parameter for all dynamic eddy-viscosity based SGS models |
| $\mathcal{E}_{\mathbf{x}}$ | any elliptic operator based on the Eulerian coordinates \mathbf{x} |
| $\mathcal{F}(\hat{\mathbf{v}})$ | linear form expressing the weak form of body force \mathbf{f} |
| \mathcal{G}_{\star} | convolution filter |
| $\mathcal{H}^{\sigma}(\hat{\mathbf{v}})$ | surface linear form associated with the stress constraint on $\partial\Omega_t^{\sigma}$ |
| \mathcal{L}_{\star} | primary LES filter |
| \mathcal{L} | modified Leonard stress tensor |
| \mathcal{M}_0^e | mapping from the reference element $\hat{\Omega}$ onto Ω_0^e |
| \mathcal{M}_t^e | mapping from the reference element $\hat{\Omega}$ onto Ω_t^e |
| \mathcal{N} | order of deconvolution in the ADM |
| \mathcal{P}_{\star} | projective grid filter |
| \mathcal{R} | modified SGS Reynolds stress tensor |
| C_S | Smagorinsky constant |
| \mathcal{T}_{\star} | test filter |
| D | discrete divergence operator associated with the spectral element method, can be time-dependent |
| \mathbf{D}^T | discrete gradient operator associated with the spectral element method, can be time-dependent |
| $\mathbf{D}_{\mathbf{x}}(\mathbf{u}), \mathbf{D}(\mathbf{u})$ | rate-of-deformation tensor in the Eulerian frame of reference |
| $\mathbf{h}(t)$ | value of the prescribed stress vector on the boundary $\partial\Omega_t^{\sigma}$ |
| $\hat{\mathbf{n}}$ | local unit outward normal vector to $\partial\Omega_t$ |
| $J_{\mathcal{A}_t}$ | Jacobian of the ALE mapping \mathcal{A}_t , $J_{\mathcal{A}_t} = \det \mathbf{J}_{\mathcal{A}_t}$ |
| $\mathbf{J}_{\mathcal{A}_t}$ | Jacobian matrix of the ALE mapping \mathcal{A}_t |
| M | mass matrix associated with the spectral element method, can be time-dependent |
| \mathbb{P}_N | functional space of polynomials of degree greater or equal to N |
| \mathbb{R}^d | Euclidian space of dimension d |
| \mathbf{f} | body force per unit mass |
| I | Identity tensor |
| $\mathbf{u}(\mathbf{x}, t)$ | Eulerian velocity field |
| $\mathbf{u}^0(\mathbf{x})$ | initial divergence-free Eulerian velocity field at $t = t_0$ |
| $\hat{\mathbf{v}}$ | time-independent velocity test functions defined on the reference fluid domain Ω_0 |
| $(\hat{\mathbf{v}} \circ \mathcal{A}_t^{-1})$ | velocity test functions on the fluid domain Ω_t |
| \mathbf{w} | arbitrary Lagrangian–Eulerian velocity field, also called “ALE mesh velocity” |
| \mathbf{x} | Eulerian space coordinate |
| \mathbf{x}^e | Eulerian coordinate in the spectral element Ω_t^e |
| Y | arbitrary Lagrangian–Eulerian space coordinate |
| \mathbf{Y}^e | arbitrary Lagrangian–Eulerian coordinate in the spectral element Ω_t^e |
| $\{\mathbf{u}_{ijk}(t)\}_{i,j,k=0}^N$ | set of nodal values of the velocity field on the GLL grid of Ω_t^e |
| $\{p_{ijk}(t)\}_{i,j,k=1}^{N-1}$ | set of nodal values of the pressure field on the GL grid of Ω_t^e |

| | |
|---------------|---|
| $a(t)$ | wave amplitude |
| d | space dimension, $d = 2, 3$ |
| E | number of non-overlapping spectral elements covering the whole discretized fluid domain |
| f | any space- and time-dependent scalar function |
| g | acceleration of gravity |
| h | half-size of the cubical cavity |
| $h(x, y, t)$ | free-surface elevation measured from the position at rest, in the z -direction |
| $H^1(\Omega)$ | first-order Sobolev space of scalar functions on Ω |
| I | time interval, $I = [t_0, T]$ |
| k | one-dimensional wave number, $k = 2\pi/\lambda$ |
| L | length and width of tank |
| $L^2(\Omega)$ | space of square-Lebesgue integrable functions on Ω |
| L_k | Legendre polynomial of degree k |
| N | polynomial degree of the spectral element discretization |
| p | pressure field or reduced pressure field (normalized by the constant fluid density) |
| p_0 | constant pressure field of the surrounding fluid, taken equal to zero |
| q | pressure test function defined on $L^2(\Omega_t)$ |
| T | final time, or period for oscillating problems |
| t | time |
| t_0 | initial time |
| u, u_x | x -component of the velocity field |
| U_0 | maximum lid velocity of the cubical cavity |
| u_θ | azimuthal component of the velocity field in cylindrical coordinates |
| u_r | radial component of the velocity field in cylindrical coordinates |
| v, u_y | y -component of the velocity field |
| w, u_z | z -component of the velocity field, also called axial velocity component in cylindrical coordinates |
| Fr | Froude number |
| Re | Reynolds number |
| Wh | Wehausen number |

Greek symbols

| | |
|--------------------------------|--|
| ω | vorticity field |
| ω^s | surface vorticity |
| σ and σ_{ij} | Cauchy stress tensor of the fluid and its entries |
| σ^* and σ_{ij}^* | reduced Cauchy stress tensor of the incompressible fluid and its entries |
| τ and τ_{ij} | subgrid scale tensor and its entries |
| ξ | running variable vector in $\hat{\Omega}$ associated with GLL discretization |
| ζ | running variable vector in $\hat{\Omega}$ associated with GL discretization |
| Δt | time-step |
| δ_{ij} | Kronecker symbol |
| η | free-surface elevation measured from its equilibrium position |
| $\eta_{\mathcal{G}}$ | filtering rate for the filter \mathcal{G}_\star |
| $\eta_{\mathcal{T}}$ | test-filter filtering rate |
| Γ | angular momentum in the lid-driven cylindrical flow, defined as $\Gamma = ru_\theta$ |
| $\hat{\tau}$ | local unit tangential vector directly orthogonal to $\hat{\mathbf{n}}$ |
| $\hat{\Omega}$ | reference parent element domain for the Legendre spectral element method, $\hat{\Omega} := [-1, 1]^d$ |
| Λ | height-to-radius aspect ratio, defined as H/R |
| λ | wavelength |
| μ | fluid dynamic viscosity |
| ν | fluid kinematic viscosity |
| ν_{eff} | effective kinematic viscosity |
| ν_{sgs} | eddy or subgrid scale viscosity |
| ω | angular frequency |
| Ω_0 | reference fluid domain or constant angular velocity of the bottom end-wall in the driven cylindrical cavity case |
| Ω_0^e | e -th spectral element of the decomposition of the reference fluid domain |
| Ω_t | fluid domain at time t |
| Ω_t^e | e -th spectral element of the decomposition of the fluid domain at time t |

| | |
|-----------------------------------|--|
| $\overline{\Delta}$ | LES filter width |
| $\overline{\Omega}_0$ | closed reference fluid domain |
| $\overline{\Omega}_t$ | closed fluid domain at time t |
| $\partial\Omega_0$ | reference fluid domain boundary |
| $\partial\Omega_t$ | fluid domain boundary at time t |
| $\partial\Omega_t^\sigma$ | stress-imposed part of the fluid domain boundary $\partial\Omega_t$ at time t |
| $\partial\Omega_t^{e,\sigma}$ | stress-imposed part of the fluid domain boundary $\partial\Omega_t$ at time t belonging to the spectral element Ω_t^e |
| $\partial\Omega_t^D$ | fixed or prescribed-in-motion part of the fluid domain boundary $\partial\Omega_t$ at time t |
| Φ | iso-parametric mapping from the parent element $\hat{\Omega}$ onto the physical spectral element |
| $\pi_i(\xi_i)$ | one-dimensional GLL-based Lagrange–Legendre interpolant of order i |
| $\pi_{i,j,k}(\xi)$ | three-dimensional tensor-product GLL-based Lagrange–Legendre interpolant of order i, j, k in the three space directions respectively |
| ρ | constant fluid density |
| Υ | region located at the interface between the inner cylindrical core and the outer cylindrical layer |
| $\varpi_i(\zeta_i)$ | one-dimensional GL-based Lagrange–Legendre interpolant of order i |
| $\varpi_{i,j,k}(\zeta)$ | three-dimensional tensor-product GL-based Lagrange–Legendre interpolant of order i, j, k in the three space directions respectively |
| $\hat{\Delta}$ | LES test filter width |
| $\{\phi_k\}_{k=0}^N$ | modal basis |
| $\Delta_{\mathbf{x}}$ or Δ | Laplacian operator based on the Eulerian coordinates \mathbf{x} |

Other symbols and operators

| | |
|--|--|
| (\cdot, \cdot) | inner product of elements in a given functional space |
| $\cdot \cdot \cdot$ | inner tensor product or double contraction |
| $\cdot \otimes \cdot$ | tensor product |
| $\frac{d}{dt}$ | total derivative in the Reynolds sense |
| $\langle \cdot \rangle$ | average quantity |
| $\nabla_{\mathbf{x}}$ or ∇ | gradient operator in the Eulerian frame of reference |
| $\nabla_{\mathbf{x}\cdot}$ or $\nabla \cdot$ | divergence operator in the Eulerian frame of reference |
| $\overline{\cdot}$ | filtered quantity |
| $\partial/\partial t _{\mathbf{x}}$ | partial time derivative in the Eulerian frame of reference |
| $\partial/\partial t _{\Upsilon}$ | partial time derivative in the ALE frame of reference or particle derivative |
| $\underline{\cdot}$ | tensorized vector containing the nodal values of a given quantity |
| $\tilde{\cdot}$ | test-filtered quantity |

Subscripts

| | |
|---------------------------|---|
| $(\cdot)_N$ | N -th order discretized quantity |
| $(\cdot)_n$ | quantity at time-step $t_n = t_0 + n\Delta t$ |
| $(\cdot, \cdot)_N$ | discretized inner product of elements in a given finite-dimensional functional space |
| $(\cdot, \cdot)_{N, GLL}$ | discretization on the GLL grid points of inner product of elements in a given finite-dimensional functional space |

Superscripts

| | |
|--------------------|----------------------------------|
| $(\cdot)'$ | subgrid scale part of a quantity |
| $(\cdot)^*$ | approximate deconvolution |
| $(\cdot)^\bullet$ | exact deconvolution |
| $(\cdot)^\diamond$ | fluctuating part of a quantity |
| $(\cdot)^T$ | transpose operation |
| $(\cdot)^d$ | deviatoric part of a tensor |

Abbreviations

| | |
|--------|-------------------------------------|
| 2D, 3D | two-, three-dimensional |
| AB k | Adams–Bashforth scheme of order k |
| ALE | arbitrary Lagrangian–Eulerian |

| | |
|---------|--|
| BDF k | backward differential formula of order k |
| CFD | computational fluid dynamics |
| CFL | Courant–Friedrich–Lewy |
| CSM | computational solid mechanics |
| DBC | dynamic boundary condition |
| DMM | dynamic mixed model |
| DNS | direct numerical simulation |
| DSM | dynamic Smagorinsky model |
| EX k | explicit extrapolation of order k |
| FDM | finite difference method |
| FEM | finite element method |
| FVM | finite volume method |
| GCL | geometric conservation law |
| GL | Gauss–Legendre |
| GLL | Gauss–Lobatto–Legendre |
| HCS | helical coherent structure |
| KBC | kinematic boundary condition |
| LES | large-eddy simulation |
| MLM | meshless method |
| MPI | message passing interface |
| ODE | ordinary differential equation |
| OIFS | operator integration factor splitting |
| PDE | partial differential equation |
| rms | root-mean-square |
| SEM | spectral element method |
| SGS | subgrid scale |
| SM | Smagorinsky model |
| TGL | Taylor–Görtler-like |
| UDNS | under-resolved direct numerical simulation |
| VB | vortex breakdown |

Part I

Introduction

Chapter 1

Introduction

The research work reported in the present dissertation is aimed at the analysis of complex physical phenomena involving instabilities and nonlinearities occurring in fluids through state-of-the-art high-order numerical modeling. Solution of intricate fluid physics problems are devised in two particularly arduous situations: fluid domains with moving boundaries and the high-Reynolds-number regime dominated by nonlinear convective effects. Shear-driven flows of incompressible Newtonian fluids enclosed in cavities are thoroughly investigated in these two frameworks: transition with a free surface and confined turbulence.

1.1 Motivations and objectives

1.1.1 Fluid physics in driven cavities

The physical system is made of an incompressible Newtonian fluid, initially quiescent and filling a bounded, or partially bounded cavity. From this initial state, a series of shear-driven flows can easily be generated by setting in motion some part of the container boundary. These driven-cavity flows are not only technologically important, they are of great scientific interest because they display almost all physical fluid phenomena that can possibly occur in incompressible flows, and this in the simplest geometrical settings. Thus corner eddies, secondary flows, longitudinal vortices, complex three-dimensional patterns, chaotic particle motions, nonuniqueness, transition, and turbulence all occur naturally and can be studied in the same geometry. This facilitates the comparison of results from experiment, analysis, and computation over a large range of Reynolds numbers. As stated by Shankar & Deshpande [225]: "... cavity flows are almost canonical and will continue to be extensively studied and used".

The flows under consideration in this dissertation are part of a larger class of confined flows driven by linear or angular momentum gradients. The two central problems discussed in this dissertation, namely transition in presence of a free surface and confined turbulence, are investigated in two different cavity geometries. First, the internal flow of a fluid enclosed in a bounded cubical cavity driven by the constant translation of its lid is considered in the locally-turbulent regime. Subsequently, the incompressible flow of a Newtonian fluid enclosed in a cylindrical container with an open top surface and driven by the steady rotation of its bottom end-wall is analyzed in the transitional regime.

In both of these cavity flows, the primary motion is due to externally imposed motion of part of the container boundary which constantly provides shear stress to the flow through viscous diffusion. The no-slip condition on the walls of the enclosing cavity imposes kinematic constraints on the flow resulting in the bending of vortex lines and in large recirculation zones in a large portion of the cavity, see Fig 1.1. In addition, this bending produces secondary motions and recirculations. The particular details of the topology of these recirculation zones depend on the geometry of the container and the strength of the driving force, yet they all result from the bending of vortex lines. In a significant part of these flows, the secondary motions can be comparable to the primary motion in terms of intensity, leading to significant nonlinear interactions. When increasing further the Reynolds number, these secondary motions start developing interactions among themselves and through the influence of the primary recirculation, leading to complex flow dynamics.

1.1.2 Moving-boundary problems and free-surface flows

Fluid flows possessing a free surface are very common in real life. The concept of free surface is often abusively used in the literature to refer to any gas-liquid interface. A free surface is an idealization of a gas-liquid interface in which the dynamics of the gas phase is neglected by setting the gas density and viscosity to zero. Free-surface flows are encountered and have applications in many disciplines of engineering and applied sciences as varied

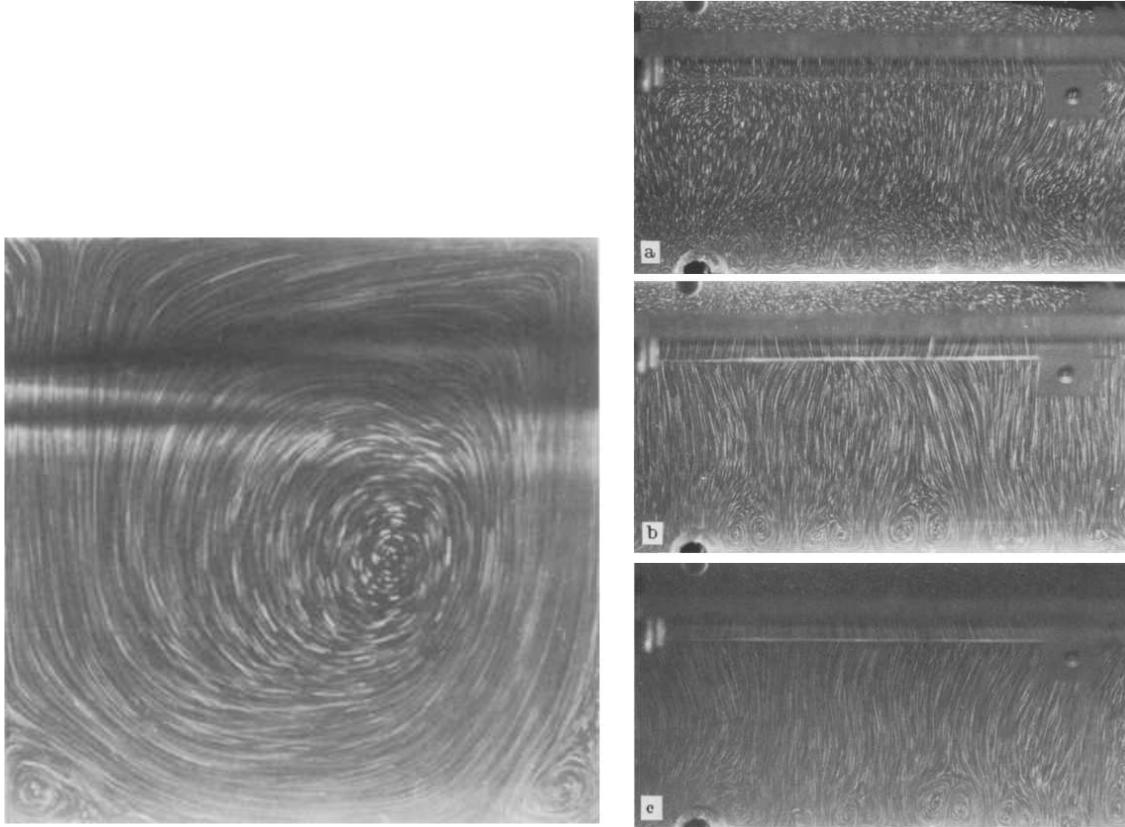


*Fig. 1.1: Experiments conducted in a three-dimensional lid-driven cavity flow to study the behavior of longitudinal Taylor–Görtler-like (TGL) vortices. Left: typical symmetry plane visualization (with a rheoscopic liquid) at $Re = 3\,300$; all three transverse secondary eddies are visible in this and all other flows for $1\,000 \leq Re \leq 10\,000$. Right: photographs of the lateral plane; in each case, (a): $Re = 2\,000$, (b): $Re = 3\,300$, and (c): $Re = 6\,000$, this location is near to that where the flow over the downstream secondary eddy reattaches to the bottom; the TGL vortex pairs are clearly visible. From Rhee *et al.* [207]. © 1984 Springer-Verlag.*

as environment, geophysics, and fundamental physics. The difficulties inherent to these problems are very challenging for mathematical, physical and computational analyses.

From a physical viewpoint, moving-boundary flows are intrinsically nonlinear. In addition to the convective nonlinearities associated with the Navier–Stokes equations in a transitional or turbulent regime, one deals with a complicated geometry changing in time and that is part of the unknown solution itself. To date all the investigations accounting for the essential mechanisms associated with the presence of the thin viscous layer beneath the free surface have been limited to flat or linearized free surface. Using a rigid-lid or a free-slip approximation to model the free surface—corresponding to the zero-Froude-number limit—not only notably simplifies the numerical treatment of the problem, but it also considerably affects the flow dynamics. The present work appears as one of the very first attempts in studying the influence of the kinematic and dynamic boundary conditions at a free surface on the dynamics of shear-driven flows in a transitional regime.

The three-dimensional character of fully-confined shear-driven cavity flows for both rectangular and cylindrical geometries, has only been recently firmly established and in some cases demonstrated in the transitional regime. The additional freedom given to the fluid motion in presence of a moving-boundary clearly increases further this three-dimensional character. Consequently, there is a crucial need to gain insight into the influence of the presence of a free surface on the flow dynamics and on the instabilities developing in the transitional regime, see Fig. 1.2 showing extreme cases.

1.1.3 Large-eddy simulation of turbulent flows

Past investigations of turbulent flows have emphasized the importance of large coherent vortical structures in the fluid dynamics. Given these physical evidences and the high-Reynolds-number regime considered here, the intricate flow dynamics in the turbulent regime can solely be deciphered by resorting to advanced numerical

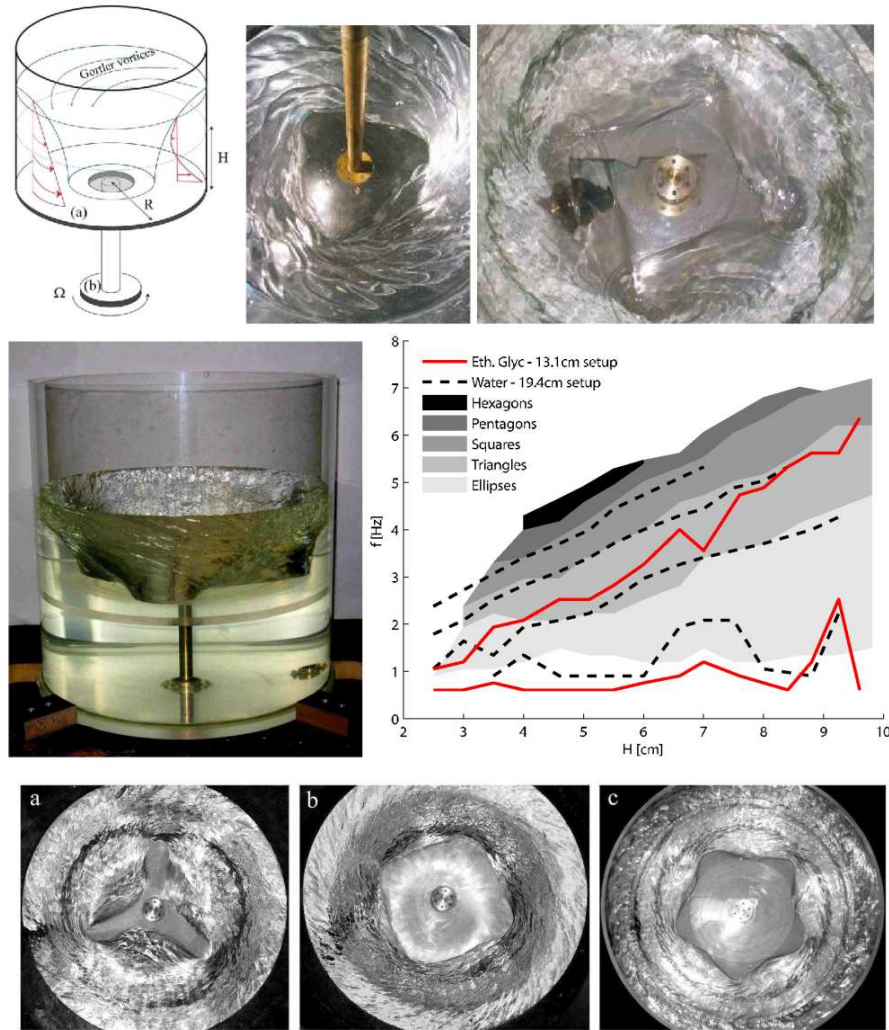


Fig. 1.2: Top row (left): Sketch of the flow in the axially symmetric basis state on top of which the rotating polygons form. The plate (a) is rotating with angular velocity, driven by a motor (b), the fluid above the plate is pressed radially outward, and a secondary flow develops as sketched. Top row (center): Triangle formed spontaneously on the surface of ethylene glycol in a cylindrical container over a rotating plate (small setup). Note the “Görtler vortices” spiraling on the surface. Top row (right): A rotating square on water. Note the vertical vortices just outside of the corners. Central row (left): Setup consisting of a stationary Plexiglas cylinder of radius 19.4 cm with a circular plate that is rotated by a motor. Water or ethylene glycol is filled to the level H above the plate. At sufficiently large rotation frequencies f , the axially symmetric surface becomes unstable and assumes the shape of a regular, rigidly rotating polygon, in this case a triangle. Central row (right): Phase diagram for “polygons” on the surface of a fluid on a rotating plate. Bottom row: Typical examples of polygons in water, as seen from above: (a) “triangle”, (b) “square”, and (c) “pentagon”. From Jansson *et al.* [133]. © 2006 The American Physical Society.

modeling tools. Throughout this research work, numerical simulations use spectral element methods for the spatial discretization. Those methods have mainly been applied to the direct numerical simulation (DNS) of fluid flow problems at low and moderate Reynolds numbers Re . With the advent of more powerful computers, especially through cluster technology, higher Reynolds number values seem to fall within the realm of feasibility. However, despite their high accuracy, spectral element methods are still far from reaching industrial applications or fundamental research problems that involve developed turbulence at Re values of the order of $10^6 - 10^7$. The reason for that dismal performance is that a resolved DNS including all scales from the largest structures to Kolmogorov scales, needs a number of degrees of freedom that grows like $Re^{9/4}$. Therefore with increasing Re , one has to increase the resolution and/or the order of the method. This places the computational load far out of the reach of present day computers. Large-eddy simulation (LES) represents an alternative to DNS insofar that it involves less degrees of freedom because the behavior of small scales are modeled.

Subgrid modeling is the cornerstone of LES and requires a very thorough validation process. Indeed for

a given numerical method, the success of a LES is essentially dependent on the quality of the underlying subgrid model and on its universality. Over the past 30 years, a considerable research effort has been devoted to developing and improving subgrid models for LES. Despite these intensive past works, there is still vast room for improvement in terms of elaborating more effective subgrid models. Furthermore, issues related to LES are too often associated with the specificities of a given numerical method. More specifically, the central concept of scale separation on which LES is built on, relies on filtering procedures which can be either explicit or implicit. In any case, the application of such filter is not performed at the continuous level but at the discretized one. An additional level of complexity appears when subgrid models are required to model the effects on the dynamics of the large eddies, of those implicit filters associated with the space (and even time) discretization.

As mentioned earlier, one decisive property that needs to be possessed by any subgrid model in order for a LES to fulfill its promises, is its universal character. Consequently, the validation of any subgrid models should therefore encompass complex turbulent flows, which challenge the model. Standard subgrid modeling validations rely on classical channel or boundary layer flows which are well-known as “forgiving” from the energetic standpoint, and which possess at least one direction of homogeneity. The lid-driven cavity flow is of particular interest in view of the richness of the fluid physics, thereby allowing to assess the effectiveness of different subgrid models. This flow possesses no direction of homogeneity, and laminar pockets coexist with transitional and turbulent zones. The confined nature of the flow avoids the evacuation of energy through an outflow section. In this context, the lid-driven cubical cavity flow in the locally-turbulent regime, represents a challenging problem in the subgrid modeling framework. As the flow is confined and recirculating, any under- or over-dissipative character of the subgrid model can be clearly identified. Moreover, the very low dissipation and dispersion induced by the spectral element method allows a pertinent analysis of the energetic action induced by any subgrid model, which is not feasible in the framework of low-order numerical methods. The coupling of the lid-driven cubical cavity flow problem with the spectral element method builds therefore a well suited framework to analyze the accuracy of any newly defined subgrid model.

Given the relative success of available subgrid models, it seems legitimate to consider more challenging subgrid models allowing to further increase the Reynolds number without increasing the simulation load. Approximate deconvolution models (ADM) have generated a very important research activity over the past six years. It has been proved to be successful in a number of flow conditions but this deconvolution procedure requires to be supplemented with another model to increase its dissipative character. Moreover, the formulation of large-eddy simulation in the ADM framework is relatively new and can therefore be challenged. To date no LES using both ADM and the spectral element method is reported in the literature, which makes the present study as one additional pioneering development of ADM.

1.1.4 High-order and spectral element method developments

From a numerical viewpoint, the accumulation of difficulties with the governing equations and boundary conditions when dealing with moving-boundary problems, calls for elaborate algorithms and numerical methods. Traditional discretization methods suffer from numerical defects like dissipation and dispersion errors affecting the prediction capabilities of the simulation. High-order methods have gained increasing attention in recent years with theoretical developments reaching a high level of sophistication. When used for solving complex real-life problems, they prove to deliver accurate solutions allowing to decipher the physical mechanisms involved. However their dissemination has been limited due to stringent implementation constraints.

There is clearly a need for high-order methods to bridge the gap between their well-defined mathematical framework and real-life problems they aim at simulating. This can be achieved by initiating further investigation in new areas: for instance complex and time-dependent geometries, treatment of singularities and nonlinearities and domain decomposition. In the context of moving-boundary problems, past implementations of high-order methods tackling moving-boundary problems were often limited to very simplified cases: steady problems, viscous-free, flat or almost-flat free surface, surface-tension free, etc. In the present dissertation, the complete mathematical framework for handling general unsteady and viscous free-surface flow problems using the spectral element method is devised.

The presence of a free surface, or more generally a moving boundary, significantly complicates all simulation methods aiming at solving the Navier–Stokes equations. The treatment in the bulk of the fluid generally poses no problem. However, the imposition of the boundary conditions on the time-evolving part of the boundary together with the correct positioning of this moving boundary are some of the most arduous problems faced when solving moving-boundary problems. From this point of view, the various methods for the interface simulation can be divided into two classes, depending on the nature, fixed or moving, of the grid used to discretize in space the problem. In this dissertation, the approach to this problem is to resort to a front-tracking and moving-grid

technique to solve the Navier–Stokes equations expressed in the arbitrary Lagrangian–Eulerian kinematics and discretized by the spectral element method; this choice being justified by the need to ensure the most accurate resolution of the surface viscous sublayer. Using this approach to simulate a transitional flow beneath a wavy free surface allows us to contradict the hypothesis of a two-dimensional vorticity field at the free surface, inferred in the flat-free-surface case.

Based on these mathematical developments, the solution of free-surface shear-driven swirling flows have been obtained. All the past simulations of free-surface swirling flows rely on the central assumptions that the free surface is flat and clean, which means that the Froude number is very small and that surface tension effects are negligible. With these assumptions, the flow is identical to the flow in the lower half part of a cylinder with two solid covers in co-rotation, *i.e.* rotating at the same angular velocity. Compared to the closed cylinder case, only some limited aspects of the open swirling flow have been investigated so far. The study of this intricate problem is relatively new and consequently the body of knowledge appears fairly limited. In addition, most of the past studies involving numerical simulations of this free-surface swirling flow, used axisymmetric streamfunction–vorticity formulations. In the present dissertation, new flow states are investigated based on a fully three-dimensional solution of the Navier–Stokes equations without the need to resort to symmetry properties by doubling the computational domain and enforcing co-rotation of both end-walls. To our knowledge, the present study provides the most general available results for this free-surface problem. Both, steady and unsteady flows are considered for different sets of governing parameters.

Additional developments in the framework of the LES using spectral element methods are necessary. As mentioned in the previous section, the central concept of scale separation used when performing LES requires to implement a filtering technique that preserves C^0 -continuity of the filtered variables across spectral elements and that is applicable at the element level. Concurrently, the effects of the implicit filter induced by the discretization of the Navier–Stokes equations on a spectral element grid needs to be considered.

1.1.5 Parallel and high-performance computations

From a practical and technical viewpoint, all the aforementioned algorithms run on large-parallel machines with the message passing interface paradigm for inter-processor communication. With a view to ensuring an adapted load balancing on the computing nodes, an investigation of the performances of the parallelized solver used is instrumental. Another crucial aspect is our capability to predict the optimal number of processors required by any simulation given the requested resolution ensuring to capture the flow physics. Furthermore, the determination of the scalability law with respect to the discretization based on the spectral element method is becoming necessary when considering the increasing parallelization trend in today’s supercomputers.

1.2 Contributions of the present work

The contributions of the present research work are in direct relation with the motivations and objectives reported in the previous section. Given the multi-disciplinary nature of the various studies described in this dissertation, contributions are grouped by fields of application.

1.2.1 Turbulence modeling and large-eddy simulation

The long-term integration of two large-eddy simulations of the lid-driven cubical cavity flow at a Reynolds number of 12 000 have been carried out for two dynamic subgrid-scale models, namely a dynamic Smagorinsky model and a dynamic mixed model. These simulations were based on an accurate spectral-element spatial discretization. All filtering levels introduced in both subgrid modelings rely on explicit modal filters in the spectral space, retaining C^0 -continuity of the numerical solution of the filtered Navier–Stokes equations. Full LES results for both dynamic models have shown very good agreement with the reference results available in the literature. The subgrid-viscosity field was shown to be strongly correlated to the turbulent energy dissipation rate in the turbulent areas of the flow.

LES of the lid-driven cubical cavity flow with approximate deconvolution models based on the van Cittert method have been performed. A coupling with a dynamic mixed scale model was introduced, which yields a novel subgrid model. The filtering operation is performed in a spectral modal space, generated by a hierarchical basis using the Legendre polynomials, through the application of a specifically designed transfer function. This transfer function is constructed in order to ensure invertibility of the filter. Accounting for the reduced sampling

and integration time, the LES performed with ADM-DMS show good agreement with the reference results. The importance of the subgrid kinetic energy as compared to the kinetic energy of the resolved field highlights the essential need for an appropriate subgrid modeling. Furthermore, regions of backscatter are identified by the subgrid model.

A new interpretation of approximate deconvolution models when used with implicit filtering as a way to approximate the projective grid filter is given. Consequently, a new category of subgrid models, the grid filter models (GFM) is defined. GFM can be either used with the standard filtered Navier–Stokes equations or with the formulation commonly used with ADM. The GFM approach gives a theoretical justification to the use of ADM without explicit filtering of the solution and explains how the use of ADM works in this context. This viewpoint allows to consider a new way of designing the convolution filter which has to approximate the grid filter and therefore a new way of improving such subgrid models. It has also been proved that the deconvoluted formulation, usually used with ADM, leads to an under-dissipative character of the subgrid model and explains the need of additional dissipative terms. Conversely, when using the filtered formulation, no additional term is needed which is of great relevance considering the confined nature of the flow and the high-order numerical method used. The GFM approach also allows to consider a more realistic methodology for *a priori* validations and its validity extends beyond the limited scope of incompressible Newtonian fluid flows considered in this dissertation.

1.2.2 Physics of shear-driven flows in cavities

At a Reynolds number of 12000, the lid-driven cubical cavity flow is placed in a locally-turbulent regime and such turbulent flow is proved to be highly inhomogeneous. The maximum production of turbulence is found to be located in the downstream-corner-eddy region just above the bottom wall. Small-scales turbulent structures were located indirectly by studying the regions of intense turbulent energy dissipation rate. Helical properties of the flow are investigated. The relative helicity spectra is shown to be decreasing at small scales, which is in agreement with the theoretical results from Borue & Orszag [31] for the three-dimensional isotropic homogeneous turbulence.

The incompressible flow of a viscous fluid enclosed in a cylindrical container with an open top surface and driven by the constant rotation of the bottom wall is considered. First, the case of a stress-free top surface is, in first approximation, maintained fixed and flat is studied. Subsequently, the most general case with an unsteady flow with a moving free-surface in the transitional regime is simulated for the first time. New flow states are investigated based on the fully three-dimensional solution of the Navier–Stokes equations for the free-surface cylindrical swirling flow, without resorting to any symmetry property unlike all other results available in the literature. To our knowledge, this study delivers the most general available results for both this flat and moving free-surface problem due to its original mathematical treatment.

1.2.3 Applied numerical mathematics

A novel numerical model based on high-order methods for solving three-dimensional moving-boundary problems is devised. This model relies on a moving-grid technique to solve the Navier–Stokes equations expressed in the arbitrary Lagrangian–Eulerian (ALE) kinematics and discretized by the spectral element method. A detailed analysis of the continuous and discretized formulations of the general problem in the ALE frame, with non-homogeneous and unsteady boundary conditions is presented for the first time. The moving-grid algorithm which is one of the key ingredient of our numerical model, is based on the computation of an ALE mesh velocity with the same accuracy and numerical technique as the fluid velocity. The coupling between the Navier–Stokes computation and the one for the mesh velocity is effective through the problem boundary conditions and the modified nonlinear convective term.

A novel isochoric moving-grid technique and mesh-transfer technique for spectral element grids have been developed. Both of these techniques are the cornerstones of our computations of transitional and turbulent free-surface flows using spectral element methods. Part of the work is to ensure that these two techniques have no effect on the exponential rate of convergence.

A thorough computational performance analysis of the parallelized high-order spectral and mortar element toolbox is presented. This toolbox is used for all simulations reported in this dissertation.

1.3 Organization of the dissertation

1.3.1 Description

The present dissertation is organized into six different parts—including the present introduction which is the first part.

- Part II contains all the details and developments associated with the numerical method. Chapter 2 reports a brief overview of the numerical context and justifies the crucial need to resort to a high-order numerical method for the present work. Necessary details associated with the spectral element method for standard fixed-grid simulations are recalled. Chapter 3 is devoted to the development of a novel numerical method to treat unsteady moving-boundary flow problems using the Legendre spectral element method.
- Part III comprises the three following chapters, which all deal with different aspects of large-eddy simulation of the turbulent flow in a lid-driven cubical cavity. Chapter 4 focuses on the flow physics while using relatively standard subgrid models. Chapter 5 presents a novel subgrid model based on the coupling of approximated deconvolution procedures and a dynamics mixed scale model. Validation of this novel model is based upon the same flow as the one considered in Chapter 4. Finally, Chapter 6 deals with the concept of subgrid modeling accounting for the effects of the implicit grid filter induced by the space discretization in large-eddy simulation.
- Part IV presents the study of the free-surface swirling flow in a cylindrical container with a rotating bottom end-wall. It is comprised of Chapter 7 and Chapter 8, which deal respectively with the flat-free-surface case and the case of a freely-evolving free surface. This part is focused on the flow physics and on the dynamics of the vortex breakdown bubbles.
- Part V reviews the conclusions of the different aspects of the work reported in the dissertation. Outlook and perspectives are finally proposed.
- Part VI groups three significant appendices, which are extensions of some chapters. Appendix A reports a mesh-update and re-meshing techniques for the moving-boundary solver introduced in Chapter 3 and practically used in Chapter 8. Appendix B is a brief study of the closed swirling flow in a cylindrical container with a rotating bottom end-wall. This study is not only useful in terms of validation but also to assess the influence of the presence of the free-surface on the swirling flow studied in Part IV. Appendix C details the practical computational performance analysis of the parallel spectral element solver used.

1.3.2 Preliminary notes

The content of the present dissertation is the result of a research effort lead by the author and in collaboration with several co-authors. Some of the chapters and appendices are revised transcriptions from published or submitted journal articles. The original text from the journal articles have been revised and amended in order to ensure a high level of coherence in the present dissertation. Nevertheless, unavoidable minor redundancies between the sections of some chapters still exist. The author would like to draw the attention of the readers on the fact that some sections may appear identical from one chapter to another, but often changes in parameters and/or definitions were made in the course of the study, thereby affecting the simulations and the methods used.

For further reference, Chapter 3 was originally published by Bodard, Bouffanais & Deville in *App. Num. Math.* [28] and by Bouffanais & Deville in *Proc. Int. Conf. on Mathematical and Numerical aspects of Waves* [33]. The contribution by N. Bodard corresponded to the applications related to fluid-structure interaction problems of Sec. 3.5.1 and Sec. 3.5.2, see [27] for full details. Chapter 4 was published by Bouffanais, Leriche & Deville in *Phys. Fluids* [37] and also by Bouffanais, Deville, Fischer, Leriche & Weill in *J. Sci. Comput.* [35]. Chapter 5 was published by Habisreutinger, Bouffanais, Leriche & Deville in *J. Comput. Phys.* [112]. Chapter 6 is in the process of being submitted for publication by Habisreutinger, Bouffanais & Deville. Chapters 7 and 8 are merged into a single article, which is currently under preparation. Appendix A has been published by Bouffanais & Deville in *J. Sci. Comput.* [34]. Appendix C has been submitted for publication by Bouffanais, Keller, Gruber & Deville to *Parallel Computing* [36].

Part II

Numerical modeling

Chapter 2

Numerical methods for simulating shear-driven flows

This chapter aims at giving a brief overview of the main numerical methods available to discretize in time and space the continuous governing equations for an isothermal flow of incompressible Newtonian fluids. Additionally, a comprehensive review of the Legendre spectral element method and of its key implementation aspects is presented, as it constitutes the backbone of all the simulations presented in this dissertation. The focus in this chapter is on fixed-grid numerical methods allowing to consider fully confined flows as well as open shear-driven flows—with a stress-free condition on fixed part of the domain boundary, for instance flat free surface. A more complex situation corresponding to the numerical modeling of moving-boundary problems is considered in detail in Chapter 3 in the spectral element framework.

2.1 Introduction

We know from experience that many flows are set into motion by shear forces, and therefore viscous effects play a crucial role in the dynamics of fluids driven by the shear. In general the viscosity depends on the shear rate. In this dissertation, however, we will restrict ourselves to the case of viscous Newtonian incompressible fluids in isothermal situations.

Based on the problem at hand, it is always physically rewarding to non-dimensionalize the governing Navier–Stokes equations which take the following general form

$$\frac{\partial \mathbf{u}}{\partial t} + \mathbf{u} \cdot \nabla \mathbf{u} = -\nabla p + \frac{1}{\text{Re}} \Delta \mathbf{u} + \mathbf{f}, \quad \forall (\mathbf{x}, t) \in \Omega \times I, \quad (2.1)$$

$$\nabla \cdot \mathbf{u} = 0, \quad \forall (\mathbf{x}, t) \in \Omega \times I, \quad (2.2)$$

where \mathbf{u} is the velocity field, p the reduced pressure (normalized by the constant fluid density), \mathbf{f} the body force per unit mass and Re the Reynolds number expressed as

$$\text{Re} = \frac{UL}{\nu}, \quad (2.3)$$

in terms of the characteristic length L , the characteristic velocity U and the constant kinematic viscosity ν . The system evolution is studied in the time interval $I = [t_0, T]$. The position of a point in the current fluid domain Ω is the Eulerian coordinate \mathbf{x} . From the physical viewpoint, Eqs. (2.1)–(2.2) are derived from the conservation of momentum and the conservation of mass respectively. For incompressible viscous fluids, the conservation of mass also called continuity equation, enforces a divergence-free velocity field as expressed by Eq. (2.2). Considering particular flows, the governing Navier–Stokes equations (2.1)–(2.2) are supplemented with appropriate boundary conditions for the fluid velocity \mathbf{u} and/or for the local stress at the boundary. For time-dependent problems, a given divergence-free velocity field is required as initial condition in the internal fluid domain.

All numerical simulations of shear-driven flows presented in this dissertation rely on the dimensionless formulation of the Navier–Stokes equations in primitive variables (\mathbf{u}, p) given by Eqs. (2.1)–(2.2). Other classical formulations use vorticity-velocity or streamfunction-vorticity formulations. In these formulations, the pressure does not appear as it is eliminated as a dependent variable and therefore automatically solves the velocity-pressure decoupling issue inherently present with the standard formulation using the primitive variables. However, the main problem with the vorticity-velocity or streamfunction-vorticity formulations lies in the boundary conditions, especially in complex geometries. For instance, neither vorticity nor its derivatives at a boundary are known in advance. A more comprehensive discussion related to these formulations and its advantages and drawbacks may be found in [25, 58, 75].

From a mathematical viewpoint, in a flow having a region of recirculation, *i.e.* flow in a sense opposite to the principal direction of flow, information may travel upstream as well as downstream. Such character is always present for both groups of lid-driven flows considered in this dissertation: the turbulent lid-driven cavity flow and the open transitional swirling flow in a cylinder. As a result, one cannot apply conditions only at the upstream end of the flow. The problem then acquires an elliptic character. It should be noted that unsteady incompressible shear-driven flows actually have a combination of both elliptic and parabolic character. The latter comes from the fact that information travels in both directions in space while the latter results from the fact that information can only flow forward in time. Such problems are called incompletely parabolic [51,75,110].

2.2 Space discretization methods

The objective of this section is to provide the reader with a rapid overview of the main groups of discretization methods at hand to simulate the two shear-driven flows of interest in this dissertation: the closed turbulent lid-driven cubical cavity flow and the transitional open swirling flow in a cylindrical cavity. This overview aims at highlighting the advantages and drawbacks associated with each group of methods, in order to justify *a priori* the choice of a spectral element method in relation with the physical problems to be investigated.

2.2.1 Finite difference methods

The finite difference method (FDM) was among the first numerical methods applied to the numerical solution of differential equations. It was first utilized by Euler, probably in 1768. It is also the easiest method to use for simple geometries. The FDM is directly applied to the differential form of the governing equations (2.1)–(2.2). The principle is to employ a Taylor series expansion for the discretization of the derivatives of the flow variables. Local expansions with truncated Taylor series are used to transform the original set of PDEs into a set of algebraic equations. Discretization by FDM leads to systems with banded matrices that are usually solved by iterative techniques.

In principle, the FDM can be applied to any grid type. However, in the vast majority of applications reported in the literature, it has been applied to structured grids. The grid lines serve as local coordinate lines. Important advantages of the FDM are its simplicity and its effectiveness. Another advantage is the possibility to easily obtain high-order approximations, and hence to achieve high-order accuracy of the spatial discretization but unfortunately at the expense of the computational cost. On the other hand, because the method requires a structured grid, the range of application is clearly restricted. Another disadvantage of the FDM is that the conservation is not enforced unless special care is taken.

Finite difference methods have been used extensively to simulate two- and three-dimensional rectangular/square cavity flow. The list of references which follows, is far from being exhaustive. Ghia *et al.* [91] performed a comprehensive study of the two-dimensional lid-driven cavity flow. Gustafson and Halasi investigated the vortex dynamics in the square cavity [108] and then the effect of increasing aspect ratio on the flow [109]. The three-dimensionality of the flow in the square cavity has been thoroughly analyzed by Iwatsu *et al.* [132], who detailed some typical 3D structures in the flow. Verstappen *et al.* [258,259] performed 2D and 3D direct numerical simulations followed by a proper orthogonal decomposition. Finally, Jordan & Ragab [135,136] used the cavity flow to test subgrid models in large-eddy simulation.

Like for the case of the square/rectangular lid-driven cavity flow, the FDM has been one of the most used numerical method to simulate the axisymmetric swirling flow in a cylindrical cavity with one or two rotating end-walls. FDM was systematically coupled with a streamfunction-vorticity formulation of the problem. The reference results for the steady and unsteady flows in an enclosed cavity driven by one single rotating end-wall is due to Lopez and Lopez *et al.* [43,158–160,166]. Sørensen's group studied similar flow configurations both experimentally and numerically but with the aim to decipher the transition mechanisms through bifurcations and the vortex breakdown bubbles generation [19,41,42,234]. They contributed importantly to the theory of the vortex breakdown formation and established several bifurcation diagrams [190,191]. More recently, the case of a steady axisymmetric flow in an open cylindrical cavity with a partially rotating bottom wall has been investigated by Piva & Meiburg [198], but considering a fixed and flat free surface.

2.2.2 Finite volume method

The finite volume method (FVM) directly utilizes the conservation laws—the integral formulation of the mass/momentum equations. As pointed out by Hirsch [120] finite-volume schemes were introduced by Godunov in 1959 [95] and they were first used in meteorological applications by Crowley in 1968 [55] and for reactive flows by McDonald in 1971 [179]. The FVM discretizes the governing equations by first dividing the physical space into a number of arbitrary polyhedral control volumes. The surface integral appearing in the integral formulation of the conservation equations is then approximated by the sum of the fluxes crossing the individual faces of the control volume. The accuracy of the spatial discretization depends on the particular scheme with which the fluxes are evaluated: cell-centered scheme, cell-vertex scheme, etc. The main advantages of the FVM are that the spatial discretization is carried out directly in the physical space and that it can be implemented on unstructured grids. This latter property renders the FVM particularly suitable for the treatment of flows in complex geometries. Because of its attractive properties, the FVM is very popular amongst CFD practitioners and in wide use.

It is undeniable that the FVM has been less employed than for instance the FDM for the simulation of both the cylindrical and square/rectangle lid-driven cavity flow. Indeed, the extremely simple geometries involved does not justify to resort to finite volume methods. Nevertheless, Albensoeder and Kuhlmann used the FVM to perform a 3D linear stability analysis of rectangular cavity flows driven by anti-parallel motion of two facing walls [5]. Albensoeder & Kuhlmann have also studied 3D instabilities of two counter-rotating vortices in a rectangular lid-driven cavity [6] and 3D centrifugal-flow instabilities [9]. Chiang *et al.* worked on the 3D flow in a rectangular cavity with a span-to-width aspect ratio of 3:1 [47–50]. A fully implicit FVM have been developed and applied to the two-dimensional lid-driven cubical cavity flow by Sahin & Owens [215,216]. To validate their dynamic mixed model, Zang *et al.* [271,272] performed a large-eddy simulation of the lid-driven cavity flow and compared their results to the experimental results of Prasad & Koseff [201].

The three-dimensional structure of vortex breakdown bubbles in swirling flows was investigated by Sotiropoulos & Ventikos [236] using FVM. Finally, in the axisymmetric case with a rotating top and bottom end-wall, a predictor-corrector method based on a cell-centered finite-volume/multi-block strategy was used by Shen *et al.* [228] in Sørensen's group.

2.2.3 Finite element methods

The finite element method (FEM) is more general the FVM. It was originally employed for structural analysis only. It was first introduced by Turner *et al.* in 1956 [251]. About ten years later, researchers started to use the FEM also for the numerical simulation of field equations in continuous media. However, only in the early eighties, did the FEM gain popularity in the solution of the Navier–Stokes equations.

The FEM is similar to the FVM in many ways. The domain is broken into a set of discrete volumes or finite elements that are generally unstructured; in 3D tetrahedra or hexahedra are most often used. The distinguishing feature of FEM is that equations are multiplied by a test function before they are integrated over the entire domain. The approximation is then substituted into a weighted integral of the conservation laws and the equations to be solved are derived by requiring the derivative of the integral with respect to each nodal value to be zero; this corresponds to selecting the best solution within the set of allowed functions (the one with minimum residual). The result is a set of nonlinear algebraic equations. An important advantage of the FEM is the ability to deal with arbitrary geometries. The grids are easily refined; each element is simply subdivided. The principal drawback of the FEM, which is shared by any method relying on unstructured grids, is that the matrices of the linearized equations are not as well structured as those for methods based on regular grids, making it more difficult to find efficient solution methods.

Surprisingly, very few three-dimensional studies of lid-driven cavity flows using the finite element method are reported in the literature. From the late nineties, Ding *et al.* [60,61] performed a 3D linear stability analysis for the cubical cavity and in two dimensions, Barragy & Carey [15] used a p -type graded finite element method.

2.2.4 Spectral and spectral element methods

Spectral methods which are based on high-order approximations (usually Chebyshev) polynomials is usually restricted to the study of problems with simple geometries. Their use for complex geometries is not an easy task unless decomposition techniques are introduced, often leading to an arduous implementation of the complete numerical method.

In relation with the simple geometry of the closed square/rectangle and cylindrical cavities, spectral methods have been recently used to achieve highly accurate direct numerical simulations. The Chebyshev collocation method was implemented by Leriche [153, 154] and, Leriche & Gavrilakis [155] for the highest Reynolds number cases ever achieved, up to $Re = 22\,000$. Albensoeder and Kuhlmann abandoned the FVM in favor of a Chebyshev collocation method which differs from the implementation due to Leriche only by the velocity-pressure decoupling technique. In addition, Albensoeder and Kuhlmann limit their study of the lid-driven cubical cavity to Reynolds number below 10 000 [7, 8, 32]. Various subgrid models have been implemented and validated against the DNS results of Leriche & Gavrilakis [155], using a Legendre spectral element method by Bouffanais *et al.* [35, 37] and Habisreutinger *et al.* [112].

For the axisymmetric swirling flow, Lopez abandoned its streamfunction-vorticity formulation discretized using FDM, in favor of efficient spectral-projection methods developed with Shen [161] and later with Marques & Shen [161, 165] for the Navier–Stokes equations expressed in primitive variables. These space discretizations allowed Marques and Lopez to investigate the precessing vortex breakdown mode [176] and also specific double Hopf bifurcations in the transition process [177]. Blackburn & Lopez also developed a mixed Fourier-axisymmetric spectral element method [21–23], which was later used in the open-cylinder case [164] to highlight the symmetry breaking due to the presence of the (flat) free surface which was first reported experimentally by Hirs *et al.* [119].

2.2.5 Meshless methods

The use of the FEM in computational fluid dynamics (CFD) is rapidly becoming commonplace. As mentioned in Sec. 2.2.3, the ability of the FEM to handle truly arbitrary geometries makes it often the most suitable choice for complex engineering applications. However, the FEM suffers from drawbacks such as locking, tedious meshing or re-meshing, large deformations of the mesh, etc. Due to these reasons, in recent years, meshless approaches in solving the boundary value problems have received a considerable attention as new ways to alleviate some of these drawbacks. Indeed, meshless methods (MLM) allows to negate the need for the human-labor intensive process of constructing geometric meshes, as well as re-meshing in an evolving solution, in a domain. Such meshless methods are especially useful in problems having discontinuities or moving boundaries, like those considered in Chapter 3 and in Part IV of the present dissertation.

The initial idea of meshless methods dates back to the smooth particle hydrodynamics (SPH) method developed by Gingold & Monaghan in 1977 [94], for modeling astrophysical phenomena. The research into MLM has become very active after the publication of the Diffuse Element Method (DEM) by Nayroles *et al.* in 1992 [187]. Several so-called meshless methods have also been reported in the literature since then: element free Galerkin, reproducing kernel particle method, the partition of unity FEM, *hp*-cloud method, natural element method, meshless Galerkin methods using radial basis functions, etc. A detailed literature review with full details regarding the corresponding references can be found in the monograph by Atluri [12]. The major differences in all these methods come only from the techniques used for interpolating the trial function. However, even though no mesh is required in these methods for the interpolation of the trial and test functions for the solution variables, the use of “shadow elements” (also called “background meshes”) is inevitable for the integration of the weak forms. Therefore, these methods are not truly meshless.

Recently, two truly meshless methods, the meshless local boundary integral equation (LBIE), and the meshless local Petrov-Galerkin (MLPG) method have been developed, see [12] for full details. Both these methods are truly meshless, as no domain/or boundary meshes are required. These methods appear very promising but are still to date far from being capable of treating the complex physics of the recirculating shear-driven flows described in the present dissertation.

2.3 Legendre spectral element method

In this section, the spectral element method (SEM) based on the Galerkin formulation of the Navier–Stokes equations (2.1)–(2.2) is presented. It was first proposed by Patera in 1984 [194]. The SEM is a high-order method which has a very low numerical dissipation and dispersion. As high-order finite element techniques, they can deal with arbitrary geometric complexity, and are capable of local mesh adaption [115] by either increasing the number of elements (*h*-refinement) or increasing the polynomial order within elements (*p*-refinement). For smooth solution spaces, the methods provide asymptotically exponential rates of spatial convergence with *p*-refinement, although in the present work it is the low numerical diffusion and dispersion exhibited by the discretization that is potentially more significant.

After having reviewed the main groups of space discretization methods in Sec. 2.2, we are now in a position to rationalize the choice of the Legendre spectral element method to elucidate the physics associated with the flows studied in the following chapters. As mentioned earlier, our first requirement is to ensure low numerical dissipation and dispersion which excludes low-order methods such as the FVM and low-order FEM and MLM. The complexity introduced by the presence of a free surface and the treatment of the stress-free boundary condition on it, is the second most important choice criterion. In the high-order subgroup of methods, spectral methods are automatically ruled out because of their severe limitations in terms of capabilities to handle complex geometries. Hence, one is left with spectral element methods or high-order FEM which are both capable of treating the stress-free boundary condition on the free surface as a natural boundary condition embodied into the weak formulation of the problem, see Sec. 2.3.1 and Sec. 3.2.3. It is worth adding that high-order MLM could become in the coming years the method of choice for this type of problems. However, to date high-order MLM are far from being capable of solving such complex 3D moving-boundary problems.

2.3.1 Weak formulation of the problem

The continuous Navier–Stokes problem (2.1)–(2.2) in its strong formulation and supplemented with appropriate Dirichlet and Neumann-like boundary conditions, is first expressed in a general weak form, which is also used in the finite element context. We denote by Ω the fluid domain subset of \mathbb{R}^d with d the space dimension. In a standard approach, first are introduced the spaces of test and trial functions used to express the initial problem in its weak form. We may note that the spaces of test and trial functions for the pressure are identical as no essential Dirichlet condition is being imposed on this field. This space is the space of functions that are square Lebesgue-integrable on the domain Ω and is denoted by $L^2(\Omega)$. In general the velocity does not necessarily vanish on the domain boundary; this general case is considered in detail in the next chapter. For the sake of simplicity, we will consider in this chapter only, problems having homogeneous Dirichlet boundary conditions on the whole boundary $\partial\Omega$ of the fluid domain Ω . From a physical viewpoint, such homogeneous essential Dirichlet boundary conditions represent the enforcement of the no-slip condition on the solid walls confining the fluid.

The solution for the velocity \mathbf{u} , of the problem (2.1)–(2.2) is sought directly in the Sobolev space of test/trial functions $H_0^1(\Omega)^d$, defined as the space of differentiable vector functions having their first-order partial derivatives in $L^2(\Omega)$ and vanishing on the domain boundary $\partial\Omega$. With the notations and spaces introduced and writing the viscous term $\Delta\mathbf{u}/\text{Re}$ in Eq. (2.1) as $2\nu\nabla\cdot\mathbf{D}(\mathbf{u})$, the weak transient formulation reads:

Find $(\mathbf{u}(t), p(t)) \in H_0^1(\Omega)^d \times L^2(\Omega)$ such that for almost every $t \geq t_0$

$$\begin{aligned} \frac{d}{dt} \int_{\Omega} \mathbf{u} \cdot \mathbf{v} \, d\Omega + \int_{\Omega} \mathbf{v} \cdot \nabla \cdot (\mathbf{u}\mathbf{u}) \, d\Omega = \int_{\Omega} (p\nabla \cdot \mathbf{v} - 2\nu\mathbf{D}(\mathbf{u}) : \nabla\mathbf{v}) \, d\Omega \\ + \int_{\Omega} \mathbf{f} \cdot \mathbf{v} \, d\Omega, \quad \forall \mathbf{v} \in H_0^1(\Omega)^d, \end{aligned} \quad (2.4)$$

and

$$- \int_{\Omega} q\nabla \cdot \mathbf{u} \, d\Omega = 0, \quad \forall q \in L^2(\Omega), \quad (2.5)$$

where $\mathbf{D}(\mathbf{u}) = \frac{1}{2}(\nabla\mathbf{u} + \nabla\mathbf{u}^T)$ is the rate-of-deformation tensor. The expression “for almost every $t \geq t_0$ ” rules out the occurrence of wild temporal behavior, for example, a step function in the velocity field, which is always detrimental in that it produces a numerical transient state with no physical meaning, see [204] for full details. It is worth noting that all constraints on the field \mathbf{u} , whether homogeneous or inhomogeneous, are by construction included into the definition of the set of admissible functions, whence the qualifier “essential” used earlier.

In order to ease the discretization of the continuous weak equations (2.4)–(2.5), we introduce the following notations and bilinear forms, such as a scalar product defined by

$$(\mathbf{u}, \mathbf{v}) := \int_{\Omega} \mathbf{u} \cdot \mathbf{v} \, d\Omega, \quad \forall \mathbf{v} \in H_0^1(\Omega)^d, \quad (2.6)$$

a so-called ‘energy bilinear form’

$$\mathcal{A}(\mathbf{u}, \mathbf{v}) := 2\nu \int_{\Omega} \mathbf{D}(\mathbf{u}) : \nabla\mathbf{v} \, d\Omega, \quad \forall \mathbf{v} \in H_0^1(\Omega)^d, \quad (2.7)$$

a bilinear form related to the weak incompressibility constraint

$$\mathcal{B}(\mathbf{v}, p) := - \int_{\Omega} p \nabla \cdot \mathbf{v} \, d\Omega, \quad \forall \mathbf{v} \in H_0^1(\Omega)^d, \quad (2.8)$$

a nonlinear form corresponding to the nonlinear convective term

$$\mathcal{C}(\mathbf{u}, \mathbf{v}) := \int_{\Omega_t} \mathbf{v} \cdot \nabla(\mathbf{u}\mathbf{u}) \, d\Omega, \quad \forall \mathbf{v} \in H_0^1(\Omega)^d, \quad (2.9)$$

and finally a linear form related to the source term \mathbf{f}

$$\mathcal{F}(\mathbf{v}) := \int_{\Omega} \mathbf{f} \cdot \mathbf{v} \, d\Omega, \quad \forall \mathbf{v} \in H_0^1(\Omega)^d. \quad (2.10)$$

With these notations, the continuous weak form of our Navier–Stokes problem can be recast as *Find* $(\mathbf{u}(t), p(t)) \in H_0^1(\Omega)^d \times L^2(\Omega)$ such that for almost every $t \geq t_0$

$$\frac{d}{dt}(\mathbf{u}, \mathbf{v}) + \mathcal{A}(\mathbf{u}, \mathbf{v}) + \mathcal{B}(\mathbf{v}, p) + \mathcal{C}(\mathbf{u}, \mathbf{v}) = \mathcal{F}(\mathbf{v}), \quad \forall \mathbf{v} \in H_0^1(\Omega)^d, \quad (2.11)$$

$$\mathcal{B}(\mathbf{u}, q) = 0, \quad \forall q \in L^2(\Omega). \quad (2.12)$$

2.3.2 Galerkin approximation

Instead of solving the previous continuous problem, an approximate projected solution is sought in finite-dimensional subspaces. The first step in the SEM discretization consists in subdividing the fluid domain $\bar{\Omega} = \Omega \cup \partial\Omega$ into E non-overlapping elements $\{\Omega^e\}_{e=1}^E$. Each element Ω^e involves a mesh constructed as a tensor product of one-dimensional grids. Although each space direction may be discretized independently of the others, without loss of generality we will consider only meshes obtained with the same number of nodes in each direction, denoted by $N + 1$, corresponding to the dimension of the space of N th-order polynomials. To describe the discretization process accurately, we adopt the same procedure as Deville *et al.* [58] and define the following spaces

$$X := H_0^1(\Omega)^d, \quad Z := L^2(\Omega). \quad (2.13)$$

We apply the Galerkin approximation to our Navier–Stokes problem in the weak form (2.11)–(2.12), and therefore select finite dimensional polynomial subspaces X_N and Z_N to represent X and Z respectively. In practice, some restrictions occur as far as the selection of polynomial degrees is concerned. In particular, the inf-sup condition imposes restrictions on the pressure subspace Z_N once the velocity subspace X_N is prescribed, to prevent locking and spurious oscillations phenomena. A staggered-grid approach with element based on $\mathbb{P}_N - \mathbb{P}_{N-2}$ spaces for the velocity and pressure field respectively was first proposed by Maday *et al.* [174] to eliminate completely the spurious pressure modes. In this context, the finite dimensional functional spaces are defined as

$$X_N := X \cap \mathbb{P}_{N,E}^d, \quad Z_N := Z \cap \mathbb{P}_{N-2,E}, \quad (2.14)$$

with

$$\mathbb{P}_{M,E} = \{\phi | \phi \in L^2(\Omega); \phi|_{\Omega^e} \text{ is a polynomial of degree } \leq M, \forall e = 1, \dots, E\}, \quad (2.15)$$

where the superscript d in (2.14) reflects the fact that test/trial velocity functions are d -dimensional. With these notations the Galerkin approximation of (2.11)–(2.12) reads

Find $(\mathbf{u}_N(t), p_N(t)) \in X_N \times Z_N$ such that for almost every $t \geq t_0$

$$\frac{d}{dt}(\mathbf{u}_N, \mathbf{v}_N) + \mathcal{A}(\mathbf{u}_N, \mathbf{v}_N) + \mathcal{B}(\mathbf{v}_N, p_N) + \mathcal{C}(\mathbf{u}_N, \mathbf{v}_N) = \mathcal{F}_N(\mathbf{v}_N), \quad \forall \mathbf{v}_N \in X_N, \quad (2.16)$$

$$\mathcal{B}(\mathbf{u}_N, q_N) = 0, \quad \forall q_N \in Z_N, \quad (2.17)$$

with

$$(\mathbf{u}_N, \mathbf{v}_N) = \sum_{e=1}^E \int_{\Omega^e} \mathbf{u}_N \cdot \mathbf{v}_N \, d\Omega, \quad \forall \mathbf{v}_N \in X_N, \quad (2.18)$$

$$\mathcal{F}_N(\mathbf{v}_N) = \sum_{e=1}^E \int_{\Omega^e} \mathbf{f}_N \cdot \mathbf{v}_N \, d\Omega, \quad \forall \mathbf{v}_N \in X_N, \quad (2.19)$$

$$(2.20)$$

\mathbf{f}_N being the projection of the fields \mathbf{f} onto the finite dimensional space $\mathbb{P}_{N,E}^d$.

The integrals within each of the spectral elements $\{\Omega^e\}_{e=1}^E$ are calculated in a discrete manner using Gaussian quadrature rules. More specifically, all the terms in (2.16)–(2.17) are integrated using a Gauss-Lobatto-Legendre (GLL) quadrature rule [44, 116] except for the two terms involving the bilinear form \mathcal{B} where functions discretized in $\mathbb{P}_{N-2,E}$ appear. For these two terms, namely the pressure term and the divergence-free condition, a Gauss-Legendre (GL) quadrature rule is chosen [44, 116]. Therefore, the $\mathbb{P}_N - \mathbb{P}_{N-2}$ Navier–Stokes problem is finally stated as

Find $(\mathbf{u}_N(t), p_N(t)) \in X_N \times Z_N$ such that for almost every $t \geq t_0$

$$\frac{d}{dt} (\mathbf{u}_N, \mathbf{v}_N)_{N,GLL} + \mathcal{A}_{N,GLL}(\mathbf{u}_N, \mathbf{v}_N) + \mathcal{B}_{N,GL}(\mathbf{v}_N, p_N) + \mathcal{C}_{N,GLL}(\mathbf{u}_N, \mathbf{v}_N) = \mathcal{F}_{N,GLL}(\mathbf{v}_N), \quad \forall \mathbf{v}_N \in X_N, \quad (2.21)$$

$$\mathcal{B}_{N,GL}(\mathbf{u}_N, q_N) = 0, \quad \forall q_N \in Z_N. \quad (2.22)$$

To simplify the notations in the sequel, we will drop the subscript GLL and unless being explicitly specified, whenever an integration rule is required, the GLL one is implicitly being used.

2.3.3 Semi-discrete Navier–Stokes formulation

In order to formulate the semi-discrete version of our problem governed by the Navier–Stokes equations, the variables are approximated with expressions involving Lagrangian interpolating polynomials based on the quadrature collocation points [44, 116, 210]. The SEM uses two tensor-product bases on the reference element $\hat{\Omega} := [-1, 1]^d$ and for the sake of simplicity we will choose the same discretization order N in each space direction:

- the Gauss-Lobatto-Legendre Lagrangian interpolation basis of degree N

$$\{\pi_{i,j,k}(\boldsymbol{\xi})\}_{i,j,k=0}^N := \{\pi_i(\xi_i)\}_{i=0}^N \otimes \{\pi_j(\xi_j)\}_{j=0}^N \otimes \{\pi_k(\xi_k)\}_{k=0}^N, \quad \forall \boldsymbol{\xi} \in \hat{\Omega}, \quad (2.23)$$

to expand the velocity field discretized on the N th-order GLL grid;

- the Gauss-Legendre Lagrangian interpolation basis of degree $N - 2$

$$\{\varpi_{i,j,k}(\boldsymbol{\zeta})\}_{i,j,k=1}^{N-1} := \{\varpi_i(\zeta_i)\}_{i=1}^{N-1} \otimes \{\varpi_j(\zeta_j)\}_{j=1}^{N-1} \otimes \{\varpi_k(\zeta_k)\}_{k=1}^{N-1}, \quad \forall \boldsymbol{\zeta} \in \hat{\Omega}, \quad (2.24)$$

to expand the pressure field discretized on the GL grid of order $N - 2$.

The expressions of the one-dimensional GLL and GL Lagrangian interpolant polynomials $\pi(\boldsymbol{\xi})$ and $\varpi(\boldsymbol{\zeta})$ appearing in (2.23)–(2.24) can be found in [58] and also partially in Sec. A.7 and Sec. A.8. The polynomials $\{\pi_{i,j,k}(\boldsymbol{\xi})\}_{i,j,k=0}^N$ and $\{\varpi_{i,j,k}(\boldsymbol{\zeta})\}_{i,j,k=1}^{N-1}$ serve as bases for the functions in the spaces X_N and Z_N

$$\mathbf{u}_N(\mathbf{x}(\boldsymbol{\xi}), t) = \sum_{i,j,k=0}^N \mathbf{u}_{ijk}(t) \pi_{i,j,k}(\boldsymbol{\xi}), \quad \forall (\boldsymbol{\xi}, t) \in \hat{\Omega} \times I, \quad (2.25)$$

$$p_N(\mathbf{x}(\boldsymbol{\zeta}), t) = \sum_{i,j,k=1}^{N-1} p_{ijk}(t) \varpi_{i,j,k}(\boldsymbol{\zeta}), \quad \forall (\boldsymbol{\zeta}, t) \in \hat{\Omega} \times I, \quad (2.26)$$

where $\mathbf{x} = \mathbf{x}^e$ is the location of the point considered in the spectral element Ω^e , $\{\mathbf{u}_{ijk}(t)\}_{i,j,k=0}^N$ is the set of nodal values of the velocity field on the GLL grid of Ω^e , and $\{p_{ijk}(t)\}_{i,j,k=1}^{N-1}$ is the set of nodal values of the pressure field on the GL grid of Ω^e .

We can now expand the trial velocity \mathbf{u}_N and the trial pressure p_N onto the GLL–GL bases like in (2.25) and (2.26) respectively. The semi-discrete equations derived from (2.16)–(2.17) are

$$\mathbf{M} \frac{d\mathbf{u}}{dt} = -\mathbf{A}\mathbf{u} - \mathbf{C}\mathbf{u} + \mathbf{D}^T \underline{p} + \mathbf{M}\mathbf{f}, \quad (2.27)$$

$$-\mathbf{D}\mathbf{u} = \underline{0}. \quad (2.28)$$

The operators appearing in (2.27)–(2.28) are: \mathbf{M} the diagonal mass matrix, \mathbf{A} the stiffness matrix, \mathbf{C} the discrete convective operator, \mathbf{D}^T the discrete gradient operator and \mathbf{D} the discrete divergence. These matrices are all composed of three blocks associated with the discretization in each space direction. For instance, the diagonal mass matrix \mathbf{M} is composed of d blocks, namely the mass matrices M which are identical when considering the same polynomial degree N in the d space directions.

2.3.4 Mortar element formulation

In order to adapt locally the numerical approximation of the flow variables in the vicinity of singularities or in special regions of the flow where the physics requires special description, it may be necessary to refine the mesh in a non-conforming way and/or modify the polynomial degree of contiguous spectral elements using the mortar element method. This latter method has been extensively described in various papers, *e.g.* [10, 18, 170]. The numerical analysis of mortar methods has been reported in detail for Stokes problems [16] and theoretical error estimates are known from which error indicators can be derive [17].

The reader is referred to the Chapter 7 of the monograph by Deville *et al.* [58] for a detailed description of the method and a presentation of the mortar operators.

2.3.5 Time discretization

Once the set of continuous equations (2.11)–(2.12) is discretized in space, the resulting semi-discrete set of nonlinear ordinary equations (2.27)–(2.28) still requires to be discretized in time. The time dependence in the previous ordinary equations obeys a first-order differential operator, which makes the time integrations schemes different from the one used for the space dependence, namely the SEM. Nevertheless, as high-order spatial discretization techniques are used for different reasons—low numerical dispersion and dissipation, accuracy of the results, low number of grid points, etc.—high temporal accuracy is concurrently required. As noted by Deville *et al.* [58], more and more industrial applications consider 3D transient calculations by direct numerical simulation (Part IV of the present dissertation) and large-eddy simulation (Part III of the present dissertation) methodologies. In order to derive and extract meaningful statistics from these large databases, accurate time integration is clearly needed.

From a mathematical viewpoint, the semi-discrete problem (2.11)–(2.12) can be seen as an unsteady Stokes problem—which embodies the coupling between velocity and pressure through the divergence-free condition—coupled to a nonlinearity corresponding to the advective term. Three-dimensional numerical simulations with a fully-coupled treatment of these subproblems are still out of reach even on the most powerful supercomputers.

Various schemes can be used to discretize in time Eqs. (2.11)–(2.12). All the simulations presented in this dissertation use in particular backward differentiation formula of order k (BDF k) for implicit (linear) terms and the extrapolation scheme of order k (EX k) for explicit (nonlinear) term as introduced by Karniadakis *et al.* [140]. Unless otherwise stated, the advective term is treated in its convective form $\mathbf{u} \cdot \nabla \mathbf{u}$. In matrix notation, the implicit-explicit discretized problem for our choice BDF2/EX2 reads

$$\left(\frac{3\mathbf{M}}{2\Delta t} + \mathbf{A} \right) \underline{\mathbf{u}}^{n+1} - \mathbf{D}^T \underline{\mathbf{p}}^{n+1} = \frac{\mathbf{M}}{\Delta t} \left(2\underline{\mathbf{u}}^n - \frac{1}{2}\underline{\mathbf{u}}^{n-1} \right) + \mathbf{M}\underline{\mathbf{f}}^{n+1} - \mathbf{C}\underline{\mathbf{u}}^{n+1}, \quad (2.29)$$

$$\mathbf{C}\underline{\mathbf{u}}^{n+1} = 2\mathbf{C}\underline{\mathbf{u}}^n - \mathbf{C}\underline{\mathbf{u}}^{n-1}, \quad (2.30)$$

$$-\mathbf{D}\underline{\mathbf{u}}^{n+1} = \underline{\mathbf{0}}, \quad (2.31)$$

where Δt is the time-step. For this scheme, there is no time-splitting error. Furthermore, following the study of Couzy [52] on the order of BDF3/EX3, one can easily show that the BDF2/EX2 scheme provides global second-order accuracy. This decoupling BDF2/EX2 has also been used in the past by Deville & Fiétier [78] for the simulation of visco-elastic flows and by Bodard [27] for fluid-structure interaction problems. The efficiency of this decoupled method depends critically on the availability of an efficient and robust solver for the underlying Stokes problem at each time-step. The approach in this dissertation consists in solving the discretized problem (2.29)–(2.31) with an efficient solver as designed by Couzy [52]. The mass-momentum set of equations is solved via a generalized block LU decomposition with pressure correction [196, 197], which can be summarized by the following steps:

1. Computation of the tentative velocity vector $\underline{\mathbf{u}}^*$ by solving

$$\mathbf{H}\underline{\mathbf{u}}^* = \mathbf{D}^T \underline{\mathbf{p}}^n + \frac{\mathbf{M}}{\Delta t} \left(2\underline{\mathbf{u}}^n - \frac{1}{2}\underline{\mathbf{u}}^{n-1} \right) + \mathbf{M}\underline{\mathbf{f}}^{n+1} - (2\mathbf{C}\underline{\mathbf{u}}^n - \mathbf{C}\underline{\mathbf{u}}^{n-1}), \quad (2.32)$$

using the old time-level pressure $\underline{\mathbf{p}}^n$ and where $\mathbf{H} = 3\mathbf{M}/(2\Delta t) + \mathbf{A}$ is the Helmholtz operator.

2. Computation of the pressure at the new time-level by solving the following problem for the pressure correction $\delta \underline{\mathbf{p}}^{n+1} = \underline{\mathbf{p}}^{n+1} - \underline{\mathbf{p}}^n$

$$-\mathbf{D}\mathbf{Q}\mathbf{D}^T \delta \underline{\mathbf{p}}^{n+1} = \frac{2}{\Delta t} \mathbf{D}\underline{\mathbf{u}}^*. \quad (2.33)$$

3. Computation of the final velocity at the time-level $n + 1$ after a pressure correction

$$\underline{\mathbf{u}}^{n+1} = \underline{\mathbf{u}}^* + \frac{\Delta t}{2} \mathbf{Q} \mathbf{D}^T \delta \underline{\mathbf{p}}^{n+1}. \quad (2.34)$$

The choice of the matrix \mathbf{Q} appearing in Eqs. (2.33)–(2.34) is instrumental. By setting $\mathbf{Q} = \mathbf{H}^{-1}$, one obtains the Uzawa algorithm [58, 171]. For the unsteady Stokes operator, the Uzawa is known to converge slowly at large computational expense. Therefore, much effort has been devoted to decoupling completely the pressure from the velocity-field calculation. This can be achieved by approximating the inverse of the Helmholtz operator by the following choice of the operator \mathbf{Q}

$$\mathbf{Q} = \frac{\Delta t}{2} \mathbf{M}^{-1}. \quad (2.35)$$

This approximation proves to first solve the issue related to the high computational expense associated with the Uzawa algorithm. Indeed, in the SEM framework the mass matrices being diagonal, their inverse can easily be computed. From an accuracy viewpoint, such block LU decomposition with the matrix \mathbf{Q} given by Eq. (2.35) leads to a pressure correction method, which is a second-order scheme, as proven by Van Kan [253].

An alternative to the extrapolation method (EX k) for computing the nonlinear term is the operator integration factor splitting (OIFS) method proposed by Maday *et al.* [173]. The advantage of the BDF k /EX k approach over the OIFS one with a BDF k scheme for linear terms, is that the local errors vanish for a converged, stationary solution. In addition, as mentioned earlier the BDF k /EX k method does not induce any time-splitting error.

2.3.6 System solving techniques

The ill-conditioning arising from high-order discretizations is a major concern in their application. As noted by Deville *et al.* [58], the condition number of the operator $M^{-1}A$ scales as $O(N^4)$ for a one-dimensional problem. As a consequence, calculations based on the SEM become increasingly ill-conditioned with the order of the method and the mesh refinement. This issue justifies the choice of preconditioned iterative solutions to finally solve the fully discretized problem. Indeed, the use of appropriate preconditioners can reduce significantly the condition number and hence converge more rapidly to the solution.

The preconditioned conjugate gradient method is used to solve the first two steps of the pressure-correction method corresponding to Eq. (2.32) and Eq. (2.33). Two different preconditioners are used: a diagonal preconditioner for the solution of Eq. (2.32) and a preconditioner developed by Couzy & Deville [53] for the pressure-correction step (2.33).

The computational performances of the above-detailed numerical method is directly related to the convergence of the preconditioned conjugate gradient and to the parallel implementation of the method. A complete assessment of the performances of the parallel implementation of the SEM used in this dissertation, is given in Appendix C considering different computer architectures and compilers.

2.3.7 Stabilization technique

As mentioned by Fischer & Mullen [80], despite the numerous advantages of the SEM, stability problems have been encountered in the past, which required very fine space and time resolutions for applications at moderate Reynolds number (10^3). Stabilization can easily be obtained with the Legendre-SEM by using a nodal filtering technique introduced by Fischer & Mullen [80]. The filter is applied at the end of each step of the Navier–Stokes time integration of the problem governed by Eqs. (2.27)–(2.28) and aims at removing nascent instabilities induced by the treatment of the nonlinear convective term. This specific technique is mainly used in the applications presented in Chapter 4 and is detailed in Sec. 4.2.4. As noted by Blackburn & Schmidt [24], this filter is applied at the element level and conveniently preserves the C^0 -continuity at the interface between elements.

2.4 Summary

In this chapter, a brief overview of the main computational methods to solve shear-driven incompressible flows is given. A Legendre spectral element method with a specific time discretization scheme has been selected since

time-dependent accurate solutions are expected for both turbulent and transitional shear-driven cavity flows considered in Part III and IV of the present dissertation. In addition, low numerical dissipation and dispersion are required if one expects to observe accurately time-dependent phenomena.

The semi-discretized problem based on the SEM is decoupled into an unsteady Stokes problem treated implicitly and the nonlinear advective term into its convective form, treated explicitly. The time-integration schemes used to treat the previous two subproblems is BDF2/EX2 respectively. No time-splitting error is induced by this choice which leads to a global second-order for the method. The details of the velocity-pressure decoupling using a generalized block LU decomposition with pressure correction has been discussed. Finally, the iterative solution of the discretized problem using the preconditioned conjugate gradient method has been briefly introduced.

Chapter 3

Spectral element method for moving-boundary problems

This chapter describes a novel numerical model aiming at solving moving-boundary problems such as free-surface flows or fluid-structure interaction. This model uses a moving-grid technique to solve the Navier–Stokes equations expressed in the arbitrary Lagrangian-Eulerian kinematics. The discretization in space is based on the spectral element method. The coupling of the fluid equations and the moving-grid equations is essentially done through the conditions on the moving boundaries. Two- and three-dimensional simulations are presented: translation and rotation of a cylinder in a fluid, and large-amplitude sloshing in a rectangular tank. The accuracy and robustness of the present numerical model is studied and discussed.

All the developments of the present chapter constitute the numerical framework for the different direct numerical simulations of free-surface swirling flows presented in Part IV of the present dissertation. These developments have also been used by Bodard in his dissertation [27] on fluid-structure interaction problems.

3.1 Introduction

With the advent of powerful computational resources like clusters of PCs or parallel computers the numericists are able to address more challenging problems involving multi-physics and multi-scale approaches. These problems cover a large spectrum of scientific and engineering applications. However, in this chapter, for the sake of conciseness, we will restrict our attention to two specific problems, namely: free-surface flows and fluid-structure interaction.

Free-surface flows occur in many industrial applications: coating flows, vertical drawing of viscous fluids, jets, die flows, etc, and in environmental flows: ocean waves, off-shore engineering, coastal habitat and management, to name a few. Two review articles have been published in recent years and report the state-of-the-art of the field [219, 248]. It can be observed that free-surface flows have been tackled by direct numerical simulation at low and moderate Reynolds numbers. This reality is essentially due to the nonlinear characters of the flow. On top of the nonlinearity associated to the Navier–Stokes equations themselves, here we deal with a complicated geometry which is changing in time and which is part of the solution itself. This accumulation of difficulties calls for elaborate algorithms and numerical techniques.

Fluid-structure interaction has been recognized for a long time as a real challenge. Indeed, this interaction is present in engineering problems like turbo-machinery, aerospace applications: buffeting, acoustics, and also in biomedical flows like blood flow in the coronary arteries. Fluid-structure interaction is also encountered in the field of vortex-induced vibrations having many important marine applications (*e.g.* related to oil exploration, cable dynamics, etc.). It is only at the present time that this type of interaction for three-dimensional cases appears to be feasible as the necessary computing power becomes available. On one hand, the computational fluid dynamics (CFD) codes integrate the full steady state or transient Navier–Stokes equations which govern the dynamics of a viscous Newtonian fluid. They mostly use finite volume or finite element approximations. On the other hand, the computational solid mechanics (CSM) codes integrate the dynamics of various solid models, incorporating for example, classical infinitesimal linear elasticity, nonlinear finite elasticity with large deformations, plasticity, visco-elasticity, etc. These problems are also highly nonlinear with respect to the complicated geometries at hand. The combination of the nonlinearities of the mathematical models for the constitutive relations and for the geometrical behavior has called for a robust approach able to deal with all the complexities and intricacies. The finite element method (FEM) with the iso-parametric elements has emerged as the leading technology and methodology in CSM—see Sec. 2.2.3 for more details.

In the present chapter, the methodological framework is the same for the fluid and the solid parts and rests upon the spectral element method [58, 172, 194, 210]. With this choice the space discretization is similar for both

problems. As in free-surface flows and fluid-structure interaction the geometry is deforming and moving, it is needed to use the arbitrary Lagrangian–Eulerian (ALE) formulation [64, 65, 82, 121]. This formulation allows to treat the full geometrical problem with respect to a reference configuration that is arbitrarily chosen. A mapping is introduced to ease the description of the current configuration with respect to a reference configuration. This process leads to an ALE velocity which will be related to a grid velocity.

In Section 3.2, the mathematical models will be presented with the associated weak formulations in the ALE context. Section 3.3 will be devoted to space and time discretizations. Section 3.4 will describe the numerical algorithms for the moving-grid technique. Section 3.5 will present numerical results and the final section will draw some conclusions.

3.2 Mathematical model

A moving boundary-fitted grid technique has been chosen to simulate the unsteady part of the boundary in our computations. In the particular cases dealt with in this work, the unsteady part of the boundary can be either the free surface in case of free-surface flows, or for fluid-structure interaction problems, the interface between the fluid and the structure. This choice of a surface-tracking technique is primarily based on accuracy requirements. With this group of techniques, the grid is configured to conform to the shape of the interface, and thus adapts continuously—at each time-step—to it and therefore provides an accurate description of the moving boundary to express the related kinematic and/or dynamic boundary conditions.

The moving-boundary incompressible Newtonian fluid flows considered, are governed by the Navier–Stokes equations comprising the momentum equation and the divergence-free condition. In the ALE formulation, a mixed kinematic description is employed: a Lagrangian description of the moving boundary, an Eulerian description of the fixed domain boundaries and a mixed description of the internal fluid domain.

3.2.1 The ALE kinematic framework

This section will introduce the notations used in this chapter to define the variables and frames of reference related to the ALE formulation. The notations adopted hereafter are borrowed from [82, 189]. We denote by Ω_t the fluid domain subset of \mathbb{R}^d with $d = 2, 3$ the space dimension, the subscript t referring to the time t as the fluid domain is changing when its boundaries are moving. Let us denote by Ω_0 a reference configuration—for instance the domain configuration at initial time $t = t_0$. The system evolution is studied in the time interval $I = [t_0, T]$. The position of a point in the current fluid domain Ω_t is denoted by \mathbf{x} —Eulerian coordinate—and in the reference frame Ω_0 by \mathbf{Y} —ALE coordinate. Let \mathcal{A}_t be a family of mappings, which at each $t \in I$ associates a point $\mathbf{Y} \in \Omega_0$ to a point $\mathbf{x} \in \Omega_t$:

$$\mathcal{A}_t : \Omega_0 \subset \mathbb{R}^d \rightarrow \Omega_t \subset \mathbb{R}^d, \quad \mathbf{x}(\mathbf{Y}, t) = \mathcal{A}_t(\mathbf{Y}). \quad (3.1)$$

\mathcal{A}_t is assumed to be continuous and invertible on $\bar{\Omega}_0$ and differentiable almost everywhere in I . The inverse of the mapping \mathcal{A}_t is also continuous on $\bar{\Omega}_0$.

The Jacobian matrix of the ALE mapping \mathcal{A}_t is given by

$$\mathbf{J}_{\mathcal{A}_t} = \frac{\partial \mathbf{x}}{\partial \mathbf{Y}}, \quad (3.2)$$

and its determinant $J_{\mathcal{A}_t} = \det \mathbf{J}_{\mathcal{A}_t}$ is the Jacobian of the mapping characterizing the metrics of Ω_t generated from the one of Ω_0 . The ALE mesh velocity \mathbf{w} is defined as

$$\mathbf{w}(\mathbf{x}, t) = \frac{\partial \mathcal{A}_t}{\partial t} \Big|_{\mathbf{Y}}. \quad (3.3)$$

The Euler expansion formula gives the relationship between the Jacobian of the mapping \mathcal{A}_t and the divergence of the ALE velocity \mathbf{w} :

$$\frac{\partial J_{\mathcal{A}_t}}{\partial t} \Big|_{\mathbf{Y}} = J_{\mathcal{A}_t} \nabla_{\mathbf{x}} \cdot \mathbf{w}, \quad \forall (\mathbf{Y}, t) \in \Omega_0 \times I, \quad (3.4)$$

supplemented by the initial condition $J_{\mathcal{A}_t} = 1$ for $t = t_0$. In real computations, \mathbf{w} will be associated to the mesh velocity. The hyperbolic partial differential equation (3.4) highlights the important role played by the divergence of the mesh velocity in the time evolution of the mapping \mathcal{A}_t . This particular point is emphasized in Section 3.4,

where one of the mesh-update techniques used in our simulations, enforces a divergence-free condition for \mathbf{w} resulting in a constant in time Jacobian $J_{\mathcal{A}_t}$ [34]. Furthermore Eq. (3.4) constitutes the evolution law for $J_{\mathcal{A}_t}$ as in our formulation the ALE mesh velocity is calculated based on the essential boundary conditions of our problem in Ω_t , thereby defining the location of the grid nodes and the value of \mathcal{A}_t .

Considering a time-dependent scalar field f defined on $\Omega_t \times I$, the notation $\partial f / \partial t|_{\mathbf{Y}}$ refers to the time derivative in the ALE frame, or in short the ALE time derivative expressed in Eulerian coordinates as opposed to the regular time derivative in Eulerian coordinates and denoted by $\partial f / \partial t|_{\mathbf{x}}$. It is worth noting that a standard application of the chain rule to the time derivative gives

$$\left. \frac{\partial f}{\partial t} \right|_{\mathbf{Y}} = \left. \frac{\partial f}{\partial t} \right|_{\mathbf{x}} + \mathbf{w} \cdot \nabla_{\mathbf{x}} f. \quad (3.5)$$

The symbol $\nabla_{\mathbf{x}}$ indicates the gradient operation applied to the scalar field f with respect to the Eulerian coordinate \mathbf{x} . If $\mathbf{w} = \mathbf{0}$, the mesh is fixed, and we recover the Eulerian description where $\partial / \partial t|_{\mathbf{Y}}$ is the classical time derivative $\partial / \partial t|_{\mathbf{x}}$. If $\mathbf{w} = \mathbf{u}$ where \mathbf{u} is the fluid velocity field, we obtain the Lagrangian description and $\partial / \partial t|_{\mathbf{Y}}$ is the particle derivative. Eq. (3.5) allows to generalize the Reynolds transport theorem for a time-dependent volume integral of a scalar field

$$\frac{d}{dt} \left(\int_{\Omega_t} f \, d\Omega \right) = \int_{\Omega_t} \left(\left. \frac{\partial f}{\partial t} \right|_{\mathbf{Y}} + f \nabla_{\mathbf{x}} \cdot \mathbf{w} \right) d\Omega. \quad (3.6)$$

3.2.2 The strong ALE formulation for the Navier–Stokes equations

The governing equations of our moving-boundary problem in the ALE kinematic description, for an incompressible Newtonian fluid flow occupying a fluid domain Ω_t whose boundary $\partial\Omega_t$ is evolving with time, are the Navier–Stokes equations which in strong form and in the Eulerian kinematic description read

$$\left. \frac{\partial \mathbf{u}}{\partial t} \right|_{\mathbf{x}} + \mathbf{u} \cdot \nabla_{\mathbf{x}} \mathbf{u} = -\nabla_{\mathbf{x}} p + 2\nu \nabla_{\mathbf{x}} \cdot \mathbf{D}_{\mathbf{x}}(\mathbf{u}) + \mathbf{f}, \quad \forall (\mathbf{x}, t) \in \Omega_t \times I, \quad (3.7)$$

$$\nabla_{\mathbf{x}} \cdot \mathbf{u} = 0, \quad \forall (\mathbf{x}, t) \in \Omega_t \times I, \quad (3.8)$$

where \mathbf{u} is the velocity field, p the pressure field (normalized by the constant fluid density ρ and relative to zero ambient), ν the kinematic viscosity of the fluid, $\mathbf{D}_{\mathbf{x}}(\mathbf{u}) = \frac{1}{2}(\nabla_{\mathbf{x}} \mathbf{u} + \nabla_{\mathbf{x}} \mathbf{u}^T)$ the rate-of-deformation tensor and \mathbf{f} the body force per unit mass, with the superscript T indicating the transpose. Eq. (3.7) expresses the conservation of momentum and the divergence-free condition (3.8) is the continuity equation in its simplified form for an incompressible flow. Equations (3.7)–(3.8) are valid in the internal fluid domain Ω_t , and have to be supplied with boundary conditions on the boundary $\partial\Omega_t$ and the problem being unsteady, an initial condition is also required. The initial velocity field is chosen as

$$\mathbf{u}(\mathbf{x}, t = t_0) = \mathbf{u}^0(\mathbf{x}), \quad \forall \mathbf{x} \in \Omega_t, \quad \text{with } \Omega_t = \Omega_{t_0} = \Omega_0, \quad (3.9)$$

such that $\nabla_{\mathbf{x}} \cdot \mathbf{u}^0 = 0$. Let the boundary $\partial\Omega_t$ be split into two non-overlapping parts $\partial\Omega_t = \partial\Omega_t^D \cup \partial\Omega_t^S$. In the sequel we will consider the two following types of boundary conditions

$$\mathbf{u} = \mathbf{g}(t), \quad \text{on } \partial\Omega_t^D \text{ and } \forall t \in I, \quad (3.10)$$

$$\boldsymbol{\sigma} \cdot \hat{\mathbf{n}} = -p\mathbf{I} \cdot \hat{\mathbf{n}} + 2\nu \mathbf{D}_{\mathbf{x}}(\mathbf{u}) \cdot \hat{\mathbf{n}} = \mathbf{h}(t), \quad \text{on } \partial\Omega_t^S \text{ and } \forall t \in I, \quad (3.11)$$

where $\boldsymbol{\sigma}$ is the stress tensor, \mathbf{I} the identity tensor and $\hat{\mathbf{n}}$ the local unit outward normal vector to $\partial\Omega_t$. Eq. (3.10) is an essential boundary condition on $\partial\Omega_t^D$ of Dirichlet type. In the cases of free-surface flows and fluid-structure interaction problems, which are of particular interest for us, $\partial\Omega_t^D$ corresponds to fixed or prescribed moving solid walls where a no-slip condition has to be satisfied. Eq. (3.11) is a natural boundary condition on $\partial\Omega_t^S$. For free-surface flows and fluid-structure interactions, $\partial\Omega_t^S$ represents prescribed inflow and/or outflow depending on the situations considered, but primarily the free surface itself or the interface between the fluid and the structure, where a mechanical equilibrium has to be enforced. Therefore (3.11) is a dynamic boundary condition (DBC) expressing the continuity of the normal stress at the moving boundary. If free-surface flows are considered and if the surface tension is neglected, $\mathbf{h} = -p_0 \hat{\mathbf{n}}$ where p_0 is the pressure of the surrounding fluid, taken as zero in the sequel.

Using Eq. (3.5), we can recast the strong form of the conservation of the momentum of the Navier–Stokes equations in the ALE frame

$$\left. \frac{\partial \mathbf{u}}{\partial t} \right|_{\mathbf{Y}} + (\mathbf{u} - \mathbf{w}) \cdot \nabla_{\mathbf{x}} \mathbf{u} = -\nabla_{\mathbf{x}} p + 2\nu \nabla_{\mathbf{x}} \cdot \mathbf{D}_{\mathbf{x}}(\mathbf{u}) + \mathbf{f}, \quad \forall (\mathbf{x}, t) \in \Omega_t \times I, \quad (3.12)$$

the divergence-free condition (3.8), the initial and boundary conditions (3.9)–(3.11) remaining unchanged in the ALE kinematic description. Indeed, boundary conditions are related to the problem and not to the kinematic description employed, be it Eulerian, Lagrangian or arbitrary Lagrangian-Eulerian. Nevertheless the ALE mesh velocity \mathbf{w} is to a certain extent part of the unknown fields of the problem even though some freedom in moving the mesh makes the ALE technique so attractive. The details related to the treatment and the computation of the mesh velocity are presented in Section 3.4.

3.2.3 The weak ALE formulation for the moving-boundary problem governed by the Navier–Stokes equations

Based on the strong formulation of the moving-boundary problem described in Section 3.2.2, one can derive the more appropriate weak transient ALE formulation. In a standard approach, first are introduced the spaces of test and trial functions used to express the initial problem in its weak form based on the reference configuration Ω_0 . We may note that the spaces of test and trial functions for the pressure are identical as no essential Dirichlet condition is being imposed on this field. This space is the space of functions that are square Lebesgue-integrable on the domain Ω_t and is denoted by $L^2(\Omega_t)$. In general the velocity does not necessarily vanish on the domain boundary; in our particular case the existence of a non-homogeneous essential Dirichlet boundary condition on $\partial\Omega_t^D$ leads us to consider different spaces for the test and trial functions for the velocity field. The solution for the velocity \mathbf{u} , of the problem (3.7)–(3.11) will be searched for directly in the Sobolev space of trial functions $H_{\mathcal{D}}^1(\Omega_t)^d$ defined as follows

$$H_{\mathcal{D}}^1(\Omega_t)^d = \{\mathbf{u} \in L^2(\Omega_t)^d, \nabla_{\mathbf{x}} u_i \in L^2(\Omega_t)^d \text{ with } i = 1, \dots, d, \mathbf{u}|_{\partial\Omega_t^D} = \mathbf{g}\}, \quad (3.13)$$

and corresponding to the current configuration Ω_t . The reference configuration Ω_0 will be used to build the velocity test functions $\hat{\mathbf{v}}$, which will be taken in the space $H_{0,\mathcal{D}}^1(\Omega_0)^d$ with

$$H_{0,\mathcal{D}}^1(\Omega_0) = \{\hat{v} \in L^2(\Omega_0), \nabla_{\mathbf{x}} \hat{v} \in L^2(\Omega_0)^d, \hat{v}|_{\partial\Omega_0^D} = 0\}, \quad (3.14)$$

to satisfy a homogenous Dirichlet condition on $\partial\Omega_0^D$. Subsequently, the dynamics of the test functions on the configuration Ω_t is obtained by means of the existing inverse of the mapping \mathcal{A}_t . Therefore the velocity test functions on the configuration at time t are the set of functions $(\hat{\mathbf{v}} \circ \mathcal{A}_t^{-1})$ with $\hat{\mathbf{v}}$ belonging to $H_{0,\mathcal{D}}^1(\Omega_0)^d$. In the sequel, the notation $(\hat{\mathbf{v}} \circ \mathcal{A}_t^{-1})$ is kept in order to emphasize two key points. First, the treatment of the weak form of the time derivative $\partial\mathbf{u}/\partial t|_{\mathbf{Y}}$ in Eq. (3.12) is based on the essential property that $\hat{\mathbf{v}}$ is not time dependent and consequently $\partial\hat{\mathbf{v}}/\partial t|_{\mathbf{Y}} = \mathbf{0}$. Second, such formulation highlights the path to follow when practically implementing the weak ALE formulation. Indeed, the time dependency is fully incorporated in the inverse mapping \mathcal{A}_t^{-1} and the functions $\hat{\mathbf{v}}$ remains the same as the ones used in fixed-grid problems. Moreover, in a more general framework where \mathcal{A}_t is still invertible but less regular, this formulation still holds and one only needs to care for the regularity of the functions $\hat{\mathbf{v}}$ and not of the functions $(\hat{\mathbf{v}} \circ \mathcal{A}_t^{-1})$. With the notations and spaces introduced, the weak transient ALE formulation reads:

Find $(\mathbf{u}(t), p(t)) \in H_{\mathcal{D}}^1(\Omega_t)^d \times L^2(\Omega_t)$ such that for almost every $t \geq t_0$

$$\begin{aligned} \frac{d}{dt} \int_{\Omega_t} (\hat{\mathbf{v}} \circ \mathcal{A}_t^{-1}) \cdot \mathbf{u} \, d\Omega + \int_{\Omega_t} (\hat{\mathbf{v}} \circ \mathcal{A}_t^{-1}) \cdot \nabla_{\mathbf{x}} \cdot [\mathbf{u}\mathbf{u} - \mathbf{u}\mathbf{w}] \, d\Omega = \\ \int_{\Omega_t} (p \nabla_{\mathbf{x}} \cdot (\hat{\mathbf{v}} \circ \mathcal{A}_t^{-1}) - 2\nu \mathbf{D}_{\mathbf{x}}(\mathbf{u}) : \nabla_{\mathbf{x}}(\hat{\mathbf{v}} \circ \mathcal{A}_t^{-1})) \, d\Omega \\ + \int_{\Omega_t} \mathbf{f} \cdot (\hat{\mathbf{v}} \circ \mathcal{A}_t^{-1}) \, d\Omega + \int_{\partial\Omega_t^{\sigma}} \mathbf{h} \cdot (\hat{\mathbf{v}} \circ \mathcal{A}_t^{-1}) \, d\partial\Omega, \quad \forall \hat{\mathbf{v}} \in H_{0,\mathcal{D}}^1(\Omega_0)^d, \end{aligned} \quad (3.15)$$

and

$$- \int_{\Omega_t} q \nabla_{\mathbf{x}} \cdot \mathbf{u} \, d\Omega = 0, \quad \forall q \in L^2(\Omega_t). \quad (3.16)$$

The above set of equations has to be intended in the sense of distribution in the interval $t > t_0$, therefore justifying the qualifier ‘‘for almost every $t \geq t_0$ ’’, see [204] for greater details. As expected the DBC (3.11) appears ‘naturally’ in the weak formulation above, corresponding to the last term on the right-hand side of (3.15) and being the only ‘surface term’ as the spatial integration is limited to $\partial\Omega_t^{\sigma}$. In addition, the DBC (3.11) defines the reference pressure level and therefore no additional condition on the mean value of the pressure is required. Finally, it is well known (see [204] for instance) that a non-homogeneous Dirichlet boundary condition

engenders a compatibility condition that the field \mathbf{u} has to satisfy. The origin of this condition is that, in order to be compatible with (3.8) the boundary condition (3.10) imposes

$$\int_{\partial\Omega_t} \mathbf{u} \cdot \hat{\mathbf{n}} \, d\partial\Omega = \int_{\partial\Omega_t^p} \mathbf{g}(t) \cdot \hat{\mathbf{n}} \, d\partial\Omega + \int_{\partial\Omega_t^{\mathcal{F}}} \mathbf{u}(t) \cdot \hat{\mathbf{n}} \, d\partial\Omega = 0, \quad \forall t \in I. \quad (3.17)$$

Eq. (3.17) is a consequence of (3.16) with $q = 1$.

In order to ease the discretization of the continuous weak equations (3.15)–(3.16), we introduce the following notations and bilinear forms, such as a scalar product defined by

$$(\mathbf{u}, \hat{\mathbf{v}}) := \int_{\Omega_t} (\hat{\mathbf{v}} \circ \mathcal{A}_t^{-1}) \cdot \mathbf{u} \, d\Omega, \quad \forall \hat{\mathbf{v}} \in H_{0,\mathcal{D}}^1(\Omega_0)^d, \quad (3.18)$$

a so-called ‘energy bilinear form’

$$\mathcal{A}(\mathbf{u}, \hat{\mathbf{v}}) := 2\nu \int_{\Omega_t} \mathbf{D}_{\mathbf{x}}(\mathbf{u}) : \nabla_{\mathbf{x}}(\hat{\mathbf{v}} \circ \mathcal{A}_t^{-1}) \, d\Omega, \quad \forall \hat{\mathbf{v}} \in H_{0,\mathcal{D}}^1(\Omega_0)^d, \quad (3.19)$$

a bilinear form related to the weak incompressibility constraint

$$\mathcal{B}(\hat{\mathbf{v}}, p) := - \int_{\Omega_t} p \nabla_{\mathbf{x}} \cdot (\hat{\mathbf{v}} \circ \mathcal{A}_t^{-1}) \, d\Omega, \quad \forall \hat{\mathbf{v}} \in H_{0,\mathcal{D}}^1(\Omega_0)^d, \quad (3.20)$$

a nonlinear form corresponding to the nonlinear convective term

$$\mathcal{C}(\hat{\mathbf{v}}; \mathbf{u}, \mathbf{w}) := \int_{\Omega_t} (\hat{\mathbf{v}} \circ \mathcal{A}_t^{-1}) \cdot \nabla_{\mathbf{x}} \cdot [\mathbf{u}\mathbf{u} - \mathbf{u}\mathbf{w}] \, d\Omega, \quad \forall \hat{\mathbf{v}} \in H_{0,\mathcal{D}}^1(\Omega_0)^d, \quad (3.21)$$

and finally two linear forms, the first one being related to the source term \mathbf{f}

$$\mathcal{F}(\hat{\mathbf{v}}) := \int_{\Omega_t} \mathbf{f} \cdot (\hat{\mathbf{v}} \circ \mathcal{A}_t^{-1}) \, d\Omega, \quad \forall \hat{\mathbf{v}} \in H_{0,\mathcal{D}}^1(\Omega_0)^d, \quad (3.22)$$

and the second one to the non-homogeneous natural boundary condition (3.11) on $\partial\Omega_t^{\mathcal{F}}$

$$\mathcal{H}^{\sigma}(\hat{\mathbf{v}}) := \int_{\partial\Omega_t^{\mathcal{F}}} \mathbf{h} \cdot (\hat{\mathbf{v}} \circ \mathcal{A}_t^{-1}) \, d\partial\Omega, \quad \forall \hat{\mathbf{v}} \in H_{0,\mathcal{D}}^1(\Omega_0)^d. \quad (3.23)$$

With these notations, the continuous weak ALE form of our moving-boundary Navier–Stokes problem can be recast as

Find $(\mathbf{u}(t), p(t)) \in H_{\mathcal{D}}^1(\Omega_t)^d \times L^2(\Omega_t)$ such that for almost every $t \geq t_0$

$$\frac{d}{dt}(\mathbf{u}, \hat{\mathbf{v}}) + \mathcal{A}(\mathbf{u}, \hat{\mathbf{v}}) + \mathcal{B}(\hat{\mathbf{v}}, p) + \mathcal{C}(\hat{\mathbf{v}}; \mathbf{u}, \mathbf{w}) = \mathcal{F}(\hat{\mathbf{v}}) + \mathcal{H}^{\sigma}(\hat{\mathbf{v}}), \quad \forall \hat{\mathbf{v}} \in H_{0,\mathcal{D}}^1(\Omega_0)^d, \quad (3.24)$$

$$\mathcal{B}(\mathbf{u}, q) = 0, \quad \forall q \in L^2(\Omega_t). \quad (3.25)$$

3.3 Numerical technique and discretization

Moving-boundary problems, either free-surface or fluid-structure interaction, represent a real challenge not only for the mathematician but also for the numericists. As presented in Section 3.2, the weak formulation of the problem (3.24)–(3.25) is an evidence of its complexity. In this section, particular emphasis will be put on the numerical space discretization of this arduous continuous problem. The general case with non-homogeneous natural and essential Dirichlet boundary conditions is dealt with, justifying the choice of a very detailed presentation. The particular case of steady problems with non-homogeneous Neumann conditions and homogeneous Dirichlet boundary conditions was first formulated by Ho & Patera in [123] in their study of free-surface flows dominated by inhomogeneous surface-tension effects. Furthermore, Rønquist extended the previous work of Ho and Patera to the more general case of steady free-surface flow problems with non-homogeneous Neumann and Dirichlet boundary conditions [211]. The specificities related to the treatment of transient problems is highlighted in the present chapter, which to our knowledge is not available in the current literature.

3.3.1 Spectral element discretization

The first step in the spectral element method (SEM) discretization consists in subdividing the fluid domain $\bar{\Omega}_t = \Omega_t \cup \partial\Omega_t$ into E non-overlapping elements $\{\Omega_t^e\}_{e=1}^E$. In the sequel we will assume that this elemental subdivision is maintained for all values of t in the interval I , therefore meaning that no re-meshing procedure is applied and leading to

$$\Omega_t^e = \mathcal{A}_t(\Omega_0^e), \quad \text{for } e = 1, \dots, E, \quad \forall t \in I. \quad (3.26)$$

A re-meshing procedure for problem using SEM is presented in [34] and can be used if needed. Each element Ω_t^e involves a mesh constructed as a tensor product of one-dimensional grids. Although each space direction may be discretized independently of the others, without loss of generality we will consider only meshes obtained with the same number of nodes in each direction, denoted by $N + 1$, corresponding to the dimension of the space of N th-order polynomials. To describe the discretization process accurately, we adopt the same procedure as in [58] and define the following spaces

$$X := H_{0,D}^1(\Omega_0)^d, \quad Y := H_D^1(\Omega_t)^d, \quad Z := L^2(\Omega_t). \quad (3.27)$$

3.3.2 Galerkin approximation

We apply the Galerkin approximation to our Navier–Stokes problem in the ALE formulation in its weak form (3.24)–(3.25), and therefore select finite dimensional polynomial subspaces X_N , Y_N and Z_N to represent X , Y and Z respectively. A staggered-grid approach with element based on $\mathbb{P}_N - \mathbb{P}_{N-2}$ spaces for the velocity and pressure field respectively, allows to eliminate completely the spurious pressure modes [172, 174]. In this context, the finite dimensional functional spaces are defined as

$$X_N := X \cap \mathbb{P}_{N,E}^d, \quad Y_N := Y \cap \mathbb{P}_{N,E}^d, \quad Z_N := Z \cap \mathbb{P}_{N-2,E}, \quad (3.28)$$

with

$$\mathbb{P}_{M,E} = \{\phi | \phi \in L^2(\Omega_t); \phi|_{\Omega_t^e} \text{ is a polynomial of degree } \leq M, \forall e = 1, \dots, E\}, \quad (3.29)$$

where the superscript d in (3.28) reflects the fact that test and trial velocity functions are d -dimensional. With these notations the Galerkin approximation of (3.24)–(3.25) reads

Find $(\mathbf{u}_N(t), p_N(t)) \in Y_N \times Z_N$ such that for almost every $t \geq t_0$

$$\begin{aligned} \frac{d}{dt}(\mathbf{u}_N, \hat{\mathbf{v}}_N) + \mathcal{A}(\mathbf{u}_N, \hat{\mathbf{v}}_N) + \mathcal{B}(\hat{\mathbf{v}}_N, p_N) + \\ \mathcal{C}(\hat{\mathbf{v}}_N; \mathbf{u}_N, \mathbf{w}_N) = \mathcal{F}_N(\hat{\mathbf{v}}_N) + \mathcal{H}_N^\sigma(\hat{\mathbf{v}}_N), \end{aligned} \quad \forall \hat{\mathbf{v}}_N \in X_N, \quad (3.30)$$

$$\mathcal{B}(\mathbf{u}_N, q_N) = 0, \quad \forall q_N \in Z_N, \quad (3.31)$$

with

$$(\mathbf{u}_N, \hat{\mathbf{v}}_N) = \sum_{e=1}^E \int_{\Omega_t^e} \mathbf{u}_N \cdot (\hat{\mathbf{v}}_N \circ \mathcal{A}_t^{-1}) \, d\Omega, \quad \forall \hat{\mathbf{v}}_N \in X_N \quad (3.32)$$

$$\mathcal{F}_N(\hat{\mathbf{v}}_N) = \sum_{e=1}^E \int_{\Omega_t^e} \mathbf{f}_N \cdot (\hat{\mathbf{v}}_N \circ \mathcal{A}_t^{-1}) \, d\Omega, \quad \forall \hat{\mathbf{v}}_N \in X_N \quad (3.33)$$

$$\mathcal{H}_N^\sigma(\hat{\mathbf{v}}_N) = \sum_{e=1}^E \int_{\partial\Omega_t^{e,\sigma}} \mathbf{h}_N \cdot (\hat{\mathbf{v}}_N \circ \mathcal{A}_t^{-1}) \, d\partial\Omega, \quad \forall \hat{\mathbf{v}}_N \in X_N \quad (3.34)$$

\mathbf{f}_N and \mathbf{w}_N being the projection of the fields \mathbf{f} and \mathbf{w} onto the finite dimensional space $\mathbb{P}_{N,E}^d$.

The integrals within each of the spectral elements $\{\Omega_t^e\}_{e=1}^E$ and on the boundaries $\{\partial\Omega_t^{e,\sigma}\}_{e=1}^E$ are performed in a discrete manner using Gaussian quadrature rules. More specifically, all the terms in (3.30)–(3.31) are integrated using a Gauss-Lobatto-Legendre (GLL) quadrature rule except for the two terms involving the bilinear form \mathcal{B} where functions discretized in $\mathbb{P}_{N-2,E}$ appear. For these two terms, namely the pressure term and the divergence-free condition, a Gauss-Legendre (GL) quadrature rule is chosen. Therefore, the $\mathbb{P}_N - \mathbb{P}_{N-2}$ Navier–Stokes problem in the ALE form is finally stated as

Find $(\mathbf{u}_N(t), p_N(t)) \in Y_N \times Z_N$ such that for almost every $t \geq t_0$

$$\begin{aligned} \frac{d}{dt}(\mathbf{u}_N, \hat{\mathbf{v}}_N)_{N,GLL} + \mathcal{A}_{N,GLL}(\mathbf{u}_N, \hat{\mathbf{v}}_N) + \mathcal{B}_{N,GL}(\hat{\mathbf{v}}_N, p_N) + \\ \mathcal{C}_{N,GLL}(\hat{\mathbf{v}}_N; \mathbf{u}_N, \mathbf{w}_N) = \mathcal{F}_{N,GLL}(\hat{\mathbf{v}}_N) + \mathcal{H}_{N,GLL}^\sigma(\hat{\mathbf{v}}_N), \end{aligned} \quad \forall \hat{\mathbf{v}}_N \in X_N, \quad (3.35)$$

$$\mathcal{B}_{N,GL}(\mathbf{u}_N, q_N) = 0, \quad \forall q_N \in Z_N. \quad (3.36)$$

To simplify the notations in the sequel, we will drop the subscript GLL and unless being explicitly specified, whenever an integration rule is required, the GLL one is implicitly being used.

3.3.3 Semi-discrete Navier–Stokes moving-boundary problem in the ALE form

In order to formulate the semi-discrete version of our moving-boundary problem governed by the Navier–Stokes equations in the ALE form, we introduce the two tensor-product bases on the reference element $\hat{\Omega} := [-1, 1]^d$ and defined with Eqs. (2.23)–(2.24) in Sec. 2.3.3. The expressions of the one-dimensional GLL and GL Lagrangian interpolant polynomials $\pi(\boldsymbol{\xi})$ and $\varpi(\boldsymbol{\zeta})$ appearing in (2.23)–(2.24) can be found in [58] and also partially in Sec. A.7. The polynomials $\{\pi_{i,j,k}(\boldsymbol{\xi})\}_{i,j,k=0}^N$ and $\{\varpi_{i,j,k}(\boldsymbol{\zeta})\}_{i,j,k=1}^{N-1}$ will serve as bases for the functions in the spaces X_N , Y_N and Z_N

$$\mathbf{u}_N(\mathbf{x}(\boldsymbol{\xi}), t) = \sum_{i,j,k=0}^N \mathbf{u}_{ijk}(t) \pi_{i,j,k}(\boldsymbol{\xi}), \quad \forall(\boldsymbol{\xi}, t) \in \hat{\Omega} \times I, \quad (3.37)$$

$$p_N(\mathbf{x}(\boldsymbol{\zeta}), t) = \sum_{i,j,k=1}^{N-1} p_{ijk}(t) \varpi_{i,j,k}(\boldsymbol{\zeta}), \quad \forall(\boldsymbol{\zeta}, t) \in \hat{\Omega} \times I, \quad (3.38)$$

where $\mathbf{x} = \mathbf{x}^e$ is the location of the point considered in the spectral element Ω_t^e , $\{\mathbf{u}_{ijk}(t)\}_{i,j,k=0}^N$ the set of nodal values of the velocity field on the GLL grid of Ω_t^e and $\{p_{ijk}(t)\}_{i,j,k=1}^{N-1}$ the set of nodal values of the pressure field on the GL grid of Ω_t^e . It is important to note that the time-dependency of the discretized velocity \mathbf{u}_N and pressure p_N is not solely accounted by the time-dependent nodal values of these two fields. Indeed, due to the motion of the grid, the mapping between the position in the reference element $\hat{\Omega}$ and the spectral element Ω_t^e at time t is also time-dependent via the ALE mapping \mathcal{A}_t . If we note \mathcal{M}_t^e (resp. \mathcal{M}_0^e) the mapping from the reference element $\hat{\Omega}$ onto Ω_t^e (resp. Ω_0^e), we can write

$$\mathbf{x}^e = \mathcal{M}_t^e(\boldsymbol{\xi}), \quad \forall(\boldsymbol{\xi}, t) \in \hat{\Omega} \times I, \quad (3.39)$$

$$\mathbf{Y}^e = \mathcal{M}_0^e(\boldsymbol{\xi}), \quad \forall(\boldsymbol{\xi}, t) \in \hat{\Omega} \times I, \quad (3.40)$$

$$\mathbf{x}^e = \mathcal{A}_t(\mathbf{Y}^e), \quad \forall(\mathbf{Y}^e, t) \in \Omega_0^e \times I, \quad (3.41)$$

leading to following relationship between the different mappings

$$\mathcal{M}_t^e = \mathcal{A}_t \circ \mathcal{M}_0^e, \quad \forall t \in I. \quad (3.42)$$

Eq. (3.42) shows that the second origin of the time-dependency of (3.37) and (3.38), after the one due to the set of GLL and GL nodal values, is the moving-grid technique via the time-dependency of the ALE mapping \mathcal{A}_t .

Before embarking on the final process of semi-discretizing the equations for the moving-boundary problem, a last issue needs to be addressed: the treatment of the non-homogeneous Dirichlet boundary condition (3.10) on $\partial\Omega_t^D$. First of all and as mentioned earlier, the non-homogeneity of (3.10) leads to different spaces for the trial and test functions for the velocity field, X_N and Y_N respectively. Therefore the basis (3.37) developed for X_N is not suitable for the solution $\mathbf{u}_N(t)$ of the problem (3.30)–(3.31) sought in Y_N . As presented earlier, the non-homogeneous Dirichlet boundary condition imposes to satisfy the compatibility condition (3.17) whose discrete version reads

$$\sum_{e=1}^E \int_{\partial\Omega_t^e} \mathbf{u}_N(t) \cdot \hat{\mathbf{n}} \, d\Omega = 0, \quad \forall t \in I. \quad (3.43)$$

Let $\mathbf{u}_{b,N}$ be a (piecewise) polynomial defined on the discrete boundary $\partial\Omega_t^e$ ($e = 1, \dots, E$) and such that its nodal boundary values are equal to the boundary data $\mathbf{g}(t)$. In practice, the GLL Lagrangian interpolation bases defined on the element boundaries are used to expand $\mathbf{u}_{b,N}$; however, in the rest of the inner domain these functions are zero. By construction, $\mathbf{u}_{b,N}$ satisfies (3.43). Setting $\mathbf{u}_N = \mathbf{u}_{0,N} + \mathbf{u}_{b,N}$, the problem reduces to finding $\mathbf{u}_{0,N}$ in the space $Y_{0,N} := H_{0,\mathcal{D}}^1(\Omega_t)^d \cap \mathbb{P}_{N,E}^d$. Therefore the problem (3.30)–(3.31) can be reformulated as follows

Find $(\mathbf{u}_{0,N}(t), p_N(t)) \in Y_{0,N} \times Z_N$ such that for almost every $t \geq t_0$

$$\frac{d}{dt} (\mathbf{u}_{0,N}, \hat{\mathbf{v}}_N)_N + \mathcal{A}_N(\mathbf{u}_{0,N}, \hat{\mathbf{v}}_N) + \mathcal{B}_{N,GL}(\hat{\mathbf{v}}_N, p_N) + \mathcal{C}_N(\hat{\mathbf{v}}_N; \mathbf{u}_{0,N}, \mathbf{w}_N) = \mathcal{F}_N(\hat{\mathbf{v}}_N) + \mathcal{H}_N^\sigma(\hat{\mathbf{v}}_N) + \mathcal{D}_{1,N}(\hat{\mathbf{v}}_N, t), \quad \forall \hat{\mathbf{v}}_N \in X_N, \quad (3.44)$$

$$\mathcal{B}_{N,GL}(\mathbf{u}_{0,N}, q_N) = \mathcal{D}_{2,N,GL}(q_N, t), \quad \forall q_N \in Z_N, \quad (3.45)$$

with

$$\begin{aligned} \mathcal{D}_{1,N}(\hat{\mathbf{v}}_N, t) &= -\frac{d}{dt}(\mathbf{u}_{b,N}(t), \hat{\mathbf{v}}_N)_N \\ &\quad - \mathcal{A}_N(\mathbf{u}_{b,N}(t), \hat{\mathbf{v}}_N) - \mathcal{C}_N(\hat{\mathbf{v}}_N; \mathbf{u}_{b,N}(t), \mathbf{w}_N), \end{aligned} \quad \forall \hat{\mathbf{v}}_N \in X_N, \quad (3.46)$$

and

$$\mathcal{D}_{2,N,GL}(q_N, t) = -\mathcal{B}_{N,GL}(\mathbf{u}_{b,N}(t), q_N), \quad \forall q_N \in Z_N. \quad (3.47)$$

The two time-dependent terms $\mathcal{D}_{1,N}$ et $\mathcal{D}_{2,N,GL}$ appearing in (3.44) and (3.45) are due to the non-homogeneity of the Dirichlet boundary condition. These values are related to the values of the discrete field $\mathbf{u}_{b,N}(t)$, which as mentioned earlier, are obtained from the values of the field $\mathbf{g}(t)$ from (3.10).

We can now expand the trial velocity $\mathbf{u}_{0,N}$ and the trial pressure p_N onto the GLL–GL bases like in (3.37) and (3.38) respectively. In the sequel we will drop the subscript 0 in $\mathbf{u}_{0,N}$, no confusion being possible as the non-homogeneous Dirichlet boundary conditions is already accounted for in (3.44)–(3.45). The semi-discrete equations derived from (3.44)–(3.45) are

$$\frac{d}{dt}(\mathbf{M}(t)\underline{\mathbf{u}}(t)) = -\mathbf{A}(t)\underline{\mathbf{u}}(t) - \mathbf{C}(\underline{\mathbf{u}}(t), \underline{\mathbf{w}}(t), t)\underline{\mathbf{u}}(t) + \mathbf{D}^T(t)\underline{p}(t) + \underline{\mathbf{F}}_1(t), \quad (3.48)$$

$$-\mathbf{D}(t)\underline{\mathbf{u}}(t) = \underline{\mathbf{F}}_2(t). \quad (3.49)$$

The matrices appearing in (3.48)–(3.49) are all time-dependent: \mathbf{M} is the mass matrix, \mathbf{A} the stiffness matrix, \mathbf{C} the discrete convective operator involving the velocity field $\underline{\mathbf{u}}$ and the ALE mesh velocity $\underline{\mathbf{w}}$, \mathbf{D}^T the discrete gradient operator and \mathbf{D} the discrete divergence. $\underline{\mathbf{F}}_1$ and $\underline{\mathbf{F}}_2$ are two vectors accounting for the presence of the body force \mathbf{f} and the time-dependent essential Dirichlet and natural non-homogeneous boundary conditions.

3.3.4 Time discretization

The set of semi-discrete equations (3.48)–(3.49) is discretized in time using finite-difference schemes in a decoupled approach. The computation of the linear Helmholtz problem—corresponding to the energy bilinear form \mathcal{A} and the stiffness matrix \mathbf{A} —is integrated based on an implicit backward differentiation formula of order 2, the nonlinear convective term—corresponding to the nonlinear form \mathcal{C} and the matrix \mathbf{C} —is integrated based on a relatively simple extrapolation method of order 2, introduced by Karniadakis *et al.* [140], see Sec. 2.3.5.

The moving-grid treatment requires the semi-discrete equations (3.48)–(3.49) to be supplemented with an equation computing the mesh nodes update

$$\frac{d\mathbf{x}}{dt} = \underline{\mathbf{w}}, \quad (3.50)$$

with \mathbf{x} being a vector containing the d -dimensional mesh nodes position at time t . The integration of Eq. (3.50) necessitates the knowledge of the values of the mesh velocity provided by the moving-grid technique employed. Two particular techniques are presented in detail in Section 3.4. The time-integration of Eq. (3.50) is based on an explicit and conditionally stable Adams–Bashforth of order 3.

Lastly the treatment of the pressure relies on a generalized block LU decomposition with pressure correction [196, 197], see Sec. 2.3.5.

The temporal order of the overall splitting scheme has proved to be equal to two for fixed-grid problems. The grid motion induces a limited reduction of the global temporal order, which is found to fall between 1.5 and 2 for the simulations presented in Section 3.5. The reasons for this reduction in the global order of the method is still not clearly understood.

3.3.5 Specificities pertaining to free-surface flows and fluid-structure interaction

Up to this point, the treatment of our moving-boundary problem was kept to a level general enough to encompass both the free-surface flow and fluid-structure interaction problems. At this stage, it appears natural to provide the specificities pertaining to each of these two sub-problems.

These specificities lie primarily in the natural and essential Dirichlet boundary conditions imposed to the system. For free-surface flows with no surface-tension effects—either of normal or tangential type—and with

no inflow nor outflow—closed system, both the natural and essential Dirichlet boundary conditions become homogeneous— $\mathbf{g} = \mathbf{0}$ on $\partial\Omega_t^D$ and $\mathbf{h} = \mathbf{0}$ on $\partial\Omega_t^\sigma$, leading to a drastic simplification of the problem. More precisely, the vector $\underline{\mathbf{E}}_1$ reduces to $\mathbf{M}(t)\underline{\mathbf{f}}$ and $\underline{\mathbf{E}}_2$ vanishes in the semi-discrete formulation (3.48)–(3.49) of the problem. For fluid-structure interaction problems, the natural boundary condition on the interface between the flow and the structure is provided by the dynamics of the structure, that can be evaluated by the SEM and the Newmark method [29]. In the sequel, we will focus our attention on the flow problem for both of these two cases of interest. Therefore, the implicit-explicit discretized problem to solve reads

$$\left(\frac{3\mathbf{M}^{n+1}}{2\Delta t} + \mathbf{A}^{n+1}\right)\underline{\mathbf{u}}^{n+1} - (\mathbf{D}^{n+1})^T \underline{\mathbf{p}}^{n+1} = \frac{1}{\Delta t} \left(2\mathbf{M}^n \underline{\mathbf{u}}^n - \frac{1}{2}\mathbf{M}^{n-1} \underline{\mathbf{u}}^{n-1}\right) + \mathbf{M}^{n+1} \underline{\mathbf{f}}^{n+1} - \mathbf{C}^{n+1} \underline{\mathbf{u}}^{n+1}, \quad (3.51)$$

$$\mathbf{C}^{n+1} \underline{\mathbf{u}}^{n+1} = 2\mathbf{C}^n(\underline{\mathbf{u}}^n, \underline{\mathbf{w}}^n) \underline{\mathbf{u}}^n - \mathbf{C}^{n-1}(\underline{\mathbf{u}}^{n-1}, \underline{\mathbf{w}}^{n-1}) \underline{\mathbf{u}}^{n-1}, \quad (3.52)$$

$$-\mathbf{D}^{n+1} \underline{\mathbf{u}}^{n+1} = \underline{\mathbf{0}}, \quad (3.53)$$

$$\underline{\mathbf{x}}^{n+1} = \underline{\mathbf{x}}^n + \Delta t \left(\frac{23}{12}\underline{\mathbf{w}}^n - \frac{16}{12}\underline{\mathbf{w}}^{n-1} + \frac{5}{12}\underline{\mathbf{w}}^{n-2}\right), \quad (3.54)$$

where Δt is the time-step.

3.4 Moving-grid techniques

When considering moving-boundary problems tackled in an interface-tracking and ALE frame, the moving boundary $\partial\Omega_t^\sigma$ is treated in a Lagrangian way whereas the boundary $\partial\Omega_t^D$ which is fixed or subject to a prescribed motion $\mathbf{g}(t)$, is studied in an Eulerian frame. Accordingly, such method allows large-amplitude motions of the moving boundary, by generating a shape-conformed grid. Hence, an accurate and simple application of the boundary conditions on $\partial\Omega_t$ is easily accessible.

As a consequence of the ALE kinematics, the boundary conditions imposed on the mesh velocity \mathbf{w} read

$$\mathbf{w} \cdot \hat{\mathbf{n}} = \mathbf{u} \cdot \hat{\mathbf{n}}, \quad \text{on } \partial\Omega_t^\sigma \text{ and } \forall t \in I, \quad (3.55)$$

$$\mathbf{w} = \mathbf{g}(t), \quad \text{on } \partial\Omega_t^D \text{ and } \forall t \in I. \quad (3.56)$$

Eq. (3.55) is a kinematic boundary condition (KBC) on the moving boundary meaning that $\partial\Omega_t^\sigma$ is a material surface with no transfer of fluid across it in the Lagrangian perspective. Eq. (3.56) expresses a kinematic boundary condition of no-slip type on the boundary of the domain which is not free to move. Given (3.55)–(3.56), it appears that the freedom left for the choice of \mathbf{w} lies in the values of this field in the internal fluid domain Ω_t and also on the tangential values of \mathbf{w} on the moving boundary $\partial\Omega_t^\sigma$.

It is important to note that the velocity boundary condition specified on walls in contact with a free surface is not well posed due to the contradiction of the moving free surface and a no-slip condition on the bounding wall. Two alternative free-surface contact wall boundary conditions have been adopted in the current work. The first one consists in strictly imposing the no-slip condition expressed by Eq. (3.56) and is used throughout the study of the free-surface swirling flow presented in Chap. 8. Such alternative does not pose any problem when a limited motion of the free surface occurs near the contact line. The second alternative consists in relaxing Eq. (3.56) by considering a free-slip wall boundary condition instead, which maintains the nonpermeability condition. Such free-slip condition relates to a shear-free condition on the walls and therefore does not lead to any production of vorticity at these walls. This second alternative is used when large-amplitude deformations of the free surface at the contact line occur, which is the case in the study of the sloshing of a viscous fluid in a tank performed in Sec. 3.5.3.

The computation of the mesh velocity \mathbf{w} in the internal fluid domain Ω_t is the corner-stone of the moving-grid technique developed in the framework of the ALE formulation. The values of the mesh velocity being prescribed on the boundary $\partial\Omega_t$ as expressed by equations (3.55)–(3.56), the evaluation of \mathbf{w} in Ω_t can be obtained as the solution of an elliptic equation:

$$\mathcal{E}_x \mathbf{w} = \mathbf{0}, \quad \forall (\mathbf{x}, t) \in \Omega_t \times I, \quad (3.57)$$

where \mathcal{E}_x represents any elliptic operator based on the Eulerian coordinates \mathbf{x} . Such an elliptic equation constitutes a classical choice for calculating the mesh velocity [122]. Two types of elliptic equations are considered in this work. The first elliptic operator used is a Laplacian operator Δ_x , and will be used extensively in the fluid-structure interaction simulations presented in Section 3.5. More details about the use of this specific operator for the computation of the mesh velocity can be found in [29]. The second strategy relies on the assumption that the

motion of the mesh nodes is equivalent to a steady Stokes flow, corresponding physically to an incompressible and elastic motion of the mesh. Therefore the problem for the mesh velocity becomes a boundary-value steady Stokes problem with the mesh velocity \mathbf{w} satisfying a divergence-free condition

$$\nabla_{\mathbf{x}} \cdot \mathbf{w} = 0 \quad \forall(\mathbf{x}, t) \in \Omega_t \times I. \quad (3.58)$$

The justifications of this additional constraint imposed to the mesh velocity problem is presented in detail in [34] and in the Appendix A. The free-surface flow simulations of a sloshing in a three-dimensional tank due to the gravity presented in Section 3.5.3, were carried out using this second strategy for \mathbf{w} .

3.5 Numerical simulations and results

In this section we will present numerical results for three problems: the steady Stokes equations in curved sub-domains, the motion of a cylinder in a square cavity and the sloshing in a three-dimensional tank.

3.5.1 Accuracy in curved domains

We want to check the error evolution in the square domain $\Omega = [-1, 1]^2$ decomposed in curved sub-domains (elements). To this aim, let us consider the steady Stokes equations

$$-\nabla_{\mathbf{x}} p + \Delta_{\mathbf{x}} \mathbf{u} + \mathbf{f} = \mathbf{0}, \quad \forall(\mathbf{x}, t) \in \Omega_t \times I, \quad (3.59)$$

$$\nabla_{\mathbf{x}} \cdot \mathbf{u} = 0, \quad \forall(\mathbf{x}, t) \in \Omega_t \times I. \quad (3.60)$$

The exact solution is given by

$$u_x = -\cos(\pi x/2) \sin(\pi y/2), \quad (3.61)$$

$$u_y = \sin(\pi x/2) \cos(\pi y/2), \quad (3.62)$$

$$p = -\pi \sin(\pi x/2) \sin(\pi y/2), \quad (3.63)$$

when the body force term is chosen as

$$f_x = -\pi^2 \cos(\pi x/2) \sin(\pi y/2), \quad f_y = 0. \quad (3.64)$$

Instead of using a regular square grid composed of elements with edges parallel to the lines of the Cartesian

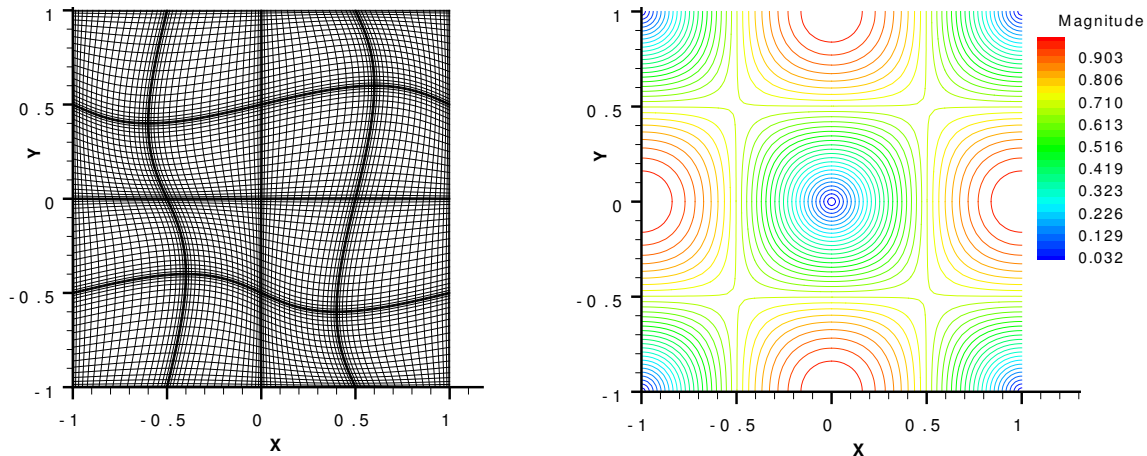


Fig. 3.1: Square domain Ω with internally deformed sub-domains with $E = 4 \times 4$ spectral elements and $N = 20$ (left) and the velocity magnitude (right).

axes, we performed the computation on the deformed mesh [97, 221] displayed in Figure 3.1 (left). Contours of the norm of the velocity field for the computed solution of problem (3.59)–(3.60), are presented on Figure 3.1 (right). Figure 3.2 shows the evolution of the relative error in H^1 -norm for the velocity and in L^2 -norm for the pressure field, with respect to an increasing polynomial degree N , for two cases— $E = 2 \times 2$ elements and

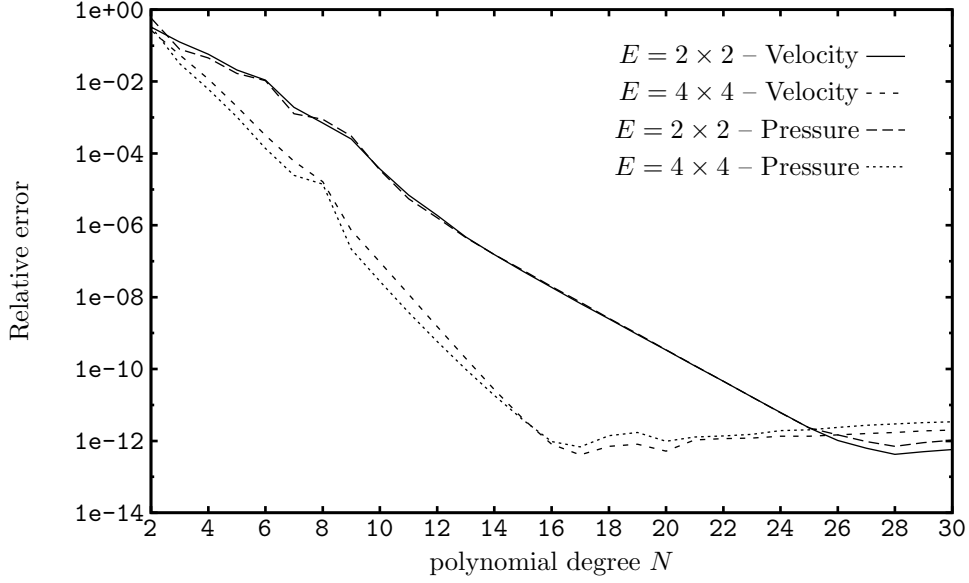


Fig. 3.2: Relative error in H^1 -norm for the velocity and in L^2 -norm for the pressure field.

$E = 4 \times 4$ elements. The convergence is slower than the one obtained with a mesh divided in several regular square sub-domains. First, we still achieve the exponential decrease of the relative error when the polynomial degree increases (which is typical of spectral or p -convergence [58]). Second, the convergence is faster when increasing the number of spectral elements E , as previously observed in [222] (which is equivalent to h -convergence in finite-element terminology [58]).

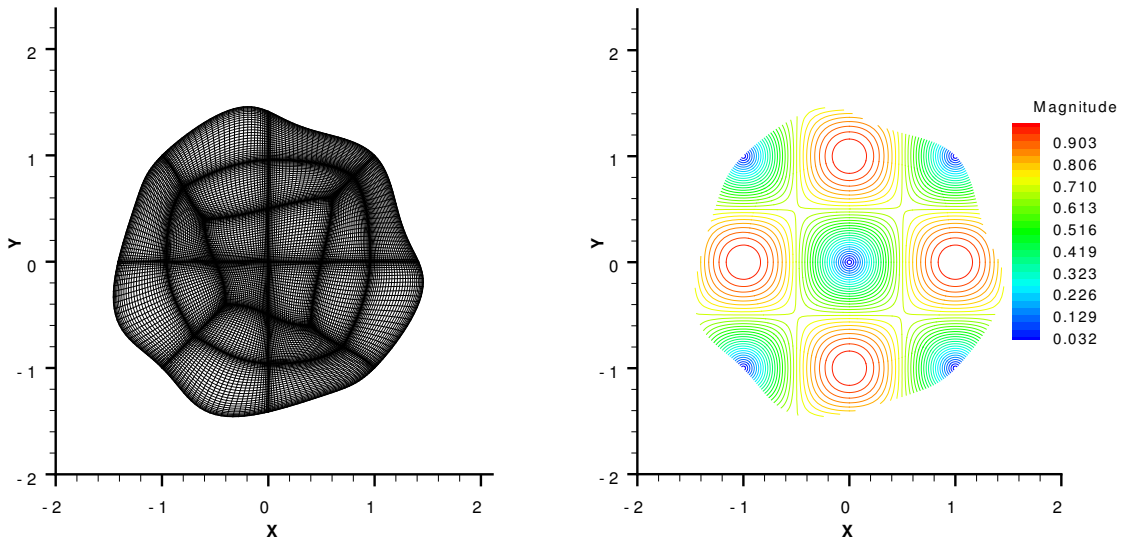


Fig. 3.3: Curvy geometry for $E = 20$ and $N = 30$ (left) and the velocity magnitude (right).

The same computation has been carried out with a geometry Ω' obtained by the transformation of coordinates of the unit square $\Omega = [-1, 1]^2$ with sine functions (Fig. 3.3)

$$x' = x + \alpha \sin(\pi x) \sin(\pi y), \quad (3.65)$$

$$y' = y + \alpha \sin(\pi x) \sin(\pi y), \quad (3.66)$$

with $(x, y) \in \Omega$, $(x', y') \in \Omega'$ and $\alpha = 1/10$. Here, the deformation of the geometry not only involves the interior of the sub-domains but also the domain boundaries.

The remarks made for the first computation, corresponding to the square domain, are still relevant for this geometry. The same behavior of the convergence is obtained as one can observe on Figure 3.4. The deformation

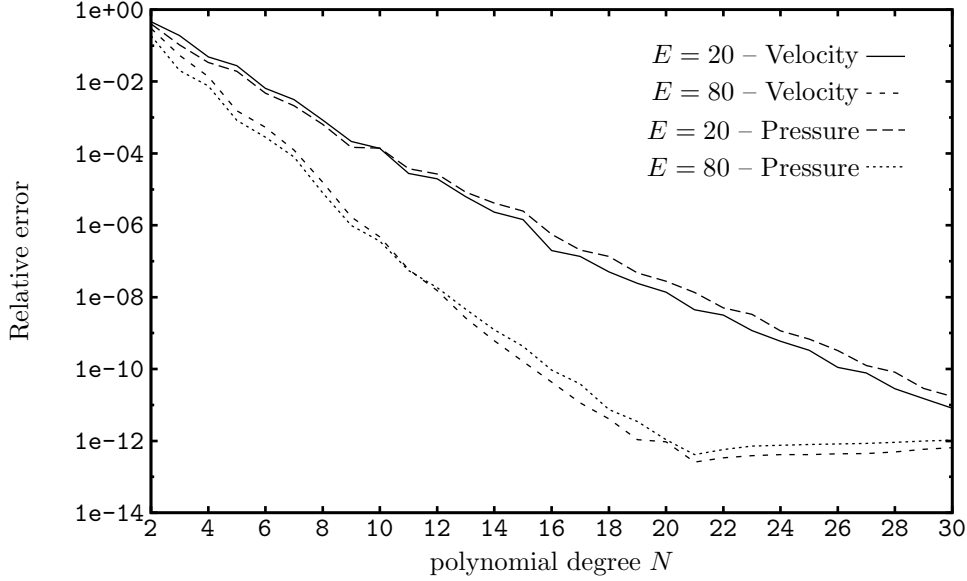


Fig. 3.4: Relative error in H^1 -norm for the velocity and in L^2 -norm for the pressure field.

of the boundaries induces obviously a slower convergence in comparison with the square domain. Nevertheless, the important result is that the spectral convergence is maintained (Fig. 3.4) even with a deformation of the domain involving its boundaries, which is a mandatory feature when solving moving-boundary problems.

3.5.2 Motion of a cylinder inside a square cavity

We solve the Navier–Stokes equations (3.7)–(3.8) in a two-dimensional square cavity. A schematic view of this cavity is given in Figure 3.5 with fixed exterior walls. A circular cylinder is immersed into the fluid and is moving with a prescribed velocity. Two types of prescribed motions are studied. In the first case, we consider a cylinder in horizontal translation from the center of the cavity with a constant velocity. Denoting the boundary of the cylinder as Γ_{cyl} , we prescribe

$$u_x|_{\Gamma_{\text{cyl}}} = w_x|_{\Gamma_{\text{cyl}}} = 1, \quad (3.67)$$

$$u_y|_{\Gamma_{\text{cyl}}} = w_y|_{\Gamma_{\text{cyl}}} = 0. \quad (3.68)$$

Denoting the exterior walls as Γ_{ext} , we have

$$\mathbf{u}|_{\Gamma_{\text{ext}}} = \mathbf{w}|_{\Gamma_{\text{ext}}} = \mathbf{0}. \quad (3.69)$$

We solve a time-dependent problem in order to study the evolution of the fluid motion caused by the translation of the cylinder in the square domain $\Omega = [-1, 1]^2$. The Reynolds number based on a unit reference length and a unit reference velocity is $\text{Re} = 1/\nu = 100$. The diameter of the cylinder is $D = 0.28$. The time-step Δt is fixed to 0.005. The discretization uses a total number of elements equal to $E = 64$ and the polynomial degree is $N = 12$ in each of the two directions. We obtain an unsteady evolution of the fluid motion and we observe a deformation of the fluid mesh as pictured in Figure 3.6, where appears the flow configuration for $t = 0.25, 0.5$ and 0.7 . If we keep on moving the cylinder closer to the right wall, the mesh deformation becomes too large. We have also focused our attention on the evaluation of an artificial “acceleration” defined as $\|\mathbf{u}_{n+1} - \mathbf{u}_n\|_{L^2}/\Delta t$, where \mathbf{u}_n denotes the velocity field at the time level n . Figure 3.7 displays the previous expression and the L^2 -norm of the velocity. The “acceleration” does not vanish, which means the solution does not become steady-state. This can be expected since the cylinder is always in motion inside the cavity. Moreover the “acceleration” increases when the cylinder gets closer to the right wall.

In the second case, the cylinder at the center of the cavity is subject to a constant counter-clockwise angular rotation $\omega = 1$ such that

$$u_x|_{\Gamma_{\text{cyl}}} = w_x|_{\Gamma_{\text{cyl}}} = -y, \quad (3.70)$$

$$u_y|_{\Gamma_{\text{cyl}}} = w_y|_{\Gamma_{\text{cyl}}} = x. \quad (3.71)$$

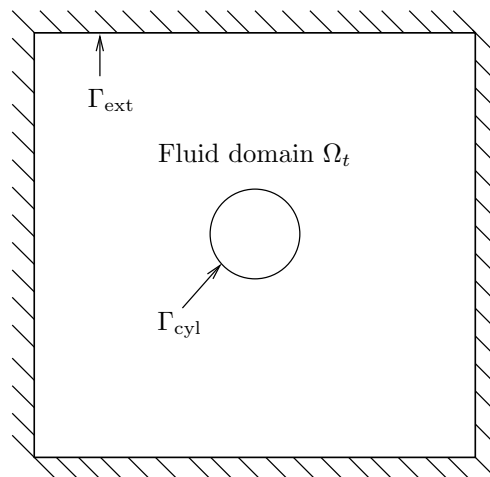


Fig. 3.5: Geometry of the fluid domain with the immersed cylinder.

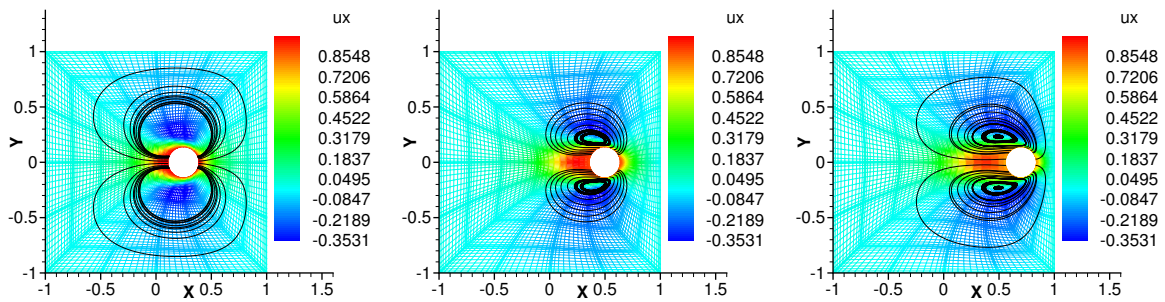


Fig. 3.6: The velocity component u_x and the corresponding streamlines (black solid lines) around a moving cylinder, $Re = 100$, for $t = 0.25$ (left), $t = 0.5$ (center) and $t = 0.7$ (right).

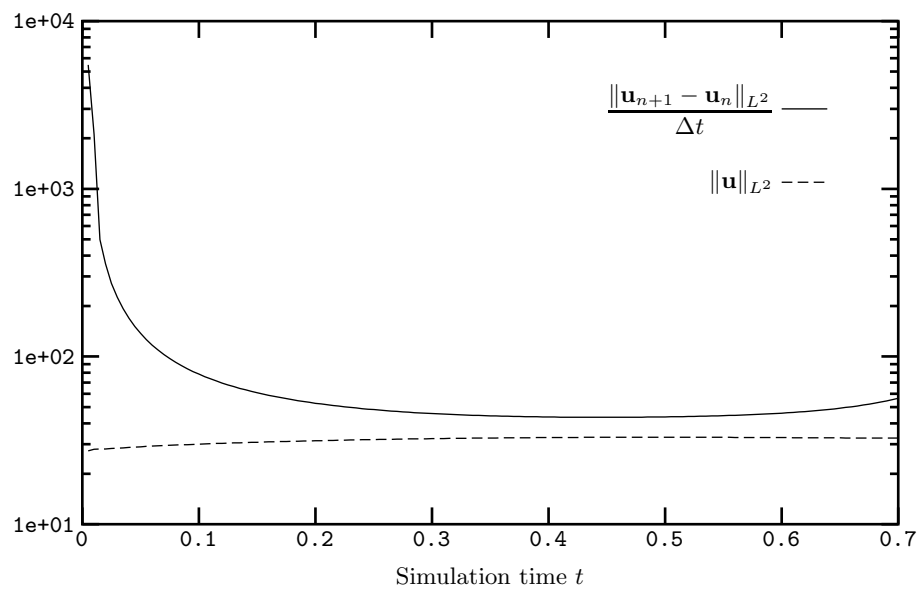


Fig. 3.7: $\|\mathbf{u}_{n+1} - \mathbf{u}_n\|_{L^2} / \Delta t$ and $\|\mathbf{u}\|_{L^2}$ versus simulation time t .

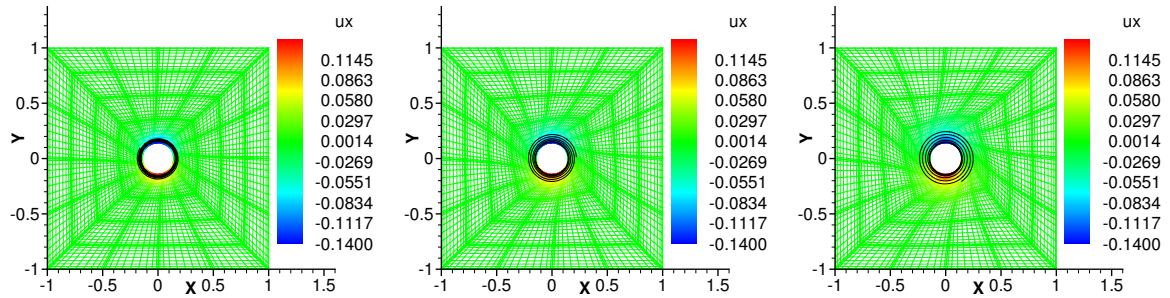


Fig. 3.8: The velocity component u_x and the corresponding streamlines (black solid lines) around a moving cylinder, $Re = 100$, for $t = 0.50$ (left), $t = 1.25$ (center) and $t = 2.0$ (right).

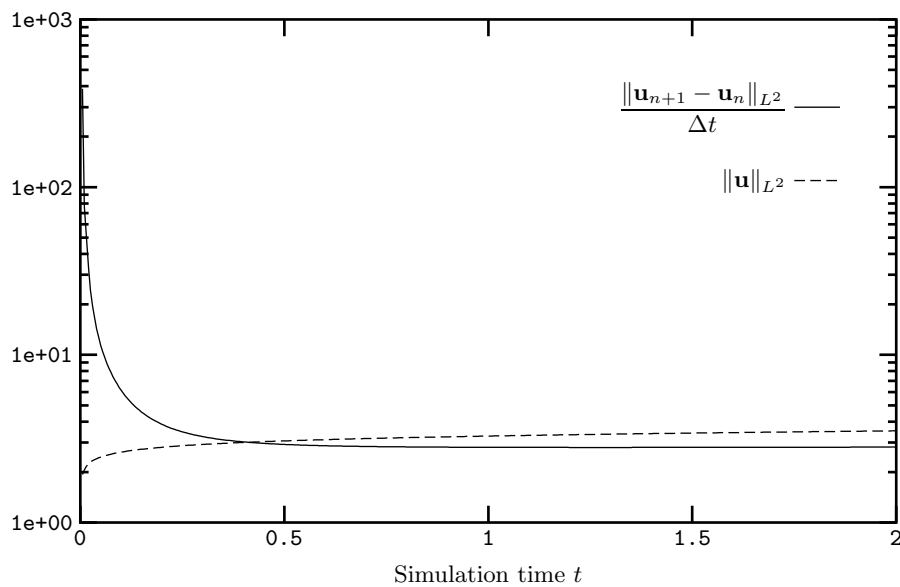


Fig. 3.9: $\|\mathbf{u}_{n+1} - \mathbf{u}_n\|_{L^2}/\Delta t$ and $\|\mathbf{u}\|_{L^2}$ versus simulation time t .

In Figure 3.8, we have maintained $E = 64$ and changed the polynomial degree to $N = 10$. We exhibit the flow configuration for $t = 0.5, 1.25$ and 2.0 . Like in the previous example, we conclude the solution does not reach a steady state due to the motion of the cylinder (Fig. 3.9). We have successfully tested these kinds of motion for large distortions of the fluid mesh.

3.5.3 Sloshing in a three-dimensional tank

To show the adaptability of our numerical model based on a moving-grid technique in the ALE frame, the analysis of large-amplitude sloshing in a three-dimensional rectangular tank has been carried out. The tank has a square-base section of dimensions $L \times L$ and a schematic view of the geometry of the problem is presented in Figure 3.10. The free-surface position is measured from the bottom of the tank: $z = L + h(x, y, t)$, where $h(x, y, t)$ is the free-surface elevation measured from its equilibrium position $z = L$. The initial shape of the free surface is varying only with x and is given by the nonlinear theory for finite-amplitude standing waves

$$h(x, t) = a(t) \cos(kx) \cos(\omega t) - \frac{ka^2(t) \cos(2kx)}{2 \tanh(kL)} \left\{ \cos^2(\omega t) + \frac{3 \cos(2\omega t) - \tanh^2(kL)}{4 \sinh^2(kL)} \right\}, \quad (3.72)$$

where the wave number is $k = 2\pi/\lambda$, the wave length $\lambda = 2L$, the initial wave amplitude $a(t = 0) = L/5$, and $\omega = \sqrt{gk \tanh(kL)}$ corresponding to the dispersion relation. For the sake of simplicity, we have taken $g = 2\pi\lambda \tanh(kL)$ which leads to a period T of the non-viscous and irrotational waves equal to one. Finally, the Reynolds number is based on the reference velocity \sqrt{gL} and is expressed as $\text{Re} = L\sqrt{gL}/\nu$.

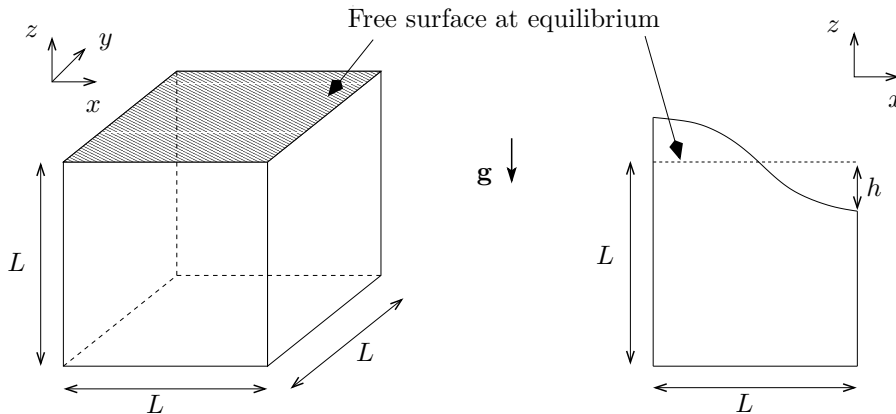


Fig. 3.10: Geometry of the simulation set-up and rectangular tank.

A no-slip condition is imposed to the velocity field at the bottom of the tank $z = 0$ and free-slip conditions on the side walls $x = 0, x = L$ and $y = 0, y = L$, likewise for the mesh velocity field \mathbf{w} which corresponds to Eq. (3.56) in the context of this problem. The Dirichlet boundary condition on the free surface for the mesh velocity is given by $\mathbf{w} = \mathbf{u}$, which includes Eq. (3.55) and also an additional condition on the tangential values of \mathbf{w} . The initial velocity field is the irrotational solution at the maximum displacement of a standing wave—corresponding to zero for all velocity components. When starting the simulation, the top surface is set free and allowed to evolve in response to the dynamic and kinematic boundary conditions (3.11) and (3.55) respectively. The nonlinearity of this problem is introduced by both boundary conditions, through the shape of the free surface in (3.55) and through the normal to the free surface in (3.11). The motion of the free surface physically corresponds to a transfer of energy between the potential energy—maximum at the initial time—and the kinetic energy, leading to a decaying oscillatory phenomenon.

Computations are performed with $E = 3^3 = 27$ spectral elements and a polynomial degree $N = 9$ in all three directions, leading to a mesh comprising 28^3 nodes. The time-step is taken equal to 0.001 and the simulation duration is 25 time units—based on the unit period T —or 25 000 iterations for 7 values of the Reynolds number $\text{Re} = 50, 100, 250, 500, 750, 1\,000$ and $1\,500$.

Using an energetic argument, Lamb [149] derived the approximate damping of a free wave due to viscosity as a function of time

$$a(t) = a(0)e^{-2\nu k^2 t}. \quad (3.73)$$

Note that this is valid for linear waves in deep water, so we can only expect this to provide a rough guide to our expected damping because the simulation waves are nonlinear with $\lambda = 2L$, which places the waves in the intermediate water regime. Figure 3.11 displays the computed relative wave amplitude $a(t)/a(0)$ with respect to the simulation time t/T . The excellent linear fits obtained for the seven values of the Reynolds number are in perfect agreement with the exponential viscous damping. Equation (3.73) also shows that the relative wave amplitude is proportional to the kinematic viscosity, if plotted in y -log scale. This second point is verified in Figure 3.12, where $a(t)/a(0)$ is plotted against the inverse of the Reynolds number which is by definition proportional to the kinematic viscosity ν .

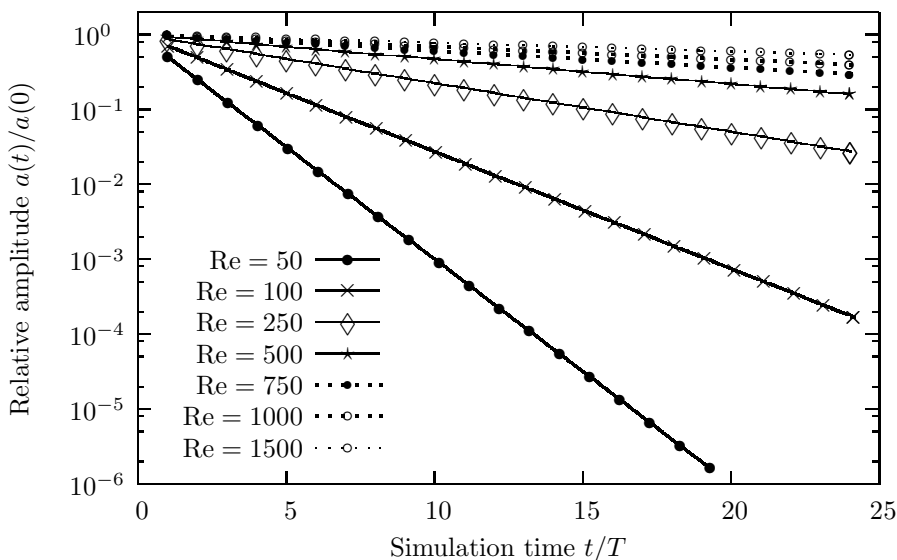


Fig. 3.11: Relative amplitude $a(t)/a(0)$ against the simulation time t/T .

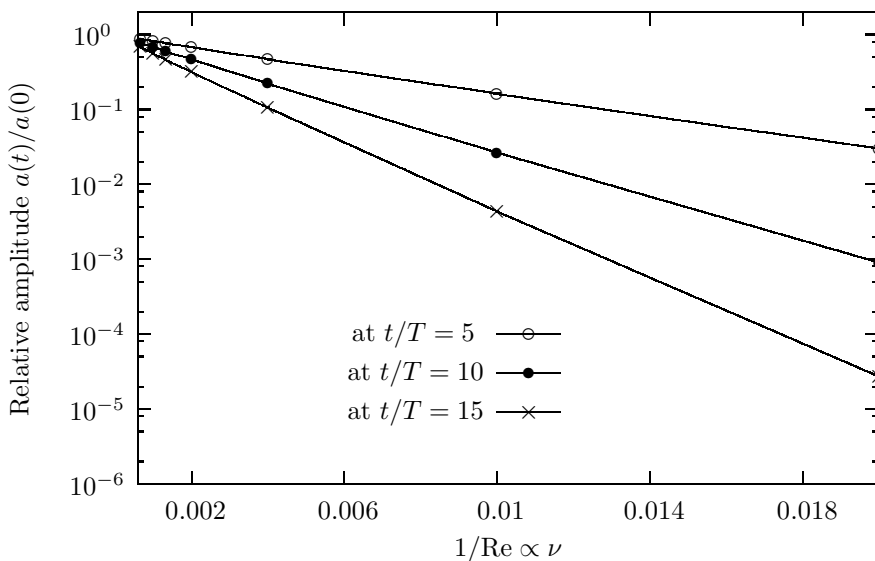


Fig. 3.12: Relative amplitude $a(t)/a(0)$ against the inverse of the Reynolds number.

Those results are evidences of the robustness and accuracy of our moving-grid technique in handling large-deformations for moving-boundary problems such as the one considered here.

3.6 Conclusions

A numerical model for solving two- and three-dimensional moving-boundary problems such as free-surface flows or fluid-structure interaction is proposed. This model relies on a moving-grid technique to solve the Navier–Stokes equations expressed in the arbitrary Lagrangian–Eulerian kinematics and discretized by the spectral element method.

A detailed analysis of the continuous and discretized formulations of the general problem in the ALE frame, with non-homogeneous and unsteady boundary conditions is presented. Particular emphasis was put on the weak formulation and its semi-discrete counterpart. The moving-grid algorithm which is one of the key ingredient of our numerical model, is based on the computation of the ALE mesh velocity with the same accuracy and numerical technique as the fluid velocity. The coupling between the Navier–Stokes computation and the one for the mesh velocity is effective through the problem boundary conditions. It is noteworthy that the coupling in the interior Navier–Stokes computation is effective through the modified convective term which is induced by what is happening at the boundaries.

Three numerical test results are presented in the two particular cases of interest, namely fluid-structure interactions and free-surface flows. First the influence of the deformation of the grid on the accuracy of the numerical model is evaluated. In a second problem, two motions (translation and rotation) of a cylinder immersed in a fluid is computed. Lastly, large-amplitude sloshing in a three-dimensional tank is simulated. The results obtained are showing very good with the theoretical results when available, therefore leading to a validation of our numerical model.

Part III

Confined shear-driven turbulent flows

Chapter 4

Turbulent lid-driven cubical cavity flow

Large-eddy simulations of the turbulent flow in a lid-driven cubical cavity have been carried out at a Reynolds number of 12 000 using the Legendre spectral element method introduced in Chapter 2. Two distinct subgrid-scales models, namely a dynamic Smagorinsky model and a dynamic mixed model, have been both implemented and used to perform long-lasting simulations required by the relevant time scales of the flow. All filtering levels make use of explicit filters applied in the physical space (on an element-by-element approach) and spectral (modal) spaces. The two subgrid-scales models are validated and compared to available experimental and numerical reference results, showing very good agreement. Specific features of lid-driven cavity flows in the turbulent regime, such as inhomogeneity of turbulence, turbulence production near the downstream corner eddy, small-scales localization and helical properties are investigated and discussed in the large-eddy simulation framework. Time histories of quantities such as the total energy, total turbulent kinetic energy or helicity exhibit different evolutions but only after a relatively long transient period. However, the average values remain extremely close.

4.1 Introduction

The study of a lid-driven flow of a Newtonian fluid in a rectangular three-dimensional cavity is of particular interest in view not only of the simplicity of the flow geometry but also the richness of the fluid flow physics manifested by multiple counter-rotating recirculating regions at the corners of the cavity depending on the Reynolds number, Taylor–Görtler-like (TGL) vortices, flow bifurcations and transition to turbulence. This flow structure is now well documented thanks to a relatively rich literature reporting both computational and experimental studies [6–9, 26, 47–50, 132, 144, 145, 148, 153–155, 201, 202]. Additionally, a comprehensive review of the fluid mechanics of driven cavities is provided by Shankar & Deshpande [225].

In the present chapter, our focus resides in relatively high-Reynolds-number and three-dimensional lid-driven cubical cavity flows. At Reynolds number higher than a critical value comprised between 2 000 and 3 000, an instability appears in the vicinity of the downstream corner eddy [7, 132, 153]. As the Reynolds number further increases, turbulence develops near the cavity walls, and at Reynolds number higher than 10 000, the flow near the downstream corner eddy becomes fully turbulent. The highest Reynolds number attained was 12 000 by direct numerical simulation (DNS) performed by Leriche & Gavrilakis [155] and 10 000 experimentally by Koseff & Street [144, 145] and Prasad & Koseff [201, 202]. In the literature, papers using the lid-driven cavity problem as a benchmark test case to evaluate the performance of numerical algorithms are proliferating, but are often limited to two space dimensions or to Reynolds numbers below 10 000. More recently, one may however notice the important developments of novel and more physical numerical methods applied to the lid-driven cavity flow such as molecular dynamics by Chen & Lin [46] and also the lattice–Boltzmann model applied by He *et al.* [114].

The results reported in this chapter correspond to the numerical simulation of the flow in a lid-driven cubical cavity at the Reynolds number of 12 000 placing us in the locally-turbulent regime. The spatial discretization relies on spectral element methods (SEM) which have been mainly applied to the DNS of fluid flow problems at low and moderate Reynolds numbers. With the advent of more powerful computers, especially through cluster technology, higher Re values seem to fall within the realm of feasibility. However, despite their high accuracy, spectral element methods are still far from reaching industrial applications that involve developed turbulence at Re values of the order of $10^6 - 10^7$. The reason for that dismal performance is that a resolved DNS including all scales from the largest structures to Kolmogorov scales, needs a number of degrees of freedom that grows like $Re^{9/4}$. Therefore with increasing Re, one has to increase the number of elements E , and the degree N of the polynomial spaces. This places the computational load far out of the reach of present day computers. Large-eddy simulation (LES) represents an alternative to DNS insofar that it involves less degrees of freedom because the behavior of the small scales are modeled. The numerical simulations presented in this chapter encompass two different LES based on two distinct subgrid-scales modeling both using an eddy-viscosity assumption, and one

using in addition a mixed model relying on the scale-similarity hypothesis, similarly to Zang *et al.* [271, 272] for $Re = 10\,000$. Compared to the previous works of Zang *et al.* [271, 272], the two LES reported in this chapter offer simulation length ten times larger therefore increasing the accuracy of the ensemble averaging and more importantly allowing to capture intermittent turbulent production. These events lead to the determination of large eddies suggested to be mainly responsible for the turbulence production near the downstream corner eddy.

Unlike low-order methods such as finite volumes or finite differences, spectral and spectral element methods allow a complete decoupling between the mathematical formulation, the subgrid modeling, the numerical technique and the filtering technique, which are introduced successively in Sec. 4.2. Specifically, we are first seeking to validate the two subgrid-scale models introduced in Sec. 4.2 which rely on explicit filtering techniques specific to spectral element spatial discretization. Sec. 4.3 presents a short, but comprehensive validation procedure. In Sec. 4.4 emphasis is put on characterizing the turbulent flow in its locally-turbulent regime. Fundamental features are qualitatively and quantitatively investigated such as the inhomogeneity of the turbulence, the turbulence production in the downstream-corner-eddy region, the small-scales turbulent structures in the cavity flow and finally the peculiar helical properties.

4.2 The model and numerical technique

4.2.1 Mathematical modeling

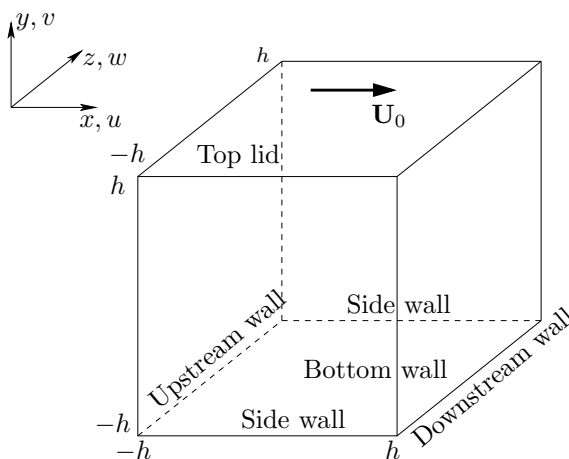


Fig. 4.1: Sketch of the geometry of the lid-driven cubical cavity.

The fluid enclosed in the cavity is assumed to be incompressible, Newtonian with uniform density and temperature. The flow is governed by the Navier–Stokes equations (2.1)–(2.2) inside the fluid domain denoted by $\mathcal{V} = [-h, +h]^3$, with no-slip boundary conditions on every cavity walls, except on the top, see Fig. 4.1. The flow is driven by imposing a prescribed velocity distribution with nonzero mean on the “top” wall—named lid in the sequel—with the velocity field maintained everywhere parallel to a given direction. The details regarding the imposition of this Dirichlet boundary condition for the velocity field at the lid is discussed in Sec. 4.2.3.3. As the flow presents turbulent zones coexisting with laminar regions, the numerical simulation incorporates the mathematical models involved by the large-eddy simulation method in order to resolve the complex dynamics of the flow. As a consequence, the governing equations of the large-eddy simulations are the filtered Navier–Stokes equations. Large-scale quantities, designated in the sequel by an “overbar”, are obtained by a filtering procedure on the computational domain $\hat{\mathcal{V}} = [-1, +1]^3$ using h for the non-dimensionalization of lengths. Such a filtering procedure relies on the definition of a convolution kernel \mathcal{G} , which is characteristic of the filter used. For any vector function \mathbf{u} , its spatially filtered or resolved part reads

$$\bar{\mathbf{u}}(\mathbf{x}, t) = \mathcal{G} \star \mathbf{u} = \int_{\mathcal{V}} \mathbf{u}(\mathbf{x}', t) \mathcal{G}(\mathbf{x} - \mathbf{x}') d^3 \mathbf{x}'. \quad (4.1)$$

The application of a low-pass inhomogeneous and anisotropic spatial filter to the Navier–Stokes equations in

the Eulerian velocity–pressure formulation and in convective form for the nonlinear term yields

$$\frac{\partial \bar{\mathbf{u}}}{\partial t} + \bar{\mathbf{u}} \cdot \nabla \bar{\mathbf{u}} = -\nabla \bar{p} + \nu \Delta \bar{\mathbf{u}} - \nabla \cdot \boldsymbol{\tau}, \quad (4.2)$$

$$\nabla \cdot \bar{\mathbf{u}} = 0, \quad (4.3)$$

in which $\bar{\mathbf{u}}$ is the filtered velocity field, t denotes the time, $\bar{p} = \bar{P}/\rho$ is the filtered static pressure and ν the assuredly constant, uniform kinematic viscosity. The symbols ∇ and Δ represent the nabla and Laplacian operators, respectively. The subgrid-scale (SGS) stress tensor $\boldsymbol{\tau}$ is given by

$$\boldsymbol{\tau} = \overline{\mathbf{u}\mathbf{u}} - \bar{\mathbf{u}}\bar{\mathbf{u}}, \quad (4.4)$$

and accounts for the effects of the unresolved- or small-scales on the dynamics of the resolved- or large-scales [213].

4.2.2 Subgrid-scale models

4.2.2.1 Under-resolved direct numerical simulation

In the same framework as it prevails among the practioners, one can resort to the DNS computations without any LES model, but with the nodal filtering technique described in Sec. 4.2.4.1 to let the numerical method dissipate locally the high-wave-number modes introduced by the insufficient space discretization. Such an approach corresponds to an under-resolved DNS (UDNS).

4.2.2.2 Smagorinsky model

The Smagorinsky model (SM) first introduced by Smagorinsky in 1963 [232] for meteorological applications, uses the concept of turbulent viscosity and assumes that the small scales are in equilibrium, balancing energy production and dissipation. This yields the following expression for the subgrid viscosity

$$\nu_{\text{sgs}} = (C_S \bar{\Delta})^2 |\bar{\mathbf{S}}|, \quad (4.5)$$

where $|\bar{\mathbf{S}}| = (2\bar{S}_{ij}\bar{S}_{ij})^{1/2}$ is the magnitude of the filtered rate-of-strain tensor with

$$\bar{S}_{ij} = \frac{1}{2} \left(\frac{\partial \bar{u}_i}{\partial x_j} + \frac{\partial \bar{u}_j}{\partial x_i} \right), \quad (4.6)$$

C_S is the Smagorinsky constant and $\bar{\Delta}$ the filter width. The Smagorinsky model has several drawbacks. The most severe one is the constant value of C_S during the computation which produces too much dissipation. Furthermore the SM does not provide the modeler with backscattering where kinetic energy is transferred from small scales to larger scales in an inverse-cascading process.

4.2.2.3 Dynamic Smagorinsky model

The dynamic Smagorinsky model (DSM) proposed by Germano *et al.* [88] overcomes the difficulty of constant C_S , by allowing it to become dependent of space and time. Now we have a dynamic parameter $C_d = C_d(\mathbf{x}, t)$. Let us introduce a test-filter length scale $\tilde{\Delta}$ that is larger than the grid length scale $\bar{\Delta}$ (*e.g.* $\tilde{\Delta} = 2\bar{\Delta}$). Using the information provided by those two filters and assuming that in the inertial range of the turbulence energy spectrum, the statistical self-similarity applies, we can better determine the features of the SGS stress. With the test filter, the former LES Eq. (4.2) yields a relation involving the subtest-scale stress tensor

$$\mathbf{T} = \widetilde{\mathbf{u}\mathbf{u}} - \tilde{\mathbf{u}}\tilde{\mathbf{u}}. \quad (4.7)$$

We introduce the Germano multiplicative identity to obtain the relation between \mathbf{T} and the filtered subgrid tensor $\tilde{\boldsymbol{\tau}}$ such that

$$\mathbf{L} = \mathbf{T} - \tilde{\boldsymbol{\tau}} = \widetilde{\mathbf{u}\mathbf{u}} - \tilde{\mathbf{u}}\tilde{\mathbf{u}}, \quad (4.8)$$

where the Leonard tensor \mathbf{L} is directly computed from the resolved fields. We apply the subgrid-viscosity model to $\boldsymbol{\tau}$ and \mathbf{T} , based on the same parameter C_d and we obtain using the self-similarity hypothesis for C_d

$$\boldsymbol{\tau}^d = -2C_d \overline{\Delta}^2 |\overline{\mathbf{S}}| \overline{\mathbf{S}} = C_d \boldsymbol{\beta}, \quad (4.9)$$

$$\mathbf{T}^d = -2C_d \widetilde{\Delta}^2 |\widetilde{\mathbf{S}}| \widetilde{\mathbf{S}} = C_d \boldsymbol{\alpha}, \quad (4.10)$$

where the superscript “d” denotes the deviatoric part of the tensor. Inserting (4.9) and (4.10) in the deviatoric part \mathbf{L}^d of \mathbf{L} produces

$$\mathbf{L}^d = C_d \boldsymbol{\alpha} - \widetilde{C}_d \widetilde{\boldsymbol{\beta}}. \quad (4.11)$$

Assuming that C_d does not vary too much over an interval of dimension at least equal to the test-filter length, one sets $\widetilde{C}_d \widetilde{\boldsymbol{\beta}} \approx C_d \widetilde{\boldsymbol{\beta}}$ and can deduce from a least-square minimization of the error related to (4.11) (see [156, 213]) that

$$C_d = \frac{(\boldsymbol{\alpha} - \widetilde{\boldsymbol{\beta}}) : \mathbf{L}^d}{(\boldsymbol{\alpha} - \widetilde{\boldsymbol{\beta}}) : (\boldsymbol{\alpha} - \widetilde{\boldsymbol{\beta}})}, \quad (4.12)$$

where the notation “:” is used for inner tensor product (double contraction).

4.2.2.4 Dynamic mixed model

The dynamic mixed model [272] introduced to tackle cavity flows is a blend of the mixed model of Bardina *et al.* [14] and the former dynamic Smagorinsky model. We notice that Bardina’s scale similarity model is not an subgrid-viscosity based model. Instead it belongs to the class of structural models [213] and relies on the scale-similarity principle. It produces almost no dissipation and for that reason needs to be used jointly with dissipative models such as the Smagorinsky model—Bardina’s mixed model—or with the dynamic Smagorinsky model. The approach of Zang *et al.* [272] was extended by Liu *et al.* [157] who proposed a new similarity subgrid-scale model for incompressible flows, in which the subgrid stress tensor is assumed to be proportional to the resolved stress tensor. Vreman *et al.* [263] later modified the DMM formulation to remove a mathematical inconsistency by expressing the scale-similarity part of the subtest-scale stress \mathbf{T} —see [35]—using only $\widetilde{\mathbf{u}}$. Salvetti & Banerjee [217] and Horiuti [126] extended the DMM to two distinct dynamic two-parameter models. Morinishi & Vasilyev [185] recommended a modification to the dynamic two-parameter mixed model of Salvetti & Banerjee [217] for large-eddy simulation of wall bounded turbulent flow. The works of Vreman *et al.* [264] and Winckelmans *et al.* [267] also closely relate to the DMM approach. As mentioned by Morinishi & Vasilyev [185] and Ghosal [92], the reliability of the results of large-eddy simulation is strongly affected by both the effectiveness of the subgrid scale model and the accuracy of the numerical method, particularly in the approximation of the non-linear convective term. As mentioned in Sec. 4.1, the SEM is decoupled from the subgrid modeling and offers a high accuracy characteristics of spectral methods. Therefore, the present work focuses on the one-parameter type of dynamic mixed model DMM as introduced by Zang *et al.* [272] for the lid-driven cavity flow. The modification suggested by Vreman *et al.* [263] was not implemented; *a priori* tests with their modified DMM using samples from the DNS results by Leriche & Gavrilakis [155] showed no noticeable improvement over the DMM of Zang *et al.* in the subgrid stress correlations. Therefore increasing the computational expense by adding an additional filtering level operation as required by the modification of Vreman *et al.* [263], seemed unjustified.

By decomposing the velocity field as

$$\mathbf{u} = \overline{\mathbf{u}} + \mathbf{u}', \quad (4.13)$$

where \mathbf{u}' represents the subgrid-scale velocity field and by inserting in Eq. (4.4), we can redefine the SGS stress as proposed by Germano [87]

$$\boldsymbol{\tau} = \mathcal{L} + \mathcal{C} + \mathcal{R}, \quad (4.14)$$

where

$$\begin{aligned} \mathcal{L} &= \overline{\mathbf{u}} \overline{\mathbf{u}} - \overline{\mathbf{u}} \overline{\mathbf{u}}, \\ \mathcal{C} &= \overline{\mathbf{u}} \mathbf{u}' + \mathbf{u}' \overline{\mathbf{u}} - (\overline{\mathbf{u}} \overline{\mathbf{u}'} + \overline{\mathbf{u}'} \overline{\mathbf{u}}), \\ \mathcal{R} &= \overline{\mathbf{u}' \mathbf{u}'} - \overline{\mathbf{u}'} \overline{\mathbf{u}'}, \end{aligned} \quad (4.15)$$

are designated as the modified Leonard stress, the SGS cross term, and the modified SGS Reynolds stress, respectively. The modified Leonard term can be calculated by resolved quantities and corresponds essentially to the mixed model. The two other terms are unresolved residual stresses and are treated through the Smagorinsky model. The dynamic procedure is applied to the parameter C_d to obtain a dynamic coefficient. Let us introduce

a test filter denoted again by a “tilde”. Applying the test filter to the Eq. (4.2), we generate the subtest-scale stress

$$\mathbf{T} = \widetilde{\mathbf{u}\mathbf{u}} - \widetilde{\mathbf{u}}\widetilde{\mathbf{u}} = \mathbf{L}^t + \mathbf{C}^t + \mathbf{R}^t, \quad (4.16)$$

with

$$\begin{aligned} \mathbf{L}^t &= \widetilde{\mathbf{u}\mathbf{u}} - \widetilde{\mathbf{u}}\widetilde{\mathbf{u}}, \\ \mathbf{C}^t &= \widetilde{\mathbf{u}\mathbf{u}'} + \mathbf{u}'\widetilde{\mathbf{u}} - (\widetilde{\mathbf{u}}\widetilde{\mathbf{u}'} + \widetilde{\mathbf{u}'}\widetilde{\mathbf{u}}), \\ \mathbf{R}^t &= \widetilde{\mathbf{u}'\mathbf{u}'} - \widetilde{\mathbf{u}'}\widetilde{\mathbf{u}'}. \end{aligned} \quad (4.17)$$

The deviatoric turbulent stress tensors related to the sub-grid and subtest filters are modeled by a mixed model as

$$\boldsymbol{\tau}^d = C_d \boldsymbol{\beta} + \mathcal{L}^d, \quad (4.18)$$

$$\mathbf{T}^d = C_d \boldsymbol{\alpha} + \mathbf{L}^{t,d}. \quad (4.19)$$

Substituting Eqs. (4.18) and (4.19) in Germano’s identity (4.8) and introducing the tensor \mathcal{G}

$$\mathcal{G} = \widetilde{\mathbf{u}\mathbf{u}} - \widetilde{\mathbf{u}}\widetilde{\mathbf{u}} = \mathbf{L}^t - \widetilde{\mathcal{L}}, \quad (4.20)$$

one can write the difference of the deviatoric parts of \mathcal{G} and \mathbf{L} —see Eq. (4.8)—as

$$\mathcal{G}^d - \mathbf{L}^d = C_d \boldsymbol{\alpha} - \widetilde{C}_d \boldsymbol{\beta}. \quad (4.21)$$

Eq. (4.21) being similar to Eq. (4.11)— \mathbf{L}^d being replaced by $\mathcal{G}^d - \mathbf{L}^d$, with the same assumptions, one can evaluate C_d following the same dynamic procedure as in Sec. 4.2.2.3 leading to the following expression

$$C_d = \frac{(\boldsymbol{\alpha} - \widetilde{\boldsymbol{\beta}}) : (\mathcal{G}^d - \mathbf{L}^d)}{(\boldsymbol{\alpha} - \widetilde{\boldsymbol{\beta}}) : (\boldsymbol{\alpha} - \widetilde{\boldsymbol{\beta}})}. \quad (4.22)$$

4.2.3 Numerical technique

4.2.3.1 Space discretization

The numerical method treats Eqs. (4.2)–(4.4) within the weak Galerkin formulation framework. The spatial discretization uses Lagrange–Legendre polynomial interpolants. The reader is referred to Chapter 2 and the monograph by Deville *et al.* [58] for full details. The velocity and pressure are expressed in the $\mathbb{P}_N - \mathbb{P}_{N-2}$ functional spaces where \mathbb{P}_N is the set of polynomials of degree lower than N in each space direction. This spectral element method avoids the presence of spurious pressure modes as it was proved by Maday & Patera [172, 174]. The quadrature rules are based on a Gauss–Lobatto–Legendre (GLL) grid for the velocity nodes and a Gauss–Legendre grid (GL) for the pressure nodes.

Borrowing the notation from Deville *et al.* [58], the semi-discrete filtered Navier–Stokes equations resulting from space discretization are

$$\mathbf{M} \frac{d\mathbf{u}}{dt} + \mathbf{C}\mathbf{u} + \nu \mathbf{A}\mathbf{u} - \mathbf{D}^T \bar{p} + \mathbf{D}_\tau \boldsymbol{\tau} = 0, \quad (4.23)$$

$$-\mathbf{D}\mathbf{u} = 0. \quad (4.24)$$

The diagonal mass matrix \mathbf{M} is composed of three blocks, namely the mass matrices M . The global vector \mathbf{u} contains all the nodal velocity components while \bar{p} is made of all nodal pressures. The matrices \mathbf{A} , \mathbf{D}^T , \mathbf{D} , \mathbf{D}_τ are the discrete Laplacian, gradient, divergence and tensor divergence operators, respectively. The matrix operator \mathbf{C} represents the action of the non-linear term written in convective form $\mathbf{u} \cdot \nabla$, on the velocity field and depends on \mathbf{u} itself. The semi-discrete equations constitute a set of non-linear ordinary differential equations (4.23) subject to the incompressibility condition (4.24).

4.2.3.2 Time integration

The state-of-the-art time integrators in spectral methods handle the viscous linear term and the pressure implicitly by a backward differentiation formula of order 2 (BDF2) to avoid stability restrictions such that

$$\nu \Delta t \leq C/N^4, \quad (4.25)$$

while all non-linearities are computed explicitly, by a second order extrapolation method (EX2), under the CFL restriction $\bar{u}_{\max} \Delta t \leq C/N^2$. Nonetheless, as the LES viscosity is not constant, we modify the standard time scheme in such a way that this space varying viscosity be handled explicitly as this was done *e.g.* [24, 35, 139]. Let us define the effective viscosity as

$$\nu_{\text{eff}} = \nu + \nu_{\text{sgs}} = \nu_{\text{cst}} + (\nu_{\text{eff}} - \nu_{\text{cst}}), \quad (4.26)$$

where ν_{cst} is the sum of the physical kinematic viscosity ν and the average of ν_{sgs} over the computational domain. The filtered semi-discrete Navier–Stokes equations become

$$\mathbf{M} \frac{d\bar{\mathbf{u}}}{dt} + \nu_{\text{cst}} \mathbf{A} \bar{\mathbf{u}} - \mathbf{D}^T \bar{p} = -\mathbf{C} \bar{\mathbf{u}} + 2\mathbf{D}_\tau (\nu_{\text{eff}} - \nu_{\text{cst}}) \bar{\mathbf{S}}, \quad (4.27)$$

$$-\mathbf{D} \bar{\mathbf{u}} = 0, \quad (4.28)$$

and the previous time splitting still applies. The viscous explicit term on the right-hand side does not harm stability as the magnitude of the term $2\mathbf{D}_\tau (\nu_{\text{eff}} - \nu_{\text{cst}}) \bar{\mathbf{S}}$ is less than that of $\mathbf{C} \bar{\mathbf{u}}$.

The implicit part is solved by a generalized block LU decomposition with a pressure correction algorithm [58, 196].

4.2.3.3 The lid-filtered velocity distribution

As already mentioned by Leriche & Gavrilakis [155], imposing a given velocity distribution on the lid of a cavity is neither an easy task experimentally nor numerically. Indeed imposing a constant lid velocity profile leads to a singularity (discontinuous behavior in the velocity boundary conditions) at the edges and at the corners of the lid, see Fig. 4.1. Without adequate treatment, this discontinuous behavior will undermine the convergence and the accuracy of any numerical method in the vicinity of the lid. For the two-dimensional case, a well known solution (but with no physical relevance) is to subtract the most singular terms of the analytical expression of the local stream-function expansion near the lid corners. The extension of such procedure to three-dimensional cases is still missing even though several recent attempts are reported, see [7, 96]. In order to explicitly filter the discontinuous behavior, the constant lid velocity profile is regularized by the use of a high-order polynomial expansion which vanishes along its first derivatives at the lid edges and corners

$$u(x, y = h, z, t) = U_0 \left[1 - (x/h)^{18} \right]^2 \left[1 - (z/h)^{18} \right]^2, \quad (4.29)$$

$$v(x, y = h, z, t) = w(x, y = h, z, t) = 0.$$

This profile flattens very quickly near the lid edges and corners while away from them, it grows rapidly to a constant value over a short distance. The exact form and the polynomial order of the profile is discussed [153, 155]. The highest polynomial order of this distribution in both x - and z -direction is 36. Such high-order polynomial expansions lead to steep velocity gradients in the vicinity of the edges of the lid. The grid refinement, in terms of spectral element distribution near the lid will be presented in greater details in Sec. 4.3. One of the constraint in the grid design is to ensure the proper resolution of the lid velocity distribution by the spectral element decomposition.

4.2.4 Filtering techniques

As spectral elements offer high spatial accuracy, we construct explicitly the filters using two spectral techniques. The first one is a nodal filter acting in physical space on the nodal velocity components (and pressure) to render the computations stable in the long range integration. The second method is designed as a modal filter and is carried out in spectral space in an element by element fashion. That filter corresponds specifically to the convolution kernel of the low-pass LES filtering.

4.2.4.1 Nodal filter

The nodal filter due to Fischer & Mullen [80] is adequately suited to parallel spectral element computation. Introducing $h_{N,j}, j = 0, \dots, N$ the set of Lagrange–Legendre interpolant polynomials of degree N based on the GLL grid nodes $\xi_{N,k}, k = 0, \dots, N$, the rectangular matrix operator I_N^M of size $(M+1) \times (N+1)$ is such that

$$(I_N^M)_{ij} = h_{N,j}(\xi_{M,i}). \quad (4.30)$$

Therefore, the matrix operator of order M

$$\Pi_M = I_M^N I_N^M, \quad (4.31)$$

interpolates on the GLL grid of degree M a function defined on the GLL grid of degree N and transfers the data back to the original grid. This process eliminates the highest modes of the polynomial representation. The one-dimensional (1D) filter is given by the relation

$$\bar{v} = [\alpha \Pi_M + (1 - \alpha) I_N^N] v. \quad (4.32)$$

The LES version of the filter sets $\alpha = 1$ and is given by

$$\bar{v} = I_M^N I_N^M v, \quad (4.33)$$

where M is equal to $N-2$ or $N-3$. The three-dimensional (3D) extension results easily from the matrix tensor product properties of the filter. It is worth noting that by construction such nodal filter constitutes a projective filter, *i.e.* $\bar{\bar{v}} = \bar{v}$.

4.2.4.2 Modal filter

Here, the variable u is approximated by a modal basis first proposed in the p -version of the finite elements and used by Boyd [38] as a filter technique. It is built up on the reference parent element as

$$\begin{aligned} \phi_0 &= \frac{1-\xi}{2}, & \phi_1 &= \frac{1+\xi}{2}, \\ \phi_k &= L_k(\xi) - L_{k-2}(\xi), & 2 \leq k \leq N. \end{aligned} \quad (4.34)$$

Conversely to the Lagrange–Legendre nodal basis used in our spectral element calculations, this modal basis (4.34) forms a hierarchical set of polynomials allowing to define in an explicit and straightforward manner a low-pass filtering procedure. The one-to-one correspondence between the nodal Lagrangian basis and the p -representation yields

$$v(\xi_i) = \sum_{k=0}^N \check{v}_k \phi_k(\xi_i), \quad (4.35)$$

which in matrix notation reads

$$\mathbf{v} = \Phi \check{\mathbf{v}}. \quad (4.36)$$

The low-pass filtering operation is performed in spectral space through a diagonal matrix \mathbb{K} with components such that

$$\mathcal{K}_0 = \mathcal{K}_1 = 1 \quad \text{and} \quad \mathcal{K}_k = \frac{1}{(1 + (k/k_c)^2)} \quad 2 \leq k \leq N, \quad (4.37)$$

where the cut-off value k_c corresponds to $\mathcal{K}_k = 1/2$. The entire filtering process for a one-dimensional problem is given by

$$\bar{\mathbf{v}} = \mathcal{G} \star \mathbf{v} = \Phi \mathbb{K} \Phi^{-1} \mathbf{v}. \quad (4.38)$$

The three-dimensional extension is again trivial by the matrix tensor product properties.

As noted by Blackburn & Schmidt [24], the effect of such modal filter onto a given field expanded in the modal basis (4.34) presents the interesting feature of maintaining the inter-element \mathcal{C}^0 -continuity. More rigorously, such \mathcal{C}^0 -continuity is enforced if and only if both ϕ_0 and ϕ_1 are not at all affected by the low-pass filtering, in other words if and only if $\mathcal{K}_0 = \mathcal{K}_1 = 1$. Nevertheless, it has been observed that such \mathcal{C}^0 -breakage does not constitute a major issue for our simulations as it only affects the subgrid viscosity field and other terms present into the modeling of the effect of the SGS tensor (4.4), and which are not used directly for constructing a solution retaining the \mathcal{C}^0 -continuity feature.

Such modal filter is invertible and consequently is not projective, *i.e.* $\bar{\bar{\mathbf{v}}} \neq \bar{\mathbf{v}}$.

4.2.4.3 The filter length

The decomposition of the computational domain into spectral elements of given sizes, within which a GLL distribution of grid points based on the polynomial degree is chosen, requires a specific definition of the filter length $\bar{\Delta}$. In order to account for both the size of each spectral element and its value of the polynomial order, and following [138], the filter length for a 1D spectral element method is chosen as

$$\bar{\Delta} = \frac{s}{p}, \quad (4.39)$$

where s is the element size and p the highest polynomial degree in the spectral decomposition Eq. (4.35) that is the closest to the cut-off frequency k_c . In the particular context of the modal filter previously introduced, p is such that

$$p = k, \text{ such that } \inf_k (\mathcal{K}_k) < \mathcal{K}_{k_c} = 1/2, \quad k = 0, \dots, N. \quad (4.40)$$

We notice that the filter length decreases when the element is refined. The straightforward extension of Eq. (4.39) to our 3D problem using rectilinear elements leads to

$$\bar{\Delta}(x, y, z) = (\bar{\Delta}_1(x)\bar{\Delta}_2(y)\bar{\Delta}_3(z))^{1/3} = \left(\frac{s_1}{p_1} \frac{s_2}{p_2} \frac{s_3}{p_3} \right)^{1/3}. \quad (4.41)$$

4.3 Physical and computational parameters

The different large-eddy simulations presented in this chapter refer to the same geometry—see Fig. 4.1—and physical parameters as the direct numerical simulation (DNS) performed by Leriche & Gavrilakis [155]. The details relative to these parameters are gathered in Table 4.1. The Reynolds number based on the maximum velocity on the lid was chosen to be $\text{Re} = U_0 2h/\nu = 12\,000$.

The kinetic energy is provided to the flow by the shear stress at the top lid through viscous diffusion. The amplitude of the Reynolds stress below the lid is negligible indicating that the flow under the lid is mainly laminar but transient. The momentum transfer from the lid induces a region of strong pressure in the upper corner of the downstream wall as the flow, mainly horizontal prior the corner, has to change direction and moves vertically downwards. This sharp turn dissipates energy in that region. Along the downstream wall the plunging flow behaves like a wall jet with a variable thickness. Near the symmetry plane the jet thickness is reduced while it increases away from this plane. This jet, laminar and unsteady at the very beginning, separates from the cavity wall at mid-height and grows as two elliptical jets on both sides of the symmetry plane. They hit the bottom wall where they produce turbulence. This turbulence is convected away by the main central vortex towards the upstream wall where the flow slows down and relaminarizes during the fluid rise.

| | |
|---|--------------------|
| Domain size (x, y, z) | $(2h, 2h, 2h)$ |
| Wall positions | $x, y, z = \pm h$ |
| Reynolds number $\text{Re} = U_0 2h/\nu$ | 12 000 |
| No. of spectral elements (E_x, E_y, E_z) | (8, 8, 8) |
| Polynomial orders (N_x, N_y, N_z) | (8, 8, 8) |
| Time-step | $0.002 h/U_0$ |
| No. of time iterations | 387 000 |
| Dynamic range | $774h/U_0$ |
| Nodal filtering – DSM & DMM | $M = N - 2 = 6$ |
| Modal filtering – DSM & DMM (1 st level) | $k_c = N - 2 = 6$ |
| Modal filtering – DSM & DMM (2 nd level) | $k'_c = N - 3 = 5$ |

Table 4.1: Numerical and physical parameters of the simulations.

In order to resolve the boundary layers along the lid and the downstream wall, the spectral elements are unevenly distributed as can be seen in Fig. 4.2. The spatial discretization has $E_x = E_y = E_z = 8$ elements in the three space directions with $N_x = N_y = N_z = 8$ polynomial degree, equivalent to 65^3 grid points in total. The spectral element calculation has two times less points per space direction than the DNS of Leriche & Gavrilakis [155] who employed a 129^3 Chebyshev discretization. Both nodal and modal filters were used in our LES computations based on DSM and DMM; the former with $M = N - 2$ to stabilize the velocity

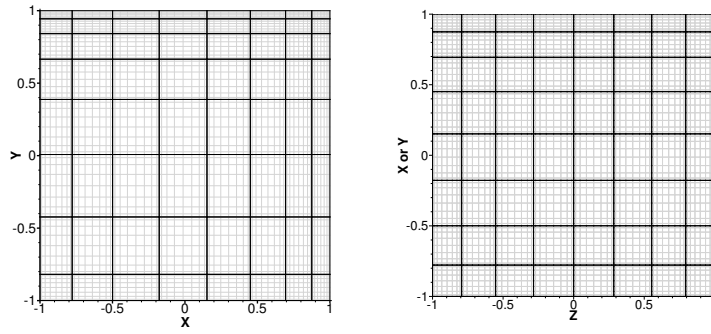


Fig. 4.2: Left: Spectral element grid in any plane normal to z ; Right: Spectral element grid in any plane normal to x or y .

field at each time-step and the latter with $k_c = N - 2$ (resp. $k'_c = N - 3$) to filter the highest modes in the modal Legendre space at the first level (resp. second level) of explicit filtering. These filtering levels refer to the overbar and the test filtering respectively. It is noteworthy recalling here that the modal filter introduced in Sec. 4.2.4 and associated with the transfer function given by Eq. (4.37), is not projective. The computations are particularly sensitive to the values of M and k_c ; smaller values will affect spectral convergence whereas higher values will have very little effect on the smallest scales of the problem. The reference results are the DNS data of Leriche [153, 155] and the experimental ones from Koseff & Street [144], corresponding to 1000 and 145.5 time units respectively. In the cavity flow, the average is obtained by time averaging.

The LES-DSM and LES-DMM were both started from the same initial condition, namely the velocity field obtained from the DNS by Leriche and Gavrilakis and re-interpolated from the Chebyshev grid onto the spectral-element GLL grid.

Non-dimensionalization is performed using h as length scale, h/U_0 as time scale and U_0 as velocity scale. All the results and data presented in the sequel will be based on this non-dimensionalization.

4.3.1 Statistical ensemble averaging

For any variable, the Reynolds statistical splitting introduces the average value denoted into brackets “ $\langle \cdot \rangle$ ” whereas the associated fluctuating part is denoted using the following superscript \diamond . It is noteworthy reminding here the filter splitting introduced in Eq. (4.13) using the overbar and prime notations to denote respectively the resolved and subgrid scales. To simplify notations, and unless otherwise stated, the overbar will be omitted in the sequel as most of the fields considered are resolved fields derived from solutions of the filtered Navier–Stokes equations (4.2)–(4.4). More precisely considering any variable \mathbf{x} can be decomposed as follows

$$\mathbf{x} = \bar{\mathbf{x}} + \mathbf{x}' = \langle \bar{\mathbf{x}} \rangle + \langle \mathbf{x}' \rangle + \bar{\mathbf{x}}^\diamond + \mathbf{x}'^\diamond, \quad (4.42)$$

where $\langle \bar{\mathbf{x}} \rangle$ (resp. $\langle \mathbf{x}' \rangle$) is the average resolved (resp. subgrid) part of \mathbf{x} and $\bar{\mathbf{x}}^\diamond$ (resp. \mathbf{x}'^\diamond) is the fluctuating resolved (resp. subgrid) part of \mathbf{x} . The subgrid scales being unknown, the term $\langle \mathbf{x}' \rangle + \mathbf{x}'^\diamond$ cannot be directly computed from the simulation. All the results presented in this chapter refer to resolved quantities be them average $\langle \bar{\mathbf{x}} \rangle$ or fluctuating $\bar{\mathbf{x}}^\diamond$. For the sake of simplicity, these quantities are directly and respectively compared to $\langle \mathbf{x} \rangle$ and \mathbf{x}^\diamond , obtained from reference results, see Sec. 4.3.3.

We assume that a statistically-steady state is attained and time averaging will be taken as ensemble averaging. The whole dynamic range—cf. Table 4.1— corresponding to 1290 equally spaced samples has been considered when averaging. As the starting point of all LES is the same DNS sample taken from a statistically-steady state, it is reasonable to also assume that these simulations will reach a statistically-steady state very quickly. These assumptions can be verified in several number of ways. First, we present in Fig. 4.3 the time histories of the volume integral of the total kinetic energy of the resolved field

$$Q(\bar{\mathbf{u}}) = \frac{1}{2} \int_{\mathcal{V}} \bar{\mathbf{u}} \cdot \bar{\mathbf{u}} d\mathcal{V}, \quad (4.43)$$

and the volume integral of the kinetic energy of the fluctuating resolved field $Q(\bar{\mathbf{u}}^\diamond)$ for the DNS and both the LES-DSM and LES-DMM. On this figure, one can observe that after approximately $80 h/U_0$ time units, the

two LES models DSM and DMM start being effective and providing different macroscopic results. Both $Q(\bar{\mathbf{u}})$ and $Q(\bar{\mathbf{u}}^\diamond)$ have different time evolutions but within the same range of fluctuations and with very close average values, see Table 4.2.

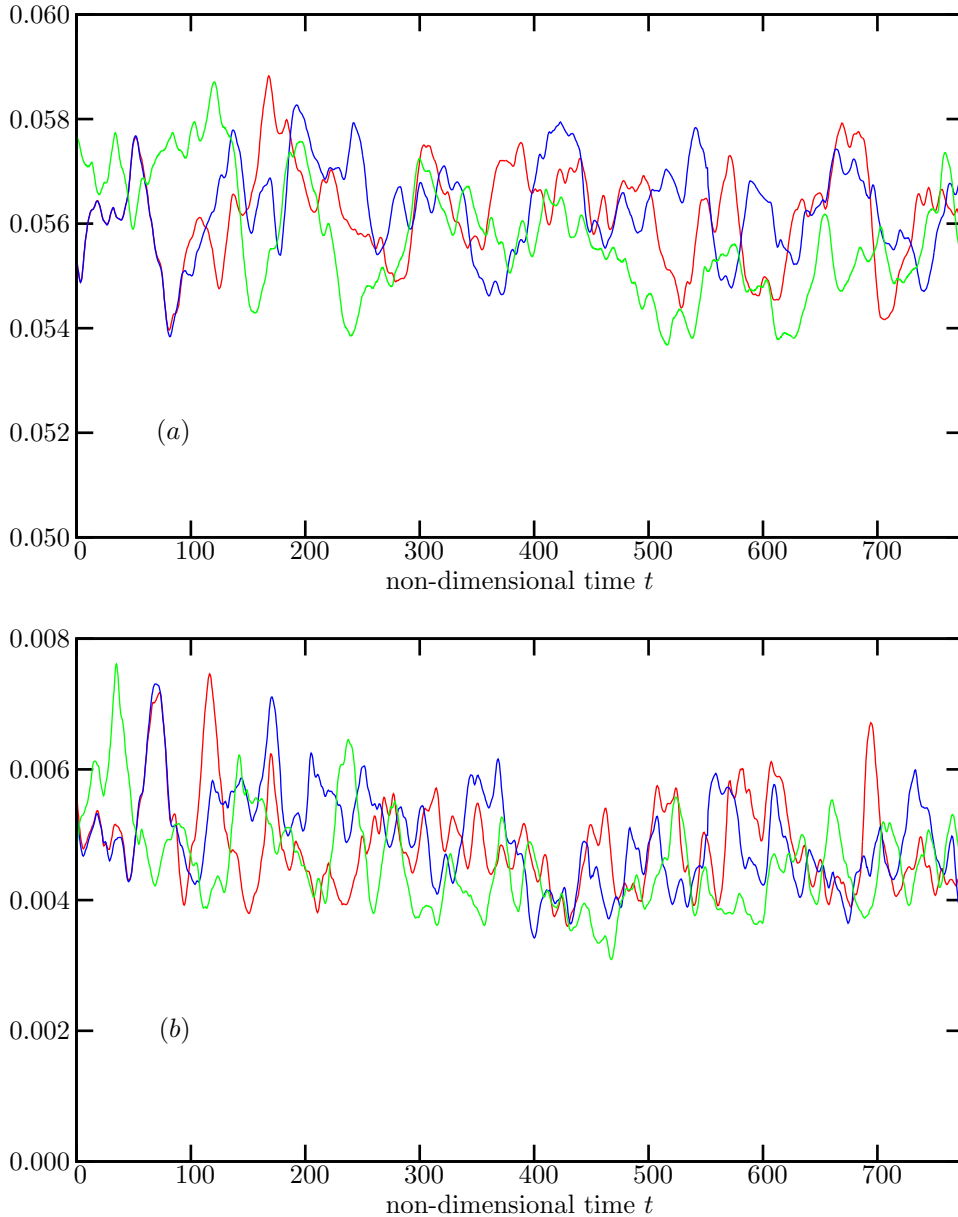


Fig. 4.3: Time histories of $Q(\bar{\mathbf{u}})$ (graphs (a): top) and of $Q(\bar{\mathbf{u}}^\diamond)$ (graphs (b): bottom) for the DNS (green lines), the LES-DSM (red lines) and the LES-DMM (blue lines).

A second way to assess the accuracy of the ensemble averaging is done by testing the property of statistical symmetry (resp. antisymmetry) with respect to the mid-plane $z/h = 0$, of some first- and second-order statistics of the resolved velocity and pressure fields. For each grid point, the relative difference between the nodal value at this point and the corresponding nodal value at the symmetric grid point is calculated. In the antisymmetric case, the opposite nodal value is considered at the symmetric grid point. The z -component of the average resolved velocity field $\langle w \rangle$ is the only field presented being statistically antisymmetric with respect to the mid-plane $z/h = 0$. The results of the maximum errors on the grid are gathered in Table 4.3 and are showing to be of the order of the error introduced by the space and time discretizations.

4.3.2 Under-resolved DNS and Smagorinsky model

Before providing the reader with a comprehensive review of results obtained for the two models LES-DSM and LES-DMM, partial results for the UDNS and the LES-SM are presented in this section. These results

| Average integral terms | Magnitude in U_0^2 units |
|---|----------------------------|
| $\langle Q(\bar{\mathbf{u}}) \rangle_{\text{DNS}}$ | 0.055527 |
| $\langle Q(\bar{\mathbf{u}}) \rangle_{\text{DSM}}$ | 0.056296 |
| $\langle Q(\bar{\mathbf{u}}) \rangle_{\text{DMM}}$ | 0.056194 |
| $\langle Q(\bar{\mathbf{u}}^\diamond) \rangle_{\text{DNS}}$ | 0.004529 |
| $\langle Q(\bar{\mathbf{u}}^\diamond) \rangle_{\text{DSM}}$ | 0.004960 |
| $\langle Q(\bar{\mathbf{u}}^\diamond) \rangle_{\text{DMM}}$ | 0.004864 |

Table 4.2: Average values of $Q(\bar{\mathbf{u}})$ and $Q(\bar{\mathbf{u}}^\diamond)$ for the DNS, LES-DSM and LES-DMM.

| Variable | Rel. diff. DSM | Rel. diff. DMM | Anti-/Symmetry |
|---|----------------|----------------|----------------|
| $\langle u \rangle$ | 4.807e-04 | 6.696e-05 | S |
| $\langle v \rangle$ | 4.591e-04 | 3.014e-04 | S |
| $\langle w \rangle$ | 6.966e-05 | 4.129e-04 | A |
| $\langle p \rangle$ | 1.120e-04 | 7.333e-05 | S |
| $\langle u^{\diamond 2} \rangle^{1/2}$ | 8.758e-05 | 8.899e-05 | S |
| $\langle v^{\diamond 2} \rangle^{1/2}$ | 1.696e-03 | 7.764e-04 | S |
| $\langle w^{\diamond 2} \rangle^{1/2}$ | 4.501e-04 | 8.447e-05 | S |
| $\langle u^\diamond v^\diamond \rangle$ | 1.107e-04 | 2.236e-04 | S |

Table 4.3: Quantitative assessment of the statistical symmetry and anti-symmetry properties of some resolved average fields in the cavity; “Rel. diff.” stands for maximum relative difference.

correspond to the same parameters as those in Table 4.1, except that the number of iterations is 33 000 corresponding to a simulation length of $66 h/U_0$ —approximately one tenth of the total simulation time of the LES-DSM and LES-DMM. Despite the shorter dynamic range, a relative good level of statistical symmetry is achieved—approximately one order less than those reported in Tab. 4.3. Moreover, for the LES-SM the value of the Smagorinsky constant C_S defined in Eq. (4.5) was taken equal to its theoretical value 0.18, see [213] for greater details, and no wall-damping procedure was implemented for these preliminary simulations. The reference result is the DNS by Leriche & Gavrilakis [155] and is represented by the solid line in the profiles in Figs. 4.4–4.5, whereas dashed (resp. dotted) lines refer to the UDNS (resp. LES-SM). The results in Figs. 4.4–4.5 are one-dimensional profiles of the average velocity field and its rms-fluctuations in the mid-plane $z/h = 0$. General conclusions can be drawn from all these figures. First, UDNS is totally inoperative in the particular context of this simulation. Even first-order statistics such as $\langle u \rangle$ and $\langle v \rangle$ are far from being well predicted, not to mention rms-fluctuations. Second, the Smagorinsky model LES-SM results show a real improvement in predicting the fields compared to the UDNS but as already known, the simplicity of this model does not allow to correctly predict the stiff physics of this simulation. These results justify the need for a more complex LES modeling such as LES-DSM and LES-DMM presented in the sequel.

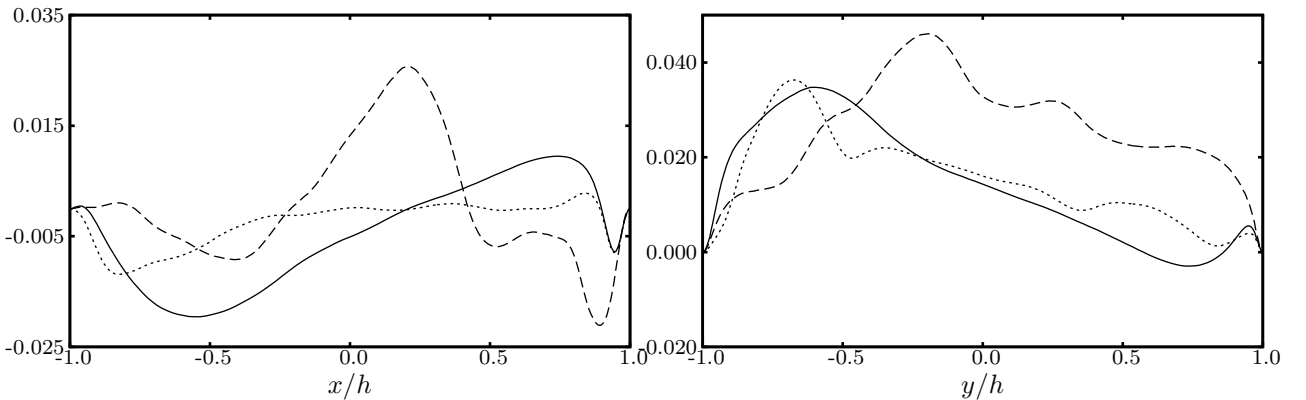


Fig. 4.4: In the mid-plane $z/h = 0$: $\langle u \rangle$ on the horizontal centerline $y/h = 0$ (top), $\langle v \rangle$ on the vertical centerline $x/h = 0$ (bottom): DNS (solid line), UDNS (dashed line) and LES-SM (dotted line).

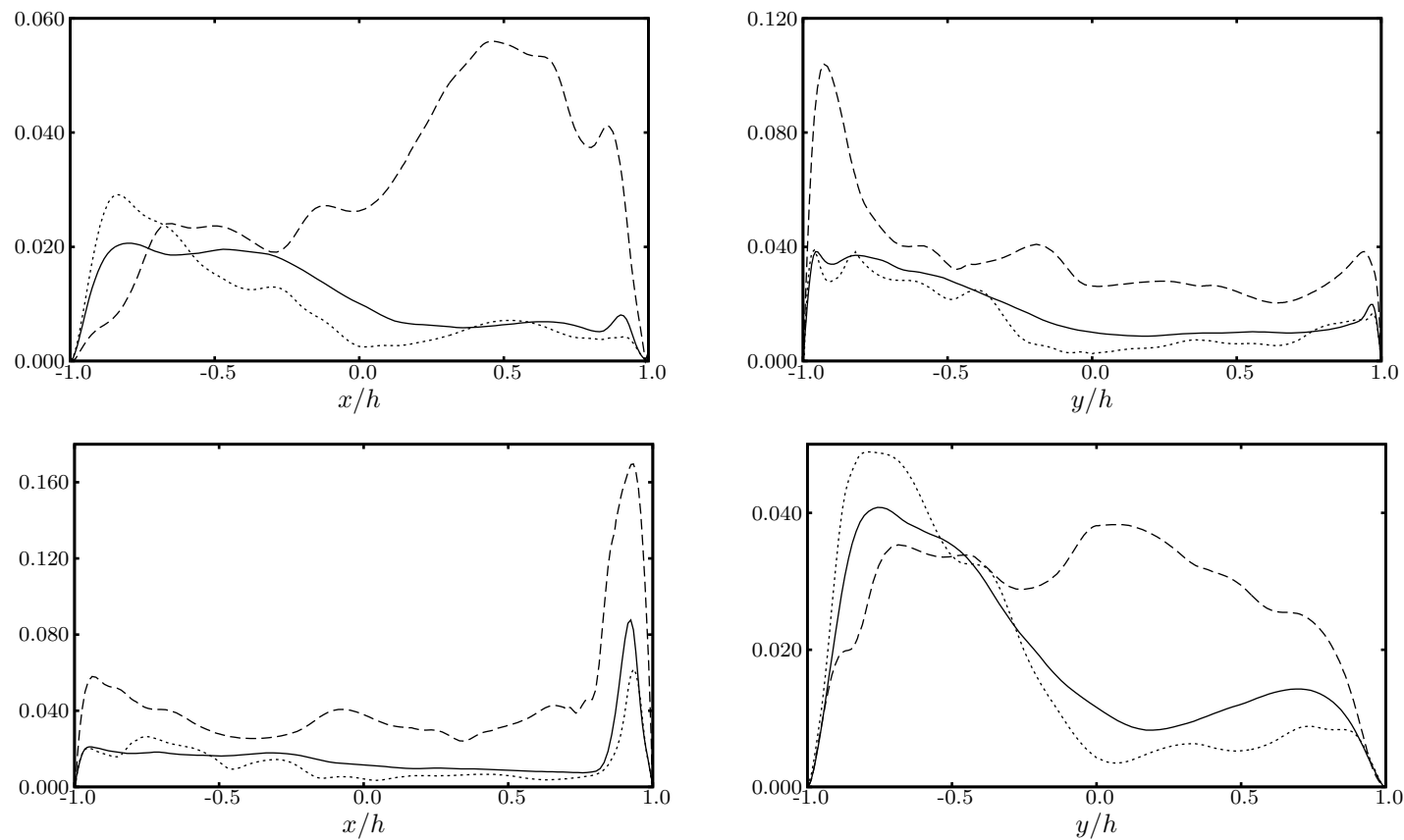


Fig. 4.5: In the mid-plane $z/h = 0$: $\langle u^{\circ 2} \rangle^{1/2}$ (top row) and $\langle v^{\circ 2} \rangle^{1/2}$ (bottom row), on the horizontal centerline $y/h = 0$ (left column) and on the vertical centerline $x/h = 0$ (right column): DNS (solid line), UDNS (dashed line) and LES-SM (dotted line).

4.3.3 Comparisons with available results

In this section, results of the LES-DSM and the LES-DMM are compared with the available reference experimental and numerical results.

4.3.3.1 One-dimensional profiles

Of the previous work available in the literature on the lid-driven cubical cavity flow, the numerical DNS data from Leriche & Gavrilakis [155], Leriche [154] and the experimental data of Prasad & Koseff [201] constitute the two main references. This work being an extension of the one by Leriche, it borrows from [155] the values of the main physical parameters—see Table 4.1. The work from Prasad & Koseff [201] includes data from a flow at Reynolds number similar to that of the present LES. The measurements that these authors reported were taken in the mid-plane $z/h = 0$, which is a statistical symmetry plane of the flow domain. As it will be shown in the sequel, the flow near the downstream secondary eddy—see Fig. 4.1—is not homogeneous in the z -direction. In the “turbulent” part of the cavity, the mid-plane is found to cut through surfaces of local minima in the intensity field with rapid changes occurring on both sides of it.

The set of experimental data corresponding to a Reynolds number $Re = 10\,000$ is used for the comparisons of the one-dimensional average velocity profiles along the vertical and horizontal symmetry axes. It is important to note that no experimental error-bars were given for any data. The only information related to the local experimental measurement error is provided by the two crosses corresponding to two different measurements in the middle ($x/h = 0$ or $y/h = 0$) of each centerline—the velocity probing system going back and forth from this point [200]. In addition the experimental data of Prasad & Koseff [200, 201] are obtained over a non-dimensional averaging time of 145.5 whereas the DNS (resp. LES) results were obtained over an averaging time of 1 000 (resp. 774). In absence of local error-bars in the measurements, this may explain the scattering (and possible non-convergence) of some experimental data, together with practical difficulties of accurately measuring fluctuating fields in region of low or almost constant velocity. A detailed analysis of the disparity between the numerical results and some experimental data can be found in [153, 155].

For the sets of experimental and DNS data, the total velocity field is considered whereas in the case of LES, only its resolved part is presented. The legend for Figs. 4.6–4.8 is as follows: crosses refer to the experimental data of Prasad and Koseff, the solid lines to the DNS by Leriche and Gavrilakis, the dashed lines to the LES-DSM and the dotted lines to the LES-DMM. All the data related to average and rms-fluctuations of the velocity field are expressed in terms of the velocity scale U_0 and $\langle u^\diamond v^\diamond \rangle$ in terms of U_0^2 .

A discussion on the comparisons between the DNS reference results and the experimental ones is available in [155]. In the sequel, we will focus on comparing the LES-DSM and LES-DMM results with the DNS and experimental ones. A rapid overview of Figs. 4.6–4.8 indicates that both LES models provide results very close to the DNS references, even for the rms-fluctuations in Fig. 4.7 and above all for the component $\langle u^\diamond v^\diamond \rangle$ of the Reynolds stress in Fig. 4.8. The differences between the profiles of the two LES models and the DNS generally coincide with the existence of local extrema; maxima tend to be slightly over-estimated in the LES whereas minima are somewhat under-estimated. These two effects can be partly justified by the reduced sampling in the LES-DSM and LES-DMM compared to the sampling of the DNS. This phenomenon have already been encountered and studied by Leriche [153]. From these results it is not possible to rank between themselves the performances of the LES-DSM and the LES-DMM.

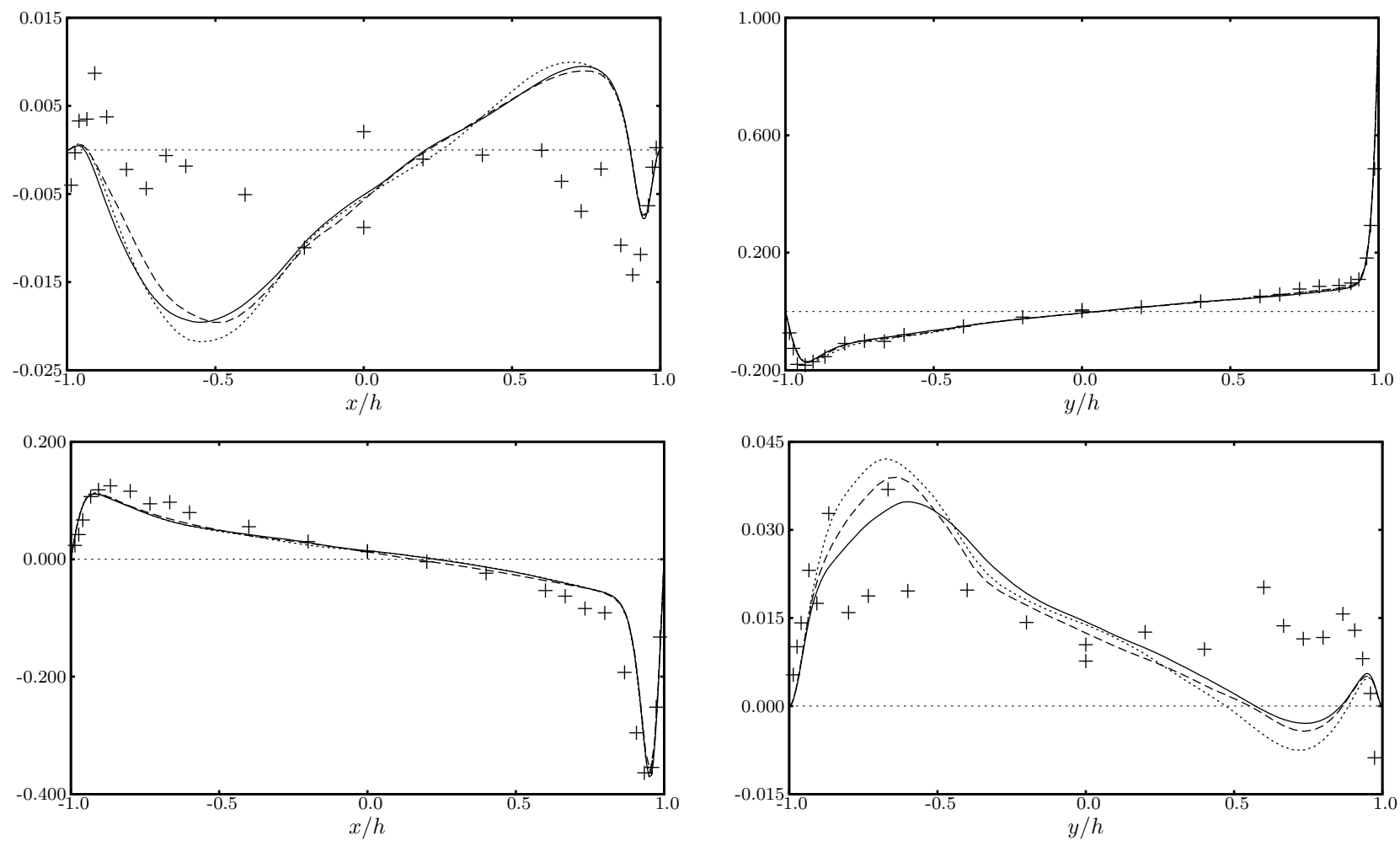


Fig. 4.6: In the mid-plane $z/h = 0$: $\langle u \rangle$ (top row) and $\langle v \rangle$ (bottom row), on the horizontal centerline $y/h = 0$ (left column) and on the vertical centerline $x/h = 0$ (right column); Experiment (crosses), DNS (solid line), LES-DSM (dashed line), LES-DMM (dotted line).

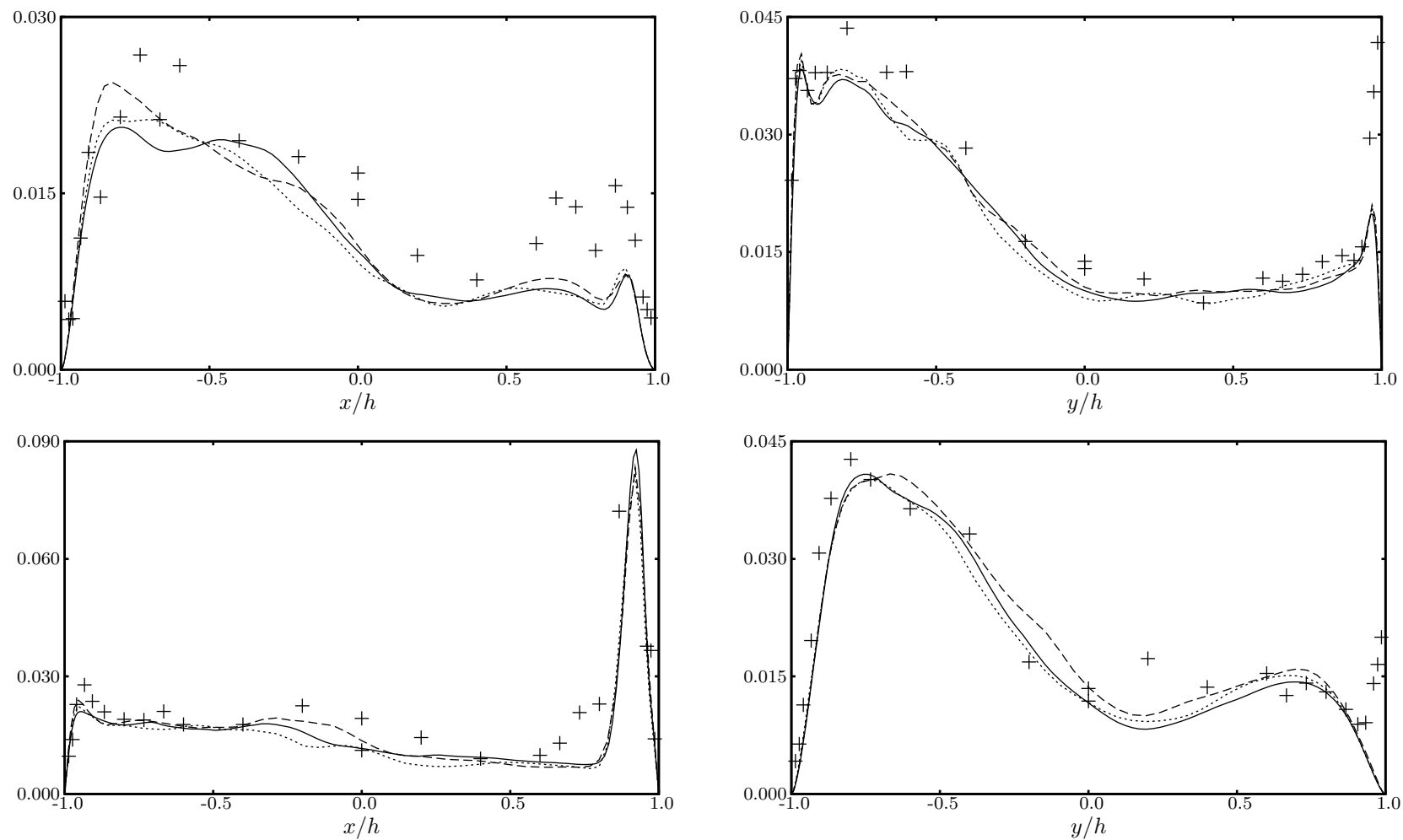


Fig. 4.7: In the mid-plane $z/h = 0$: $\langle u^{\circ 2} \rangle^{1/2}$ (top row) and $\langle v^{\circ 2} \rangle^{1/2}$ (bottom row), on the horizontal centerline $y/h = 0$ (left column) and on the vertical centerline $x/h = 0$ (right column); Experiment (crosses), DNS (solid line), LES-DSM (dashed line), LES-DMM (dotted line).

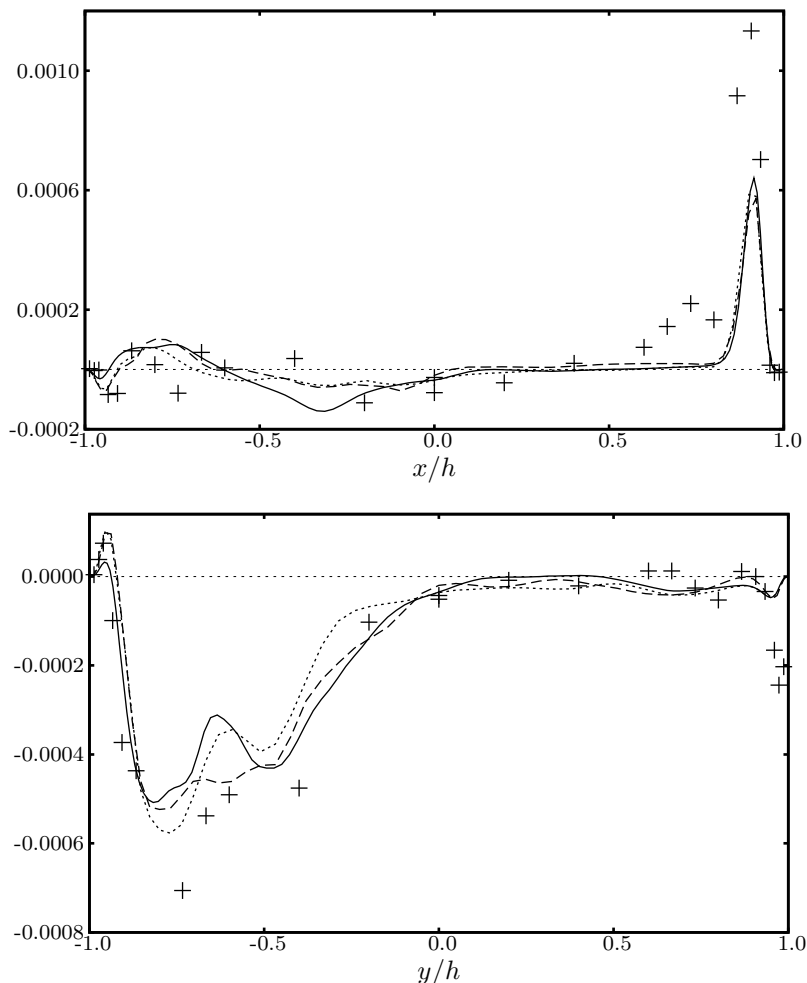


Fig. 4.8: In the mid-plane $z/h = 0$: $\langle u^\diamond v^\diamond \rangle$ on the horizontal centerline $y/h = 0$ (top), $\langle u^\diamond v^\diamond \rangle$ on the vertical centerline $x/h = 0$ (bottom); Experiment (crosses), DNS (solid line), LES-DSM (dashed line), LES-DMM (dotted line).

4.3.3.2 Two-dimensional profiles

The comparisons with the DNS results started in Sec. 4.3.3.1 are now extended to the whole mid-plane $z/h = 0$ by plotting identical series of contour levels of average velocity components in Fig. 4.9 and of rms-fluctuations of the velocity in Fig. 4.10, for the DNS (left column), the LES-DSM (central column) and the LES-DMM (right column).

As previously noted with the one-dimensional profiles, the results provided by the LES-DSM and LES-DMM are both very close to the reference DNS results. Secondary corner eddies located above the bottom wall and below the lid next to the upstream wall are correctly captured in the mean flow. Other finer structures visible in Fig. 4.10 (bottom), for $\langle v^{\diamond 2} \rangle^{1/2}$ near the upstream wall are also correctly captured by both LES modelings. The rms-fluctuations of the x -component u of the velocity field is accurately resolved just below the lid which is a high-gradient region for the mean flow. Moreover, in the region near the downstream wall where the wall jet—separated into two elliptical jets—are impinging on the bottom wall, the high gradients of velocity fluctuations are well reproduced. As it will be presented in the following sections, the maximum of turbulence production belongs to this region of the flow domain which will be indeed of particular interest in the remaining.

The flow below the lid and near the corner with the downstream wall presents wiggles in the LES contours for $\langle v \rangle$, see Fig. 4.9 (bottom). Although less intense, these wiggles are also noticeable on the contours for $\langle v^{\diamond 2} \rangle^{1/2}$ at the same location, see Fig. 4.10 (bottom). More limited effects are noticeable for the equivalent x -component fields. These very limited defects in both simulations find their origin in a slight under-resolution of the spectral-element grid in this small region of the cavity where high gradients are present.

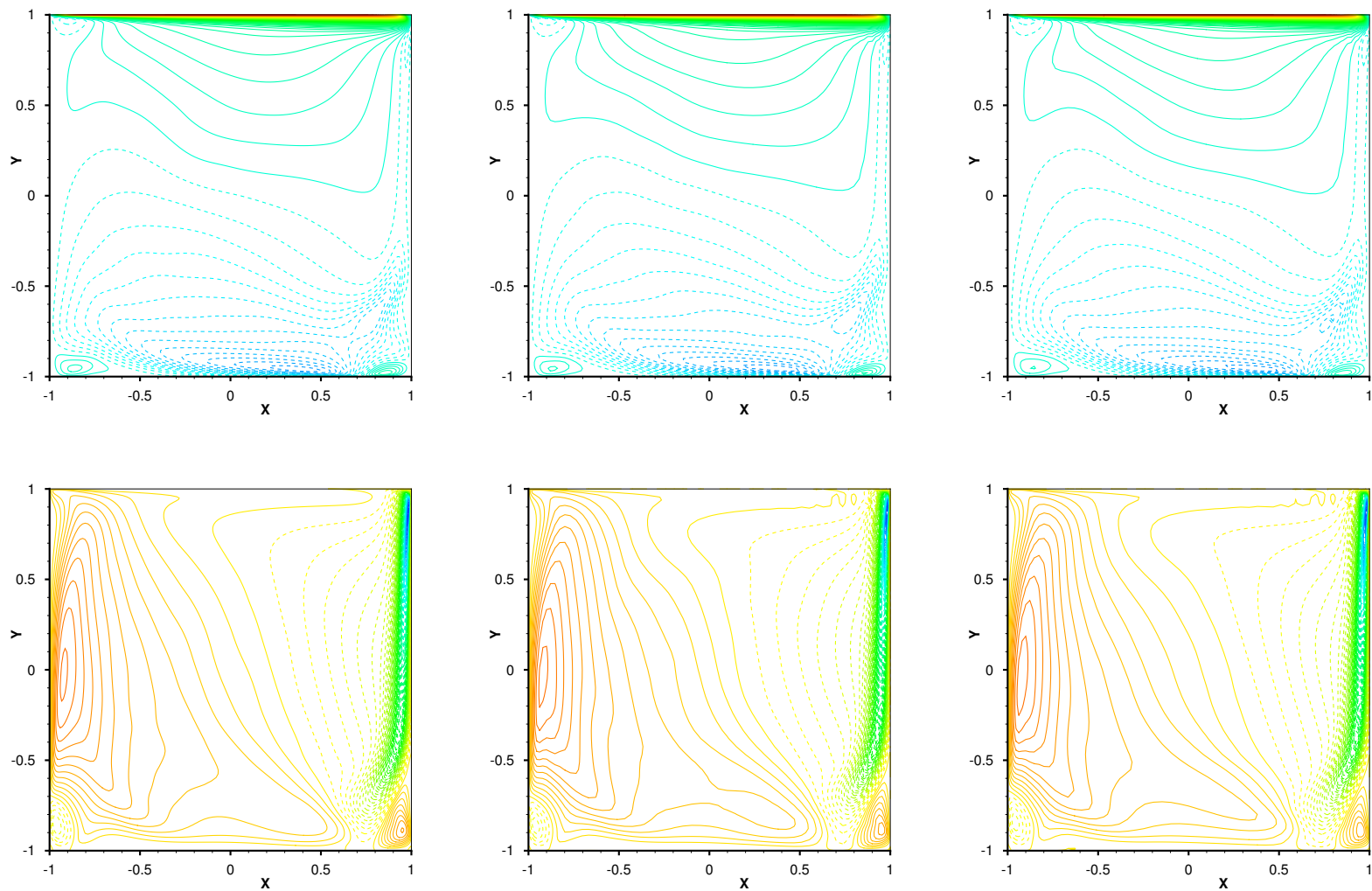


Fig. 4.9: Contours of average velocity in the mid-plane $z/h = 0$; DNS (left), LES-DSM (center) and LES-DMM (right)—100 contours levels taken between -0.4 and 1 for $\langle u \rangle$ (top) and between -0.7 and 0.2 for $\langle v \rangle$ (bottom). Dashed contours lines correspond to negative levels.

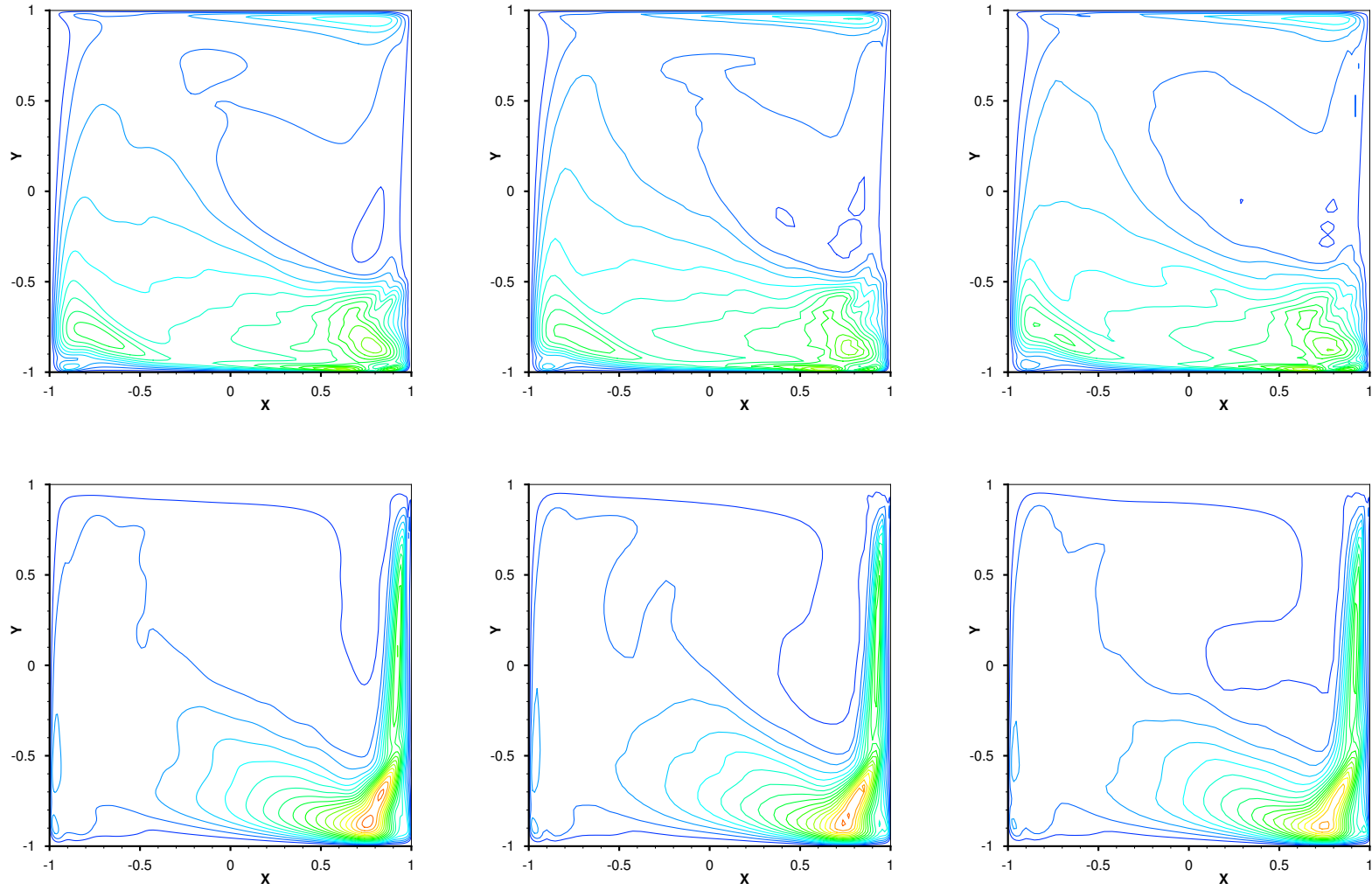


Fig. 4.10: Contours of rms-fluctuations of the velocity in the mid-plane $z/h = 0$; DNS (left), LES-DSM (center) and LES-DMM (right); 20 contours equally spaced between 0 and 0.1 for $\langle u^2 \rangle^{1/2}$ (top) and between 0 and 0.15 for $\langle v^2 \rangle^{1/2}$ (bottom).

4.3.4 Physical parameters of the LES modeling

The LES modeling for both the LES-DSM and LES-DMM involves the calculation of two scalar fields, namely the dynamic parameter C_d and the subgrid viscosity ν_{sgs} which are inter-related. As some values of C_d produced by the two dynamic procedures (4.12) and (4.22) may locally reach relatively “high values” destabilizing the time-integration procedure for the filtered Navier–Stokes computations. Hence it is common to use *ad hoc* averaging or limiting of the dynamic parameter C_d to ensure stability. Various procedures are reported in the literature: averaging in homogeneous directions [88, 146], temporal smoothing [40], integral constraint [93], Lagrangian averaging [180] and clipping [24, 272]. In the present work the latter procedure of clipping is used due to the explicit treatment of the subgrid terms. First the maximum admitted value of the dynamic parameter was $C_{d,\text{max}} = (0.18)^2$, 0.18 corresponding to the theoretical value of the Smagorinsky constant—see [213]. The negative values of C_d are also clipped and set to zero for the LES-DSM and LES-DMM. The amount of grid points clipped is indeed very limited and correspond to 0.2% and 0.08% of the total number of grid points for LES-DSM and LES-DMM respectively. It was found that the clipping of C_d to the interval comprised between $-(0.18)^2$ and $+(0.18)^2$ —therefore allowing for local negative values of the subgrid viscosity—was not affecting at all the stability of the spectral-element filtered Navier–Stokes computation. The difference between the results with or without the negative values of C_d was found to be negligible in the particular context of the lid-driven cubical cavity flow which is related to the limited amount of backscattering for this flow at a Reynolds number of 12 000.

Fig. 4.11 displays contour lines of the average subgrid viscosity for the LES-DSM in the mid-plane $z/h = 0$ and in the plane $z/h = 0.241$ where the maximum of average turbulent energy dissipation rate was localized—cf. Sec. 4.4.3 for greater details. First, the C^0 -continuity breakage in the inter-element continuity is obvious—see Fig. 4.2 to compare with the spectral element grid in the mid-plane—and is directly related to the discontinuous nature of the filter length field Δ defined in Sec. 4.2.4.2, Eq. (4.41). The effect of such discontinuity of the subgrid viscosity has been analyzed and discussed by Blackburn & Schmidt [24] using the same numerical framework as ours, namely the SEM. They found that the inter-element discontinuity of the subgrid term does not have a noticeable effect on their physical results which is confirmed by the present work. Finally, it appears clearly that the reasons for resorting to a dynamic procedure are fully justified by Fig. 4.11. Indeed, the dynamic procedure automatically turns on the dynamic parameter C_d which in turn activates subgrid-scale viscous effects in the regions of the flow where turbulent dissipation at the small-scales level occurs—see Sec. 4.4.3.

Similar results are obtained for the subgrid viscosity and the dynamic parameter in the case of the dynamic mixed model LES-DMM. The same clipping procedure, with the same clipping values as described earlier for LES-DSM was implemented.

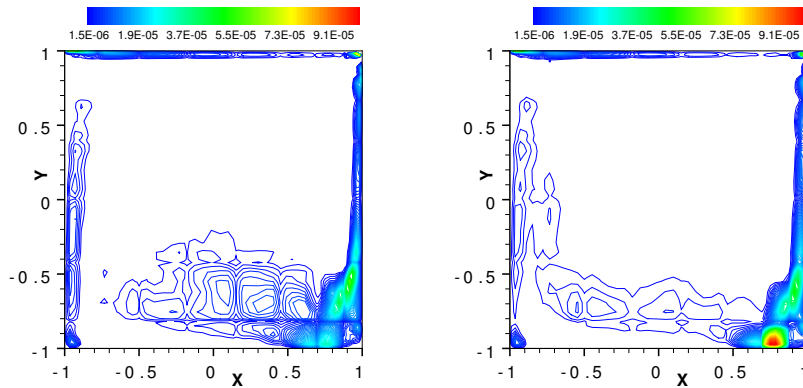


Fig. 4.11: Contours of the average subgrid viscosity $\langle \nu_{\text{sgs}} \rangle$ for the LES-DSM in the mid-plane $z/h = 0$ (left) and in the plane $z/h = 0.241$ (right); same series of contour levels is used in the two planes.

4.4 Characterization of turbulence in the flow

This section is devoted to a thorough analysis of some specific features of the flow in the region of the cavity where turbulence occurs. The aims are to ensure that the LES-DSM and LES-DMM are both capable of reproducing the fine physics observed in these regions and also to gain insights in the turbulent mechanisms involved.

4.4.1 Inhomogeneity of turbulence

It is easily predictable that such a confined flow will produce an inhomogeneous turbulence but it is worth determining in greater details the turbulent inhomogeneous zones in the cavity. In order to access this information we use the average turbulent energy dissipation rate $\langle \varepsilon \rangle$ defined by

$$\langle \varepsilon \rangle = \frac{1}{2} \nu \left\langle \left(\frac{\partial u_i^\diamond}{\partial x_j} + \frac{\partial u_j^\diamond}{\partial x_i} \right) \left(\frac{\partial u_i^\diamond}{\partial x_j} + \frac{\partial u_j^\diamond}{\partial x_i} \right) \right\rangle = 2\nu \langle S_{ij}^\diamond S_{ij}^\diamond \rangle. \quad (4.44)$$

Here and in the sequel, we use index notation and the summation convention, where repeated indices imply summation. The velocity fluctuations being divergence-free, one can rewrite

$$\langle \varepsilon \rangle = \nu \left\langle \frac{\partial u_i^\diamond}{\partial x_j} \frac{\partial u_i^\diamond}{\partial x_j} \right\rangle + \nu \frac{\partial^2 \langle u_i^\diamond u_j^\diamond \rangle}{\partial x_i \partial x_j}, \quad (4.45)$$

which in turn can be recast in terms of ω^\diamond the fluctuating vorticity, ω being the total resolved vorticity field

$$\langle \varepsilon \rangle = \nu \langle \omega_i^\diamond \omega_i^\diamond \rangle + 2\nu \frac{\partial^2 \langle u_i^\diamond u_j^\diamond \rangle}{\partial x_i \partial x_j}. \quad (4.46)$$

We define the average difference $\langle \delta \rangle$ by the difference between the average turbulent energy dissipation rate, divided by ν , and the average fluctuating enstrophy

$$\langle \delta \rangle = \left\langle \frac{\varepsilon}{\nu} \right\rangle - \langle \omega_i^\diamond \omega_i^\diamond \rangle = 2 \frac{\partial^2 \langle u_i^\diamond u_j^\diamond \rangle}{\partial x_i \partial x_j}. \quad (4.47)$$

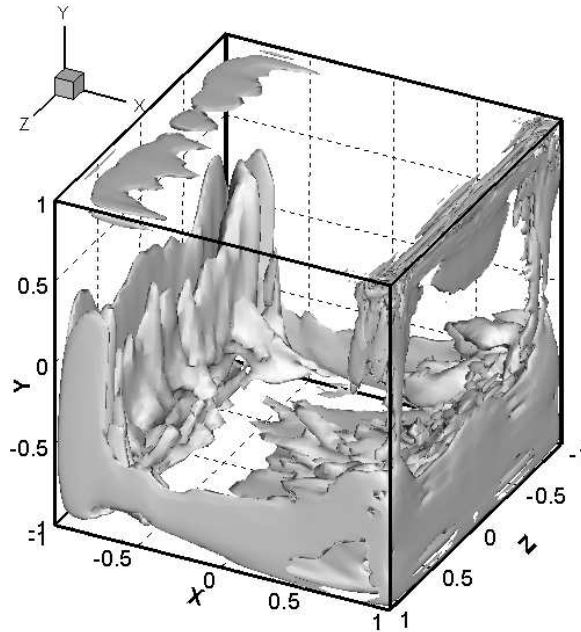


Fig. 4.12: Region of the cavity where the turbulent flow is inhomogeneous according to the criterion $|\langle \delta \rangle|/|\langle \delta \rangle_{\max}| > 1/100$; LES-DMM.

For homogeneous flow, the spatial derivatives of the Reynolds stress components $\langle u_i^\diamond u_j^\diamond \rangle$ are zero, and subsequently $\langle \delta \rangle = 0$. The average difference $\langle \delta \rangle$ was calculated for both databases LES-DSM and LES-DMM. Figure 4.12 displays a 3D view of the volume of the cavity where the flow is inhomogeneous according to the following heuristic criterion: $|\langle \delta \rangle|/|\langle \delta \rangle_{\max}| > 1/100$, where $|\langle \delta \rangle_{\max}^{\text{DSM}}| = 159.8 U_0^2/h^2$ and $|\langle \delta \rangle_{\max}^{\text{DMM}}| = 155.6 U_0^2/h^2$. In other words, it shows the region of the flow where the inhomogeneity of the turbulence—measured by $\langle \delta \rangle$ —is above 1% of its maximum absolute value.

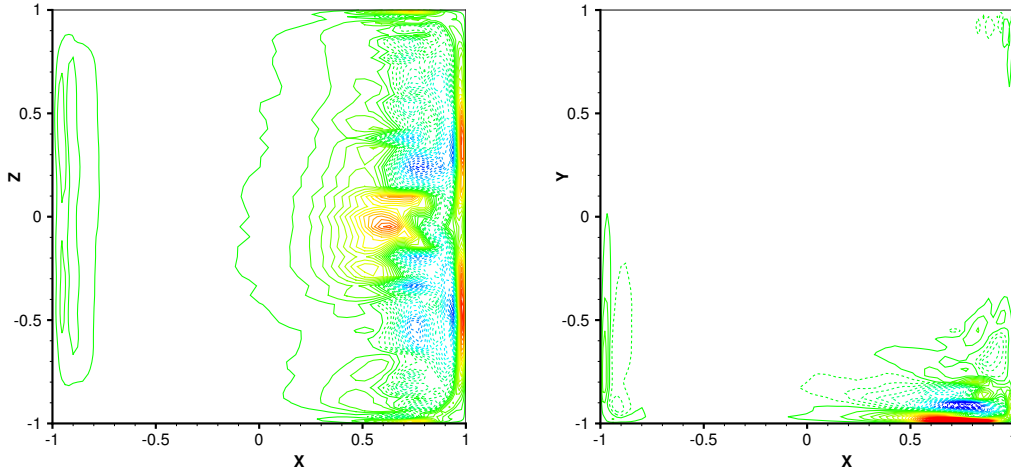


Fig. 4.13: Contours of $\langle \delta \rangle$ in the plane $y/h = -0.968$ just above the bottom wall (left) and in the mid-plane $z/h = 0$ (right); 100 equally spaced contours corresponding to levels between the threshold $0.01|\langle \delta \rangle_{\max}|$; dashed contours correspond to negative levels with a colormap ranging from blue to red; LES-DMM.

As expected, one can observe in Fig. 4.13 that in the region near the downstream wall where the two primary elliptical jets are impinging on the bottom wall, the flow is highly inhomogeneous. More specifically, the inhomogeneity is more important in the zone in between the two elliptical jets where the flow is ejected and recirculating. Likewise similar patterns with lower magnitudes are detected in the regions where the secondary jets and the tertiary jets are impinging. The secondary jets are impinging on the bottom of the upstream wall producing an inhomogeneous turbulence visible in Fig. 4.13 for values of x/h close to -1 . For the tertiary jets, impinging on the upstream part of the lid, the inhomogeneity is only visible in the 3D view in Fig. 4.12.

4.4.2 The turbulence production near the downstream wall

As mentioned by Leriche & Gavrilakis [155], the largest turbulence production rates in the cavity are to be found in the primary elliptical jets parallel to the downstream wall, near the impact points just above the bottom wall. The budget equations of the resolved second-order moments $\langle u_i^\diamond u_j^\diamond \rangle$ governing the turbulence energetics—see [178] and [199] for greater details—comprise a term named here P_{ij} , defined by

$$P_{ij} = -\langle u_i^\diamond u_k^\diamond \rangle \frac{\partial \langle u_j \rangle}{\partial x_k} - \langle u_j^\diamond u_k^\diamond \rangle \frac{\partial \langle u_i \rangle}{\partial x_k}, \quad (4.48)$$

and corresponding to the interaction of the resolved mean flow and the resolved Reynolds stress tensor. P_{ij} can be interpreted as responsible for the production of Reynolds stresses or in other words for the production of turbulence.

4.4.2.1 Maximum of turbulence production near the downstream wall

In the specific case of the separated downstream-wall jet, the term P_{22} is the largest out of the set of turbulence production terms $\{P_{ij}\}$. After probing in the cavity, the maxima of the resolved field P_{22} is to be found in the plane $y/h = -0.9388$ just at a very short distance above the bottom wall. The maximum values obtained are $P_{22_{\max}}^{\text{DSM}} = 0.070 U_0^3/h$ and $P_{22_{\max}}^{\text{DMM}} = 0.064 U_0^3/h$. The contours of the turbulence production term P_{22} in this plane $y/h = -0.9388$ are shown in Fig. 4.14 for both LES models. First, it can be noted that these contours are qualitatively very close to the ones obtained by Leriche & Gavrilakis [155]. For $x/h > 0.5$, the distribution of contours of the production of turbulence allow to clearly visualize the trace of the separated elliptical jets.

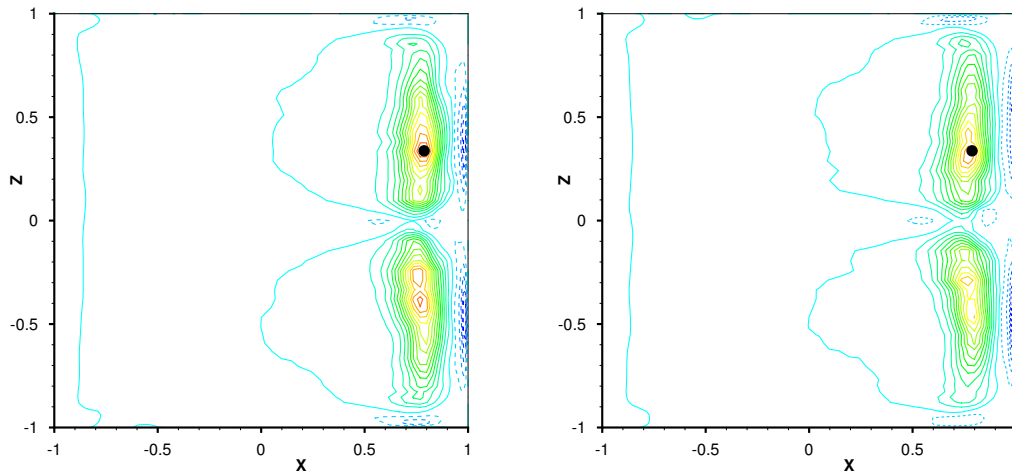


Fig. 4.14: Contours of the resolved production of turbulence term P_{22} in the plane $y/h = -0.9388$; LES-DSM (left) and LES-DMM (right); 20 contour levels equally spaced between $-0.025 U_0^3/h$ and $0.070 U_0^3/h$; dashed lines refer to negative contour levels; bullet points \bullet refer to the same grid node of coordinates $(x/h = 0.7874, y/h = -0.9388, z/h = 0.3371)$.

4.4.2.2 Time histories and power spectra at the maximum of turbulence production

In Fig. 4.14, one can notice that for each LES model, one grid point—identical for both DSM and DMM—has been highlighted with a bullet point \bullet . This point denoted by Θ_0 whose coordinates are $x/h = 0.7874$, $y/h = -0.9388$, $z/h = 0.3371$, is the closest grid point to the two maxima of P_{22} for LES-DSM and LES-DMM. The point Θ_0 provides the optimal search position for probing time histories of various turbulent fields in the sequel.

First, the values of the x -component of the fluctuating resolved velocity field u^\diamond , of the fluctuating resolved pressure p^\diamond and the resolved turbulent kinetic energy $q = u_i^\diamond u_i^\diamond / 2$, have been extracted of the LES-DSM database for each and every sample. These time histories are shown in Fig. 4.15—note that only the last 1024 samples out of the total of 1290 that constitutes the database are presented.

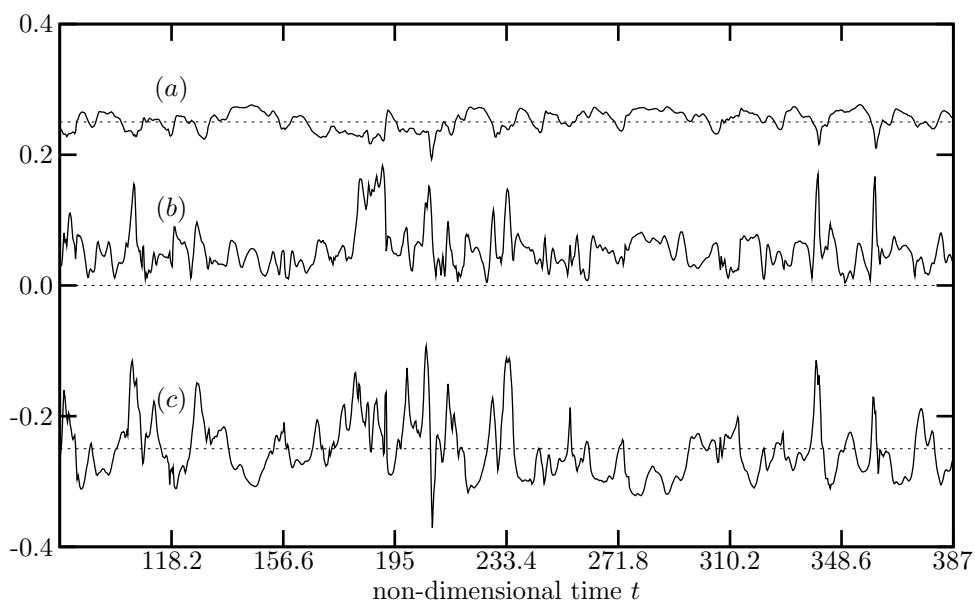


Fig. 4.15: Time histories of p^\diamond (graph (a) shifted of $+0.25$), the resolved turbulent kinetic energy q (graph (b)) and u^\diamond (graph (c) shifted of -0.25), at the point of coordinates $(0.7874, -0.9388, 0.3371)$; LES-DSM database.

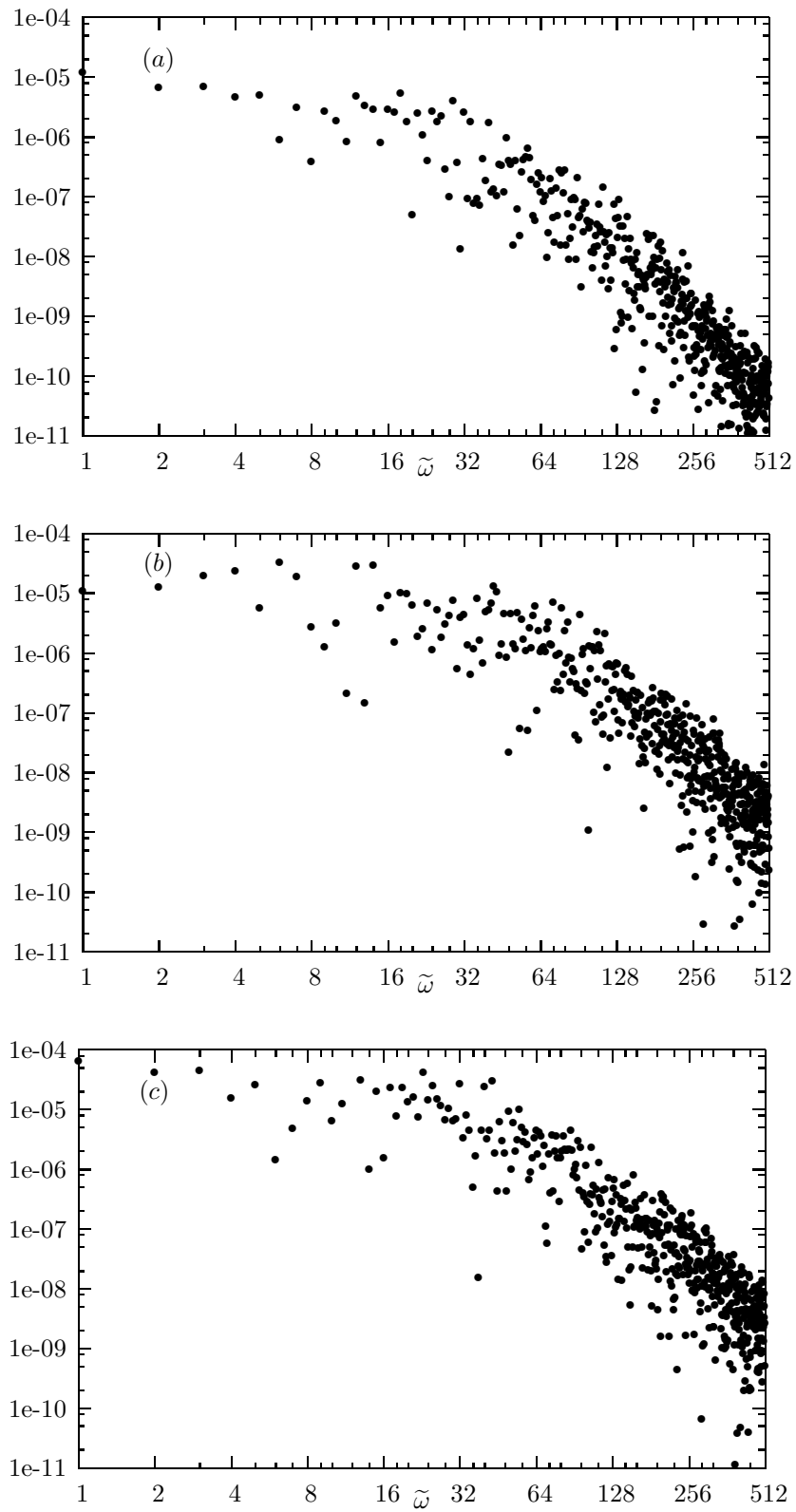


Fig. 4.16: Power spectra for the fluctuating resolved pressure p^\diamond (a), the resolved turbulent kinetic energy q (b), and the fluctuating resolved velocity field u^\diamond (c), obtained from the time histories in Fig. 4.15; LES-DSM database.

Based on these results the corresponding power spectra have been computed by fast Fourier transform—*a posteriori* justifying the choice of 1024 samples in the previous time histories—and are presented in Fig. 4.16. The scattering of points in the high-wavenumber zone is expected for spectra of non-spatially average fields. For such inhomogeneous flow with highly localized turbulent effects, averaging in space the fields not only pleasantly reduce the scattering of points but concurrently strongly modifies the high-wavenumber scaling which is the main source of information brought by the spectra. Nevertheless, the spectra offer a qualitative information regarding the Eulerian time scales of the spatial structures of turbulence convected past the point Θ_0 . The resolved mean flow depicted in Fig. 4.17—highlighting the presence of the core central primary vortex and secondary corner vortices—serves merely to advect turbulence at the bullet-spotted point Θ_0 . A careful scrutinizing of the resolved mean flow in the vicinity of Θ_0 shows that this point is exactly positioned at the “interface” between the core central vortex and the bottom corner vortex. The power spectra in Fig. 4.16 feature

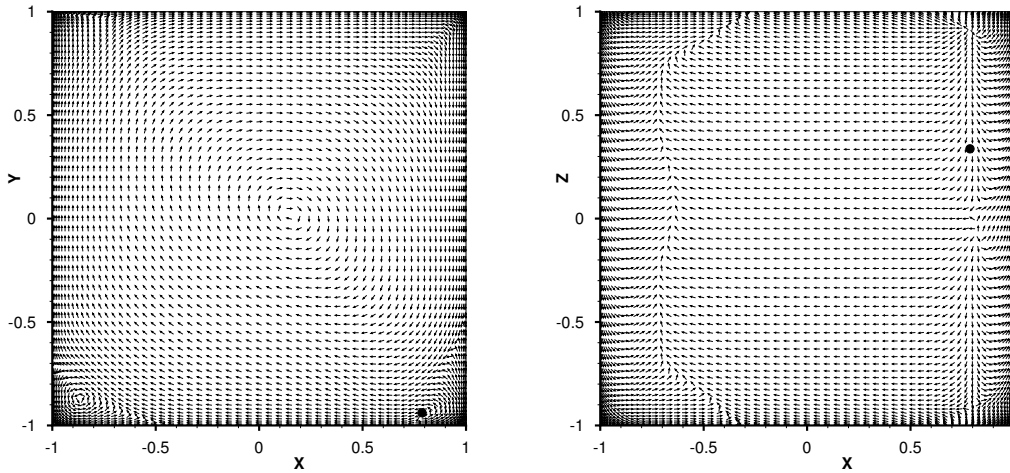


Fig. 4.17: Two-dimensional projected average resolved velocity vectors in the mid-plane $z/h = 0$ (left) and in the plane $y/h = -0.9388$ (right); bullet point refers to Θ_0 ; LES-DSM; bullet points \bullet refer to the same grid node of coordinates $(x/h = 0.7874, y/h = -0.9388, z/h = 0.3371)$.

the distribution of frequencies—or equivalently of time scales. These frequencies $\tilde{\omega}$ refer to the convection past Θ_0 of turbulent structures of size of order ℓ at a velocity of order $\langle u \rangle(\Theta_0)$, leading to the relation

$$\tilde{\omega} = \frac{\langle u \rangle(\Theta_0)}{\ell}. \quad (4.49)$$

The average resolved velocity field at Θ_0 being given, the spectra hence instruct us on the distribution of spatial scales of resolved turbulent structures convected by the mean flow at this point where the production of turbulence is maximum. Unfortunately, the relatively low sampling of the LES-DSM database and the not-long-enough simulation range interval does not permit to reach the highest frequencies of the order of $\langle u \rangle(\Theta_0)/\Delta$ where Δ is the filter length—see Eq. (4.41)—defining the LES scale separation.

4.4.2.3 Determination of coherent structures responsible for the peaks of turbulence production

In an attempt to provide a comprehensive and thorough assessment of the performances of both LES models, the determination of the coherent structures responsible for the intense turbulence production at the point Θ_0 has been considered as an ultimate challenge for both SGS modeling. The first step towards this goal necessitates to study the instantaneous distribution of the resolved term $-v^{\diamond 2} \partial \langle v \rangle / \partial y$ which was found to be the predominant term in P_{22} , see [155]. Figure 4.18 displays the time histories of this term for the DNS, LES-DSM and LES-DMM. Both LES present a limited number of high-value peaks which are assumed to be engendered by specific coherent vortices or large eddies. The intensity of the peaks produced by the LES-DMM is lower than those generated by the LES-DSM. This is supposed to be due to an over-evaluation of the subgrid viscosity by the dynamic procedure of the DMM. In addition, this is consistent with the observation made in Sec. 4.4.2.1 where $P_{22_{\max}}^{\text{DMM}} < P_{22_{\max}}^{\text{DSM}}$ was found and with the values of resolved $\langle Q(\bar{\mathbf{u}}) \rangle$ and $\langle Q(\bar{\mathbf{u}}^\diamond) \rangle$ in Table 4.2.

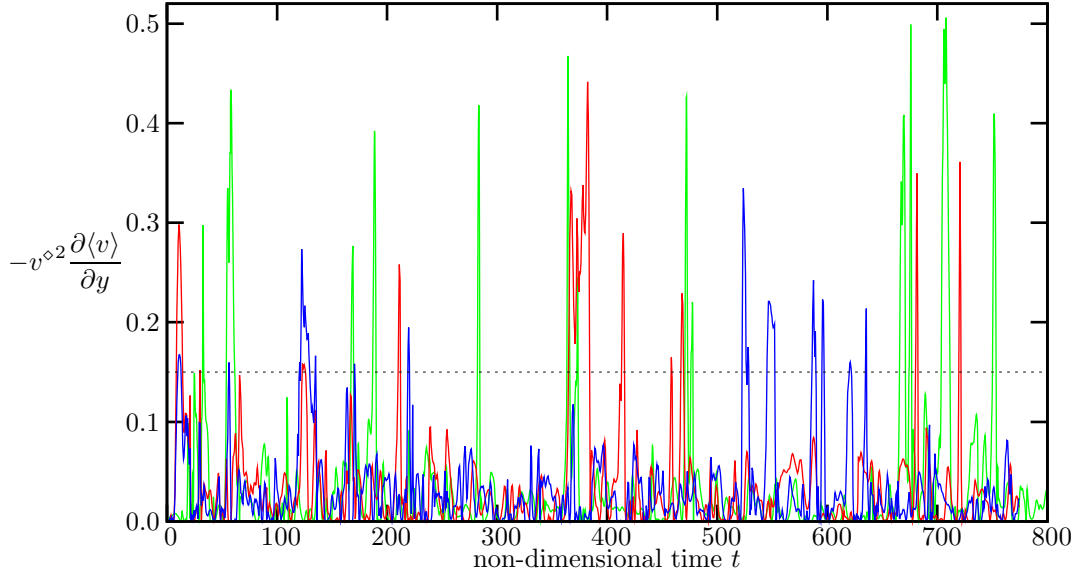


Fig. 4.18: Time histories of the resolved term $-v^{\circ 2} \partial \langle v \rangle / \partial y$ in U_0^3/h units for the DNS (green), LES-DSM (red) and the LES-DMM (blue); the dotted lines represent the threshold value $0.15 U_0^3/h$.

In order to finally characterize possible large eddies which would be responsible for these peaks, database samples producing a resolved term $-v^{\circ 2} \partial \langle v \rangle / \partial y$ above the threshold value $0.15 U_0^3/h$ were put aside to form a subset of the complete databases. The size of the subset of samples for LES-DSM (resp. LES-DMM) is approximately 6% (resp. 5%) of the size of the complete database. Based on these two subsets a conditional averaging of the streamwise resolved vorticity field ω_x is performed. Figure 4.19 displays the contours of this quantity in the vicinity of Θ_0 —the domain represented corresponds to only 4% of the surface of a normal section of the cavity—for both models. Two counter-rotating vortices are clearly exhibited by both models, together with the intense influenced shear layers laying on the bottom wall at $y/h = -1$. This vortex pair is identified as the coherent eddy responsible for the turbulence peaks and production in this region. The characteristic length scale of this large eddy is of the order of $0.1h$. Having identified this vortex pair we can further analyze the time histories at Θ_0 of the resolved pressure and the resolved turbulent kinetic energy depicted on Fig. 4.15, graph (a) and (b) respectively. One can notice that the intense peaks of the resolved term $-v^{\circ 2} \partial \langle v \rangle / \partial y$ on Fig. 4.18 correspond to intense peaks of resolved turbulent kinetic energy on Fig. 4.15 (b) and to low-pressure peaks on Fig. 4.15 (a). The vortex pairs generated by this turbulent flow are responsible for the low pressures and the high turbulent kinetic energy thereby justifying the observed correlations between these three time histories. Moreover the intensity of the vortex pair calculated by the LES-DSM is again higher than the one from the LES-DMM: $\langle \omega_x^{\text{DSM}} \rangle_{\text{ca,max}} = 18.6 U_0/h$ and $\langle \omega_x^{\text{DMM}} \rangle_{\text{ca,max}} = 14.0 U_0/h$, where the subscript “ca” stands for conditionally averaged. The intensity, the more regular structure and the localization of the vortex pair are three features suggesting that the dynamic Smagorinsky model provides a better SGS modeling than the dynamic mixed model. Nevertheless, the DMM performances in terms of SGS modeling are more than satisfactory. When considering the complete averaging of the x -component of the resolved vorticity field in the region where the vortex pair has been localized by conditional averaging, see Fig. 4.19, $\langle \omega_x \rangle$ was found almost constant and of magnitude approximately $0.9 U_0/h$.

4.4.3 Small-scales turbulent structures

A characteristic of high-Reynolds-number turbulence is that the vorticity possesses intense small-scale, random variations in both space and time. The spatial scale for vorticity fluctuations is the smallest in the continuum of turbulent scales, *i.e.* the Kolmogorov scale. Analogously to the vorticity fluctuations, for large-Reynolds-number turbulence velocity gradients $\partial u_i^{\circ} / \partial x_j$ are also dominated by the small scales of turbulence and the overall energy dissipation rate of kinetic energy is dominated by the average turbulent energy dissipation rate $\langle \varepsilon \rangle$ defined in Eq. (4.44). In the LES framework, the interest for small scales is twofold. First, small scales fall into the range of subgrid scales and therefore are not simulated but wholly modeled to properly reproduce their interactions with larger resolved scales of the flow. Second, the small scales have the crucial role to terminate the turbulent energy cascade by dissipating the energy originating from large eddies. An incorrect SGS modeling

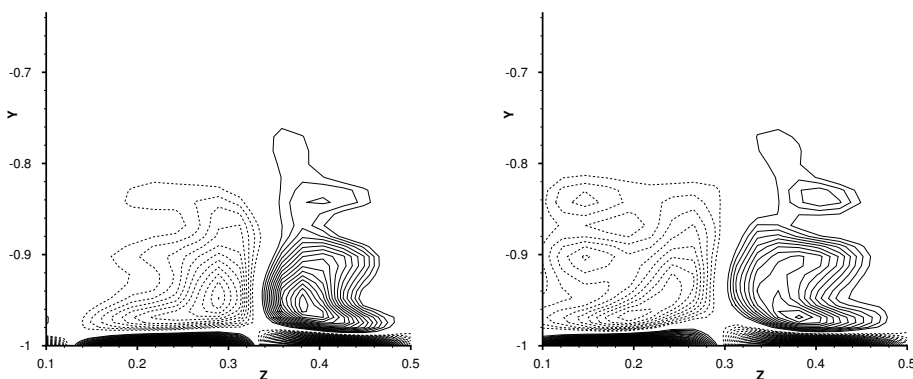


Fig. 4.19: Contours of the conditionally averaged resolved vorticity field $\langle \omega_x \rangle_{ca}$ in the plane $x/h = 0.7874$ for the LES-DSM (left) and the LES-DMM (right); dashed lines refer to negative contour levels.

will produce either an over-dissipation or conversely an under-dissipation of kinetic energy. The time histories of the total kinetic energy of the cavity flow $Q(\bar{\mathbf{u}})$ and of the total turbulent fluctuating energy $Q(\bar{\mathbf{u}}^\circ)$ presented in Fig. 4.3 are in this framework a precious proof of the correct global prediction of the energy dissipation by the modeled small scales in volume.

4.4.3.1 Localization of small-scales structures

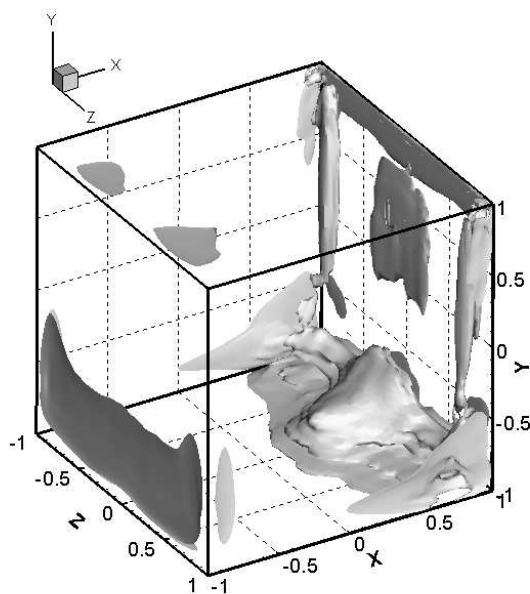


Fig. 4.20: Visualization of the region of the cavity where the average turbulent energy dissipation rate $\langle \varepsilon \rangle$ is above 1% of its maximum value $3570 \nu U_0^2 / h^2$; LES-DMM.

In this context, it appears relevant to first locate small-scales turbulent structures in the cavity and afterwards to check the correlation between the small-scales positioning and the activation of the SGS modeling represented in Fig. 4.11. Small scales can be indirectly localized by investigating the zones of intense average turbulent energy dissipation rate. Indeed $\langle \varepsilon \rangle$ involves products of fluctuating velocity gradients, see Eq. (4.44). First qualitatively, the region of the cavity flow corresponding to values of $\langle \varepsilon \rangle$ above 1% of its maximum value is shown in Fig. 4.20 for the LES-DMM. As foreseen, the wall-jet-impinging regions are subject to intense turbulent energy dissipation at the small-scales level. The two-dimensional cuts in Fig. 4.21 offer a more detailed information regarding the intensity of $\langle \varepsilon \rangle$ in four different planes of specific interest. It is worth keeping in mind that the more intense

$\langle \varepsilon \rangle$ the more small scales are involved in the dissipation process. Figure 4.21 displays with decreasing intensity, the dissipation due to the impingements of the separated wall jets on the bottom wall (bottom-left), on the upstream wall (bottom-right) and on the lid-plane (top-left). It appears that the LES-DSM is not able to properly reproduce the same intensity for the two symmetric jets impinging on the upstream wall (bottom-right). The same asymmetry in the intensity of $\langle \varepsilon \rangle$ is observed for the LES-DMM which could presumably be due to the observed asymmetry—with respect to the mid-plane—of the subgrid viscosities generated by the dynamic procedures of both SGS modeling.

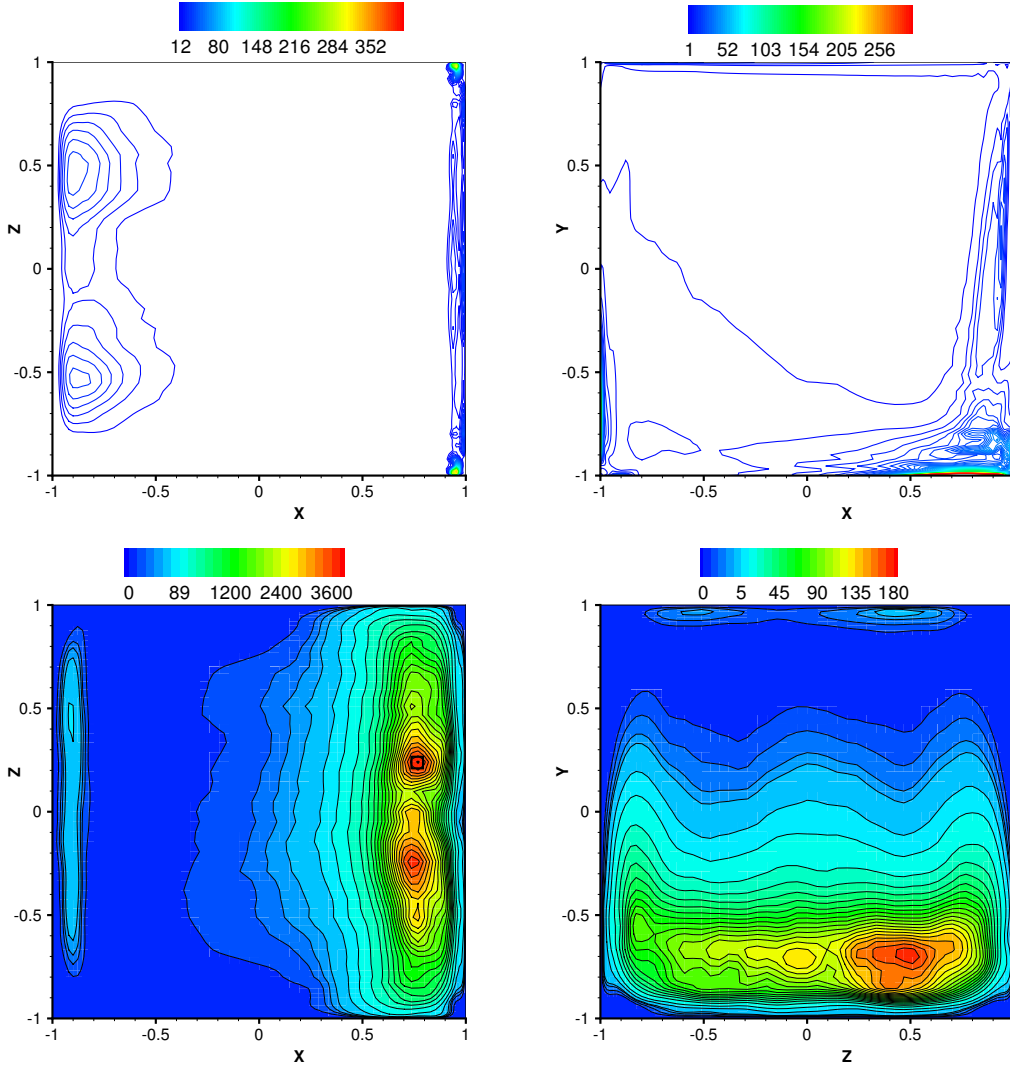


Fig. 4.21: Two-dimensional contour lines of $\langle \varepsilon \rangle$ in the following planes: lid-plane $y/h = 1$ (top-left), plane $z/h = 0.241$ (top-right), bottom-plane $y/h = -1$ (bottom-left), upstream-plane $x/h = -1$ (bottom-right); LES-DSM; black rectangle \square refers to the grid node of coordinates $(x/h = 0.7685, y/h = -1, z/h = 0.2410)$.

In Fig. 4.21 (bottom-left), one can notice that one grid point has been highlighted with a black rectangle \square . This point denoted by Ξ_0 whose coordinates are $x/h = 0.7685$, $y/h = -1$, $z/h = 0.2410$, is the closest grid point to the maximum of $\langle \varepsilon \rangle$ for LES-DSM. The point Ξ_0 provides the optimal search position for probing small-scales related fields. The plane-cut $z/h = 0.241$ —passing by Ξ_0 —of $\langle \varepsilon \rangle$ in Fig. 4.21 (top-right) exhibits a qualitative correlation with the same plane-cut for the average subgrid viscosity $\langle \nu_{\text{sgs}} \rangle$ in Fig. 4.11 (right).

4.4.3.2 Correlation between small-scales localization and subgrid viscosity

Such correlation between the small-scales localization and the activation of the LES dynamic Smagorinsky modeling is important in practice to ensure the effectiveness of the SGS modeling. Therefore a more quantitative approach is required, which relies on the calculation of a correlation field based on the instantaneous values of

ε and ν_{sgs} . The following correlation coefficient \mathcal{C} , defined by

$$\mathcal{C} = \mathcal{C}(\varepsilon, \nu_{\text{sgs}}) = \frac{\langle \varepsilon \nu_{\text{sgs}} \rangle - \langle \varepsilon \rangle \langle \nu_{\text{sgs}} \rangle}{(\langle \varepsilon^2 \rangle \langle \nu_{\text{sgs}}^2 \rangle)^{1/2}}, \quad (4.50)$$

was calculated for the complete set of samples LES-DSM.

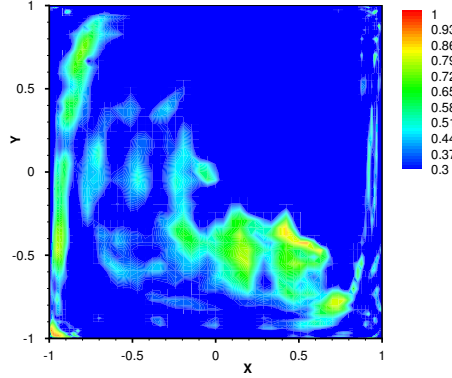


Fig. 4.22: Contours of the correlation coefficient \mathcal{C} in the plane $z/h = 0.241$ containing the point Ξ_0 ; LES-DSM.

Contours of \mathcal{C} in the plane $z/h = 0.241$, passing by Ξ_0 are presented in Fig. 4.22. The high-correlation zones reproduce in essence the turbulent-dominated regions of the cavity and even suggest the mean-flow convective effect of the central core vortex and other secondary corner vortices on the turbulent pockets. Nevertheless, higher correlations would have been expected in the vicinity of Ξ_0 . Such low correlations are evidences of the limitations of the LES in this region of the cavity flow. Conversely, the high correlations near the upstream wall are in good agreement with the small-scales localization. More precisely the poor correlation in the vicinity of Ξ_0 is imputed to the fact that in this region, the term $S_{ij}^\diamond S_{ij}^\diamond$ in the turbulent energy dissipation rate—see Eq. (4.44)—varies very rapidly in space likewise the subgrid viscosity. At this point, the information provided by the analysis of the subgrid-scale activity in the next section is a good complement to the previous correlation study.

4.4.3.3 Subgrid-scale activity

The filtered kinetic energy can be decomposed into the kinetic energy of the resolved velocity field and the residual kinetic energy which is equal to $\tau_{ii}/2$. The conservation equation for the kinetic energy of the resolved velocity field—see pp. 585–586 in [199] for greater details—comprises transport terms as well as source/sink terms which are of prime interest. First is the sink term $\bar{\varepsilon}_\nu = 2\nu \bar{S}_{ij} \bar{S}_{ij} = 2\bar{S}_{ij} \bar{S}_{ij} / \text{Re}$ corresponding to the viscous dissipation associated with the resolved velocity field. The second sink term $\bar{\varepsilon}_{\text{sgs}} = -\tau_{ij}^d \bar{S}_{ij}$ corresponds to the SGS contribution and represents the rate of transfer of energy from the resolved scales of the flow to the subgrid scales. This term $\bar{\varepsilon}_{\text{sgs}}$ is often inappropriately referred to as the SGS dissipation in the literature. Indeed $\bar{\varepsilon}_{\text{sgs}}$ does not correspond to any physical dissipation but finds its origin in inertial processes. In addition, it is important to note that locally $\bar{\varepsilon}_{\text{sgs}}$ can take negative values.

The SGS activity, denoted by \mathcal{A}_{sgs} in the sequel, allows to study the local energy fluxes due to the SGS effects. Following Geurts & Fröhlich [90] and Meyers *et al.* [181], \mathcal{A}_{sgs} is defined as

$$\mathcal{A}_{\text{sgs}} = \frac{\bar{\varepsilon}_{\text{sgs}}}{\bar{\varepsilon}_{\text{sgs}} + \bar{\varepsilon}_\nu} = \frac{-\tau_{ij}^d \bar{S}_{ij}}{-\tau_{ij}^d \bar{S}_{ij} + 2\nu \bar{S}_{ij} \bar{S}_{ij}}. \quad (4.51)$$

The SGS activity \mathcal{A}_{sgs} measures the importance of the subgrid scales in the overall dissipation process of the kinetic energy of the resolved velocity field. As mentioned by Meyers *et al.* [181], the SGS activity varies between zero and one where a value of zero corresponds to DNS and $\mathcal{A}_{\text{sgs}} = 1$ is associated with LES at infinite Reynolds number. Moreover the value of \mathcal{A}_{sgs} is directly related to the filter width $\bar{\Delta}$ and measures the “distance” between a DNS resolving all flow features at sufficiently high spatial resolution and an actual LES

corresponding to a specific filter width and mesh spacing. In the particular case of the LES-DSM, the SGS sink term is $\bar{\epsilon}_{\text{sgs}} = 2\nu_{\text{sgs}}\bar{\mathcal{S}}_{ij}\bar{\mathcal{S}}_{ij} = 2C_d\bar{\Delta}^2|\bar{\mathcal{S}}|\bar{\mathcal{S}}_{ij}$, leading to

$$\mathcal{A}_{\text{sgs}}^{\text{DSM}} = \frac{\nu_{\text{sgs}}}{\nu_{\text{sgs}} + \nu} = \frac{C_d\bar{\Delta}^2|\bar{\mathcal{S}}|/\nu}{1 + C_d\bar{\Delta}^2|\bar{\mathcal{S}}|/\nu}. \quad (4.52)$$

Fig. 4.23 displays the average value $\langle \mathcal{A}_{\text{sgs}} \rangle$ of the SGS activity in the plane $z/h = 0.241$ containing Ξ_0 and where the turbulent energy dissipation rate is maximum. First, it appears that the SGS activity is slightly higher for the LES-DMM than for the LES-DSM. Moreover, it appears very clearly that the SGS modeling is activated in the region of the cavity where the different wall jets are present, with maxima in the impingement zones. The LES-DMM is more effective in activating the subgrid scales in these particular zones. In the zone where the tertiary wall jet is impinging on the lid, SGS dissipation for the LES-DSM is less than 25% of the total dissipation, whereas it is above 45% for the LES-DMM.

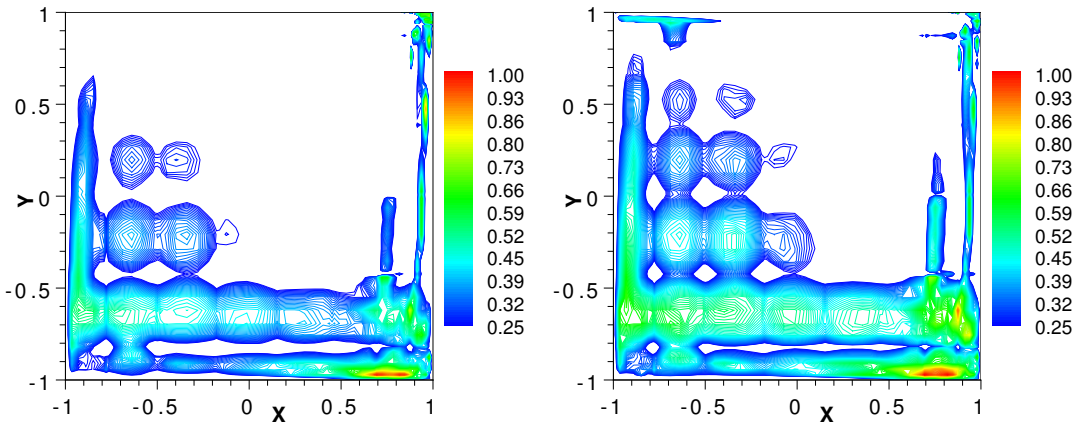


Fig. 4.23: Contours of the average SGS activity $\langle \mathcal{A}_{\text{sgs}} \rangle$ in the plane $z/h = 0.241$ containing the point Ξ_0 : LES-DSM (left) and LES-DMM(right); same series of contour levels is used for both models.

4.4.4 Helical properties of the cavity flow

The helicity \mathcal{H} of the fluid flow confined in the cavity \mathcal{V} at instant t is defined by

$$\mathcal{H}(t) = \int_{\mathcal{V}} \mathbf{u} \cdot \boldsymbol{\omega} \, d\mathcal{V}, \quad (4.53)$$

and is a measure of linkages and knots between the vorticity lines of the flow. The quantity $h(\mathbf{x}, t) = \mathbf{u} \cdot \boldsymbol{\omega}$ is the helicity density and is a pseudo-scalar quantity just like \mathcal{H} . The helicity is an important flow quantity because just like the total energy of the flow $Q(\bar{\mathbf{u}})$, it is an invariant of three-dimensional homogeneous turbulence [184]. The study of the resolved helicity \mathcal{H} and the average resolved helicity density $\langle h \rangle$ in the particular context of the lid-driven cavity flow in a locally-turbulent regime allows to gain insights into very important features of the turbulence dynamics as noted by Moffat & Tsinober [184]. For instance TGL vortices and secondary corner eddies are structures encountered in the lid-driven cavity flow which are well known as typical helical structures.

Mappings of the average resolved helicity density in Fig. 4.24 allows to locate resolved helical coherent structures (HCS). These HCS are particularly intense in the secondary-corner-eddy region and are consistent with the experimentally observed typical HCS, namely streamwise counter-rotating vortices [249]. This pairing of coherent helical structures correspond to a pairing of coherent vortical structures having opposite vorticity and consequently opposite helicity. Such observation justifies the relatively small—but non-zero—resolved average helicity reached by both LES models: $\langle \mathcal{H}^{\text{DSM}} \rangle = 0.00764 U_0^2 h^2$ and $\langle \mathcal{H}^{\text{DMM}} \rangle = -0.00572 U_0^2 h^2$. Smaller HCS have been identified earlier in Sec. 4.4.2.3, where streamwise counter-rotating vortices—cf. Fig. 4.19—near the bottom wall, have been identified by the conditional averaging as the principal coherent structures responsible for the high-intensity peaks in the production of turbulence in this region of the flow. Finally, it is noteworthy

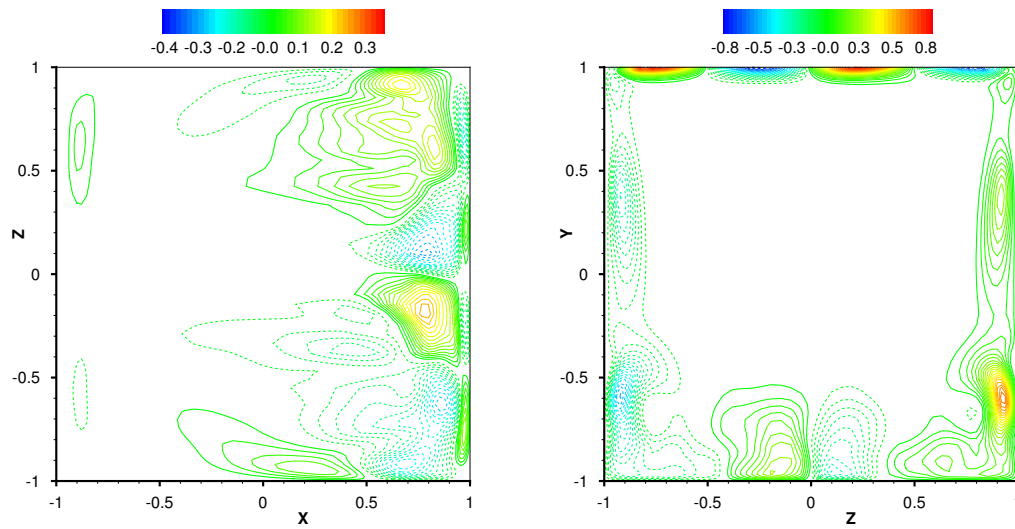


Fig. 4.24: Contours of the average resolved helicity density $\langle h \rangle$ in the bottom plane $y/h = -1$ (left) and in the plane $x/h = 0.7874$ (right) containing Θ_0 ; LES-DSM.

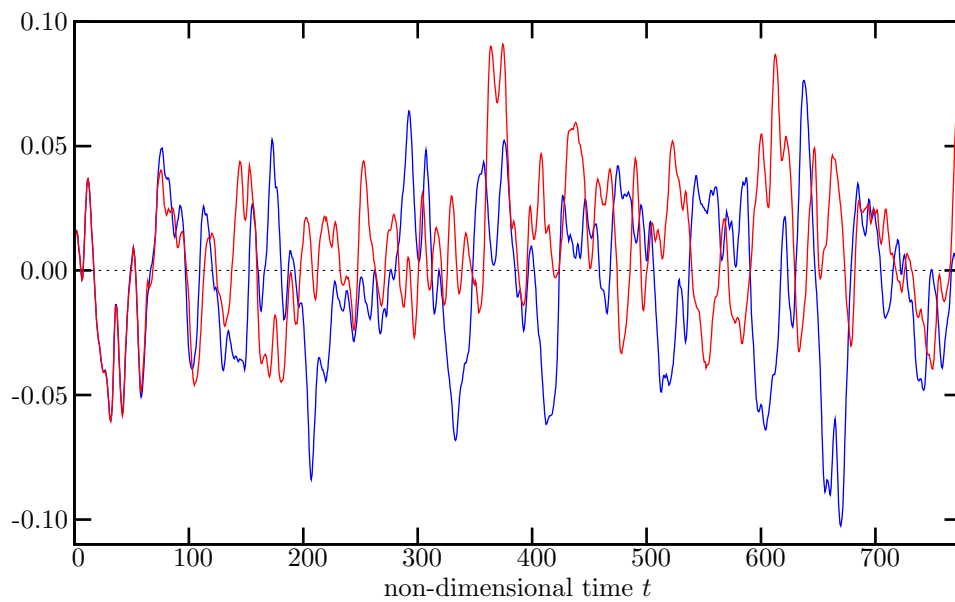


Fig. 4.25: Time histories of resolved $\mathcal{H}(t)$ for the LES-DSM (red lines) and the LES-DMM (blue lines).

to emphasize the strong link between average resolved helicity density contours and average resolved turbulent kinetic energy dissipation rate ones in Fig. 4.21.

As mentioned previously the average resolved helicity of the flow is non-zero. The time histories of the resolved helicity for the whole simulations are shown in Fig. 4.25 for both LES-DSM and LES-DMM. In Sec. 4.3.1 was mentioned that both SGS models start being effective and producing different global results after a transient period of about $80 h/U_0$ time units, and likewise the helicity as can be seen in Fig. 4.25. Moreover, the amplitude of the resolved helicity fluctuations is not decaying during the simulation and the LES-DMM qualitatively produces more high-amplitude negative helical values therefore justifying its negative average value.

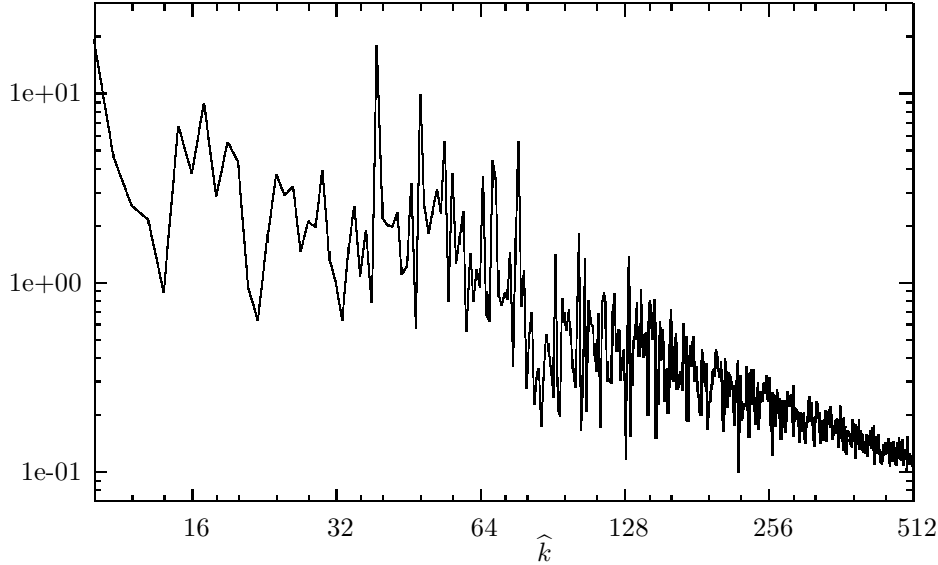


Fig. 4.26: One-dimensional relative helicity spectrum $\alpha(\hat{k})$; LES-DMM.

Helicity, like energy, is cascaded from large scales down to the Kolmogorov dissipation scale, where it is destroyed. Unfortunately, the relatively low Reynolds number of both LES does not permit the determination of quantitative scalings of energy and helicity spectra which could be compared to the Kolmogorov scalings in $\hat{k}^{-5/3}$ in helical three-dimensional homogeneous isotropic turbulence, as mentioned by Borue & Orszag [31]. In the same paper, Borue and Orszag conclude that helicity is inherently a large-scale quantity which behaves similarly to a passive scalar. Consequently the one-dimensional relative helicity spectrum defined by

$$\alpha(\hat{k}) = \frac{\hat{\mathcal{H}}(\hat{k})}{2\hat{k}\hat{Q}(\hat{k})}, \quad (4.54)$$

where $\hat{\mathcal{H}}$ (resp. \hat{Q}) is the one-dimensional resolved helicity (resp. energy) spectrum, decreases at small scales. Even if in our context, the turbulence is not homogeneous nor isotropic, the previous assertion is undeniably verified by both LES as can be seen only for the LES-DMM in Fig. 4.26, for high values of \hat{k} corresponding to small scales. Similar relative helicity spectrum is obtained for the LES-DSM. This suggests that the decreasing trend at small scales of the relative helicity spectrum is more general and not only limited to the homogeneous and isotropic turbulence theoretical framework, just like the Kolmogorov scale in the inertial range.

4.5 Conclusions

The long-integration results of two LES of the lid-driven cubical cavity flow at a Reynolds number of 12 000 have been presented for two dynamic subgrid-scale models, namely a dynamic Smagorinsky model and a dynamic mixed model. These simulations were based on an accurate spectral-element spatial discretization, having two times less points per space direction than the direct numerical simulation reference result from Leriche & Gavrilakis [155]. All filtering levels introduced in both SGS modelings rely on explicit modal filters in the spectral space, retaining \mathcal{C}^0 -continuity of the numerical solution of the filtered Navier–Stokes equations. An

additional nodal filter was used to stabilize both LES. Time-averaging was shown to be equivalent to ensemble-averaging, with respect to the global precision level of the numerical integration.

Partial simulation results using the UDNS and the Smagorinsky model as subgrid-scale models, have served to prove the necessity of a dynamic SGS procedure. Full LES results for both dynamic models have shown very good agreement with the DNS reference results. The agreement with the experimental reference results from Prasad & Koseff [201] is qualitatively good.

At a Reynolds number of 12000, the lid-driven cavity flow is placed in a locally turbulent regime and such turbulent flow is proved to be highly inhomogeneous in the secondary-corner regions of the cavity where turbulence production and dissipation are important. The maximum production of turbulence was found to be located in the downstream-corner-eddy region just above the bottom wall. An analysis of the spectra of turbulent quantities at this point allowed us to determine the distribution of the scales of the turbulent structures convected past this maximum. Moreover, both LES were able to capture the coherent counter-rotating pair of vortices which are mainly responsible for the peaks of turbulence production still at this point. LES-DSM have shown globally more intense and better results than the LES-DMM in this matter.

Small-scales turbulent structures were located indirectly by studying the regions of intense turbulent energy dissipation rate ε . The subgrid-viscosity field was shown to be strongly correlated to ε in the turbulent areas of the flow, but the clipping procedure—necessary for stabilizing the numerics—imposed to the dynamic parameters strongly diminishes this correlation in the intense turbulent zones. Subgrid-scales activity has been analyzed and the higher SGS activity is associated with the LES-DMM.

Helical properties of the flow were investigated. Typical helical coherent structures were identified in the secondary-corner regions. These structures appear to be correlated to the turbulent energy dissipation rate ε . The relative helicity spectra is shown to be decreasing at small scales, which is in agreement with the theoretical results from Borue & Orszag [31] for the three-dimensional isotropic homogeneous turbulence.

Chapter 5

A coupled approximate deconvolution and dynamic mixed scale model for LES

Large-eddy simulations of incompressible Newtonian fluid flows with approximate deconvolution models based on the van Cittert method are reported in this chapter. The Legendre spectral element method is used for the spatial discretization to solve the filtered Navier–Stokes equations. A novel variant of approximate deconvolution models blended with a mixed scale model using a dynamic evaluation of the subgrid-viscosity constant is proposed. This model is validated by comparing the large-eddy simulation with the direct numerical simulation of the flow in a lid-driven cubical cavity, performed at a Reynolds number of 12 000. Subgrid modeling in the case of a flow with coexisting laminar, transitional and turbulent zones such as the lid-driven cubical cavity flow represents a challenging problem [79]. Moreover, the coupling with the spectral element method having very low numerical dissipation and dispersion builds a well suited framework to analyze the efficiency of a subgrid model. First- and second-order statistics obtained using this new model are showing very good agreement with the direct numerical simulation. Filtering operations rely on an invertible filter applied in a modal basis and preserving the C^0 -continuity across elements. No clipping on dynamic parameters was needed to preserve numerical stability.

5.1 Introduction

As previously mentioned in Chapter 4, large-eddy simulation (LES) represents a way of reducing the number of degrees of freedom of the simulation with respect to the requirements of the direct numerical simulation (DNS). This is done by calculating only low-frequency modes in space and modeling high-frequency ones, the scale separation being performed by filtering in space the Navier–Stokes equations. Large-scale structures are obtained by the computed flow dynamics while the behavior of subgrid scales and their interaction with large eddies are modeled by the additional term in the LES governing equations resulting from filtering the Navier–Stokes equations. The expression of the additional term as a function of the resolved field is referred to as subgrid modeling.

Approximate deconvolution models (ADM) constitute a particular family of subgrid models. They rely on the attempt to recover, at least partially, the original unfiltered fields, up to the grid level, by inverting the filtering operator applied to the Navier–Stokes equations. The focus here is on the approximate iterative method introduced by Stolz & Adams [243] which is based on the van Cittert procedure. This method was subsequently applied to incompressible wall-bounded flows [246], to compressible flows and to shock-boundary layer interaction [245] using a new variant ADM-RT, blending ADM with a relaxation term (RT) increasing the dissipative character of the model. Transitional flows were also investigated by Schlatter *et al.* [220]. Over the past five years, ADM spread over various fields of application. Gullbrand & Chow studied the effect of explicit filtering in the case of channel flow [107]. ADM were also more recently applied to the LES of a rectangular jet and to computational aero-acoustics by Rembold & Kleiser [206]. Particle-laden turbulent flows were investigated in the ADM framework by Shotorban & Mashayek [229]. From the numerical viewpoint, Schlatter *et al.* [220] used a parallel implementation of a mixed Fourier–Chebyshev spectral method. These models were also implemented in a finite volume framework in the semi-industrial code NSMB, Navier–Stokes Multi–Block, by von Kaenel *et al.* who applied it to shock-boundary layer interaction and channel flow in [261, 262]. To our knowledge, the only implementation based on the spectral element method (SEM) is due to Iliescu & Fischer [128] who used ADM based on the rational LES model (RLES) instead of the van Cittert one. More recently, Pruett *et al.* proposed a temporal ADM for LES [203] and a stability analysis of the LES-ADM equations was performed by Dunca & Epshteyn [68].

LES of Newtonian incompressible fluid flows with ADM based on the van Cittert method using Legendre-SEM as spatial discretization to solve the filtered Navier–Stokes equations are considered for the first time in this

chapter. Following the idea of Winckelmans & Jeanmart [266] who coupled the ADM based on the van Cittert method and the Smagorinsky model [232], and Gullbrand & Chow [107] who proposed a dynamic version of the previous model, a new variant which blends ADM and the mixed scale model introduced by Sagaut [212] with a dynamic evaluation of the subgrid-viscosity constant based on a Germano–Lilly type of procedure [88, 156] is proposed.

A specific filtering operation adapted to SEM and preserving continuity across elements is applied in a modal basis which was proposed in the p -version of finite elements and first used by Boyd [38] as a filtering technique. Depending on the transfer function, this filter is not projective and is therefore invertible, this property being essential for the deconvolution procedure.

A DNS of the flow in a lid-driven cubical cavity performed at Reynolds number of 12 000 with a Chebyshev collocation method due to Leriche & Gavrilakis [155] is taken as the reference solution to validate the new model. Subgrid modeling in the case of a flow with coexisting laminar, transitional and turbulent zones such as the lid-driven cubical cavity flow represents a challenging problem. As the flow is confined and recirculating, any under- or over-dissipative character of the subgrid model can be clearly identified. Moreover, the very low dissipation and dispersion induced by SEM allows a pertinent analysis of the energetic action induced by any subgrid model, which is not feasible in the framework of low-order numerical methods. The coupling of the lid-driven cubical cavity flow problem with the SEM builds therefore a well suited framework to analyze the accuracy of the newly defined subgrid model. Bouffanais *et al.* [35, 37] have performed LES of the flow in a lid-driven cubical cavity at a Reynolds number of 12 000 using the same physical parameters as the DNS from Leriche & Gavrilakis [155]. The numerical framework of [35, 37] is the same as the one used in the present chapter. Standard subgrid models were used in [35, 37]: dynamic Smagorinsky [88, 156] or dynamic mixed models [272].

This chapter is organized as follows. In Section 5.2, the filtered Navier–Stokes equations are given, followed by a brief description of the space-time discretization using the spectral element method. The subgrid modeling is dealt in detail in Section 5.3 and the numerical filters are described in Section 5.4. LES of the flow in the lid-driven cubical cavity, based on the subgrid models introduced in Section 5.3, is presented and thoroughly analyzed in Section 5.5. Finally, in Section 5.6 we present the conclusions.

5.2 Governing equations and numerical method

5.2.1 Governing equations

In the case of isothermal flows of Newtonian incompressible fluids, the LES governing equations for the filtered quantities denoted by an *overbar*, obtained by applying a convolution filter \mathcal{G}_\star to the Navier–Stokes equations, read

$$\frac{\partial \bar{u}_i}{\partial t} + \frac{\partial}{\partial x_j} (\bar{u}_i \bar{u}_j) = -\frac{\partial \bar{p}}{\partial x_i} + \nu \frac{\partial}{\partial x_j} \left(\frac{\partial \bar{u}_i}{\partial x_j} + \frac{\partial \bar{u}_j}{\partial x_i} \right) - \frac{\partial \tau_{ij}}{\partial x_j}, \quad (5.1)$$

$$\frac{\partial \bar{u}_j}{\partial x_j} = 0, \quad (5.2)$$

the filtered velocity field $\bar{\mathbf{u}} = \mathcal{G}_\star \mathbf{u}$ satisfying the divergence-free condition (5.2) through the filtered reduced pressure field \bar{p} . The components of the subgrid tensor $\boldsymbol{\tau}$ are given by

$$\tau_{ij} = \overline{u_i u_j} - \bar{u}_i \bar{u}_j, \quad (5.3)$$

and ν is the kinematic viscosity. The closure of the filtered momentum equation (5.1) requires $\boldsymbol{\tau}$ to be expressed in terms of the filtered field which reflects the subgrid scales modeling and the interaction among all space scales of the solution.

5.2.2 Space discretization

The numerical method and the space discretization is the same as the ones used in Chapter 4 and introduced in Chapter 2. For the sake of clarity, the central lines and ideas are briefly recalled here. The numerical method treats Eqs. (5.1)–(5.2) within the weak Galerkin formulation framework. The SEM consists in dividing the computational domain into a given number of spectral elements. In each spectral element, the velocity and pressure fields are approximated using Lagrange–Legendre polynomial interpolants. The reader is referred to

the monograph by Deville *et al.* [58] for full details. The velocity and pressure are expressed in the $\mathbb{P}_N - \mathbb{P}_{N-2}$ functional spaces where \mathbb{P}_N is the set of polynomials of degree lower than N in each space direction. This spectral element method avoids the presence of spurious pressure modes as it was proved by Maday & Patera [172, 174]. The quadrature rules are based on a Gauss–Lobatto–Legendre (GLL) grid for the velocity nodes and a Gauss–Legendre grid (GL) for the pressure nodes.

Borrowing the notation from Deville *et al.* [58], the semi-discrete filtered Navier–Stokes equations resulting from space discretization are

$$\mathbf{M} \frac{d\bar{\mathbf{u}}}{dt} + \mathbf{C}\bar{\mathbf{u}} + \nu \mathbf{A}\bar{\mathbf{u}} - \mathbf{D}^T \bar{\mathbf{p}} + \mathbf{D}_\tau \boldsymbol{\tau} = 0, \quad (5.4)$$

$$-\mathbf{D}\bar{\mathbf{u}} = 0. \quad (5.5)$$

The diagonal mass matrix \mathbf{M} is composed of three blocks, namely the mass matrices M . The global vector $\bar{\mathbf{u}}$ contains all the nodal velocity components while $\bar{\mathbf{p}}$ is made of all nodal pressures. The matrices \mathbf{A} , \mathbf{D}^T , \mathbf{D} , \mathbf{D}_τ are the discrete Laplacian, gradient, divergence and tensor divergence operators, respectively. The matrix operator \mathbf{C} represents the action of the nonlinear term written in convective form $\bar{\mathbf{u}} \cdot \nabla$, on the velocity field and depends on $\bar{\mathbf{u}}$ itself. The semi-discrete equations constitute a set of nonlinear ordinary differential equations (5.4) subject to the weak incompressibility condition (5.5).

5.2.3 Time integration

Standard time integrators in the SEM framework handle the viscous linear term and the pressure implicitly by a backward differentiation formula of order 2 (BDF2) to avoid stability restrictions such that $\nu \Delta t \leq C/N^4$, while all nonlinearities, including the discretized subgrid term $-\mathbf{D}_\tau \boldsymbol{\tau}$, are computed explicitly, *e.g.* by a second order extrapolation method (EX2), under the CFL restriction

$$\bar{u}_{\max} \Delta t \leq C/N^2. \quad (5.6)$$

The implicit part is solved by a generalized block LU decomposition with a pressure correction algorithm [54, 58, 196]. The overall order-in-time of the afore-presented numerical method is two.

5.3 Subgrid modeling

5.3.1 General considerations

The problem of subgrid modeling consists in taking into account the interaction between resolved and subgrid scales which is represented by the subgrid term $\nabla \cdot \boldsymbol{\tau}$ in the filtered momentum equation (5.1).

Following the terminology introduced by Sagaut [213], two modeling strategies are defined. A first group of models, called structural, aims at making the best approximation of the tensor $\boldsymbol{\tau}$ by reconstructing it formally from the resolved field $\bar{\mathbf{u}}$. The closure consists in finding a relation such that

$$\boldsymbol{\tau}^m = \mathcal{C}_\tau(\bar{\mathbf{u}}), \quad (5.7)$$

where the upper index ‘m’ distinguishes the modeled from the exact subgrid tensor. This group of models does not require any foreknowledge about the nature of the interactions between resolved and subgrid scales. The second group, called functional, consists in modeling the action of subgrid scales on the resolved field $\bar{\mathbf{u}}$ using physical concepts and not at approximating the subgrid tensor $\boldsymbol{\tau}$ itself, even if a subgrid tensor is explicitly constructed as for subgrid-viscosity models. Most of these models assume that the action of subgrid scales on resolved ones is essentially energetic, so that the balance of energy transfers between both scales categories is sufficient to describe the interaction.

The focus hereafter is on ADM which attempts to recover, at least partially, the original unfiltered fields, up to the grid level, by inverting the filtering operator applied to the Navier–Stokes equations. Following the idea of Winkelmanns & Jeanmart [266] who coupled the ADM based on the van Cittert method and the Smagorinsky model [232], and Gullbrand & Chow [107] who proposed a dynamic version of the previous model, a new variant blending ADM and the dynamic mixed scale model introduced by Sagaut [212] is proposed.

5.3.2 Approximate deconvolution model

The deconvolution approach aims at reconstructing the unfiltered fields from the filtered ones. The subgrid modes are not modeled but reconstructed using an *ad hoc* mathematical procedure which falls in the structural modeling category. Writing formally the Navier–Stokes momentum equation (5.1) as

$$\frac{\partial \mathbf{u}}{\partial t} + \mathbf{f}(\mathbf{u}) = \mathbf{0}, \quad (5.8)$$

the evolution equation of the filtered quantities becomes

$$\frac{\partial \bar{\mathbf{u}}}{\partial t} + \mathbf{f}(\bar{\mathbf{u}}) = [\mathbf{f}, \mathcal{G}\star](\mathbf{u}), \quad (5.9)$$

where the convolution filter $\mathcal{G}\star = (\mathcal{L} \circ \mathcal{P})\star$ embodies the LES filter $\mathcal{L}\star$ and the projective grid filter $\mathcal{P}\star$ [107, 266], the latter being therefore implicitly accounted for in the sequel. It is important to note that the LES filter and the grid filter do not commute since the effect of the SEM discretization is not a spectral cutoff filter, unlike the case of spectral methods as reported by Gullbrand & Chow [107]. The subgrid commutator reads then

$$[\mathbf{f}, \mathcal{G}\star](\mathbf{u}) = \mathbf{f}(\mathcal{G}\star \mathbf{u}) - \mathcal{G}\star \mathbf{f}(\mathbf{u}) = \mathbf{f}(\bar{\mathbf{u}}) - \overline{\mathbf{f}(\mathbf{u})}, \quad (5.10)$$

which is strictly equivalent to Eq. (5.1) given

$$[\mathbf{f}, \mathcal{G}\star](\mathbf{u}) = -\nabla \cdot \boldsymbol{\tau}. \quad (5.11)$$

The exact subgrid contribution appears as a function of the non-filtered field, which is not computed when performing a LES. This field being unknown, the idea is to approximate it using the following deconvolution procedure

$$\mathbf{u} \simeq \mathbf{u}^* = \mathcal{Q}_N \star \bar{\mathbf{u}} = (\mathcal{Q}_N \circ \mathcal{G}) \star \mathbf{u} = (\mathcal{Q}_N \circ \mathcal{L} \circ \mathcal{P}) \star \mathbf{u} = (\mathcal{Q}_N \circ \mathcal{L}) \star \hat{\mathbf{u}}, \quad (5.12)$$

where $\hat{\mathbf{u}} = \mathcal{P}\star \mathbf{u}$ is the grid-filtered velocity. The operator $\mathcal{Q}_N\star$ is an N th-order approximation of the inverse of the filter $\mathcal{L}\star$, since the grid filter is projective and therefore not invertible, such that

$$(\mathcal{Q}_N \circ \mathcal{L}) = \mathcal{I} + O(\bar{\Delta}^{-N}), \quad (5.13)$$

with $\mathcal{I}\star$ the identity filtering operator and $\bar{\Delta}$ the filter cutoff length associated to $\mathcal{G}\star$. Stolz & Adams proposed in [243] an iterative deconvolution procedure based on the van Cittert method. If the filter $\mathcal{L}\star$ has an inverse, it can be computed using the truncated van Cittert expansion series

$$\mathcal{L}^{-1} \simeq \mathcal{Q}_N = \sum_{i=0}^N (\mathcal{I} - \mathcal{L})^i, \quad (5.14)$$

which is known to be convergent if

$$\|\mathcal{I} - \mathcal{L}\| \ll 1. \quad (5.15)$$

The deconvolution error induced by the approximation (5.14) can be represented by a filter $\mathcal{H}_N\star$ defined by

$$\mathcal{H}_N = \mathcal{I} - \mathcal{Q}_N \circ \mathcal{L}. \quad (5.16)$$

The subgrid term is then approximated as

$$[\mathbf{f}, \mathcal{G}\star](\mathbf{u}) \simeq [\mathbf{f}, \mathcal{G}\star](\mathcal{Q}_N \star \bar{\mathbf{u}}) = [\mathbf{f}, \mathcal{G}\star](\mathbf{u}^*), \quad (5.17)$$

and the model resulting from this approach is obtained by introducing Eq. (5.17) into the filtered Navier–Stokes momentum equation (5.9)

$$\frac{\partial \bar{\mathbf{u}}}{\partial t} + \mathbf{f}(\bar{\mathbf{u}}) = [\mathbf{f}, \mathcal{G}\star](\mathbf{u}^*). \quad (5.18)$$

Using once more approximation (5.12) in Eq. (5.18) implies $\mathbf{f}(\bar{\mathbf{u}}) = \mathbf{f}(\bar{\mathbf{u}}^*)$ and leads to the formulation commonly used with ADM

$$\frac{\partial \bar{\mathbf{u}}}{\partial t} + \mathcal{G}\star \mathbf{f}(\mathbf{u}^*) = 0. \quad (5.19)$$

It is noteworthy that this latter formulation introduces the deconvolution error and the error related to the non-inversion of $\mathcal{P}\star$ into the nonlinear advection term, thereby breaking the Galilean invariance [238]. Furthermore, the expression of the subgrid tensor of Bardina’s scale similarity model [13] is not recovered from the deconvoluted formulation (5.19) when $\mathcal{Q}_N = \mathcal{I}$, which is again due to the difference between the filtered and the deconvoluted velocities. Based on the previous comments, the filtered formulation (5.18) appears to be the most general and therefore, all LES presented in the sequel rely on it. No numerical instabilities were observed using the formulation (5.18) associated with our explicit treatment of the nonlinear terms, see Sec. 5.2.3.

5.3.3 Coupling with a dynamic mixed scale model

Coupling ADM with a subgrid-viscosity model can be formally achieved by adding a source term $\mathbf{s}(\bar{\mathbf{u}})$ to the right-hand side of Eq. (5.18)

$$\frac{\partial \bar{\mathbf{u}}}{\partial t} + \mathbf{f}(\bar{\mathbf{u}}) = [\mathbf{f}, \mathcal{G}\star](\mathbf{u}^*) + \mathbf{s}(\bar{\mathbf{u}}), \quad (5.20)$$

where $\mathbf{s}(\bar{\mathbf{u}})$ is expressed in terms of the filtered rate-of-strain tensor $\bar{\mathbf{S}}$ by

$$\mathbf{s}(\bar{\mathbf{u}}) = \nabla \cdot (\nu_{\text{sgs}}(\nabla \bar{\mathbf{u}} + \nabla \bar{\mathbf{u}}^T)) = \nabla \cdot (2\nu_{\text{sgs}}\bar{\mathbf{S}}), \quad (5.21)$$

the superscript ‘T’ denoting the transpose operation and ν_{sgs} the subgrid viscosity. For such functional models, only the deviatoric part of the subgrid stress is modeled. On the other hand, the ADM part $[\mathbf{f}, \mathcal{G}\star](\mathbf{u}^*)$ includes both isotropic and deviatoric parts. Using such subgrid-viscosity model, the only unknown is the subgrid viscosity itself which implies a closure of the form

$$\nu_{\text{sgs}} = C_\nu(\bar{\mathbf{u}}). \quad (5.22)$$

5.3.3.1 Mixed scale model

In the sequel, we focus on a subgrid-viscosity model proposed by Sagaut [212] having a triple dependency on the large and small structures of the resolved field, and the filter cutoff length. With respect to the Smagorinsky model used by Winckelmans & Jeanmart [266], the model proposed by Sagaut offers the advantage of automatically vanishing if subgrid scales are absent of the solution. This model, which makes up the one-parameter mixed scale family, is derived by taking a weighted geometric average of the models based on large scales and those based on the energy at cutoff. The closure is given by

$$\nu_{\text{sgs}} = C_\gamma |\mathcal{F}(\bar{\mathbf{u}})|^\gamma (\bar{q}_c)^{\frac{1-\gamma}{2}} \bar{\Delta}^{1+\gamma}, \quad (5.23)$$

where C_γ and γ are the subgrid-viscosity and mixed-scale constants, \bar{q}_c is the resolved kinetic energy at cutoff and

$$\mathcal{F}(\bar{\mathbf{u}}) = \mathbf{S}(\bar{\mathbf{u}}) = \bar{\mathbf{S}} \quad \text{or} \quad \mathcal{F}(\bar{\mathbf{u}}) = \nabla \times \bar{\mathbf{u}} = \bar{\boldsymbol{\omega}}. \quad (5.24)$$

The resolved kinetic energy at cutoff can be evaluated using the formula

$$\bar{q}_c = \frac{1}{2} \tilde{u}_{c,i} \tilde{u}_{c,i}, \quad (5.25)$$

where the cutoff velocity field $\tilde{\mathbf{u}}_c$ represents the high-frequency part of the resolved field, defined using a second filter, referred to as test filter, designated by the *tilde* symbol and associated with the cutoff length $\Delta > \bar{\Delta}$

$$\tilde{\mathbf{u}}_c = \bar{\mathbf{u}} - \tilde{\tilde{\mathbf{u}}}. \quad (5.26)$$

We note that for $\gamma \in [0, 1]$, the subgrid viscosity is always defined. The constant C_γ can be evaluated by theories of turbulence in the case of statistically homogeneous and isotropic turbulent flow

$$C_\gamma = C_q^{1-\gamma} C_s^{2\gamma}, \quad (5.27)$$

where the Smagorinsky constant $C_s \simeq 0.18$ and $C_q \simeq 0.20$.

5.3.3.2 Dynamic evaluation of the subgrid-viscosity constant

Theoretical values of the subgrid-viscosity constant cannot be used in our case because they are derived if the model is used without the ADM structural contribution, that is to model the whole subgrid tensor. In order to overcome this issue, we introduce a dynamic procedure of Germano–Lilly type to evaluate this parameter as a function of space and time. Such procedure completes the definition of the subgrid model based on the coupling of ADM with the dynamic mixed scale (DMS) model, called ADM-DMS in the sequel. This requires the introduction of the twice-filtered Navier–Stokes equations. Applying the test filter $\mathcal{T}\star$, represented by a *tilde*, to the filtered Navier–Stokes momentum equation (5.9) gives

$$\frac{\partial \tilde{\tilde{\mathbf{u}}}}{\partial t} + \mathbf{f}(\tilde{\tilde{\mathbf{u}}}) = [\mathbf{f}, \mathcal{T}\star](\bar{\mathbf{u}}) + \mathcal{T}\star[\mathbf{f}, \mathcal{G}\star](\mathbf{u}), \quad (5.28)$$

which can be recast in the form

$$\frac{\partial \widetilde{\mathbf{u}}}{\partial t} + \mathbf{f}(\widetilde{\mathbf{u}}) = -\nabla \cdot (\mathbf{L} + \widetilde{\boldsymbol{\tau}}) = -\nabla \cdot \mathbf{T}, \quad (5.29)$$

where $\mathbf{T} = \mathbf{L} + \widetilde{\boldsymbol{\tau}}$ is an expression of the Leibniz identity referred to as multiplicative Germano identity in the LES framework [88]. The components of $\boldsymbol{\tau}$ are given in Eq. (5.3) and those of \mathbf{L} by

$$L_{ij} = \widetilde{u_i u_j} - \widetilde{u_i} \widetilde{u_j}, \quad (5.30)$$

leading to the following expression for the subgrid tensor \mathbf{T} corresponding to the twice-filtered Navier–Stokes equations

$$T_{ij} = \widetilde{\widetilde{u_i u_j}} - \widetilde{u_i} \widetilde{u_j}. \quad (5.31)$$

The tensors corresponding to filtered and twice-filtered equations are modeled by blending ADM with the mixed scale model previously introduced. Assuming each subgrid tensor can be modeled using the same dynamic parameter C_d replacing the constant C_γ , which relies on the scale similarity hypothesis between test filter and primary filter cutoff lengths $\widetilde{\Delta}$ and $\overline{\Delta}$, we obtain

$$\tau_{ij}^m = \overline{u_i^* u_j^*} - \overline{u_i^*} \overline{u_j^*} + C_d \beta_{ij}, \quad \beta_{ij} = -2\overline{\Delta}^{1+\gamma} |\mathcal{F}(\overline{\mathbf{u}})|^\gamma (\overline{q_c})^{\frac{1-\gamma}{2}} \overline{S}_{ij}, \quad (5.32)$$

$$T_{ij}^m = \widetilde{\widetilde{u_i^* u_j^*}} - \widetilde{\widetilde{u_i^*}} \widetilde{\widetilde{u_j^*}} + C_d \alpha_{ij}, \quad \alpha_{ij} = -2\widetilde{\Delta}^{1+\gamma} |\mathcal{F}(\widetilde{\mathbf{u}})|^\gamma (\widetilde{q_c})^{\frac{1-\gamma}{2}} \widetilde{S}_{ij}, \quad (5.33)$$

where $\boldsymbol{\alpha}$ and $\boldsymbol{\beta}$ are the subgrid-viscosity terms deprived of their constant. The parameter C_d is evaluated in order to minimize the residual

$$E_{ij} = L_{ij} - L_{ij}^m, \quad (5.34)$$

where $\mathbf{L}^m = \mathbf{T}^m - \widetilde{\boldsymbol{\tau}}^m$. Using Eqs. (5.32)–(5.33), Eq. (5.34) reads

$$E_{ij} = L_{ij} - [(\widetilde{\widetilde{u_i^* u_j^*}} - \widetilde{\widetilde{u_i^*}} \widetilde{\widetilde{u_j^*}} + C_d \alpha_{ij}) - (\overline{u_i^* u_j^*} - \overline{u_i^*} \overline{u_j^*} + \widetilde{C_d} \beta_{ij})]. \quad (5.35)$$

Assuming C_d is constant over an interval at least equal to the test-filter cutoff length such that $\widetilde{C_d} \beta_{ij} = C_d \widetilde{\beta}_{ij}$, we have

$$E_{ij} = L_{ij} - (H_{ij} + C_d m_{ij}), \quad (5.36)$$

where

$$m_{ij} = \alpha_{ij} - \widetilde{\beta}_{ij} \quad \text{and} \quad H_{ij} = \overline{u_i^* u_j^*} - \overline{u_i^*} \overline{u_j^*}, \quad (5.37)$$

which consists in a system of six independent equations leading to six possible different values of the constant. In a similar framework and in order to obtain a single value, Lilly [156] proposed an evaluation based on a least-squares minimization of the form

$$\frac{\partial E_{ij} E_{ij}}{\partial C_d} = 0, \quad (5.38)$$

leading to the solution of the following single scalar equation

$$C_d = \frac{(L_{ij} - H_{ij}) m_{ij}}{m_{ij} m_{ij}}. \quad (5.39)$$

Smaller values than theoretical ones are expected for C_d using the previous dynamic procedure because of the small difference between the tensors \mathbf{L} and \mathbf{H} , only induced by the deconvolution error. Indeed, the tensor \mathbf{H} can be explicitly written as

$$H_{ij} = \frac{\widetilde{\widetilde{(\mathcal{Q}_N \star u_i)}}}{\widetilde{\widetilde{(\mathcal{Q}_N \star u_j)}}} - \frac{\widetilde{\widetilde{(\mathcal{Q}_N \star u_i)}}}{\widetilde{\widetilde{(\mathcal{Q}_N \star u_i)}}} \frac{\widetilde{\widetilde{(\mathcal{Q}_N \star u_j)}}}{\widetilde{\widetilde{(\mathcal{Q}_N \star u_j)}}}, \quad (5.40)$$

and if the deconvolution order $\mathcal{N} \rightarrow \infty$, corresponding to $\mathcal{Q}_N \rightarrow \mathcal{G}^{-1}$ if the series (5.14) is convergent, one has

$$\lim_{\mathcal{N} \rightarrow \infty} H_{ij} = L_{ij}, \quad (5.41)$$

which implies that the subgrid-viscosity term vanishes if exact deconvolution is performed up to the grid level. This behavior of the eddy-viscosity part of our model, when the deconvolution order tends to infinity is strictly equivalent to the one observed by Sagaut *et al.* [214] and Stolz *et al.* [246] using high-pass filtered subgrid-viscosity models. Furthermore the relaxation term introduced by Stolz *et al.* [244, 245] to stabilize their ADM-based LES has the same behavior in the infinite deconvolution order limit. The choice of the deconvolution order \mathcal{N} can be interpreted as a way of tuning the relative part taken by the subgrid-viscosity term which compensates the deconvolution error to minimize the difference between \mathbf{L} and \mathbf{L}^m , in a least-squares sense. In the limit of \mathcal{N} going to infinity, the modeled subgrid stress tensor defined in Eq. (5.32) reduces solely to its ADM contribution

$$\tau_{ij}^m = \overline{\hat{u}_i \hat{u}_j} - \overline{\hat{u}_i} \overline{\hat{u}_j}, \quad (5.42)$$

where $\hat{\mathbf{u}} = \mathcal{P} \star \mathbf{u}$ is the grid-filtered velocity.

5.3.4 Particular cases of ADM-DMS

In this section we highlight two particular cases of ADM-DMS. The first one is the model proposed by Zang *et al.* [272], based on Bardina and Smagorinsky models with a dynamic evaluation of the subgrid-viscosity constant. The ADM-DMS expression of the subgrid tensor given by (5.32) can be explicitly written as

$$\tau_{ij}^m = \overline{(\mathcal{Q}_N \star \bar{u}_i)(\mathcal{Q}_N \star \bar{u}_j)} - \overline{(\mathcal{Q}_N \star \bar{u}_i)} \overline{(\mathcal{Q}_N \star \bar{u}_j)} + C_d \beta_{ij}. \quad (5.43)$$

Then choosing $\gamma = 1$, $\mathcal{N} = 0$ and $\mathcal{F}(\bar{\mathbf{u}}) = \bar{\mathbf{S}}$ leads to

$$\tau_{ij}^m = \overline{\bar{u}_i \bar{u}_j} - \overline{\bar{u}_i} \overline{\bar{u}_j} + C_d \beta_{ij}, \quad \beta_{ij} = -2\bar{\Delta}^2 |\bar{\mathbf{S}}| \bar{S}_{ij}, \quad (5.44)$$

which is the expression of the one-parameter dynamic mixed model. For $\mathcal{N} = 0$, the tensor \mathbf{H} explicitly expressed by Eq. (5.40) reads

$$H_{ij} = \widetilde{\overline{\bar{u}_i \bar{u}_j}} - \widetilde{\overline{\bar{u}_i}} \widetilde{\overline{\bar{u}_j}}. \quad (5.45)$$

The second particular case of ADM-DMS is DMS, a dynamic version of the mixed scale model proposed by Sagaut [212]. This model is formally obtained by imposing $\mathcal{Q}_N = 0$ in the developments of Sect. 5.3.3.2, which leads to $\mathbf{H} = \mathbf{0}$ and to the following expression of the subgrid tensor

$$\tau_{ij}^m = C_d \beta_{ij}, \quad \beta_{ij} = -2\bar{\Delta}^{1+\gamma} |\mathcal{F}(\bar{\mathbf{u}})|^\gamma (\bar{q}_c)^{\frac{1-\gamma}{2}} \bar{S}_{ij}, \quad (5.46)$$

with the dynamic parameter of DMS given by

$$C_d = \frac{L_{ij} m_{ij}}{m_{ij} m_{ij}}. \quad (5.47)$$

Without the ADM contribution, higher values of the dynamic parameter are expected since the difference between \mathbf{L} and \mathbf{H} occurring in Eq. (5.39) disappears in Eq. (5.47). This phenomenon is in direct relation with the fact that the subgrid viscosity term is used to model the whole subgrid tensor in this particular case.

5.4 Filtering

Filtering techniques suited to SEM and LES must preserve \mathcal{C}^0 -continuity of the filtered variables across spectral elements and be applicable at the element level. In the sequel, we present a filter satisfying these constraints which is based on spectral techniques ensuring the element-level filtering property. The filtering operation is performed by applying a given transfer function in a modal basis. Depending on this transfer function, this filter may not be projective, therefore ensuring its invertibility which is a key feature needed by the deconvolution procedure. Hence, we will focus on the choice of the transfer function to fulfill this constraint.

5.4.1 Description of the filter

The modal basis introduced in the p -version of finite elements and first used by Boyd [38] as filtering technique is presented in its one-dimensional version, the extension to three dimensions being straightforward by tensor product. It is built up on the reference parent element $\hat{\Omega} = [-1, 1]$ of the SEM as

$$\begin{aligned} \phi_0 &= \frac{1-\xi}{2}, & \phi_1 &= \frac{1+\xi}{2}, \\ \phi_j &= L_j(\xi) - L_{j-2}(\xi), & 2 \leq j \leq N, \end{aligned} \quad (5.48)$$

where L_j is the Legendre polynomial of degree j . Unlike the Lagrange–Legendre nodal basis used in our spectral element calculations, this modal basis forms a hierarchical set of polynomials allowing to define in an explicit and straightforward manner a low-pass filtering procedure. Any variable v can be expressed in this basis by the relation

$$v(\xi) = \sum_{j=0}^N \check{v}_j \phi_j(\xi), \quad \xi \in \hat{\Omega}, \quad (5.49)$$

which in matrix notation reads

$$\mathbf{v} = \mathbf{\Phi} \check{\mathbf{v}}, \quad (5.50)$$

where

$$\Phi_{ij} = \phi_j(\xi_i). \quad (5.51)$$

The filtering operation is performed in the spectral modal space through a diagonal matrix \mathbf{K} whose components are chosen in order to fulfill the required properties of the filter. The filtering process for a one-dimensional problem is expressed by

$$\bar{\mathbf{v}} = \Phi \mathbf{K} \Phi^{-1} \mathbf{v} = \mathbf{G} \mathbf{v}. \quad (5.52)$$

5.4.2 Transfer function

\mathcal{C}^0 -continuity, conservation of constants, invertibility and low-pass filtering are obtained by properly choosing the transfer function represented by the diagonal transfer matrix \mathbf{K} . Imposing all these requirements to the filter could seem like an intractable issue but appears feasible when visualizing the modal basis functions presented in [24] and reported in Fig. 5.1. As the filter acts in another basis than the one used for our spectral element calculations, \mathcal{C}^0 -continuity is preserved if the boundaries of the elements are not affected by the filtering procedure. One can notice that the only shape functions having non-zero values at the element boundaries are ϕ_0 and ϕ_1 , while ϕ_j , $j \geq 2$ are bubble functions. The functions ϕ_0 and ϕ_1 are responsible for imposing the non-zero values on element edges. Therefore, the transfer function coefficients must satisfy

$$K_{ij} = \delta_{ij}, \quad i, j \leq 1, \quad (5.53)$$

with δ_{ij} the Kronecker operator. If K_{ij} verifies (5.53), the constants are conserved after filtering because they are expressed as a linear combination of ϕ_0 and ϕ_1 . The modal filter is not projective if all diagonal coefficients K_{ii} are non-zeros. The last required property is to perform low-pass filtering in frequency. As this modal basis forms a hierarchical set of polynomials, low-pass filtering is done by damping the high-degree polynomial contributions. The transfer matrix is expressed by

$$K_{ij} = \delta_{ij} \mathcal{K}(i), \quad (5.54)$$

with the continuous transfer function

$$\mathcal{K}(k) = \frac{1}{1 + \left(\eta \frac{\max(0, k-1)}{N} \right)^2}, \quad \eta \geq 0, \quad (5.55)$$

where η is referred to as filtering rate (Fig. 5.2). The transfer function is such that the filter verifies all the required properties previously described. The cutoff frequency \bar{k} is arbitrarily defined by $\mathcal{K}(\bar{k}) = 1/2$. Such filtering technique has already been used by Blackburn & Schmidt for the LES of channel flow using SEM [24]. In the present work, the transfer function given by Eq. (5.55) and depicted on Fig. 5.2 ensures the invertibility of the filter contrary to [24]. Moreover, the shape of the transfer function in Fig. 5.2 is similar to the one classically used by Stolz *et al.* [244, 245]. However, in the SEM framework the transfer function is defined element by element in the spectral modal space which prevents from a direct comparison with the discrete filter implemented by Stolz *et al.* [244, 245].

5.4.3 Filter cutoff length

The subgrid-viscosity term of ADM-DMS makes explicitly use of the filter cutoff length which needs to be defined. For a one-dimensional problem, *e.g.* in the x -direction, using the SEM, a common choice of filter width [35, 37] is

$$\bar{\Delta}_x = \frac{\hat{\Delta}_x}{p_{x,c}}, \quad (5.56)$$

where $\hat{\Delta}_x$ is the element size and $p_{x,c}$ the highest polynomial degree in the spectral decomposition (5.49) that is the closest to the cutoff frequency \bar{k}

$$p_{x,c} = \max(i), \quad \text{such that } i \leq \bar{k}, \quad i = 0, \dots, N. \quad (5.57)$$

We notice that the filter length decreases when the element is refined and the polynomial degree augmented. The straightforward three-dimensional extension for problems with rectilinear spectral elements is

$$\bar{\Delta}(x, y, z) = (\bar{\Delta}_x(x) \bar{\Delta}_y(y) \bar{\Delta}_z(z))^{1/3} = \left(\frac{\hat{\Delta}_x}{p_{x,c}} \frac{\hat{\Delta}_y}{p_{y,c}} \frac{\hat{\Delta}_z}{p_{z,c}} \right)^{1/3}. \quad (5.58)$$

5.4.4 Filtering operators related to ADM

The filtering operators $\mathcal{Q}_{\mathcal{N}\star}$ and $\mathcal{H}_{\mathcal{N}\star}$ are defined with respect to $\mathcal{G}\star$, see Eq. (5.14) and (5.16) respectively and explicitly depend on the deconvolution order \mathcal{N} . By representing in Figure 5.2 the transfer function associated with $\mathcal{H}_{\mathcal{N}\star}$, one can observe that the deconvolution error is important at the end of the modal spectrum, so that $\mathcal{H}_{\mathcal{N}\star}$ constitutes a high-pass filter. When increasing the deconvolution order \mathcal{N} , the transfer function associated with the filter $\mathcal{H}_{\mathcal{N}\star}$ diminishes, showing the increasing accuracy of the approximate deconvolution procedure.

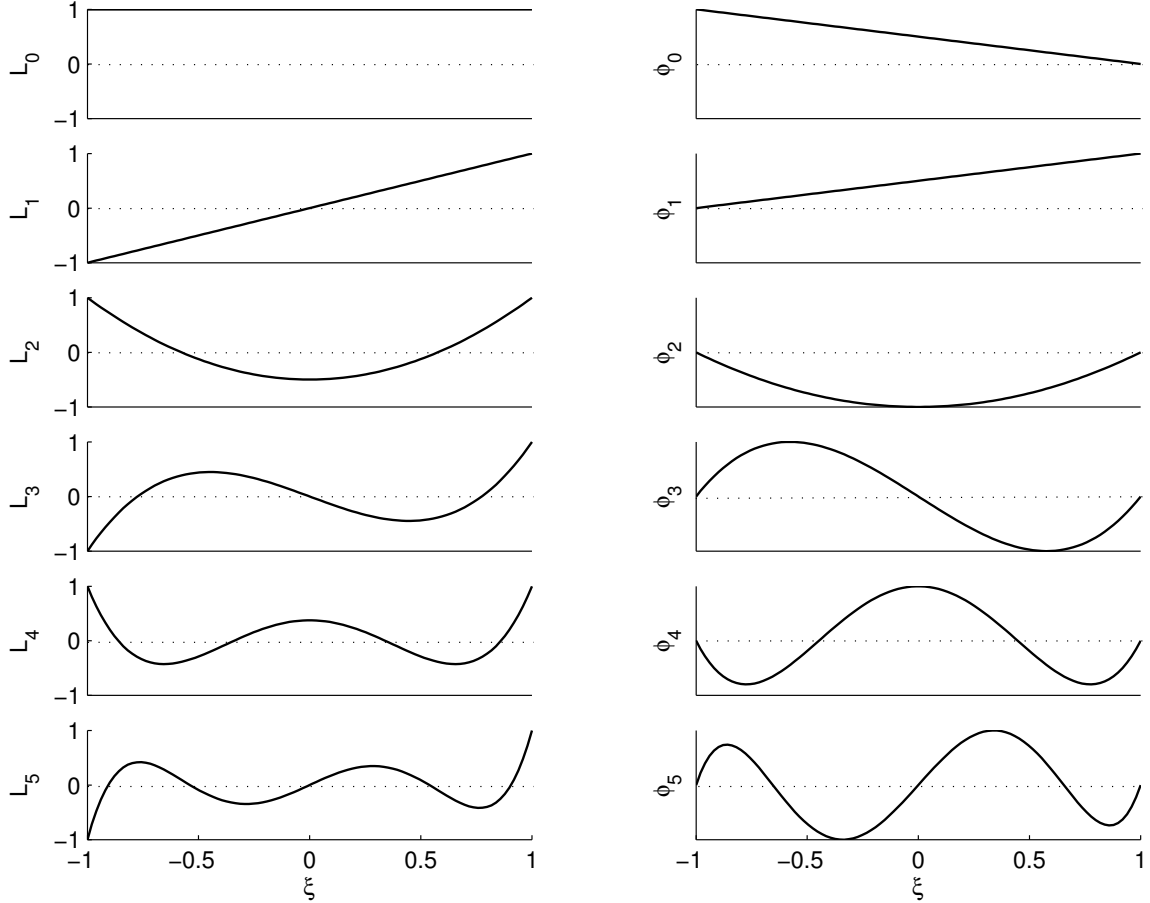


Fig. 5.1: Bases associated with the filtering operation, shown for polynomial order $N = 5$ on the reference parent element $\hat{\Omega} = [-1, 1]$. The Legendre polynomials (left column), the modal polynomials (right column).

5.5 LES of the lid-driven cubical cavity flow

5.5.1 General considerations

The different LES presented hereafter refer to the flow in a lid-driven cubical cavity performed at Reynolds number of 12 000. The flow domain Ω consists in a cubical cavity such that $\Omega = (-h, h)^3$, the axis origin being assigned at the center of the cavity (Fig. 4.1). The flow is driven by imposing a non-zero velocity parallel to the x -axis on the “top” wall. On the other walls, no-slip conditions are imposed. The moving wall will be referred to as the lid while the faces normal to the z -axis will be referred to as side walls. The upstream and downstream walls are normal to the x -axis and characterized by their relative position with respect to the lid motion. The remaining face parallel to the lid is called bottom wall. As far as the velocity imposed on the lid is concerned, the unit velocity induces severe discontinuities along the top edges. In order to avoid these defects, the imposed velocity on the lid is given by the polynomial expression

$$u_x(x, h, z) = U_0(1 - (x/h)^n)^2(1 - (z/h)^n)^2, u_y = u_z = 0, \quad (5.59)$$

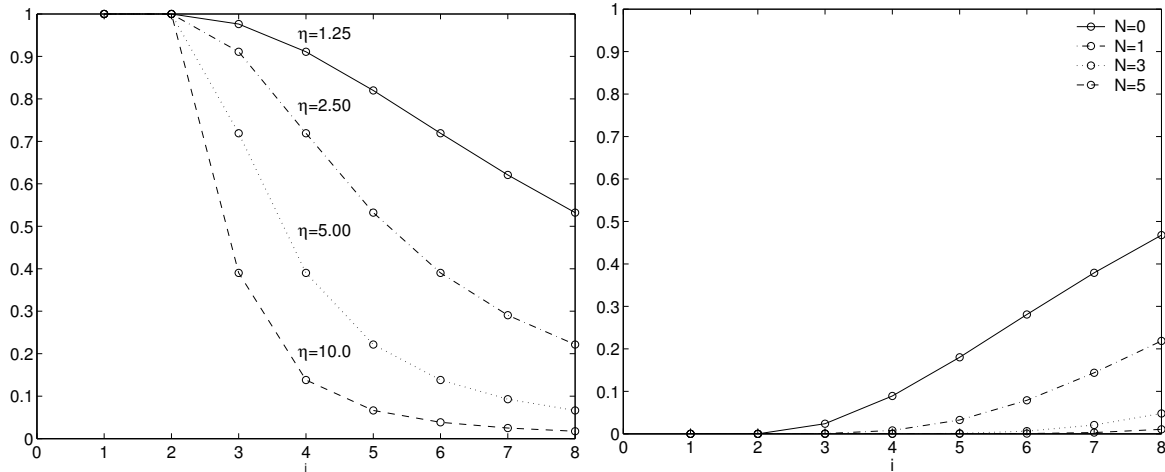


Fig. 5.2: Transfer functions associated with $\mathcal{G}\star$ for different values of the filtering rate $\eta = 1.25, 2.50, 5.00, 10.0$ (left) and, $\mathcal{H}\star$ for different values of the deconvolution order $\mathcal{N} = 0, 1, 3, 5$ with $\eta = 1.25$ (right). Polynomial order $N = 8$.

where U_0 is a constant. The Reynolds number is defined using the maximum velocity U_0

$$\text{Re} = \frac{2hU_0}{\nu}. \quad (5.60)$$

Although the geometry is very simple, the flow presents complex physical phenomena [37, 155], no direction of homogeneity and a large variety of flow conditions. For such Reynolds numbers, the flow over most of the domain is laminar and turbulence develops near the cavity walls. Its main feature is a large scale recirculation which spans the cavity in the z -direction. Aside this large flow structure, the relatively high momentum fluid near the lid is deviated by the downstream wall into a down flowing nonparallel wall jet which separates ahead of the bottom wall. A region of high pressure and dissipation located at the top of downstream wall results from this deviation. The energy resulting from the impingement of the separated layer against the bottom wall is lost to turbulence and partly recovered by an emerging wall jet near the upstream wall where the flow slows down and relaminarizes during the fluid rise. The flow is also characterized by multiple counter-rotating recirculating regions at the corners and edges of the cavity.

| | Time-step h/U_0 | Lid vel. n | Int. time h/U_0 | Nb. elements (E_x, E_y, E_z) | Polynomial degree (N_x, N_y, N_z) |
|-----|----------------------|-----------------|----------------------|-----------------------------------|--|
| DNS | 0.0025 | 18 | 1 000 | (1, 1, 1) | (128, 128, 128) |
| LES | 0.0020 | 18 | 80 | (8, 8, 8) | (8, 8, 8) |

Table 5.1: Numerical and physical parameters of the DNS [155] and LES.

The physical and numerical parameters of the DNS and the LES are gathered in Table 5.1. The DNS constitutes the reference solution and was obtained with a Chebyshev collocation method on a grid composed of 129 collocation points in each spatial direction [155]. For LES, the spectral elements are unevenly distributed (Fig. 4.2) in order to resolve the boundary layers along the lid and the downstream wall. The spatial discretization has $E_x = E_y = E_z = 8$ elements in the three space directions with $p_x = p_y = p_z = 8$ polynomial degree, equivalent to 65^3 grid points in total. The mesh used for LES has therefore twice less points per space direction than the DNS grid of Leriche and Gavrilakis but it is important to note that to achieve a DNS using the SEM would require more than 129^3 grid points due to the lower order of the SEM as compared to the Chebyshev collocation method [58]. The space discretization is strictly equivalent to the one used for the LES reported by Zang *et al.* [272] for a lower Reynolds number of 10 000. One should notice that the time-step for LES is slightly smaller than for the DNS which is due to different CFL constraints for the two different numerical schemes used, namely SEM and Chebyshev collocation.

The mixed scales constant is set to $\gamma = 0.5$ in order to have the triple dependency on the large and small structures of the resolved field as a function of the filter cutoff length. Furthermore, the ratio between both filtering rates $\eta_{\mathcal{T}}$ and $\eta_{\mathcal{G}}$ in Eq. (5.55), corresponding to the test and primary filters $\mathcal{T}\star$ and $\mathcal{G}\star$ respectively, is taken equal to two leading to a ratio of the filter cutoff lengths $\tilde{\Delta}/\bar{\Delta} = 7/4$. The parameters chosen for all

LES analyzed hereafter are summarized in Table 5.2. The choice of the deconvolution order is based on the observations of Stolz *et al.* [244, 245] and, Gullbrand & Chow [107] who found that the value $\mathcal{N} = 5$ for the deconvolution order is a good compromise between the precision in the approximate deconvolution and the computational cost induced by higher \mathcal{N} in the van Cittert expansion series. This choice is further justified by the analysis of the approximate deconvolution error developed in Sec. 5.5.2.

A LES based on ADM-DMS with the same parameters as the ones in Table 5.2, except for $\mathcal{F} = \overline{\omega}$ has been carried out and has provided results extremely close to those from ADM-DMS with $\mathcal{F} = \overline{\mathbf{S}}$. Consequently, ADM-DMS results for the case $\mathcal{F} = \overline{\mathbf{S}}$ are the only ones reported in this chapter. A LES based on DMS, see Sec. 5.3.4, with the same parameters as ADM-DMS for its dynamic mixed scale part, is also presented and compared to ADM-DMS in order to identify the improvement induced by coupling ADM with DMS.

| LES model | \mathcal{N} | $\eta_{\mathcal{G}}$ | $\eta_{\mathcal{T}}$ | γ | \mathcal{F} |
|-----------|---------------|----------------------|----------------------|----------|-------------------------|
| ADM-DMS | 5 | 1.25 | 2.50 | 0.50 | $\overline{\mathbf{S}}$ |
| DMS | - | 1.25 | 2.50 | 0.50 | $\overline{\mathbf{S}}$ |

Table 5.2: Models parameters for both ADM-DMS and DMS.

The different LES are all started from the same initial condition, namely an instantaneous velocity field obtained from the DNS in the statistically-steady range and re-interpolated onto the spectral element grid. The projective filter due to this re-interpolation induces the unrecoverable loss of the subgrid scales.

In order to verify that our mesh is coarse enough and does not resolve all scales of the flow, a DNS of the lid-driven cubical cavity flow was performed with SEM and with exactly the same physical and numerical parameters as the ones reported in Table 5.1. One can observe on Fig. 5.3 that this under-resolved DNS (UDNS) is totally inoperative in the particular context of this simulation. Even first-order statistics are far from being well predicted, not to mention second-order ones. These results allow us to confirm the sufficient under-resolution of the flow using the 65^3 SEM mesh.

We assume that a statistically-steady state is reached and time averaging will be taken as ensemble averaging. For any variable v , we recall the Reynolds statistical decomposition

$$v = \langle v \rangle + v^\diamond \quad (5.61)$$

introduces the time-averaged value denoted into brackets $\langle v \rangle$ and its fluctuating part v^\diamond . It is noteworthy reminding here the difference between the filter splitting $v = \overline{v} + v'$ and the Reynolds decomposition, see Eq. (4.42) and Sec. 4.3.1 in Chapter 4. As the initial condition of all LES is the same DNS instantaneous velocity field taken from the statistically-steady-state range, it is reasonable to also assume that LES will reach a statistically-steady state very quickly, if subgrid modeling is efficient [37]. These assumptions are easily verified by evaluating the total kinetic energy of the resolved field

$$Q(\overline{\mathbf{u}}) = \frac{1}{2} \int_{\Omega} \overline{u}_i \overline{u}_i \, d\Omega, \quad (5.62)$$

which is expected to evolve within a relatively small fluctuation range. For figure 5.4, the results reported for ADM-DMS correspond to a longer dynamic range of $200 h/U_0$ time units. However, all the statistical results presented hereafter for both ADM-DMS and DMS are limited to the first $80 h/U_0$ time units. The time histories of $Q(\overline{\mathbf{u}})$ presented in Fig. 5.4 for ADM-DMS and DMS show an evolution within the same fluctuation range as the DNS and around the average value of the total kinetic energy predicted by the DNS. As reported in Chapter 4 and also by Bouffanais *et al.* [37] using a dynamic Smagorinsky model, which is a particular case of the present DMS over $800 h/U_0$ time units, further confirms the evolution of $Q(\overline{\mathbf{u}})$ for DMS in the long run.

Additionally the time histories of the kinetic energy of the fluctuating resolved field $Q(\overline{\mathbf{u}}^\diamond)$ presented on Fig. 5.5 is also evolving in the same fluctuation range as the DNS. The results on Fig. 5.4 and Fig. 5.5 for both $Q(\overline{\mathbf{u}})$ and $Q(\overline{\mathbf{u}}^\diamond)$ allow to conclude that the turbulent flow reaches a statistically-steady state extremely quickly. No transient can be clearly identified in this case. The same conclusion is made in Sec. 4.3.1 and also by Bouffanais *et al.* [37] for LES using more classical subgrid models.

Since the scale separation used for LES leads to the removal of subgrid scales mainly responsible for the energy dissipation, the subgrid model has to take into account this phenomenon. The flow in the cavity is confined and recirculating so that the same fluid is conserved inside the cavity. Moreover, kinetic energy is constantly provided to it by viscous diffusion. Hence, integral energy quantities over the flow domain such as $Q(\overline{\mathbf{u}})$ and $Q(\overline{\mathbf{u}}^\diamond)$ are a direct indication of any under- or over-dissipative character of the subgrid model, keeping in mind the very low numerical dissipation and dispersion of the SEM. The results obtained for $Q(\overline{\mathbf{u}})$ using ADM-DMS and DMS clearly show that the energy balance is achieved when using these models in this context.

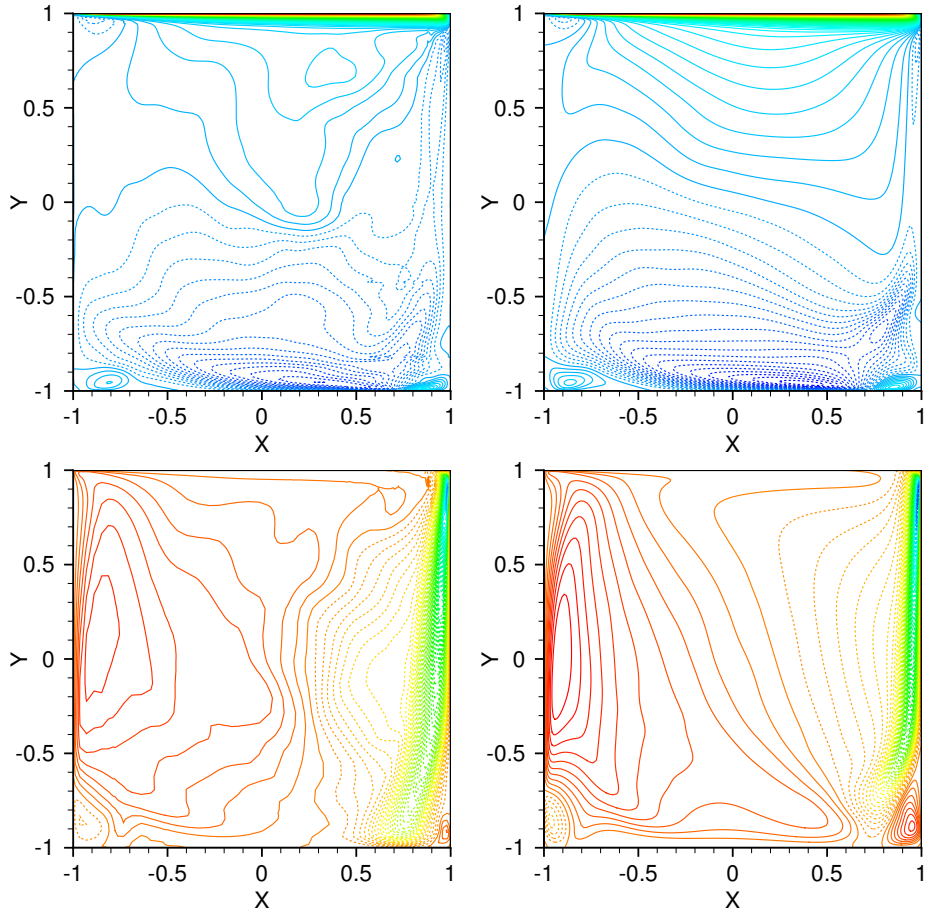


Fig. 5.3: In the mid-plane $z/h = 0$, UDNS (left column) and DNS (right column). Top row: contours of the x -component of the average resolved velocity field from -0.2 to 1 by increments of 0.01 . Bottom row: contours of the y -component of the average resolved velocity field from -0.7 to 0.1 by increments of 0.01 . Color scale from blue to red. Dashed contours correspond to negative levels. Levels in U_0 units.

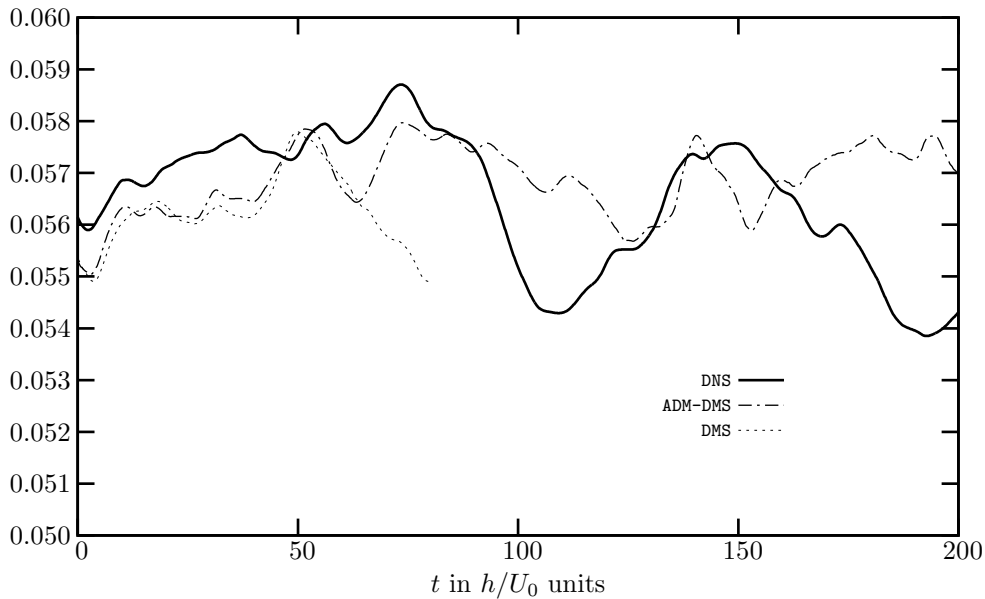


Fig. 5.4: Total resolved kinetic energy $Q(\bar{\mathbf{u}})$ in $U_0^2 h^3$ units with respect to the time t in h/U_0 units and, for the DNS, ADM-DMS and DMS (limited to 80 time units).

5.5.2 Validation of the approximate deconvolution procedure

The first step towards a complete validation of the ADM-DMS model, resides in investigating the accuracy of the deconvolution procedure based on the van Cittert method, with respect to the deconvolution order \mathcal{N} . For

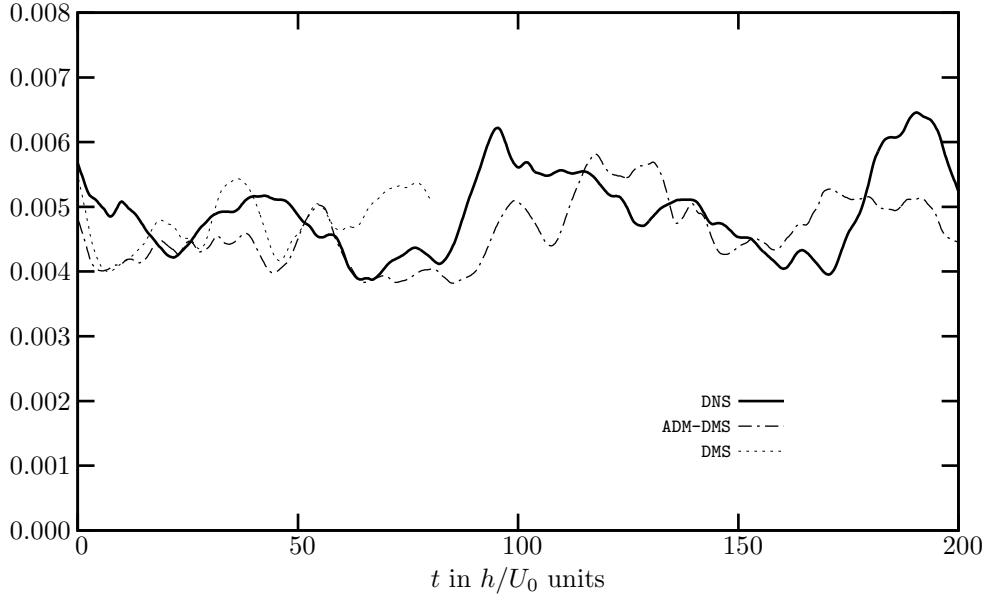


Fig. 5.5: Fluctuating resolved kinetic energy $Q(\bar{\mathbf{u}}^\circ)$ in $U_0^2 h^3$ units with respect to the time t in h/U_0 units and, for the DNS, ADM-DMS and DMS (limited to 80 time units).

this purpose, we define the relative error in L^2 -norm between a non-filtered DNS velocity field, extracted from the DNS database of Leriche & Gavrilakis [155], and its deconvoluted counterpart $\mathcal{Q}_{\mathcal{N}} \star \bar{\mathbf{u}}$

$$e_{\mathbf{u}} = \frac{\|\mathbf{u} - \mathcal{Q}_{\mathcal{N}} \star \bar{\mathbf{u}}\|_{L^2(\Omega)}}{\|\mathbf{u}\|_{L^2(\Omega)}}. \quad (5.63)$$

Figure 5.6 displays the parametric analysis of the relative error with respect to the deconvolution order, with the filtering rate $\eta_{\mathcal{G}}$ as parameter. One can notice that the van Cittert expansion series is convergent and the error increases with the filtering rate $\eta_{\mathcal{G}}$. In practical tests the deconvolution order must be set lower to 30 in order to avoid having binomial coefficients of very high values which would inevitably induce precision errors. This numerical issue justifies the “apparent divergence” of the approximate deconvolution procedure for all filtering rates observed in Fig. 5.6 for large values of \mathcal{N} . The filtering rate is increased from 1 to 9 by unit increments showing that the deconvolution error is larger with higher values of the filtering rate, which corresponds to the expected result. One can also notice that the error growth in the “apparent divergence” occurs earlier with lower filtering rates. It is very interesting to note that the error analysis is being performed using a velocity field corresponding to a turbulent flow including laminar regions. The resulting deconvolution error is clearly higher than the one obtained with a smooth analytically-defined field.

5.5.3 *A posteriori* validations

In this section, results of the LES are compared with the available reference results by analyzing first- and second-order statistics. The measurements reported by Leriche & Gavrilakis [155] were taken in the mid-plane $z/h = 0$, which is the statistical symmetry plane of the flow domain. For the sets of DNS data, the total velocity field is considered whereas in the case of LES, only its resolved part is presented. In consequence, the statistical moments computed from the resolved field cannot be equal to those computed from the DNS. One solution to overcome this issue would have been to apply the same filtering as is used for the scale separation to the reference solution [183]. We refer the reader to the monograph by Sagaut [213] for more details. The statistics for all LES and UDNS are based on a sampling approximately 10 times smaller than the one of the original DNS, but about twice longer than the one of the LES of Zang *et al.* [272]; more precisely 400 samples are collected over $80 h/U_0$ time units. The original reference DNS statistics were performed using 4 000 samples extracted over an integration range of $1 000 h/U_0$. Therefore, the LES statistics are not expected to be identical to the reference ones, especially the second-order ones.

The comparisons with the DNS results are performed by plotting identical series of contour levels of the average velocity. Figures 5.8 displays the average values of the velocity field for DMS, ADM-DMS, and the DNS in the mid-plane of the cavity. This figure is complemented by the corresponding one-dimensional plots presented

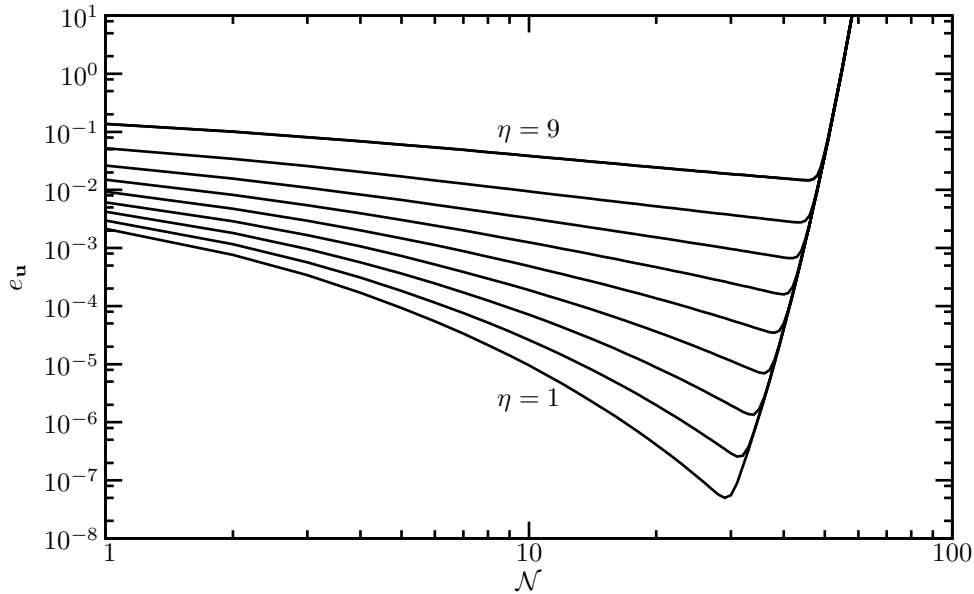


Fig. 5.6: Parametric analysis of the deconvolution error $e_{\mathbf{u}}$ with respect to the deconvolution order \mathcal{N} . The filtering rate η is increased from 1 to 9 with unit increments.

in Fig. 5.7 on the horizontal/vertical centerlines in the mid-plane $z/h = 0$. A rapid overview of these figures indicates that ADM-DMS provides results very close to the DNS references, which has to be compared with the UDNS results of Figure 5.3. In addition, it appears that ADM-DMS results are more satisfactory than those from DMS. Secondary corner eddies located above the bottom wall and below the lid next to the upstream wall are correctly resolved in the mean flow. The flow below the lid and near the corner with the downstream wall presents wiggles in the LES contours for $\langle \bar{u}_y \rangle$. More limited effects are noticeable for the equivalent x -component field. We assume that these very limited defects find their origin in a local too important under-resolution due to the very high shear rate near the downstream corner right below the lid [37]. The previous comparisons of ADM-DMS with the DNS and DMS for first-order moments require to be complemented by plotting identical series of contours of three components of the resolved Reynolds stress tensor. Figure 5.9 showcases the improvement achieved in terms of subgrid modeling by coupling ADM with DMS. Moreover, Fig. 5.10–5.12 provide the associated one-dimensional plots of these quantities in the vertical and horizontal centerlines of the mid-plane of the cavity. Indeed, the variations of $\langle \bar{u}_x^{\circ 2} \rangle^{1/2}$, $\langle \bar{u}_y^{\circ 2} \rangle^{1/2}$ and $\langle \bar{u}_x^{\circ} \bar{u}_y^{\circ} \rangle$ for ADM-DMS reproduce quite accurately the intense-fluctuations zones in the mid-plane $z/h = 0$, and more specifically in the vicinity of the downstream corner eddy. DMS appears clearly not as effective as ADM-DMS. The lower intensity of the Reynolds stress components for ADM-DMS as compared to the DNS are induced by the lower sampling of all LES. A longer dynamic range would produce more intense results as reported in [37].

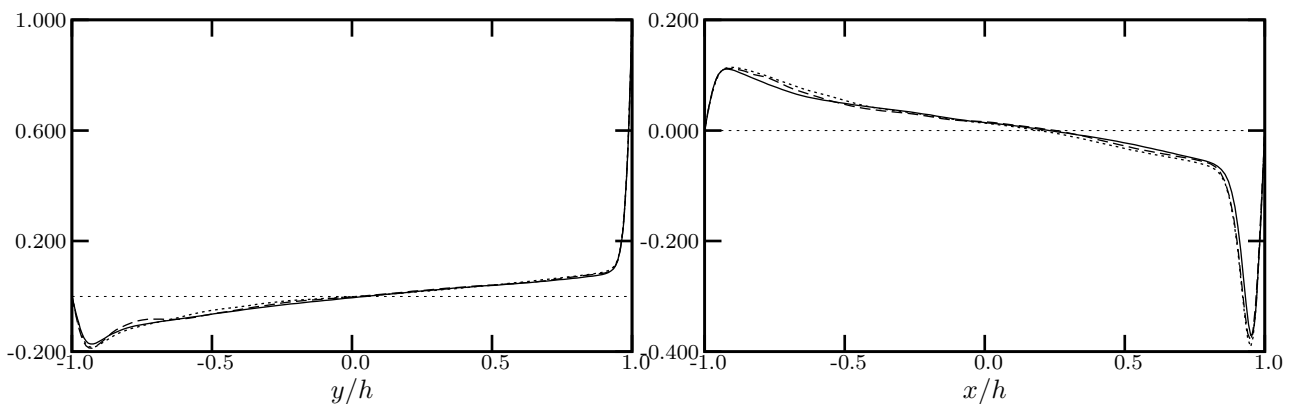


Fig. 5.7: In the mid-plane $z/h = 0$, DMS (dashed lines), ADM-DMS (dotted lines) and DNS (solid lines). Left: $\langle \bar{u}_x \rangle$ on the horizontal centerline $x/h = 0$. Right: $\langle \bar{u}_y \rangle$ on the vertical centerline $y/h = 0$.

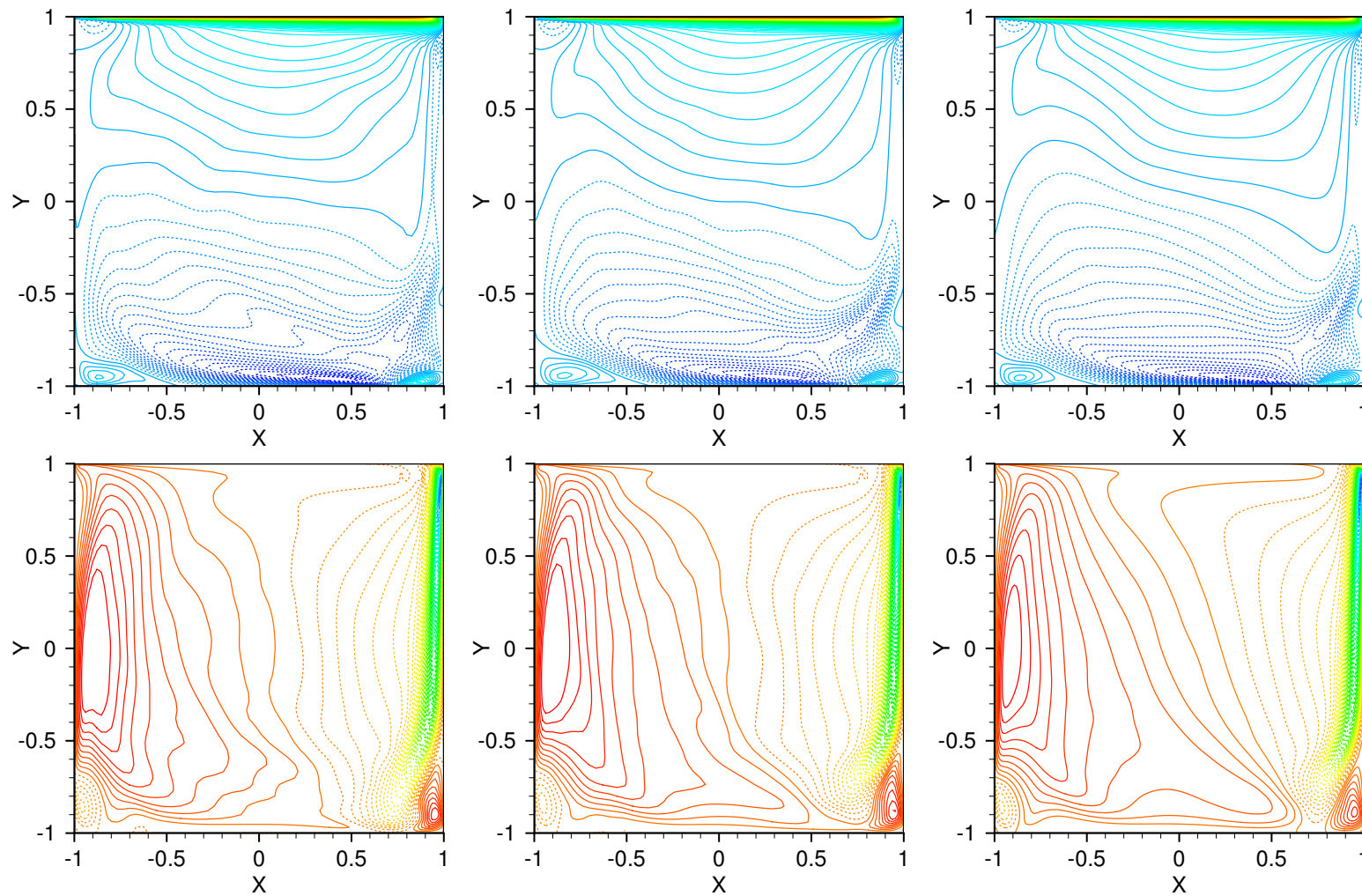


Fig. 5.8: In the mid-plane $z/h = 0$, DMS (left column), ADM-DMS (central column) and DNS (right column). Top row: contours of $\langle \bar{u}_x \rangle$ from -0.2 to 1 by increments of 0.01 . Bottom row: contours of $\langle \bar{u}_y \rangle$ from -0.7 to 0.1 by increments of 0.01 . Color scale from blue to red. Dashed contours correspond to negative levels. Levels in U_0 units.

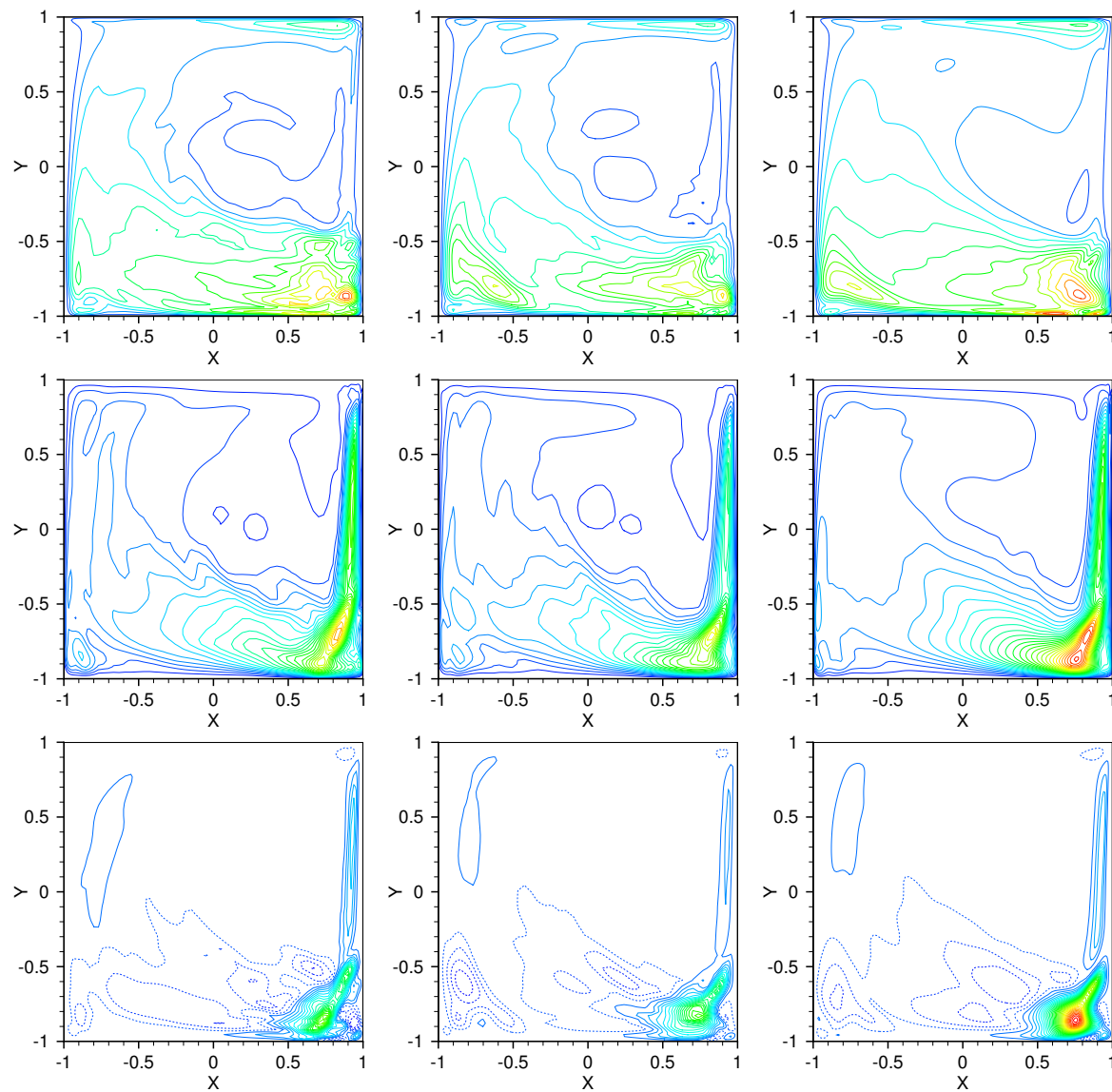


Fig. 5.9: In the mid-plane $z/h = 0$, DMS (left column), ADM-DMS (central column) and DNS (right column). Top row: contours of $\langle \overline{u_x^2} \rangle^{1/2}$ from 0 to 0.07 by increments of 0.005. Central row: contours of $\langle \overline{u_y^2} \rangle^{1/2}$ from 0 to 0.15 by increments of 0.005. Bottom row: contours of $\langle \overline{u_x u_y} \rangle$ from -0.0007 to 0.0065 by increments of 0.0002 . Color scale from blue to red. Dashed contours correspond to negative levels. Levels in U_0 units for $\langle \overline{u_x^2} \rangle^{1/2}$ and $\langle \overline{u_y^2} \rangle^{1/2}$ and in U_0^2 units for $\langle \overline{u_x u_y} \rangle$.

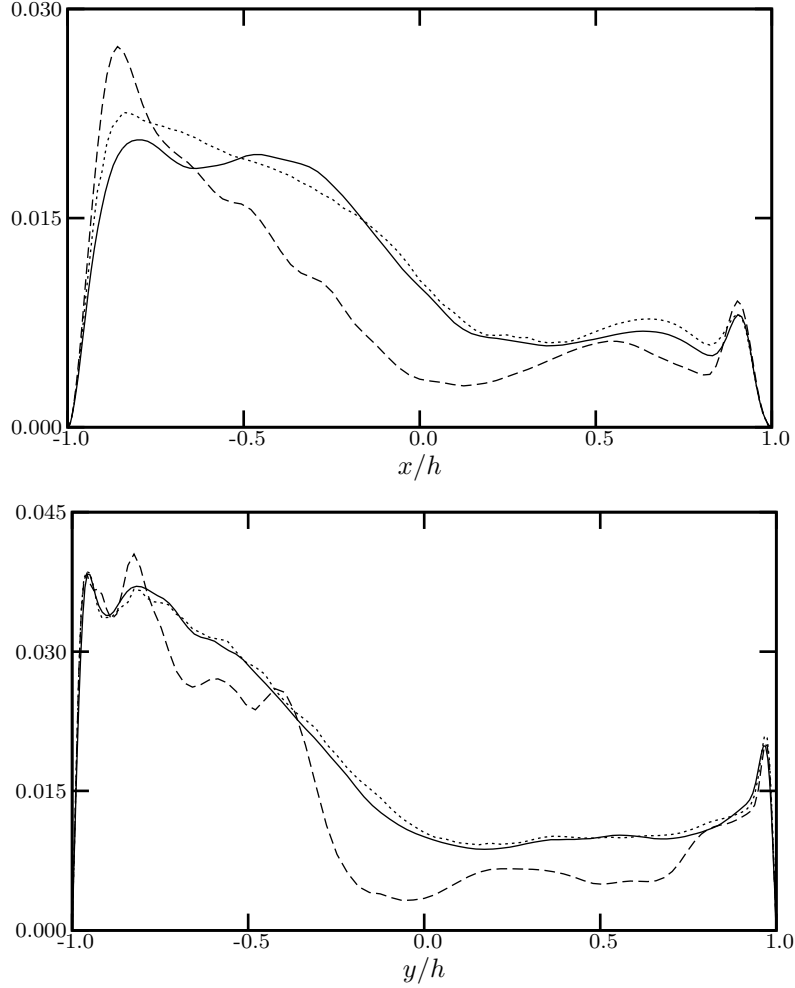


Fig. 5.10: In the mid-plane $z/h = 0$, DMS (dashed lines), ADM-DMS (dotted lines) and DNS (solid lines). $\langle \overline{u_x^{\diamond 2}} \rangle^{1/2}$ on the vertical centerline $y/h = 0$ (Top) and on the horizontal centerline $x/h = 0$ (Bottom).

5.5.4 Reynolds stresses production

As mentioned by Leriche & Gavrilakis [155], the largest Reynolds stresses production rates in the cavity are to be found in the primary elliptical jets parallel to the downstream wall, near the impact points just above the bottom wall. The budget equations of the resolved second-order moments $\langle \overline{u_i^{\diamond} u_j^{\diamond}} \rangle$ governing the resolved Reynolds stresses, see [178, 199], comprise a term named here \overline{P}_{ij} , defined by

$$\overline{P}_{ij} = -\langle \overline{u_i^{\diamond} \overline{u_k^{\diamond}}} \rangle \frac{\partial \langle \overline{u_j} \rangle}{\partial x_k} - \langle \overline{u_j^{\diamond} \overline{u_k^{\diamond}}} \rangle \frac{\partial \langle \overline{u_i} \rangle}{\partial x_k} \quad (5.64)$$

and corresponding to the interaction of the mean flow and the Reynolds stress tensor. This quantity can be interpreted as responsible for the production of resolved Reynolds stresses and couples first- and second-order statistical moments.

In the specific case of the separated downstream-wall jet, the term \overline{P}_{22} is the largest out of the set of \overline{P}_{ij} terms. After probing in the cavity, the maxima of the field \overline{P}_{22} was found in the plane $y/h = -0.9384$ just at a very short distance above the bottom wall. The contours of the resolved Reynolds stress production term \overline{P}_{22} in this plane are shown in Figure 5.13. First, it can be noted that these contours are qualitatively very close to the ones obtained by Leriche & Gavrilakis [155] and presents secondary structures of negative Reynolds stress production. The distribution of contours allows to clearly visualize the trace of the separated elliptical jets just before their impingement on the bottom wall. This separation is clearer for ADM-DMS than for DMS which shows once again the superiority of the coupled model.

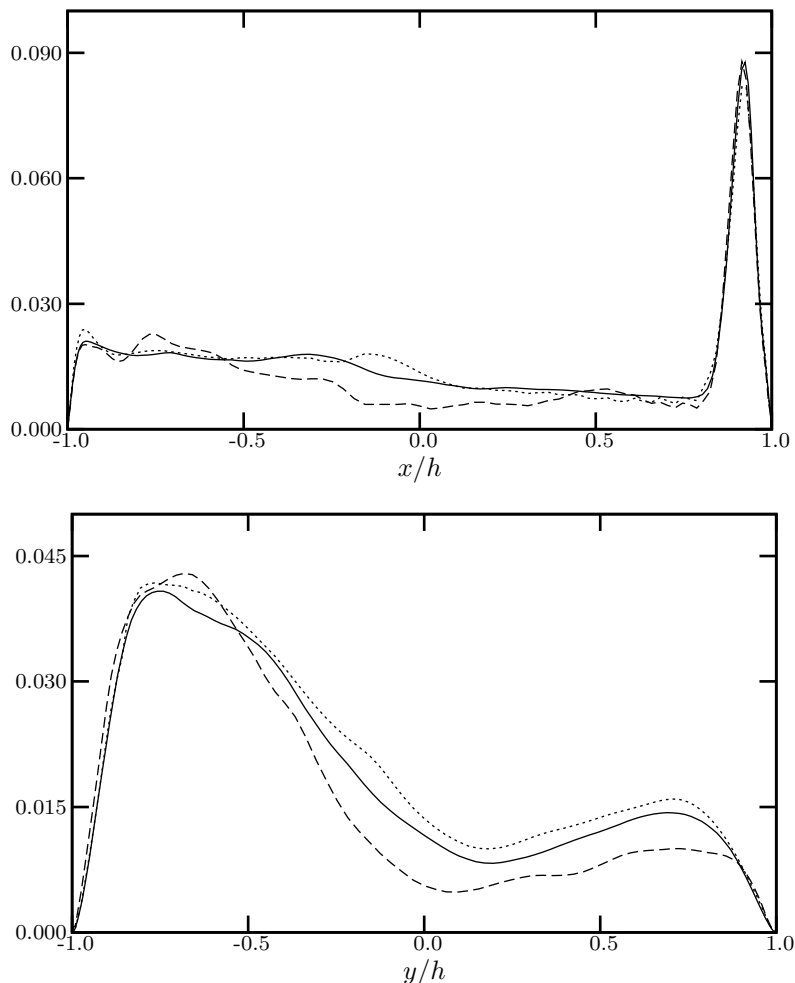


Fig. 5.11: In the mid-plane $z/h = 0$, DMS (dashed lines), ADM-DMS (dotted lines) and DNS (solid lines). $(\overline{u_y'^2})^{1/2}$ on the vertical centerline $y/h = 0$ (Top) and on the horizontal centerline $x/h = 0$ (Bottom).

5.5.5 Dynamic parameter for ADM-DMS

In practical LES presented in the sequel, local negative values of the dynamic parameter C_d are encountered. It was not found necessary to clip them as commonly done—*e.g.* in [24, 272]—to conveniently get rid of locally destabilizing negative values.

It is worth analyzing the variations of the dynamic parameter C_d for ADM-DMS in the plane $y/h = -0.9384$ where the maximum of the resolved Reynolds stress production is found. As discussed in Sec. 5.3.3.2, we expect that, by employing ADM as the base model for the scale-similarity part of the subgrid stress tensor, the magnitude of the dynamic parameter C_d will be reduced compared with that from the dynamic mixed model and even more reduced compared with that from the dynamic Smagorinsky model [272]. This is confirmed by our LES where three orders of magnitude separate the dynamic parameters for DMS and ADM-DMS. The distribution of contours of the average dynamic parameter C_d in Figure 5.14 appears clearly correlated with the contours of the resolved Reynolds stress production \overline{P}_{22} in the same plane and presented in Figure 5.13. Indeed, the trace of the separated elliptical jets is discernibly apparent in Figure 5.14.

In addition, the maximum of \overline{P}_{22} localized at the point Θ_0 of coordinates $x/h = 0.7874$, $y/h = -0.9384$, $z/h = -0.3371$ (see Fig. 5.13) corresponds to a region of maximal values for the dynamic parameter. The time history of the local value of C_d at the point Θ_0 is reported in Figure 5.15 and present a limited number of high-value peaks. Leriche & Gavrilakis [155] and Bouffanais *et al.* [35] identified in this region of the cavity a pair of counter-rotating vortices responsible for the intermittent and intense production of Reynolds stresses. The presence of this coherent vortical structure seems to be detected by the intense values of the dynamic parameter.

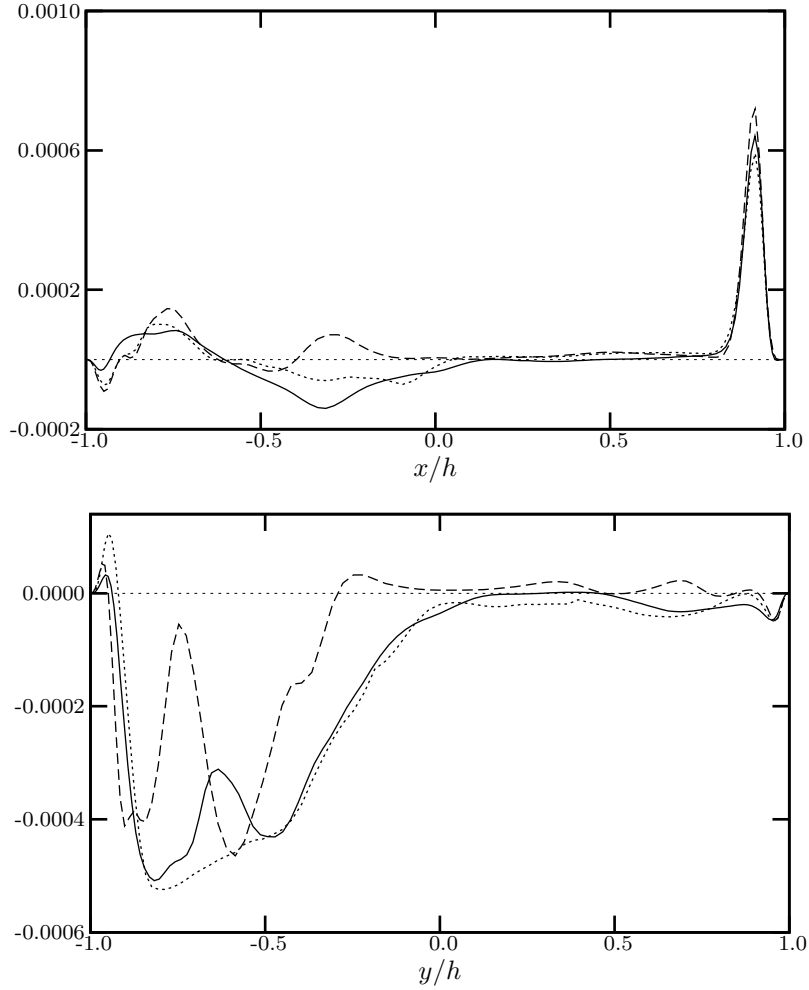


Fig. 5.12: In the mid-plane $z/h = 0$, DMS (dashed lines), ADM-DMS (dotted lines) and DNS (solid lines). $\langle \widehat{u}_x \widehat{u}_y \rangle$ on the vertical centerline $y/h = 0$ (Top) and on the horizontal centerline $x/h = 0$ (Bottom).

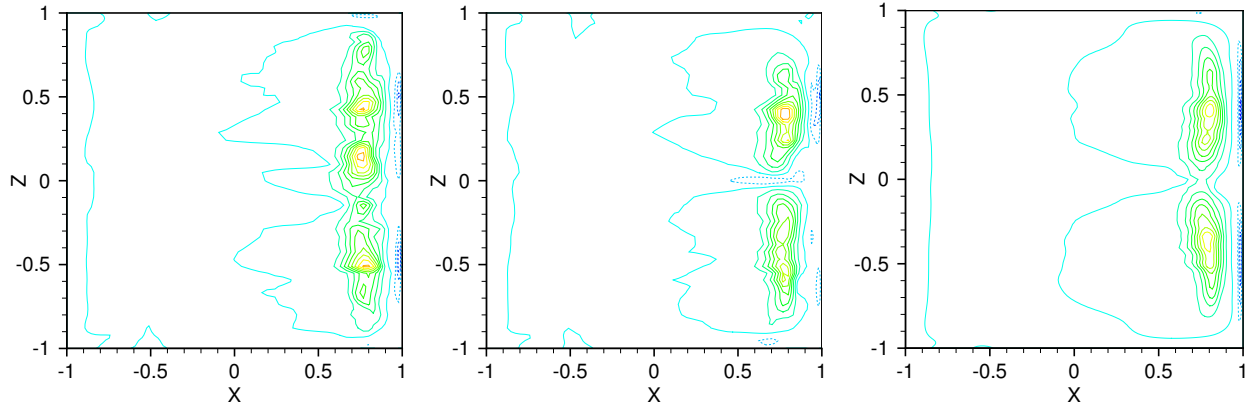


Fig. 5.13: Contours of \overline{P}_{22} from -0.04 to 0.11 by increments of 0.01 . DMS (left), ADM-DMS (center), DNS (right). Plane $y/h = -0.9384$. Color scale from blue to red. Dashed contours correspond to negative levels. Levels in U_0^3/h units.

5.5.6 Subgrid activity

As a next step, we are mostly interested in identifying the regions where turbulence occurs inside the cavity. For this purpose, we assume that if subgrid scales exist, the flow is locally turbulent and energy is exchanged between subgrid and resolved scales. In other words, the activity of the term modeling subgrid scales is a direct indication of the turbulence occurring in the cavity flow. A measure of subgrid activity is given by the subgrid

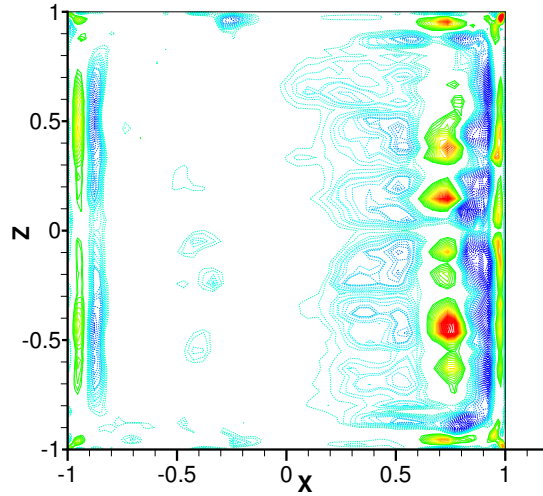


Fig. 5.14: Contours of the average dynamic parameter C_d from -0.001 to 0.001 for ADM-DMS. Plane $y/h = -0.9384$. Color scale from blue to red. Dashed contours correspond to negative levels.

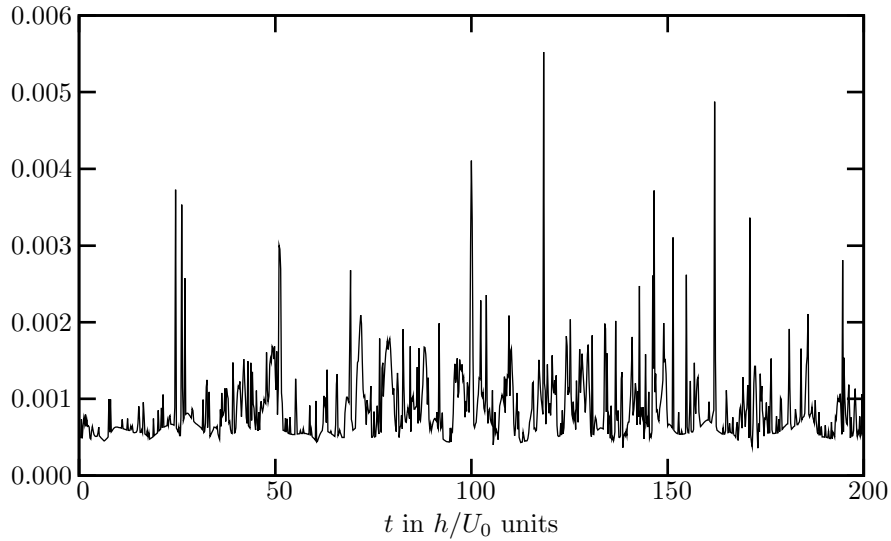


Fig. 5.15: Time history of the local value of the dynamic parameter C_d for ADM-DMS at the point Θ_0 whose coordinates are $x/h = 0.7874$, $y/h = -0.9384$, $z/h = -0.3371$.

energy transfer $\bar{\varepsilon}_{\text{sgs}}^m$ defined by

$$\bar{\varepsilon}_{\text{sgs}}^m = -\tau_{ij}^m \bar{S}_{ij}. \quad (5.65)$$

This latter quantity is only relative in value because the dissipation induced by the fluid viscosity, denoted by $\bar{\varepsilon}_\nu$,

$$\bar{\varepsilon}_\nu = 2\nu \bar{S}_{ij} \bar{S}_{ij}, \quad \bar{\varepsilon}_\nu \geq 0, \quad (5.66)$$

is also responsible for an energetic action. It appears therefore legitimate to define and analyze the relative subgrid energy transfer

$$\mathcal{A}_{\text{sgs}} = \frac{|\bar{\varepsilon}_{\text{sgs}}^m|}{\bar{\varepsilon}_\nu + |\bar{\varepsilon}_{\text{sgs}}^m|}, \quad (5.67)$$

which is referred to as subgrid activity in the sequel. If it is close to zero, the energetic phenomena are mainly induced by the viscous effects showing that the fluid is mainly laminar. Conversely, values close to the unit indicate a strong energetic action of the subgrid model reflecting that turbulence is mainly responsible of energy transfers.

As one can see in Fig. 5.16, turbulence essentially occurs in the vicinity of the cavity walls but, as expected, very close to the walls the energetic action is essentially due to viscous effects. High values of subgrid activity

are also identified at the bottom of the cavity and near upstream and downstream walls. One can also notice that subgrid activity is clearly reduced at the edges of the elements. This is a direct consequence of the nature of the filter which is not active at the element-boundaries. This issue cannot be avoided in this framework since C^0 -continuity of the variables across elements is essential for numerical stability and physical consistency reasons.

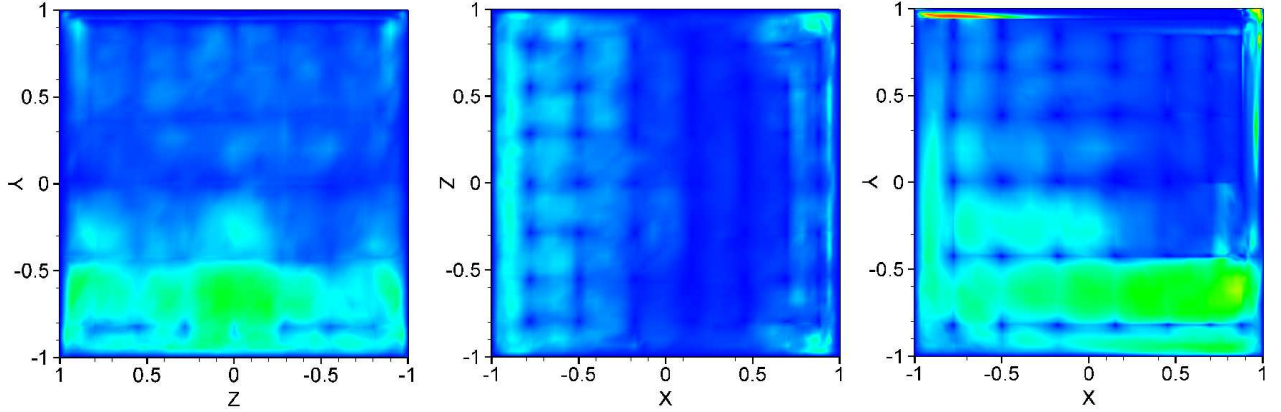


Fig. 5.16: Map of the average relative subgrid energy transfer $\langle A_{\text{sgs}} \rangle$ from 0 (blue) to 1 (red) for ADM-DMS. Upstream wall $x/h = 0$ (left), bottom wall $y/h = 0$ (center) and mid-plane $z/h = 0$ (right).

5.5.7 Subgrid kinetic energy

In order to complement the previous study of the subgrid activity and give further details about the importance of the subgrid terms in the ADM-DMS simulation, energetic quantities related to the subgrid scales are analyzed. For this purpose, we consider the filtered subgrid kinetic energy \bar{q}' which is expressed—see [199, 213]—as the difference between the total filtered kinetic energy and the kinetic energy of the resolved field $\bar{q} = \bar{u}_i \bar{u}_i / 2$,

$$\bar{q}' = \frac{1}{2}(\bar{u}_i \bar{u}_i - \bar{u}_i \bar{u}_i) = \frac{1}{2}\tau_{ii} \simeq \frac{1}{2}\tau_{ii}^m, \quad (5.68)$$

where τ^m is the modeled subgrid tensor defined in Eq. (5.32). In order to provide the reader with deeper insight into the relative importance of the subgrid terms, we introduce the relative subgrid kinetic energy κ as the ratio between the subgrid kinetic energy and the kinetic energy of the resolved field

$$\kappa = \frac{\bar{q}'}{\bar{q}}. \quad (5.69)$$

As one can notice on Fig. 5.17, the average values of κ reported in the plane $z/h = 0.9384$, have negative values mainly located at the top-left corner of the cavity. This shows that the subgrid model predicts backscattering, that is the energy transfer from subgrid to resolved scales. This region of inverse energy transfer corresponds to the region of intense subgrid activity as reported in Fig. 5.16 in the mid-plane $z/h = 0$.

The importance of the subgrid terms already observed for the local energy fluxes and analyzed through the subgrid activity, is further confirmed by the presence of regions of intense $\langle \kappa \rangle$. More precisely, four regions with high values of $\langle \kappa \rangle$ and corresponding to the zones where the wall-jets detach from their respective walls [155] are easily identified in Fig. 5.16.

In order to highlight the zones where backscattering occurs, the iso-surface $\langle \bar{q}' \rangle = 0$ is plotted in Fig. 5.18 thereby defining the boundary between the backscattering and the forward-energy transfer regions. This figure shows that this phenomenon mainly occurs below the lid and in the down flowing jet next to the downstream wall. It also demonstrates the need for a complex subgrid model with such anisotropic flows containing various flow conditions and no direction of homogeneity.

5.6 Conclusions

LES of Newtonian incompressible fluid flows with ADM based on the van Cittert method using Legendre-SEM have been performed. A coupling with a dynamic mixed scale model was introduced. The coupling of the

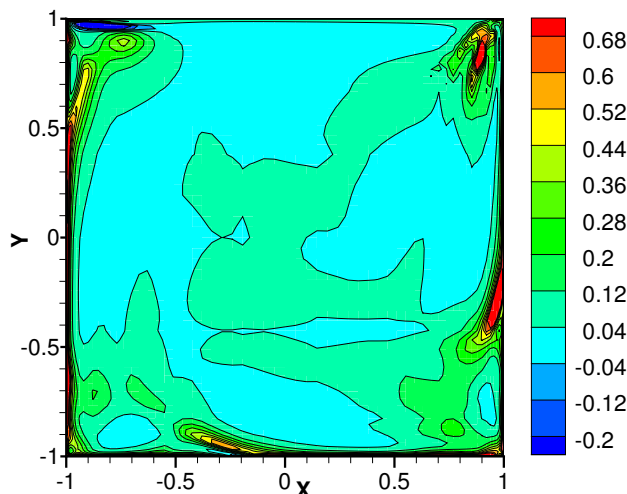


Fig. 5.17: Map of the ratio between the resolved and the subgrid kinetic energy in the plane $z/h = 0.9384$.

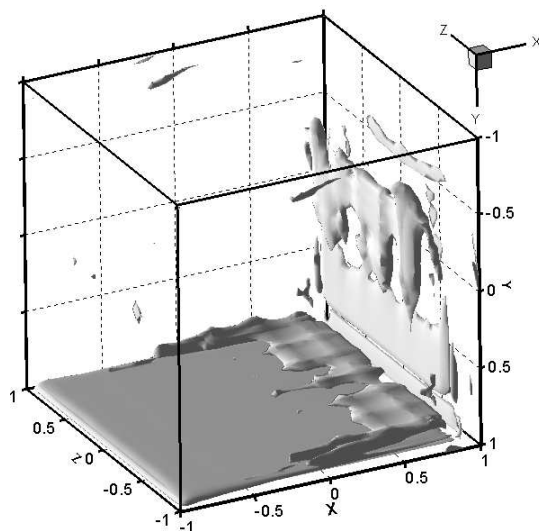


Fig. 5.18: Iso-surface of vanishing subgrid kinetic energy in the cavity.

lid-driven cubical cavity flow problem at Reynolds number of 12 000 with the SEM having very low numerical dissipation and dispersion appears to be a well suited framework to analyze the accuracy of the proposed subgrid model.

The filtering operation is performed in a spectral modal space, generated by a hierarchical basis using the Legendre polynomials, through the application of a specifically designed transfer function. This transfer function is constructed in order to ensure continuity across elements, conservation of the constants, invertibility of the filter and to perform low-pass filtering. From the computation viewpoint, the filtering technique presented in this chapter, is the essential link between the SEM and ADM-based subgrid models.

The validation of the deconvolution procedure performed using a DNS velocity sample, shows that the van Cittert method is convergent. Accounting for the reduced sampling and integration time, the LES performed with ADM-DMS show good agreement with the reference results. More precisely, first- and second-order statistics are in good agreement when compared to their DNS counterparts. Results for the Reynolds stresses production, coupling first- and second-order statistical moments, are also well predicted using this new model even with such reduced sampling. The analysis of the results obtained with DMS allows us to clearly identify the improvement induced by coupling ADM with DMS. Subgrid activity has been analyzed showing a qualitative correlation with the localization of small-scale structures in the cavity depicted in [37]. The importance of the

subgrid kinetic energy as compared to the kinetic energy of the resolved field highlights the essential need for an appropriate subgrid modeling. Furthermore, regions of backscatter are identified by ADM-DMS.

All the presented results emphasize the efficiency of ADM-DMS when dealing with laminar, transitional and turbulent flow conditions such as those occurring in the lid-driven cubical cavity flow at $Re = 12\,000$.

Chapter 6

Grid filter models for LES of shear-driven confined flows

The work on subgrid modeling based on approximate deconvolution models initiated in Chapter 5 is continued but focused now on implicit filtering [45,62]. The details related to the filtering technique as well as the numerical method are simply briefly recalled. The reader is referred to the previous chapters for missing details.

In this chapter, a new interpretation of approximate deconvolution models (ADM) when used with implicit filtering as a way to approximate the projective grid filter is given. Consequently, a new category of subgrid models, the grid filter models (GFM) is defined. ADM appear as a particular case of GFM since only approximate deconvolution is achieved. GFM can be either used with the standard filtered Navier–Stokes equations or with the formulation commonly used with ADM. The latter formulation requires an additional assumption leading to an incomplete modeling of the subgrid scales.

6.1 Introduction

The main subject of this chapter is a new approach to the problem of subgrid modeling. This approach is aimed at a partial recovery of the full velocity field from its filtered counterpart based on inverse filtering operations. Such a procedure is equally well called deconvolution or defiltering. Several types of deconvolution procedures have been considered in the past, *e.g.* discrete-kernel and polynomial regularizations by Shah & Ferziger [224], Geurts [89], and Kuerten *et al.* [147]. Approximate deconvolution models based on the van Cittert method, were introduced by Stolz & Adams [243] as a particular family of subgrid models for large-eddy simulation. They have also been detailed and used in the previous chapter, coupled to a dynamic mixed scale model. As a reminder, these models rely on the attempt to recover, at least partially, the original unfiltered fields by inverting the filtering operator applied to the Navier–Stokes equations, and by resorting to an iterative procedure. As already mentioned in Chapter 5, over the past five years ADM spread over various fields of application, such as LES of incompressible wall-bounded flows [244], compressible flows applied to shock-boundary layer interaction [245] and transitional flows [220]. A temporal ADM for LES was also recently proposed in [203]. Implicit subgrid-scale modeling by adaptive deconvolution has also been investigated by Adams *et al.* [4] and complemented by a study on an adaptive local deconvolution method for implicit LES due to Hickel *et al.* [118]. This important research activity initiated by the original ADM formulation reveals the substantial need for improvement in terms of subgrid modeling for the LES of complex turbulent flows [62].

Defiltering models are purely algorithmic as they only rely on the definition of the filter without the need to resort to any physical modeling. As noted by Domaradzki & Adams [62], “since the need for the physical models is removed this approach seems to be more promising than the classical models. However, this promise is not fulfilled if the effects of numerical discretization are accounted for”. Moreover, for a given filter, its inverse may be analytically determined which theoretically allows to express the full velocity field as a function of the filtered field. Therefore, solving the filtered Navier–Stokes should in principle deliver as much information as the solution to the standard non-filtered Navier–Stokes equations. This apparent paradox is resolved by acknowledging the unavoidable effects of the filter associated with the numerical discretization. This point has long been noted by LES practitioners, *e.g.* by the earlier work of Zhou *et al.* [274], and more recently by Langford & Moser [150], Domaradzki & Loh [63], and Winkelmanns *et al.* [267]. Nevertheless, the discretization effects are very often considered for the simple case of node-based methods—see Chapter 2— but very few studies for function-based methods—*e.g.* spectral and spectral element methods—are reported in the literature. Consequently, many of the arguments commonly expressed about grid filtering, are not valid nor applicable when, like in the present study, a function-based method is used. Recently, Hesthaven & Kirby [117] started investigating this instrumental point in the particular case of Legendre spectral methods. Consequently, when no explicit filter is applied but only the implicit grid filter is considered, deconvolution models can actively contribute to subgrid modeling but

in a very different way than the one associated with LES relying on explicit filtering techniques. The objective of this chapter is to gain insight into the use of deconvolution procedures for implicitly-filtered LES.

This chapter is organized as follows. Section 6.2 introduces the notations and more importantly the two distinct formulations of the problem. The grid filter models are defined and characterized in Sec. 6.3, which is followed by *a posteriori* validations detailed in Sec. 6.4. This chapter ends with conclusions in Sec. 6.5.

6.2 Different formulations of the problem

In the case of isothermal flows of Newtonian incompressible fluids, the LES governing equations for the filtered quantities denoted by an *overbar*, obtained by applying a convolution filter \mathcal{G}_\star to the Navier–Stokes equations, read

$$\frac{\partial \bar{u}_i}{\partial t} + \frac{\partial}{\partial x_j} (\bar{u}_i \bar{u}_j) = -\frac{\partial \bar{p}}{\partial x_i} + \nu \frac{\partial}{\partial x_j} \left(\frac{\partial \bar{u}_i}{\partial x_j} + \frac{\partial \bar{u}_j}{\partial x_i} \right) - \frac{\partial \tau_{ij}}{\partial x_j}, \quad (6.1)$$

where the filtered velocity field $\bar{\mathbf{u}}$ satisfies the divergence-free condition. The components of the subgrid tensor $\boldsymbol{\tau}$ are defined by $\tau_{ij} = \overline{u_i u_j} - \bar{u}_i \bar{u}_j$ and ν is the kinematic viscosity. Again, the closure of the filtered momentum equation (6.1) requires $\boldsymbol{\tau}$ to be expressed in terms of the filtered field.

6.2.1 General considerations

Following the notation adopted in Chapter 5, the filtered Navier–Stokes momentum equation is written formally as

$$\frac{\partial \bar{\mathbf{u}}}{\partial t} + \mathbf{f}(\bar{\mathbf{u}}) = [\mathbf{f}, \mathcal{G}_\star](\mathbf{u}), \quad (6.2)$$

where $[\mathbf{f}, \mathcal{G}_\star](\mathbf{u})$ is the subgrid commutator, which only retains the nonlinear and noncommutating terms. This equation is strictly equivalent to Eq. (6.1) with

$$[\mathbf{f}, \mathcal{G}_\star](\mathbf{u}) = -\nabla \cdot \boldsymbol{\tau}. \quad (6.3)$$

In the inverse filtering framework, the idea is to approximate this unknown field by inverting the filtering operator \mathcal{G}_\star applied to the Navier–Stokes equations

$$\mathbf{u} \simeq \mathbf{u}^* = \mathcal{Q}_\mathcal{N} \star \bar{\mathbf{u}} = (\mathcal{Q}_\mathcal{N} \circ \mathcal{G}) \star \mathbf{u}, \quad (6.4)$$

where $\mathcal{Q}_\mathcal{N}$ is an \mathcal{N} th-order approximation of the inverse of the filter \mathcal{G}_\star such as $\mathcal{Q}_\mathcal{N} \circ \mathcal{G} = \mathcal{I} + O(\bar{\Delta}^\mathcal{N})$, $\bar{\Delta}$ being the filter cutoff length and \mathcal{I} the identity filtering operator. The subgrid term is then approximated as

$$[\mathbf{f}, \mathcal{G}_\star](\mathbf{u}) \simeq [\mathbf{f}, \mathcal{G}_\star](\mathcal{Q}_\mathcal{N} \star \bar{\mathbf{u}}) = [\mathbf{f}, \mathcal{G}_\star](\mathbf{u}^*). \quad (6.5)$$

The model resulting from this approach can take two distinct forms, which are referred to as “filtered” and “deconvoluted” formulations. Both formulations are detailed in the following sections.

6.2.2 Filtered formulation

The so-called “filtered formulation” is the most commonly used LES formulation with the large majority of classical subgrid models, *e.g.* Smagorinsky model, dynamic Smagorinsky models, dynamic mixed models, etc. It is obtained by introducing the approximate expression (6.5) of the subgrid commutator directly into the filtered momentum equation (6.2)

$$\frac{\partial \bar{\mathbf{u}}}{\partial t} + \mathbf{f}(\bar{\mathbf{u}}) = [\mathbf{f}, \mathcal{G}_\star](\mathbf{u}^*). \quad (6.6)$$

Stolz and Adams [243] refer to it as a generalized scale similarity formulation. Indeed, using the simplest choice for the approximate inverse filtering operator, that is $\mathcal{Q}_\mathcal{N} = \mathcal{I}$ —which corresponds to the zero-th order in the van Cittert expansion—one recovers the subgrid tensor of Bardina’s scale similarity model [13]. Thus, Bardina’s scale similarity subgrid model appears as a particular case of ADM. Other similarity models have been introduced, such as the ones investigated by Liu *et al.* [157] and O’Neil & Meneveau [192], in which the velocity field appearing in the subgrid tensor is simply substituted by a velocity filtered by a wider filter.

The term “filtered formulation” introduced earlier is justified by the fact that the problem formulated by Eq. (6.6) is a set of equations for the filtered velocity field having for source term the subgrid term expressed in terms of the deconvoluted velocity field.

6.2.3 Deconvoluted formulation

The deconvoluted formulation is the one commonly used for LES with ADM by Stolz & Adams [243], Stolz *et al.* [244, 245] and the subsequent studies based on these pioneering works, *e.g.* Schlatter *et al.* [220], Shotorban & Mashayek [229], Pruet *et al.* [203], etc. Writing explicitly the subgrid commutator of Eq. (6.6) yields

$$\frac{\partial \bar{\mathbf{u}}}{\partial t} + \mathbf{f}(\bar{\mathbf{u}}) = \mathbf{f}(\bar{\mathbf{u}}^*) - \mathcal{G} \star \mathbf{f}(\mathbf{u}^*). \quad (6.7)$$

Using once more approximation (6.4) in Eq. (6.7) implies $\mathbf{f}(\bar{\mathbf{u}}) = \mathbf{f}(\bar{\mathbf{u}}^*)$ and leads to

$$\frac{\partial \bar{\mathbf{u}}}{\partial t} + \mathcal{G} \star \mathbf{f}(\mathbf{u}^*) = 0. \quad (6.8)$$

It is noteworthy that this formulation introduces the deconvolution error into the nonlinear advection term, thereby breaking the Galilean invariance [238]. Furthermore, the expression of the subgrid tensor of Bardina's scale similarity model is not recovered from the deconvoluted formulation when $\mathcal{Q}_{\mathcal{N}} = \mathcal{I}$, which is again due to the difference between the filtered and the deconvoluted velocities. Despite these inconsistencies, the deconvoluted formulation has been extensively used due its attractive expression, which does not exhibit explicitly the subgrid terms. Nevertheless, based on the previous comments, the filtered formulation introduced in Sec. 6.2.2 appears to be the most general.

6.2.4 Implicit projective grid filter

The previous theoretical developments only hold if the filter $\mathcal{G} \star$ is explicitly imposed to the solution, that is when performing LES with explicit filtering [62, 213], which was the case in the previous chapter. It is worth recalling here that in Sec. 5.3.2, the convolution filter $\mathcal{G} \star$ was expressed as

$$\mathcal{G} \star = (\mathcal{L} \circ \mathcal{P}) \star, \quad (6.9)$$

thereby embodying the explicit LES filter $\mathcal{L} \star$ and the implicit projective grid filter $\mathcal{P} \star$ [107, 266]. Using the previous decomposition of the filter $\mathcal{G} \star$, the filtered Navier–Stokes are rewritten as

$$\frac{\partial (\hat{\mathbf{u}})^{\mathcal{L}}}{\partial t} + \mathbf{f}((\hat{\mathbf{u}})^{\mathcal{L}}) = [\mathbf{f}, (\mathcal{L} \circ \mathcal{P})](\mathbf{u}), \quad (6.10)$$

where the superscript $(\cdot)^{\mathcal{L}}$ denotes the application of the explicit filter $\mathcal{L} \star$, and $\hat{\mathbf{u}} = \mathcal{P} \star \mathbf{u}$ is the grid-filtered velocity field.

In the case where no explicit LES filter $\mathcal{L} \star$ is applied and solely the implicit filter is effective, the previous interpretation of ADM no longer holds. Indeed, it would be a non-sense to invert a filter that has never been applied to the solution. Moreover, the previous developments do not account for the implicit grid filter induced by the space discretization of characteristic length $\hat{\Delta}$ [45, 62]. In order to use ADM only with implicit filtering, another interpretation must be found which is the main goal of this chapter and will lead to the definition of a new class of subgrid models. If only implicit grid filtering is considered, the filtered Navier–Stokes equations read

$$\frac{\partial \hat{\mathbf{u}}}{\partial t} + \mathbf{f}(\hat{\mathbf{u}}) = [\mathbf{f}, \mathcal{P} \star](\mathbf{u}), \quad (6.11)$$

where $\hat{\mathbf{u}}$ is the grid filtered velocity, or in other word the part of the velocity field that can be resolved by the grid used to perform the LES. In this framework, subgrid modeling based on deconvolution models requires the subgrid commutator of the previous equation to be expressed solely in terms of the known projected velocity $\hat{\mathbf{u}}$, which reads

$$[\mathbf{f}, \mathcal{P} \star](\mathbf{u}) = [\mathbf{f}, \mathcal{P} \star](\mathcal{P}^{-1} \star \hat{\mathbf{u}}), \quad (6.12)$$

where

$$\mathbf{u} = \mathcal{P}^{-1} \star \hat{\mathbf{u}}, \quad (6.13)$$

is the formal inverse grid filtering operation to be devised. It is important adding here that due to its implicit nature, the grid filter $\mathcal{P} \star$ entirely depends on the nature of the numerical method used to discretize in space the Navier–Stokes equations.

6.3 Grid filter models

6.3.1 Definition

The problem with Eq. (6.12) is that $\mathcal{P}^{-1}\star$ does not exist, this filter being a projector. The idea formulated by Habisreutinger [111], is then to approximate $\mathcal{P}\star$ with an invertible filter reproducing as closely as possible its effect

$$\mathcal{P}\star \simeq \mathcal{G}\star, \quad (6.14)$$

in order to have

$$[\mathbf{f}, \mathcal{P}\star](\mathbf{u}) \simeq [\mathbf{f}, \mathcal{G}\star](\mathcal{G}^{-1}\star \hat{\mathbf{u}}). \quad (6.15)$$

For such subgrid models, modeling only requires to build $\mathcal{G}\star$ in order to achieve the best approximation of $\mathcal{P}\star$, as stated in Eq. (6.14). The problem is exactly solved if $\mathcal{P}\star = \mathcal{G}\star$, which is not achievable since $\mathcal{P}\star$ applies on an infinite spectrum while $\mathcal{G}\star$ only applies to computable wave numbers [62]. Moreover, $\mathcal{G}\star$ must be invertible and $\mathcal{P}\star$ is projective. The approximation (6.14) being the only required modeling, the subgrid models arising from this new approach are referred to as grid filter models (GFM). Depending on $\mathcal{G}\star$, its inverse can be either determined analytically or by approximate methods such as ADM. In the latter case, one has $\mathcal{G}^{-1}\star \simeq \mathcal{Q}_{\mathcal{N}}\star$ leading to

$$[\mathbf{f}, \mathcal{P}\star](\mathbf{u}) \simeq [\mathbf{f}, \mathcal{G}\star](\mathcal{Q}_{\mathcal{N}}\star \hat{\mathbf{u}}), \quad (6.16)$$

which is the expression (6.5) of the subgrid commutator for ADM. Consequently, ADM appear as a way to approximate the projective grid filter and as a particular case of GFM since only approximate deconvolution is achieved.

At this stage, it is important noting three central points related to the afore-introduced grid filter modeling approach. First, the GFM is by essence an approximate subgrid model as it relies on the approximation (6.14), which cannot become a true equality. This approximate character of GFM should not be mixed up with the approximate character of ADM, which is essentially dependent on our capacity to achieve an exact deconvolution. For instance, if an explicitly invertible filter is used, ADM reduces to simply an exact deconvolution model whereas GFM conserves its approximate character. Secondly, from a conceptual viewpoint, GFM belong to the structural group of subgrid models aiming at reconstructing the velocity field from its filtered counterpart. Finally, any method achieving even partially, the inverse filtering procedure can be used in the GFM framework. This includes, as mentioned earlier ADM but also all other discrete-kernel and polynomial regularizations, *e.g.* [89, 147, 224].

6.3.2 Interpretation

The new interpretation of ADM resulting from the definition of GFM builds a theoretical basis that allows the use of such subgrid models without any explicit filtering of the solution. Moreover, this viewpoint allows to consider a new way of designing the filter $\mathcal{G}\star$ which has to approximate the grid filter $\mathcal{P}\star$ as accurately as possible. GFM can use standard ADM techniques originally meant to solve the soft deconvolution problem [62], to solve the hard deconvolution one since only implicit filtering is considered. This is made possible by the newly introduced GFM approach.

Furthermore, GFM allow to consider a more realistic methodology for *a priori* validations taking into account the implicit grid filtering, see Habisreutinger [111]. *A priori* validations rely on the use of a reference solution provided by experimental results or a direct numerical simulation (DNS). The reference velocity field \mathbf{u} is filtered leading to the definition of fully determined resolved and subgrid fields $\bar{\mathbf{u}}$ and \mathbf{u}' , respectively. The modeled subgrid commutator is computed using the filtered field and compared to the exact one computed with the non-filtered field. If an invertible filter is used, $\mathcal{G}\star$ for instance, the modeled subgrid tensor is computed using the deconvoluted field which is equal to the non-filtered one if exact deconvolution is achieved. Using this method, referred to as classical in Table 6.1, one does not measure the efficiency of the model but solely the accuracy of the deconvolution procedure. This is therefore a validation of the deconvolution method and not of the subgrid models which justifies why the classical *a priori* methodology produces highly correlated results with ADM.

In order to account for these effects and measure a more realistic efficiency of the subgrid models, one has to take into account the non-invertible filter induced by the grid in practical LES. In the framework of GFM based on Eq. (6.15), a novel method for *a priori* validations taking into account the implicit grid filtering is straightforward and referred to as GFM-*a priori* in Table 6.1. In addition to the construction of the filter $\mathcal{G}\star$ for the modeled commutator, one has to make use of a projective filter to compute the exact commutator.

| Methodology | Exact commutator | Modeled commutator |
|----------------------|--|---|
| Classical | $[\mathbf{f}, \mathcal{G}\star](\mathbf{u})$ | $[\mathbf{f}, \mathcal{G}\star](\mathcal{G}^{-1}\star\bar{\mathbf{u}})$ |
| GFM- <i>a priori</i> | $[\mathbf{f}, \mathcal{P}\star](\mathbf{u})$ | $[\mathbf{f}, \mathcal{G}\star](\mathcal{G}^{-1}\star\hat{\mathbf{u}})$ |

Table 6.1: *A priori* validation methodologies.

6.4 Numerical results

6.4.1 *A priori* validations

Following the methodology introduced in the previous section, an *a priori* validation test has been carried out using the reference DNS results from Leriche & Gavrilakis [155] for the lid-driven cubical cavity flow. The Reynolds number $\text{Re} = 2hU_0/\nu$, where $2h$ is the size of the cavity and U_0 the imposed lid velocity, is equal to 12 000. The mesh used for this LES *a priori* test has eight times less points than the DNS grid of Leriche and Gavrilakis who employed a 129^3 Chebyshev discretization. The reader is referred to Chapters 4 & 5 for full details on the grid used and on the space discretization based on the Legendre spectral element method. A set of velocity samples \mathbf{u} taken from the statistically-steady state range of the DNS by Leriche & Gavrilakis is reinterpolated onto the LES *a priori* grid—see Fig. 4.2—therefore enforcing the effect of the projective grid filter $\mathcal{P}\star$, and yielding the grid-filtered velocity samples $\hat{\mathbf{u}}$.

The filter $\mathcal{G}\star$ used to approximate the grid filter in Eq. (6.14) relies on the application of a given low-pass transfer function in a hierarchical modal basis, as reported in Sec. 5.4. Since the filter $\mathcal{G}\star$ defined in detail in Sec. 5.4 is analytically invertible, its inverse is computed analytically for exact deconvolution. One can easily verify that the continuous transfer function \mathcal{S} associated with $\mathcal{G}^{-1}\star$ is simply obtained by taking the inverse of Eq. (5.55), leading to

$$\mathcal{S}(k) = \frac{1}{\mathcal{K}(k)} = 1 + \left(\eta \frac{\max(0, k-1)}{N} \right)^2, \quad \eta \geq 0. \quad (6.17)$$

Using the notations introduced in Sec. 5.4.1, the exact deconvolution process for any scalar quantity reads

$$\mathbf{v}^\bullet = \Phi \mathbf{S} \Phi^{-1} \hat{\mathbf{v}} = \mathbf{G}^{-1} \hat{\mathbf{v}}, \quad (6.18)$$

where the superscript \bullet denotes the exact deconvolution in opposition to the approximate deconvolution formerly denoted by $*$.

Based on the filter $\mathcal{G}\star$ and its analytical inverse $\mathcal{G}^{-1}\star$ defined respectively by Eq. (5.55) and Eq. (6.17), we are now equipped to perform the *a priori* test. The first step consists in calculating the exact subgrid terms associated with the projective grid filter, which according to Eq. (6.3), read

$$[\mathbf{f}, \mathcal{P}\star](\mathbf{u}) = -\nabla \cdot \boldsymbol{\tau}^{\text{exact}}, \quad (6.19)$$

where the exact subgrid stress tensor is

$$\boldsymbol{\tau}^{\text{exact}} = \widehat{\mathbf{u}} \widehat{\mathbf{u}} - \hat{\mathbf{u}} \hat{\mathbf{u}}. \quad (6.20)$$

In order to access the exact subgrid tensor, one first needs to first calculate the term $\mathbf{u}\mathbf{u}$ onto the DNS grid prior to projecting it onto the LES *a priori* grid leading to $\widehat{\mathbf{u}}\widehat{\mathbf{u}}$. Afterwards, the divergence of the exact subgrid stress tensor is calculated. The second step consists in calculating the modeled subgrid terms, which according to Table 6.1, read

$$[\mathbf{f}, \mathcal{G}\star](\mathcal{G}^{-1}\star\hat{\mathbf{u}}) = [\mathbf{f}, \mathcal{G}\star](\mathbf{u}^\bullet) = -\nabla \cdot \boldsymbol{\tau}^{\text{modeled}}. \quad (6.21)$$

The above equation is strictly equivalent to writing

$$\boldsymbol{\tau}^{\text{modeled}} = \overline{\mathbf{u}^\bullet \mathbf{u}^\bullet} - \overline{\mathbf{u}^\bullet} \overline{\mathbf{u}^\bullet}. \quad (6.22)$$

Finally, the last step aims at measuring the correlation between two meaningful quantities both derived from the exact and modeled subgrid tensor, namely the rates of transfer of energy from the resolved scales of the flow to the subgrid scales

$$\hat{\epsilon}_{\text{sgs}} = -\tau_{ij}^{\text{d}} \widehat{S}_{ij}, \quad (6.23)$$

where the superscript “d” still refers to the deviatoric part of the subgrid tensor, and \widehat{S}_{ij} is the grid-filtered rate-of-strain tensor. This quantity has been introduced in Chapter 4 for the study of the subgrid activity detailed in Sec. 4.4.3.3. The following correlation coefficient \mathcal{C} , defined by

$$\mathcal{C} = \mathcal{C}(\alpha, \beta) = \frac{\langle \alpha, \beta \rangle - \langle \alpha \rangle \langle \beta \rangle}{(\langle \alpha^2 \rangle \langle \beta^2 \rangle)^{1/2}}, \quad (6.24)$$

with $\alpha = \hat{\epsilon}_{\text{sgs}}^{\text{exact}}$ and $\beta = \hat{\epsilon}_{\text{sgs}}^{\text{modeled}}$, and $\alpha^\diamond = \alpha - \langle \alpha \rangle$. The reader is referred to Chapter 4, Sec. 4.3.1 for details and notations used in the present averaging procedure—denoted into brackets $\langle \cdot \rangle$. This coefficient was calculated for a complete set of 105 velocity samples available from the DNS by Leriche & Gavrilakis [155]. Results are presented on Fig. 6.1, and show a relatively high correlation between the exact and the modeled inter-scales rate of transfer of energy. More importantly, the regions of high intensity of the correlation coefficient observed in the mid-plane of the cavity, are very close to the high regions of subgrid activity calculated for the dynamic mixed model (DMM) in Chapter 4, Sec. 4.4.3.3 and represented in Fig. 4.23, even though these results are reported in a plane parallel to the mid-plane. These promising *a priori* results call for a more complete validation based on *a posteriori* tests.

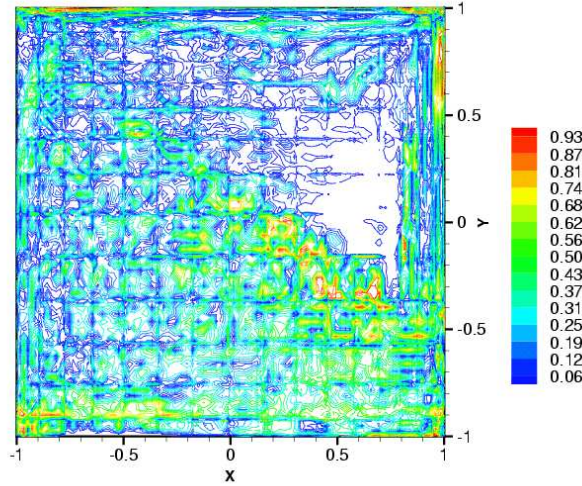


Fig. 6.1: Contours of the correlation coefficient $\mathcal{C}(\hat{\epsilon}_{\text{sgs}}^{\text{exact}}, \hat{\epsilon}_{\text{sgs}}^{\text{modeled}})$, in the mid-plane z/h of the cavity.

6.4.2 *A posteriori* validations

The next step is to perform *a posteriori* validations using GFM with exact and approximate deconvolution in both formulations and without resorting to any additional dissipative or relaxation term. To our knowledge, all simulations in the ADM framework and based on the deconvoluted formulation, required the use of an additional sink term into the filtered momentum equation. Originally, Stolz *et al.* [244, 245] introduced a relaxation term having the following expression

$$-\chi(\mathcal{I} - \mathcal{Q}_{\mathcal{N}} \star \mathcal{G}) \star \bar{\mathbf{u}} = -\chi(\bar{\mathbf{u}} - \bar{\mathbf{u}}^*), \quad (6.25)$$

where χ has the dimension of a time and can either be constant in space and time [244], or can be dynamically evaluated [220, 245]. This regularization term has no physical meaning and is only intended to increase the dissipative character of ADM expressed in the deconvoluted formulation. Subsequently, Winckelmans & Jeanmart [266] suggested to replace the relaxation term (6.25) by a constant subgrid-viscosity term of Smagorinsky type. Gullbrand & Chow [107] followed the path open by Winckelmans & Jeanmart [266], by evaluating dynamically the subgrid viscosity in the dissipative Smagorinsky term.

An under-resolved DNS (UDNS), *i.e.* without using any subgrid model, is also presented to emphasize the action of the considered models and to make sure that the space discretization is not refined enough to represent all scales of the solution, see Sec. 4.2.2.1. Besides this under-resolved DNS, four different LES have been carried out corresponding to four distinct grid filter models. Two of them use an exact analytical deconvolution procedure, while the two others rely on approximate deconvolution based on the van Cittert method. The two different formulations, namely filtered and deconvoluted, have been considered. For the sake of clarity, we will expose the formal expressions of the momentum equation for these modes. The use of the exact deconvolution together with the filtered formulation (6.6) defined GFM-F, which is governed by

$$\frac{\partial \hat{\mathbf{u}}}{\partial t} + \mathbf{f}(\hat{\mathbf{u}}) = [\mathbf{f}, \mathcal{G}\star](\mathbf{u}^\bullet), \quad (6.26)$$

where \mathbf{u}^\bullet denotes the analytically defiltered velocity field. From the previous model, it is straightforward to define ADM-F by simply replacing the exact deconvolution with the approximate deconvolution. The formulation used

is still the filtered formulation (6.6) and consequently the governing equation reads

$$\frac{\partial \hat{\mathbf{u}}}{\partial t} + \mathbf{f}(\hat{\mathbf{u}}) = [\mathbf{f}, \mathcal{G}\star](\mathbf{u}^*), \quad (6.27)$$

where \mathbf{u}^* still denotes the approximately deconvoluted velocity field. The second group of cases make use of the deconvoluted formulation (6.8). Coupling this deconvoluted formulation with the exact deconvolution procedure defines GFM-D, which is governed by

$$\frac{\partial \hat{\mathbf{u}}}{\partial t} + \mathcal{G} \star \mathbf{f}(\mathbf{u}^\bullet) = 0. \quad (6.28)$$

Finally, instead of exact deconvolution, ADM-D relies on approximate deconvolution for its modeling

$$\frac{\partial \hat{\mathbf{u}}}{\partial t} + \mathcal{G} \star \mathbf{f}(\mathbf{u}^*) = 0. \quad (6.29)$$

These four models and their respective names are summarized in Table 6.2.

| Deconvolution | Filtered form. | Deconvoluted form. |
|---------------|----------------|--------------------|
| Exact | GFM-F | GFM-D |
| Approximate | ADM-F | ADM-D |

Table 6.2: Models and formulations.

LES of the lid-driven cubical cavity flow presented here are performed using the Legendre spectral element method (SEM) and refer to the same computational parameters as in Chapters 4 & 5, and the same physical parameters as the DNS performed by Leriche & Gavrilakis [155], taken as the reference solution. The space discretization is strictly equivalent to the one used for the LES reported by Zang *et al.* [272] for a lower Reynolds number of 10 000. To allow comparisons with LES results, DNS data are all re-interpolated onto the LES mesh therefore accounting for the effect of the grid filter. The same filter $\mathcal{G}\star$ as the one used for *a priori* tests has been used for these *a posteriori* tests, and likewise for the exact analytical deconvolution and the inverse analytical filter $\mathcal{G}^{-1}\star$. When approximate deconvolution is used, it relies on the van Cittert method with the deconvolution order being set to $\mathcal{N} = 5$ as recommended by Stolz *et al.* [243].

It is worth noting that any improvement in the design of the filter $\mathcal{G}\star$ as an approximation of the grid filter will consequently lead to better modeling. Nevertheless, in the present work this aspect of filter design is not dealt with as our focus resides on the influences of the formulation and deconvolution procedure used. Moreover, no stabilizing nodal filter—*e.g.* stabilization of Fischer & Mullen [80], see Sec. 2.3.7—has been used.

6.4.3 Evolution of total resolved kinetic energy and enstrophy of the flow

As observed in Chapter 4 and Chapter 5, subgrid modeling in the case of a flow with coexisting laminar, transitional and turbulent zones such as the lid-driven cubical cavity flow for such Reynolds number represents a challenging problem. Kinetic energy is constantly provided to the fluid by the viscous diffusion induced by the lid motion and the confined nature of the flow avoids the evacuation of energy through an outflow section. Hence, integral energy quantities over the flow domain are a direct indication of any under- or over-dissipative character of the subgrid model since the scale separation used for LES leads to the removal of subgrid scales mainly responsible for the energy dissipation. In addition, the very low dissipation induced by SEM allows a pertinent analysis of the energetic action of the models, which is not feasible in the framework of low-order numerical methods. The coupling of the lid-driven cubical cavity flow problem with the SEM provides a well suited framework to analyze and compare the accuracy of the different subgrid models introduced in the previous section and summarized in Table 6.2.

Since all LES were started from the same instantaneous DNS velocity field corresponding to a statistically steady state, the total resolved kinetic energy,

$$\hat{Q} = \frac{1}{2} \int_{\Omega} \hat{u}_i \hat{u}_i \, d\Omega, \quad (6.30)$$

is expected to evolve within a small fluctuation range. However, the time history of this quantity reported in Fig. 6.2 for ADM-D shows a monotonous growth which clearly reflects an under-dissipative character in the deconvoluted formulation. Since this formulation is the one commonly used by all the authors using ADM, this is probably at the origin of the introduction of additional dissipative terms, such as the relaxation term used by

Stolz *et al.* [244, 245], Winckelmans & Jeanmart [266], and Gullbrand & Chow [107], to increase the dissipation. This behavior, also observed for GFM-D, occurs with any of the convective, conservative and skew-symmetric formulations of the nonlinear advective term. The results for GFM-D being limited to the first four time units due to a divergence of the simulation, are not reported here. Indeed, increasing the accuracy of the deconvolution and to the limit performing exact deconvolution leads to numerical instabilities if the deconvoluted formulation is used. This observation is in direct relation with the low deconvolution orders \mathcal{N} used in most LES based on ADM. Moreover, the relaxation term introduced in [244, 245] vanishes if exact deconvolution is achieved, leading to even more unstable simulations with the deconvoluted formulation.

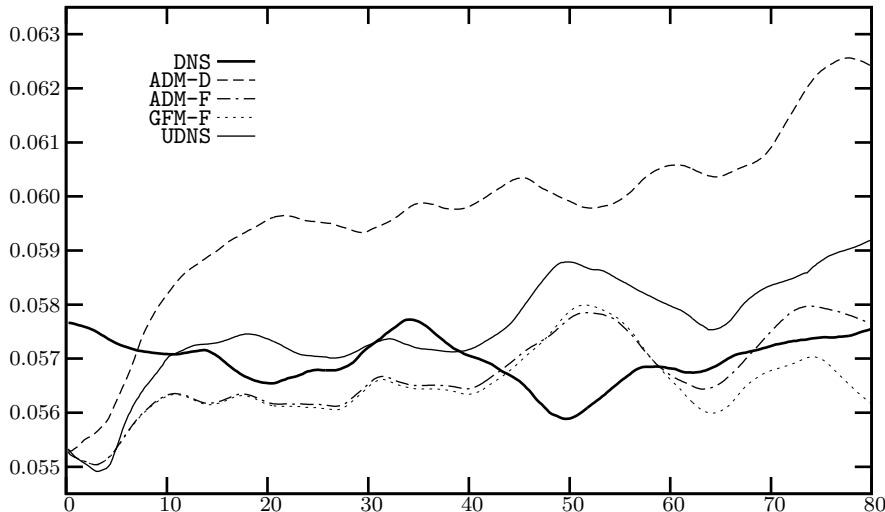


Fig. 6.2: Total resolved kinetic energy \hat{Q} in $U_0^2 h^3$ units with respect to the time t in h/U_0 units.

When considering the filtered formulation, GFM-F and ADM-F, the energy balance is achieved without resorting to any additional relaxation or dissipative term. The time evolution of \hat{Q} is comprised in the same range of fluctuations as the reference DNS. Considering the confined nature of the flow and the low dissipative character of the SEM, the previous observation is of great relevance.

A characteristic of turbulence is that the vorticity possesses intense small-scale, random variations in both space and time. Therefore, another important integral quantity is the total resolved enstrophy of the flow defined by

$$\hat{E} = \frac{1}{2} \int_{\Omega} \hat{\omega}_i \hat{\omega}_i \, d\Omega, \quad (6.31)$$

where $\hat{\omega} = \nabla \times \hat{\mathbf{u}}$ is the resolved vorticity field. Indeed, \hat{E} provides an insightful information regarding the smallest resolved scales of the flow. Figure 6.3 shows that the enstrophy obtained from the deconvoluted formulation is clearly too low when compared to the enstrophy of the grid-filtered DNS. The low level of enstrophy reflects the under-representation of small scales which directly induces the under-dissipative character and the over-estimation of \hat{Q} . Conversely, the filtered formulation gives rise to higher levels of resolved enstrophy, which in turn explains the better subgrid modeling leading to a correct energy balance.

6.4.4 Assessment based on the Reynolds stress tensor

In an attempt to provide a comprehensive assessment of the performances of all subgrid scales models, the determination of the Reynolds stress tensor components has been considered as a challenge in the framework of the lid-driven cubical cavity flow. The Reynolds statistical decomposition $\mathbf{u} = \langle \mathbf{u} \rangle + \mathbf{u}^\diamond$, introduces the average value denoted into brackets and its fluctuating part \mathbf{u}^\diamond . The statistics for all LES are based on a sampling approximately 10 times smaller than the one of the DNS, but about twice longer than the one of the LES of Zang *et al.* [272]; more precisely 400 samples are collected over $80 h/U_0$ time units.

Figure 6.4 displays the low-amplitude cross term $\langle \hat{u}_x^\diamond \hat{u}_y^\diamond \rangle$ in the symmetry plane of the cavity. The contours for UDNS show that implicit modeling is totally inoperative in the SEM framework and highlight the need for explicit subgrid modeling. Approximate deconvolution (ADM-F) provides contours extremely close to those obtained with exact deconvolution (GFM-F) and are therefore not reported here (also noticeable with integral

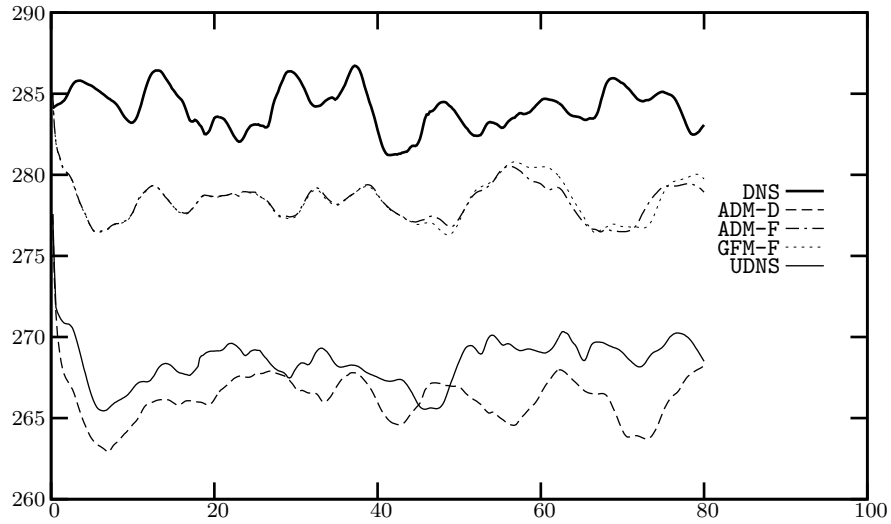


Fig. 6.3: Total resolved kinetic enstrophy \hat{E} in $U_0^2 h$ units with respect to the time t in h/U_0 units.

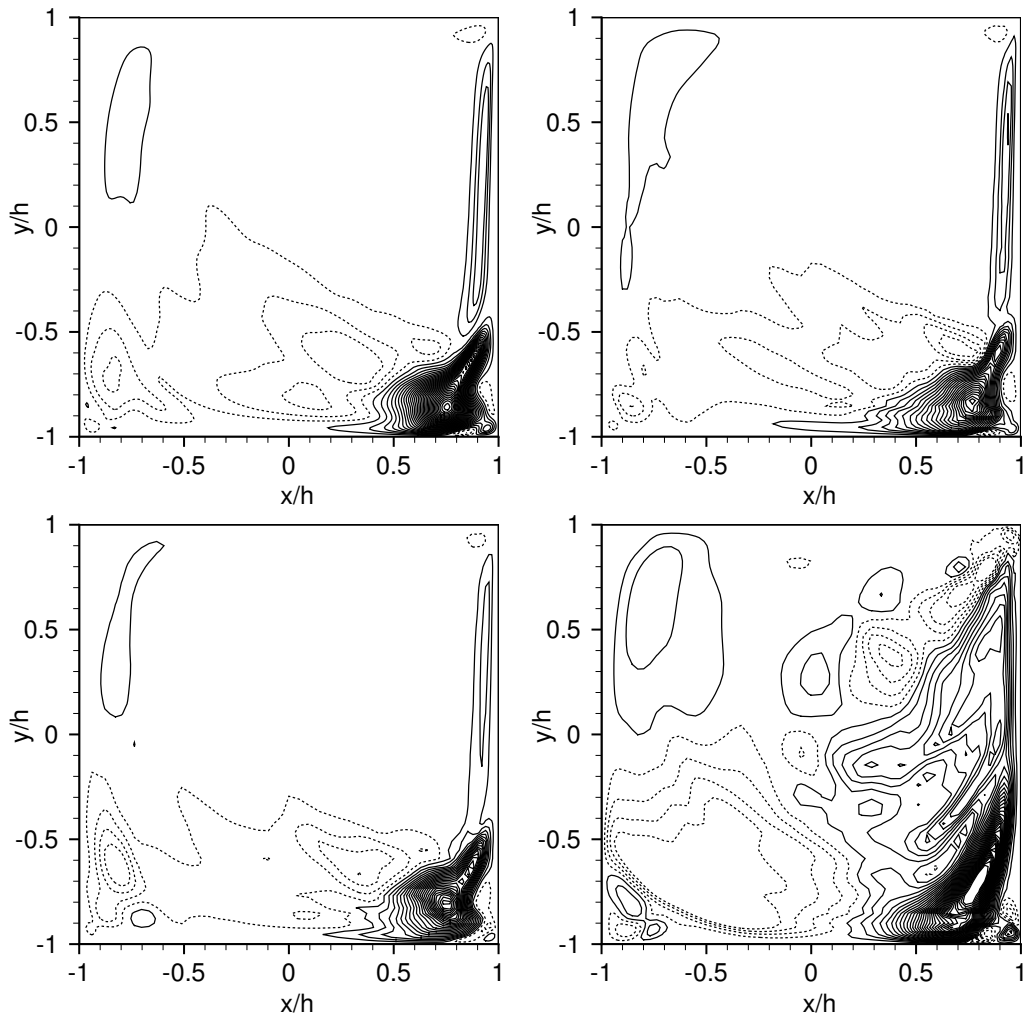


Fig. 6.4: Contours of $\langle \hat{u}_x^2 \hat{u}_y^2 \rangle$ from -0.0007 to 0.0065 in U_0^2 units, by increments of 0.0002 in the midplane $z/h = 0$. DNS (top-left), ADM-D (top-right), GFM-F (bottom-left), UDNS (bottom-right). Dashed contours correspond to negative levels. The cavity lid $y/h = 1$, moves at U_0 in the x -direction.

quantities on Figs. 6.2 and 6.3). The nature of the deconvolution procedure (exact or approximate) has a very limited influence on modeling. The contours for GFM-F and ADM-D are relatively close to the DNS ones.

At this stage, it appears that the statistics in the deconvoluted formulation for ADM-D do not reflect the incomplete subgrid modeling observed with \hat{Q} and \hat{E} . The study of these two integral quantities for this confined flow using a very low-dissipative numerical scheme allows us to highlight the under-dissipation associated with the deconvoluted formulation. This important observation would have not been possible using validations based on statistics of unbounded flows (*e.g.* channel flow) or with dissipative numerical methods.

6.5 Conclusions

The GFM approach gives a theoretical justification to the use of ADM without explicit filtering of the solution and explains how the use of ADM works in this context. This viewpoint allows to consider a new way of designing the convolution filter which has to approximate the grid filter and therefore a new way of improving such subgrid models. It has also been proved that the deconvoluted formulation, usually used with ADM, leads to an under-dissipative character of the subgrid model and explains the need of additional dissipative terms. Conversely, when using the filtered formulation, no additional term is needed which is of great relevance considering the confined nature of the flow and the high-order numerical method used.

The GFM approach also allows to consider a more realistic methodology for *a priori* validations and its validity extends beyond the limited scope of incompressible Newtonian fluid flows considered in this chapter. LES of compressible and visco-elastic fluid flows can also be considered using GFM. From a numerical viewpoint, GFM can be implemented with all numerical methods allowing filtering operations only needed to compute the subgrid commutator.

Part IV

Open shear-driven transitional swirling flows

Chapter 7

Transitional open swirling flow

This chapter is devoted to the study of the incompressible flow of a viscous fluid partly enclosed in a cylindrical container with an open top surface and driven by the constant rotation of the bottom wall. Such type of flows constitutes another group of recirculating lid-driven cavity flows with geometrical axisymmetry of the container and of the prescribed boundary conditions of Dirichlet type—no-slip on the cavity walls. The previous Part III of the present dissertation was dealing with the fully-confined internal cubical lid-driven cavity flow at a relatively high Reynolds number, where no-slip conditions are enforced on all cavity walls. In the present part, which includes this chapter and the next one, the top surface of the cylindrical cavity is left open and a stress-free boundary condition is imposed on it, while a no-slip condition is imposed on the side-wall and on the rotating bottom wall. More specifically, in the present chapter the stress-free top surface is, in first approximation, maintained fixed and flat. The most general case involving a moving free surface is dealt with in Chapter 8. The Reynolds regime corresponds to transitional flows with some incursions in the fully laminar regime. Both steady and unsteady non-oscillatory swirling flows are considered.

In the present chapter, new flow states are investigated based on a fully three-dimensional solution of the Navier–Stokes equations for the free-surface cylindrical swirling flow, without resorting to any symmetry property unlike all other results available in the literature. To our knowledge, the present study delivers the most general available results for this flat-free-surface problem due to its original mathematical treatment.

7.1 Introduction

Besides the differences in terms of geometry, boundary conditions and of Reynolds number regime, the lid-driven cubical cavity flow and the cylindrical swirling flow investigated in this chapter and the next one, present similar features typical of shear-driven recirculating flows such as intense wall-jets and shear layers in the vicinity of the driven wall, and secondary recirculating flows, which are very dependent on the flow parameters. Nevertheless, the geometry—cubical on one hand and cylindrical on the other hand—dramatically influences the nature and structure of these secondary flows: corner eddies for the cubical cavity and recirculation bubbles in the cylindrical case.

7.1.1 General considerations

Following the pioneering work of Bogatyrev & Gorin [30] and Koseff & Street [144, 145], it was shown that contrary to intuition, the lid-driven cubical cavity flow is essentially three dimensional, even when considering large aspect ratio. It is only recently that the three dimensionality of the lid-driven cylindrical cavity flow was confirmed numerically by Blackburn & Lopez [21, 22] after it was suggested but not fully proved experimentally by Sørensen [233], Spohn *et al.* [240], Sotiropoulos & Ventikos [235], and Pereira & Sousa [195]. In 2001, Sotiropoulos & Ventikos [236] gave full experimental evidence of the three-dimensional character of the flow with the onset of non-axisymmetric modes. The three-dimensional nature of these driven cavity flows is therefore a general characteristic of internal recirculating shear-driven flows.

In the sequel, we will only consider the cylindrical lid-driven cavity flow also referred to as “swirling” flow without any additional precision. The first experiments by Vogel [260] and later Ronnenberg [209] showed that Ekman suction and pumping, induced by the Ekman layers on the rotating and stationary disks, lead to the formation of a concentrated vortex core along the axis in the closed cavity case. The two dimensionless groups characterizing this flow are the height-to-radius aspect ratio $\Lambda = H/R$ and the Reynolds number $\text{Re} = R^2\Omega/\nu$, where H and R are respectively the height and radius of the cylinder, Ω the constant angular velocity of the bottom end-wall, and ν the kinematic viscosity of the Newtonian fluid. For specific values of the aspect ratio Λ , and above a critical Reynolds number, the vortex core breaks down in the form of one or more recirculation

bubbles which are on-axis in the closed cavity case and on- or off-axis in the open cavity one. Owing to the enormous extent of work in the area of vortex breakdown (VB), (see reviews by Hall [113], Leibovich [152], Shtern & Hussain [231], Kerswell [142], and Arnt [11]), we will only briefly recall the central features of VB. As defined by Leibovich in its review on the structure of vortex breakdown [152], the term “vortex breakdown” refers to a disturbance characterized by the formation of an internal stagnation point on the vortex axis, followed by reversed flow in a region of limited axial extent. Two forms of vortex breakdown predominate, one called “near-axisymmetric” (sometimes “axisymmetric” or “bubble-like”) and clearly visible in Fig. 7.1, and the other called “spiral” also visible on the far-right of Fig. 7.1. The practical importance of vortex breakdown lies mainly

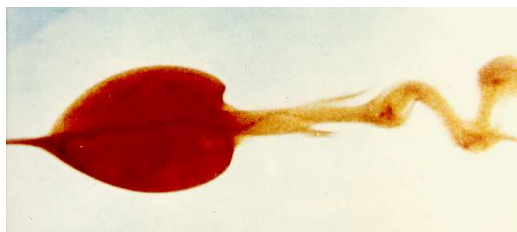


Fig. 7.1: Laboratory vortex breakdown obtained under highly controlled conditions: a bubble-like or B-mode breakdown is nicely illustrated and is followed by an S-mode breakdown. © Prof. T. Sarpkaya, Naval Postgraduate School, Monterey, California.

in the field of aeronautics, where they can be observed over wings—mainly delta wings—with highly swept leading edges when the angle of incidence exceeds a critical value, see Fig. 7.2 & Fig. 7.3. Vortex breakdown can be a limiting factor on the operating attitude of slender-winged flying vehicles. Moreover, the occurrence of VB in the wake of a large aircraft is relevant to the safety of flight in dense air-traffic, which is becoming more and more frequent with the constant increase in air-traffic over the years. VB is also important in other fields. It has been observed in the swirling flows through nozzles and diffusers [72], and in the field of reactive flows, in combustion chambers. Besides the tremendous importance of VB in engineering applications, it is also a prototypical phenomenon allowing to elucidate the fundamental aspects of the bubble mode.

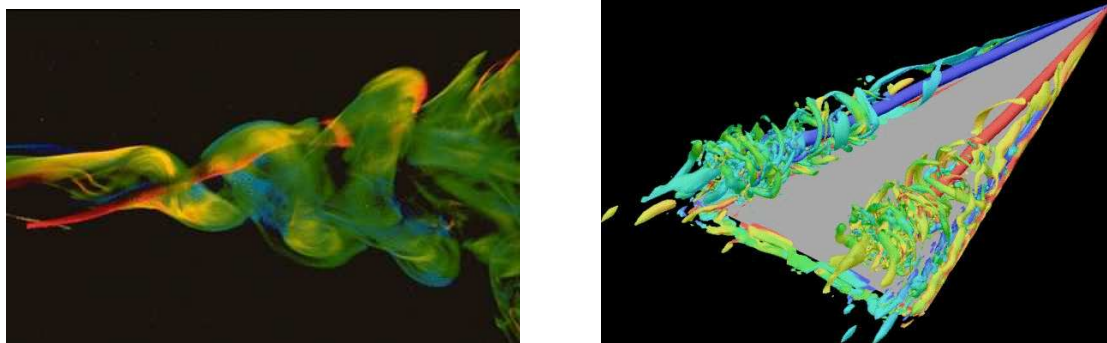


Fig. 7.2: Left: Vortex breakdown at the end of an airfoil; visualization with liquid dye tracers. Right: Vortex breakdown on a delta wing with high angle of attack. © ONERA.

7.1.2 The lid-driven cylindrical cavity flow

The first comprehensive experimental study of the closed cylindrical container case was undertaken by Escudier [69], and Escudier & Keller [71], who extended the earlier results of Vogel [260] and Ronnenberg [209] to obtain the first map of VB transitions with respect to the aspect ratio Λ and the Reynolds number. Escudier [69] revealed flow states with one, two or even three successive breakdowns, as well as a transition from steadiness to unsteadiness. Sørensen [233] extended to a broader range of Reynolds number in the same experiment as Escudier [69] for the closed container, and inferred that above a critical Reynolds number in the unsteady flow regime, the meridional flow becomes highly asymmetric. The first experimental study of the open cylindrical container case with a free surface on the top, was undertaken by Spohn *et al.* [239], who highlighted the significant change in the structure, the occurrence and the location of the breakdown bubbles. In the steady closed cylinder case, Hourigan *et al.* [127] investigated the asymmetric spiraling effects along the cylinder axis prior to the first vortex breakdown. They argued that the observed asymmetry was purely an experimental



Fig. 7.3: A NASA F-18 at 20 degrees angle of attack. The strake vortex has been made visible with smoke showing the vortex breakdown which occurs toward the trailing edge of the wing. Courtesy of NASA: <http://www.dfrc.nasa.gov/gallery/photo/>.

artifact and not an evidence of the three-dimensional nature of the flow. Spohn *et al.* [240] were the first to investigate experimentally the origin of possible asymmetric features of the instabilities at their onset. The steady breakdown bubbles reported by Spohn *et al.* [240] showcase asymmetric features comparable to earlier measurements, and also to unsteady bubbles observed in circular diffusers by Faler & Leibovich [72]. As a matter of fact, the work of Spohn *et al.* [240] is really a pioneering work in the acceptance of the axisymmetry breaking, amongst fluid experimentalists. It is noteworthy at this point, that the complex physics associated with these intricate phenomena occurring in closed/open rotating cylindrical container is still not clearly understood.

Like for the lid-driven cubical cavity flow, and in relation with the simple geometry of the flow, the rotating cylindrical cavity flow has been extensively studied using direct numerical simulations. A non-exhaustive list of references using different numerical methods has been given in Sec. 2.2 of Chapter 2. It is important to note that since the early seventies, the method of choice has consisted in solving the streamfunction-vorticity formulation of the axisymmetric incompressible Navier–Stokes equations. Without being exhaustive, the following list of references gives an overview of the numerical simulation of the closed lid-driven cylindrical flow over three decades: Pao [193], Lugt & Haussling [168, 169], Dijkstra & van Heijst [59], Lugt & Abboud [167], Neitzel [188], Daube & Sørensen [56], Lopez [158], Brown & Lopez [43], Lopez & Perry [166], Sørensen & Christensen [234], Watson & Neitzel [265], Gelfgat *et al.* [84, 85], Tsitverblit & Kit [250], and Brøns *et al.* [41]. All these works were able to reproduce with a reasonable accuracy, the basic features observed experimentally and reported earlier including the size, shape and number of recirculation bubbles. The onset of vortex breakdown was to some extent captured by several of these numerical simulations. Part of this work has been reproduced and is reported in the Appendix B, and constitutes a preliminary work for the study of open swirling flows. Lopez [158], and Brown & Lopez [43] suggested a physical mechanism for the intricate phenomena observed. They prove the existence of a standing centrifugal wave, whose amplitude increases with the Reynolds number and which can create a stagnation point on the cylinder axis, initiating the breakdown process. It is worth recalling that the streamfunction-vorticity formulation is adequate and appropriate only for the study of flow dynamics preserving the property of axisymmetry. At the inception of any instability breaking the axisymmetry of the flow, a three-dimensional solution of the Navier–Stokes equations is required, thereby increasing considerably the complexity of the task. The last remark justifies the observed changes in terms of numerical modeling of Lopez’ group and Sørensen’s group reported in Sec. 2.2, to allow them to investigate axisymmetry breaking in the closed cylinder case [19, 21–23, 228]. Therefore, three-dimensional flow structures have started being simulated more recently, see Gelfgat *et al.* [86], Sotiropoulos & Ventikos [236], Sotiropoulos *et al.* [237], Marques & Lopez [176], Blackburn & Lopez [21, 22], Serre & Bontoux [223], Blackburn [20], and Lopez [162].

Apart from the canonical case with a single driving lid in rotation at a constant angular velocity, different variations of the problem have been extensively studied in the past years: *e.g.* cylinder with co- and counter-rotating end-covers by Brøns *et al.* [41], steady axisymmetric flow in an open cylindrical container with a partially rotating bottom wall by Piva & Meiburg [198], vortex scenario and bubble generation in a cylindrical cavity with rotating top and bottom by Okulov *et al.* [191], swirling flow of a viscoelastic fluid by Escudier & Cullen [70], Day *et al.* [57], Xue *et al.* [268], and Stokes *et al.* [241, 242]. Mullin *et al.* [186] also included a rod at the axis to control the breakdown, and Pereira & Sousa [195] significantly changed the configuration by replacing the flat rotating bottom cover by a cone. As noted by Brøns *et al.* [42], all these studies show a large

set of flow structures which are quite sensitive to variations of external parameters.

7.1.3 Open swirling flow

The focus in the present chapter is on the canonical problem of a cylinder with a rotating bottom end-wall but replacing the stationary solid top end-wall by a free surface. The flow associated with this problem was first studied experimentally by Spohn *et al.* [239,240]. They observed the influence of the top free surface—assuredly clean of surfactants—on the onset, structure, nature and number of recirculating bubbles. Their central observations are that breakdown bubbles still appear, but are off-axis and may be attached to the free surface, depending on the aspect ratio Λ and the Reynolds number. Of course, such structures could not be observed in the closed case because of the no-slip condition imposed on the top wall. All the past simulations of free-surface swirling flows rely on the central assumptions that the free surface is flat and clean, which means that the Froude number is very small and that surface tension effects are negligible. With these assumptions, the flow is identical to the flow in the lower half part of a cylinder with two solid covers in co-rotation, *i.e.* rotating at the same angular velocity. Brøns *et al.* reported a wide range of topologies of vortex breakdown bubbles in a bottom-driven cylinder with a free surface, see Fig. 7.4. Valentine & Jahnke [252], observed in their

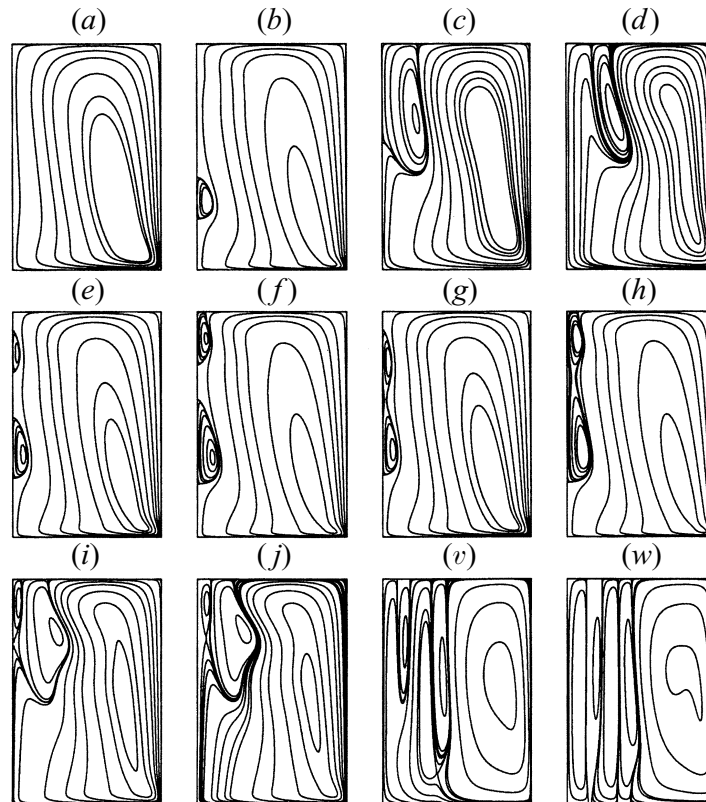


*Fig. 7.4: Typical representatives of the observed flow topologies (contours of the stream function) found in the steady domain. The drawings are scaled to the same normalized aspect ratio. Only the right half of a meridional plane is shown. The vertical line to the left is the axis. (a) $Re = 1000$, $\Lambda = 2.0$, no bubble. (b) $Re = 2800$, $\Lambda = 4.0$, axis bubble. (c) $Re = 1000$, $\Lambda = 1.0$, corner bubble. (d) $Re = 1700$, $\Lambda = 1.0$, surface bubble. (e) $Re = 1950$, $\Lambda = 3.0$, two axis bubbles. (f) $Re = 3000$, $\Lambda = 4.0$, one axis bubble and one corner bubble. (g) $Re = 1700$, $\Lambda = 2.7$, axis bubble with inner structure. (h) $Re = 3100$, $\Lambda = 4.0$, corner bubble with inner structure. (i) $Re = 2500$, $\Lambda = 1.9$, corner bubble with inner corner bubble. (j) $Re = 2800$, $\Lambda = 2.0$, surface bubble and in-flow saddle loop. (v) $Re = 1500$, $\Lambda = 0.3$, transition towards multi-cell topology. (w) $Re = 2100$, $\Lambda = 0.3$, Multi-cell topology with separatrices joining stagnation points at the surface and bottom. From Brøns *et al.* [42]. © 2001 Cambridge University Press.*

simulations the existence of one or two toroidal-like types of recirculation bubble having their stagnation lines attached to the free surface, depending on the value of the Reynolds number. Their study was complemented by the work of Lopez [159] for oscillating unsteady flows. Information relevant to the present problem with a free surface all indicate consistent flow behavior at small aspect ratio *i.e.*, $0.5 \leq \Lambda \leq 1.0$ in that stagnation

occurs off-axis and associated secondary flow creates a toroidal recirculation bubble. Steady free-surface flows have been computed by Iwatsu [130,131] providing flow state classifications with new flow patterns not revealed in the previous studies.

Recent experiments by Jansson *et al.* [133] and Suzuki *et al.* [247] at high angular velocity or equivalently high Reynolds number reported spectacular instabilities of the fluid surface. In those systems, the axisymmetry is spontaneously broken and polygonal shapes appear at the free surface: triangles, squares, pentagons and even hexagons [133, 255–257].

7.1.4 Motivations and objectives

The present study is motivated by several factors. Firstly, compared to the closed cylinder case, only some limited aspects of the open swirling flow have been investigated so far. The study of this intricate problem is relatively new and consequently the body of knowledge in some (Λ, Re) -parameter regions appears fairly limited. Secondly, most of the past studies involving numerical simulations of this free-surface swirling flow, used axisymmetric streamfunction-vorticity formulations: Brøns *et al.* [42], Iwatsu [130,131], and Piva & Meiburg [198]. To our knowledge, the only fully three-dimensional numerical simulation is due to Lopez *et al.* [164], who investigated mainly symmetry breaking issues. Finally, the work in this chapter aims at delivering results supporting the developments in the next chapter, where the free surface is no longer considered as fixed and flat.

In the present chapter, new flow states are investigated based on a fully three-dimensional solution of the Navier–Stokes equations without the need to resort to symmetry properties by doubling the computational domain and enforcing co-rotation of both end-walls. To our knowledge, the present study provides the most general available results for this flat-free-surface problem. Both, steady and unsteady flows are considered for different sets of governing parameters (Λ, Re) . A Legendre spectral element method is used to provide an accurate solution of the governing equations, while the stress-free boundary condition is naturally enforced into the weak formulation of the problem.

The mathematical model and the problem formulation are detailed in Sec. 7.2, while the original computational approach of this study is presented in Sec. 7.3. Subsequently, Sec. 7.4 contains all the numerical results corresponding to various physical situations and flow states. Finally, this chapter ends with Sec. 7.5 providing summary and conclusions on the present work.

7.2 Mathematical model and problem formulation

7.2.1 Mathematical description of the problem

The fluid enclosed in the cylindrical cavity is assumed to be incompressible, Newtonian with uniform density and temperature. The flow is governed by the Navier–Stokes equations

$$\frac{\partial u_i}{\partial t} + u_j \frac{\partial u_i}{\partial x_j} = \frac{\partial \sigma_{ij}^*}{\partial x_j} + g_i, \quad (7.1)$$

$$\frac{\partial u_j}{\partial x_j} = 0, \quad (7.2)$$

where $\sigma_{ij}^* = -p\delta_{ij} + 2\nu D_{ij}$ is the reduced Cauchy stress tensor of the fluid, p the static or reduced pressure, D_{ij} the rate-of-deformation tensor, ν the assuredly constant and uniform kinematic viscosity, and g_i the components of the acceleration of gravity ($g_1 = g_2 = 0$ and $g_3 = -g$). Inside the fluid domain denoted by \mathcal{V} , no-slip boundary conditions are imposed on all cavity walls: the tubular side-wall, the bottom end-wall in steady rotation, see Fig. 7.5. The mathematical expression of the no-slip condition on the tubular side-wall simply reads

$$u(r = R, \theta, z, t) = v(r = R, \theta, z, t) = w(r = R, \theta, z, t) = 0, \quad 0 \leq \theta \leq 2\pi, \quad 0 \leq z \leq H. \quad (7.3)$$

The flow is driven by imposing a prescribed angular velocity distribution of the bottom end-wall, which transfers its kinetic energy to the fluid above. The details regarding the imposition of this Dirichlet boundary condition for the velocity field at the lid are discussed in the next section 7.2.2. The top surface is left open and is modeled as a flat, fixed and clean free surface. The details regarding the imposition of this stress-free condition on the free surface are discussed in Sec. 7.2.3. As mentioned in the Introduction, Sec. 7.1.1, two parameters that determine completely the flow state are the height-to-radius aspect ratio $\Lambda = H/R$ and the Reynolds number $\text{Re} = R^2\Omega_0/\nu$, based on the maximal prescribed angular velocity Ω_0 of the bottom end-wall.

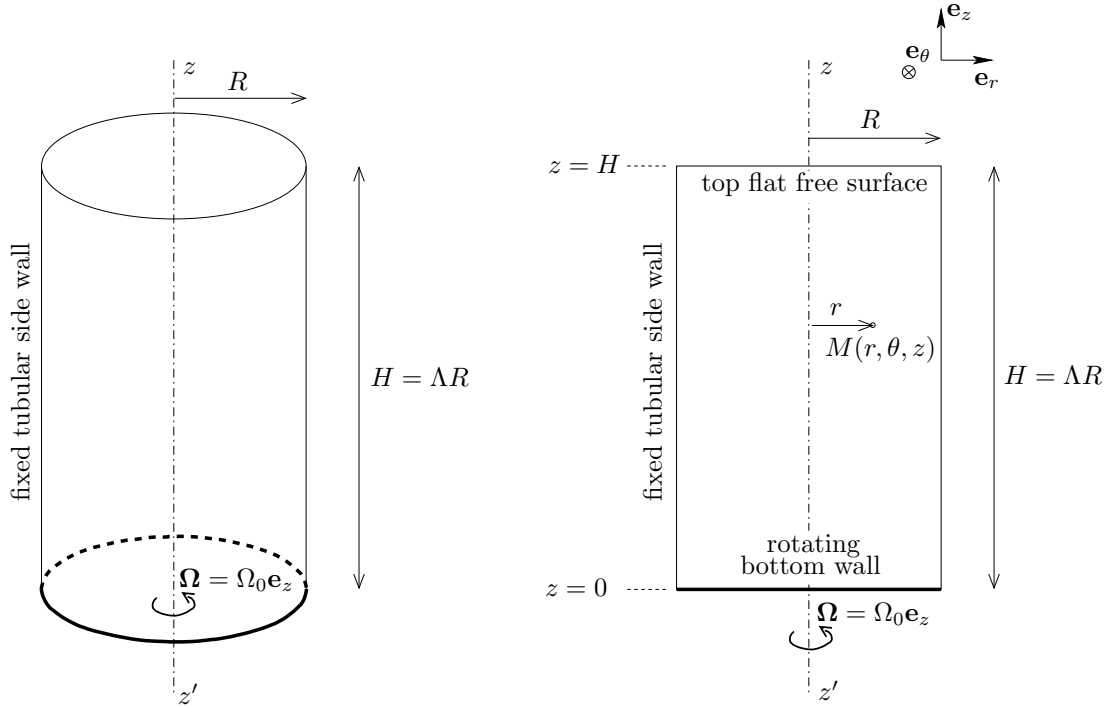


Fig. 7.5: Left: sketch of the three-dimensional geometry of the cylindrical cavity. Right: meridional cut of the cylindrical cavity.

In the sequel, the length, time, velocity, vorticity, helicity, streamfunction, (reduced) pressure and kinetic energy, and enstrophy are non-dimensionalized with respect to the reference scales R , Ω_0^{-1} , $R\Omega_0$, Ω_0 , $R\Omega_0^2$, $R^3\Omega_0$, $R^2\Omega_0^2$, Ω_0^2 respectively.

7.2.2 Angular velocity distribution

As already mentioned in Sec. 4.2.3.3 for the study of the lid-driven cubical cavity flow, imposing a given angular velocity distribution on the bottom end-wall of a cavity is not an easy task numerically. Indeed, imposing a constant angular velocity profile leads to a singularity (discontinuous behavior in the velocity boundary conditions) at the circular edge between the bottom end-wall and the tubular side-wall, see Fig. 7.5. Without adequate treatment, this discontinuous behavior will undermine the convergence and the accuracy of any numerical method in the vicinity of the lid. The same remedy as in the lid-driven cubical cavity problem of Part III is used here for the same reasons and with analogous justifications. A regularized angular velocity profile is employed by prescribing the following high-order polynomial expansion which vanishes along its first derivatives on the circular edge

$$\Omega(r, \theta, z = 0, t) = \Omega_0 \left[1 - \left(\frac{r}{R} \right)^{16} \right]^2 \mathbf{e}_z, \quad (7.4)$$

which leads to the following expressions in Cartesian coordinates of the components of the prescribed velocity field on the bottom end-wall

$$u(x, y, z = 0, t) = u_x(x, y, z = 0, t) = -y\Omega_0 \left[1 - \left(\frac{\sqrt{x^2 + y^2}}{R} \right)^{16} \right]^2, \quad (7.5)$$

$$v(x, y, z = 0, t) = u_y(x, y, z = 0, t) = +x\Omega_0 \left[1 - \left(\frac{\sqrt{x^2 + y^2}}{R} \right)^{16} \right]^2, \quad (7.6)$$

$$w(x, y, z = 0, t) = u_z(x, y, z = 0, t) = 0. \quad (7.7)$$

This profile flattens very quickly near the circular edge ($r/R = 1, \theta, z/H = 0$) while away from it, it grows rapidly to a constant value Ω_0 of the angular velocity over a short distance. The highest polynomial order of this distribution is 32. Such high-order polynomial expansions lead to steep velocity gradients in the vicinity of the circular edge of the bottom end-wall. The grid refinement, in terms of spectral element distribution near the disk will be presented in greater details in Sec. 7.3. One of the constraint in the grid design is to ensure the proper resolution of the lid velocity distribution by the spectral element decomposition.

7.2.3 Free-surface modeling

The analysis of a two-phase flow is based on the coupled hydrodynamics interactions between adjacent layers over a broad range of space and time scales. This analysis can be significantly simplified if the dynamics of the interface is almost entirely dependent—from the hydrodynamics and physico-chemistry viewpoints—on one phase, *e.g.* a liquid phase, and almost independent of the dynamics of the second phase, *e.g.* a gas phase. Based on this hypothesis, the surface is said to be *free*. Consequently, the two fluid phases can only exert constant normal stresses. Sarpkaya in his review entitled “Vorticity, free surface and surfactants” [218] gives a clear characterization and definition of a free surface: “Although, the exterior of a free surface is free from externally imposed shear, the interior is not necessarily free from the shear generated internally. In fact, surface deformations and contaminants give rise to surface-gradients and tangential stresses in the internal side of the bounding interface. From a mathematical viewpoint, a free surface means that the density and the viscosity of the upper fluid are zero and that the existence of a continuum above the interface is inconsequential. From a practical point of view, the free surface means that the dynamics of the continuum above the interface has negligible influence on the lower phase, *i.e.* a free surface is a simplifying approximation for an *almost free surface*.”

In the study presented in this chapter, the modeling of the interface between the fluids in the cylindrical cavity as a free surface is supplemented by an additional simplifying approximation: the free surface is supposed to remain flat and fixed all along the dynamic range of investigation. In general, the dynamics of the free surface depends on the non-dimensional Froude number defined here as

$$\text{Fr} = \frac{R^2 \Omega_0^2}{gH}, \quad (7.8)$$

which measures the relative importance of the inertial effects compared to the stabilizing gravitational effects. Therefore, assuming a flat free surface corresponds mathematically to a Froude number identically zero. As a consequence and in consistency with the latter assumption, the axial component of the velocity $w = u_z$ needs to vanish at the free surface $z/H = 1$

$$w(x, y, z = H, t) = 0, \quad x^2 + y^2 \leq R^2, \quad (7.9)$$

thereby expressing the kinematic boundary condition at the free surface. This latter condition on the axial velocity w is to be supplemented with the stress-free condition at the free surface

$$\sigma_{ij}^* \hat{n}_j = -p \delta_{ij} \hat{n}_j + 2\nu D_{ij} \hat{n}_j = 0, \quad (7.10)$$

where $\hat{\mathbf{n}}$ is the local outward unit vector normal at the free surface, which in the present particular situation is the unit normal vector \mathbf{e}_z in the z -direction. Consequently, the stress-free condition (7.10) reduces to $\sigma_{i3}^* = \sigma_{iz}^* = 0$, $i = 1, 2, 3$ at $z = H$, and is explicitly stated as

$$\sigma_{13}^* = 2\nu D_{13} = 0, \quad (7.11)$$

$$\sigma_{23}^* = 2\nu D_{23} = 0, \quad (7.12)$$

$$\sigma_{33}^* = -p + 2\nu D_{33} = 0, \quad (7.13)$$

which under the zero-deformation condition (7.9), simplifies to

$$\left(\frac{\partial u}{\partial z} + \frac{\partial w}{\partial x} \right) = \frac{\partial u}{\partial z} = 0, \quad (7.14)$$

$$\left(\frac{\partial v}{\partial z} + \frac{\partial w}{\partial y} \right) = \frac{\partial v}{\partial z} = 0, \quad (7.15)$$

$$-p + 2\nu \frac{\partial w}{\partial z} = 0. \quad (7.16)$$

The vorticity at the free surface often plays an important role in free-surface flows, and differs substantially from that for the free-slip or no-slip wall. Let the vorticity be denoted by $\boldsymbol{\omega}$ with components

$$\omega_x = \frac{\partial w}{\partial y} - \frac{\partial v}{\partial z}, \quad (7.17)$$

$$\omega_y = \frac{\partial u}{\partial z} - \frac{\partial w}{\partial x}, \quad (7.18)$$

$$\omega_z = \frac{\partial v}{\partial x} - \frac{\partial u}{\partial y}, \quad (7.19)$$

in Cartesian coordinates. The surface vorticity defined as $\boldsymbol{\omega}^s := (\omega_x, \omega_y)|_{z=H}$, is thereby identically zero in the particular case of the flat free surface. The axial component ω_z of the vorticity field is non-zero and is a measure of the internal shear at the free surface generated by the flow.

7.3 Computational approach

This section is aimed at providing the reader with a brief description of the numerical treatment of the equations governing the problem studied throughout this chapter.

7.3.1 Space discretization

The Navier–Stokes equations (7.1)–(7.2), supplemented with the boundary conditions (7.3), (7.5)–(7.7), (7.9), (7.14)–(7.16), constitute the set of governing equations for this free-surface swirling flow to be discretized and ultimately solved. The numerical method treats Eqs. (7.1)–(7.2) within the weak Galerkin formulation framework. The spatial discretization uses Lagrange–Legendre polynomial interpolants. The reader is referred to Chapter 2, Chapter 3 and the monograph by Deville *et al.* [58] for full details. The treatment of the governing equations is very similar to the one described in the past chapters and we only briefly recall here the fundamentals of the method. The velocity and pressure are expressed in the $\mathbb{P}_N - \mathbb{P}_{N-2}$ functional spaces where \mathbb{P}_N is the set of polynomials of degree lower than N in each space direction. This spectral element method avoids the presence of spurious pressure modes as it was proved by Maday & Patera [172, 174]. The quadrature rules are based on a Gauss–Lobatto–Legendre (GLL) grid for the velocity nodes and a Gauss–Legendre grid (GL) for the pressure nodes. The spectral element grid used for all simulations reported in this chapter is presented on Fig. 7.6 and Fig. 7.7, in the particular case $\Lambda = 1$. This mesh comprises 440 spectral elements distributed into 10 cylindrical layers of different heights, but all made of the same distribution of 44 spectral elements, see Fig. 7.6 (right). In order to resolve the boundary layer along the tubular side-wall, the Ekman shear layer above the rotating bottom end-wall and the surface shear layer below the free surface, the spectral elements are unevenly distributed as can be seen in Figs. 7.6 & 7.7. The choice of polynomial order in the three space directions, defining the inner GLL and GL grid into each spectral element is deferred to Sec. 7.3.3.

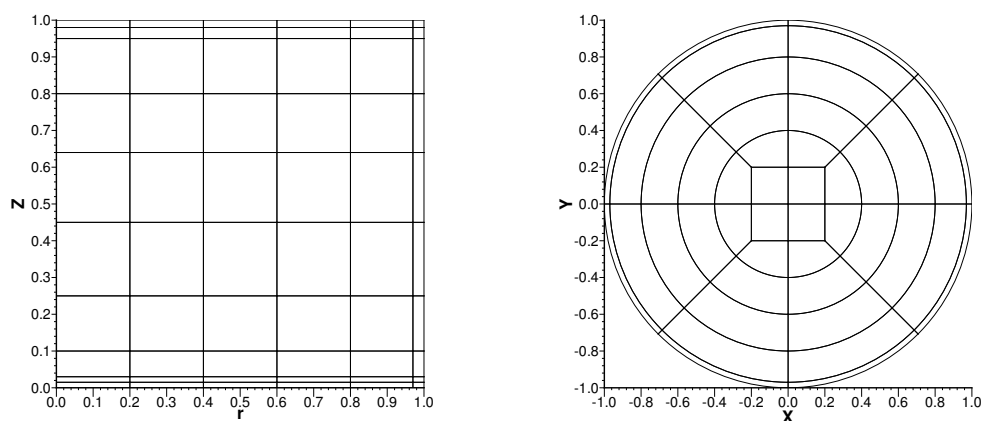


Fig. 7.6: Left: half-meridional grid. Right: spectral-element grid in any plane normal to the z -direction. Case $\Lambda = 1$.

The essential Dirichlet boundary conditions—homogeneous for \mathbf{u} on the tubular side-wall as expressed by Eq. (7.3), homogeneous for $w = u_z$ on the free surface as expressed by Eq. (7.9), and non-homogeneous for \mathbf{u} on the rotating bottom end-wall as expressed by Eqs. (7.5)–(7.7)—are embodied into the choice of test and trial functions chosen for the velocity field.

The stress-free condition (7.10) at the free surface, further expressed by Eqs. (7.14)–(7.16), appears as a homogeneous natural boundary condition in the weak Galerkin framework. This central point is discussed in detail and in a more general framework, in Chapter 3, Sec. 3.2.3, where a non-homogenous natural boundary condition is accounted for in the weak formulation of the problem. Based on this previous analysis, the treatment

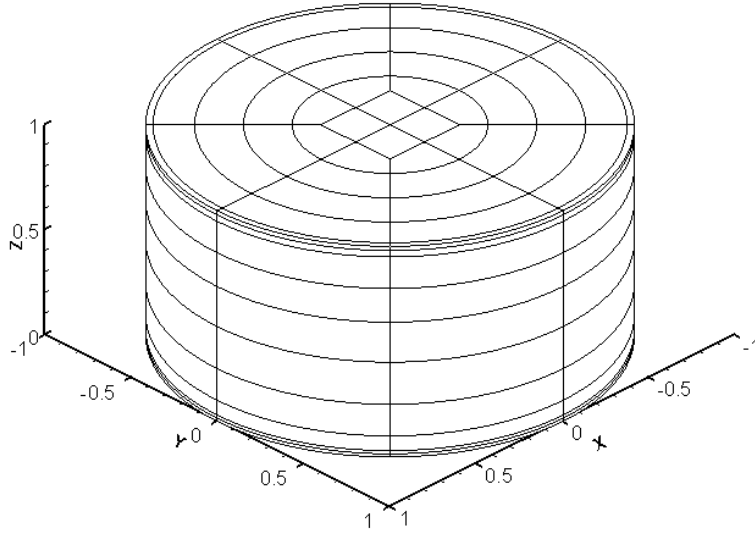


Fig. 7.7: Three-dimensional grid comprising 10 cylindrical layers of nonuniform heights made of 44 spectral elements each. Case $\Lambda = 1$.

of the present stress-free condition at the free surface appears straightforward and is automatically incorporated into the weak formulation of the problem.

Borrowing the notation from Deville *et al.* [58], the semi-discrete Navier–Stokes equations resulting from space discretization are

$$\mathbf{M} \frac{d\mathbf{u}}{dt} + \mathbf{C}\mathbf{u} + \nu \mathbf{A}\mathbf{u} - \mathbf{D}^T \underline{p} = 0, \quad (7.20)$$

$$-\mathbf{D}\mathbf{u} = 0. \quad (7.21)$$

The diagonal mass matrix \mathbf{M} is composed of three blocks, namely the mass matrices M . The global vector \mathbf{u} contains all the nodal velocity components while \underline{p} is made of all nodal pressures. The matrices \mathbf{A} , \mathbf{D}^T , \mathbf{D} are the discrete Laplacian, gradient and divergence operators, respectively. The matrix operator \mathbf{C} represents the action of the non-linear term written in convective form $\mathbf{u} \cdot \nabla$, on the velocity field and depends on \mathbf{u} itself. The semi-discrete equations constitute a set of non-linear ordinary differential equations (7.20) subject to the incompressibility condition (7.21).

7.3.2 Time integration

The time discretization of the semi-discrete set of governing equations (7.20)–(7.21) is the same as the one previously used in Chapter 3–Chapter 6, and detailed in Sec. 3.3.4, Sec. 4.2.3.2, and Sec. 5.2.3. We only briefly recall here the fundamentals of the method. The set of semi-discrete equations (7.20)–(7.21) obtained in the previous section is discretized in time using finite-difference schemes in a decoupled approach. The computation of the linear Helmholtz problem—corresponding to the stiffness matrix \mathbf{A} —is integrated based on an implicit backward differentiation formula of order 2, the nonlinear convective term—corresponding to the operator \mathbf{C} —is integrated based on a relatively simple extrapolation method of order 2, introduced by Karniadakis *et al.* [140], see Sec. 2.3.5 for full details.

7.3.3 Convergence tests

In order to demonstrate the spatial and temporal convergence of the simulation method, time series data have been analyzed, while varying separately the time-step Δt and the polynomial order N of the GLL basis in

each space direction, at the upper bound in Reynolds number $\text{Re} = 6000$, and with $\Lambda = H/R = 1$. As no experimental, nor numerical reference results are available for the present problem, three integral and one local quantities have been computed and compared. These three integral quantities are the total kinetic energy Q , enstrophy E and helicity \mathcal{H} of the flow, which definitions are recalled

$$Q = \frac{1}{2} \int_{\mathcal{V}} \mathbf{u} \cdot \mathbf{u} \, d\mathcal{V}, \quad (7.22)$$

$$E = \frac{1}{2} \int_{\mathcal{V}} \boldsymbol{\omega} \cdot \boldsymbol{\omega} \, d\mathcal{V}, \quad (7.23)$$

$$\mathcal{H} = \int_{\mathcal{V}} \mathbf{u} \cdot \boldsymbol{\omega} \, d\mathcal{V}. \quad (7.24)$$

The local quantity monitored is the axial velocity component $w = u_z$ at the point Π_0 of coordinates $(r/R = 0, z/H = 0.75)$, located along the cylinder axis. The location choice of this monitoring point is motivated by the study of Piva & Meiburg [198] for a very similar configuration but at smaller Reynolds numbers. They show that in the vicinity of this point, the axial velocity component reaches a local maximum. Given the relatively high Reynolds number of our benchmark simulation, a quite long transient—approximately 500 time units in Ω_0^{-1} units—is observed. Performing convergence tests involving a simulation time of the order of this transient time would simply be prohibitive. Consequently, it was chosen to assess the convergence after only 50 time units of simulations, which corresponds to the appearance of the first vortex-breakdown recirculation bubble in the fluid domain.

First, the spatial convergence is assessed by varying the polynomial order in the range $6 \leq N \leq 10$, while keeping the time-step values constant $\Delta t = 0.0025$. Results are reported in Table 7.1, and suggest that the spatial convergence is achieved using a polynomial order $N = 8$ in all three space directions. This value is used for all the direct numerical simulations presented in the sequel, except for one single case corresponding to the steady laminar case ($\Lambda = 1, \text{Re} = 900$), for which $N = 7$ is chosen.

| N | Q | E | \mathcal{H} | $w(\Pi_0)$ |
|-----|-------------|-------------|---------------|-------------|
| 6 | 2.02745e-02 | 2.11900e+01 | 1.29876e-01 | 3.28923e-03 |
| 7 | 2.08244e-02 | 2.18923e+01 | 1.33612e-01 | 3.40034e-03 |
| 8 | 2.19036e-02 | 2.37953e+01 | 1.66448e-01 | 3.81373e-03 |
| 9 | 2.19034e-02 | 2.37957e+01 | 1.66450e-01 | 3.81376e-03 |
| 10 | 2.19035e-02 | 2.37955e+01 | 1.66447e-01 | 3.81375e-03 |

Table 7.1: Spatial convergence analysis for the case ($\text{Re} = 6000, \Lambda = 1$) with $\Delta t = 0.0025 \Omega_0^{-1}$. Q in $R^3(R\Omega_0)^2$ units, E in $R^3\Omega_0^2$ units, \mathcal{H} in $R^4\Omega_0^2$ units, and w in $R\Omega_0$ units. Instant $t = 50\Omega_0^{-1}$.

Finally, the temporal convergence is assessed by varying the time-step, while keeping the polynomial order constant at the value $N = 8$, in agreement with the earlier spatial convergence analysis. Results are reported in Table 7.2 below, and suggest that the temporal convergence is achieved using a time-step $\Delta t = 0.0025$. At a reduced Reynolds number compared to the one employed for this convergence analysis $\text{Re} = 6000$, greater values of the time-step have been chosen in relation with the more laminar nature of the flow without affecting the convergence of the simulations.

| Δt | Q | E | \mathcal{H} | $w(\Pi_0)$ |
|------------|-------------|-------------|---------------|-------------|
| 0.005 | 2.08574e-02 | 2.14302e+01 | 1.36342e-01 | 3.49221e-03 |
| 0.0035 | 2.11896e-02 | 2.25311e+01 | 1.48303e-01 | 3.61923e-03 |
| 0.0025 | 2.19036e-02 | 2.37953e+01 | 1.66448e-01 | 3.81373e-03 |
| 0.001 | 2.19034e-02 | 2.37960e+01 | 1.66446e-01 | 3.81379e-03 |

Table 7.2: Temporal convergence analysis for the case ($\text{Re} = 6000, \Lambda = 1$) with $N = 8$. Δt in Ω_0^{-1} units, Q in $R^3(R\Omega_0)^2$ units, E in $R^3\Omega_0^2$ units, \mathcal{H} in $R^4\Omega_0^2$ units, and w in $R\Omega_0$ units. Instant $t = 50\Omega_0^{-1}$.

7.4 Numerical simulations and results

7.4.1 General physical characteristics of the flow

The central characteristics of the flow in a closed cylindrical container with a bottom rotating end-wall is a large recirculation of the fluid. The features of the intense shear layer induced by the rotation of the bottom wall can be obtained from the analogy with the analysis by von Kármán for the flow generated by a spinning plate in an unbounded fluid domain, see the review by Zandbergen & Dijkstra [270] for full details. The rotation of the bottom wall has a suction effect on the fluid in the near-axis region and a pumping effect, while accelerating the fluid radially outwards in an Ekman shear layer of thickness $O(\text{Re}^{-1/2})$. In the framework of our problem, this Ekman layer is bounded by the tubular cylinder side-wall, which forces the recirculation of the fluid in the upward direction along the side-wall, and towards the top wall. As the fluid approaches the curved corner, the radial velocity contribution to the kinetic energy is progressively transformed into an axial velocity contribution to the kinetic energy. It has been observed that the fluid turns and subsequently spirals upward along the tubular side-wall.

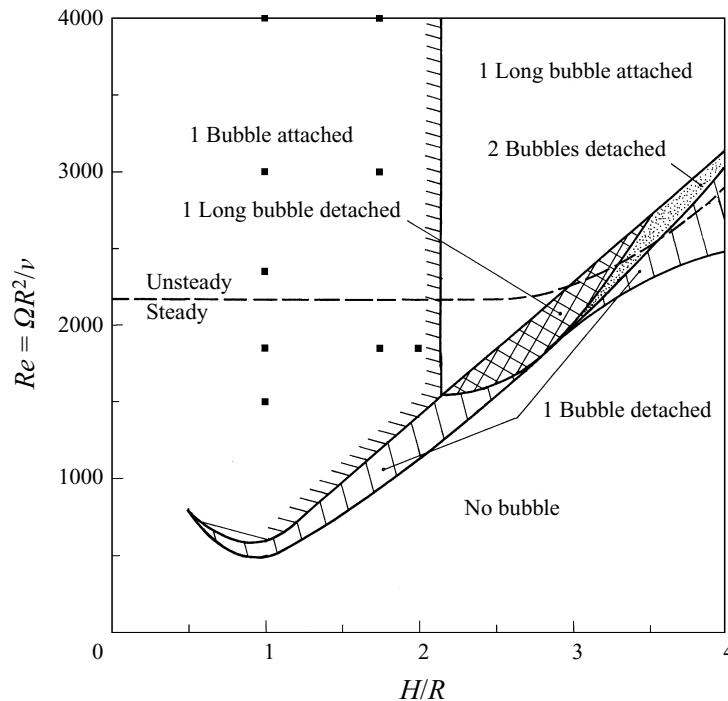


Fig. 7.8: Comparisons of flow states with a free surface for some selected parameter combinations ($\Lambda = H/R$, Re) with the results obtained by Spohn *et al.* [239]. Regimes where experiments have been carried out are indicated by symbol: ■, one bubble. From Spohn *et al.* [240]. © 1998 Cambridge University Press.

As mentioned in Sec. 7.1.3, replacing the fixed top solid wall with a free surface changes significantly the physics of the flow and the recirculation mechanisms. In absence of tangential stresses at the free surface, the boundary layer is replaced by a surface layer in the sense of Shen *et al.* [226, 227]. In addition, the inward spiraling fluid elements conserve their angular momentum at the free surface. When the related centrifugal force is large enough to balance the radial pressure gradient, the flow separates from the free surface and leads to the generation of a vortex breakdown bubble. The most striking difference between the flow patterns observed in the present open cylinder case and compared to the close cylinder one—see Appendix B for a brief introduction—are the possible appearances of recirculation bubbles, which are generally attached to the free surface. Such flow patterns are simply impossible in presence of the no-slip condition imposed on the top wall in the closed cylinder case. More precisely, Iwatsu [131] determined 24 different flow states in the steady regime according to the meridional streamline patterns observed. Some of these flow states are depicted in Fig. 7.4. Spohn *et al.* [240] summarized those flow states in a simplified bifurcation diagram in the (Λ, Re) space, which is shown in Fig. 7.8. Based on his extensive and comprehensive study, Iwatsu [131] came out with a more detailed and complex bifurcation diagram.

In subsequent studies, the stability of those steady axisymmetric flows were investigated. Young *et al.* [269], Miraghaie *et al.* [182], Lopez *et al.* [164], and Lopez & Marques [163] observed unstable azimuthal modes which are triggered at different values of the Reynolds number depending on the nature “shallow” ($\Lambda < 1$) or “deep” ($\Lambda > 1$) of the system. Valentine & Jahnke [252], Lopez [159], and Brøns *et al.* [42] associated the axisymmetry breakage to instability modes. These modes appear following a Hopf bifurcation which generally occurs at relatively high Reynolds number.

7.4.2 Cases studied

As mentioned in the previous sections, the physics of these free-surface swirling flows depends critically on the Reynolds number. Nevertheless, the height-to-radius aspect ratio Λ also has considerable impact on the observed nature of the flow. Very often, situations corresponding to extreme values of Λ have been studied, as they generally lead to simplified flow mechanisms. For instance, shallow systems ($\Lambda < 1$) are often referred to as “rotor-stator” configurations, in which the fluid is almost in a state of solid-body rotation. On the other hand, deep systems associated with large values of Λ , generate recirculation bubbles away from the free surface and generally on the cylinder axis. Consequently, systems corresponding to values of Λ close to the unity are intermediate in the sense that the physics of the flow observed is a complex combination of the general features reported for the shallow and deep systems.

| Case | Re | $\Lambda = H/R$ | Time-step Δt | Time evolution | Vortex breakdown |
|------|-------|-----------------|----------------------|----------------|------------------------------|
| (a) | 900 | 1.0 | 0.005 | steady | one attached bubble |
| (b) | 1 500 | 1.0 | 0.005 | steady | one attached toroidal bubble |
| (c) | 6 000 | 1.0 | 0.0025 | unsteady | complex dynamics |
| (d) | 2 000 | 1/3 | 0.004 | steady | two long attached bubbles |
| (e) | 2 000 | 3.0 | 0.004 | steady | one short detached bubble |

Table 7.3: Parameters and characteristics of the cases considered. The time-step Δt is expressed in Ω_0^{-1} units.

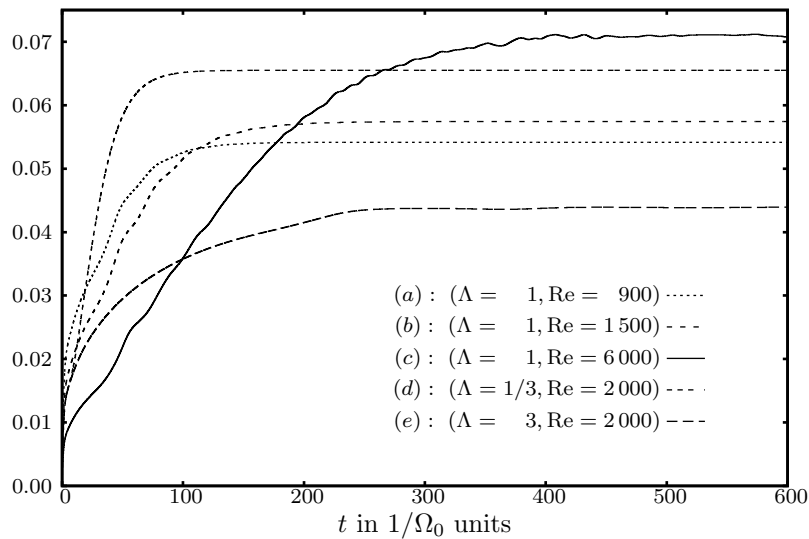


Fig. 7.9: Time history of the volume integral of the kinetic energy Q of the flow, in $R^5 \Omega_0^2$ units for cases (a)–(e).

The details related to the five cases considered in this chapter are summarized in Table 7.3. In the study reported in this chapter and the next one, the primary focus is on the flow defined by $\text{Re} = 6\,000$ and $\Lambda = 1$. The value of the Reynolds number is intentionally set to a high value compared to previous studies—the highest to our knowledge, in order to ensure producing fields of a relative intensity at the free surface. The choice of the value of Λ follows the earlier comment on systems being intermediate between shallow and deep. This central case ($\Lambda = 1, \text{Re} = 6\,000$) is supplemented with four secondary cases described in Table 7.3. The study of those secondary flows is of prime importance for the understanding of the complex dynamics of the primary case ($\Lambda = 1, \text{Re} = 6\,000$).

In terms of initial conditions, the steady rotation is impulsively started from a quiescent fluid state for all cases presented in the sequel. At this point, it is worth noting the timescales of the evolution of these flows.

Figure 7.9 displays the time history of the volume integral of the kinetic energy of the flow Q . For all cases except case (c), the flow reaches a steady state after a given time scale, which is, as expected, shorter for shallow systems. Case (c) leads to an unsteady flow which does not display any oscillatory evolution. The value of the Reynolds number for this case is large enough to produce a non-trivial evolution of the recirculation zones as will be seen in the sequel.

The time histories of the volume integral of the kinetic energy Q for the five cases (a) – (e) can be compared to the ones, reported in Sec. B.2.2 of Appendix B, for the closed swirling flow problem with $\Lambda = 2.5$, see Fig B.4. It should be noted that for a fixed value of Λ , the total kinetic energy Q of the flow decreases with the Reynolds number for the closed cylinder case, while it increases in the open cylinder case. This decreasing trend for Q in the closed cylinder case can easily be resolved by transposing the analysis given by Leriche & Gavrilakis [155] in their study of the closed lid-driven cubical cavity flow. Leriche & Gavrilakis argue that the most significant part of the kinetic energy of the flow is contained in the viscous layer developing on the driving wall. Consequently, the total energy varies like the energy contained in this viscous layer which can approximately be expressed as $U_0^2 \mathcal{V} \text{Re}^{-1/2}$, where U_0 is the characteristic velocity of the driving wall and \mathcal{V} the volume of the cavity. Such argument and estimate can easily be transposed for the closed swirling flows studied in Appendix B, and explains the decreasing trend for Q with respect to Re . Furthermore this argument is confirmed by the measurements of the kinetic energy $Q(L_1)$ of the cylindrical layer of fluid L_1 located right above the spinning disk and of height $0.015H$, reported in Table 7.4. This thin layer of fluid which only represents 1.5% of the total volume of fluid, contributes for approximately 10% to the total kinetic energy of the flow. Concurrently, its contribution to the total kinetic energy of the flow decreases with the Reynolds number.

| Re | $Q(L_1)$ | $E(L_1)$ | $E_z(L_1)$ |
|-------|-------------|-------------|---------------|
| 900 | 7.42243e-03 | 3.04128e+00 | 3.99817e-01 |
| 1 500 | 7.05011e-03 | 4.46885e+00 | 4.03147e-01 |
| 6 000 | 5.71943e-03 | 1.18305e+01 | 4.25622e-01 |
| Re | $Q(L_{10})$ | $E(L_{10})$ | $E_z(L_{10})$ |
| 900 | 3.88037e-04 | 6.14708e-03 | 5.99848e-03 |
| 1 500 | 5.47285e-04 | 9.04519e-03 | 8.25633e-03 |
| 6 000 | 1.21966e-03 | 6.43344e-02 | 2.00737e-02 |

Table 7.4: Measurements of the kinetic energy Q , enstrophy E , and enstrophy associated solely with the axial vorticity component E_z for the cylindrical layer L_1 comprised between $z = 0$ and $z = 0.015H$, and for the cylindrical layer L_{10} comprised between $z = 0.98H$ and $z = H$. Q in $R^3(R\Omega_0)^2$ units, E and E_z in $R^3\Omega_0^2$ units. Instant $t = 600\Omega_0^{-1}$.

On the contrary, a reverse trend is observed for the variations of Q with respect to Re in the open swirling flow. It therefore requires another physical justification. Nevertheless, the previous energetic argument associated with the viscous layer still holds for the viscous layer above the spinning disk and near the tubular side-wall in the open cylinder swirling flow. Below the surface at $z = H$, the viscous layer in the closed cylinder case is replaced by an intense shear layer. As mentioned in Sec. 7.2.3, in the present flat-free-surface problem, the axial vorticity ω_z is the only component of the vorticity field which is not vanishing at the free surface and it provides a measure of the internal shear at the free surface. The part E_z of the enstrophy associated with the axial vorticity component is measured in the cylindrical layer of fluid L_{10} , of height $0.02H$ and located below the free surface. Results are reported in Table 7.4 and clearly show a significant increase of E_z with respect to Re in the layer L_{10} , while it is almost constant in L_1 . These results allow us to infer that the shear layer below the free surface becomes more and more intense and energetic—see $Q(L_{10})$ — when increasing the Reynolds number. But this observed energetic trend of the free-surface shear layer is not the only factor responsible for counterbalancing the decreasing trend of the viscous layers. The internal structure of the free-surface layer is itself physically different as reported by Shen *et al.* [226, 227]. The so-called surface layer corresponds to a thin region adjacent to the free surface characterized by fast variations of the tangential vorticity components. This surface layer is caused by the dynamic zero-stress boundary conditions (7.10) at the free surface and lies inside a thicker blockage (or “source”) layer, which is due to the kinematic boundary condition (7.9) at the free surface. The importance of the outer blockage layer is manifested mainly in the redistribution of the kinetic energy, *i.e.* in the increase of the kinetic energy of the tangential velocity components at the expense of the kinetic energy of the axial velocity component. This point is to be further discussed in Sec. 7.4.3.2, where a comprehensive comparison of the flow below the surface $z = H$ for the case (c) with a free surface and the equivalent closed case in Appendix B is given.

7.4.3 Physical description of flow states

7.4.3.1 Steady flows

As a first step, we present the two steady flows for $\Lambda = 1$ and $\text{Re} = 900, 1500$ corresponding to cases (a) and (b) respectively. Figure 7.10 displays the streamlines of these flows into any meridional plane. Both of these flows present a large axisymmetric vortex breakdown bubble attached to the free surface in agreement with the experimental results from Spohn *et al.* [240] summarized by the bifurcation diagram reported in Fig. 7.8. These recirculation zones are characteristic of these swirling flows due to the conjugate effects of the centrifugal force and the overturning flow induced by the presence of the tubular side-wall. The central difference between the low-Reynolds-number cases (a) and (b) is the shape of the recirculation, which becomes toroidal after leaving the axis when the Reynolds number is increased from 900 up to 1500, see the three-dimensional representations given in Fig. 7.12. These results can be further validated by comparing them to the experimental steady dye lines obtained by Piva for $\text{Re} = 1120$ and shown in Fig. 7.11. Finally, case (a) ($\Lambda = 1, \text{Re} = 900$) has been computed by Piva & Meiburg [198] and four series of the contour lines of their results are presented in Fig. 7.13.

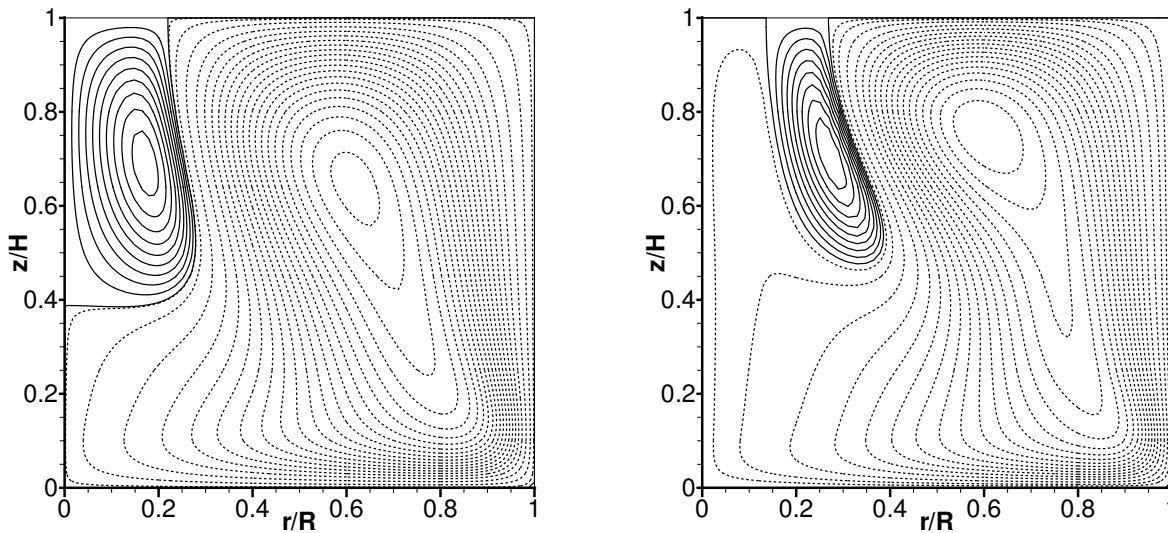


Fig. 7.10: Contours of streamlines in a meridional plane, case $\Lambda = 1$. Left: case $\text{Re} = 900$; Right: case $\text{Re} = 1500$. The 30 contours are non-uniformly spaced for visualization purposes, 20 equally-spaced negative contours and 10 equally-spaced positive contours for $\text{Re} = 900$ and $\text{Re} = 1500$.

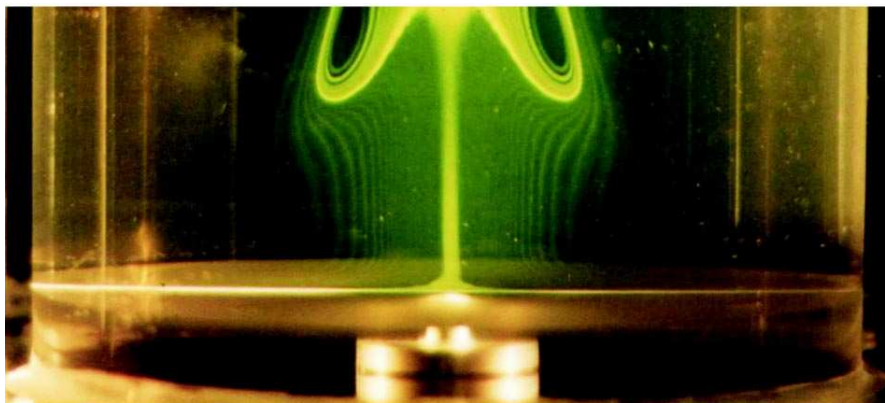


Fig. 7.11: Snapshot of the meridional flow field obtained by dye injection in the case $\Lambda = 1$ and $\text{Re} = 1120$. © M. Piva, Ph.D. thesis, Universidad de Buenos Aires, 2000.

As a second step, the contours of the radial, azimuthal and axial velocity components in any meridional plane are given in Fig. 7.14. These data are supplemented with the contours of the axial component of the

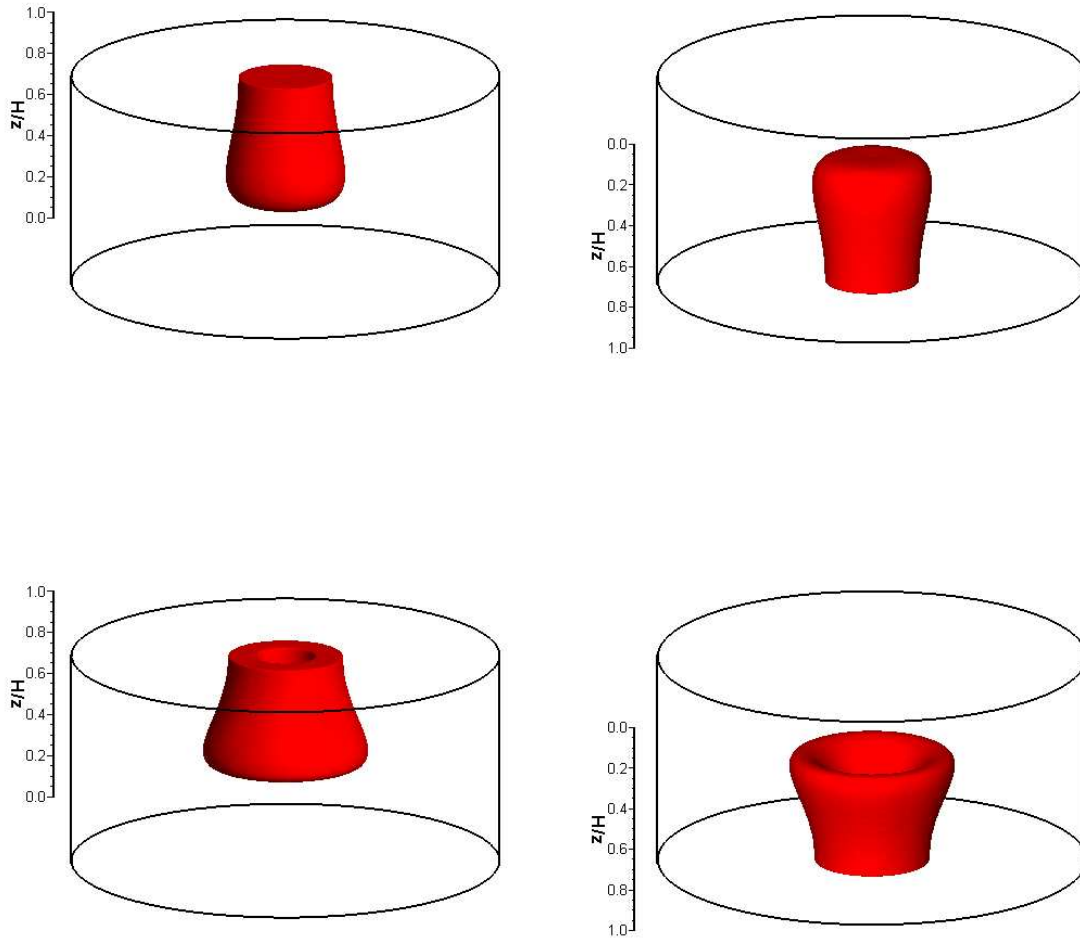


Fig. 7.12: Visualization of the shape of the recirculation bubble attached to the free surface for case $\Lambda = 1$. Top row: $Re = 900$; Bottom row: $Re = 1500$. Left column: normal view; Right column: upside-down view.

angular momentum $\Gamma = ru_\theta$ still in Fig. 7.14, extreme right column. The interest for Γ lies in the fact that it plays the role of a streamfunction for the part of the velocity field comprised in any meridional plane, see Bragg & Hawthorne [39] and Keller [141] for full details. Therefore, the contours of Γ deliver the intersection of vortex surfaces with the corresponding meridional plane where they are drawn, and as such provide us with the local direction of the meridional vorticity field. One can notice from the velocity components and axial angular momentum component that the meridional structure of these flows is far from being trivial. It consists of an intense boundary layer above the spinning bottom end-wall that is turned into the interior by the presence of the tubular side-wall, forming a shear layer having a jet-like velocity profile in the azimuthal direction. The contour lines of the axial component of the angular momentum shown in Fig. 7.14 (extreme right column) simply represent the vortex lines, which all emanate from the rotating disk; the structure of the shear layer is apparent. It is worth noting here that the vortex lines distribution at their origin varies like r^2 . As a consequence of the regularized profile of angular velocity of the rotating disk—see Sec. 7.2.2, this distribution in r^2 is slightly affected in the vicinity of $r = R$. This regularization of this profile has the advantage of preventing the appearance of vortex lines terminating at the circular corner ($r = R, z = 0$), which are deprived of any physical meaning. The overturning nature of these flows is also apparent in the vicinity of the tubular side-wall, which is the vortex surface corresponding to $\Gamma = 0$, together with the cylinder axis. As non-zero azimuthal velocities are possible at the free surface, vortex lines emanating from the rotating end-wall have the option of terminating orthogonally to the free surface. This observation is one of the major difference with the closed cylinder swirling flow where all vortex lines have to terminate in the corner, see Fig. B.3 and Fig. B.9 in

Appendix B. Furthermore, the termination of vortex lines at the free surface is responsible for the possibility of having vortex breakdown bubbles being attached to the free surface as observed in Fig. 7.10 and Fig. 7.11. A careful analysis of Fig. 7.14 (extreme right column) reveals that one vortex line marks the limit between an inner region comprising only vortex lines terminating at the free surface, and an outer region, where they terminate near the circular corner, like in the closed cylinder case. In summary, it appears that the main effect of this overturning flow is to bring high-angular-momentum fluid towards the cylinder axis.

The results for case (a) ($\Lambda = 1, \text{Re} = 900$) presented in Fig. 7.10 (left) and Fig. 7.14 (top row) show a qualitative good agreement with the numerical results of Piva & Meiburg [198] reproduced in Fig. 7.13.

The differences related to the features of the recirculation bubbles for cases (a) and (b) have been discussed earlier. One can notice in Fig. 7.14 (two left columns), as expected, that the thicknesses of the intense radial velocity layer as well as the axial wall jet are reduced when the Reynolds number is increased from 900 to 1 500. The contours of the axial velocity component reveal that the downward-directed flow induced by the suction effect of the Ekman layer, is more intense at higher Reynolds number. In addition, the region of the flow where $w = u_z$ has a negative extremum tends to move closer to the free surface when increasing Re. Regarding the vortex lines shown in the extreme right column, their bending towards the cylinder axis is more pronounced at the higher Reynolds number of 1 500. In relation with the previous analysis, this latter observation highlights the fact that more high-angular-momentum fluid is brought towards the axis when increasing Re.

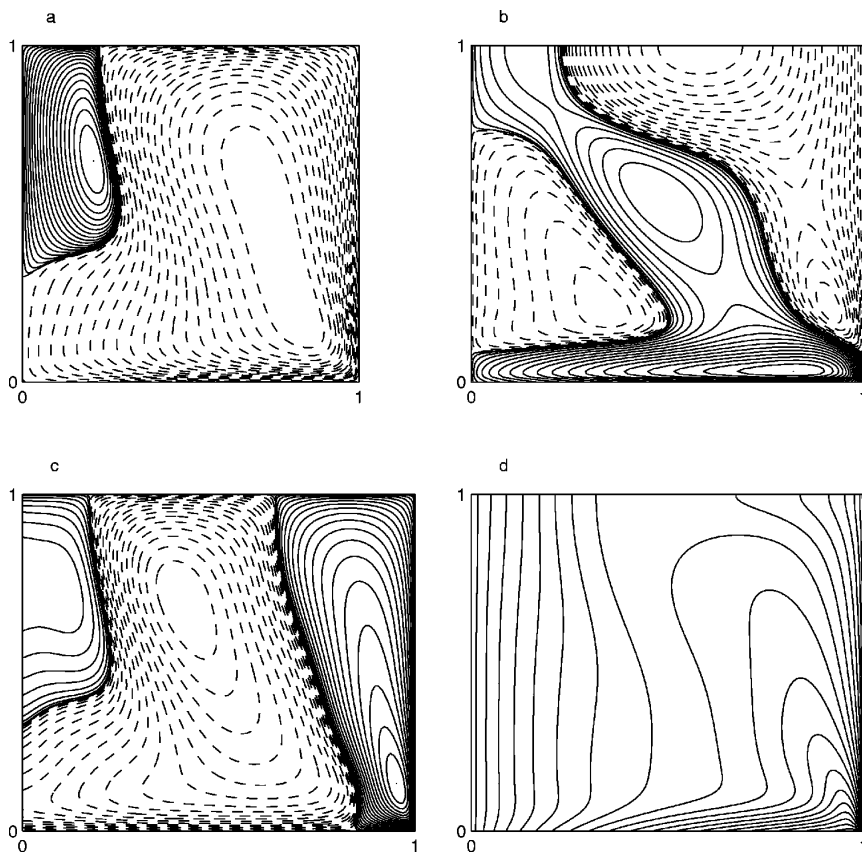


Fig. 7.13: Contours of (a) streamlines; (b) radial velocity; (c) axial velocity; (d) angular momentum in a meridional plane. Case $\Lambda = 1$ and $\text{Re} = 900$. For visualization purposes, the contour levels are nonuniformly spaced. From Piva & Meiburg [198]. © 2005 American Institute of Physics.

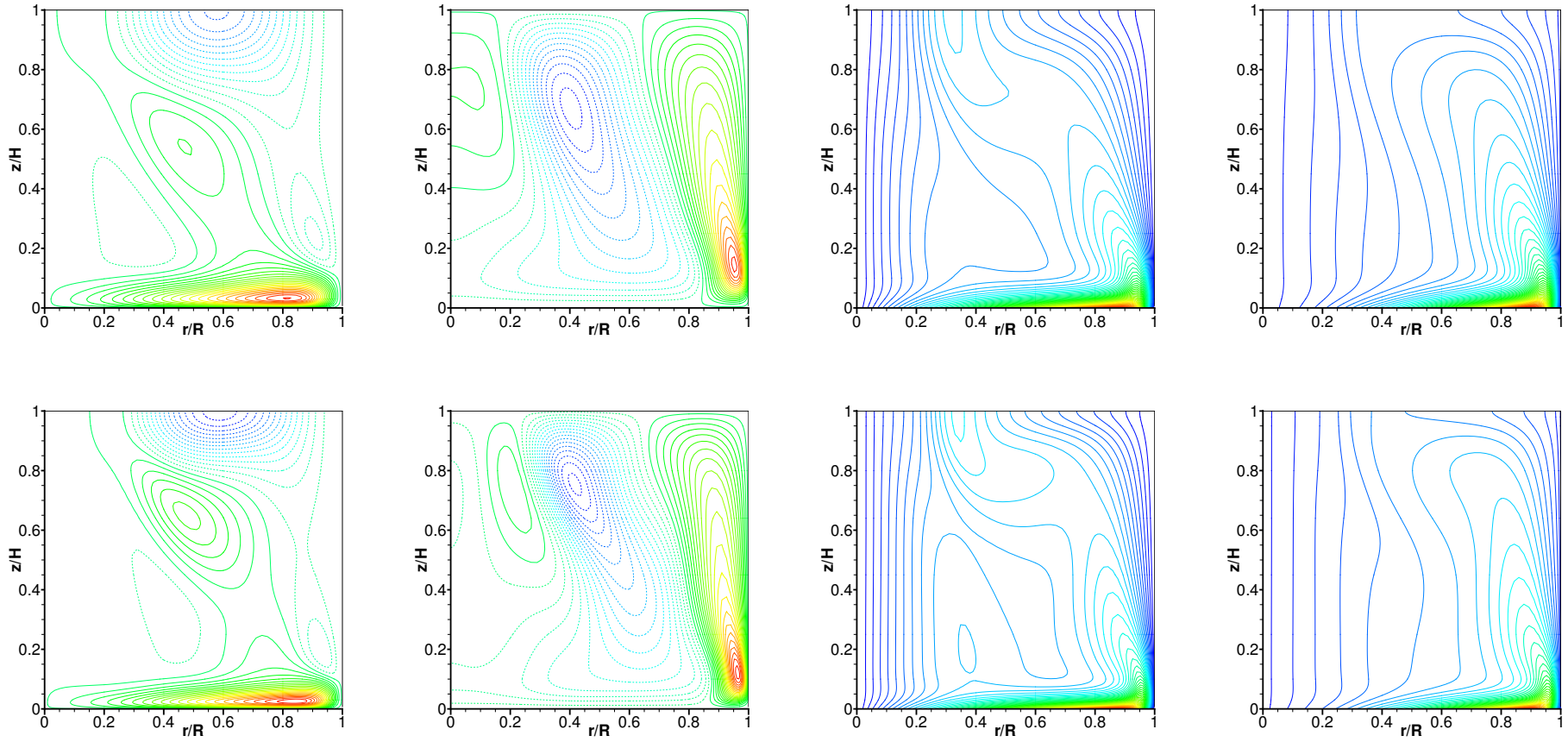


Fig. 7.14: Contours in a meridional plane for the case $\Lambda = 1$. Top row: case $\text{Re} = 900$; Bottom row: case $\text{Re} = 1500$. From left column to right column: radial velocity component u_r ; axial velocity component $w = u_z$; azimuthal velocity component u_θ ; axial angular momentum component $\Gamma = ru_\theta$. The 35 contours are uniformly spaced, between -0.1 and 0.145 for u_r ; and between -0.08 and 0.115 for u_z ; The 50 contours are uniformly spaced, between 0 and 1 for u_θ and Γ .

As mentioned in Sec. 7.4.2, our primary interest lies in case (c) ($\Lambda = 1$, $\text{Re} = 6000$), thereby justifying the study of cases (a) and (b), having the same aspect ratio Λ but corresponding to laminar cases. Nevertheless, the study of cases (d) and (e), which both correspond to “extreme” cases in terms of height-to-radius aspect ratio, illustrate some essential features of the open swirling flow. In case (c) some of these features may prevail only in specific regions of the flow as it corresponds to an intermediate case between a shallow system characterized by case (d) and a deep system characterized by case (e). These features are as follows:

- solid-body rotation of the inner core region, predominantly for small Λ ;
- radial jet of angular momentum at the free surface;
- lateral jet-like shear layer along the tubular side-wall;

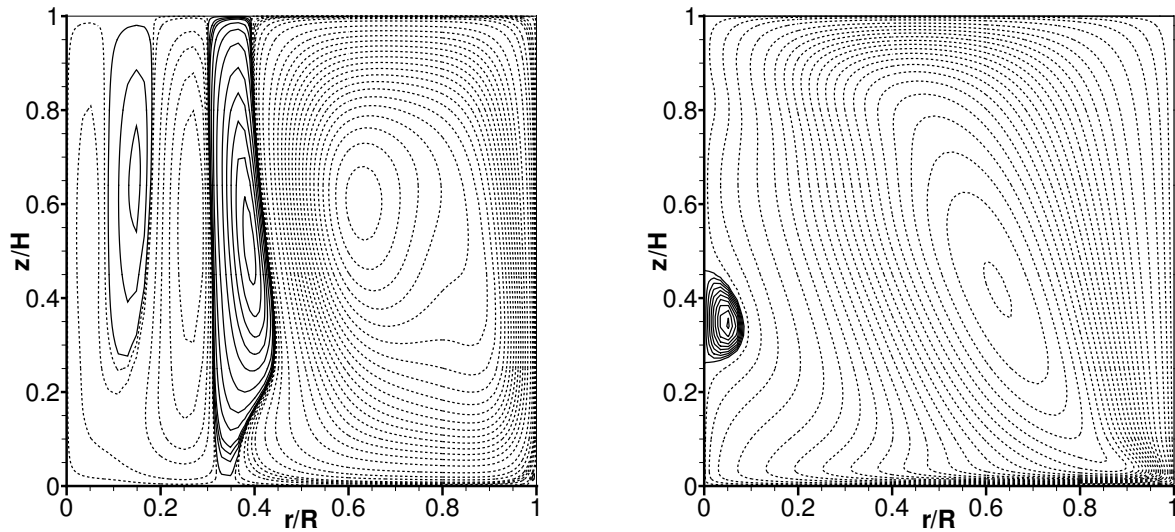


Fig. 7.15: Contours of streamlines in a meridional plane. Left: case (d) : ($\Lambda = 1/3$, $\text{Re} = 2000$); Right: case (e) : ($\Lambda = 3$, $\text{Re} = 2000$). The 30 contours are non-uniformly spaced for visualization purposes, 20 equally-spaced negative contours and 10 equally-spaced positive contours for (d) and (e).

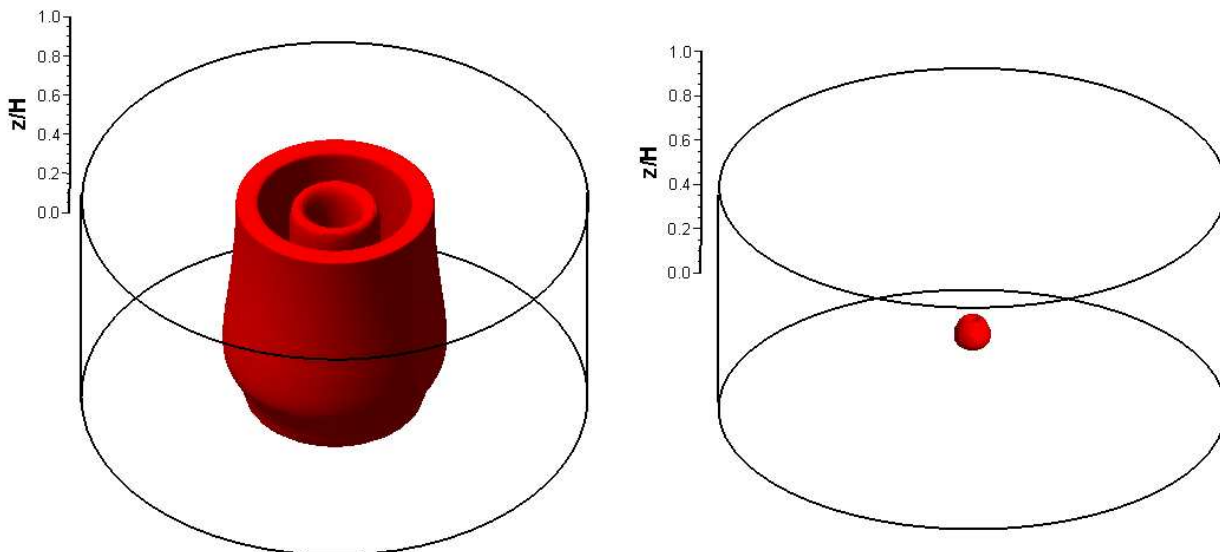


Fig. 7.16: Visualization of the shape of the recirculation bubble(s) attached to the free surface. Left: case $\Lambda = 1/3$ and $\text{Re} = 2000$; Right: case $\Lambda = 3$ and $\text{Re} = 2000$.

The very different flow patterns developed by both cases (*d*) and (*e*) are highlighted by the very distinctive streamlines shown in Fig. 7.15 and with the 3D visualizations in Fig. 7.16. The shallow case (*d*) yields two vortex breakdown bubbles, which are off the cylinder axis while remaining attached to the free surface. The recirculation is more intense in the largest bubble, which is elongated enough to produce a recirculation of the fluid from the free surface all the way down to the rotating disk, and so forth. Consequently, this elongated bubble completely separates the outer region of the flow ($r/R \geq 0.5$) from the inner core, where the second less intense, vortex breakdown occurs. Comparatively, the recirculation in case (*e*) is fairly limited. A vortex breakdown still occurs in this case, leading to the formation of a small on-axis bubble, which is detached from the free surface. One can notice from the bending of the streamlines near the axis at the height $z/H = 0.8$, that another vortex breakdown is in preparation—compare this effect to the similar effect on the streamlines prior the vortex breakdown in the closed swirling flow at $Re = 1900$, shown in Fig. B.2.

The shallow system (d) ($\Lambda = 1/3, Re = 2000$) possesses some very distinctive features as can be seen in Fig. 7.17 (top row). The vortex lines for $r/R < 0.4$ being aligned with the rotation axis, one can easily conclude that the flow is essentially in solid-body rotation in this inner core region of the cavity. The meridional flow in this inner part of the cavity has a very weak intensity as attested by the values close to zero of the contours of the axial and radial velocity components—solid contour lines are positive and negative contour lines being dashed. In contrast, for $r > 0.4$ the primary recirculation of the flow is intense and predominates. The vortex lines bending is limited to this region and again is at the origin of the vortex breakdown appearing near $r/R = 0.4$. The boundary layer on the rotating disk is limited to the region $r/R > 0.5$ and the internal jet-like shear layer close the tubular side-wall has a structure quite different from the cases with $\Lambda = 1$. Indeed in this shear layer, the axial velocity is relatively intense all along the tubular side-wall, unlike cases (*a*), (*b*) and (*e*), where the axial velocity u_z decreases rapidly with z/H . This observation is easily explained by the shorter height in the case studied, but has several considerable consequences on the flow itself. A more intense wall-jet implies a more intense angular momentum jet at the free surface, which facilitates the vortex breakdown phenomena. The intense angular momentum free-surface jet produces an elongated recirculation bubble located as seen earlier, around $r/R = 0.4$. In this elongated bubble, the axial velocity field is globally positive, thereby producing an effect similar to the jet-like shear layer near the tubular side-wall. In turn it generates a secondary angular momentum free-surface wall jet responsible for the second vortex breakdown.

Increasing the height-to-radius aspect ratio to $\Lambda = 3$, modifies considerably the flow dynamics as can be seen in Fig. 7.17 (bottom row). It seems clear from the previous analysis for the shallow case (*d*), that the influence of the free surface on the flow is more important when Λ is small. The proximity between the driving disk, which generates the primary flow and the free surface with its specific boundary conditions, leads to the complex flow dynamics earlier explained. Conversely, for large values of Λ the important distance between the spinning disk and the free surface is so important that it significantly reduces the effect of the presence of the free surface. The flow pattern presents *in fine* a structure very similar to the flow pattern observed in the closed cylinder swirling flow presented in Appendix B, except very close to the free surface. As mentioned earlier the recirculation bubble itself is fairly small and located on the cylinder axis likewise in the closed cylinder case. Finally, it is worth adding that the region of solid-body rotation is almost completely eliminated. Even the closest-to-the-axis vortex lines present some bending.

As a brief conclusion of the previous study of the steady and laminar free surface swirling flows, it appears that the choice $\Lambda = 1$ for the height-to-radius aspect ratio of the cavity in presence of a free surface, ensures us to deal with a complex flow dynamics. Different mechanisms are in competition in different regions of the cavity, and in the end make the cases with $\Lambda = 1$ physically more challenging and more interesting. This conclusion—valid in presence of a free surface—stops being valid for the closed cylinder swirling flow, and thereby explains the focus in the literature on cases with $\Lambda \geq 2$.

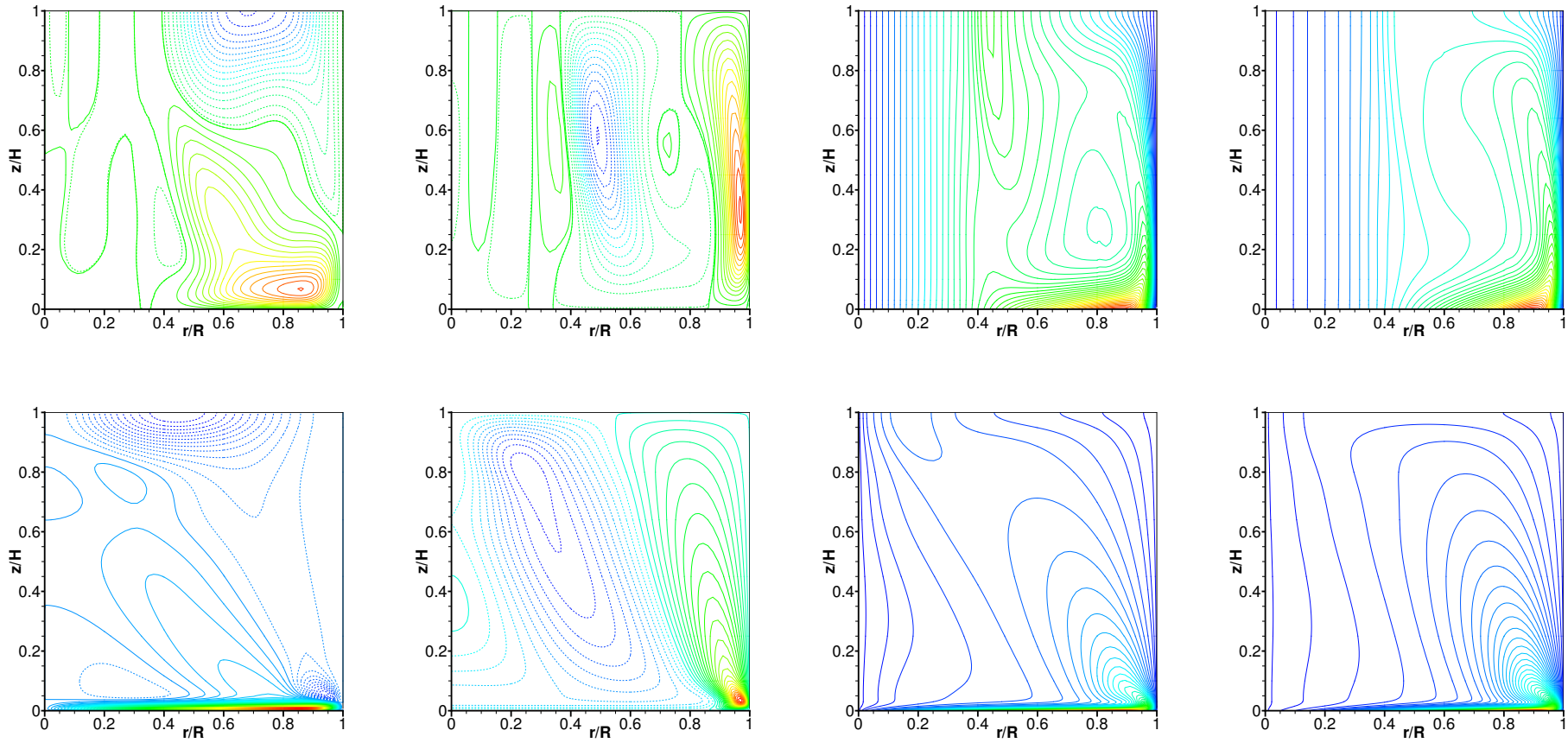


Fig. 7.17: Contours in a meridional plane for the case (d) : ($\Lambda = 1/3, \text{Re} = 2000$) (top row) and case (e) : ($\Lambda = 3, \text{Re} = 2000$) (bottom row). From left column to right column: radial velocity component u_r ; axial velocity component $w = u_z$; azimuthal velocity component u_θ ; axial angular momentum component $\Gamma = ru_\theta$. All contours are uniformly spaced; 35 contours between -0.17 and 0.15 for u_r case (d); 90 contours between -0.03 and 0.15 for u_r case (e); 35 contours between -0.1 and 0.12 for u_z case (d); 35 contours between -0.05 and 0.12 for u_z case (e); 50 contours between 0 and 1 for u_θ and Γ , cases (d) and (e).

7.4.3.2 Unsteady flow

For sufficiently small Reynolds number and irrespective of Λ , the basic flow state is stable. As noted by Lopez *et al.* [164], when Re is increased, the basic flow state loses stability via a variety of Hopf bifurcations. It is worth noting that when Re tends to infinity, the stream surfaces and vortex surfaces—giving the streamlines and vortex lines by intersection with a meridional plane—must coincide. At this point, the presence of a flat free surface poses problem because of the constraint of having orthogonal streamlines and vortex lines on it. This apparent paradox is unraveled by simply letting the free surface move, which is done in next chapter. Nevertheless, we know from the experiments carried out by Spohn *et al.* [239,240], that even at a $Re = 6\,000$ the tangential flow is extremely intense compared to the normal one, leading to small free-surface deformations. It is very likely that these small amplitude deformations are not sufficient to solve our apparent paradox. At low Reynolds number, like those of cases (a), (b), (d), and (e), the viscosity acts on the velocity field to allow the latter condition of orthogonality to be fulfilled. But when the Reynolds number is increased, the action of viscosity and the limited deformation of the free surface are not sufficient to bring back the orthogonality of the two sets of lines. Therefore, the flow must either lose its axisymmetry or become unsteady in order to allow to drop the orthogonality condition. The experiments by Spohn *et al.* [240] suggest that the open swirling flow first go through the unsteady path.

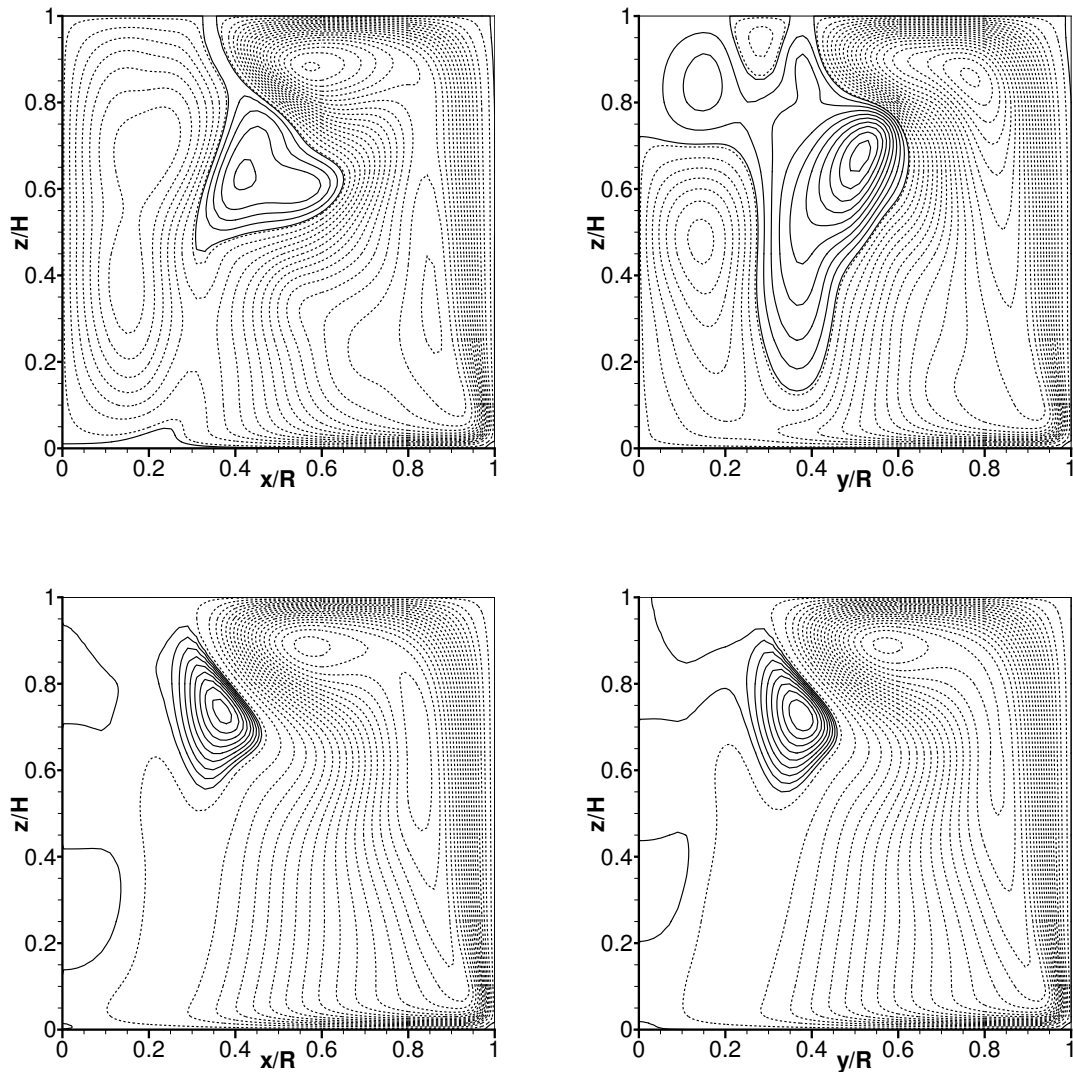


Fig. 7.18: Contours of streamlines in two orthogonal meridional planes, case $\Lambda = 1$ and $Re = 6\,000$. Top row: instantaneous flow; Bottom row: mean flow. Left column: meridional plane $y/R = 0$; Right column: meridional plane $x/R = 0$. The 30 contours are non-uniformly spaced for visualization purposes, 20 equally-spaced negative contours and 10 equally-spaced positive contours.

As discussed in detail in Sec. 7.1.3, the loss of axisymmetry of this flow has been a controversial subject among fluid dynamicists for a long time. When high angular velocities are considered, experiments like those of Jansson *et al.* [133] and Suzuki *et al.* [247] show concurrently large surface deformations and an undeniable loss of axisymmetry. Therefore, the feeling is that the loss of axisymmetry is related to free surface deformations. Thus, the problem is to know if the loss of axisymmetry can occur with a flat free surface.

In this section, the study is focused on the unsteady swirling flow corresponding to case (c) ($\Lambda = 1$, $\text{Re} = 6000$). To our knowledge, such transitional regime at this relatively high Re has never been investigated nor reported in the literature. At this Reynolds number the loss of axisymmetry in this flat-free-surface case is evident from the observation of the three-dimensional shape of the recirculation bubbles shown in Fig. 7.19. As the flow is unsteady, these recirculation bubbles are instantaneous and correspond to a flow sample taken in the statistically-steady regime for $t > 600$ in Ω_0^{-1} units, see Fig. 7.9.

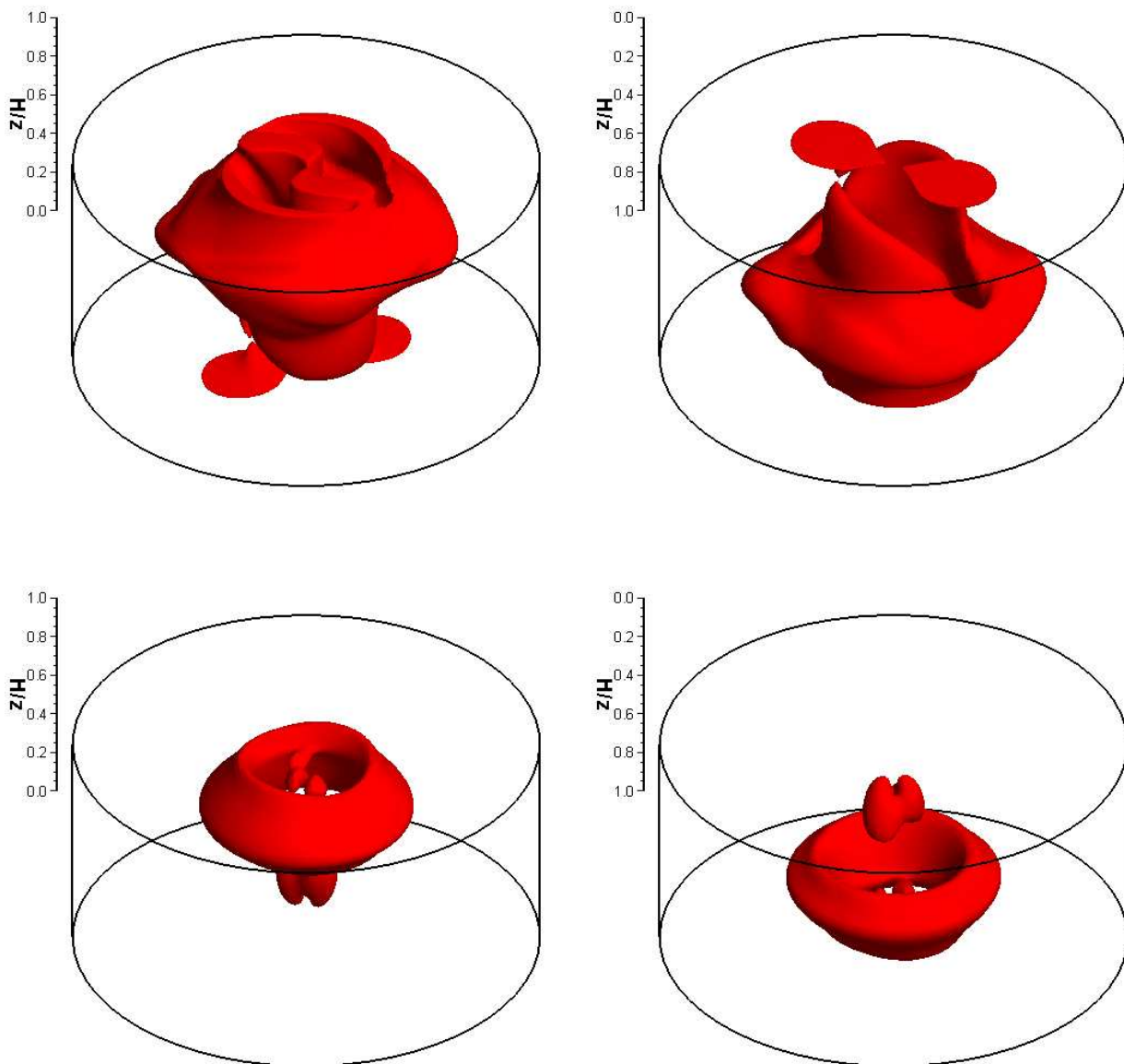


Fig. 7.19: Visualization of the shape of the recirculation bubble attached to the free surface. Case $\Lambda = 1$ and $\text{Re} = 6000$. Top row: instantaneous flow; Bottom row: mean flow; Left column: normal view; Right column: upside-down view.

The streamlines of this flow sample are represented in two orthogonal meridian planes corresponding to $y/R = 0$ and $x/R = 0$, in Fig. 7.18 (top row). Once again, the loss of axisymmetry appears clearly from the complex and nonaxisymmetric structure of the recirculation bubbles. Compared to the laminar and steady

cases (a) and (b), the recirculation bubbles have their own dynamics and evolution. In a common approach to such unsteady problems, this complex dynamics is analyzed by the means of an averaging process, which is supplemented with an analysis of instantaneous flow samples equally-spaced in time. The reader is referred to Chapter 4, Sec. 4.3.1 for details and notations used in the present averaging procedure. The mean flow is obtained by averaging 500 flow samples corresponding to successive flow states extracted every 0.25 times units (or equivalently every 100 iterations). Subsequently, the root-mean-square (rms) fluctuations of flow fields are calculated using the same extracted flow samples and the mean flow field obtained earlier.

The streamlines associated with the mean flow are shown in Fig. 7.18 (bottom row), as well as the recirculation bubbles in Fig. 7.19 (bottom row). The most surprising characteristic is that the mean flow itself appears to be slightly nonaxisymmetric. This point is still under investigation and we feel that this nonaxisymmetric feature of the mean flow is simply a side-effect of a limited sampling. We are currently investigating the effect of an increased sampling—averaging procedure using two times more samples—on the mean flow field. Besides this striking feature, the streamlines of the mean flow reveal the existence of a toroidal recirculation bubble, located off the cylinder axis and more surprisingly detached from the free surface. The toroidal shape and off-axis location of the mean recirculation bubble is in agreement with the increased-Re trend observed with cases (a) and (b) in Sec. 7.4.3.1. Regarding the detachment from the free surface of the mean bubble, it is more relevant here to notice that the instantaneous bubbles are still attached to the free surface. More precisely, one may notice two points:

- in the meridional plane $y/R = 0$, a small recirculation zone appears attached to the rotating disk for $r/R \simeq 0.2$;
- in the meridional plane $x/R = 0$, the recirculation bubble is stretched from the free surface $z/H = 1$ down to $z/H = 0.15$, in a radial position $r/R \simeq 0.4$.

These two observations remind the streamline patterns described in the case (d) ($\Lambda = 1/3, \text{Re} = 2000$), with a long bubble stretching from the free surface down to the driving disk. The previous analysis is further confirmed by the contours of the three velocity components and of the axial angular momentum for both an instantaneous flow sample and the mean flow, presented in Fig. 7.22, in the meridional plane $x/R = 0$. A careful analysis of the vortex lines for the instantaneous flow sample shows a bending in the whole meridian plane. This bending is very significant in the region $0.3 \leq r/R \leq 0.8$ and $0.4 \leq z/H \leq 1$, which corresponds to the limit between the primary recirculation of the flow and the secondary recirculation bubble. On the contrary, the vortex lines structure of the mean flow is as expected much more regular. The inner core region of the flow $r/R \leq 0.4$ displays a state of solid-body rotation. For both the instantaneous and mean flow, the jet-like shear layer along the tubular side-wall is turned into the interior of the flow by the free surface. Compared to the previous cases (a), (b), (d), (e), and also the closed swirling flow ($\Lambda = 1, \text{Re} = 6000$) of Appendix B, the structure of this shear layer at $\text{Re} = 6000$ reveals the presence of an intense radial jet of angular momentum at the free surface.

The fluctuations of the flow with respect to its mean state have been calculated with the same flow samples as before. It should be noted that the fluctuation level corresponds to less than 5% of the maximal intensity of the respective mean flow fields. Despite the relatively low level of fluctuation encountered, these fluctuations are very localized in space as can be seen in Fig. 7.23. Similarly to the mean flow fields, the rms fluctuations of the velocity field and of Γ appear to be slightly nonaxisymmetric. All the three velocity components present a noticeable level of fluctuation near the free surface for radii close to 0.4. In this region, the free-surface radial jet of angular momentum reaches the inner flow, which is solid-body rotation. These fluctuations are therefore located in the vicinity of the stagnation point where the vortex breakdown is initiated. The rms-fluctuations of the vortex lines, *i.e.* Γ , are the highest in the corner region between the free surface and the tubular side-wall. It is in this corner, where the shear layer is turned into the interior by the presence of the free surface.

The analysis of 24 equally-spaced in time flow samples—shown in Fig 7.20 and Fig. 7.21—delivers some fruitful information on the dynamics of the recirculation bubbles. The samples are extracted every 0.5 time units, which correspond to half a rotation of the bottom end-wall, and covers a dynamic range of length 12 time units comprised between $t_1 = 665.5$ and $t_{24} = 677.5$. The dynamics of the vortex breakdown bubbles are a succession of separation and coalescence. Even if the flow dynamics is not oscillatory, some sort of “cycle” is observed. A typical “cycle” starts from a bubble attached to the free surface near $r/R \simeq 0.4$. The bubble becomes more and more intense, is stretched down to approximately $z/H = 0.2$. Afterwards, the bubble keeps growing and tends to occupy the inner core region of the flow, until it becomes an on-axis attached bubble. Subsequently, this large bubble separates into one attached and off-axis bubble and another internal bubble, which tends to disappear. From the remaining off-axis bubble attached to the free surface, starts another cycle. Such cycle is clearly visible in Fig 7.20 and Fig. 7.21.

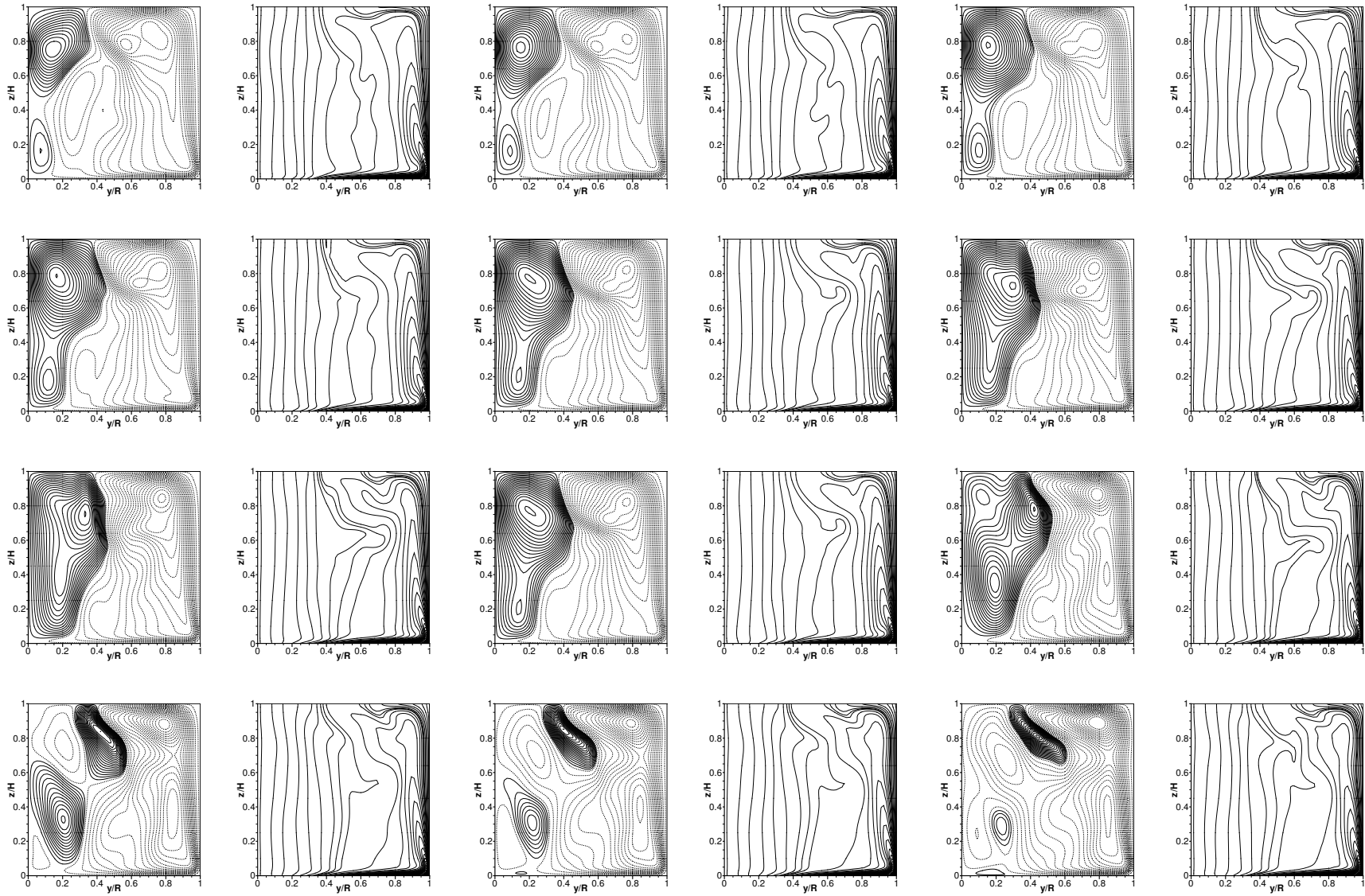


Fig. 7.20: Contours of streamlines and vortex lines in the meridional plane $x/R = 0$, case $\Lambda = 1$ and $Re = 6000$. Each pair of contours of streamlines and vortex lines refers to the same instant: from left to right, and from top to bottom the successive instants are given by $t_k = 665 + k0.5$, $k = 1, \dots, 12$.

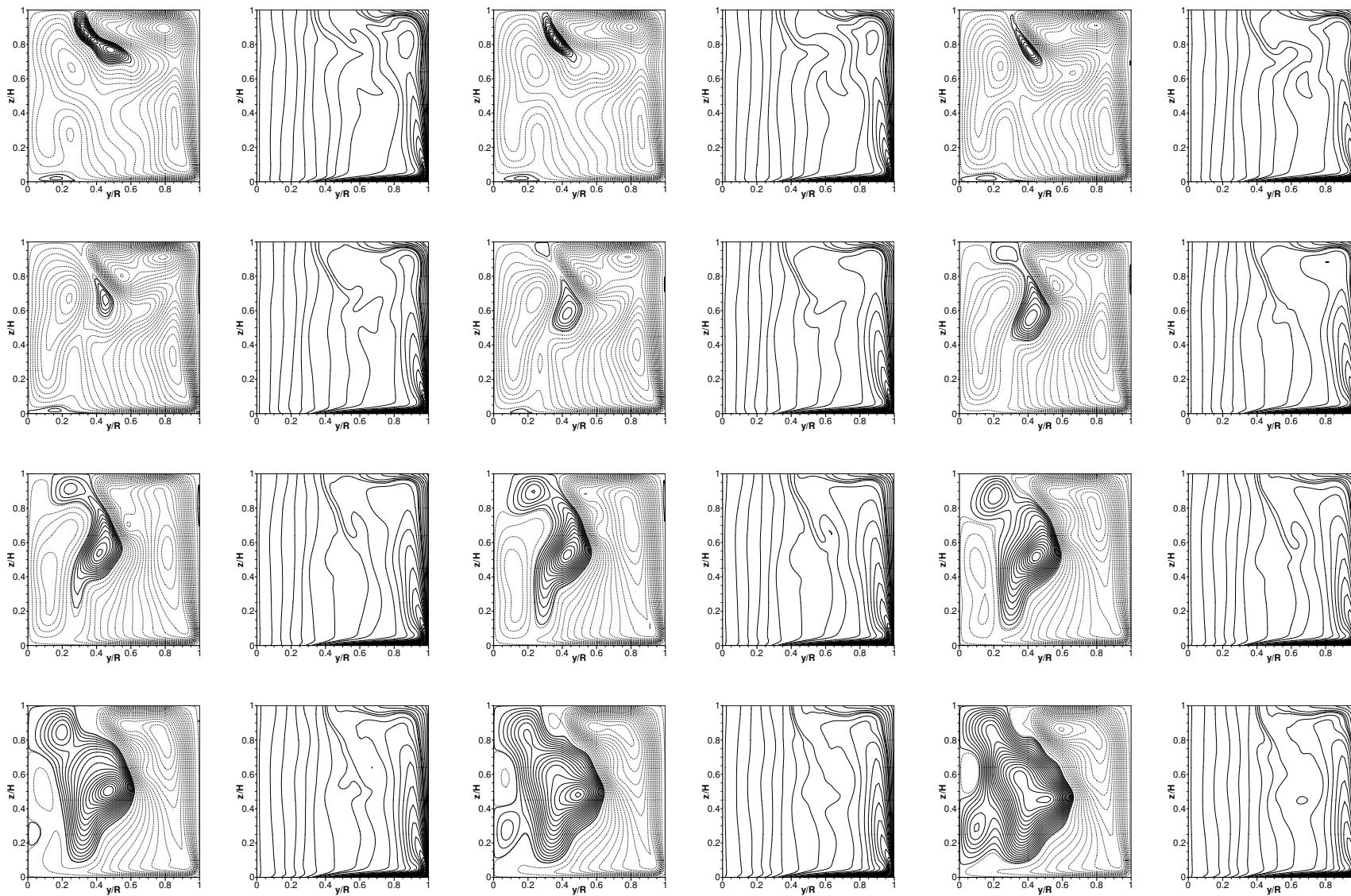


Fig. 7.21: Contours of streamlines and vortex lines in the meridional plane $x/R = 0$, case $\Lambda = 1$ and $\text{Re} = 6000$. Each pair of contours of streamlines and vortex lines refers to the same instant: from left to right, and from top to bottom the successive instants are given by $t_k = 665 + k0.5$, $k = 13, \dots, 24$.

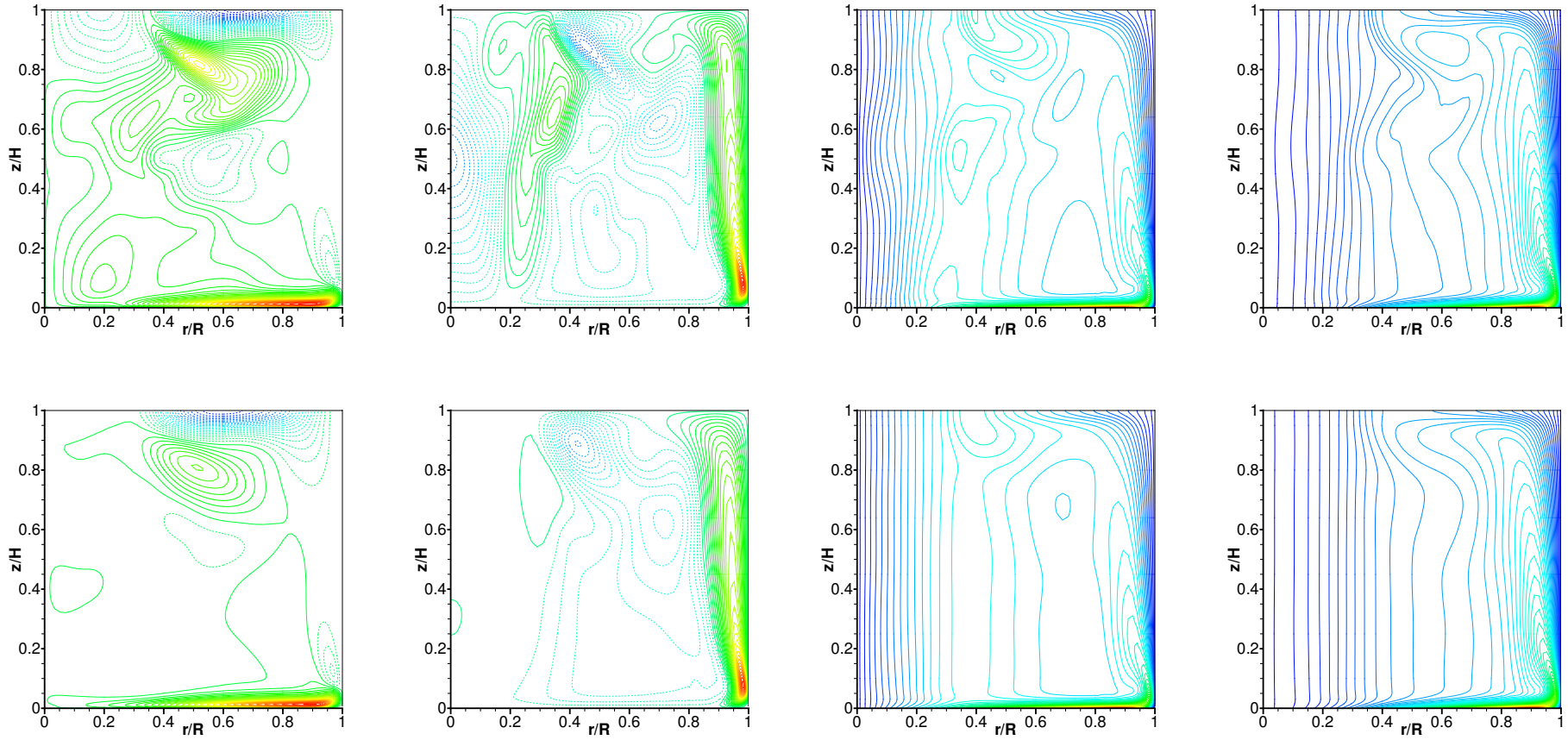


Fig. 7.22: Contours in a meridional plane for the case $\Lambda = 1$ and $\text{Re} = 6000$. Top row: instantaneous flow; Bottom row: mean flow. From left column to right column: radial velocity component u_r ; axial velocity component u_z ; azimuthal velocity component u_θ ; axial angular momentum $\Gamma = ru_\theta$. The 50 contours are uniformly spaced, between -0.13 and 0.16 for u_r ; between -0.09 and 0.14 for u_z ; and between 0 and 1 for u_θ . The 100 contours are uniformly spaced between 0 and 1 for Γ .

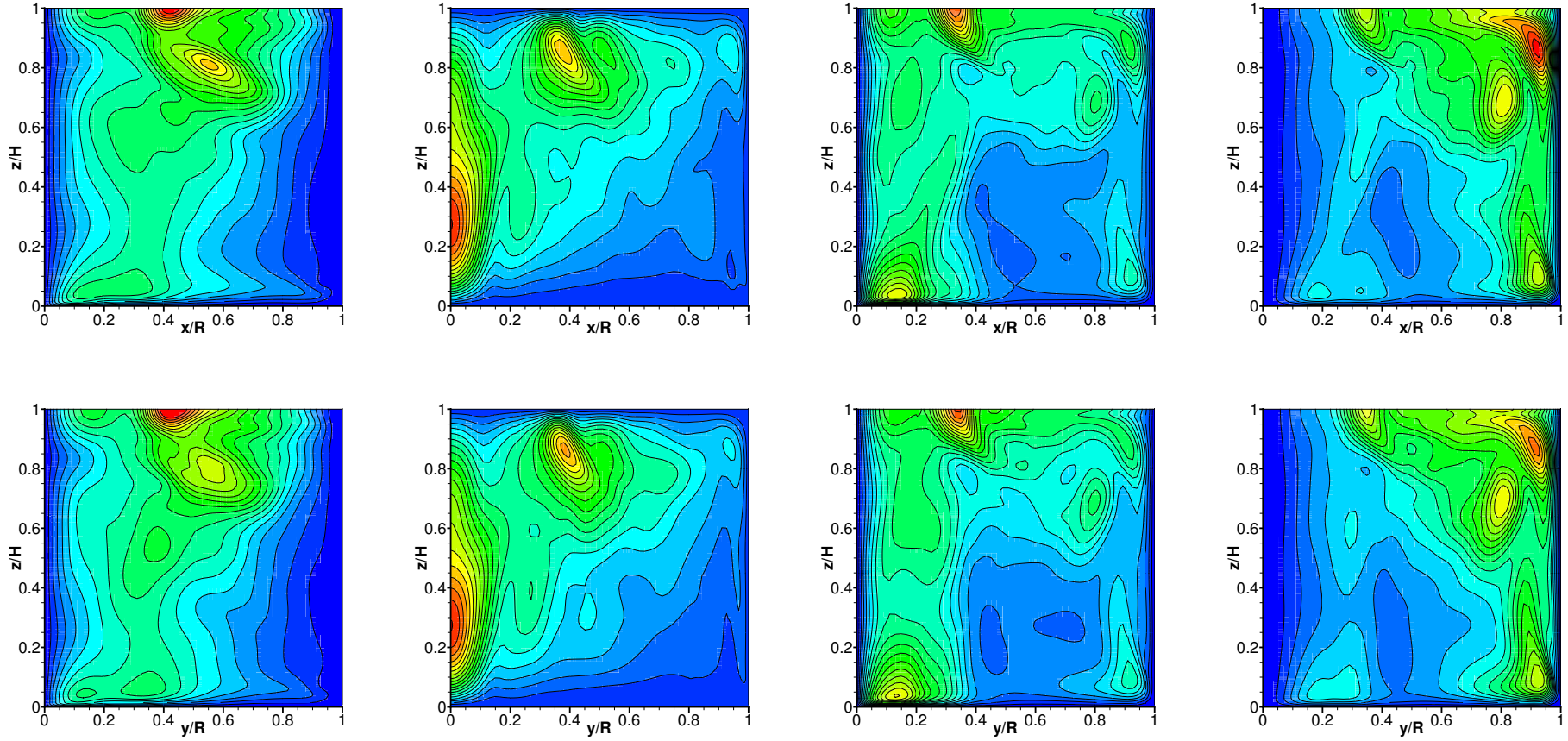


Fig. 7.23: Contours in a meridional plane for the case $\Lambda = 1$ and $\text{Re} = 6000$. Top row: in the meridional plane $y/R = 0$; Bottom row: in the meridional plane $x/R = 0$. From left column to right column: rms fluctuations of radial velocity component u_r ; rms fluctuations of the axial velocity component u_z ; rms fluctuations of the azimuthal velocity component u_θ ; and rms fluctuations of the axial angular momentum $\Gamma = ru_\theta$. The 20 contours are uniformly spaced, between 0 and 0.002 for $\text{rms-}u_r$; between 0 and 0.0024 for $\text{rms-}u_z$; between 0 and 0.004 for $\text{rms-}u_\theta$; and between 0 and 0.001 for $\text{rms-}\Gamma$.

7.4.4 One-dimensional momentum budgets

This section is devoted to the careful analysis of the momentum balance for the radial, azimuthal and axial components. This study is performed along different radial and axial lines within the cavity. It is of interest to determine the predominant physical terms, which are responsible for the complex flow dynamics depicted in the previous sections. As noticed in these previous sections, the structure of the flow in the inner core region is far different from the one close to the tubular side-wall. Similarly, the flow above the rotating driving disk has properties, which are not comparable to the ones below the flat free surface. For the sake of conciseness, this momentum balance analysis is limited to cases (a) – (c) for which $\Lambda = 1$.

7.4.4.1 General considerations

The numerical integration of the Navier–Stokes equations using the spectral element method as described in Sec. 7.3, is performed in Cartesian coordinates (x, y, z) for the velocity components (u, v, w) . Nevertheless, the axisymmetric nature of the container and of the boundary conditions imposed to the flow suggests the use of cylindrical coordinates. Indeed, the different physical terms involved in the momentum equation represented here by the Navier–Stokes equations—nonlinear advective term, viscous strain, pressure gradient, etc.—are better apprehended when expressed in cylindrical coordinates. Accordingly, all vectors and physical terms are recast as functions of (r, θ, z) , and for instance the velocity components are (u_r, u_θ, u_z) .

The complete expression of the momentum equations in cylindrical coordinates reads

$$\frac{\partial u_r}{\partial t} + u_r \frac{\partial u_r}{\partial r} + \frac{u_\theta}{r} \frac{\partial u_r}{\partial \theta} - \frac{u_\theta^2}{r} + u_z \frac{\partial u_r}{\partial z} = -\frac{\partial p}{\partial r} + \frac{1}{\text{Re}} \left[\frac{\partial}{\partial r} \left(\frac{1}{r} \frac{\partial (ru_r)}{\partial r} \right) + \frac{1}{r^2} \frac{\partial^2 u_r}{\partial \theta^2} - \frac{2}{r^2} \frac{\partial u_\theta}{\partial \theta} + \frac{\partial^2 u_r}{\partial z^2} \right], \quad (7.25)$$

$$\frac{\partial u_\theta}{\partial t} + u_r \frac{\partial u_\theta}{\partial r} + \frac{u_\theta}{r} \frac{\partial u_\theta}{\partial \theta} + \frac{u_r u_\theta}{r} + u_z \frac{\partial u_\theta}{\partial z} = -\frac{1}{r} \frac{\partial p}{\partial \theta} + \frac{1}{\text{Re}} \left[\frac{\partial}{\partial r} \left(\frac{1}{r} \frac{\partial (ru_\theta)}{\partial r} \right) + \frac{1}{r^2} \frac{\partial^2 u_\theta}{\partial \theta^2} + \frac{2}{r^2} \frac{\partial u_r}{\partial \theta} + \frac{\partial^2 u_\theta}{\partial z^2} \right], \quad (7.26)$$

$$\frac{\partial u_z}{\partial t} + u_r \frac{\partial u_z}{\partial r} + \frac{u_\theta}{r} \frac{\partial u_z}{\partial \theta} + u_z \frac{\partial u_z}{\partial z} = -\frac{\partial p}{\partial z} + \frac{1}{\text{Re}} \left[\frac{1}{r} \frac{\partial}{\partial r} \left(r \frac{\partial u_z}{\partial r} \right) + \frac{1}{r^2} \frac{\partial^2 u_z}{\partial \theta^2} + \frac{\partial^2 u_z}{\partial z^2} \right], \quad (7.27)$$

where successively appears, the velocity time derivative, the nonlinear advective term, the pressure gradient and the viscous strain. The central objective of this study is to compare the relative importance of some of these terms along different lines. Equation (7.25) (resp. (7.26)) represents the momentum balance in the radial (resp. azimuthal) direction, and is analyzed along four radial lines at four different heights $z/H = 0.03, 0.64, 0.95, 1$, ranging from right above the rotating disk up to the free surface. Equation (7.27) represents the momentum balance in the axial direction, and is analyzed along three different axial vertical lines at three radial positions $r/R = 0.08, 0.48, 0.98$, ranging from near the cylinder axis to near the tubular side-wall.

For the sake of simplicity, some of the terms appearing in (7.25)–(7.27) are identified and denoted specifically in Table 7.5. In the sequel, the various graphs reporting the variations of these terms will use this nomenclature.

| Name | Expression | Name | Expression | Name | Expression |
|------|--|------|---|------|---|
| NLr1 | $-u_r \frac{\partial u_r}{\partial r}$ | NLt1 | $-u_r \frac{\partial u_\theta}{\partial r}$ | NLa1 | $-u_r \frac{\partial u_z}{\partial r}$ |
| NLr2 | $+\frac{u_\theta^2}{r}$ | NLt2 | $-\frac{u_r u_\theta}{r}$ | NLa2 | $-u_z \frac{\partial u_z}{\partial z}$ |
| NLr3 | $-u_z \frac{\partial u_r}{\partial z}$ | NLt3 | $-u_z \frac{\partial u_\theta}{\partial z}$ | PGa | $-\frac{\partial p}{\partial z}$ |
| PGr | $-\frac{\partial p}{\partial r}$ | VSt1 | $\frac{1}{\text{Re}} \left[\frac{\partial}{\partial r} \left(\frac{1}{r} \frac{\partial (ru_\theta)}{\partial r} \right) \right]$ | VSa1 | $\frac{1}{\text{Re}} \left[\frac{1}{r} \frac{\partial}{\partial r} \left(r \frac{\partial u_z}{\partial r} \right) \right]$ |
| VSr | $\frac{1}{\text{Re}} \left[\frac{\partial}{\partial r} \left(\frac{1}{r} \frac{\partial (ru_r)}{\partial r} \right) + \frac{\partial^2 u_r}{\partial z^2} \right]$ | VSt2 | $\frac{1}{\text{Re}} \left(\frac{\partial^2 u_\theta}{\partial z^2} \right)$ | VSa2 | $\frac{1}{\text{Re}} \left(\frac{\partial^2 u_z}{\partial z^2} \right)$ |

Table 7.5: Name definitions of different terms appearing in the momentum budget equations (7.25)–(7.27).

7.4.4.2 Steady flows

As discussed in Sec. 7.4.3.1, the steady swirling flows are also fully axisymmetric. The first-order time derivative of the velocity fields is identically zero in Eqs. (7.25)–(7.27). The axisymmetric property makes the velocity field independent of the azimuthal angle θ , and consequently all partial derivatives with respect to this variable vanish. Therefore, the balance in the momentum equation solely involves the terms described in Table 7.5.

As a first step, the momentum balance in the radial direction is presented in Fig. 7.24 for case (a) (left column) and case (b) (right column). At the free surface $z/H = 1$ (top row), the viscous terms are insignificant, and the flow is driven by the radial pressure deceleration, which is mainly counterbalanced by the centrifugal acceleration $NLr2 = u_\theta^2/r$ and to a certain extent by $NLr1$. This analysis at the free surface still holds below the free surface at $z/H = 0.94$ and at $z/H = 0.64$. At this latter height, both the radial pressure deceleration and the centrifugal acceleration $NLr2$ have a lower magnitude than at the free surface but their magnitude is less localized than at the free surface. As expected, above the disk, at $z/H = 0.03$, all the terms have a higher magnitude and the momentum balance is more complex as only one single term $NLr3$ does not really contribute to the balance. The centrifugal acceleration $NLr2$ keeps its predominant position, but its maximum is now shifted towards the outer radial region, which corresponds to the region of highest angular momentum $0.8 \leq r/R \leq 1$. The other acceleration term $NLr1$ becomes relatively important. Both of these acceleration terms are counterbalanced by the radial pressure gradient and now also by the viscous strain. The importance of the viscous strain at this height $z/H = 0.03$ can easily be understood, as we are located in the viscous layer generated by the motion of the disk. One may add that in the inner core region of the flow, say $r/R < 0.15$, the linear trend observed for both the centrifugal acceleration and the pressure deceleration are well-known features of a flow in solid-body rotation, as observed with the vertical vortex lines in Fig. 7.14 (extreme right column).

The evolution of those momentum balances along radial lines at different heights does not really change when increasing Re from 900 up to 1500. But some noticeable trends are observable. For instance, even if the viscous strain does not play a central role at the free surface, it is worth noting that its effect is increased with Re , while conversely it is decreased when getting closer to the rotating bottom end-wall.

As a second step, we aim at analyzing the momentum balance in the azimuthal direction along radial lines at the same different heights as before. The results are presented in Fig. 7.25 for case (a) (left column) and case (b) (right column). It is important to note at this point that the two terms $NLt1$ and $VSt1$ involve partial derivatives with respect to the radial variable r . Given the fact that our solution is continuous and first-order differentiable within a spectral element and only continuous at the element edges, one expects some slight unphysical deformations of the plots associated with these two terms. Along the radial lines of interest, the spectral element edges are located at $r/R = 0.2, 0.4, 0.6, 0.8, 0.97$. As a consequence, some rapid variations of the terms $VSt1$ and $NLt1$ are going to be simply disregarded in the coming discussions.

A rapid glance at all the plots in Fig. 7.25 allows to conclude that the importance of the azimuthal momentum transfers resides in the near bottom end-wall region. The magnitude of all terms is over ten times smaller at $z/H = 0.64, 0.95, 1$, compared to $z/H = 0.03$. Given the solid-body rotation in the inner core region of the flow $r/R < 0.15$, most of the terms are vanishing small—excluding the unphysical values of $VSt1$.

At $z/H = 0.03$, one can notice the vigorous action of the viscous strain term $VSt2$ which literally drives the fluid in the viscous Ekman layer. This driving viscous term is being compensated by the convective terms $NLt1$ and $NLt3$, and by the Coriolis term $NLt2$. As one gets closer to corner between the rotating disk and the tubular side-wall, say $r/R \geq 0.8$, the interplay between the various terms is being reversed. The term $VSt2$, which is driving the fluid in the inner region of the cavity is now a dissipative term in the jet-like shear layer. Conversely, the convective term $NLt1$ becomes large and is driving the fluid in the shear layer. Very close to the tubular side-wall, this term starts being counterbalanced by the second viscous term $VSt1$.

The viscous driving effect of the term $VSt2$ becomes insignificant at $z/H = 0.64$, but when z/H is increased, $VSt2$ starts growing again to reach a local maximum value at the free surface, but with a magnitude slightly smaller than the two other nonlinear convective terms $NLt1$ and $NLt2$. Close to the free surface and at the free surface, the flow is primarily driven by the Coriolis term $NLt2$ together with the viscous term $VSt2$. Their global action is counterbalanced the nonlinear convective term $NLt1$. This momentum balance at the free surface in the outer region $r/R \geq 0.4$ reflects the central effect of the free-surface jet of angular momentum. Again the viscous effects are more intense at the free surface when Re is increased from 900 to 1500, despite the presence of the kinematic viscosity term $1/Re$ in their definitions.

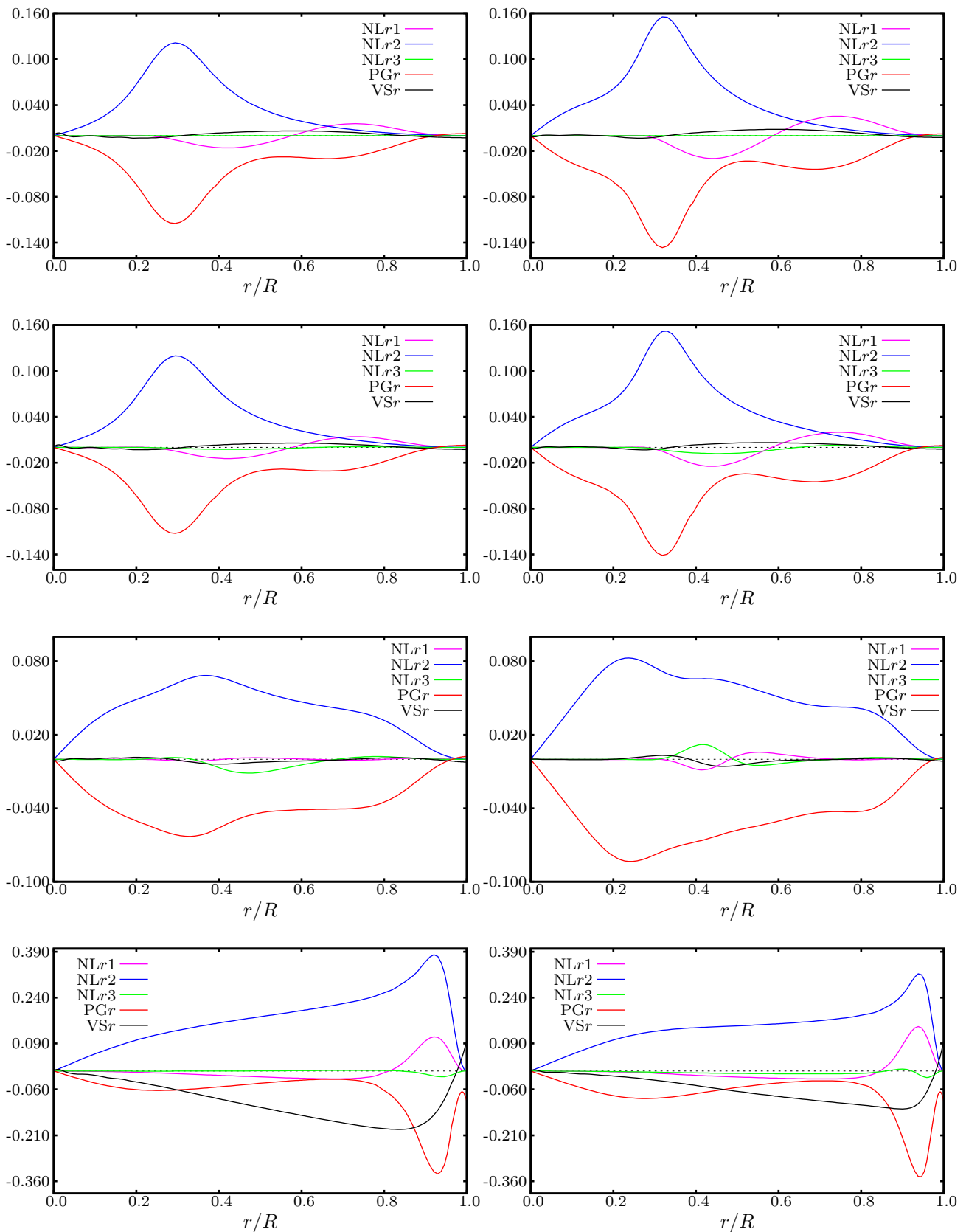


Fig. 7.24: Momentum balance in radial direction plotted along horizontal radial lines at four different vertical positions. First row: $z/H = 1$; second row: $z/H = 0.95$; third row: $z/H = 0.64$; fourth row: $z/H = 0.03$. Left column: case $Re = 900$; Right column: case $Re = 1500$. Case $\Lambda = 1$. The terminology refers to Tab. 7.5.

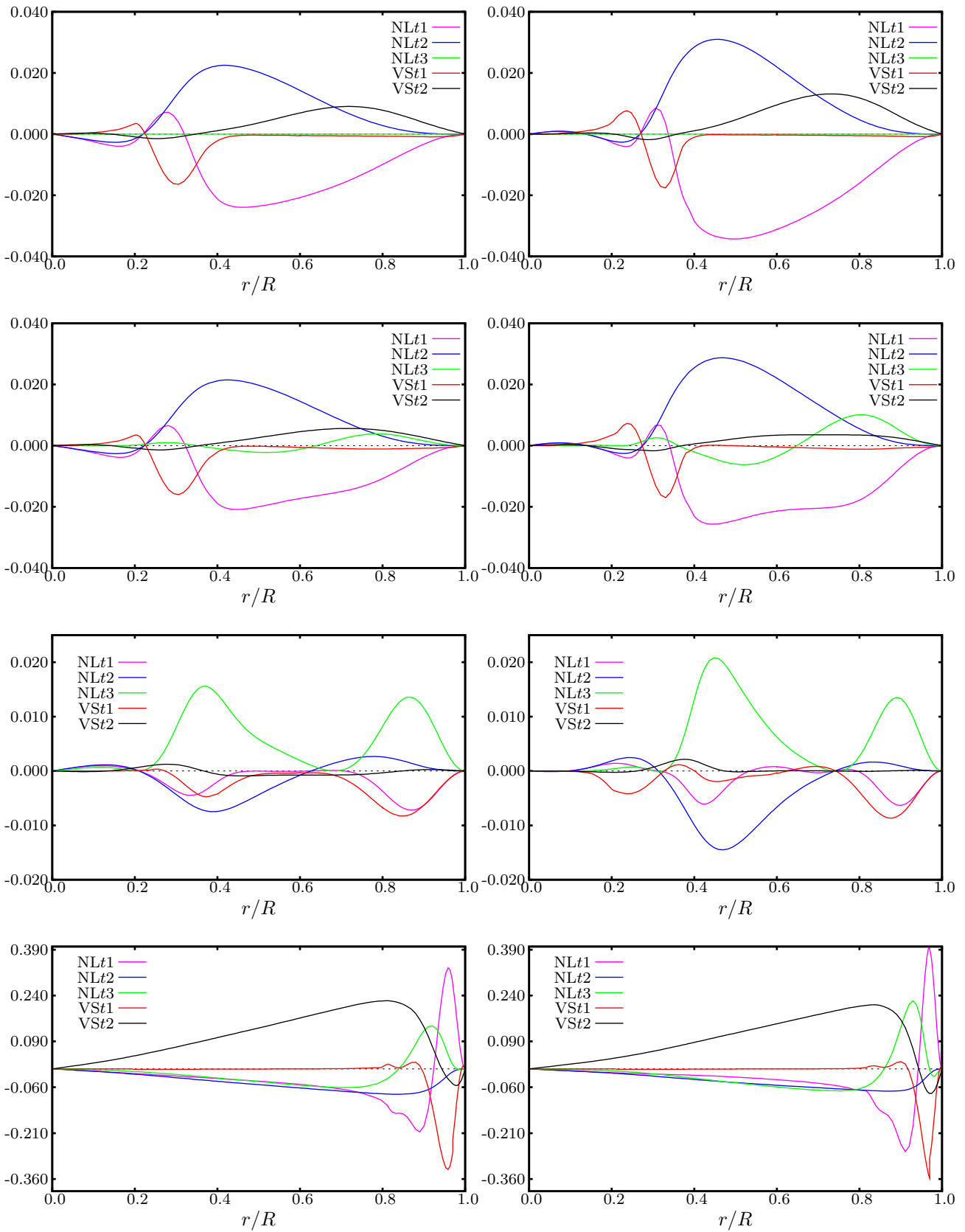


Fig. 7.25: Momentum balance in azimuthal direction plotted along horizontal radial lines at four different vertical positions. First row: $z/H = 1$; second row: $z/H = 0.95$; third row: $z/H = 0.64$; fourth row: $z/H = 0.03$. Left column: case $Re = 900$; Right column: case $Re = 1500$. Case $\Lambda = 1$. The terminology refers to Tab. 7.5.

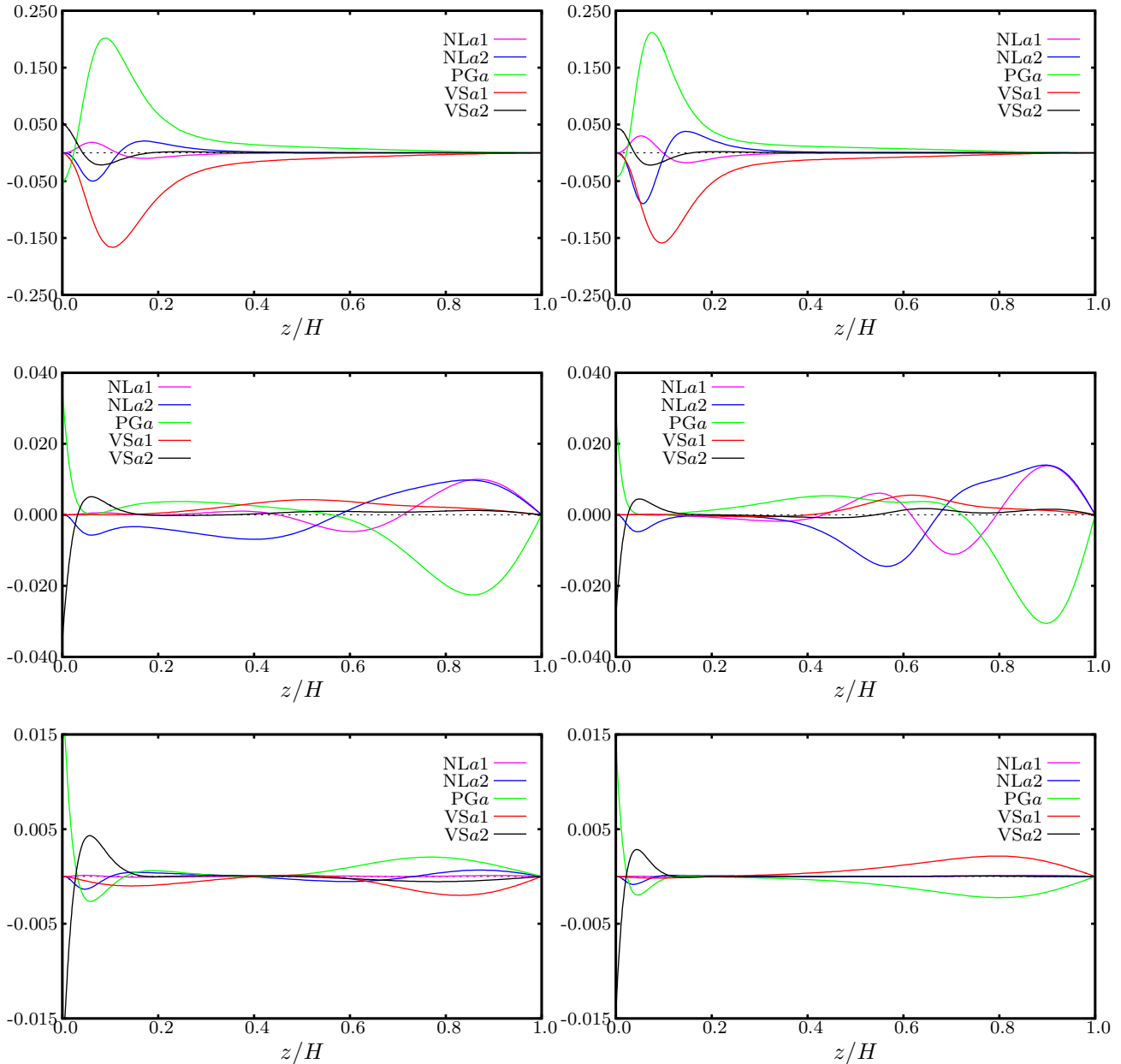


Fig. 7.26: Momentum balance in axial direction plotted along vertical lines at three different radial positions. First row: $r/R = 0.98$; second row: $r/R = 0.48$; third row: $r/R = 0.08$. Left column: case $Re = 900$; Right column: case $Re = 1500$. Case $\Lambda = 1$. The terminology refers to Tab. 7.5.

As a last step for these two steady flows (a) and (b), we investigate the momentum transfer in the axial direction, but now along three different vertical lines corresponding to three different radii $r/R = 0.08, 0.48, 0.98$. The graphs for the five different terms involved are reported in Fig. 7.26. We start from the top row, which is associated with the results for $r/R = 0.98$ in the jet-like shear layer and which present the highest magnitudes of all radii considered. The lack of axial momentum transfers is clearly visible in the region $z/H \geq 0.4$ and even inexistent at the free surface. Conversely, in the corner between the rotating bottom end-wall and the tubular side-wall the flow is driven by the axial pressure gradient, and to some extent by the two nonlinear terms $NLa1$ and $NLa2$ independently. The viscous term $VSa1$ is primarily responsible for counterbalancing the driving pressure effects. The second viscous term $VSa2$ has a less important effect in terms of magnitude but is driving very close to the disk (viscous Ekman layer), when z/H is increased it becomes dissipative as we are out of the Ekman layer but within the wall-jet shear layer.

Near the medium radial position $r/R = 0.48$, the axial momentum transfers near the free surface show the relative importance of the two nonlinear terms $NLa1$ and $NLa2$, which are driving the fluid against the axial pressure gradient, which is negative as a consequence of the kinematic boundary condition imposing a vanishing axial velocity component at the free surface.

Near the cylinder axis, for $r/R = 0.08$, the axial momentum transfers are limited and relatively simples. Nonlinear convective effects seem almost insignificant and the axial component of the flow is obtained from the balance between the axial pressure gradient and the two viscous terms: $VSa2$ in the bottom of the cavity and $VSa1$ in the top of the cavity.

7.4.4.3 Unsteady flow

The momentum balance analysis developed in the previous section for the two steady flows (*a*) and (*b*) cannot be directly transposed to the unsteady case (*c*). The two reasons for that are first the unsteady character requiring to account for the first-order time derivative $\partial\mathbf{u}/\partial t$. The second reason is the loss of axisymmetry of case (*c*) imposing to account for all the terms involving a partial derivative with respect to θ in Eqs. (7.25)–(7.27). One can overcome the issue associated with $\partial\mathbf{u}/\partial t$ by performing the analysis on the mean flow, which is obtained from the statistically steady regime. On the other hand, the momentum equations for the mean flow involve the Reynolds stress terms, expressing the influence of the fluctuating velocity field onto the dynamics of the mean field. Despite all these considerations and issues, we have deliberately omitted the terms involving derivatives with respect to the time and to the azimuthal coordinate, and we have calculated the values of the terms in Table 7.5 on the same lines as in Sec. 7.4.4.2. By doing so, the objective is not to reproduce a similar analysis as with the steady cases, but more to investigate the evolution of the different terms for the instantaneous flow and the mean flow as compared to the laminar cases (*a*) and (*b*).

We compare the radial terms for the instantaneous and mean flows presented in Fig. 7.27, to their laminar and steady counterparts in Fig. 7.24. In terms of magnitude, the leading terms have a slightly higher magnitude at $Re = 6000$. The general observations given in Sec. 7.4.4.2 remain valid here for $z/H = 0.64, 0.95, 1$. However, the influence of the intense recirculation bubble modifies locally and significantly the terms in the region $0.2 \leq r/R \leq 0.4$, for the instantaneous flow. Indeed, in this interval around the radial position $r/R = 0.3$ and close to the free surface, the centrifugal acceleration $NLr2$ presents a local minimum, while the decelerating radial pressure gradient presents a local maximum. These localized effects are directly related to the presence of the recirculation bubble as can be seen in Fig. 7.18. A similar observation can be done for the mean flow but the effect is much less visible.

Close to the rotating disk, at $z/H = 0.03$, the variations of the five axial terms are notably different from their laminar counterparts, but extremely similar for the instantaneous and mean flows. More precisely, the viscous term VSr has mainly a dissipative action in the laminar regime, while it is slightly driving the flow at $Re = 6000$, except very close to the tubular side-wall where it gets back its dissipative action in the jet-like shear layer. Moreover, the two leading terms, namely the centrifugal acceleration $NLr2$ and the radial pressure gradient, both presents a local maximum in the region $0.2 \leq r/R \leq 0.3$, for the case (*c*), while it keeps growing in the laminar regime. This particular observation is again related to the presence of the recirculation bubbles in this region, which locally strongly modifies the momentum transfers. Finally, the third radial convective term $NLr3$, which is very small in the laminar regime, acquires a magnitude as important as the two other convective terms for $r/R \geq 0.9$.

Let us consider now the radial variations of the five azimuthal terms as shown in Fig. 7.28. A rapid overlook of all variations for the instantaneous flow sample (left column) allows to conclude to a general agreement with the results obtained in the laminar cases (*a*) and (*b*). The variations of the different terms are similar for the instantaneous and mean flows in the outer radial region, which implies again a relative steadiness of those terms for $r/R \geq 0.7$. On the other hand, the mean flow yields vanishingly small terms in the inner core region $r/R \leq 0.4$, where the instantaneous flow have the three nonlinear convective terms $NLt1$ – $NLt3$ with a relatively high magnitude. The unsteady activity of those three nonlinear terms and the intense fluctuating activity generated by them is further discussed in Sec. 7.4.5.

As a last step, we compare the axial terms for the instantaneous and mean flows presented in Fig. 7.29 to their laminar and steady counterparts in Fig. 7.26. We start from the outer radial line $r/R = 0.98$, where the results for the instantaneous flow and the mean flow are extremely close, revealing an almost steady behavior of the jet-like wall shear layer surrounding the tubular side-wall. The comparison of these results with those of cases (*a*) and (*b*) leads to several comments. First, the variations of all the terms are limited to a smaller zone above the disk at $Re = 6000$. The magnitude of the axial pressure gradient is increased with Re . More surprisingly the axial pressure gradient is no longer counterbalanced by the convective term $NLa1$, but is now counterbalanced by $NLa2$. By extension, one can infer that the jet-like shear layer is dominated by axial effects at high Reynolds number.

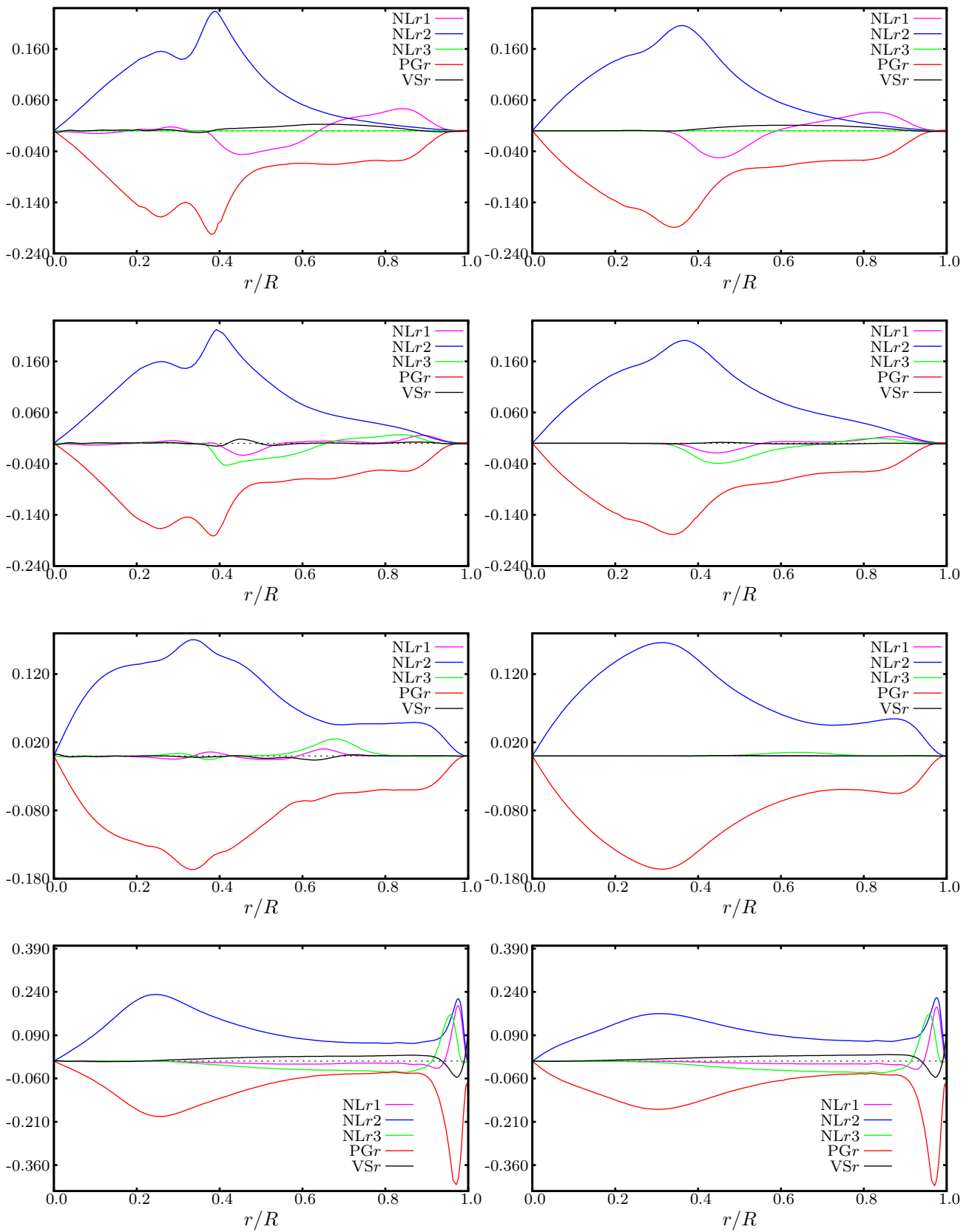


Fig. 7.27: Momentum balance in radial direction plotted along horizontal radial lines at four different vertical positions. First row: $z/H = 1$; second row: $z/H = 0.95$; third row: $z/H = 0.64$; fourth row: $z/H = 0.03$. Left column: instantaneous flow; Right column: mean flow. Case $\Lambda = 1$ and $Re = 6000$. The terminology refers to Tab. 7.5.

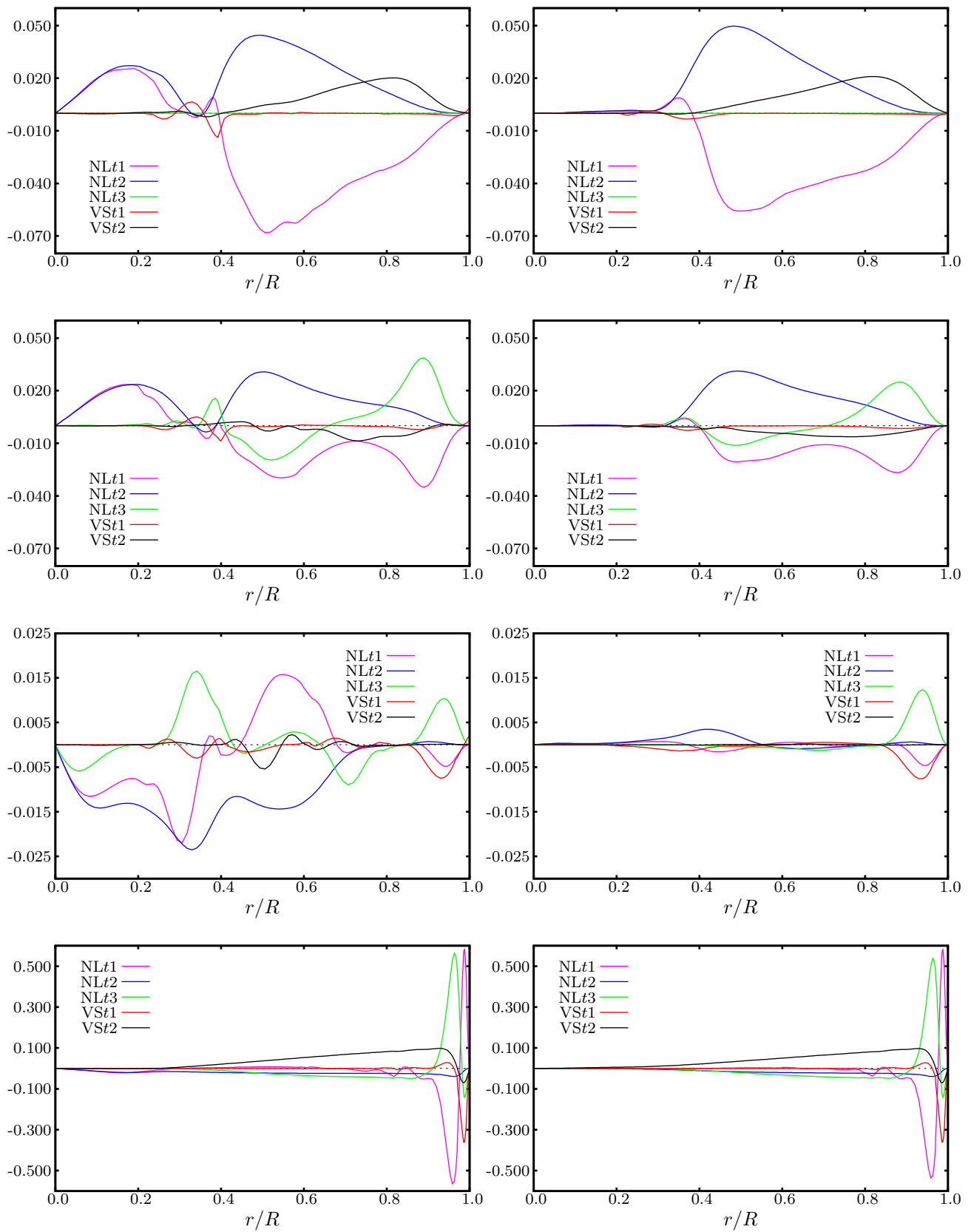


Fig. 7.28: Momentum balance in azimuthal direction plotted along horizontal radial lines at four different vertical positions. First row: $z/H = 1$; second row: $z/H = 0.95$; third row: $z/H = 0.64$; fourth row: $z/H = 0.03$. Left column: instantaneous flow; Right column: mean flow. Case $\Lambda = 1$ and $Re = 6000$. The terminology refers to Tab. 7.5.

For the two other radii $r/R = 0.08, 0.48$, the instantaneous flow terms are far different from their mean counterparts. As consequence, the flow in the inner core region appears much more unsteady than the flow in the outer region of the cavity. In addition, given the high level of fluctuation in the inner core region of the flow—see Fig. 7.23—it appears irrelevant to further analyze the results for the mean flow. On the other hand, variations of the different axial terms for the instantaneous flow reveals that the axial momentum transfers are more important at high Re and are predominant in the top half of the cavity, including below the free surface. The viscous terms are still insignificant and the two axial convective terms $NLa1$ and $NLa2$, and the axial pressure gradient dominate the transfers with other unsteady and nonaxisymmetric terms not shown here.

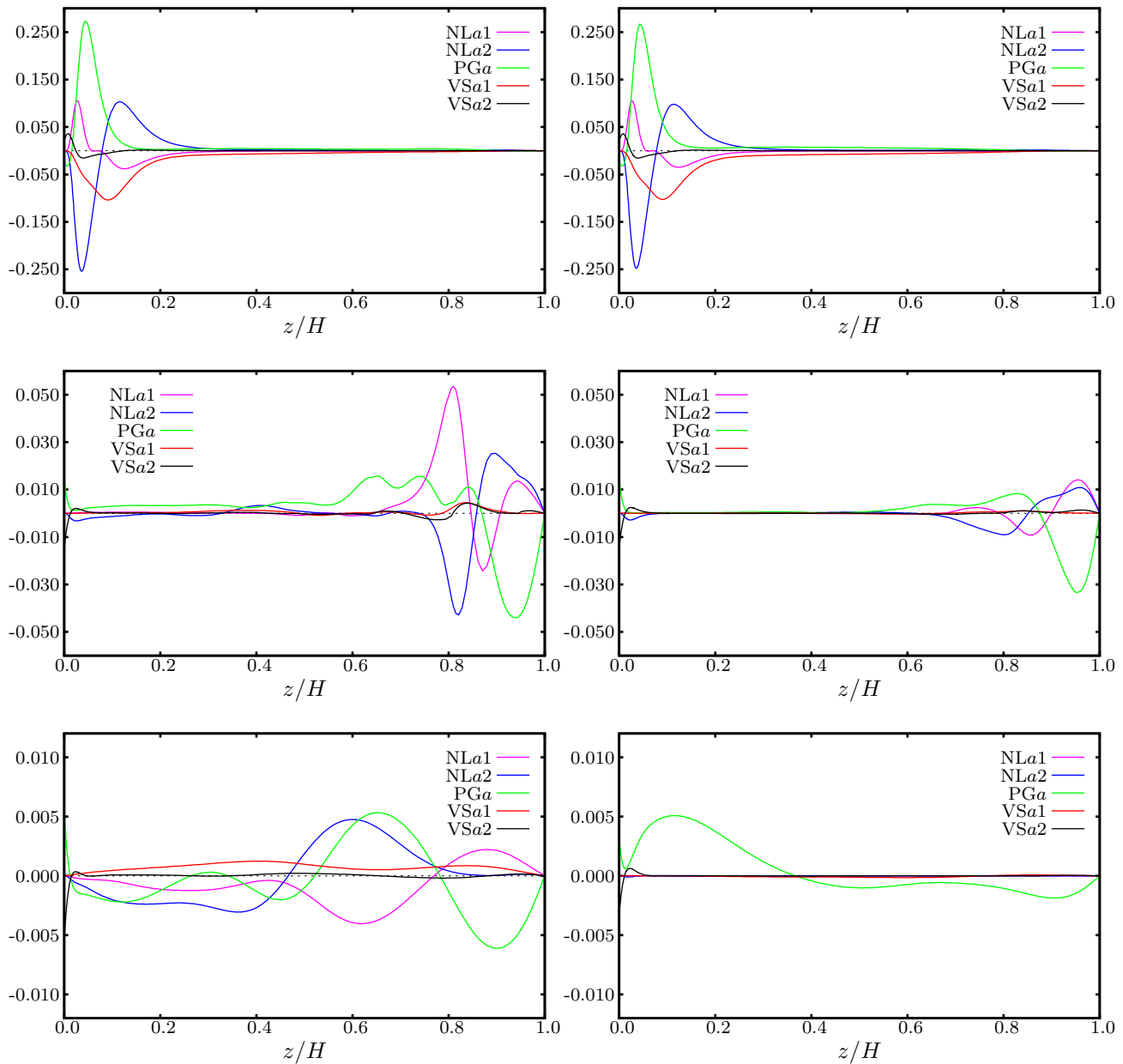


Fig. 7.29: Momentum balance in axial direction plotted along vertical lines at three different radial positions. First row: $r/R = 0.98$; second row: $r/R = 0.48$; third row: $r/R = 0.08$. Left column: instantaneous flow; Right column: mean flow. Case $\Lambda = 1$ and $Re = 6000$. The terminology refers to Tab. 7.5.

7.4.5 Nonaxisymmetric modes in the unsteady transitional flow

All the previous results dealing with the transitional case (c) reveals a complex flow dynamics due to instabilities developing from a steady stable flow similar to the steady laminar cases (a) and (b). The objective of this section is to discuss the physical origin of this instability based on the results presented earlier and also to characterize, at least qualitatively, its effect on the flow field.

As mentioned on several occasions in Sec. 7.4.3 and Sec. 7.4.4, the inner core region of the flow $r/R \leq 0.2$ is globally governed by a quasi-solid-body rotation and in the outer radial region, a wall-jet along the tubular side-wall drives the flow. As already discussed, this latter axial wall-jet is turned into a radial surface jet by the presence of the free surface. It seems therefore legitimate to consider the interfacial zone—denoted Υ in the sequel—between the inner core region and the radially-inward coming jet as prone to developing instabilities. Given the stress-free condition imposed on the free surface, the effect of the instabilities should persist all the way to the free surface itself. Consequently, we consider the variations at the free surface $z/H = 1$ of the radial and azimuthal velocity components—the axial component vanishes at the free surface because of the kinematic boundary condition on it—and of the axial angular momentum $\Gamma = ru_\theta$. These variations for the instantaneous flow are shown in Fig. 7.31 (top row), while the corresponding rms fluctuations are presented in the row below.

The most significant feature highlighted in these graphs is the presence of an annular region with $0.3 \leq r/R \leq 0.4$, where the fluctuations of u_r , u_θ and Γ are intense. Such intense fluctuating activity brings the interfacial zone Υ to light. Focusing now on the rms fluctuations of the axial angular momentum, one may notice the presence of a second outer annular region comprised in the interval $0.6 \leq r/R \leq 0.9$, which is nonaxisymmetric and relatively intense. This outer region of intense rms fluctuations for Γ correspond to the zone where the jet-like shear layer is turned into the interior by the free surface. This outer wall jet injects high-angular-momentum fluid towards the cylinder axis. This radial jet impinges on the cylindrical core of the fluid that is in solid-body rotation. When increasing the Reynolds number, the radius of the cylindrical core in solid-body rotation is reduced, while the intensity of the radial jet is increased. Above a given value of the Reynolds number, the action of the impingement of the radial jet on the inner core region starts developing unstable modes.

The origin of these unstable modes is to be found in the analysis of the momentum transfers performed in the previous section. Returning on the radial variations of the five azimuthal terms below the free surface at $z/H = 0.95$, Fig. 7.30 reproduces these variations for $Re = 900, 1\,500, 6\,000$ (instantaneous flow), $6\,000$ (mean flow) from top to bottom. All these results have been shown separately before and are now shown together to facilitate the discussion. The flow in the outer region $r/R > 0.5$ has a strong steady character given the fact that the variations for the mean flow are fairly close to those of the instantaneous flow. The Coriolis term $NLt2 = -u_r u_\theta / r$ keeps the same radially-outward decreasing trend. On the other hand, the two other nonlinear terms $NLt1$ and $NLt3$ develops opposed and equally-intense peaks around $r/R = 0.9$. These opposite peaks have an increasing intensity with the Reynolds number. In the interfacial zone Υ , all the terms involved present brutal variations and changes of behavior, which give another characterization of this interfacial zone Υ . In the inner core region $r/R \leq 0.4$, the flow possesses a strong unsteady character brought to light by the vanishingly small values of the various terms for the mean flow. Consequently, the unstable azimuthal modes are to be found into this inner cylindrical region. Indeed, one may notice that the convective term $NLt1 = -u_r \partial u_\theta / \partial r$ and the Coriolis term $NLt2 = -u_r u_\theta / r$ are negative and have a low magnitude in the laminar cases (a) and (b), but acquires large positive values at $Re = 6\,000$. Moreover, all the three other terms $NLt3$, $VSt1$ and $VSt2$ have very low magnitudes, and thus cannot counterbalance the azimuthal momentum injected by $NLt1$ and the Coriolis term $NLt2$. Only an unsteady and nonaxisymmetric flow can support such azimuthal momentum effects. The effect of these two destabilizing terms on the flow apparently leads to the formation of azimuthal rotating waves superimposed to the stable base flow. The variations at the free surface $z/H = 1$, of the radial and azimuthal velocity components, and of the axial angular momentum shown in Fig. 7.31 (top row), suggest the conjugate effect of several rotating waves. These rotating waves correspond to even azimuthal Fourier modes, mainly $n = 2$ and $n = 4$. A comprehensive azimuthal Fourier analysis is currently in progress in order to determine quantitatively two points: (1) the relative amplitude of the different present modes with respect to the fundamental mode; (2) the eventual parity (even) of the Fourier modes.

As a final step to the study of the nonaxisymmetric modes present in these unsteady transitional swirling flows, we offer to the reader three visualizations of given iso-surfaces for case (c) ($\Lambda = 1, Re = 6\,000$). These iso-surfaces are placed in Fig. 7.32 and represent on the left: one iso-surface of the radial velocity component (value 0.01), on the center: one iso-surface of the axial angular momentum (value 0.11) and on the right: one iso-surface of the axial velocity component (value -0.24). The effect of unstable modes are clearly visible on each of these three iso-surfaces.

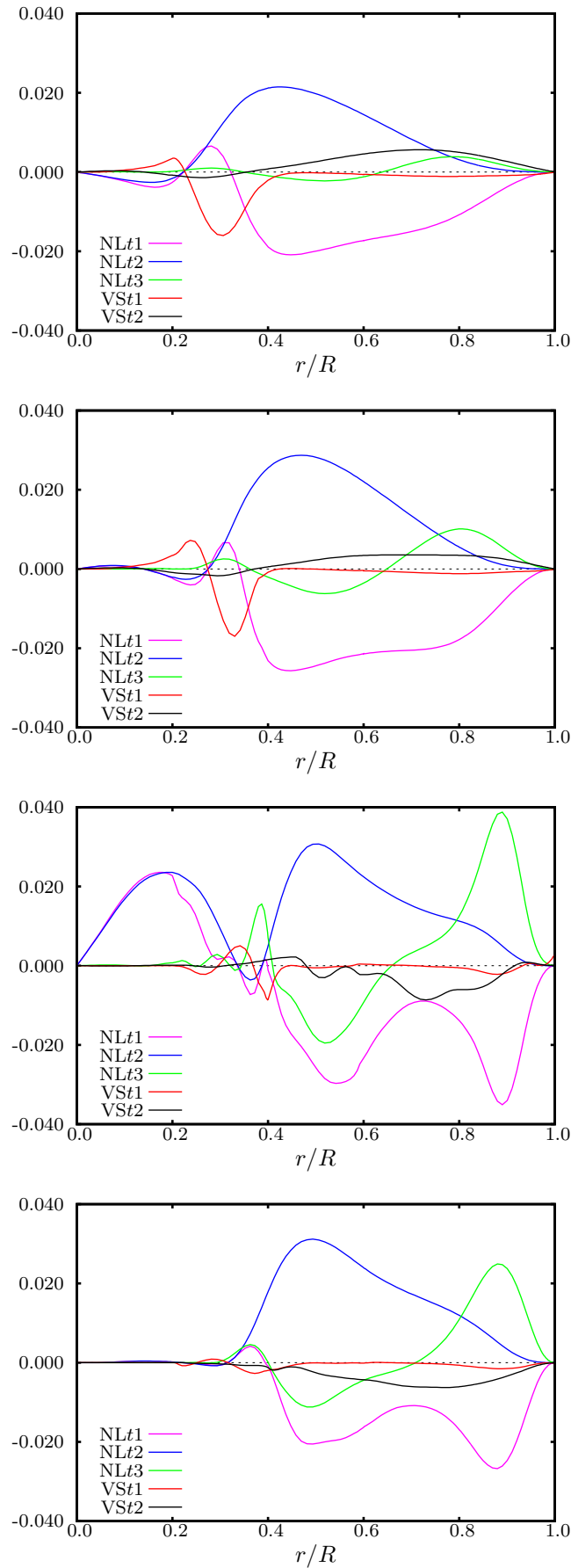


Fig. 7.30: Momentum terms in azimuthal direction plotted along the horizontal radial line at $z/H = 0.95$. From top to bottom: case (a); case (b); case (c) instantaneous; case (c) mean flow. The terminology refers to Tab. 7.5.

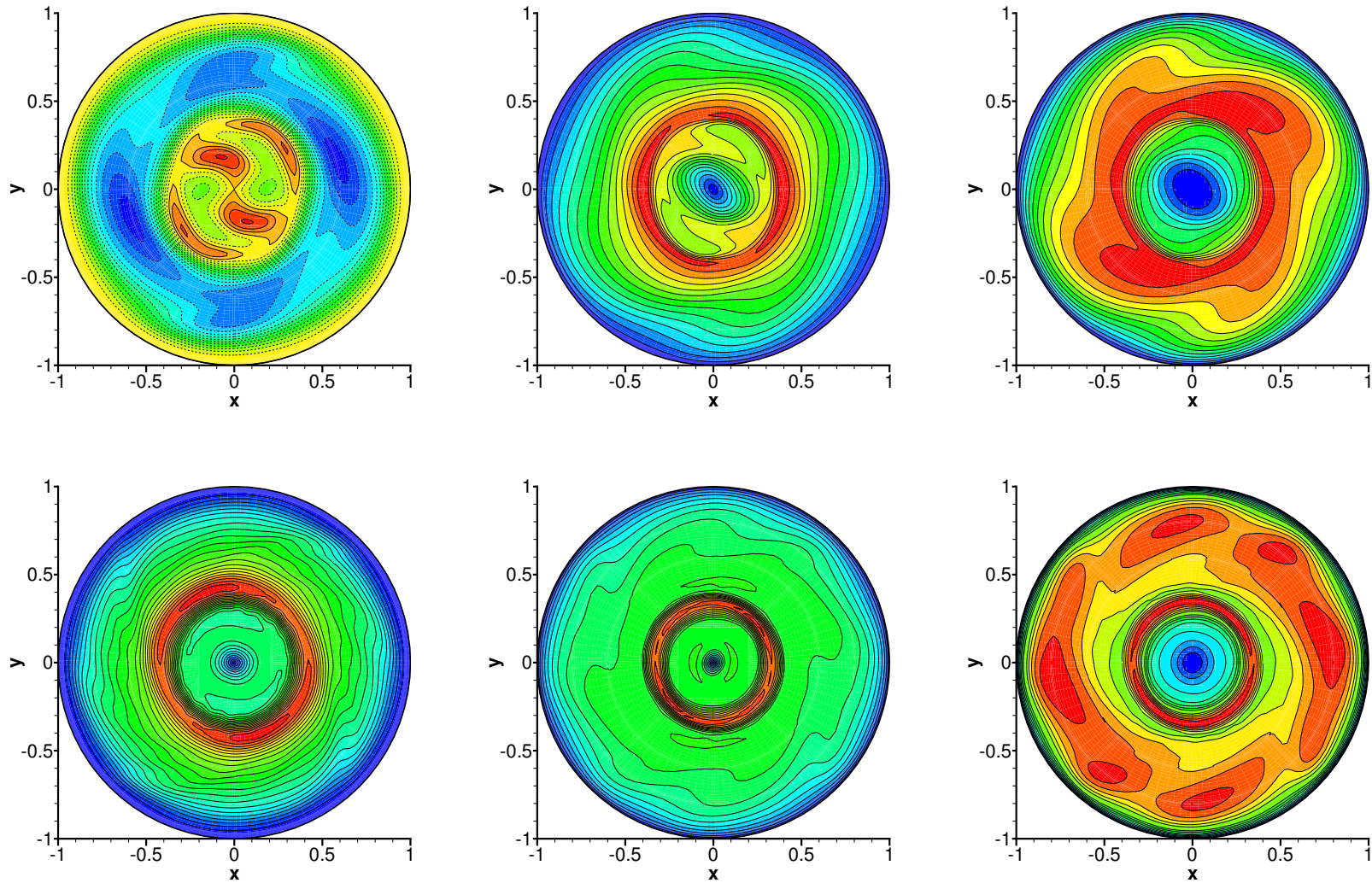


Fig. 7.31: Contours on the free surface $z/H = 1$ for the case $\Lambda = 1$ and $Re = 6000$. Top row: instantaneous flow; Bottom row: rms fluctuations. Left column: radial velocity component u_r ; Central column: azimuthal velocity component u_θ ; Right column: axial component of the angular momentum $\Gamma = ru_\theta$. The 15 contours are uniformly spaced, between -0.13 and 0.03 for u_r ; between 0 and 0.35 for u_θ ; and between 0 and 0.2 for Γ . The 20 contours are uniformly spaced, between 0 and 0.002 for $rms-u_r$; between 0 and 0.024 for $rms-u_\theta$; and between 0 and 0.001 for $rms-\Gamma$.

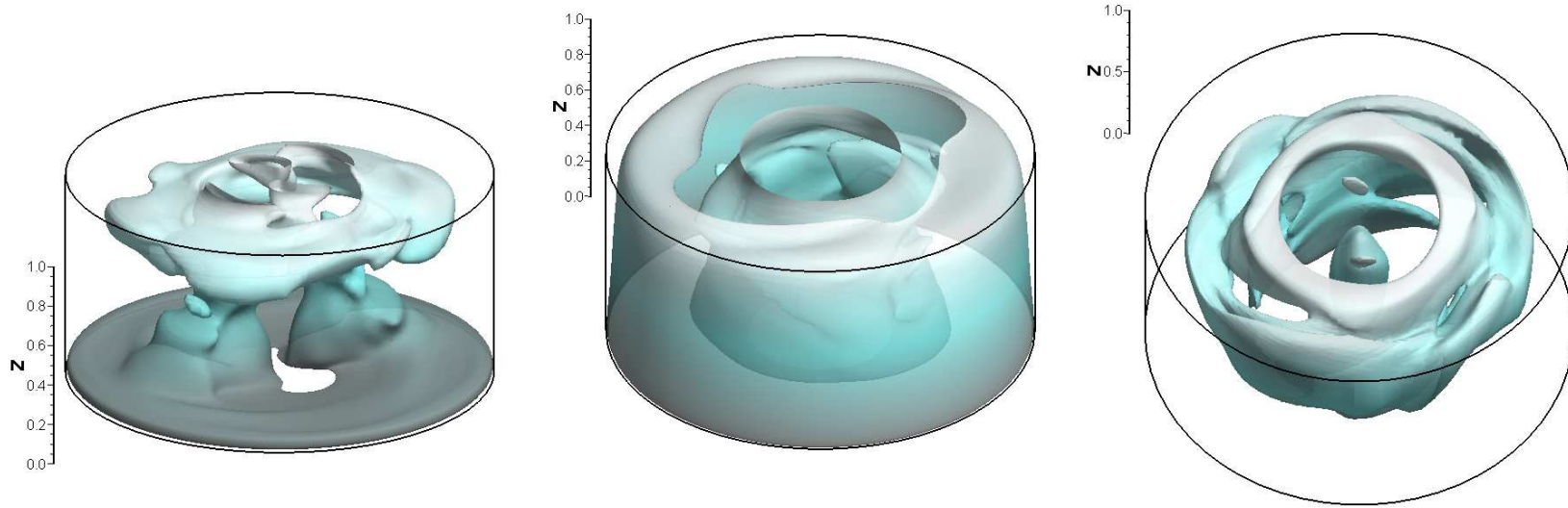


Fig. 7.32: Visualization of three-dimensional iso-surfaces for the instantaneous flow. Case $\Lambda = 1$ and $\text{Re} = 6000$. Left: iso-surface $u_r = 0.01$; Central: iso-surface $\Gamma = ru_\theta = 0.11$; Right: iso-surface $u_z = -0.24$.

7.5 Conclusions

The incompressible flow of a viscous fluid enclosed in a cylindrical container with an open top flat surface and driven by the constant rotation of the bottom wall has been thoroughly investigated in this chapter. The top surface of the cylindrical cavity is left open with a stress-free boundary condition imposed on it. No-slip condition imposed on the side-wall and also on the rotating bottom end-wall by means of a regularized angular velocity profile. More specifically, the stress-free top surface is, in first approximation, maintained fixed and flat.

In the present chapter, new flow states have been investigated based on a fully three-dimensional solution of the Navier–Stokes equations for the free-surface cylindrical swirling flow, without resorting to any symmetry property unlike all other results available in the literature. To our knowledge, the present study delivers the most general available results for this flat-free-surface problem due to its original mathematical treatment.

Five different cases corresponding to different pairs of governing parameters (Λ, Re) have been considered. The Reynolds regime corresponds to transitional flows with some incursions in the fully laminar regime. Both steady and unsteady non-oscillatory swirling flows are considered with a particular emphasis on the case $(\Lambda = 1, \text{Re} = 6\,000)$. Of great concern to this study is the question of space resolution. This is particularly important for the bifurcated case at $\text{Re} = 6\,000$. Convergence tests in space and time have been carried out on this upmost problematic case, and optimal values of the polynomial order and time-step have been deduced.

The evolution of the total kinetic energy of this open flow has been carefully studied for increasing Reynolds numbers and has been compared to the results for the closed swirling flow. The presence of the free surface on the top of the cylinder is found to strongly modify the observed trend: the total kinetic energy is increased with Re in the open cylinder case, while the converse is observed in the closed cylinder case. A physical analysis of the energetic action of the surface layer below the free surface allows to justify the above results. A comprehensive physical description of all flow states has been given with particular emphasis on the vortex breakdown bubbles and on the structure of the vortex lines. The unsteady case at $\text{Re} = 6\,000$ has retained more attention, given its unsteady transitional character. The mean flow and the corresponding rms fluctuations have been calculated and the results analyzed accordingly. Based on 24 flow samples equally-distributed in time, the general dynamics of the recirculation bubbles has been determined and described. The momentum transfers in the radial, azimuthal and axial directions have been studied along various one-dimensional lines. For the transitional case at $\text{Re} = 6\,000$, the flow in an inner cylindrical core is in solid-body rotation, while the outer radial layer is dominated by the jet-like shear layer along the tubular side-wall. This axial wall-jet is turned into a radial jet of angular momentum, which prevails all the way up to the free surface. The impingement of this radial jet onto the inner cylindrical core in solid-body rotation leads to the development of unstable azimuthal modes. The nonlinear terms, which includes a Coriolis effect, responsible for the development of these unstable modes have been found using the azimuthal momentum imbalance below the free surface. These unstable modes seem to take the form of even-order azimuthal rotating waves. A comprehensive azimuthal Fourier analysis is currently in progress in order to complement the available results.

The extension to the most general case involving a moving free surface is dealt with in the next Chapter.

Chapter 8

Free-surface swirling flow

The present chapter is aimed at the study of a specific shear-driven flow with a moving free-surface. Like in the previous chapter, we consider the incompressible flow of a viscous fluid partly enclosed in a cylindrical container driven by the steady rotation of the bottom wall. In this chapter, instead of considering the simplest case with a top flat and fixed surface, we consider the most general case with a moving free surface that evolves according to the flow dynamics, while participating to it. Consequently, the study in this chapter is a direct extension to the one in the previous chapter. The top surface of the cylindrical cavity is again left open and a stress-free boundary condition is imposed on it, while a no-slip condition is imposed on the side-wall and on the rotating bottom wall. The kinematic boundary condition which was reduced to a free-slip condition at the fixed surface in the previous chapter, is now imposed in its most general form by resorting to the arbitrary Lagrangian–Eulerian kinematics.

The flow states studied in this chapter correspond to the same governing parameters as the cases considered in Chapter 7. The Reynolds regime leads to transitional flows with some incursions in the fully laminar regime. Both steady and unsteady non-oscillatory swirling flows are studied.

8.1 Introduction

8.1.1 General considerations

As mentioned in Sec. 7.2.3, flat gas–liquid interfaces are often modeled as flat, fixed and stress-free surfaces. This idealization is commonly used by fluid dynamicists performing numerical simulations. Indeed, by resorting to this assumption the physical problem is significantly simplified and thus standard solution techniques can be used to deliver the flow fields. However, this idealization is never realized physically, even in well-controlled experimental set-ups and this mainly because of the presence of small amounts of surfactants. In addition, even for small angular velocities of the bottom end-wall, *i.e.* for small Reynolds numbers, limited deformations of the top surface are always present. These deformations are very often difficult to access by any of the measurement techniques available in laboratory experiments.

As discussed in detail in Chapter 7, the vortex breakdown of a swirling cylindrical flow refers to the flow state with recirculation zones appearing over a given range of the governing parameters $\Lambda = H/R$ and Re . Compared with swirling flows in a closed cylinder, the vortex breakdown phenomena occur in different conditions for an open cylinder flow: lower critical Reynolds number; smaller lower-limit aspect ratio Λ at which vortex breakdown occurs; large size of breakdown bubbles; possible attachment to the top free surface; etc. Moreover, for the relatively “shallow” system corresponding to $\Lambda = 1$, the loss of axisymmetry of these free-surface swirling flows is due to unstable azimuthal modes developing at the interface between the “inner” fluid in quasi-solid-body rotation and the “outer” fluid, where a surface jet of angular momentum exists and is directed towards the cylinder axis. The reader is referred to Chapter 7 for full details.

8.1.2 Motivations and objectives

The present study is mainly motivated by the need to gain insight into the influence of an unsteady and non-flat free surface onto the cylindrical swirling flow. It is important to note that even if the deformation amplitude of the free surface is limited compared to the cylinder height, the relative deformation amplitude may have rapid variations along radial lines. Those rapid variations could potentially have an impact on the various physical terms appearing in the governing Navier–Stokes equations. Ultimately, the reported effects of the relative deformations of the free surface on the physical terms—nonlinear convective terms, pressure gradient, viscous stress—may be extrapolated to cases where the amplitude of the surface deformations is more

important. Lower-Reynolds-number cases display a steady flow behavior which persists in presence of a free surface, which acquires a steady shape. In addition, for the unsteady case corresponding to ($\Lambda = 1$, $\text{Re} = 6000$), the free surface displays an unsteady evolution.

As already discussed in the previous chapter, all attempts to simulate this free-surface flow were limited to the fixed and flat free-surface case. Such lack of study in the scientific literature of this open swirling flow with a moving free surface can be understood when reading the following statement from Sarpkaya in his review entitled “Vorticity, free surface and surfactants” [218]: “... the modeling of free-surface phenomena still poses difficulties, not only because of an insufficient understanding of the physics of the vorticity/free-surface interaction, but also because of the necessity to devise and use mathematical formulations, numerical schemes, and physical-property experiments of far greater complexity than had hitherto been used...”. Indeed, when considering a real moving free surface, the complexity of the physical problem is dramatically increased. On top of the nonlinearity associated to the Navier–Stokes equations themselves, here we deal with a complicated geometry, which is changing in time and which is part of the solution itself. In addition, the nature of the boundary conditions on the free surface makes their imposition much more difficult compared to standard no-slip or free-slip boundary conditions. This particular point explains why all past studies of this flow problem prior to the one reported in this dissertation, used symmetry properties combined with a double-sized computational domain to enforce the stress-free condition at the flat free surface.

This accumulation of difficulties calls for elaborate algorithms and numerical techniques. All the developments of the present chapter use the numerical framework detailed in Chapter 3 and supplemented with the techniques reported in Appendix A.

8.2 Mathematical model and problem formulation

8.2.1 Mathematical description of the problem

The fluid enclosed in the cylindrical cavity is assumed to be incompressible, Newtonian with uniform density and temperature. In the arbitrary Lagrangian–Eulerian kinematics, the flow is governed by the modified Navier–Stokes equations

$$\frac{\partial u_i}{\partial t} + (u_j - w_j) \frac{\partial u_i}{\partial x_j} = \frac{\partial \sigma_{ij}^*}{\partial x_j} + g_i, \quad (8.1)$$

$$\frac{\partial u_j}{\partial x_j} = 0, \quad (8.2)$$

where $\sigma_{ij}^* = -p\delta_{ij} + 2\nu D_{ij}$ is the reduced Cauchy stress tensor of the fluid, p the static or reduced pressure, D_{ij} the rate-of-deformation tensor, ν the assuredly constant and uniform kinematic viscosity, g_i the components of the acceleration of gravity ($g_1 = g_2 = 0$ and $g_3 = -g$), and w_i the components of the ALE mesh velocity. The reader is referred to Chapter 3 for a comprehensive introduction of the ALE kinematics and for the definition of the ALE mesh velocity \mathbf{w} . For the sake of clarity, we briefly present here the central details of the mathematical description of this problem in the ALE framework. Inside the fluid domain denoted by \mathcal{V} , no-slip boundary conditions are imposed on all cavity walls: the tubular side-wall, the bottom end-wall in steady rotation. A sketch of the fluid domain along with additional information, is depicted in Fig. 8.1. The mathematical expressions of the no-slip condition on the tubular side-wall now account for the varying fluid height and read

$$u(r = R, \theta, z, t) = v(r = R, \theta, z, t) = w(r = R, \theta, z, t) = 0, \quad 0 \leq \theta \leq 2\pi, \quad 0 \leq z \leq H + \eta(r, \theta, t), \quad (8.3)$$

where $\eta(r, \theta, t)$ is the algebraic free-surface elevation at the point of polar coordinates (r, θ) , and measured from its equilibrium position $z = H$. The flow is driven by imposing a regularized angular velocity profile to the bottom end-wall, which transfers its kinetic energy to the fluid above. The details regarding the imposition of this Dirichlet boundary condition for the velocity field at the spinning disk are exactly identical to the ones discussed in Sec. 7.2.2. The top surface is left open and is modeled as a moving and yet clean free surface. The details regarding the imposition of the dynamic and kinematic boundary conditions at the free surface are discussed in the next section.

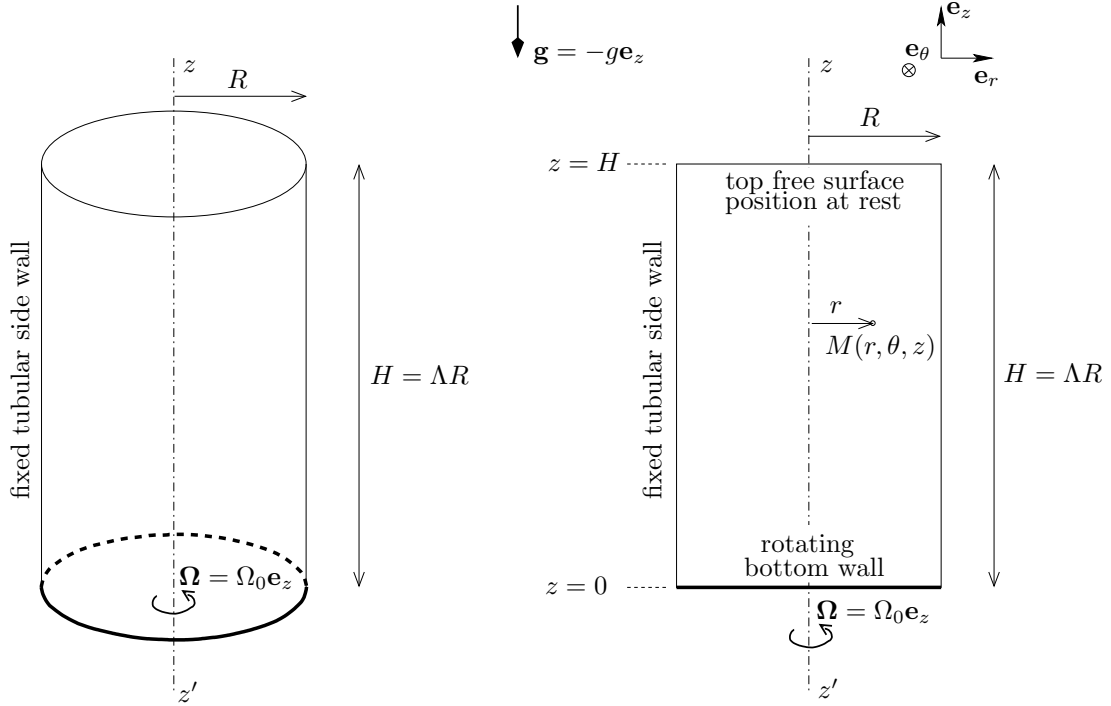


Fig. 8.1: Left: sketch of the three-dimensional geometry of the cylindrical cavity. Right: meridional cut of the cylindrical cavity.

8.2.2 Free-surface modeling

The mathematical problem corresponding to Eqs. (8.1)–(8.2) requires the definition of three independent non-dimensional parameters to determine completely the flow state. These three parameters are the height-to-radius aspect ratio $\Lambda = H/R$, the Reynolds number $\text{Re} = R^2\Omega_0/\nu$, and the Froude number $\text{Fr} = R^2\Omega_0^2/(gH) = R\Omega_0^2/(g\Lambda)$, based on the maximal prescribed angular velocity Ω_0 of the bottom end-wall and the acceleration of gravity g . It is sometimes convenient to introduce an additional non-dimensional number: the Wehausen number denoted as Wh , and defined as the ratio between Re and $\text{Fr}^{1/2}$

$$\text{Wh} = \frac{\text{Re}}{\sqrt{\text{Fr}}} = R^{3/2} \frac{\sqrt{g\Lambda}}{\nu}. \quad (8.4)$$

This non-dimensional number is obviously dependent on the three other non-dimensional numbers, and may be regarded as a measure of the relative magnitudes of the diffusive and macroscopic time scales, see Eq. (3.73) for one possible physical introduction to the notion of diffusive time scale. The interest for the Wehausen number lies in the fact that for a given fluid—*i.e.* for a given kinematic viscosity ν —under the effect of gravitational forces, Wh solely depends on the problem length scale—here the cylinder radius R , the dependence on the aspect ratio Λ being marginal. The Wehausen number has been introduced in the past for the study of large-scale free surface flows, see Marcus & Berger [175], to justify the use of an irrotational flow hypothesis away from the free surface. These arguments correspond to typical free-surface flows encountered in ocean engineering. In the present case, the length scales correspond to typical laboratory experimental set-ups and are therefore clearly smaller. In the International System of Units, using $g = 9.81 \text{ m}\cdot\text{s}^{-2}$ and the kinematic viscosity of tap water at ambient temperature $\nu = 10^{-6} \text{ m}^2\cdot\text{s}^{-1}$, one can evaluate the order of the Wehausen number for a prototypical cylinder of radius $R = H = 0.1 \text{ m}$: $\text{Wh} = O(10^5)$. Such a high order for Wh is a further validation of the flat and fixed free-surface approximation used in the previous chapter. However, this estimate loses some of its interest when considering the dynamics of some local effects at the free surface that we are trying to highlight in the present study. Indeed, as mentioned earlier, Wh does not depend on any characteristic velocity scale but solely on the characteristic length scale of the problem. The study presented in the previous chapter has revealed some small-scale structures near the free surface. These small-scale structures lead to significantly smaller values of the Wehausen number, and this independently of their characteristic velocity or vorticity scales.

In the previous chapter, the hypothesis of flat free surface was shown to be equivalent to a zero-Froude-number condition, which in turn led to the simplified kinematic boundary condition $u_z = 0$ at the free surface $z = H$. The kinematic boundary condition (KBC) expresses the fact that the free surface is a material surface

with no transfer of fluid across it in the Lagrangian perspective. In the ALE framework, the KBC at the free surface in its most general form reads

$$\mathbf{u} \cdot \hat{\mathbf{n}} = \mathbf{w} \cdot \hat{\mathbf{n}}, \quad (8.5)$$

where $\hat{\mathbf{n}}$ represents the local unit outward normal vector to the free surface. The scalar equation (8.5) only constrains the normal component of the mesh velocity \mathbf{w} . Some freedom remains for the choice of the values of the tangential part of \mathbf{w} . To simplify the implementation, a pure Lagrangian description of the free surface is chosen by imposing the tangential part of \mathbf{w} to be identical to corresponding one for the fluid velocity. Thus, the KBC takes the very simple form of the following vector equation

$$\mathbf{u} = \mathbf{w}, \quad (8.6)$$

at the free surface.

The pressure and velocity boundary conditions on the free surface are both formulated from the dynamic constraint of continuity of normal momentum flux across the free surface, whilst assuming negligible momentum on the air side and neglecting surface tension effects—hypothesis of clean surface without any surfactant. This dynamic boundary condition (DBC) reads

$$\sigma_{ij}^* \hat{n}_j = -p \delta_{ij} \hat{n}_j + 2\nu D_{ij} \hat{n}_j = 0, \quad (8.7)$$

for zero atmospheric pressure. Unlike in the flat and fixed free-surface case dealt with in the previous chapter, the DBC (8.7) does not simplify further but leads to a vanishing surface term $\mathcal{H}^\sigma = 0$, into the weak ALE formulation of the problem, see Sec. 3.2.3. As emphasized in Chapter 3, this homogeneous DBC is automatically incorporated into the complete weak formulation of the problem expressed in its strong form by Eqs. (8.1)–(8.2). This automatic imposition of the DBC through the weak formulation of the problem is one of the most attractive feature of the newly-developed numerical method. Along the same line, the specific choice of the ALE kinematics allows to automatically account for the KBC through Eq. (8.5), or equivalently Eq. (8.6).

8.2.3 Mesh velocity problem and boundary conditions

When considering this free-surface swirling flow problem tackled in an interface-tracking and ALE frame, the free surface is treated in a Lagrangian way, whereas the fixed tubular side-wall and the prescribed-in-motion bottom end-wall, is studied in the Eulerian frame. It is worth noting that the vector expression (8.6) of the KBC is mathematically compatible with the no-slip condition on the tubular side-wall expressed by Eq. (8.3), if and only if one imposes the same no-slip condition to the ALE mesh velocity at the contact line defined by $(r = R, \theta, z = H + \eta)$. This compatibility condition at the contact line is easily enforced by imposing a no-slip condition on the whole tubular side-wall, which mathematically reads

$$w_r(r = R, \theta, z, t) = w_\theta(r = R, \theta, z, t) = w_z(r = R, \theta, z, t) = 0, \quad 0 \leq \theta \leq 2\pi, \quad 0 \leq z \leq H + \eta(r, \theta, t). \quad (8.8)$$

This homogeneous Dirichlet boundary condition for the mesh velocity on the tubular side-wall is supplemented by another homogeneous Dirichlet condition on the bottom end-wall of the cylindrical cavity and expressed by the following vector equation

$$\mathbf{w}(r, \theta, z = 0) = \mathbf{0}. \quad (8.9)$$

As a consequence of the choice of kinematics on the fluid domain boundary—Lagrangian and Eulerian but not yet arbitrary, the values of the mesh velocity are prescribed by the boundary conditions given by Eq. (8.6), Eq. (8.8) and Eq. (8.9). The freedom left for the choice of \mathbf{w} lies solely in the values of this field in the internal fluid domain.

The details associated with the underlying moving-grid technique are dealt with in Sec. 3.4 and Appendix A. For the sake of clarity, we briefly recall here the central details of this method. The determination of the mesh velocity \mathbf{w} in the internal fluid domain is the corner-stone of the moving-grid technique developed in the framework of the ALE formulation. The values of the mesh velocity being prescribed on the boundary, the evaluation of \mathbf{w} are obtained as the solution of the following steady Stokes problem

$$\nabla_{\mathbf{x}} \cdot \tilde{\boldsymbol{\sigma}} = \mathbf{0}, \quad (8.10)$$

$$\nabla_{\mathbf{x}} \cdot \mathbf{w} = 0, \quad (8.11)$$

where $\tilde{\boldsymbol{\sigma}}$ is the Cauchy stress tensor of the mesh defined by

$$\tilde{\boldsymbol{\sigma}} = -\tilde{p}\mathbf{I} + \tilde{\nu}(\nabla_{\mathbf{x}}\mathbf{w} + \nabla_{\mathbf{x}}\mathbf{w}^T), \quad (8.12)$$

with \tilde{p} and $\tilde{\nu}$ being respectively the fictitious mesh pressure and the fictitious kinematic viscosity of the mesh, characterizing the elasticity of the mesh in its motion. The reader is referred to Sec. A.4 in Appendix A for the justifications of this choice of elastic and incompressible motion of the mesh. Finally, the update of the position \mathbf{x} of the mesh points is performed by integrating the following equation

$$\frac{d\mathbf{x}}{dt} = \mathbf{w}. \quad (8.13)$$

8.3 Computational approach

This section is aimed at providing the reader with a brief description of the numerical treatment of the equations governing the problem studied throughout this chapter in the specific context of the ALE moving-grid technique jointly used with the Legendre spectral element method.

8.3.1 Space discretization

A classical Galerkin approximation is applied to the set of governing equations expressed in the weak transient ALE form in order to determine the pressure and the fluid velocity. The Galerkin approximation is then discretized by using the spectral element method with the classical staggered $\mathbb{P}_N - \mathbb{P}_{N-2}$ approach to avoid the development of spurious pressure modes [174]. Discontinuous and continuous approximations are respectively taken for the pressure and fluid velocity. The mesh velocity is discretized using the same polynomial space as the fluid velocity, namely \mathbb{P}_N , based on a Gauss–Lobatto–Legendre (GLL) grid of order N . For the discontinuous approximation of the pressure, a Gauss–Legendre (GL) grid of order $N - 2$ is used. Consequently the ALE Navier–Stokes semi-discrete equations reads:

$$\frac{d}{dt}(\mathbf{M}\underline{\mathbf{u}}) + \mathbf{C}(\underline{\mathbf{u}}, \underline{\mathbf{w}})\underline{\mathbf{u}} + \mathbf{A}\underline{\mathbf{u}} + \mathbf{D}^T \underline{p} = \underline{\mathbf{F}}, \quad (8.14)$$

$$-\mathbf{D}\underline{\mathbf{u}} = \mathbf{0}, \quad (8.15)$$

\mathbf{M} denoting the tensorized mass matrix, \mathbf{A} the tensorized stiffness matrix, \mathbf{D}^T the tensorized discrete gradient operator, \mathbf{D} the tensorized discrete divergence operator, $\mathbf{C}(\underline{\mathbf{u}}, \underline{\mathbf{w}})$ the tensorized discrete convective operator depending both on the fluid and mesh velocities and $\underline{\mathbf{F}}$ the discrete body force which accounts for the macroscopic effects of the acceleration of gravity g . The update of the position \mathbf{x} of the mesh points is performed by integrating the discrete counterpart of Eq. (8.13)

$$\frac{d\mathbf{x}}{dt} = \underline{\mathbf{w}}. \quad (8.16)$$

8.3.2 Time integration

The set of semi-discrete equations (8.14)–(8.16) is discretized in time using a decoupled approach detailed in Sec. 3.3.4 and Sec. 3.3.5 in Chapter 3. The discrete body force vector $\underline{\mathbf{F}}$ appearing in Eq. (8.14) may be expressed in a more intuitive way as $\mathbf{M}\underline{\mathbf{g}}$, where \mathbf{M} denotes the tensorized mass matrix. The fully-discretized set of governing equations reads

$$\left(\frac{3\mathbf{M}^{n+1}}{2\Delta t} + \mathbf{A}^{n+1} \right) \underline{\mathbf{u}}^{n+1} - (\mathbf{D}^{n+1})^T \underline{p}^{n+1} = \frac{1}{\Delta t} \left(2\mathbf{M}^n \underline{\mathbf{u}}^n - \frac{1}{2}\mathbf{M}^{n-1} \underline{\mathbf{u}}^{n-1} \right) + \mathbf{M}^{n+1} \underline{\mathbf{g}}^{n+1} - \mathbf{C}^{n+1} \underline{\mathbf{u}}^{n+1}, \quad (8.17)$$

$$\mathbf{C}^{n+1} \underline{\mathbf{u}}^{n+1} = 2\mathbf{C}^n(\underline{\mathbf{u}}^n, \underline{\mathbf{w}}^n) \underline{\mathbf{u}}^n - \mathbf{C}^{n-1}(\underline{\mathbf{u}}^{n-1}, \underline{\mathbf{w}}^{n-1}) \underline{\mathbf{u}}^{n-1}, \quad (8.18)$$

$$-\mathbf{D}^{n+1} \underline{\mathbf{u}}^{n+1} = \underline{\mathbf{0}}, \quad (8.19)$$

$$\underline{\mathbf{x}}^{n+1} = \underline{\mathbf{x}}^n + \Delta t \left(\frac{23}{12} \underline{\mathbf{w}}^n - \frac{16}{12} \underline{\mathbf{w}}^{n-1} + \frac{5}{12} \underline{\mathbf{w}}^{n-2} \right), \quad (8.20)$$

where Δt is the time-step. The reader is referred to Sec. 3.3.4 and Sec. 3.3.5 for full details.

8.3.3 Computational parameters

The simulations carried out in this chapter are limited to the three cases (a) – (c) corresponding to three different values of the Reynolds number, but to the same aspect ratio $\Lambda = 1$. Given the non-dimensionalization

used, these three cases correspond to the same Froude number. Building on the convergence analysis developed in Sec. 7.3.3, the same spatial resolution as the one used in Chapter 7 has been used throughout this chapter. The spectral element grid prior to any motion in the ALE framework is identical to the one used in the previous chapter and depicted in Figs. 7.6 & 7.7. In terms of initial conditions, the steady rotation is started from the steady state (resp. statistically-steady state) reached in the fixed and flat free-surface simulations (a) – (b) (resp. (c)) reported in Chapter 7, see Fig. 7.9 and Sec. 7.4.2.

The physical and computational parameters corresponding to the three moving cases are reported in Table 8.1.

| Case | Re | $\Lambda = H/R$ | Fr | Wh | Time-step Δt | Time evolution | N |
|------|-------|-----------------|-----|--------|----------------------|----------------|-----|
| (a) | 900 | 1.0 | 0.1 | 2 846 | 0.0025 | steady | 7 |
| (b) | 1 500 | 1.0 | 0.1 | 4 743 | 0.0025 | steady | 8 |
| (c) | 6 000 | 1.0 | 0.1 | 18 974 | 0.001 | unsteady | 8 |

Table 8.1: Parameters and characteristics of the cases considered. The time-step Δt is expressed in Ω_0^{-1} units and N refers to the same polynomial order used in all space directions.

8.4 Numerical simulations and results

Numerical results revealed in the present dissertation are intended to contribute to the exposition of the open swirling cylinder problem in unsteady and non-axisymmetric configurations. Indeed, much attention has been paid to the steady and/or axisymmetric flow states.

As mentioned in Sec. 7.4.1, the experimental studies of deep systems—corresponding to $\Lambda > 1$ —performed independently and successively by Young *et al.* [269], Hirs *et al.* [119], and Miraghaie *et al.* [182], revealed that the instability mode is concentrated in the vicinity of the wall-jet along the tubular side-wall. This wall-jet is generated by the rotation of the bottom end-wall and is turned upwards by the presence of the tubular side-wall. As mentioned by Piva and Meiburg [198]: “this instability mode does not lead to a surface deflection, so that it can be captured in numerical simulations assuming a flat, stress-free surface”. Conversely, the instability modes for shallow systems—corresponding to $\Lambda \leq 1$ —are concentrated in the interfacial region denoted by Υ in Sec. 7.4.5 and where the surface radial jet of angular momentum impinges onto the inner cylindrical core in a state of quasi solid-body rotation. As it is shown in the sequel, these unstable modes yield free-surface deflection, which becomes non-axisymmetric at sufficiently large Reynolds number. For those shallow cases, the flat and stress-free modeling of the free surface is less effective compared to deep systems.

8.4.1 Free surface profiles

After having extensively studied the flat free-surface swirling flow in Chapter 7, our primary focus resides in the determination of the free-surface elevation η . Figure 8.2 displays the relative surface elevation η/H in any meridional plane for both steady cases (a) – (b). Three-dimensional views of these two cases are available in Fig. 8.5. One clearly distinguishes two regions corresponding to surface elevations of opposite signs. In the inner-core region of the flow, say $r/R \leq 0.4$, the algebraic surface elevation is the largest in absolute value and a large trough forms. This internal trough is surrounded by a outer region of strictly positive surface elevation all the way to the circular contact line along the tubular side-wall. The radial position of this ring crest is located around $r/R = 0.9$ and its amplitude is much smaller than the one of the trough measured on the cylinder axis.

Such observations can easily be justified based on the physical analysis of the flow presented in Chapter 7. The outer ring of positive η is generated by the impingement of the tubular wall-jet, which is therefore a consequence of the pumping effect of the Ekman layer above the rotating disk. The inner trough is itself another consequence of this Ekman layer, but through its sucking effect which complete the large meridional circulation generated by the motion of the disk. It also corresponds to the region of the flow in a state of quasi-solid-body rotation.

As far as the comparison between the cases at $\text{Re} = 900$ and $\text{Re} = 1\,500$ is concerned, one may globally note a more pronounced free-surface deformation at higher Re : the deepness of the trough is more important in case (b), and the crest of the outer ring is higher in case (b). On top of those global remarks, three important specific items are to be pointed out. First, one could expect the deepest free surface point to be located on axis. This is the case at $\text{Re} = 1\,500$ but not at $\text{Re} = 900$, where the presence of the on-axis vortex breakdown bubble limits the sucking effect of the Ekman layer. At $\text{Re} = 1\,500$, the recirculation bubble becomes off-axis and toroidal,

which therefore allows for a more important sucking effect along the cylinder axis. The second point is related to the radial location of the maximum of the ring crest: the radius of this maximum appears to be shifted towards the cylinder radius when increasing Re . Bearing in mind that the crest is generated by the tubular wall-jet, one may recall that the thickness of this wall-jet is reduced with increasing Re , which therefore explains the observed maximum shift of the crest. The third item refers to the transition region between the positive and negative regions of η . This transition region is in relationship with the interfacial zone Υ : for $Re = 900$ almost no elevation of the free surface is observed, while at $Re = 1500$ an additional small crest is observed followed radially by a second small trough before reaching the largest crest ring.

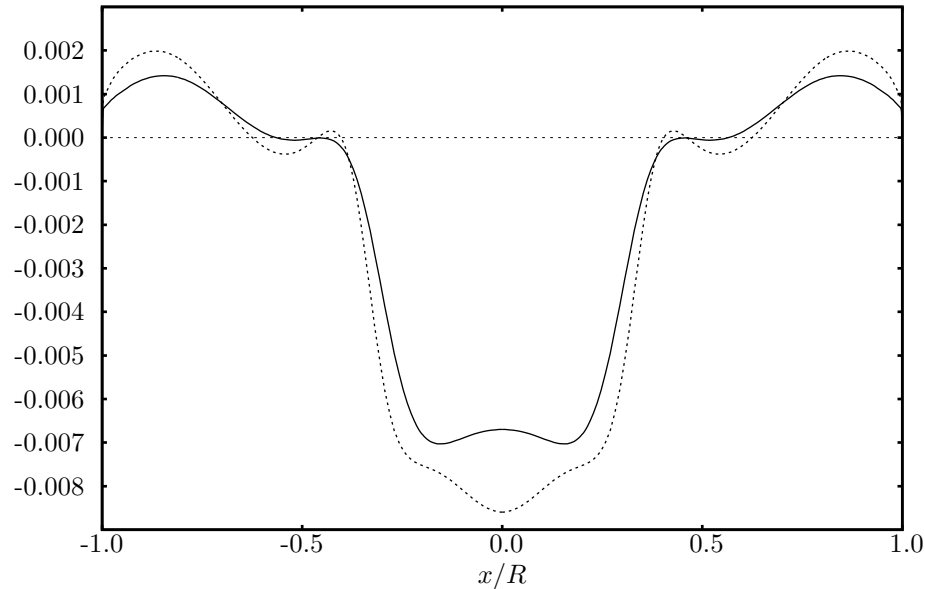


Fig. 8.2: Relative free-surface elevation η/H measured from the position $z = H$ at rest, in any meridional plane. Solid line: $Re=900$; Dotted line: $Re=1500$.

Based on axisymmetric steady state results, Piva & Meiburg [198] have extrapolated the leading order free surface deflection—denoted by h in their journal article—using the balance of normal stresses at the free surface. In their study, Piva & Meiburg focused on the steady axisymmetric open swirling flow with a partially rotating bottom end-wall. It is important to note that their results shown in Fig. 8.3 are only extrapolated results from numerical data obtained using a flat stress-free modeling for the free surface. In Fig. 8.3, only the case $D = 1$ corresponding to a complete rotation of the bottom wall is of interest to us as it corresponds exactly to our case (a). It appears that their results for $D = 1$ do not capture any of the three important items discussed above.

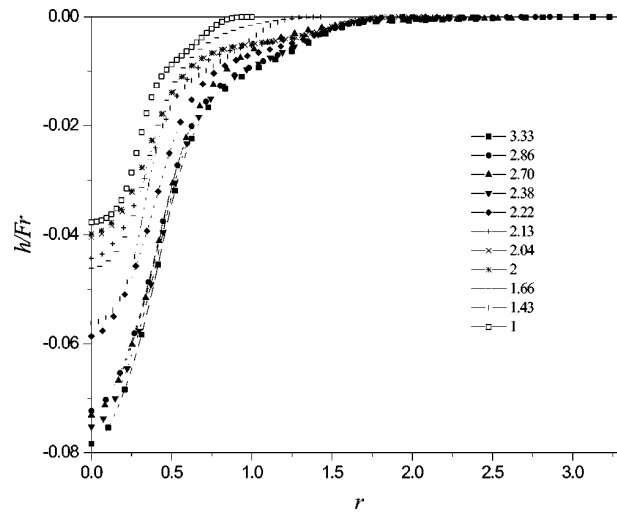


Fig. 8.3: Surface deflection for $\Lambda = 1$, $Re = 900$, and various ratios $D = R_c/R_d$, where R_c is the cylinder radius and R_d the radius of the rotating disk. From Piva & Meiburg [198]. © 2005 American Institute of Physics.

When increasing the Reynolds number up to $Re = 6000$, the numerical simulation yields a non-axisymmetric

free-surface shape as can be seen in two orthogonal meridional planes in Fig. 8.4 and in 3D in Fig. 8.5. The comments related to the comparison of cases (a) and (b) remain valid for this higher-Reynolds-number case. One may however note in Fig. 8.4 the more complex radial variations of η in the larger transition region between the inner trough and the outer crest ring. In Chapter 7, the unstable modes were found to be active in this region, which comprised the interfacial zone Υ . The 3D view in the bottom row of Fig. 8.5 reveals a free-surface shape of “bathtub sink-vortex” type.

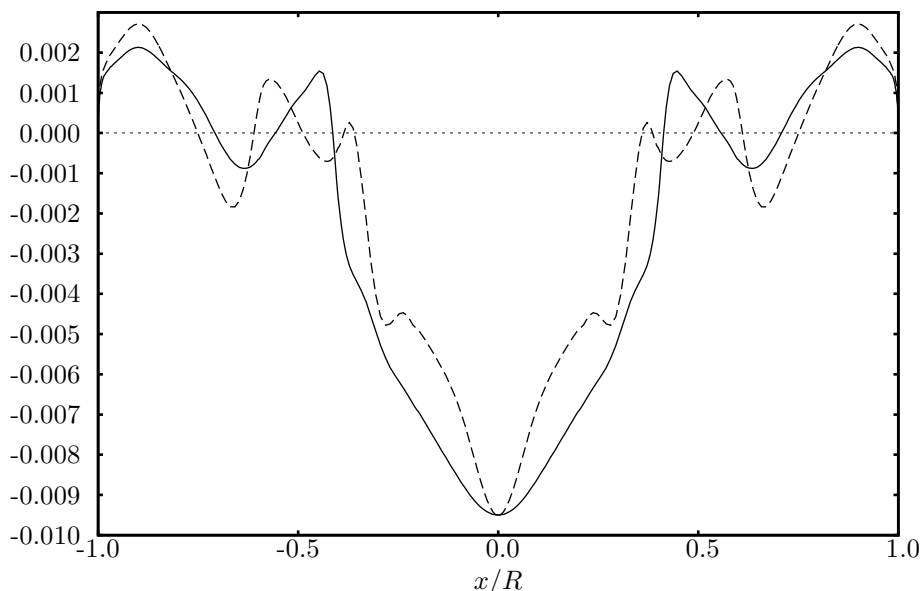


Fig. 8.4: Relative free-surface elevation η/H measured from the position $z = H$ at rest, for case (c) ($\Lambda = 1$, $\text{Re} = 6\,000$). Solid line: meridional plane $y/R = 0$; Dotted line: meridional plane $x/R = 0$.

8.4.2 Vortex breakdown bubbles and meridional flow fields

We consider now the two steady flows for $\Lambda = 1$ and $\text{Re} = 900, 1\,500$ corresponding to cases (a) and (b) respectively. Figure 8.6 displays the streamlines of these flows into any meridional plane. For both of these flows, the streamlines are extremely close to those obtained in the flat stress-free model—see Fig. 7.10—except near the contact line ($r = R, \theta, z = H + \eta$). A small recirculation bubble appears near this contact line. It is attached to the free surface and stretched from about half-height of the cavity up to the free surface. This vortex breakdown bubble is related to the crest ring described in the previous section. It is important to note that experimentally this small recirculation bubble may be difficult to obtain because of the presence of small amounts of surfactants affecting the cleanliness of the surface. This notably modifies the contact angle and the free-surface shape near the contact line. The same observation and conclusions apply to case (c). The streamlines for this case are represented in two orthogonal meridian planes corresponding to $y/R = 0$ and $x/R = 0$, in Fig. 8.7. Once again, the loss of axisymmetry appears clearly from the complex and asymmetric structure of the recirculation bubbles.

As a second step, the contours of the radial, azimuthal and axial velocity components in any meridional plane are given in Fig. 8.8. These data are supplemented with the contours of the axial component of the angular momentum $\Gamma = ru_\theta$ still in Fig. 8.8, extreme right column. Given the small Reynolds numbers in both cases, it is clear that the structures of these fields are extremely close to those obtained using the flat stress-free model in Chapter 7 and shown in Fig. 7.14. The only notable difference lies in the contours the axial velocity component u_z . Indeed, the zero-Froude-number condition imposed in Chapter 7 in lieu of the kinematic boundary condition, led to a vanishing axial velocity at the free surface. In this study, this condition is relaxed and the real kinematic boundary condition is imposed allowing to have non-zero axial velocity at the free surface. Consequently, we observe now non-zero contours terminating at the free surface, which was impossible previously. The distribution of contours of u_z are to be put together with the surface elevations depicted in Fig. 8.2. Given the limited surface deflection of the free surface, its local unit normal vector $\hat{\mathbf{n}}$ is everywhere close to the unit vector in the z -direction. As the normal component of the fluid velocity is responsible for free-surface deformations, in this case it is u_z that is mainly responsible for the observed surface elevation. One may notice that we recover from the distribution of contours of u_z at the free surface, the two regions of positive and negative η defined in the previous section.

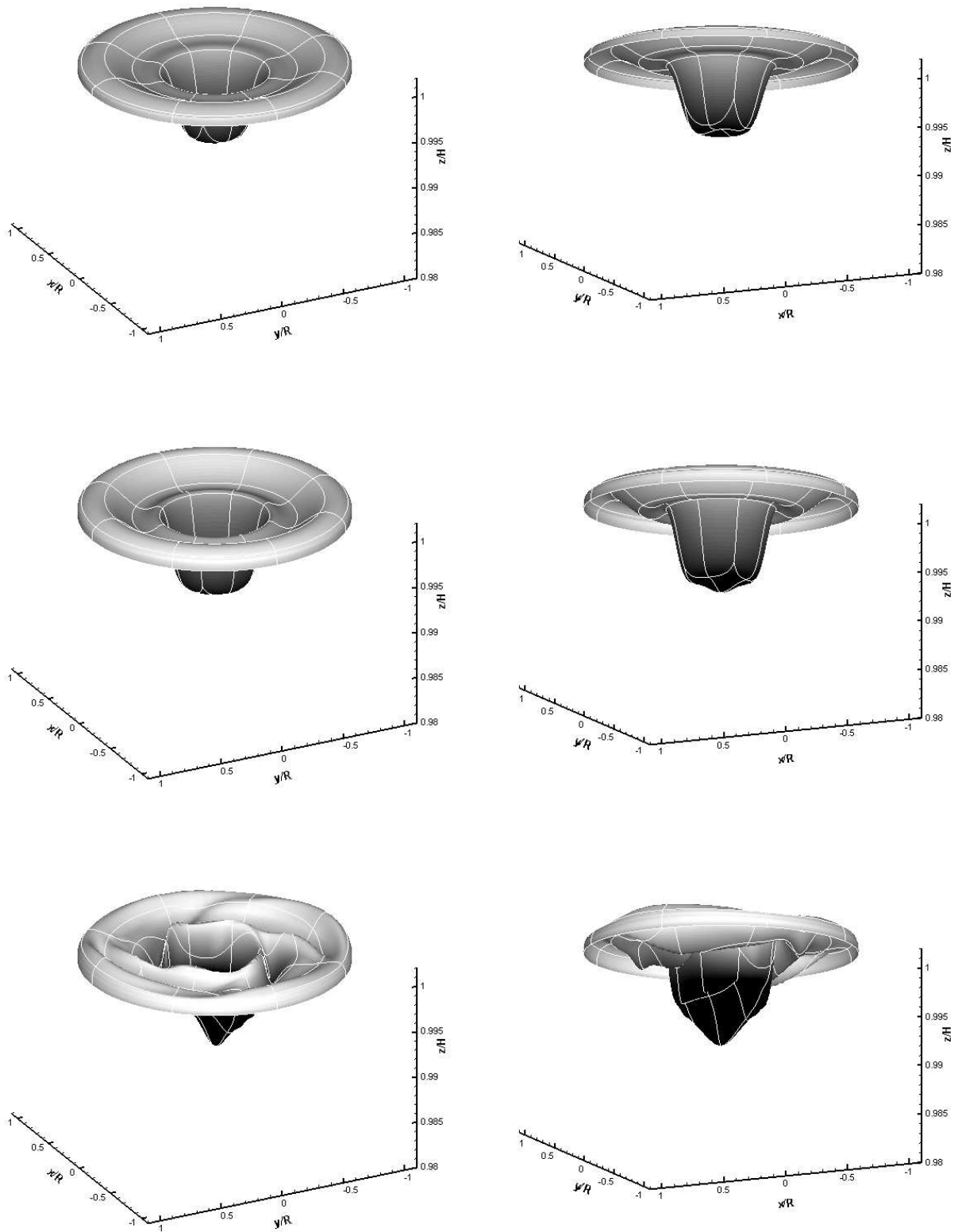


Fig. 8.5: Three-dimensional views of the free-surface shape η/H measured from the position $z = H$ at rest. Top row: $Re = 900$; Central row: $Re = 1500$; Bottom row: $Re = 6000$. Left column: high-angle view; Right column: low-angle view. The spectral element grid appears in solid white line to improve the 3D visualization.

The previous analysis is further confirmed by the contours of the three velocity components and of the axial angular momentum for an instantaneous flow sample, presented in Fig. 8.9, in the meridional plane $x/R = 0$. No statistical analysis of the flow at $Re = 6000$ is yet available because of technical issues that still need to be overcome. Without going into detail, it is important to notice that each flow sample corresponds to a different flow dynamics and consequently to a different mesh velocity, and ultimately to a different mesh. Performing statistical analyses on hundreds of flow samples corresponding to hundreds of computational meshes is a complex and time-consuming task that we are still trying to simplify and optimize.

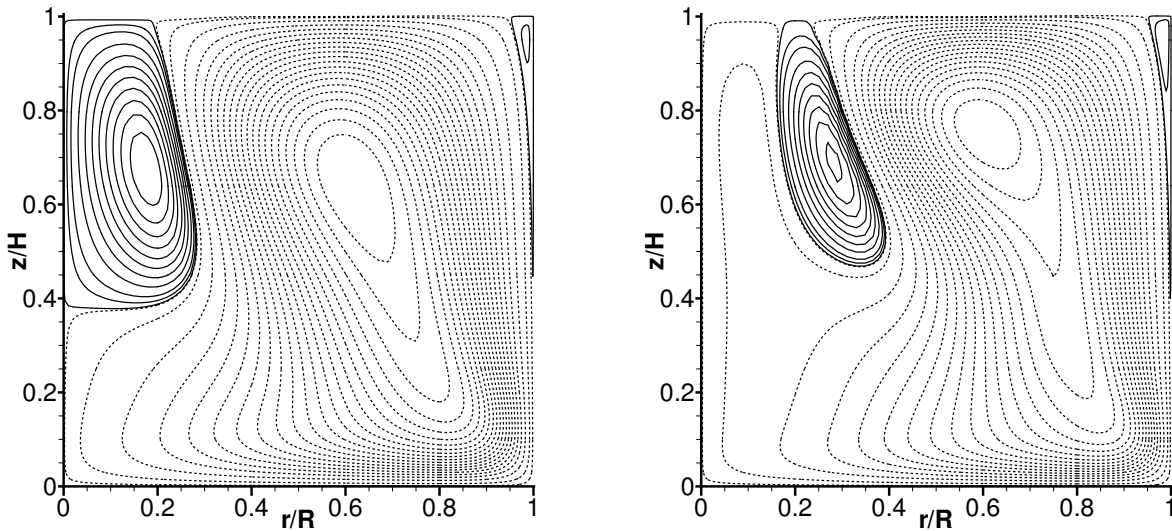


Fig. 8.6: Contours of streamlines in a meridional plane, case $\Lambda = 1$ with a free surface. Left: case $Re = 900$; Right: case $Re = 1500$. The 30 contours are non-uniformly spaced for visualization purposes, 20 equally-spaced negative contours and 10 equally-spaced positive contours for $Re = 900$ and $Re = 1500$.

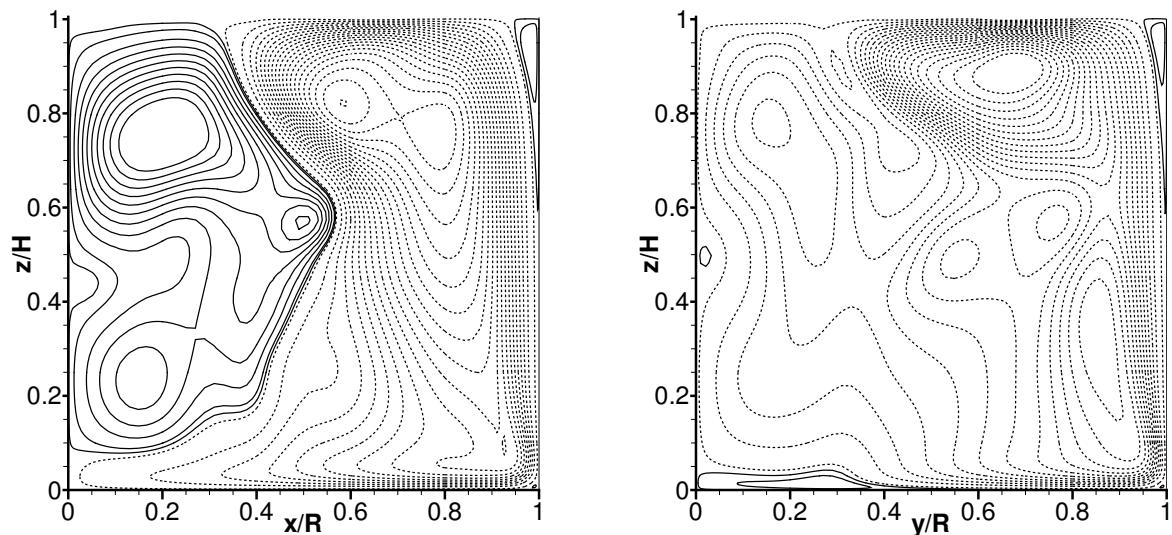


Fig. 8.7: Contours of streamlines in two orthogonal meridional planes, case $\Lambda = 1$ and $Re = 6000$ with a free surface. Instantaneous flow sample. Left column: meridional plane $y/R = 0$; Right column: meridional plane $x/R = 0$. The 30 contours are non-uniformly spaced for visualization purposes, 20 equally-spaced negative contours and 10 equally-spaced positive contours.

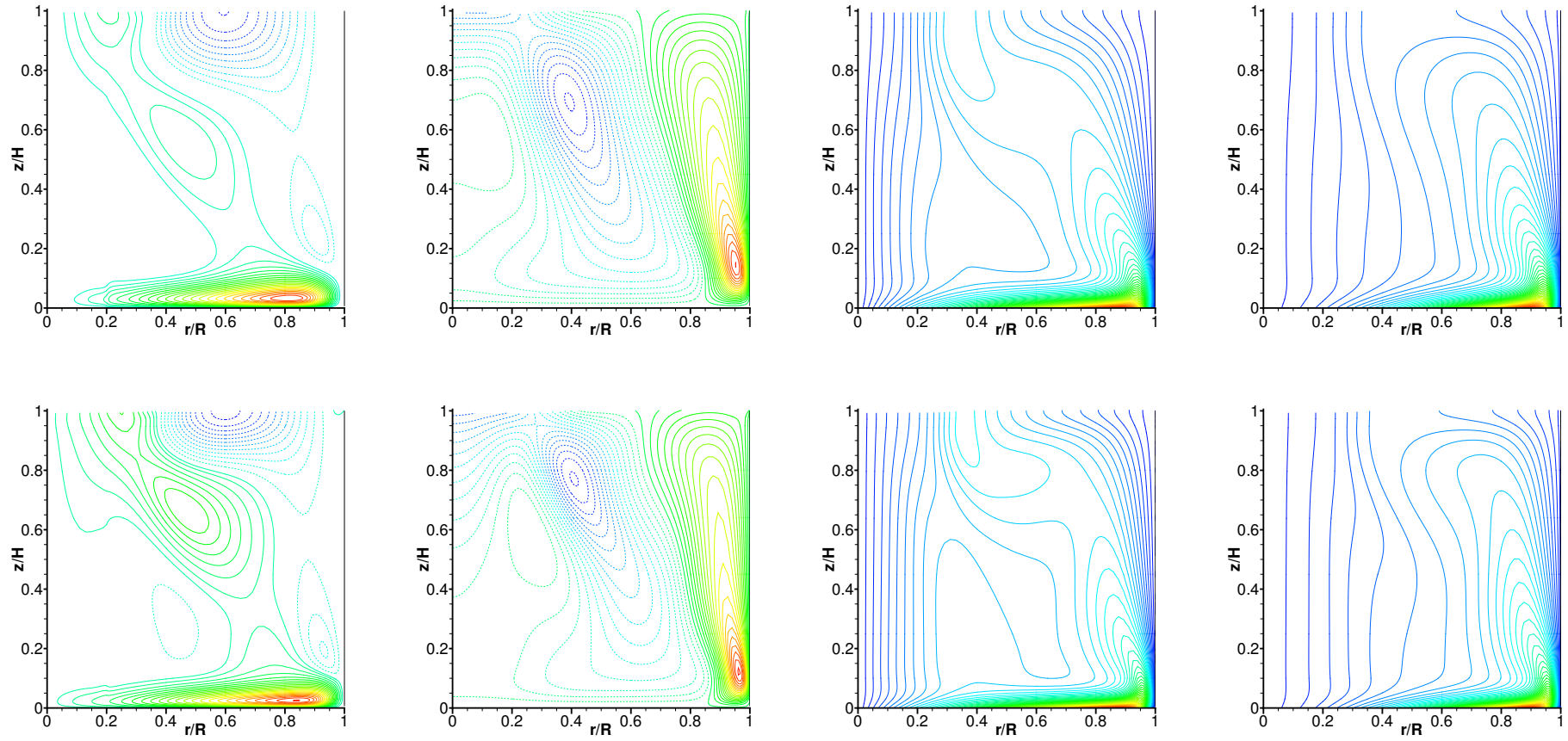


Fig. 8.8: Contours in a meridional plane for the case $\Lambda = 1$ with a free surface. Top row: case $\text{Re} = 900$; Bottom row: case $\text{Re} = 1500$. From left column to right column: radial velocity component u_r ; axial velocity component $w = u_z$; azimuthal velocity component u_θ ; axial angular momentum component $\Gamma = ru_\theta$. The 35 contours are uniformly spaced, between -0.06 and 0.145 for u_r ; and between -0.09 and 0.12 for u_z ; The 50 contours are uniformly spaced, between 0 and 1 for u_θ and Γ .

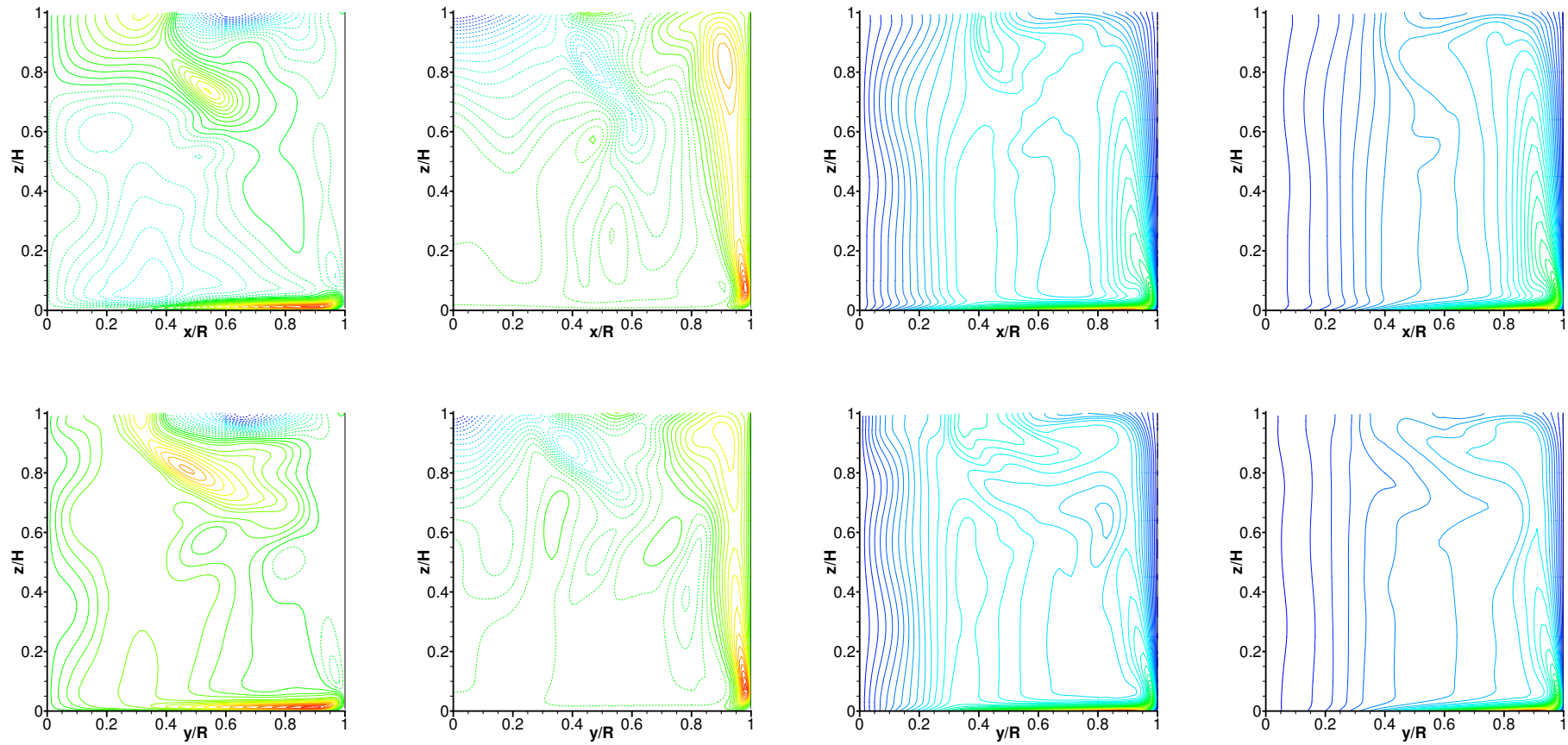


Fig. 8.9: Contours in two orthogonal meridional planes for the case $\Lambda = 1$ and $\text{Re} = 6000$ with a free surface. Instantaneous flow sample. Top row: meridional plane $y/R = 0$; Bottom row: meridional plane $x/R = 0$. From left column to right column: radial velocity component u_r ; axial velocity component u_z ; azimuthal velocity component u_θ ; axial angular momentum $\Gamma = ru_\theta$. The 50 contours are uniformly spaced, between -0.13 and 0.16 for u_r ; between -0.09 and 0.14 for u_z ; and between 0 and 1 for u_θ . The 100 contours are uniformly spaced between 0 and 1 for Γ .

A careful analysis of the vortex lines for the instantaneous flow sample shows a bending in the whole meridian plane. This bending is very significant in the region $0.4 \leq r/R \leq 0.8$ and $0.4 \leq z/H \leq 1$, which corresponds to the limit between the primary recirculation of the flow and the secondary recirculation bubble. The jet-like shear layer along the tubular side-wall is turned into the interior of the flow by the free surface. Focusing on the axial velocity component u_z , the comparison of the respective contours of u_z in Fig. 7.22 and Fig. 8.9 highlights the higher intensity of this shear layer in the moving-free-surface case. In the flat case, the axial velocity has monotone decreasing variations in the increasing z -direction, while we observe a local maximum of u_z near the position ($r/R = 0.9, z/H = 0.9$). The structure of the jet-like shear layer appears therefore modified by the presence of the free surface.

The distribution of contours of u_z at the free surface $z = H + \eta$ again reflects well the calculated free surface elevation shown in Fig. 8.4. For instance, the local positive extrema of η at $r/R \simeq 0.5$, and the local negative extrema at $r/R \simeq 0.4$ and $r/R \simeq 0.6$ are well predicted by the variations of u_z at the free surface.

8.4.3 Free-surface flow fields

All the previous results in this chapter and the previous one, dealing with the transitional case (c) reveals a complex flow dynamics due to instabilities developing from a steady stable flow similar to the steady laminar case (b). The study of the rms fluctuations of the flow fields at the free surface presented in Sec. 7.4.5 revealed the existence on an annular region with $0.3 \leq r/R \leq 0.4$, where the fluctuations of u_r , u_θ and Γ are intense. This region was related to the interfacial zone Υ and in the sequel both of these zones will be indifferently denoted by Υ . The future statistical analysis of the flow samples corresponding to case (c) will allow the study of the rms fluctuations of u_z at the free surface. We expect to have intense rms fluctuations of u_z in Υ , given the very clear and unsteady deformation of the free surface in Fig. 8.4 for $r/R \simeq 0.4$.

Figure 8.10 presents the flooded contours of the three cylindrical velocity components and of Γ on the deformed free surface for two different three-dimensional view angles. Besides the esthetically pleasing character of these pictures, it is noteworthy focusing our comments on the last row associated to the axial angular momentum Γ . Four radial jets (two groups of two jets) are visible at the free surface. The two groups of two jets are of different intensity and the most intense one leads to more important surface deflections in the region Υ . This observation can be justified as follows: when the radial free-surface jet of angular momentum impinges on the inner fluid in quasi-solid-body-rotation, the larger part of momentum is redirected downward, while a non-negligible part of it is redirected upward thereby deforming the free surface.

8.4.4 Study of some nonlinear convective terms

Before concluding this study of the moving-free-surface swirling flow, we present the variations of some radial and azimuthal nonlinear terms at the free surface. The magnitude of the terms $NLrk$ and $NLtk$, $k = 1, 2, 3$ —see Table 8.2 for mathematical expressions—has been calculated along a radial line ($r, \theta = 0, z = H + \eta$) that follows the shape of the free surface. These results are compared to those corresponding to the flat-and-fixed free-surface case obtained in Chapter 7, Sec. 7.4.4, for cases (a) – (c). Theses radial variations of the terms in Table 8.2 are reported in Fig. 8.11 for cases (a) – (b) and in Fig. 8.12 for cases (b) – (c). The goal of the study in this section is to highlight the differences in those terms when considering the moving-free-surface model as opposed to the flat-and-fixed one, denoted as “FS” and “SF” respectively in Figs. 8.11 & 8.12.

| Name | Expression | Name | Expression |
|------|--|------|---|
| NLr1 | $-u_r \frac{\partial u_r}{\partial r}$ | NLt1 | $-u_r \frac{\partial u_\theta}{\partial r}$ |
| NLr2 | $+\frac{u_\theta^2}{r}$ | NLt2 | $-\frac{u_r u_\theta}{r}$ |
| NLr3 | $-u_z \frac{\partial u_r}{\partial z}$ | NLt3 | $-u_z \frac{\partial u_\theta}{\partial z}$ |

Table 8.2: Name definitions of different terms appearing in the momentum budget equations (7.25)–(7.27).

Starting first with the term $NLr1 = -u_r \partial u_r / \partial r$, one should observe no substantial change in the variations trend, but for all three Reynolds numbers the “FS” terms have a reduced magnitude compared to their “SF”

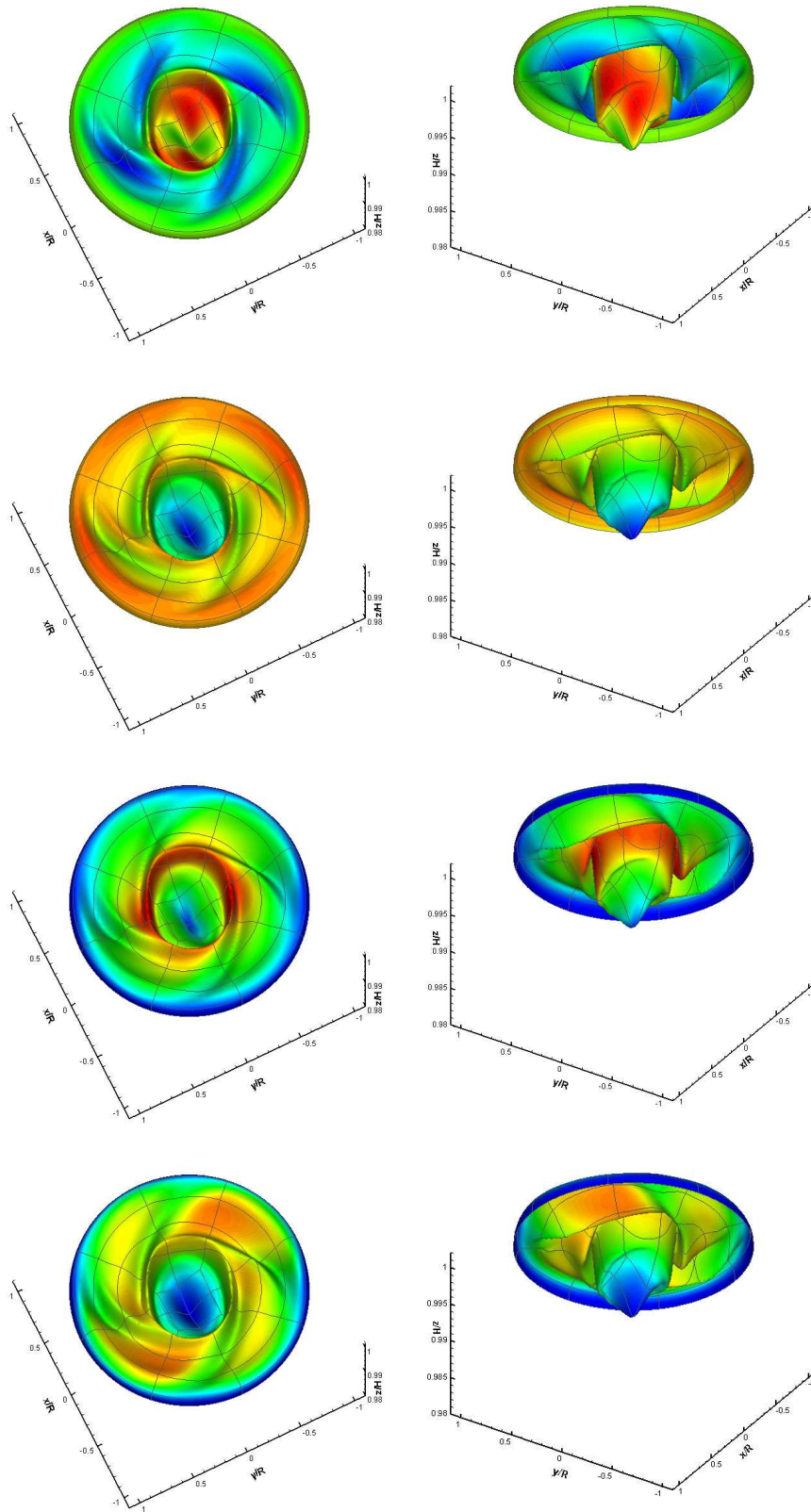


Fig. 8.10: Contours on the free surface $z = H + \eta$ for the case $\Lambda = 1$ and $Re = 6000$. First row: u_r ; Second row: u_z ; Third row: u_θ ; Fourth row: $\Gamma = ru_\theta$. Left column: high-angle view; Right column: low-angle view. Contour levels are the same as those in Fig. 8.8 & Fig. 8.9. The spectral element grid appears in solid dark-grey line to improve the 3D visualization.

counterparts. The flat-and-fixed free surface assumption used in Chapter 7 leads to a systematic over-estimation of the radial nonlinear term $NLr1$.

Exactly the same analysis and comments can be made for the radial variations of the centrifugal acceleration $NLr2 = u_\theta^2/r$. In addition, it has been pointed out in Sec. 7.4.4 for case (c), the appearance of a local minimum for the centrifugal acceleration in the interfacial zone Υ . This local minimum is still observable for the “FS” term $NLr2$, and it is even more pronounced and affects a broader radial interval $0.05 \leq r/R \leq 0.45$.

By definition, the nonlinear term $NLr3 = -u_z \partial u_r / \partial z$ vanishes at the free surface when considering the flat-and-fixed free surface hypothesis. For cases (a)–(b), the magnitude of $NLr3$ is extremely small compared to $NLr1$ and $NLr2$, Consequently, we can conclude to a very limited influence of this term in the flow dynamics, even for case (c) at $Re = 6000$. The low magnitude of the axial velocity at the free surface seems responsible for this fact. Again, exactly the same analysis and comments can be made for the azimuthal term $NLt3 = -u_z \partial u_\theta / \partial z$.

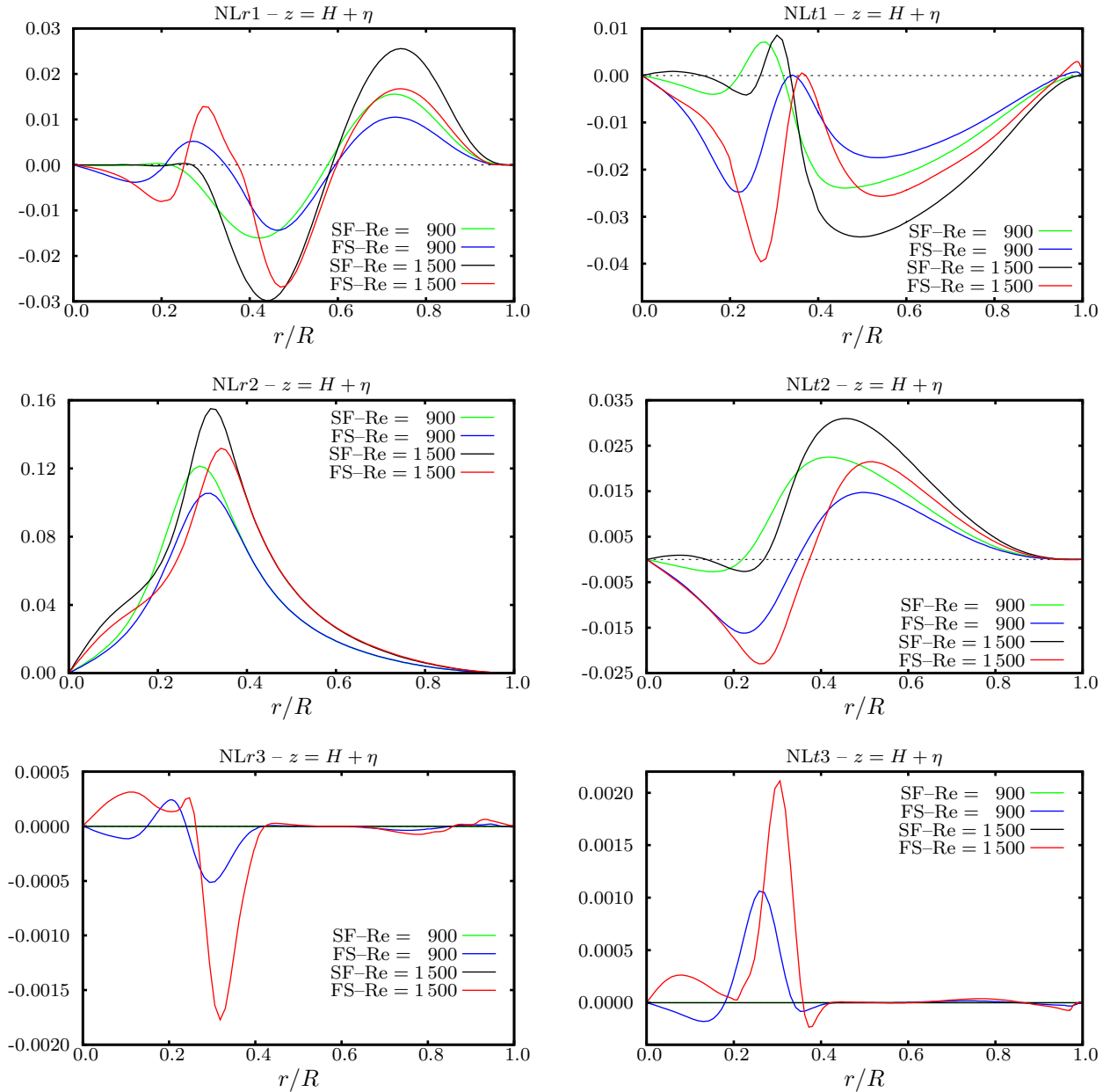


Fig. 8.11: Variations at the free surface of nonlinear terms along a radial line that follows the shape of the free surface. Cases (a) – (b). Left column: terms $NLrk$, $k = 1, 2, 3$; Right column: terms $NLtk$, $k = 1, 2, 3$. “SF” stands for stress-free and refers to the flat stress-free model and “FS” stands for free surface. The terminology refers to Tab. 8.2.

On the contrary to what have been observed for the radial terms $NLr1$ and $NLr2$, the azimuthal terms $NLt1$ and $NLt2$ have their first local minimum in the interval $0.2 \leq r/R \leq 0.4$, under-estimated in the flat-and-fixed free surface framework. For case (c) at $Re = 6000$, the “SF” term $NLt1$ shows a local maximum instead of a high-magnitude local minimum found for the “FS” $NLt1$ term. In addition, the Coriolis term $NLt2$ is globally under-estimated in the flat-and-fixed case.

All the results presented in this section confirm some deficiencies of the flat-and-fixed free surface model when dealing with some nonlinear terms appearing in the governing equations. These deficiencies are obviously more important at the free surface than closer to the rotating disk.

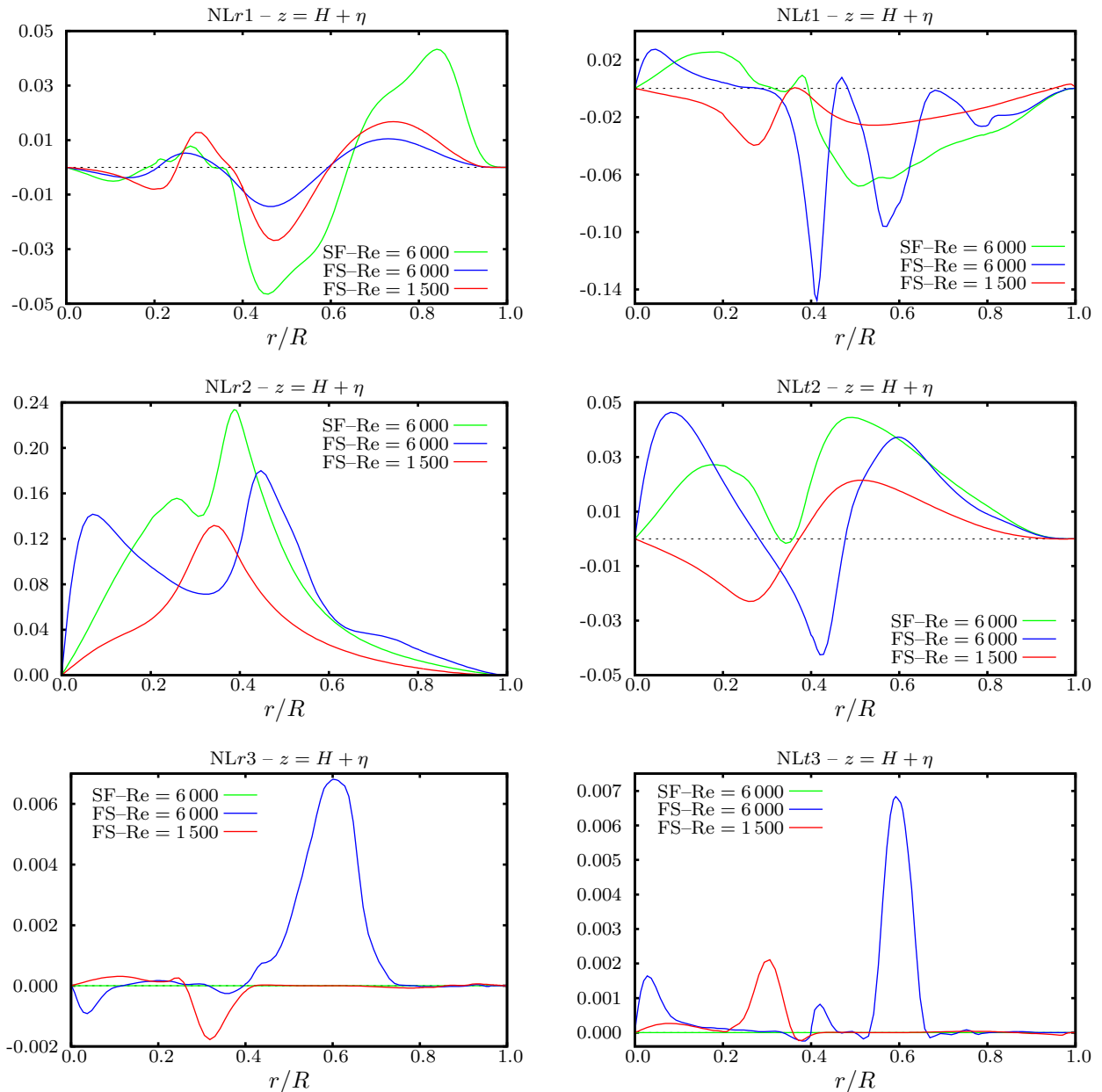


Fig. 8.12: Variations at the free surface of nonlinear terms along a radial line that follows the shape of the free surface. Cases (b) – (c). Left column: terms $NLrk$, $k = 1, 2, 3$; Right column: terms $NLtk$, $k = 1, 2, 3$. “SF” stands for stress-free and refers to the flat stress-free model and “FS” stands for free surface. The terminology refers to Tab. 8.2.

8.5 Conclusions

The incompressible flow of a viscous fluid enclosed in a cylindrical container with a moving free surface and driven by the constant rotation of the bottom wall has been thoroughly investigated in this chapter. The top surface of the cylindrical cavity is left open with a clean free surface subject to a kinematic and dynamic boundary conditions. No-slip conditions are imposed on the side-wall and on the rotating bottom end-wall by means of a regularized angular velocity profile.

In the present chapter, new flow states have been investigated based on a fully three-dimensional solution of the Navier–Stokes equations for the free-surface cylindrical swirling flow, using a moving-grid technique in the arbitrary Lagrangian–Eulerian framework. The dynamic boundary condition is automatically incorporated into the complete weak formulation of the problem. This automatic imposition of this dynamic boundary condition through the weak formulation of the problem is one of the most attractive feature of the newly-developed numerical method. Along the same line, the specific choice of the ALE kinematics allows to automatically account for the kinematic boundary condition. To our knowledge, the present study delivers the first results for this free-surface swirling flow problem.

Three different cases corresponding to three different values of the Reynolds number have been considered, while fixing $\Lambda = 1$. The shape of the free surface leads globally to a deep trough around the axis generated by the sucking effect of the Ekman layer above the rotating disk. A small crest ring appears due to the impingement of the tubular wall-jet onto the free surface. The location of the vortex breakdown bubble influences locally the shape of the free surface. At $Re = 6000$, the shape of the free surface loses its axisymmetry and reveals secondary smaller crests and troughs in the interfacial region Υ . For all Re , a smaller recirculation bubble forms near the contact line and the axial velocity component is the most affected by the motion of the free surface. The distribution of axial velocity at the free surface is in good agreement with the free-surface shapes calculated. In the highest-Reynolds-number case considered, the analysis of the flow at the free surface reveals the presence of two groups of two radial jets of axial angular momentum, which are impinging onto the inner core in quasi-solid-body rotation.

The study presented in this chapter needs to be supplemented with a proper statistical analysis to analyze the influence of the moving free surface on the mean flow and on the rms fluctuations. More specifically, the rms fluctuations of the axial velocity component u_z at the free surface should reveal an intense activity in the interfacial zone Υ , where the unstable modes are active.

Part V

Summary and conclusions

Chapter 9

Summary and conclusions

9.1 Outcomes and summary

The contributions of the present research work are in direct relation with the motivations and objectives reported in the Introduction, in Chapter 1. The description of the outcomes and summary of this work follows the structure of the dissertation: (1) the developments of the numerical method, (2) the turbulent internal lid-driven cavity flow, and (3) the free-surface transitional swirling flow in a cylindrical cavity. The details below are gathered from the multiple conclusions presented at the end of each chapter and appendix. They are aimed at providing the reader with a global review of the various outcomes in the various fields of study covered in this dissertation.

A numerical model for solving two- and three-dimensional moving-boundary problems such as free-surface flows or fluid-structure interaction is proposed. This model relies on a moving-grid technique to solve the Navier–Stokes equations expressed in the arbitrary Lagrangian–Eulerian kinematics and discretized by the spectral element method. A detailed analysis of the continuous and discretized formulations of the general problem in the ALE frame, with non-homogeneous and unsteady boundary conditions is presented. Particular emphasis is put on the weak formulation and its semi-discrete counterpart. The moving-grid algorithm which is one of the key ingredient of our numerical model, is based on the computation of the ALE mesh velocity with the same accuracy and numerical technique as the fluid velocity. The coupling between the Navier–Stokes computation and the one for the mesh velocity is effective through the problem boundary conditions. It is noteworthy that the coupling in the interior Navier–Stokes computation is effective through the modified convective term which is induced by what is happening at the boundaries. Three numerical test results are presented in the two particular cases of interest, namely fluid-structure interactions and free-surface flows. First the influence of the deformation of the grid on the accuracy of the numerical model is evaluated. In a second problem, two motions (translation and rotation) of a cylinder immersed in a fluid is computed. Lastly, large-amplitude sloshing in a three-dimensional tank is simulated. The results obtained are showing very good with the theoretical results when available, therefore leading to a validation of our numerical model. A novel isochoric moving-grid technique and mesh-transfer technique for spectral element grids have been presented and have allowed to automatically enforce the geometric conservation laws. Both of these techniques are the corner-stones of our computations of transitional and turbulent free-surface flows using spectral element method. Part of the work was to ensure that these two techniques have no effect on the exponential rate of convergence, the main reason of our choice of the Legendre spectral element method. We have obtained positive results all along the extensive series of tests carried out to verify the behavior of this rate of convergence.

The long-term integration results of two LES of the lid-driven cubical cavity flow at a Reynolds number of 12 000 is presented for two dynamic subgrid-scale models, namely a dynamic Smagorinsky model and a dynamic mixed model. These simulations are based on an accurate spectral-element spatial discretization, having two times less points per space direction than the direct numerical simulation reference result from Leriche & Gavrilakis [155]. All filtering levels introduced in both SGS modelings rely on explicit modal filters in the spectral space, retaining C^0 -continuity of the numerical solution of the filtered Navier–Stokes equations. An additional nodal filter was used to stabilize both LES. Time-averaging is shown to be equivalent to ensemble-averaging, with respect to the global precision level of the numerical integration. Partial simulation results using the UDNS and the Smagorinsky model as subgrid-scale models, have served to prove the necessity of a dynamic SGS procedure. Full LES results for both dynamic models show very good agreement with the DNS reference results. The agreement with the experimental reference results from Prasad & Koseff [201] is qualitatively good. At a Reynolds number of 12 000, the lid-driven cavity flow is placed in a locally turbulent regime and such turbulent flow is proved to be highly inhomogeneous in the secondary-corner regions of the cavity where turbulence production and dissipation are important. The maximum production of turbulence is found to be located in the downstream-corner-eddy region just above the bottom wall. An analysis of the spectra of turbulent quantities at this point allowed us to determine the distribution of the scales of the turbulent structures convected

past this maximum. Moreover, both LES are able to capture the coherent counter-rotating pair of vortices which are mainly responsible for the peaks of turbulence production still at this point. LES-DSM shows globally more intense and better results than the LES-DMM in this matter. Small-scales turbulent structures are located indirectly by studying the regions of intense turbulent energy dissipation rate ε . The subgrid-viscosity field is shown to be strongly correlated to ε in the turbulent areas of the flow, but the clipping procedure—necessary for stabilizing the numerics—imposed to the dynamic parameters strongly diminishes this correlation in the intense turbulent zones. Subgrid-scales activity is analyzed and the higher SGS activity is associated with the LES-DMM. Helical properties of the flow were investigated. Typical helical coherent structures are identified in the secondary-corner regions. These structures appear to be correlated to the turbulent energy dissipation rate ε . The relative helicity spectra is shown to be decreasing at small scales, which is in agreement with the theoretical results from Borue & Orszag [31] for the three-dimensional isotropic inhomogeneous turbulence.

LES of Newtonian incompressible fluid flows with ADM based on the van Cittert method using Legendre-SEM have been performed. A coupling with a dynamic mixed scale model is introduced. The coupling of the lid-driven cubical cavity flow problem at Reynolds number of 12 000 with the SEM having very low numerical dissipation and dispersion appears to be a well suited framework to analyze the accuracy of the proposed subgrid model. The filtering operation is performed in a spectral modal space, generated by a hierarchical basis using the Legendre polynomials, through the application of a specifically designed transfer function. This transfer function is constructed in order to ensure continuity across elements, conservation of the constants, invertibility of the filter and to perform low-pass filtering. From the computation viewpoint, the filtering technique presented in Chapter 5, is the essential link between the SEM and ADM-based subgrid models. The validation of the deconvolution procedure performed using a DNS velocity sample, shows that the van Cittert method is convergent. Accounting for the reduced sampling and integration time, the LES performed with ADM-DMS show good agreement with the reference results. More precisely, first- and second-order statistics are in good agreement when compared to their DNS counterparts. Results for the Reynolds stresses production, coupling first- and second-order statistical moments, are also well predicted using this new model even with such reduced sampling. The analysis of the results obtained with DMS allows us to clearly identify the improvement induced by coupling ADM with DMS. Subgrid activity has been analyzed showing a qualitative correlation with the localization of small-scale structures in the cavity depicted in Chapter 4. The importance of the subgrid kinetic energy as compared to the kinetic energy of the resolved field highlights the essential need for an appropriate subgrid modeling. Furthermore, regions of backscatter are identified by ADM-DMS. All the presented results emphasize the efficiency of ADM-DMS when dealing with laminar, transitional and turbulent flow conditions such as those occurring in the lid-driven cubical cavity flow at $Re = 12\,000$.

A new interpretation of approximate deconvolution models (ADM) when used with implicit filtering as a way to approximate the projective grid filter is given. Consequently, a new category of subgrid models, the grid filter models (GFM) is defined. ADM appear as a particular case of GFM since only approximate deconvolution is achieved. GFM can be either used with the standard filtered Navier–Stokes equations or with the formulation commonly used with ADM. The latter formulation requires an additional assumption leading to an incomplete modeling of the subgrid scales. The GFM approach gives a theoretical justification to the use of ADM without explicit filtering of the solution and explains how the use of ADM works in this context. This viewpoint allows to consider a new way of designing the convolution filter which has to approximate the grid filter and therefore a new way of improving such subgrid models. It has also been proved that the deconvoluted formulation, usually used with ADM, leads to an under-dissipative character of the subgrid model and explains the need of additional dissipative terms. Conversely, when using the filtered formulation, no additional term is needed which is of great relevance considering the confined nature of the flow and the high-order numerical method used. The GFM approach also allows to consider a more realistic methodology for *a priori* validations and its validity extends beyond the limited scope of incompressible Newtonian fluid flows considered in this chapter. LES of compressible and visco-elastic fluid flows can also be considered using GFM. From a numerical viewpoint, GFM can be implemented with all numerical methods allowing filtering operations only needed to compute the subgrid commutator.

The incompressible flow of a viscous fluid enclosed in a cylindrical container with an open top flat surface and driven by the constant rotation of the bottom wall has been thoroughly investigated. The top surface of the cylindrical cavity is left open with a stress-free boundary condition imposed on it. No-slip condition imposed on the side-wall and also on the rotating bottom end-wall by means of a regularized angular velocity profile. More specifically, the stress-free top surface is, in first approximation, maintained fixed and flat. New flow states have been investigated based on a fully three-dimensional solution of the Navier–Stokes equations for the free-surface cylindrical swirling flow, without resorting to any symmetry property unlike all other results available in the literature. To our knowledge, the present study delivers the most general available results for this flat-free-surface problem due to its original mathematical treatment. Five different cases corresponding

to different pairs of governing parameters (Λ, Re) have been considered. The Reynolds regime corresponds to transitional flows with some incursions in the fully laminar regime. Both steady and unsteady non-oscillatory swirling flows are considered with a particular emphasis on the case ($\Lambda = 1, \text{Re} = 6000$). Of great concern to this study is the question of space resolution. This is particularly important for the bifurcated case at $\text{Re} = 6000$. Convergence tests in space and time have been carried out on this upmost problematic case, and optimal values of the polynomial order and time-step is deduced. The evolution of the total kinetic energy of this open flow has been carefully studied for increasing Reynolds numbers and has been compared to the results for the closed swirling flow. The presence of the free surface on the top of the cylinder is found to strongly modify the observed trend: the total kinetic energy is increased with Re in the open cylinder case, while the converse is observed in the closed cylinder case. A physical analysis of the energetic action of the surface layer below the free surface allows to justify the above results. A comprehensive physical description of all flow states has been given with particular emphasis on the vortex breakdown bubbles and on the structure of the vortex lines. The unsteady case at $\text{Re} = 6000$ has retained more attention, given its unsteady transitional character. The mean flow and the corresponding rms fluctuations have been calculated and the results analyzed accordingly. Based on 24 flow samples equally-distributed in time, the general dynamics of the recirculation bubbles has been determined and described. The momentum transfers in the radial, azimuthal and axial directions have been studied along various one-dimensional lines. For the transitional case at $\text{Re} = 6000$, the flow in an inner cylindrical core is in solid-body rotation, while the outer radial layer is dominated by the jet-like shear layer along the tubular side-wall. This axial wall-jet is turned into a radial jet of angular momentum, which prevails all the way up to the free surface. The impingement of this radial jet onto the inner cylindrical core in solid-body rotation leads to the development of unstable azimuthal modes. The nonlinear terms, which includes a Coriolis effect, responsible for the development of these unstable modes have been found using the azimuthal momentum imbalance below the free surface. These unstable modes seem to take the form of even-order azimuthal rotating waves.

The incompressible flow of a viscous fluid enclosed in a cylindrical container with a moving free surface and driven by the constant rotation of the bottom wall has been thoroughly investigated in this chapter. The top surface of the cylindrical cavity is left open with a clean free surface subject to a kinematic and dynamic boundary conditions. No-slip conditions are imposed on the side-wall and on the rotating bottom end-wall by means of a regularized angular velocity profile. In the present chapter, new flow states have been investigated based on a fully three-dimensional solution of the Navier–Stokes equations for the free-surface cylindrical swirling flow, using a moving-grid technique in the arbitrary Lagrangian–Eulerian framework. The dynamic boundary condition is automatically incorporated into the complete weak formulation of the problem. This automatic imposition of this dynamic boundary condition through the weak formulation of the problem is one of the most attractive feature of the newly-developed numerical method. Along the same line, the specific choice of the ALE kinematics allows to automatically account for the kinematic boundary condition. To our knowledge, the present study delivers the first results for this free-surface swirling flow problem. Three different cases corresponding to three different values of the Reynolds number have been considered, while fixing $\Lambda = 1$. The shape of the free surface leads globally to a deep trough around the axis generated by the sucking effect of the Ekman layer above the rotating disk. A small crest ring appears due to the impingement of the tubular wall-jet onto the free surface. The location of the vortex breakdown bubble influences locally the shape of the free surface. At $\text{Re} = 6000$, the shape of the free surface loses its axisymmetry and reveals secondary smaller crests and troughs in the interfacial region Υ . For all Re , a smaller recirculation bubble forms near the contact line and the axial velocity component is the most affected by the motion of the free surface. The distribution of axial velocity at the free surface is in good agreement with the free-surface shapes calculated. In the highest-Reynolds-number case considered, the analysis of the flow at the free surface reveals the presence of two groups of two radial jets of axial angular momentum, which are impinging onto the inner core in quasi-solid-body rotation.

9.2 Outlook and perspectives

The most logical straightforward extension to this thesis work would be to consider free-surface flows in a turbulent regime. This could easily be obtained by increasing the Reynolds number in the free-surface swirling flows studied in Part IV. One ultimate goal could be to better understand the mechanisms justifying the existence of long-lasting vortical structures observed at a free surface. For that reason it would be interesting to focus on the high-Froude-number regime as it corresponds to significant deformations of the free surface dominated by nonlinearities. From a practical viewpoint, large-eddy simulations using the subgrid models developed in Part III could be carried out. These LES should be coupled to the numerical method developed in Chapter 3 to handle moving-boundary problems in the spectral element framework. It is important to note that such coupling is far from being straightforward. Indeed, the novel numerical method detailed in Chapter 3 relies on the ALE kinematics and on a moving-grid technique, which modify the structure of the nonlinear term in the Navier–

Stokes equations, see Eq. (3.12). In addition, large-eddy simulations rely on scale-separation procedure, which is ultimately performed by considering the application of a low-pass filter to the Navier–Stokes equations. This highlights a crucial issue faced with such coupling: how does the presence of the mesh velocity in the nonlinear convective term influence the dynamics of the subgrid scales and subgrid modeling in general?

The present research work on turbulent flows and free-surface flows addresses the particular case of Newtonian fluids. The numerous aforementioned developments and achievements in large-eddy simulation of turbulent flows and free-surface flows make a very good framework to start investigating some phenomena in non-Newtonian fluids. Viscoelastic flows are of great importance for complex biological and engineering applications. When compared to Newtonian fluids, they exhibit typical exotic flow phenomena induced by their peculiar chemical composition. The study of this new source of hydrodynamics instabilities is highly challenging and interesting. In the near future, two specific viscoelastic problems could be studied. The first one is the recently discovered elastic turbulence phenomenon. The second one deals with elastic-capillary instabilities at the free surface of a viscoelastic fluid. For both problems, advanced analytical modeling supplemented with numerical simulations using high-order methods could be used to gain invaluable insight into these two phenomena.

The phenomenon of elastic turbulence in viscoelastic fluid flows has been discovered very recently by Groisman and Steinberg [99–101]. Irregular flows excited by the elastic stresses in polymer solutions can lead to efficient mixing at very low Reynolds number. The presence of polymers affects the laminar flow stability. Consequently, the flow stretches further the polymer molecules, and in a retroactive process becomes increasingly turbulent until some saturated dynamic state is reached. Transition to elastic turbulence has been observed at extremely small Reynolds number (order 10^{-3}). Although the Reynolds number can be arbitrary small, the resulting flow displays all the main features of developed turbulence, as the enhancement of mixing and the power law spectrum of velocity fluctuations. The objective of such study would be to understand how the polymers destabilize the laminar flow by increasing the flux of energy from large eddies to small scales in the energy cascade using in the first place an Oldroyd-B constitutive model. First, a linear stability analysis could be carried out to establish the influence of both the Reynolds and the Deborah numbers on the onset of this elastic instability. As a second step, one could perform series of numerical simulations of an Oldroyd-B flow in the multiple smoothly connected half-rings channels originally designed by Groisman and Steinberg for their experiments [99–101]. This will allow to analyze the influence of the Deborah number on the energy spectrum and hopefully could contribute significantly to the understanding of elastic turbulence given its important applications in mixing at low Reynolds number in microfluidics devices.

The penetration of a long gas bubble through a tube filled with a Newtonian fluid has been extensively studied in the past. To date very little numerical work has been done to increase our understanding of non-Newtonian fluids behavior in such flows. It would be deeply interesting to study such nonlinear systems in order to understand their pattern selection process near the elastic instability onset. Building on this thesis work, we propose performing steady numerical simulations using the ALE-moving-grid spectral-element solver developed. It will allow for an accurate way of imposing the free-surface boundary conditions, which include the surface-tension effects. These capillary effects at the interface are in competition with the elastic effects in the bulk of the viscoelastic fluid. The objective of this prospective work would be twofold. On one hand, it would focus on the near-interface region of the flow to quantitatively describe the properties of what can be called an elastic surface sublayer. A thorough analysis of this fine interfacial physics would be possible with different simulations corresponding to varying capillary and Weissenberg numbers. On the other hand, it would aim at confirming the very limited influence of the capillary effects on this viscoelastic flow far from the interface. Such study is motivated by important engineering applications, including enhanced oil recovery.

Part VI

Appendices

Appendix A

Mesh update techniques for free-surface flow solvers

This appendix presents a novel mesh-update technique for unsteady free-surface Newtonian flows using spectral element method and relying on the arbitrary Lagrangian–Eulerian kinematic description for moving the grid. Selected results showing compatibility of this mesh-update technique with spectral element method are given.

A.1 Introduction

Incompressible free-surface flows are encountered in a wide range of engineering and environmental flows. In the nineties the more specific case of transitional and turbulent free-surface flows started to be investigated with numerical computation based on high-order methods [122, 125]. In our work, we aim at computing direct numerical simulations of unsteady, incompressible and Newtonian turbulent free-surface flows by using the spectral element method (SEM) [172, 194]. The choice of interface-tracking technique was made to ensure an accurate description of the free surface.

This appendix highlights the computational techniques developed for simulating incompressible free-surface flows using the SEM. These techniques include the arbitrary Lagrangian–Eulerian (ALE) formulation [64, 121, 205], mesh update and re-meshing methods [106, 134].

This appendix is organized as follows. The governing equations in the ALE framework for general free-surface flows developed in Section 3.2 are recalled and summarized in Section A.2. Then the discretization methods and numerical technique are presented in Section A.3. Sections A.4 and A.5 are dedicated to the moving-grid technique and the mesh-transfer operation, respectively. Section A.6 delivers conclusions and details of the remeshing algorithms are given in Annexes 1 and 2 in Sections A.7–A.8

A.2 Governing Equations

A moving boundary-fitted grid technique has been chosen to simulate the free surface in our computations. This choice of a *surface-tracking* technique is primarily based on accuracy requirements. With this group of techniques, the grid is configured to conform to the shape of the interface, and thus adapts continually (at each time-step) to it and therefore provides an accurate description of the free surface to express the related kinematic and dynamic boundary conditions.

The free-surface incompressible Newtonian flows that we have considered are governed by the Navier–Stokes equations comprising the momentum equation and the divergence-free condition. In the arbitrary Lagrangian–Eulerian (ALE) formulation, a mixed kinematic description is employed: Lagrangian description of the free surface $\partial\Omega_t^\sigma$, Eulerian description of the fixed domain boundaries $\partial\Omega_t^D$ and mixed description of the internal fluid domain $\Omega(t)$, subset of \mathbb{R}^d with $d = 2, 3$ the space dimension, t referring to the time as the fluid domain is changing when its boundaries are moving. Let us denote by Ω_0 a reference configuration (for instance the domain configuration at initial time $t = t_0$). The system evolution is studied in the time interval $I = [t_0, T]$. The position of a point in the current fluid domain $\Omega(t)$ is denoted by \mathbf{x} (Eulerian coordinate) and in the reference frame Ω_0 by \mathbf{Y} (ALE coordinate). Let \mathcal{A}_t be a family of mappings, which at each $t \in I$ associates a point $\mathbf{Y} \in \Omega_0$ to a point $\mathbf{x} \in \Omega_t$:

$$\mathcal{A}_t : \Omega_0 \subset \mathbb{R}^d \rightarrow \Omega_t \subset \mathbb{R}^d, \quad \mathbf{x}(\mathbf{Y}, t) = \mathcal{A}_t(\mathbf{Y}). \quad (\text{A.1})$$

\mathcal{A}_t is assumed to be continuous and invertible on $\overline{\Omega_0}$ and differentiable almost everywhere in I . The inverse of

the mapping \mathcal{A}_t is also continuous on $\bar{\Omega}_0$. With these notations the set of equation reads:

$$\frac{\partial \mathbf{u}}{\partial t} \Big|_{\mathbf{Y}} + (\mathbf{u} - \mathbf{w}) \cdot \nabla_{\mathbf{x}} \mathbf{u} = -\nabla_{\mathbf{x}} p + 2\nu \nabla_{\mathbf{x}} \cdot \mathbf{D}_{\mathbf{x}}(\mathbf{u}) + \mathbf{f} \quad \text{in } \Omega(t), \quad (\text{A.2})$$

$$\nabla_{\mathbf{x}} \cdot \mathbf{u} = 0 \quad \text{in } \Omega(t), \quad (\text{A.3})$$

with $\mathbf{u}(\mathbf{x}, t)$ the velocity field, $p(\mathbf{x}, t)$ the pressure field (normalized by the constant density ρ), $\mathbf{D}_{\mathbf{x}}(\mathbf{u}) = \frac{1}{2}(\nabla_{\mathbf{x}} \mathbf{u} + \nabla_{\mathbf{x}} \mathbf{u}^T)$ the rate-of-deformation tensor, ν the kinematic viscosity of the fluid and \mathbf{f} the body force. The ALE mesh velocity $\mathbf{w}(\mathbf{x}, t)$ appearing in (A.2) is defined as

$$\mathbf{w}(\mathbf{x}, t) = \frac{\partial \mathbf{x}}{\partial t} \Big|_{\mathbf{Y}} = \frac{\partial \mathcal{A}_t}{\partial t} \Big|_{\mathbf{Y}}. \quad (\text{A.4})$$

Surface tension effects are assumed to be negligible. The associated boundary conditions are:

- the kinematic boundary condition on $\partial\Omega_t^{\mathcal{F}}$:

$$\mathbf{u} \cdot \hat{\mathbf{n}} = \mathbf{w} \cdot \hat{\mathbf{n}}, \quad (\text{A.5})$$

$\hat{\mathbf{n}}$ being the local outward unit normal to the free surface;

- the dynamic boundary condition on $\partial\Omega_t^{\mathcal{F}}$:

$$-p\hat{\mathbf{n}} + 2\nu \mathbf{D}_{\mathbf{x}}(\mathbf{u}) \cdot \hat{\mathbf{n}} = \mathbf{0}, \quad (\text{A.6})$$

assuming an inviscid air and zero ambient pressure;

- homogeneous Dirichlet boundary condition on $\partial\Omega_t^{\mathcal{D}}$:

$$\mathbf{u} = \mathbf{w} = \mathbf{0}. \quad (\text{A.7})$$

In addition to the set of governing equations (A.2)–(A.7), the closure of this free-surface problem based on a moving-grid formulation requires one more equation governing the evolution of the mesh velocity \mathbf{w} in the internal fluid domain $\Omega(t)$. The boundary values of \mathbf{w} being prescribed by the equations (A.5) and (A.7) on the boundary $\partial\Omega_t^{\mathcal{F}} \cup \partial\Omega_t^{\mathcal{D}}$ of the fluid domain. This last governing equation for \mathbf{w} will be presented in detail in Section A.4.

As our focus is on transient problems, proper initial conditions at time $t = t_0$ for the fluid velocity \mathbf{u} and for the mesh velocity \mathbf{w} have to be provided. The initial fluid velocity must satisfy the divergence-free condition and the values of the initial mesh velocity have to be given together with the initial shape of the free surface.

Based on the strong formulation of this free-surface problem given above, one can derive the more appropriate weak transient ALE formulation:

Find $(\mathbf{u}(t), p(t)) \in H_{0,\mathcal{D}}^1(\Omega(t))^d \times L^2(\Omega(t))$ such that for almost every $t \geq t_0$

$$\begin{aligned} \frac{d}{dt} \int_{\Omega(t)} \mathbf{u} \cdot (\hat{\mathbf{v}} \circ \mathcal{A}_t^{-1}) d\Omega + \int_{\Omega(t)} (\hat{\mathbf{v}} \circ \mathcal{A}_t^{-1}) \cdot \nabla_{\mathbf{x}} \cdot [\mathbf{u}\mathbf{u} - \mathbf{u}\mathbf{w}] d\Omega = \\ \int_{\Omega(t)} (p \nabla_{\mathbf{x}} \cdot (\hat{\mathbf{v}} \circ \mathcal{A}_t^{-1}) - 2\nu \mathbf{D}_{\mathbf{x}}(\mathbf{u}) : \nabla_{\mathbf{x}} (\hat{\mathbf{v}} \circ \mathcal{A}_t^{-1})) d\Omega \\ + \int_{\Omega(t)} \mathbf{f} \cdot (\hat{\mathbf{v}} \circ \mathcal{A}_t^{-1}) d\Omega \quad \forall \hat{\mathbf{v}} \in H_{0,\mathcal{D}}^1(\Omega_0)^d, \end{aligned} \quad (\text{A.8})$$

and

$$- \int_{\Omega(t)} q \nabla_{\mathbf{x}} \cdot \mathbf{u} d\Omega = 0 \quad \forall q \in L^2(\Omega(t)). \quad (\text{A.9})$$

with the functional space $H_{0,\mathcal{D}}^1(\Omega(t))$ defined by

$$H_{0,\mathcal{D}}^1(\Omega(t)) = \{v \in L^2(\Omega(t)), \nabla_{\mathbf{x}} v \in L^2(\Omega(t))^d, v|_{\partial\Omega_t^{\mathcal{F}}} = 0\}.$$

It is worth noting that the weak formulation (A.8)–(A.9) is only valid in our particular case where homogeneous natural and essential boundary conditions, respectively (A.6) and (A.7) are applied to the system.

A.3 Numerical technique and discretization

A classical Galerkin approximation is applied to the set of governing equations in its weak transient ALE form (A.8)–(A.9) on the flow domain $\Omega(t)$, in order to determine the pressure and the fluid velocity, keeping in mind that the mesh velocity is obtained by the moving-grid technique developed in the next section. The Galerkin approximation is then discretized by using the spectral element method with the classical staggered $\mathbb{P}_N - \mathbb{P}_{N-2}$ approach to avoid the development of spurious pressure modes [174]. Discontinuous and continuous approximations are respectively taken for the pressure and fluid velocity. The mesh velocity is discretized using the same polynomial space as the fluid velocity, namely \mathbb{P}_N , based on a Gauss–Lobatto–Legendre (GLL) grid of order N . For the discontinuous approximation of the pressure, a Gauss–Legendre (GL) grid of order $N - 2$ is used. Consequently the ALE Navier–Stokes semi-discrete equations can be derived from (A.8)–(A.9):

$$\frac{d}{dt}(\mathbf{M}\mathbf{u}) + \mathbf{C}(\mathbf{u}, \mathbf{w})\mathbf{u} = -\mathbf{A}\mathbf{u} + \mathbf{D}^T \underline{p} + \underline{\mathbf{F}}, \quad (\text{A.10})$$

$$-\mathbf{D}\mathbf{u} = \mathbf{0}, \quad (\text{A.11})$$

\mathbf{M} denoting the mass matrix, \mathbf{A} the stiffness matrix, \mathbf{D}^T the discrete gradient operator, \mathbf{D} the discrete divergence operator, $\mathbf{C}(\mathbf{u}, \mathbf{w})$ the discrete convective operator depending both on the fluid and mesh velocities and $\underline{\mathbf{F}}$ the discrete body force. The update of the position \mathbf{x} of the mesh points is performed by integrating the following discrete equation:

$$\frac{d\mathbf{x}}{dt} = \mathbf{w}. \quad (\text{A.12})$$

The set of semi-discrete equations (A.10)–(A.12) is discretized in time using a decoupled approach: the linear Stokes computation (linear viscous diffusive term) is integrated based on an implicit backward differentiation formula of order 2, the nonlinear convective term is integrated based on a simple method used by Karniadakis *et al.* [140], consisting in an explicit extrapolation of order 2. Finally the update of the position of mesh points is based on an explicit and conditionally stable Adams–Bashforth of order 3 (AB3).

Lastly the treatment of the pressure relies on a generalized block LU decomposition, using a standard fractional-step method with pressure correction [196, 197].

A.4 Moving-grid technique

As already mentioned in the previous sections, our free-surface flow computations are of interface-tracking type and rely on a moving-grid technique, allowing large amplitude motions of the free surface, generating a grid conforming to the shape of the free surface for an accurate and easy application of the boundary conditions on $\partial\Omega_t^\sigma$. Moreover a description as accurate as possible of the free-surface boundary layer is essential to our work. These points justify by themselves the choice of a moving-grid technique that increases the difficulty of the marginally intractable problem of turbulent viscous flow computations.

The computation of the mesh velocity \mathbf{w} in the internal fluid domain $\Omega(t)$ is the corner-stone of the moving-grid technique developed in the framework of the ALE formulation. The values of the mesh velocity being prescribed on the boundary $\partial\Omega(t) = \partial\Omega_t^\sigma \cup \partial\Omega_t^D$ as expressed by equations (A.5) and (A.7), the evaluation of \mathbf{w} in $\Omega(t)$ can be obtained as the solution of an elliptic equation:

$$\mathcal{E}_\mathbf{x}\mathbf{w} = \mathbf{0} \quad \text{in } \Omega(t). \quad (\text{A.13})$$

This elliptic equation constitutes a classical choice for calculating the mesh velocity [122]. In the present case it is desirable to impose an additional constraint to the mesh velocity problem, in order to ensure the incompressibility of the mesh by imposing a divergence-free condition to \mathbf{w} :

$$\nabla_\mathbf{x} \cdot \mathbf{w} = 0 \quad \text{in } \Omega(t). \quad (\text{A.14})$$

Our choice for the elliptic operator $\mathcal{E}_\mathbf{x}$ is based on the assumption that the motion of the mesh nodes is equivalent to a steady Stokes flow, corresponding physically to an incompressible and elastic motion of the mesh. The boundary-value steady Stokes problem for the mesh velocity can be formulated as follows:

$$\mathbf{w} \cdot \hat{\mathbf{n}} = \mathbf{u} \cdot \hat{\mathbf{n}} \quad \text{on } \partial\Omega_t^\sigma, \quad (\text{A.15})$$

$$\mathbf{w} \cdot \hat{\boldsymbol{\tau}} = 0 \quad \text{on } \partial\Omega_t^\sigma, \quad (\text{A.16})$$

$$\mathbf{w} = \mathbf{0} \quad \text{on } \partial\Omega_t^D, \quad (\text{A.17})$$

where $\hat{\boldsymbol{\tau}}$ is the local unit vector directly orthogonal to $\hat{\mathbf{n}}$, and

$$\nabla_{\mathbf{x}} \cdot \tilde{\boldsymbol{\sigma}} = \mathbf{0} \quad \text{in } \Omega(t), \quad (\text{A.18})$$

$$\nabla_{\mathbf{x}} \cdot \mathbf{w} = 0 \quad \text{in } \Omega(t), \quad (\text{A.19})$$

denoting by $\tilde{\boldsymbol{\sigma}}$ the Cauchy stress tensor of the mesh defined by:

$$\tilde{\boldsymbol{\sigma}} = -\tilde{p}\mathbf{I} + \tilde{\nu}(\nabla_{\mathbf{x}}\mathbf{w} + \nabla_{\mathbf{x}}\mathbf{w}^T), \quad (\text{A.20})$$

with \tilde{p} and $\tilde{\nu}$ being respectively the fictitious mesh pressure and the fictitious kinematic viscosity of the mesh, characterizing the elasticity of the mesh in its motion.

The choice of this boundary-value problem for the mesh velocity has several justifications. Constraining the elliptic equation by a divergence-free condition for \mathbf{w} allows to ensure the conservation of the volume of the spectral elements, condition that is helpful in practice to have rapidly convergent computations [58]. In general the global volume of the computational domain may not be conserved, *e.g.* with an inflow-outflow imbalance, which requires (A.17) to be relaxed. In addition, the mesh velocity \mathbf{w} appears in the convective part of equations (A.2), (A.8) and (A.10), together with the divergence-free fluid velocity \mathbf{u} . Moreover it is worth remembering that the divergence-free condition imposed to \mathbf{w} leads to a conservation of the metrics (the Jacobian being constant in time) when moving the mesh. Finally the unavoidable issue of fulfilling the geometric conservation law (GCL) in the ALE framework [73, 74, 83] is automatically solved when considering a divergence-free mesh velocity as a consequence of the work of Formaggia and Nobile in [83].

From a numerical point of view, the problem corresponding to the set of equations (A.15)–(A.19) is discretized using the SEM, with a staggered grid $\mathbb{P}_N - \mathbb{P}_{N-2}$ for the couple mesh (\mathbf{w}, \tilde{p}) . An Uzawa decoupling technique is employed for the treatment of the fictitious pressure.

Based on the technique described earlier, we have developed the following moving-grid algorithm:

1. Input data: mesh \mathcal{M}_n at $t = t_n$, with nodal coordinates \mathbf{x}_n , fluid velocity \mathbf{u}_n on $\partial\Omega_{t_n}^\sigma$,
2. Step 1: steady Stokes computation of \mathbf{w}_{n+1} by Eqs. (A.15)–(A.19);
3. Step 2: update of the nodal coordinates Eq. (A.12); spectral element vertices are moved according to the AB3 scheme:

$$\mathbf{x}_{n+1} = \mathbf{x}_n + \frac{\Delta t}{12}(23\mathbf{w}_n - 16\mathbf{w}_{n-1} + 5\mathbf{w}_{n-2}); \quad (\text{A.21})$$

4. Creation of the new mesh \mathcal{M}_{n+1} with the new Gauss–Legendre and Gauss–Lobatto–Legendre grids for each new spectral element;
5. Output data: mesh \mathcal{M}_{n+1} at time-step $t = t_{n+1}$, with nodes coordinates \mathbf{x}_{n+1} , mesh velocity \mathbf{w}_{n+1} in $\Omega_{n+1} \cup \partial\Omega_{n+1}$.

Two performance tests have been carried out on a study case where one edge of a squared mesh is deformed by a sine profile. Both of these tests aimed at verifying the spectral element volume conservation that is theoretically imposed by the divergence-free condition on \mathbf{w} . The first test is dedicated to the verification of the global volume conservation, by computing the relative change of the volume of the computational domain when moving the grid from the initial square to the deformed one. For several number of spectral elements and for a polynomial interpolation order ranging from 1 up to 12, the relative change of the volume of the computational domain is found to be smaller than the machine precision. The second test is also devoted to the volume conservation but now from a local perspective and by numerically computing the $L^2(\Omega)$ - and $L^2(\omega)$ -norm of the divergence of the mesh velocity \mathbf{w} for a polynomial interpolation order N ranging from 5 up to 12, where ω is interior of the computational domain made of the spectral of elements of Ω not sharing an edge with $\partial\Omega$. Results are presented on Fig. A.1 and it is found that these norms are exponentially decreasing with N as expected when using a spectral element method [58]. Moreover we can note that the $L^2(\omega)$ -norm of $\nabla \cdot \mathbf{w}$ has a faster rate of convergence than the $L^2(\Omega)$ -norm. This is justified by the fact that the divergence-free constraint cannot easily be enforced at the grid points located in the vicinity of the boundaries of the computational domain Ω .

A.5 Mesh-transfer operation

In the previous section was presented the moving-grid technique used in our work to move the grid points at each time-step, generating a new mesh. Depending on the amplitude of the mesh deformation at each time-step, this technique can be applied during an important number of iterations. Nevertheless the mesh obtained

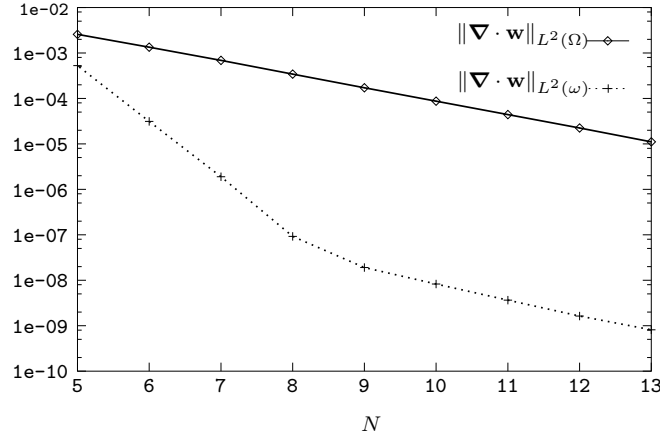


Fig. A.1: L^2 -norms of the divergence of the mesh velocity \mathbf{w} versus polynomial interpolation order N (Log scale).

by moving the grid nodes can be too convoluted therefore affecting the accuracy and the convergence of the simulation. Consequently a re-meshing operation is to be called by a specific control parameter (*e.g.* a discrete Jacobian positiveness criterion [129]) to provide a new mesh topology. Before starting the ALE Navier–Stokes computation at the next time-step on this newly created mesh, it is mandatory to transfer some information from the previous mesh to the new one. The main requirement imposed to this so-called mesh-transfer operation is to conserve the spectral accuracy of the SEM. The information to be transferred comprises six fields: the fluid velocities \mathbf{u}_n , \mathbf{u}_{n-1} and the mesh velocities \mathbf{w}_n , \mathbf{w}_{n-1} , \mathbf{w}_{n-2} (time-integration schemes are of order 2 for \mathbf{u} and 3 for \mathbf{w}) and also the pressure at the current time-step (use of a pressure correction technique). As written in Section A.3, the velocities are expanded over a GLL grid and the pressure over a GL one. Therefore our mesh-transfer technique must be capable of transferring fields defined over GL and GLL grids.

Our mesh-transfer algorithm for GL grids being based on the one for GLL grids, we will start presenting in detail the latter. Let us consider two meshes \mathcal{M}_1 and \mathcal{M}_2 corresponding to different mesh topologies of the same computational domain and the mesh-transfer operation from \mathcal{M}_1 to \mathcal{M}_2 . In the sequel it is assumed that the following decompositions in terms of spectral elements hold:

$$\Omega_i \cup \partial\Omega_i = \bigcup_{e=1}^{E_i} \Omega_i^e \quad \text{for } i = 1, 2. \quad (\text{A.22})$$

As the computational domain remains unchanged, for each spectral element Ω_2^e of \mathcal{M}_2 we have:

$$\Omega_2^e \subset (\Omega_1 \cup \partial\Omega_1) \quad \forall e = 1, \dots, E_2. \quad (\text{A.23})$$

Due to Eq. (A.23) our mesh-transfer technique only requires an interpolation procedure. Let us note the physical location of the set of GLL grid points of a spectral element $\Omega_2^{e_2}$ ($e_2 = 1, \dots, E_2$) by $\{\mathbf{x}_{ij,2}^{e_2}\}$ with ($i = 1, \dots, N_{x,2} + 1; j = 1, \dots, N_{y,2} + 1$), $N_{x,2}$ (resp. $N_{y,2}$) being the order of the polynomial interpolation in the x -direction (resp. y -direction) for the mesh \mathcal{M}_2 (with the same notations, $N_{x,2}$ and $N_{y,2}$ can be different from $N_{x,1}$ and $N_{y,1}$ respectively). The proposed algorithm can be summarized in three steps:

1. Find the spectral element $\Omega_1^{e_1}$ of \mathcal{M}_1 containing $\mathbf{x}_{ij,2}^{e_2}$;
2. Determine the position $\mathbf{r}_1^{e_1}$ of $\mathbf{x}_{ij,2}^{e_2}$ within the parent element $\hat{\Omega}_1^{e_1}$ of $\Omega_1^{e_1}$;
3. Compute the value of the field at the point $\mathbf{x}_{ij,2}^{e_2}$ given $\mathbf{r}_1^{e_1}$, the GLL Lagrangian interpolation basis and the values of the field at the GLL grid points of $\Omega_1^{e_1}$.

The first step causes no difficulty in its implementation as it fully relies on a coarse element positioner coupled to the mapping inversion techniques described hereafter. The second step uses a transfinite interpolation procedure in each spectral element, in order to invert the iso-parametric mapping Φ :

$$\mathbf{r}_1^{e_1} = (r_1^{e_1}, s_1^{e_1}) = \Phi^{-1}(\mathbf{x}_2^{e_2}) \quad \text{with} \quad \mathbf{r}_1^{e_1} \in \hat{\Omega}_1^{e_1} = [-1, 1]^2. \quad (\text{A.24})$$

In practice, the inversion is carried out differently depending on the topology of the spectral element. With quadrangular spectral elements, our algorithm performs a direct analytical inversion of the affine mapping Φ

which is computationally inexpensive and detailed at the end of this appendix in Annex 1. With deformed spectral elements [58], the inversion of Φ relies on the so-called ‘inverse iso-parametric mapping technique’ from Lee and Bathe [151] which is based on a Newton–Raphson type iterative procedure.

Finally in the last step, efficient routines compute the following spectral interpolation:

$$\mathbf{u}(\Phi^{-1}(\mathbf{x}_{ij,2}^{e_2})) = \mathbf{u}(r_1^{e_1}, s_1^{e_1}) = \sum_{k=0}^{N_{1,x}} \sum_{l=0}^{N_{1,y}} \mathbf{u}_{kl} \pi_k(r_1^{e_1}) \pi_l(s_1^{e_1}), \quad (\text{A.25})$$

with $\{\pi_j(\xi)\}_{j=0}^{N_{p,1}}$ and $p = x, y$, the one-dimensional GLL Lagrangian interpolation basis of degree $N_{p,1}$. As said earlier the mesh-transfer technique for GL grids relies on the one for the GLL grids, and is detailed at the end of this appendix in Annex 2. In our simulations, the only GL-interpolated field that has to be mesh-transferred is the pressure field. Therefore, by interpolating the pressure on the GLL grid, then by applying the GLL mesh-transfer operation introduced earlier and finally by interpolating back on the GL grid, we manage to perform the requested operation. It is important to minimize the occurrence of a re-meshing as our mesh-transfer technique is computationally expensive even for quadrangular elements (affine iso-parametric mapping). A more detailed assessment of the performance of this technique is provided at the end of this section.

This mesh-transfer operation has been extensively tested in order to ensure its compatibility with the SEM, regarding its exponential rate of convergence. Tests involving the following two key parameters have been carried out: the polynomial interpolation order N and the amplitude of the change in topology of the grid when re-meshing.

The set-up is presented in Fig. A.2 and is made of a mesh comprising four spectral elements. The change in topology of the mesh is prescribed by moving only the vertex ω (see Fig. A.2) common to all four spectral elements and afterwards the mesh-transfer operation is performed.

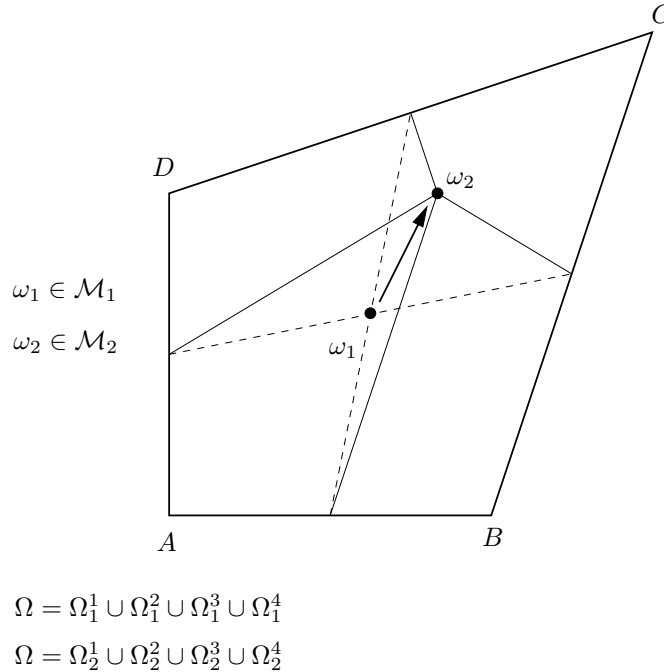


Fig. A.2: Sketch of the computational domain Ω , the two meshes \mathcal{M}_1 and \mathcal{M}_2 and their spectral element decompositions before and after a prescribed re-meshing operation obtained by moving the central vertex ω .

To evaluate the dependence of our technique with the interpolation order N , the central vertex is moved to produce a topological change in the mesh by a factor of approximately 10 %. An analytical field f is calculated on the initial mesh and mesh-transferred onto the distorted mesh, leading to the interpolated field \tilde{f} . The interpolation error is defined by $\varepsilon = \|f - \tilde{f}\|_{L^2(\Omega)}$ and computed values are presented in Table A.1, showing a conservation of the exponential rate of convergence.

| N | $\varepsilon = \ f - \tilde{f}\ _{L^2(\Omega)}$ | N | $\varepsilon = \ f - \tilde{f}\ _{L^2(\Omega)}$ |
|-----|---|-----|---|
| 3 | 7.232e-03 | 12 | 4.400e-12 |
| 4 | 1.487e-03 | 13 | 9.850e-14 |
| 5 | 1.367e-04 | 14 | 1.252e-14 |
| 6 | 2.307e-05 | 15 | 3.602e-15 |
| 7 | 1.457e-06 | 16 | 3.354e-15 |
| 8 | 2.067e-07 | 17 | 1.843e-15 |
| 9 | 8.382e-09 | 18 | 1.585e-15 |
| 10 | 1.172e-09 | 19 | 1.105e-15 |
| 11 | 3.383e-11 | 20 | 1.151e-15 |

Table A.1: Evolution of the error ε with the spectral interpolation order N .

To characterize the effect of the distortion of the mesh on our mesh-transfer operation, all possible positions of the moving vertex within the computational domain Ω were considered. In particular, we present here the case where ω is moved along the diagonal AC of the computational domain Ω as shown in Fig. A.2. Its motion is characterized by the set of coordinates (α, β) of ω in the parent domain $\hat{\Omega} = [-1, 1]^2$. The interpolation error ε was again computed for three values of N and results appearing in Table A.2, show that our technique is totally independent on the amplitude of topological change of the mesh due to the re-meshing operation.

| $\alpha = \beta$ | $\varepsilon = \ f^2 - \tilde{f}^2\ _{L^2(\Omega)}$ | | |
|------------------|---|-----------|-----------|
| | $N = 8$ | $N = 10$ | $N = 12$ |
| -0.9 | 2.100e-07 | 1.005e-09 | 3.849e-12 |
| -0.8 | 2.267e-07 | 1.111e-09 | 4.448e-12 |
| -0.7 | 2.000e-07 | 1.006e-09 | 3.906e-12 |
| -0.6 | 1.928e-07 | 1.106e-09 | 4.073e-12 |
| -0.5 | 2.289e-07 | 1.033e-09 | 3.786e-12 |
| -0.4 | 1.847e-07 | 1.053e-09 | 4.199e-12 |
| -0.3 | 2.326e-07 | 1.160e-09 | 4.166e-12 |
| -0.2 | 2.231e-07 | 1.204e-09 | 4.332e-12 |
| -0.1 | 2.067e-07 | 1.172e-09 | 4.400e-12 |
| 0.0 | 4.563e-16 | 1.199e-15 | 7.886e-16 |
| 0.1 | 2.067e-07 | 1.172e-09 | 4.400e-12 |
| 0.2 | 2.231e-07 | 1.204e-09 | 4.332e-12 |
| 0.3 | 2.326e-07 | 1.160e-09 | 4.166e-12 |
| 0.4 | 1.847e-07 | 1.053e-09 | 4.199e-12 |
| 0.5 | 2.289e-07 | 1.033e-09 | 3.786e-12 |
| 0.6 | 1.928e-07 | 1.106e-09 | 4.073e-12 |
| 0.7 | 2.000e-07 | 1.006e-09 | 3.906e-12 |
| 0.8 | 2.267e-07 | 1.111e-09 | 4.448e-12 |
| 0.9 | 2.100e-07 | 1.005e-09 | 3.849e-12 |

Table A.2: Evolution of the error ε when ω moves along the diagonal AC , for three different values of N .

Lastly, the computational expense of the mesh-transfer has been evaluated for a polynomial degree $N = 10$ in both directions (19^2 grid points for this 2D grid), and as previously for a topological change in the mesh by a factor of approximately 10 %, corresponding to a ‘small’ 2D case. The results confirm the afore-mentioned cost: a complete mesh-transfer corresponds to approximately 100 Navier–Stokes solves depending on the value of the time-step.

A.6 Conclusion and future studies

A novel isochoric moving-grid technique and mesh-transfer technique for spectral element grids have been presented. Both of these techniques are the corner-stones of our computations of transitional and turbulent free-surface flows using spectral element method. Part of the work was to ensure that these two techniques have no effect on the exponential rate of convergence, the main reason of our choice of the Legendre spectral

element method. We have obtained positive results all along the extensive series of tests carried out to verify the behavior of this rate of convergence. The development of an automatized re-meshing scheme coupled to a re-meshing control parameter is still under investigation.

Our next goal would be to simulate three-dimensional transitional and turbulent free-surface flows using the techniques presented in this appendix with the difficult task of gaining a better insight into the physics involved in the thin boundary layer near the free surface.

A.7 Annex 1

In this annex, the details of the iso-parametric mapping inversion in the particular case of quadrangular elements with straight edges, mentioned in Section A.5, is given. We consider a given quadrangular spectral element Ω^e and the parent element $\hat{\Omega} = [-1, 1]^2$ for a two-dimensional problem. The geometry of this general problem is presented in Fig. A.3. A transfinite interpolation [97, 98] of the parent element $\hat{\Omega}$ leads to the following

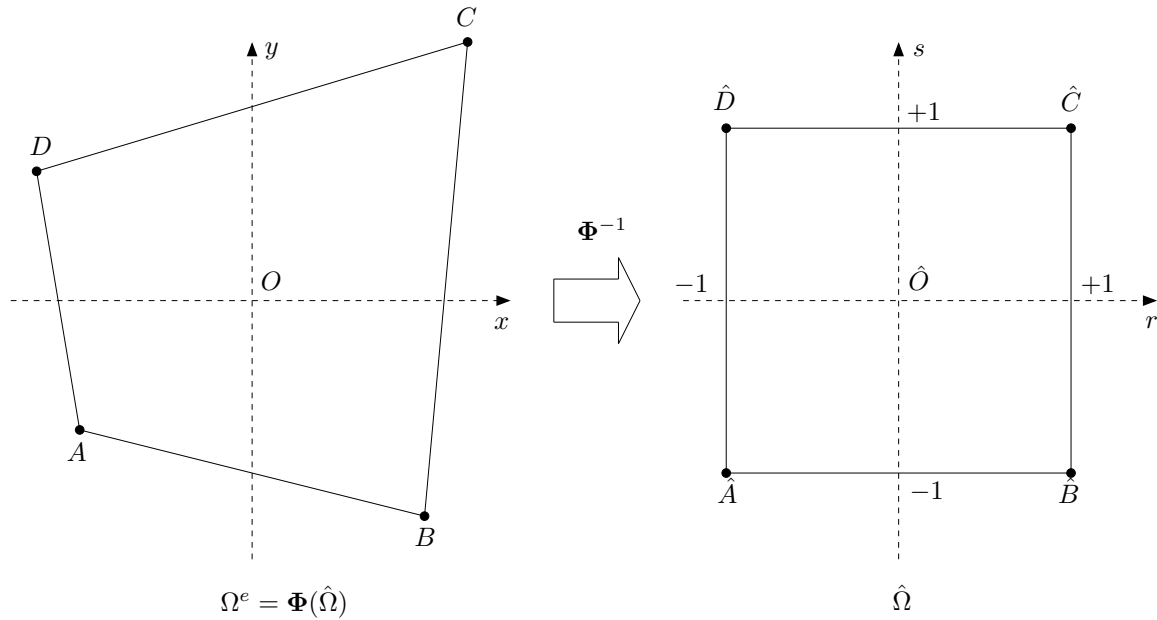


Fig. A.3: Description of the geometry for the inversion of the iso-parametric mapping.

parameterizations:

$$r = r(x, s) = \frac{\left[x - \left(\frac{1+s}{2}\right)(x_C + x_D)\right] + \left[x - \left(\frac{1-s}{2}\right)(x_B + x_A)\right]}{\left(\frac{1+s}{2}\right)(x_C - x_D) + \left(\frac{1-s}{2}\right)(x_B - x_A)}, \quad (\text{A.26})$$

$$s = s(y, r) = \frac{\left[y - \left(\frac{1+r}{2}\right)(y_C + y_B)\right] + \left[y - \left(\frac{1-r}{2}\right)(y_D + y_A)\right]}{\left(\frac{1+r}{2}\right)(y_C - y_B) + \left(\frac{1-r}{2}\right)(y_D - y_A)}. \quad (\text{A.27})$$

The above equations can be reformulated as follows:

$$r = r(x, s) = \frac{\alpha_1(x) + \beta_1 s}{\alpha_2 + \beta_2 s}, \quad (\text{A.28})$$

$$s = s(y, r) = \frac{\lambda_1(y) + \mu_1 r}{\lambda_2 + \mu_2 r}, \quad (\text{A.29})$$

introducing the following eight coefficients:

$$\begin{aligned}
\alpha_1(x) &= 4x - (x_A + x_B + x_C + x_D), \\
\beta_1 &= x_A + x_B - x_C - x_D, \\
\alpha_2 &= x_B + x_C - x_D - x_A, \\
\beta_2 &= x_A + x_C - x_B - x_D, \\
\lambda_1(y) &= 4y - (y_A + y_B + y_C + y_D), \\
\mu_1 &= y_A + y_D - y_B - y_C, \\
\lambda_2 &= y_C + y_D - y_A - y_B, \\
\mu_2 &= y_A + y_C - y_B - y_D.
\end{aligned} \tag{A.30}$$

As we aim at finding the expression of $r = r(x, y)$ and $s = s(x, y)$, we inject Eq. (A.29) into Eq. (A.28), therefore yielding an implicit quadratic form $r = r(x, s(y, r))$:

$$(\alpha_2\mu_2 + \beta_2\mu_1) r^2 + (\alpha_2\lambda_2 + \beta_2\lambda_1(y) - \alpha_1(x)\mu_2 - \beta_1\mu_1) r - (\alpha_1(x)\lambda_2 + \beta_1\lambda_1(y)) = 0. \tag{A.31}$$

The property of invertibility of the iso-parametric mapping ensures a unique real solution to the quadratic Eq. (A.31). It is possible to show that the constraint $|r| \leq 1$ leads to the only possible explicit expression of r if $\alpha_2\mu_2 + \beta_2\mu_1 \neq 0$:

$$r(x, y) = \frac{-(\alpha_2\lambda_2 + \beta_2\lambda_1(y) - \alpha_1(x)\mu_2 - \beta_1\mu_1) + \sqrt{\Delta(x, y)}}{2(\alpha_2\mu_2 + \beta_2\mu_1)}, \tag{A.32}$$

where $\Delta(x, y)$ is the strictly positive discriminant of Eq. (A.31)

$$\Delta(x, y) = (\alpha_2\lambda_2 + \beta_2\lambda_1(y) - \alpha_1(x)\mu_2 - \beta_1\mu_1)^2 + 4(\alpha_2\mu_2 + \beta_2\mu_1)(\alpha_1(x)\lambda_2 + \beta_1\lambda_1(y)). \tag{A.33}$$

The particular case $\alpha_2\mu_2 + \beta_2\mu_1 = 0$ yields the following trivial explicit expression:

$$r(x, y) = \frac{\alpha_1(x)\lambda_2 + \beta_1\lambda_1(y)}{\alpha_2\lambda_2 + \beta_2\lambda_1(y) - \alpha_1(x)\mu_2 - \beta_1\mu_1}. \tag{A.34}$$

One can note that the denominator in Eq. (A.34) is never vanishing because of the property of invertibility of the mapping Φ . In both cases, the explicit expression of $r(x, y)$ is injected into Eq. (A.29) to deliver the associated explicit expression of $s(x, y)$.

In Speculoos [66,67], the mapping-inversion has been implemented in the class `Quad`:

```
RealVector* Quad :: GetPositionInParentElement(Point *P)
```

Given the `Point` $P(x, y)$ contained by the face `Quad`, the above routine returns a two-component real vector, whose components are r and s respectively. This routine is extremely efficient; it has a very low computational cost due to the small number of elementary operations involved in it.

A.7.1 Parent-element point positioning algorithm

The algorithm implemented in the previous section assumes that any GLL grid point $\mathbf{x}_{ij,2}^{e_2}$ of the mesh \mathcal{M}_2 can be assigned to a single spectral element $\Omega_1^{e_1}$ of the mesh \mathcal{M}_1 containing it. This assignment procedure has been implemented using the previous inversion-mapping algorithm. It is again based on the property of local invertibility of the iso-parametric mapping Φ . If a GLL grid point $\mathbf{x}_{ij,2}^{e_2}$ is not contained by a spectral element of \mathcal{M}_1 , then three cases are encountered when applying the mapping-inversion algorithm:

1. $|r| > 1$;
2. $\Delta(x, y) < 0$;
3. $\alpha_2\mu_2 + \beta_2\mu_1 = 0$ and also $\alpha_2\lambda_2 + \beta_2\lambda_1(y) - \alpha_1(x)\mu_2 - \beta_1\mu_1 = 0$.

In Speculoos, this parent-element point-positioning algorithm has been implemented in the class `Quad`:

```
Boolean Quad :: ContainsPoint(Point *P)
```

Given the `Point` $P(x, y)$ and the face `Quad`, the above routine returns `true` if P is contained by the `Quad` (meaning that none of the three cases above are encountered) and `false` if it is not the case (meaning that at least one of the three cases above is encountered). The same remark on the efficiency of this routine as for the case of the mapping-inversion routine is still valid. Nevertheless, it is worth noting that in the worst case scenario, with a hashing scheme the number of calls of this routine reduces to $O(1)$ for a given GLL grid point of \mathcal{M}_2 .

A.7.2 Implementation of the field-spectral interpolation algorithm

At this stage, we are able to position all the GLL grid points $\mathbf{x}_{ij,2}^{e_2}$ of \mathcal{M}_2 into its associated parent element $\hat{\Omega}_1^{e_1}$ of the spectral element $\Omega_1^{e_1}$ containing it. Working at this parent element level, we recall here again the interpolation for any field \mathbf{u} given by the SEM [58]:

$$\mathbf{u}(\Phi^{-1}(\mathbf{x}_{ij,2}^{e_2})) = \mathbf{u}(r_1^{e_1}, s_1^{e_1}) = \sum_{k=0}^{N_{1,x}} \sum_{l=0}^{N_{1,y}} \mathbf{u}_{kl} \pi_k(r_1^{e_1}) \pi_l(s_1^{e_1}), \quad (\text{A.35})$$

with $\{\pi_j(\xi)\}_{j=0}^{N_{p,1}}$ and $p = x, y$, the one-dimensional GLL Lagrangian interpolation basis of degree $N_{p,1}$. The generic expression of the polynomial elements of this basis is given by [58]

$$\pi_j(\xi) = \frac{1}{N(N+1)L_N(\xi_j)} \frac{(\xi^2 - 1)}{(\xi - \xi_j)} L'_N(\xi), \quad 0 \leq j \leq N, \quad \xi \in \hat{\Omega}_1^{e_1}, \quad (\text{A.36})$$

with N being a simplified expression standing for $N_{p,1}$, noting $\{\xi_j\}_{j=0}^N$ the set of $(N+1)$ GLL grid points such that $\xi_0 = -1 < \xi_1 < \dots < \xi_{N-1} < \xi_N = +1$ and $\{\xi_j\}_{j=1}^{N-1}$ being the $N-1$ roots of $L'_N(\xi)$, the first-order derivative of the Legendre polynomial of order N , $L_N(\xi)$. L'_N is an irreducible and separable polynomial in the parent element $\hat{\Omega} = [-1, 1]$. Therefore one may re-write $L'_N(\xi)$ as a product of $N-1$ monomials in ξ :

$$L'_N(\xi) = \Gamma_N \prod_{i=1}^{N-1} (\xi - \xi_i), \quad \xi \in \hat{\Omega}_1^{e_1}, \quad (\text{A.37})$$

Γ_N being the real coefficient associated with the highest-order monomial (which is equal to $N-1$, the degree of L'_N) of $L'_N(\xi)$. Noting also that $(\xi^2 - 1) = (\xi - \xi_0)(\xi - \xi_N)$, leads us to a new formulation of Eq. (A.36):

$$\pi_j(\xi) = \frac{\Gamma_N}{N(N+1)L_N(\xi_j)} \prod_{i=0, i \neq j}^N (\xi - \xi_i), \quad \xi \in \hat{\Omega}_1^{e_1}, \quad (\text{A.38})$$

From a computational viewpoint the expression of $L_N(\xi)$ given by Eq. (A.38) is much more preferable to the one given by Eq. (A.36) because of the monomial $(\xi - \xi_j)$ at the denominator, giving rise to unacceptable numerical errors.

Efficient routines from MIT, calculating the values of any Legendre polynomial and its first derivative are already implemented in Speculoos. Similarly, a routine calculating the one-dimensional GLL quadrature nodes is also available in Speculoos. As a consequence the coefficient Γ_N is the last parameter required to be computed. Analytically Γ_N can be calculated indirectly by setting ξ to a well-chosen value $\tilde{\xi}$. The value $\tilde{\xi} = 1$ gives a straightforward solution to our problem because $L'_N(\tilde{\xi} = 1)$ can be analytically expressed for all values of N :

$$L'_N(1) = \frac{1}{2}N(N+1), \quad \forall N \in \mathbb{N}, \quad (\text{A.39})$$

which leads to the following expression for Γ_N

$$\Gamma_N = \frac{N(N+1)}{2 \prod_{i=1}^{N-1} (1 - \xi_i)}, \quad \forall N \in \mathbb{N}, \quad (\text{A.40})$$

and finally allowing to find the most computationally appropriate expression of the GLL Lagrangian interpolation polynomials:

$$\pi_j(\xi) = \frac{1}{2L_N(\xi_j)} \frac{\prod_{i=0, i \neq j}^N (\xi - \xi_i)}{\prod_{i=1}^{N-1} (1 - \xi_i)}, \quad \xi \in \hat{\Omega}_1^{e_1}, \quad (\text{A.41})$$

Eq. (A.41) only involves the known GLL quadrature nodes $\{\xi_i\}_{i=0}^N$ and a value of the Legendre polynomial that can efficiently be calculated by an already implemented routine as mentioned above.

Using Eq. (A.41) the SEM interpolation of any field \mathbf{u} can be formulated as follows

$$\mathbf{u}(\Phi^{-1}(\mathbf{x}_{ij,2}^{e_2})) = \frac{1}{4} \sum_{k=0}^{N_{1,x}} \sum_{l=0}^{N_{1,y}} \frac{\mathbf{u}(\xi_k, \xi_l)}{L_{N_{1,x}}(\xi_k) L_{N_{1,y}}(\xi_l)} \frac{\prod_{i=0, i \neq k}^{N_{1,x}} (r_1^{e_1} - \xi_i)}{\prod_{i=1}^{N_{1,x}-1} (1 - \xi_i)} \frac{\prod_{i=0, i \neq l}^{N_{1,y}} (s_1^{e_1} - \xi_i)}{\prod_{i=1}^{N_{1,y}-1} (1 - \xi_i)}. \quad (\text{A.42})$$

Eq. (A.42) is not directly implemented in Speculoos, but instead several intermediate routines are used to achieve the same computation as the one described by this equation. For the user the algorithm presented above can be reached by using two similar routines implemented in the classes `FlatField` and `MortaredField` respectively:

```
void FlatField :: ApplyGLLMeshInterpolation(FlatField *f1)

void MortaredField :: ApplyGLLMeshInterpolation(MortaredField *f1)
```

These two routines have been developed using MPI to ensure a correct parallel behavior of the final Speculoos code. Performance testings have been carried out for some benchmark problems and are presented in the next section.

A.7.3 Performance of the Field-spectral interpolation algorithm

A quadrangular computational domain Ω is chosen to carry out this performance test. The vertices are located at the following positions: $(0, 0)$, $(1, 0)$, $(1.5, 1.5)$ and $(0, 1)$, see Fig. A.2, and the resulting domain is uniformly divided into $E_x \times E_y$ spectral elements, with E_x (resp. E_y) the number of spectral elements in the x -direction (resp. y -direction). The mesh generated by this mean is structured and we have also chosen to have conforming spectral elements within the mesh, meaning that all elements have the same degree of interpolation N_x and N_y , in the x - and y -direction respectively. For the sake of simplicity we will assume in the sequel that $E_x = E_y = E$ and $N_x = N_y = N$.

It is necessary to create a ‘test signal’ that is known analytically in order to be able to evaluate the interpolation error at any point of the computational domain (and not only at the GLL grid points of the mesh). Moreover this test signal should preferably be smooth enough in order to have a good spectral element representation over the GLL grid of our computational domain Ω (if the spectral element representation of the test signal is not good enough, it is meaningless to try any kind of interpolation). The analytical field $f(\mathbf{x}) = f(x, y) = \sin(\pi x) \sin(\pi y)$ is smooth enough to qualify as a good test signal for our test.

Lastly, the following procedure has been put in place to measure the interpolation error:

1. a uniform grid made of $10^2 \times 10^2$ equally-spaced points \mathbf{x}_{ij} is stacked over the GLL grid of Ω ;
2. for each of the 10^4 points \mathbf{x}_{ij} , the test signal $f(\mathbf{x})$ is interpolated using the implemented algorithm and the following error is measured: $\varepsilon(\mathbf{x}_{ij}) = |\tilde{f}_{ij} - f(\mathbf{x}_{ij})|$ where \tilde{f}_{ij} is the interpolated value at the point \mathbf{x}_{ij} and $f(\mathbf{x}_{ij})$ is the calculated value;
3. the field interpolation error ε is taken as the maximum of the point-wise interpolation error which is quantified using: $\varepsilon = \max_{i,j} (\varepsilon(\mathbf{x}_{ij}))$.

The results of the above test are presented on Fig. A.4, where the field interpolation error ε is plotted against the degree of interpolation N for different values of E ranging from 1 to 10. These results clearly show a spectral behavior for our point-wise interpolation procedure, as for any value of E the interpolation is decreasing exponentially with N (Fig. A.4 uses a y -logscale) until the machine precision is reached. In addition, by increasing the number of spectral elements E^2 of the mesh, one reaches the machine precision ‘faster’: with a single spectral element, machine precision is reached for approximately $N = 18$ whereas with 100 spectral elements, it is reached for only $N = 9$.

A.8 Annex 2

In this annex, the details of the GL mesh-transfer algorithm is given. We aim at implementing an algorithm capable of transferring a field defined over a GL grid from one mesh to another. In practice this GL mesh-transfer algorithm will be used to transfer the pressure field from \mathcal{M}_1 to \mathcal{M}_2 .

To prevent the development of spurious pressure oscillations our ALE Navier–Stokes computation classically uses a staggered-grid $\mathbb{P}_N - \mathbb{P}_{N-2}$ approach [52, 58], in which the pressure field is the only field not defined over a GLL grid. Instead a Gauss–Legendre (GL) grid of order $N - 2$ is used. It is important to bear in mind that the mesh made of the union of the GL grids for each spectral element does not produce a full coverage of the computational domain.

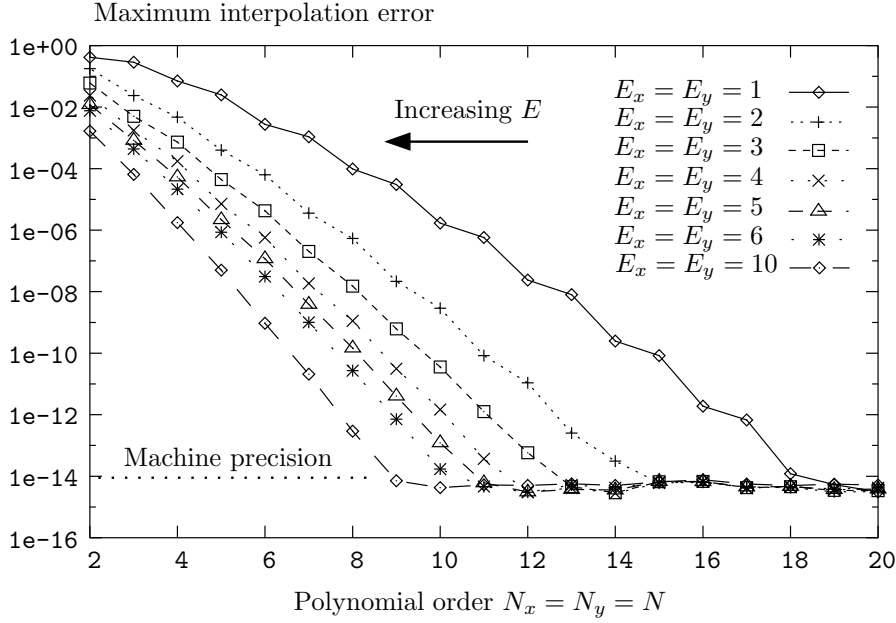


Fig. A.4: Maximum interpolation error ε vs. degree of interpolation N for different number of elements.

A.8.1 GL polynomial bases and interpolation algorithm

Working at the parent element level, we recall here the interpolation for any field \mathbf{u} given by the SEM [58] using a GL polynomial basis of order $N - 2$:

$$\mathbf{u}(\Phi^{-1}(\mathbf{x}_{ij,2}^{e_2})) = \mathbf{u}(r_1^{e_1}, s_1^{e_1}) = \sum_{k=1}^{N_{1,x}-1} \sum_{l=1}^{N_{1,y}-1} \mathbf{u}_{kl} \varpi_k^p(r_1^{e_1}) \varpi_l^p(s_1^{e_1}), \quad (\text{A.43})$$

with $\{\varpi_j^p(\zeta)\}_{j=1}^{N_{p,1}-1}$ and $p = x, y$, the one-dimensional GL Lagrangian interpolation basis of degree $N_{p,1} - 2$. The generic expression of the polynomial elements of this Gauss–Legendre basis are given by [58]

$$\varpi_j^p(\zeta) = \frac{L_{N-1}(\zeta)}{(\zeta - \zeta_j) L'_{N-1}(\zeta_j)} \quad 1 \leq j \leq N - 1, \quad \zeta \in \hat{\Omega}_1^{e_1}, \quad (\text{A.44})$$

noting $\{\zeta_j\}_{j=1}^{N-1}$ the set of $(N - 1)$ GL grid points such that $-1 < \zeta_1 < \zeta_2 < \dots < \zeta_{N-1} < +1$ and $\{\zeta_j\}_{j=1}^{N-1}$ being the $N - 1$ roots of $L_{N-1}(\zeta)$, the Legendre polynomial of order $N - 1$. L_{N-1} is an irreducible and separable polynomial in the parent element $\hat{\Omega} = [-1, 1]$. Therefore one may re-write $L_{N-1}(\zeta)$ as a product of $N - 1$ monomials in ζ :

$$L_{N-1}(\zeta) = \Theta_{N-1} \prod_{i=1}^{N-1} (\zeta - \zeta_i), \quad \zeta \in \hat{\Omega}_1^{e_1}, \quad (\text{A.45})$$

Θ_{N-1} being the real coefficient associated with the highest-order monomial of $L_{N-1}(\zeta)$. The analytical expression of Θ_{N-1} can easily be found using the well-known property of Legendre polynomials: $L_{N-1}(\zeta = 1) = 1$ for all values of N , leading to

$$\Theta_{N-1} = \frac{1}{\prod_{i=1}^{N-1} (1 - \zeta_i)}. \quad (\text{A.46})$$

This separation of the polynomial L_{N-1} and the expression of Θ_{N-1} lead us to a new formulation of Eq. (A.44):

$$\varpi_j^p(\zeta) = \frac{1}{L'_N(\zeta_j)} \frac{\prod_{i=1, i \neq j}^{N-1} (\zeta - \zeta_i)}{\prod_{i=1}^{N-1} (1 - \zeta_i)}, \quad \zeta \in \hat{\Omega}_1^{e_1}. \quad (\text{A.47})$$

Similarly to the case of the GLL field-spectral interpolation algorithm presented earlier, Eq. (A.47) allows an efficient computation of the interpolated pressure field over the new GL grid points $\mathbf{x}_{ij,2}^{e_2}$. Nevertheless, a

problem arises when trying to follow-up a deeper analogy with the GLL mesh-transfer algorithm. The origin of this problem lies in the fact that in general, some new GL grid points $\mathbf{x}_{ij,2}^{e_2}$ (belonging to the GL mesh associated to the new GLL mesh \mathcal{M}_2) appear to be located in the space of the computational domain that is not covered by the old GL mesh.

Two paths can be followed in order to solve this problem:

- *to use a spectral extrapolation algorithm* to find the values of the pressure field corresponding to points that do not lie in the GL grid associated with \mathcal{M}_1 ;
- *to interpolate the pressure field over the GLL mesh* associated with \mathcal{M}_1 , then use the previously presented GLL mesh-transfer technique to interpolate the pressure from \mathcal{M}_1 onto \mathcal{M}_2 , and finally to interpolate back the pressure over the GL mesh associated with \mathcal{M}_2 .

This second option can easily be implemented in our code as it uses previously implemented techniques that have shown great efficiency. Performance test of this second option corresponding now to our GL mesh-transfer technique were carried out and are presented in the next section.

A.8.2 GL mesh-transfer algorithm performance tests

To evaluate the performance of the GL mesh-transfer technique introduced in the previous section, we stick to the same configuration as for the GLL mesh-transfer (same computational domain and same notations). The error is still measured using the $L^2(\Omega)$ -norm of the difference between the test field and the computed field. The test field is the same as before but now its spectral decomposition is made over the GL mesh associated with \mathcal{M}_2 .

The outcome of the computation of this GL mesh-transfer is presented in Table A.3 for $\omega_2 = (0.1, 0.1)$. Comparing these results with those presented in Table A.1 for the case of the GLL mesh-transfer technique, we can conclude to an excellent agreement with the theory for the following reasons:

- the spectral behavior observed for the GLL mesh-transfer technique is still observable in this case;
- the spectral element decomposition of the pressure being of two-order lower compared to all other fields defined on the GLL grid, it was expected to have a higher error ε for a given value of the interpolation order N . The machine precision is still reachable but for a higher value of N .

| N | $\varepsilon = \ f^2 - \tilde{f}^2\ _{L^2(\Omega)}$ | N | $\varepsilon = \ f^2 - \tilde{f}^2\ _{L^2(\Omega)}$ |
|-----|---|-----|---|
| 3 | 3.714691e-02 | 13 | 1.5373920e-11 |
| 4 | 1.721680e-02 | 14 | 1.9687020e-12 |
| 5 | 3.582591e-03 | 15 | 4.2342865e-14 |
| 6 | 7.234110e-04 | 16 | 7.2800141e-15 |
| 7 | 6.037107e-05 | 17 | 2.0363273e-15 |
| 8 | 1.122697e-05 | 18 | 2.1848130e-15 |
| 9 | 6.128462e-07 | 19 | 1.4084790e-15 |
| 10 | 9.428244e-08 | 20 | 1.4801411e-15 |
| 11 | 5.047457e-09 | | |
| 12 | 5.134571e-10 | | |

Table A.3: Evolution of the error ε with the spectral interpolation order N , for $\omega_2 = (0.1, 0.1)$ for a GL mesh transfer.

Appendix B

Closed cylindrical swirling flow

This appendix is in direct relation with the studies of the flow in an open cylindrical container driven by a rotating bottom end-wall treated in Chapter 7 and Chapter 8 of Part IV of the present dissertation. The work reported hereafter corresponds to a preliminary study to the developments and simulations presented in Chapters 7 & 8. The internal and incompressible shear-driven flow of a Newtonian fluid enclosed in a cylindrical container and driven by the steady rotation of its bottom end-wall is briefly discussed. The main objective here is to provide the reader with insight into the basic axisymmetric flow states encountered in the steady and unsteady closed swirling flow.

B.1 Introduction

The reader is referred to Sec. 7.1.2 for a detailed introduction and literature review regarding the “standard” case that constitutes the study of vortex breakdown in a closed cylindrical cavity. It is worth recalling here that Escudier [69] revealed flow states with one, two or even three successive breakdowns, as well as a transition from steadiness to unsteadiness. Sørensen [233] extended to a broader range of Reynolds number in the same experiment as Escudier [69] for the closed container, and inferred that above a critical Reynolds number in the unsteady flow regime, the meridional flow becomes highly asymmetric. These results are summarized and depicted in Fig. B.1

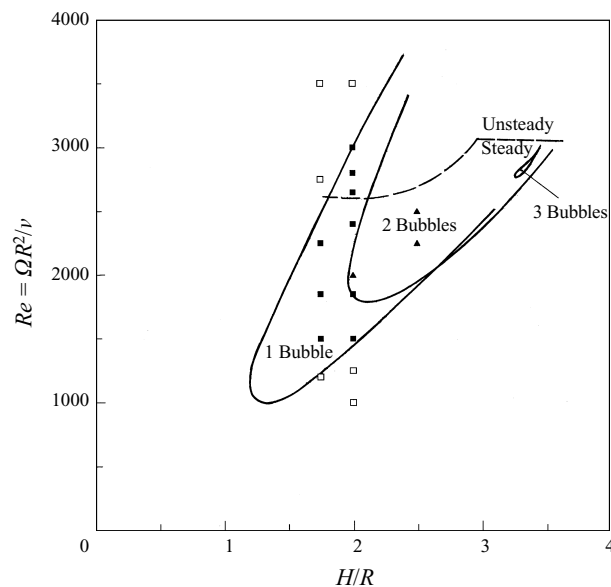


Fig. B.1: Stability boundaries for single, double and triple breakdowns, and boundary between steady and unsteady oscillatory flow, in the $(\Lambda = H/R, Re)$ -plane with the results obtained by Escudier [69]. Regimes where experiments have been carried out are indicated by symbols: \square , no bubble; \blacksquare , one bubble; \blacktriangle , two bubbles. From Spohn *et al.* [240]. © 1998 Cambridge University Press.

Direct numerical simulations of the swirling flow in an enclosed cylinder have been carried out. Numerical results are presented in the next section, and will be useful to compare with results obtained in the open cylinder case.

B.2 Numerical results

The comprehensive experimental and numerical studies of this flow have shown that it undergoes a series of transitions when varying both governing parameters Λ and Re . The short study described in the sequel focuses on the development of the flow characteristics with the Reynolds number Re for a given value of the height-to-radius aspect ratio $\Lambda = 2.5$, and up to the point where the flow no longer reaches a steady state. The particular choice of the value for Λ has mainly two justifications. First, as one can see in Fig. B.1, varying the Reynolds number while keeping $\Lambda = 2.5$, allows to generate a wide spectrum of flow states: *e.g.* no recirculation bubble, two vortex breakdowns, steady and unsteady flows. The second justification of the choice $\Lambda = 2.5$, lies in the existence of a large body of experimental and numerical results available in the literature and corresponding to this specific value, which is therefore very useful to validate some aspects of the numerical simulation. In particular, in the region of parameter space considered, *i.e.* $1\,600 \leq Re \leq 3\,000$ and $\Lambda = 2, 5$, the flow is observed to remain axisymmetric, laminar, and mainly steady.

The numerical method is the one detailed in Sec. 7.3, except for the treatment of the top surface, which is replaced here by a fixed solid wall imposing a homogeneous Dirichlet boundary condition for the velocity field

$$u(x, y, z = H, t) = v(x, y, z = H, t) = w(x, y, z = H, t) = 0. \quad (\text{B.1})$$

As the highest Reynolds number considered for this study is $Re = 3\,000$, a coarser grid than the one used for the past simulations in Chapters 7 & 8, has been employed. This grid is made up with 6 cylindrical layers comprising each 28 spectral elements, which are arranged in a similar manner to the one presented in Figs. 7.6 & 7.7. The details related to the four test cases considered in this appendix are summarized in Table B.1. The choice of the four values of the Reynolds number were made in accordance with the results from Escudier [69], which are depicted in Fig. B.1.

| Re | $\Lambda = H/R$ | Time-step Δt | Time evolution | Vortex breakdown |
|-------|-----------------|----------------------|----------------|---------------------|
| 1 600 | 2.5 | 0.01 | steady | no |
| 1 900 | 2.5 | 0.01 | steady | no |
| 2 200 | 2.5 | 0.005 | steady | 2 separate bubbles |
| 3 000 | 2.5 | 0.005 | unsteady | 2 connected bubbles |

Table B.1: Parameters and characteristics of the four test cases considered. The time-step Δt is expressed in Ω_0^{-1} units.

B.2.1 Vortex breakdowns with increasing Reynolds number

In this section, the evolution of the streamline contours—defined as the intersections of the streamfunction surfaces with any meridional plane—is investigated with an increasing Reynolds number. Figure B.2 displays two series of contours for the cases defined in Table B.1. The first series of contours is for the cases at $Re = 1\,600$ and $Re = 1\,900$, which only contain negative values of ψ in absence of any recirculation bubble. On the contrary, the second series of contours, for the cases at $Re = 2\,200$ and $Re = 3\,000$, possesses positive values, which correspond to the two recirculation bubbles that have appeared after the vortex breakdown. As can be seen from the results of Escudier [69] in Fig. B.1, the case at $Re = 1\,900$ is very close to the breakdown. This appears clearly in Fig. B.2 with the two local bending of the contours in the near-axis region. The structure of the recirculation regions determined by the present simulations at $Re = 2\,200$ (see Fig. B.2, bottom left) is compared in detail with the numerical simulation from Lopez [158] and the experimental observation from Escudier [69], see Fig. 4(a) in [158]. A very good agreement is found between the present results and the ones from Lopez [158] and Escudier [69].

The distribution of axial angular momentum is of particular interest for this flow driven by the constant torque imposed to the bottom end-wall. The axial angular momentum is denoted by Γ and can easily be expressed in terms of the azimuthal component of the velocity field as $\Gamma = ru_\theta$. Figure B.3 (top row) displays the contours of the angular momentum for the four cases considered in this study. For all values of Re , one can clearly observe how the fluid acquires angular momentum by the shear stress generated by the rotating bottom end-wall and how it loses it in the viscous boundary layers on the tubular side-wall and on the top wall. For low values of the Reynolds number, Γ is nearly constant on all stream surfaces in the near-axis region. As expected, the presence of the recirculation bubble after the vortex breakdown process, influences the distribution of axial angular momentum. Far from the recirculation bubbles, the angular momentum distribution corresponds to

essentially solid-body rotation of the fluid. As mentioned by Lopez in [158]: “In essence, in these flows, the breakdown regions is like a transition region from a concentrated vortical flow to solid-body rotation”.

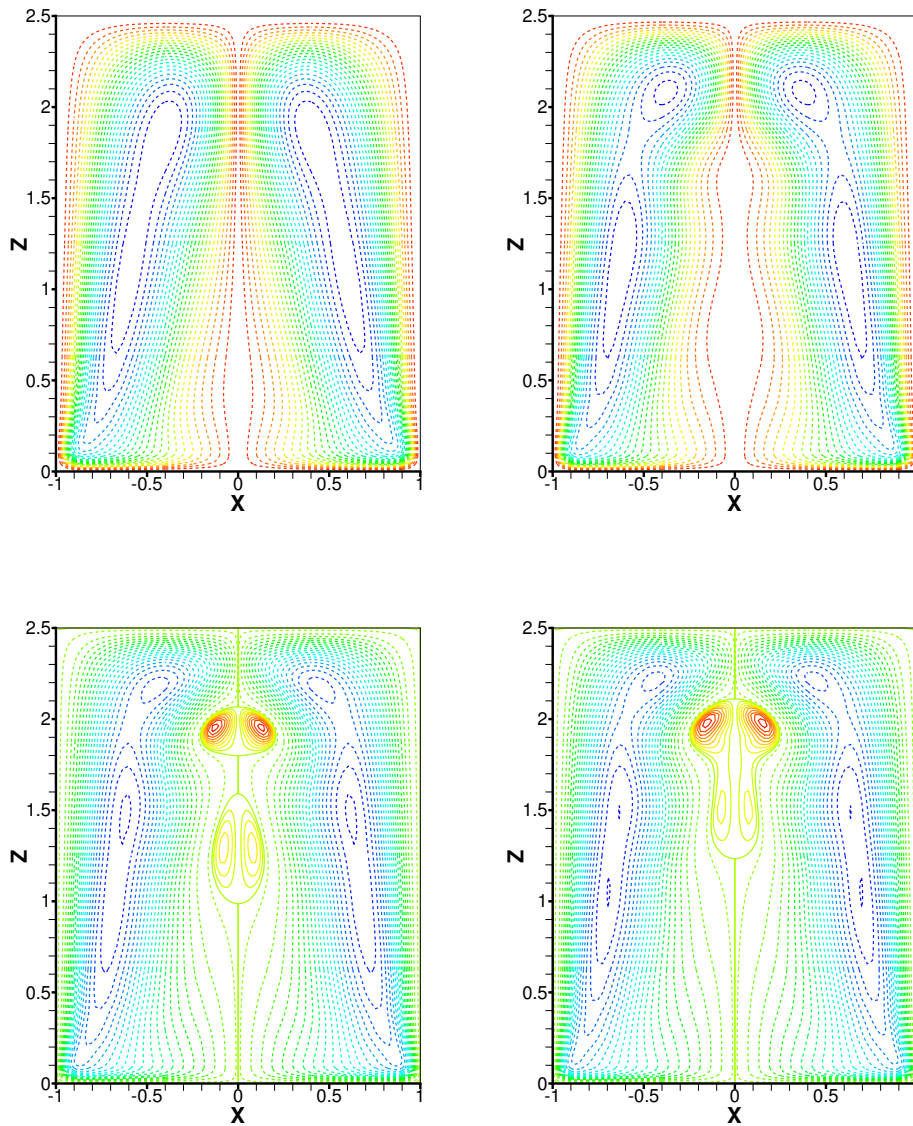


Fig. B.2: Contours of the streamfunction ψ in the meridional plane corresponding to $y/R = 0$. Top & left: $Re = 1600$; top & right: $Re = 1900$; bottom & left: $Re = 2200$; bottom & right: $Re = 3000$. The 30 are uniformly spaced contours between minimal value and zero for $Re = 1600$ and $Re = 1900$; The 30 contours are non-uniformly spaced for visualization purposes, 20 equally-spaced negative (dashed) contours and 10 equally-spaced positive (solid) contours for $Re = 2200$ and $Re = 3000$.

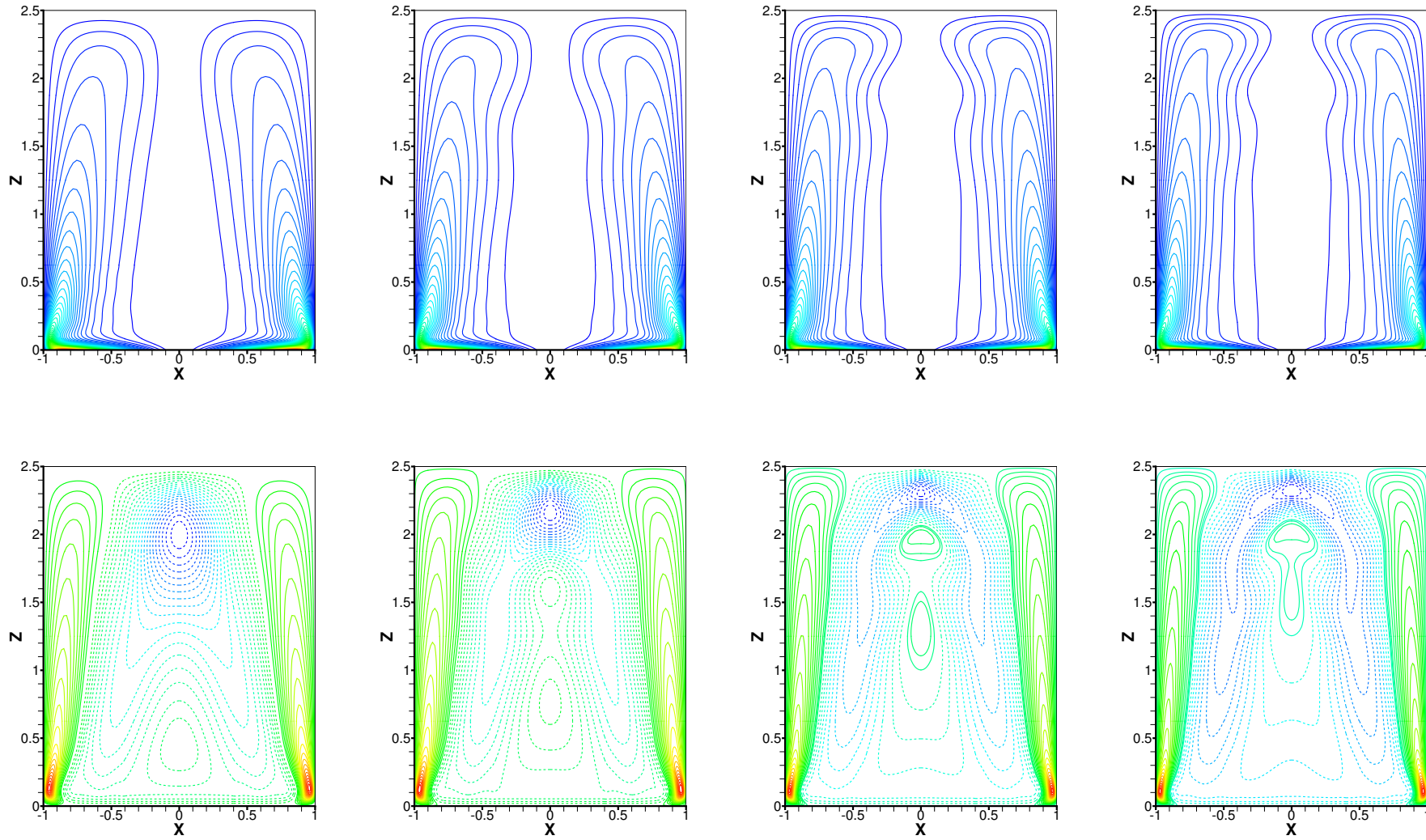


Fig. B.3: Contours of the angular momentum $\Gamma = ru_\theta$ (top row) and of the axial velocity component $w = u_z$ (bottom row), in the meridional plane corresponding to $y/R = 0$. The 50 contours are uniformly spaced between 0 and 1 for Γ ; The 40 contours are uniformly spaced between ± 0.20 for w . From left column to right column: $Re = 1600, 1900, 2200, 3000$.

Finally, the distribution of axial velocity is shown in Fig. B.3 (bottom row). It allows to visualize the axial recirculation flows within any meridional plane. For all values of Re , the upward-directed wall-jet along the tubular side-wall is clearly visible. It originates from the strong turning at the circular corner ($r/R = 1, z/H = 0$) of the flow radially ejected by the centrifugal force induced by the rotation of the bottom end-wall. Before the vortex breakdowns, the central flow along the cylinder axis forms a cylindrical jet oriented downward. This central jet originates from the pumping effect—low pressure gradient along the axis of the rotating bottom end-wall—in the Ekman layer. The presence of recirculation bubble after the vortex breakdowns, strongly modifies the structure of this central cylindrical jet into a toroidal jet still oriented downward. As expected, the fluid inside the recirculation bubbles is upward-directed, in an opposite direction to one of the central toroidal jet.

B.2.2 Transition to unsteadiness

As already observed in Fig. B.1, for a given value of the aspect ratio Λ , the first transition process associated with the vortex breakdown, and described in the previous section, is followed by a second transition from a steady flow to an unsteady oscillatory flow.

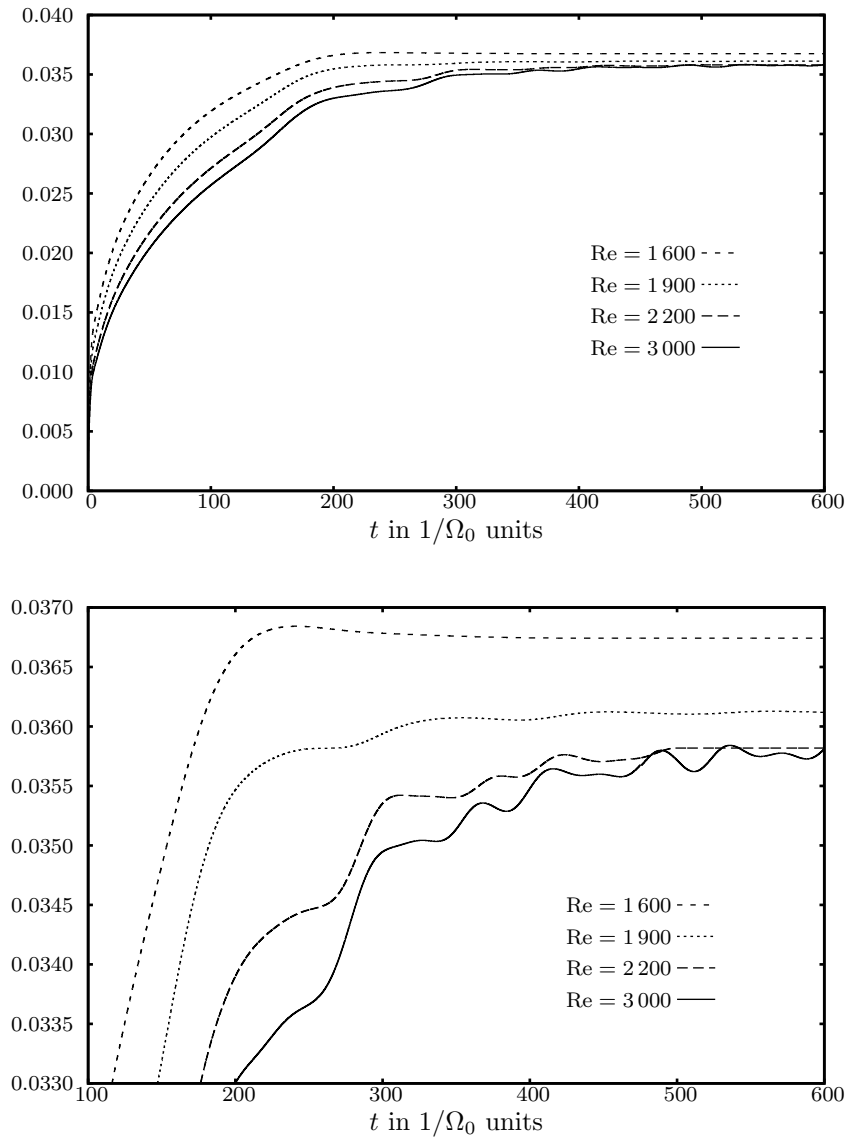


Fig. B.4: Time history of the volume integral of the kinetic energy Q of the flow. $Re = 1600, 1900, 2200, 3000$. Top: complete dynamic range including transient; bottom: zoom-in of the stationary region.

At this point, it is worth noting the timescales of the evolution of these flows. Figure B.4 displays the time history of the volume integral of the kinetic energy of the flow Q . For the first three cases, *i.e.* $Re = 1600, 1900, 2200$, the flow reaches a steady state after approximately 500 rotations of the bottom end-wall

and following an impulsive start from a quiescent fluid state. The fourth case, which corresponds to $Re = 3\,000$, leads to an unsteady flow with an oscillatory evolution of the structure of the recirculation bubbles. The flow structure in the central core region over one cycle is given in Fig. B.6 for 12 instants equally spaced in time and represented by circles in Fig. B.5. As noted by Lopez in [158], the unsteady character of the flow is due to the interaction between the two bubbles—coalescing and separating, and coalescing, etc.

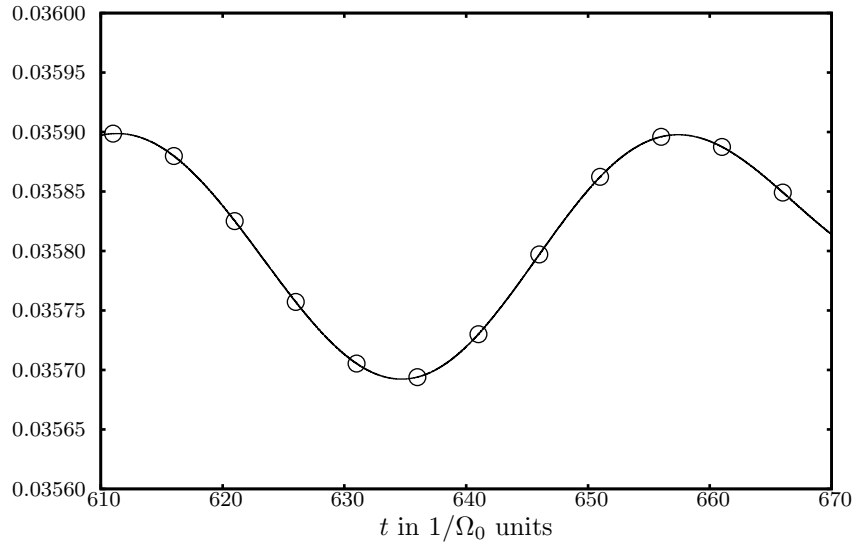


Fig. B.5: Time history of the volume integral of the kinetic energy Q of the flow for $610 \leq \Omega_0 t \leq 670$. $Re = 3\,000$. The circles \circ correspond to the instantaneous structures in Fig. B.6.

B.3 Conclusions

This appendix briefly described the basic features of the swirling flow in an enclosed cylinder. The study focused on the observed transitions while increasing the Reynolds number for a given value of the height-to-radius aspect ratio $\Lambda = 2.5$. The first transition is associated with the vortex breakdown process, and its effects on the recirculation flows and jets within the cavity. The second transition investigated, is the transition from a steady flow towards an unsteady flow, induced by the interactions between the two recirculation bubbles.

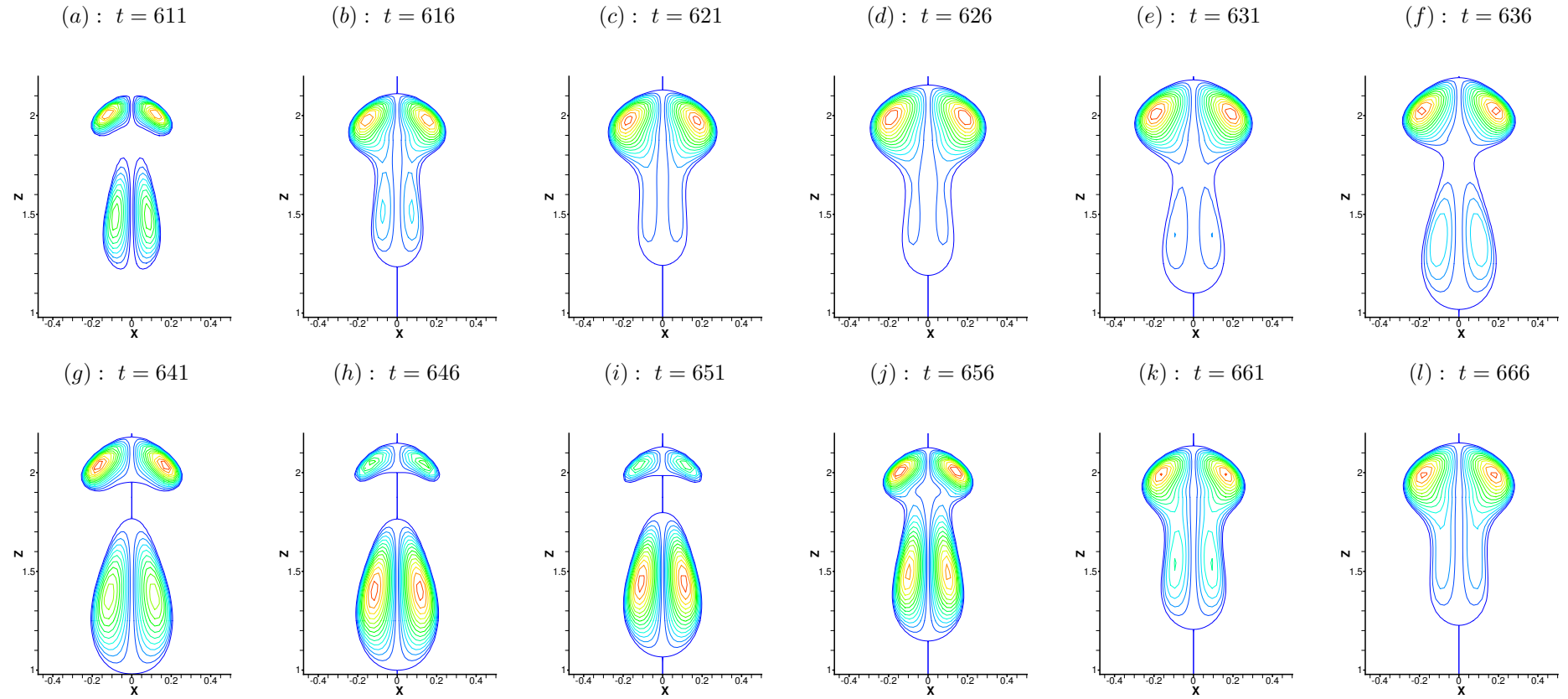


Fig. B.6: Instantaneous streamlines $\psi = \text{Cst.}$ in the central region $r/R \leq 0.5$, of the meridional plane corresponding to $y/R = 0$ for the case $\text{Re} = 3000$. Only 14 equally-spaced contours are represented. Different instants t correspond to circles in Fig. B.5.

B.4 Annex: Closed swirling flow without recirculation bubble

This annex presents results of the closed cylindrical swirling flow corresponding to the case ($\Lambda = 1, \text{Re} = 6000$). These results are placed in this appendix as they correspond to the swirling flow in a closed cylindrical cavity unlike the open case dealt with in Part IV. Nevertheless, as the value of the height-to-radius aspect ratio Λ is different from the cases above—consequently preventing a vortex breakdown to occur—the results are placed in this annex at the end of the present appendix.

The case ($\Lambda = 1, \text{Re} = 6000$) in the open cylinder flow of Part IV is the central case of the study in the transitional regime. Therefore, it seems appropriate to compare the results in the open cylinder case with the ones in the closed case with exactly the same parameters and same numerical method. The only difference being the imposition of a homogeneous Dirichlet boundary condition on the top end-wall of the cylinder, in order to enforce the no-slip condition imposed by the presence of the steady disk. As expected from the bifurcation diagram shown in Fig B.1, no vortex breakdown occurs for the value $\Lambda = 1$, independently of the value of the Reynolds number. Nevertheless, even without any recirculation bubble, a notable unsteady character is measured for this flow. Figure B.7 displays the streamlines of this instantaneous flow into any half-meridional plane. Even at such a relatively high Reynolds number, one can prove that the flow maintains its axisymmetry. To this aim, the following quantity

$$\frac{\Delta X}{X} = \frac{\|X(r, \theta = 0, z) - X(r, \theta = \pi/2, z)\|_{L^2}}{\|X(r, \theta = 0, z)\|_{L^2}}, \quad (\text{B.2})$$

has been calculated for all three components of the velocity field, using the L^2 -norm in the meridional plane ($r, \theta = 0, z$). The results are gathered in Table B.2 and are showing to be of the order of the error introduced by the space and time discretizations. This observation is crucial as it allows us to infer that the axisymmetry breaking observed at $\text{Re} = 6000$ in the open cylinder case with $\Lambda = 1$, is due to the presence and the dynamics of the recirculation bubble(s).

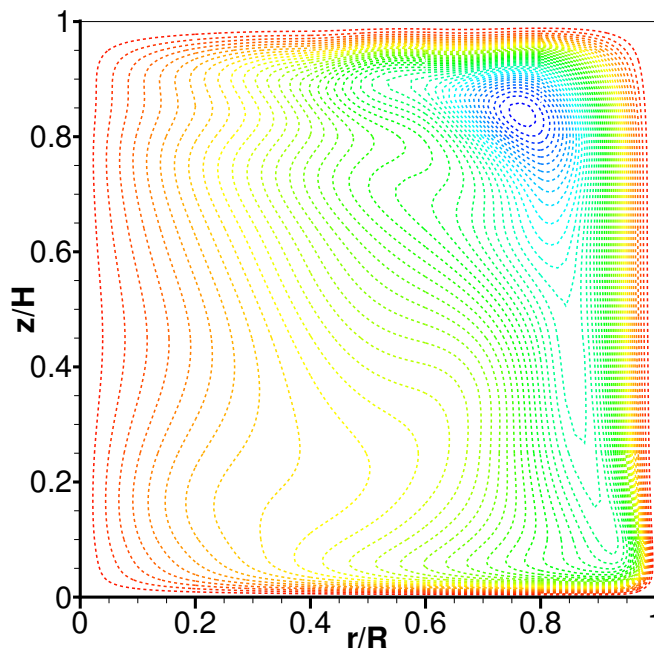


Fig. B.7: Contours of streamlines in a half-meridional plane for an instantaneous flow sample. Closed cylinder case with ($\Lambda = 1, \text{Re} = 6000$). The 40 contours are uniformly spaced, between -0.008 and 0 .

As a second step, the contours of the radial and axial velocity components in any meridional plane are given in Fig. B.8. These data are supplemented with the contours of the azimuthal velocity component u_θ and of the axial component of the angular momentum $\Gamma = ru_\theta$ in Fig. B.9. The behavior of the velocity field and axial angular momentum right below the top end-wall is of prime importance when comparing these data with those of Part IV corresponding to an open cylinder.

| Variable | Relative difference $\Delta X/X$ |
|------------|----------------------------------|
| u_r | 2.927e-06 |
| u_θ | 3.182e-06 |
| u_z | 6.855e-07 |

Table B.2: Quantitative assessment of the axisymmetry of the velocity field in the cylinder.

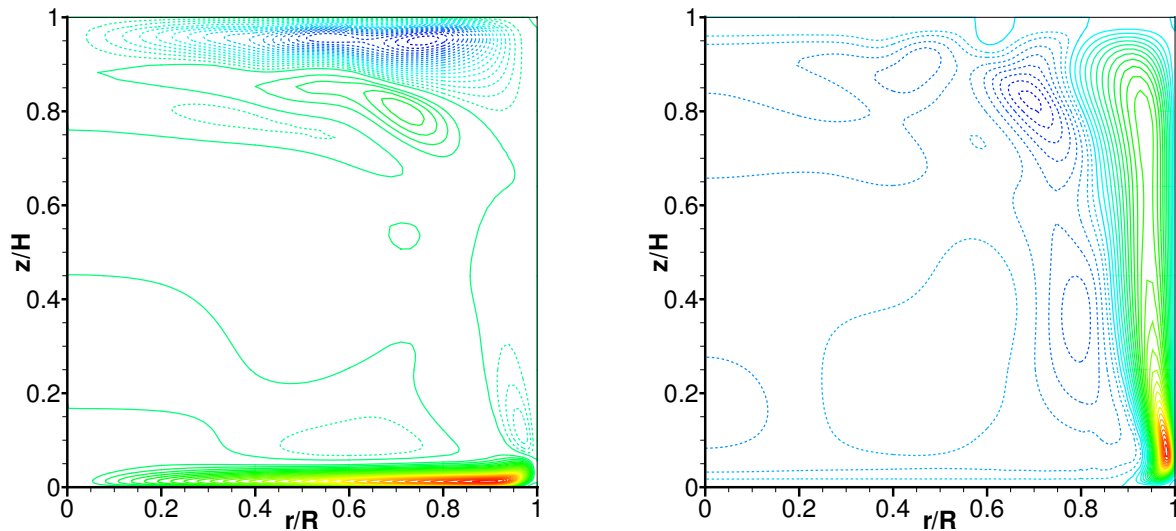


Fig. B.8: Contours in a half-meridional plane for an instantaneous flow sample. Closed cylinder case with ($\Lambda = 1, Re = 6000$). Left: radial velocity component u_r ; Right: axial velocity component u_z . The 50 contours are nonuniformly spaced for visualization purposes, between -0.100 and 0.155 for u_r , and between -0.04 and 0.14 for u_z .

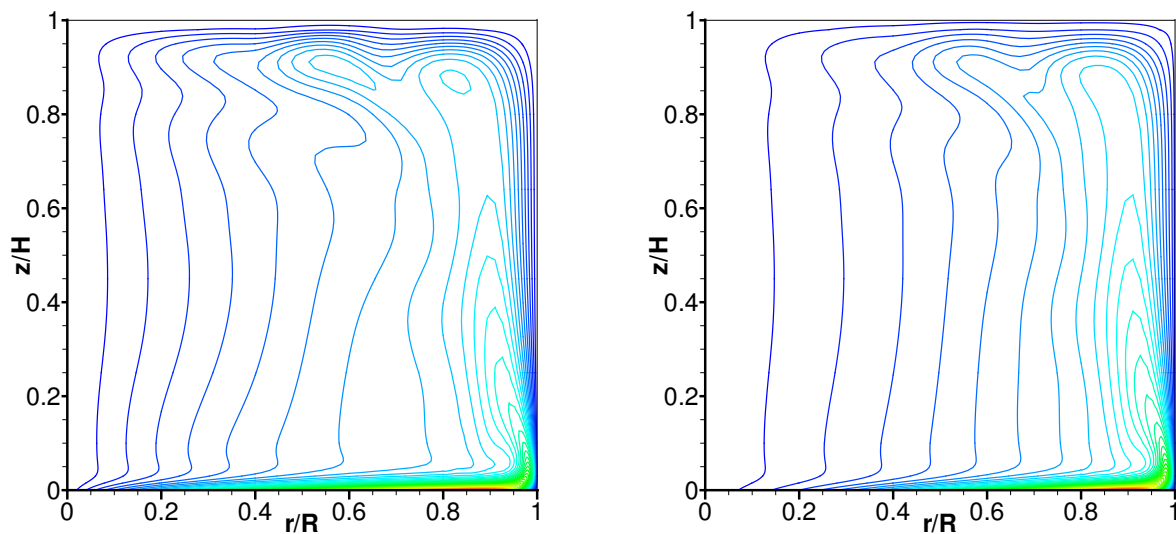


Fig. B.9: Contours in a half-meridional plane for an instantaneous flow sample. Closed cylinder case with ($\Lambda = 1, Re = 6000$). Left: azimuthal velocity component u_θ ; Right: axial angular momentum Γ . The 50 contours are uniformly spaced, between 0 and 1.

Appendix C

Computational performance analysis of a parallelized high-order spectral and mortar element toolbox

In this appendix, a comprehensive performance review of a MPI-based high-order spectral and mortar element method C++ toolbox is presented. The focus is put on the performance evaluation of several aspects at the hardware and software levels with a particular emphasis on the parallel efficiency, the C++ implementation weaknesses and the influence of the concurrent and subsequent implementation layers in a multi-programming environment. The performance evaluation is analyzed and compared to predictions given by a heuristic model, the so-called Γ model. Three tailor-made CFD computation benchmark cases are introduced and used to carry out this review on different serial and parallel architectures, stressing the particular interest for commodity clusters. Conclusions are drawn from this extensive series of analyses and modeling leading to specific recommendations concerning such toolbox development and implementation.

C.1 Introduction

This appendix provides a detailed performance evaluation of the C++ toolbox named Speculoos (for Spectral Unstructured Elements Object-Oriented System). Speculoos is a spectral and mortar element analysis toolbox for the numerical solution of partial differential equations and more particularly for solving incompressible unsteady fluid flow problems. It was initiated by Prof. Michel O. Deville and Dr. Vincent Van Kemenade [254] in 1995 at the Laboratory of Fluid Mechanics of the École Polytechnique Fédérale de Lausanne (EPFL). The main architecture choices and the parallel implementation were elaborated and implemented by Van Kemenade and Dubois-Pèlerin [66,67]. Subsequently, Speculoos' C++ code has been growing up with additional layers enabling to tackle and simulate more specific and arduous CFD problems: viscoelastic flows by Fiétier and Deville [76–78], fluid-structure interaction problems by Bodard and Deville [29], large-eddy simulations of confined turbulent flows by Bouffanais *et al.* [35] and free-surface flows by Bouffanais and Deville [34].

It is well known that spectral element methods are amenable easily to parallelization as they are intrinsically a natural way of decomposing a geometrical domain [81].

The numerous references previously given and the ongoing simulations based on Speculoos highlight the achieved versatility and flexibility of this C++ toolbox. Nevertheless, ten years have passed between the first version of Speculoos' code and the present appendix, and tremendous changes have occurred at both hardware and software levels: fast dual DDR memory, RISC architectures, 64-bit memory addressing, compilers improvement, libraries optimization, libraries parallelization, increase in inter-connecting switch performance, etc.

Back in 1995, Speculoos was commonly compiled and was running on HP, Silicon Graphics workstations and also on the Swiss-Tx machine, a commodity-technology based computer with enhanced interconnect link between processors [103]. Currently most of the simulations based on Speculoos are compiled and are running on commodity clusters. The workstation world experienced a technical revolution with the advent of 'cheap' RISC processors leading to the ongoing impressive development of parallel architectures such as massively parallel clusters and commodity clusters. As a matter of fact, Speculoos benefited from this fast technical evolution as it was originally developed as to run in a single program, multiple data mode (SPMD) on a distributed-memory computer. The performance evaluations presented in this appendix are demonstrating the correlation between the good performances measured with Speculoos and the adequation of this code structure with the current hardware and software evolutions.

This appendix is organized as follows. In Section C.2 we introduce the numerical context in which Speculoos

was initiated, the software aspects related to its implementation and the variable-size benchmark test case used for the performance evaluation presented in the subsequent sections. In Section C.3 we present the performance analysis carried out on single-processor architectures and involving different compilers and compilation parameters. Section C.4 is devoted to the parallel performance analysis achieved on a RISC-based commodity cluster. It is followed by an advanced parallel benchmarking presented in Sec. C.5. Finally, in Section C.6 we draw some conclusions on the results obtained.

C.2 Speculoos numerical and software context

In this section, is gathered the necessary background information regarding the numerical method—namely the spectral and mortar element method—, the object-oriented concept and the parallel paradigm, essential roots embodied in Speculoos. The final Section C.2.4 introduces the two simulations used throughout this appendix as benchmark evaluation test cases.

C.2.1 Spectral and mortar element method

The spectral element method (SEM) is a high-order spatial discretization method for the approximate Galerkin solution of partial differential equations expressed in weak forms. The SEM relies on expansions on Lagrangian interpolants bases used in conjunction with particular Gauss–Lobatto and Gauss–Lobatto–Jacobi quadrature rules [172, 194]. As high-order finite element techniques, the SEM can deal with arbitrary complex geometry where h -refinement is achieved by increasing the number of spectral elements and p -refinement by increasing the Lagrangian polynomial order within the elements. From a high-order precision viewpoint, SEM is comparable to spectral methods as an exponential rate-of-convergence is observed when smooth solutions to regular problems are sought.

C^0 -continuity across element interfaces requires the exact same interpolation in each and every spectral elements sharing a common interface. The associated caveat to such conforming configurations is the over-refinement meshing generated in low-gradient zones. The adopted remedy to such nuisance is a technique developed by Bernardi *et al.* [18] referred to as the mortar element method. Mortars can be viewed as variational patches of the discontinuous field along the element interfaces. They relax the C^0 -continuity condition while preserving exponential rate-of-convergence, and thus allow polynomial nonconformities along element interfaces. Geometrical nonconformities are not implemented yet.

C.2.2 Object-oriented programming

As mentioned in [67], the reasons for choosing C++ as the implementation language for such a spectral and mortar element simulation toolbox are numerous [230]: object-oriented concepts, widespread, non-proprietary, portability, efficiency, possibility to interface with C and Fortran subroutines. Joyner [137] noted that C++ embodies several weak points: it is complex, cryptic, uselessly permissive, it has no garbage collector—in one word, low-level. Dubois-Pèlerin and Van Kemenade [67] have attempted to overcome these drawbacks in Speculoos by the use of a restrictive but sufficient set of different C++ instructions and of several programming guidelines and style conventions which had pervaded the implementation.

Nevertheless, as compared to other widespread efficient programming languages such as Fortran 90, C++ constitutes a high-level programming approach, facilitating the know how transfer from one programmer to the other. In the past decade, this crucial feature has proved its relevance and efficiency as attested by the aforementioned references [34, 35, 66, 67, 76–78]. However it seems reasonable to assess the impact of the accumulation of several implementation layers by different programmers over the years on the current efficiency of this C++ toolbox.

C.2.3 Parallel implementation

The complexity and the size of the large three-dimensional problems tackled by numericists in their simulations require top computational performance accessible from highly parallelized algorithms running on parallel architectures. As mentioned in [67], the implementation of concurrency in Speculoos was based on the concept

that concurrency is a painful implementation constraint going against the high-level object-oriented programming concepts introduced in Section C.2.2. As a matter of consequence, Speculoos parallelization was kept very low-level. In most higher-level operations parallelism does not even show up.

From a computational viewpoint, systems discretized with a high-order spectral element method rely mainly on optimized tensor-product operations taking place at the spectral element level. The natural data distribution for high-order spectral element methods is based on an elemental decomposition in which the spectral elements are distributed to the processors available for the run. It is worth noting that for very large computations, the number of spectral elements can become relatively important as compared to the number of processors available for the computation. The design of Speculoos makes it possible to have several elements sitting on a single processor. Nodal values on subdomain interface boundaries are stored redundantly on each processor corresponding to the spectral elements having this interface in common. Moreover, this approach is consistent with the element-based storage scheme which minimizes the inter-processor communications. Inter-processor communication is completed by MPI instructions [102].

C.2.4 Benchmark evaluation test cases description

As a common practice in performance evaluation, it is important to build a tailor-made benchmark based on a numerical simulation corresponding to a concrete situation for the numericist. Before proceeding to the first step of our performance evaluation, we have short-listed some key parameters that have the most significant impact on the performance of our toolbox: single-processor optimization on the three architectures described above, single-processor profiling analysis, parallel implementation and scalability (including speedup, efficiency, communication times) and parallel implementation and processor dispatching. The main characteristics of the different computer architectures are presented in Table C.1. In the advanced parallel benchmarking presented in Sec. C.5, other machines and computer architectures have been used and are presented in Table C.6.

Two test cases have been developed for this benchmark and an additional one for the advanced parallel benchmarking, see Sec. C.5. All these three test cases belong to the field of CFD and consist in solving the Navier–Stokes equations (2.1)–(2.2), for a Newtonian incompressible fluid. The general formulation of the physical problems corresponding to these test cases is the one introduced in Sec. 2.1.

The first two test cases are based respectively on a two-dimensional (2D) and pseudo three-dimensional (3D) Navier–Stokes simulations of the incompressible flow of decaying vortices in the domain Ω . An analytical solution of these 2D and pseudo 3D Navier–Stokes problems are available and a numerical solution is sought in a 2D or 3D framework. The discretization errors can therefore be explicitly calculated. The accuracy of the results of this benchmark is monitored using relative errors based on the $H^1(\Omega)$ -norm (resp. $L^2(\Omega)$ -norm) for the velocity field \mathbf{v} (resp. pressure field p):

$$\varepsilon_{\mathbf{v}} = \frac{\|\mathbf{v} - \mathbf{v}_{\text{exact}}\|_{H^1(\Omega)}}{\|\mathbf{v}_{\text{exact}}\|_{H^1(\Omega)}} \quad \text{and} \quad \varepsilon_p = \frac{\|p - p_{\text{exact}}\|_{L^2(\Omega)}}{\|p_{\text{exact}}\|_{L^2(\Omega)}} . \quad (\text{C.1})$$

The unsteady flow of decaying vortices has the following exact solution in a 3D framework

$$u(x, y, t) = -\cos x \sin y e^{-2t} , \quad (\text{C.2})$$

$$v(x, y, t) = +\sin x \cos y e^{-2t} , \quad (\text{C.3})$$

$$w(x, y, t) = 0 , \quad (\text{C.4})$$

$$p(x, y, t) = -\frac{1}{4} [\cos(2x) + \cos(2y)] e^{-2t} . \quad (\text{C.5})$$

Computations are carried out in the domain $\Omega = [0, \pi]^d$, where $d = 2, 3$ is the space dimension, with a Reynolds number Re equals to unity. This flow is very well documented [124, 125, 143, 208, 273] and therefore constitutes a suitable choice to test the accuracy of numerical methods and boundary conditions. As the exact solution is exponentially time-decaying, it is important to run the calculations on a short time interval $[0, t_{\text{final}}]$ to prevent a too important analytical decay of the solution, leading to a convergent solution anyway. A choice of $t_{\text{final}} = 10^{-2}$ seems reasonable, associated with a time-step $\Delta t = 10^{-3}$.

All our computations were carried out using two time integrators: the implicit backward-differentiation formula (BDF) of order 2 for the treatment of the viscous diffusive term and an extrapolation scheme (EX) [52, 140] of same order for the nonlinear convective term. One type of pressure decomposition mode, based on a fractional-step method using pressure correction namely BP1 [53, 196, 197] is used.

| | Pleiades | Pleiades2 | ielnx2 | Itanium |
|-----------------------|-----------|------------------|----------------|---------------------|
| Processor | Pentium 4 | Xeon (mono-proc) | Xeon (bi-proc) | Itanium 2 (bi-proc) |
| Nprocs | 1 | 1 | 1 | 1 |
| R_∞ [GFlops/s] | 5.6 | 5.6 | 3.4 | 5.3 |
| Memory addressing | 32-bit | 64-bit | 32-bit | 64-bit |
| Memory type | Dual DDR | Dual DDR | Fast Rambus | Fast Rambus |
| Memory size | 2 GB | 4 GB | 4 GB | 4 GB |

Table C.1: The computer architectures used.

| | Pleiades | Pleiades2 | ielnx2 | Itanium |
|-----------------------|----------|-----------|---------|---------|
| M_∞ [GWords/s] | 0.8 | 0.8 | 0.538 | 0.3 |
| V_m [Flops/Word] | 7 | 7 | 6.32 | 8.67 |
| Compilers | gcc, icc | gcc | gcc | ecc |
| T_5 [s] | 15 749 | 13 827 | 35 6584 | 50 131 |

Table C.2: The computer architectures characteristics: gcc the GNU project C/C++ compiler, icc (resp. ecc) the Intel C++ compiler, 32-bit (resp. 64 bit) version. T_5 is the process duration for test case 5 defined in Table C.3.

Speculoos uses a Legendre SEM [58, 172, 194] for the spatial discretization of the Navier–Stokes equations. For the sake of simplicity the same polynomial order has been chosen in the different spatial directions ($N_x = N_y = N = 10$). Moreover, to prevent any spurious oscillations in our Navier–Stokes computations, the choice of a staggered $\mathbb{P}_N - \mathbb{P}_{N-2}$ interpolation method for the velocity and pressure respectively, has been made [58, 174]. As a consequence of this choice of a staggered grid, the inner-element grid for the x - and y -component of the velocity field is a Gauss–Lobatto–Legendre grid made up with 121 ($= (N + 1)^2$) quadrature (nodal) points and the grid for the pressure is a Gauss–Legendre grid made up with 81 ($= [(N - 2) + 1]^2$) quadrature (nodal) points, in each spectral element. Given E_x (resp. E_y) the number of spectral elements (or subdomains in the finite element nomenclature) in the x -direction (resp. y -direction), the total number of degrees of freedom dof is

$$\text{dof} = 2 \times (10E_x + 1)(10E_y + 1) + 81E_x \times E_y.$$

Table C.3 summarizes the seven cases of variable size studied throughout this appendix, ranging from around 0.1 million dofs up to around 5 millions of degrees of freedom.

| Case | $E_x \times E_y$ | Nb. of elements | Total nb. of dof | Size in memory |
|------|------------------|-----------------|------------------|----------------|
| 1 | 16×16 | 256 | 72 578 | 15.73 MB |
| 2 | 16×32 | 512 | 144 834 | 31.39 MB |
| 3 | 32×32 | 1 024 | 289 026 | 62.64 MB |
| 4 | 64×32 | 2 048 | 577 410 | 125.14 MB |
| 5 | 128×32 | 4 096 | 1 154 178 | 250.13 MB |
| 6 | 256×32 | 8 192 | 2 307 714 | 500.13 MB |
| 7 | 256×64 | 16 384 | 4 610 306 | 999.15 MB |

Table C.3: Information on the variable-size test cases studied.

Two major concerns regarding the specificities of this benchmark case need to be addressed before performing extensive series of tests and afterwards drawing conclusions. The first concern is related to the scalability of the problem, in terms of computer effort, with respect to the number of degrees of freedom of the problem when increasing its dimension from a two-dimensional case to a three-dimensional one. The second concern is also related to the same problem of scalability as before, but now with respect to the number of degrees of freedom when varying the polynomial order in the two directions of the 2D problem. These issues are concurrently dealt with by measuring, on a single-processor architecture, the process durations for variable-size jobs for two- and three-dimensional cases based on the unsteady flow of decaying vortices. The 2D problem described by (C.2)–(C.5) is straightforwardly extended to a three-dimensional one. To maintain a number of degrees of freedom comparable to the ones for the 2D cases presented in Table C.3, the number of spectral elements in the third dimension was kept to the unity— $E_z = 1$ —the polynomial order in this direction, N_z , varying, with $N_x = N_y = 10$, just like in the 2D cases. The results of these computations are reported in Figure C.1. The 2D cases correspond to $N_x = N_y = 10$, the size is adjusted by changing the number of spectral elements E_x and E_y . Two series of 3D cases have been computed, the first one—crosses on Figure C.1—represents $32 \times 32 \times 1$ spectral elements, with $N_x = N_y = 10$ and N_z varying between 2 up to 6. Finally, the second series of 3D cases—squares on Figure C.1—represents $64 \times 32 \times 1$ spectral elements, with $N_x = N_y = 10$ and N_z varying between 2 up to 6.

As expected from the tensor-product formulation of the SEM within each spectral element, Figure C.1 shows a good scalability, in terms of computer effort, of Speculoos with respect to the number of degrees of freedom of the problem when changing both the dimension and/or the polynomial order in one or more directions. It is worth noting that the scalability may be affected by the use of specific preconditioners [52, 53].

The third test case is the fully three-dimensional simulation of the flow enclosed a in lid-driven cubical cavity. It corresponds to the case denoted under-resolved DNS (UDNS) in Part III of the present dissertation. The reader is referred to Chapter 4 for full details on the numerical method and on the parameters used throughout the advanced parallel benchmark described in Sec. C.5.

C.3 Single-processor performance analysis

Single-processor tests have been carried out and are presented in this section, relating to computer architectures, compiler optimization and finally profiling information.

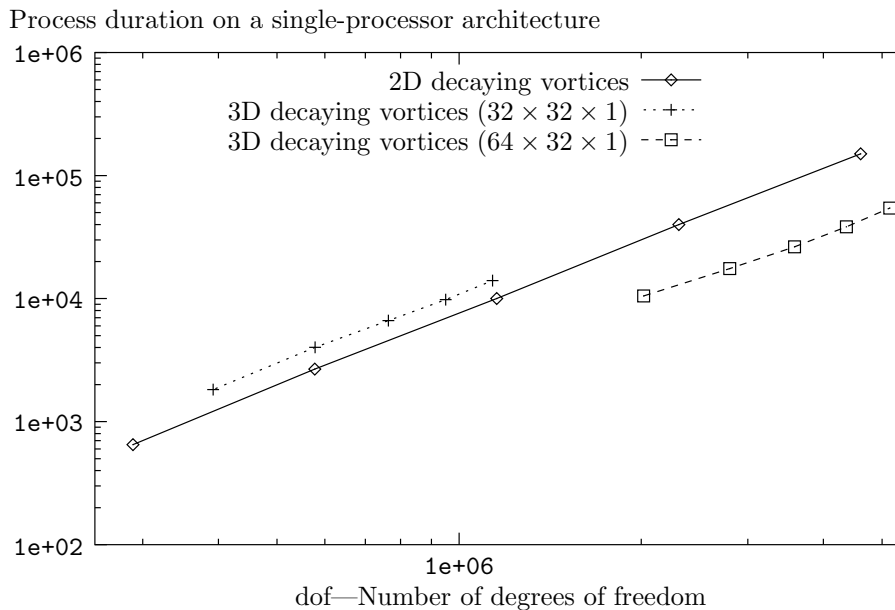


Fig. C.1: Process duration for variable-size jobs running on a single-processor architecture (log-log scale). Diamonds, crosses and squares represent 2D cases with $N_x = N_y = 10$, 3D cases with $E_x = E_y = 32$ and $E_z = 1$, and 3D cases with $E_x = 64$, $E_y = 32$ and $E_z = 1$, respectively.

C.3.1 Influence of the computer architecture

In this section, we will look into the hardware part of our performance analysis. The results described hereafter are obtained using test case 5, corresponding to 128×32 spectral elements. This choice of test case 5 is primarily based on the fact that it is an *intermediate case* in terms of memory resources and also in terms of computing time. In the sequel we will refer to this job run on a single-processor on the three different architectures described in Table C.1 and Table C.2.

The last row of Table C.2 gives the process duration T_5 (for test case 5) obtained compiling in 32-bit mode with `gcc` (the GNU compiler, see C.3.2) on `Pleiades` and on `ielnx2`, and compiling in 64-bit mode with `icc` (the Intel C++ compiler) on Itanium 2. As expected from the architectures characteristics, `Pleiades` is the fastest platform: 2.3 times faster than `ielnx2` and 3.2 times faster than Itanium 2. These results are justified by the higher frequency of the Pentium 4 but also by its very efficient Dual DDR bus memory.

C.3.2 Compiler optimization

For the same C++ code, two compilers are available on the `Pleiades` cluster: `gcc` (or more precisely `g++` that is calling `gcc`) the GNU project C/C++ compiler and `icc` the Intel C++ compiler. Linking for both `gcc` and `icc` used the Intel `mk1_lapack 6.1`, `libmk1_def`, `libguide` and `libF90` libraries. Both of them have been tested with different options, mainly two families of options:

- *Optimization parameters*, offering different levels of optimizations from `00` (no optimization) until `03` where the code optimization is maximum;
- *Processor architecture and CPU type parameters*; on the cluster `Pleiades` where Pentium 4 CPUs are used, options `i686` and `pentium4` are notified to the compilers `gcc` and `icc` respectively.

Table C.4 contains the results of several computations run on the same Navier–Stokes test case described in section C.2.4 with 128×32 spectral elements (case 5—corresponding to approximately one million dofs). The second column shows the process duration in second for a single-processor run and the third column corresponds to the relative performance improvement for the run studied compared to the same run with the same options but with the other compiler (`gcc` if `icc` is considered and conversely).

The results presented in the Table C.4 lead us to the following remarks and conclusions:

| Compiler optimization parameters | Process duration (s) | R.P.I. g++/icc (%) |
|---|----------------------|--------------------|
| g++ (all options off) | 22'291 | + 6.8% |
| g++ -O3 -march=i686 | 16'189 | + 1.9% |
| g++ -O3 -mcpu=i686 | 16'192 | + 2.1% |
| g++ -O3 -march=i686 -mcpu=i686 | 15'749 | + 4.9% |
| g++ -O3 -march=i686 -mcpu=i686 -finline-functions | 16'210 | |
| g++ -O3 -march=i686 -mcpu=i686 -finline-functions -msse2 | 16'192 | |
| icc -O0 | 23'918 | - 7.3% |
| icc (all options off) | 16'729 | |
| icc -O3 | 16'553 | |
| icc -O3 -march=pentium4 | 16'508 | - 2.0% |
| icc -O3 -mcpu=pentium4 | 16'537 | - 2.1% |
| icc -O3 -march=pentium4 -mcpu=pentium4 | 16'570 | - 5.2% |
| icc -O3 -march=pentium4 -mcpu=pentium4 -xW -ip | 16'560 | |

Table C.4: Comparisons of the performances of two compilers `icc` and `gcc` (R.P.I standing for Relative performance improvement).

- For all cases studied with different compiler options, the compiler `gcc` provides better results than `icc`. In the usual case, where the architecture and CPU types are defined and when the optimization is maximum (flag `-O3`), using `gcc` shortens the process duration by approximately 5% compared to the usage of `icc`. This performance improvement is non-negligible and for a run lasting 30 days, the choice of `gcc` will save one and a half day of computer resources;
- as `icc` is a compiler dedicated to Intel Pentium processors and architectures, it automatically detects the CPU and architecture types. This explains why the results of the computation with `icc` with all options off is close to the results where CPU and architecture types are specified. In addition, as the CPU and architecture types are automatically specified with `icc`, it is therefore possible to just optimize it by flagging with `-O3` when compiling. On the other hand, `gcc` requires the CPU or architecture type when flagging `-O3` for optimization purpose;
- we can also notice that by default `icc` optimizes the code (comparison of cases with flags `-O0` and `-O3`) that is not the case of `gcc`. More importantly, one can notice that the difference between an aggressive optimization `-O3` and a size and locality optimization `-O1`—which corresponds by default to the case where all options are off—is only more than 1%. This suggests that Speculoos is well optimized, but indeed solely reflects the optimization of the libraries `Blas` and `Lapack`, which are substantially used by the code.

As a conclusion of this section on performance improvement due to compilation, we can say that with Speculoos, the GNU project compiler `gcc` is recommended, specifying both architecture and CPU type and with the maximum code optimization parameter on. To our knowledge, Speculoos is far from being the only C++ code producing more cost-effective simulations when compiled with `gcc` instead of its proprietary counterpart `icc`. The choice of `gcc` as compiler for Speculoos is primarily based on performance requirements but also on portability requirement, `gcc` being available on most of the current platforms—if not sources are available.

C.3.3 Linking optimization

Choosing `gcc` as compiler—see Section C.3.2—, we have tested out linking the 32 Speculoos object files with three different groups of libraries. Speculoos requires `Blas`, `Lapack` and also a library ensuring the conversion from Fortran to C/C++. The same test case as in the previous section is used:

- Using `Blas 3.0`, `Lapack 3.0` and `libg2c` from the GNU project, the computing time is 18'680 s;
- Using the Intel `mk1_lapack 6.1`, `libmkl_def`, `libguide` and `libF90`, the computing time is 15'750 s;
- Using the Intel `mk1_lapack 6.1`, `libmkl_p4`, `libguide` and `libpthread`, the computing time is 26'833 s.

As a conclusion of this section, it appears clearly that the proprietary optimized libraries from Intel with the Fortran 90 converter, coupled with the non-proprietary compiler `gcc` produce the most efficient binary executable file. These results highlight the room for improvement for the GNU project in the framework of their optimized libraries associated to its efficient compiler.

C.3.4 Profiling

In annex is presented the most significant part of the profiling information, namely the flat profile. This information was gathered by `gprof` the GNU profiler after compiling and linking on Pentium 4 of *Pleiades*, the 32 object files comprised by *Speculoos* using `gcc` together with the flag `-pg`.

For ease of presentation only the function calls representing the top 90% of the cumulative running time appears in the flat profile in annex.

In general the flat profile allows the programmer to spot the functions monopolizing the major part of the CPU resources. For scientific computations, these functions should correspond to fundamental operations such as multiplication-summation of vector-Matrix/Matrix-vector. Therefore optimizing these functions lead to a significant reduction of the computing time.

In our case, the intermediate test case 5 (128×32 elements) has been profiled and the most striking piece of information delivered by the flat profile is that no function represents a large and significant part of the running time. For instance the most costly function called, the first one in the profile

```
RealVector::Multiply(RealVector*)
```

represents a bit less than 15% of the cumulative computing time. It means that optimizing this function could in the best case reduce its “cost” by 10 to 20%, representing finally a “saving” of only 1 to 3% of the total running time.

Knowing the complexity of the *Speculoos* C++ code—see Sec C.2.2—, the optimization of the four first functions in the flat profile, namely:

1. `RealVector::Multiply(RealVector*)`
2. `FlatField::Multiply(Field*, int, int)`
3. `Element::CopyAddValuesFrom(Element*)`
4. `ElementaryField::MultiplyByWeights(int)`

corresponding each of them to more than 5% of the total computing time, is not worth the time to be invested by the programmer.

The second important piece of information revealed by the flat profile is gathered in the fourth column “calls” corresponding to the number of times a function was invoked by the code. A quarter of the functions listed in the flat profile (including the most costly (1): `RealVector::Multiply(RealVector*)`) are invoked a number of times reaching extremely high values with an order of magnitude of the billion! This remark highlights one of the weaknesses of *Speculoos* due to its implementation with very structured classes, templates and repeated function calls.

As a last point, it is important to notice that the flat profile obtained is somehow different from what could be expected from the profiling output of an optimized scientific computation. Several functions not involved in pure calculations appear to occupy a non-negligible part of the cumulative time. From the flat profile in annex, 9 functions are of this type and cumulate about 12% of the total computing time. In addition, these functions are usually invoked a very large number of times as discussed earlier.

As a conclusion, the profiling information presented in this appendix is a proof of some weaknesses of *Speculoos*, in particular related to its excessive structured C++ implementation [137, 230].

C.4 Parallel implementation

In the sequel, we will assume that the reader is familiar with the basics of parameterization on a parallel machine. For a complete introduction to these notions we refer the reader to the following references [104, 105].

The speedup A of an application on a given parallel machine can be described as

$$A = \frac{\text{Computing time on one processor}}{\text{CPU plus communication times on } P \text{ processors}} = \frac{T_1}{T_P + T_C}. \quad (\text{C.6})$$

If we suppose that the computing effort strictly scales with P , then $T_1 = PT_P$ and the speedup can be written as

$$A = \frac{T_1}{T_P + T_C} = \frac{PT_P}{T_P + T_C} = \frac{P}{1 + \gamma_m/\gamma_a} = \frac{P}{1 + 1/\Gamma}, \quad (\text{C.7})$$

where γ_m and γ_a are introduced in [105], and $\Gamma = \gamma_a/\gamma_m$. The efficiency E of a parallel machine is defined by

$$E = \frac{A}{P} = \frac{1}{1 + 1/\Gamma}. \quad (\text{C.8})$$

The quantity $P_{1/2}$ denotes the number of processors for which the efficiency E is half, and $A_{1/2} = A(P_{1/2})$ is the speedup for $P = P_{1/2}$ processors.

C.4.1 Influence of processor dispatching on performance

In this section we will discuss the effect of specifying the way of dispatching the spectral elements—or subdomains—to the processors for a job running in parallel on a cluster architecture such as **Pleiades** for instance in our case.

With **Speculoos**, the first basic procedure to assign a processor to every spectral element is called

`DispatchElements()`.

It is a non-optimized algorithm in which the spectral elements are assigned to a processor following a cycle, with a cycle-length equal to the number of processors available for the run. It is clear that this non-optimized method will increase the communications between processors.

In order to improve on this point and to optimize the communications between the processors a new procedure to assign a processor to every spectral element, called

`DispatchElementsByBlocks(nx, ny)`,

has been implemented. The computational grid is assumed to be structured, in the sense that its elements are assumed to be generated by a `nx*ny` distribution on a face element. The elements are assigned by blocks, in order to minimize inter-processor communications.

The functions `DispatchElements()` and `DispatchElementsByBlocks(nx, ny)` have been tested on our intermediate test case 5 (128×32 spectral elements) with a number of processors ranging between 1 and 16. Figure C.2 summarizes the results in terms of parallel efficiency E . The increase in efficiency E between the non-optimized and the optimized processor dispatching procedures is almost constant with the number of processors `Nprocs` and is equal to 7–8%.

C.4.2 Scalability study and influence of the size of the problem

As expected from the theory, the scaling of our computations depends highly on the load-balancing of our cases among the processors available for the run. Therefore the smaller the case studied (in terms of memory and CPU resources) the longer the communications, reducing *ipso facto* the speedup A and the efficiency $E = A/P$ measuring the scalability.

As can be seen on Fig C.4 and C.5, cases 5–7 (128×32 – 256×64 elements) scale almost perfectly for a number of processors up to four. Cases 1–2 (16×16 – 16×32 elements) are too small and therefore do not load sufficiently the processors and their associated shared memory. In these cases, parallel computations are not justified: $P_{1/2}$ is close to 4 and 6 (see Table C.5), corresponding to an efficiency of only 50%. The waste of resources is due to communications and a detailed analysis is given in the next section.

For small values of the number of processors P ($P \leq 4$), the load-balancing is acceptable for all cases studied leading to efficiencies very close to 1 (see Fig. C.7) and an almost perfect scalability.

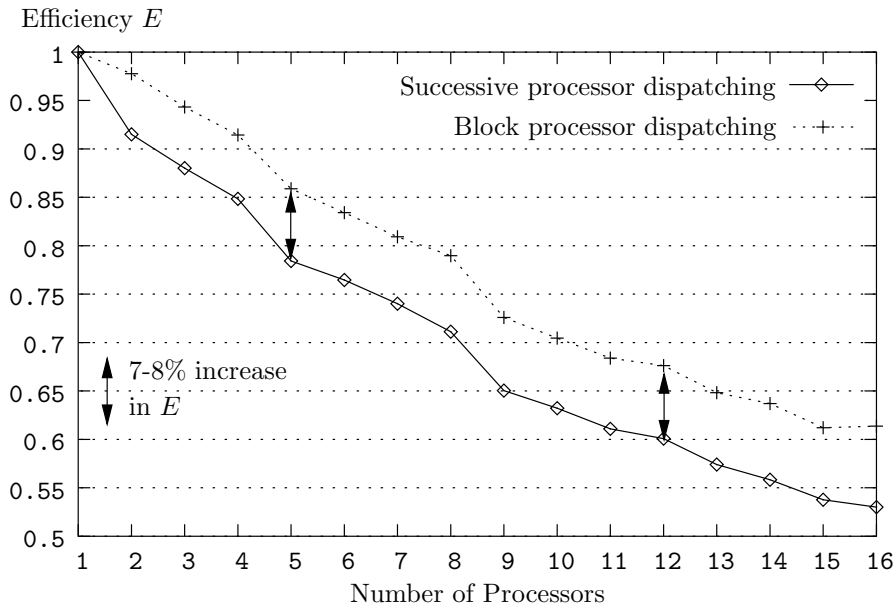


Fig. C.2: Performance improvement due to an optimized dispatching of the spectral elements by blocks.

| Case | $E_x \times E_y$ | $P_{1/2} \Leftrightarrow E(P_{1/2}) = 0.5$ | $A_{1/2} = A(P_{1/2})$ |
|------|------------------|--|------------------------|
| 1 | 16×16 | 4 | $\gtrsim 2$ |
| 2 | 16×32 | 6 | $\gtrsim 3$ |
| 3 | 32×32 | 9 | ≈ 4.5 |
| 4 | 64×32 | 12 | $\gtrsim 7$ |
| 5 | 128×32 | ≈ 20 | ≈ 11 |
| 6 | 256×32 | 32 | ≈ 17 |
| 7 | 256×64 | > 32 | > 20 |

Table C.5: Values of $P_{1/2}$ and $A_{1/2}$ for the seven test cases.

For a larger number of processors ($16 \leq P \leq 32$) Fig. C.6 (magnification on the left side) shows a very poor load-balancing for the small cases. The speedups comprised between $A(P = 16)$ and $A(P = 32)$ are smaller than the speedup $A(P = 8)$ and even $A(P = 4)$ for $A(P = 32)$. These observations translate into very poor efficiencies (smaller than 0.15) observed on Fig. C.7.

For information, a dimensionalized graph showing the computing time T_P in seconds, with the number of processors varying between 1 and up to 32 is given on Fig. C.3.

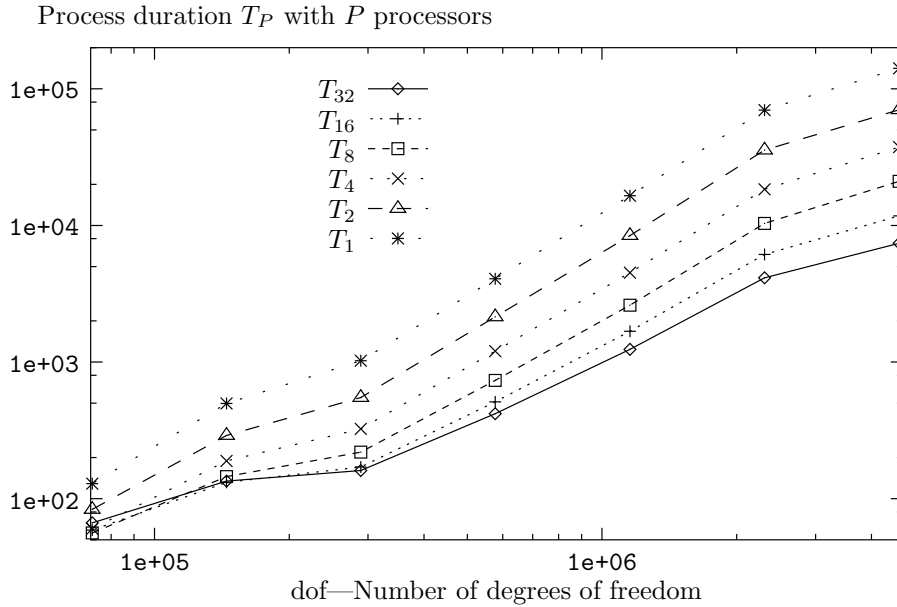


Fig. C.3: Process durations for variable-size jobs running on 1 up to 32 processors (log-log scale).

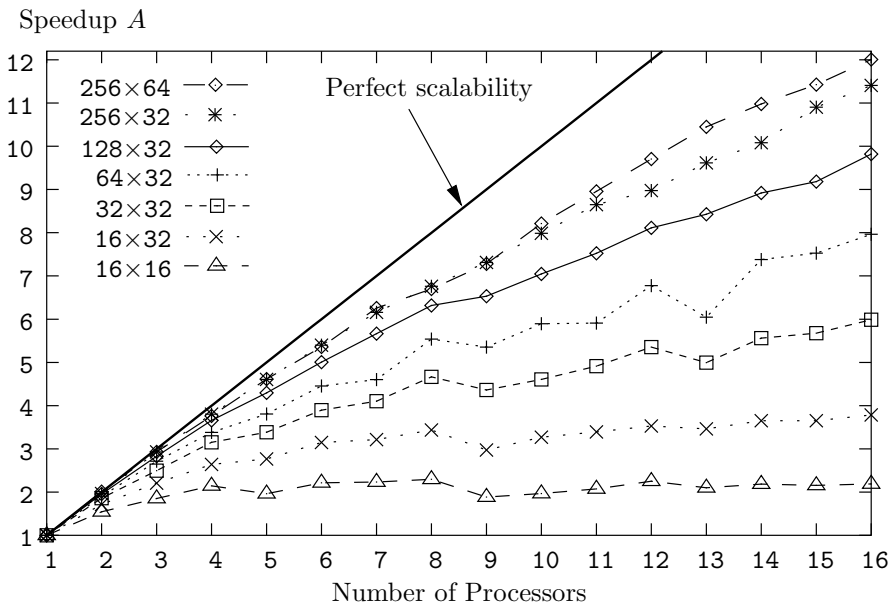


Fig. C.4: Evolution of the speedup A against the number of processors N_{procs} for the seven test cases 1–7.

C.4.3 Communications

One major concern when running jobs on a parallel architecture is to have the inter-processor communications taking a too important part of the computing time. This is even more important when the network switch is like in the case of Pleiades a Fast Ethernet switch running at only 10 MB/s. Even with a Gigabit Ethernet switch, communications still remain a point of special attention.

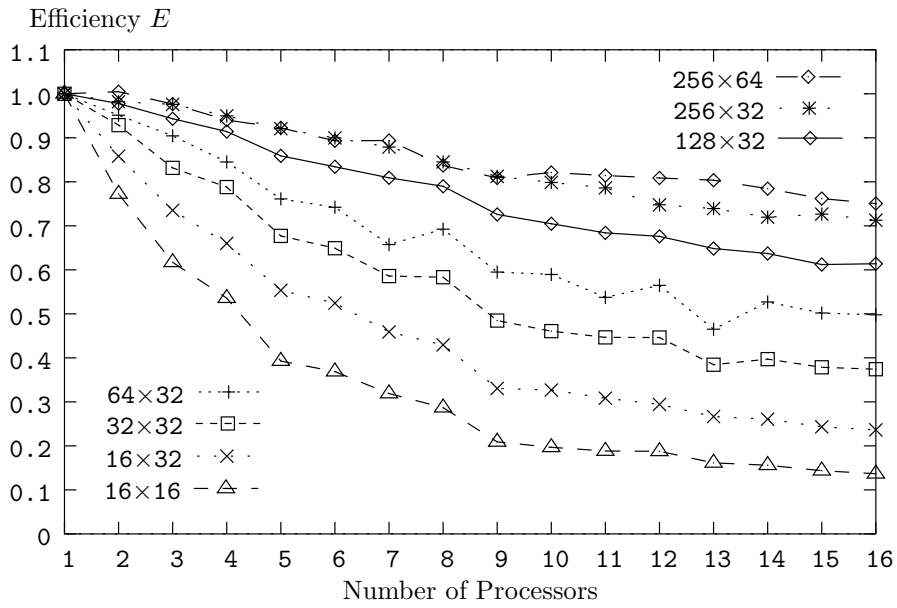


Fig. C.5: Evolution of the efficiency E with the number of processors N_{procs} for the seven test cases 1–7.

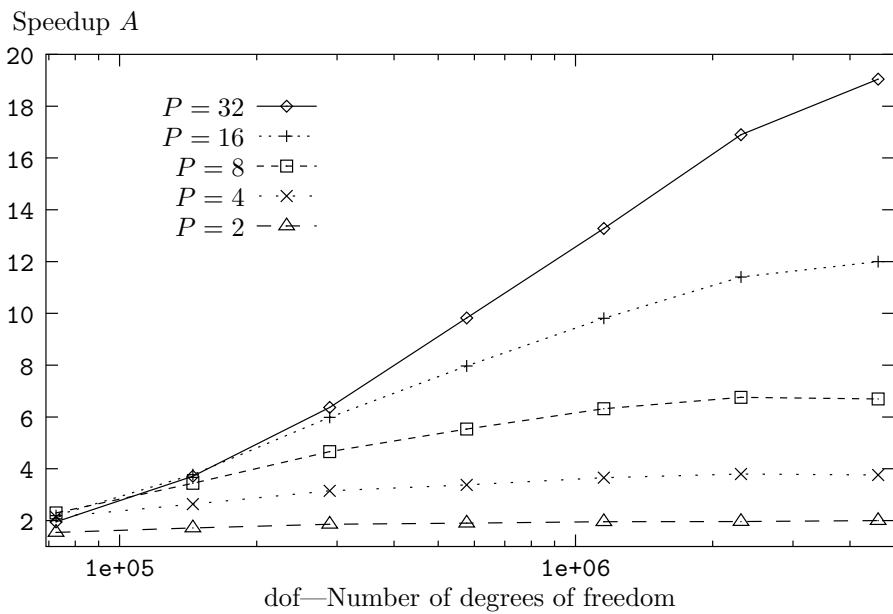


Fig. C.6: Evolution of the speedup A as a function of the size of the test case, for $N_{procs}=2^k$, with $k=1, \dots, 5$.

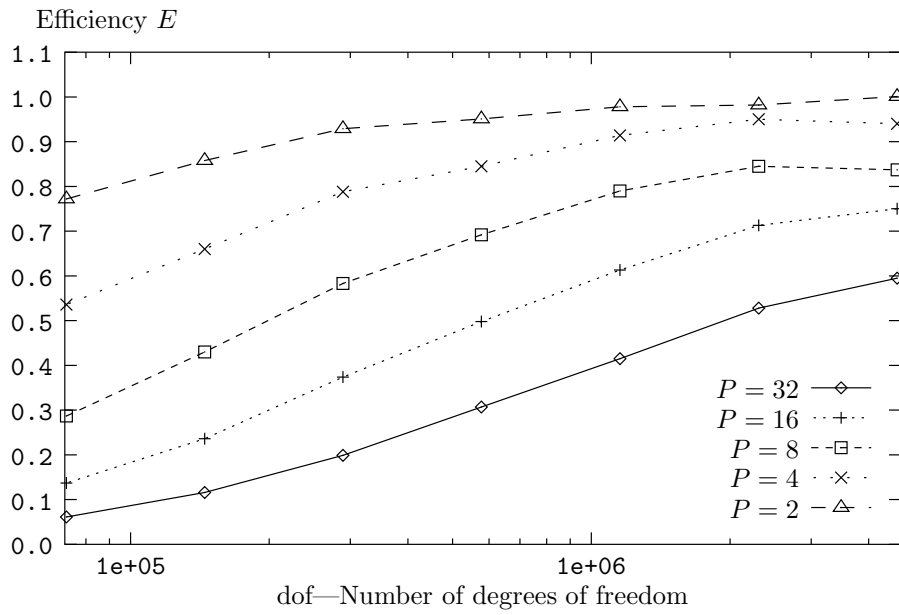


Fig. C.7: Evolution of the efficiency E as a function of the size of the test case, for $N_{\text{procs}} = 2^k$, with $k = 1, \dots, 5$.

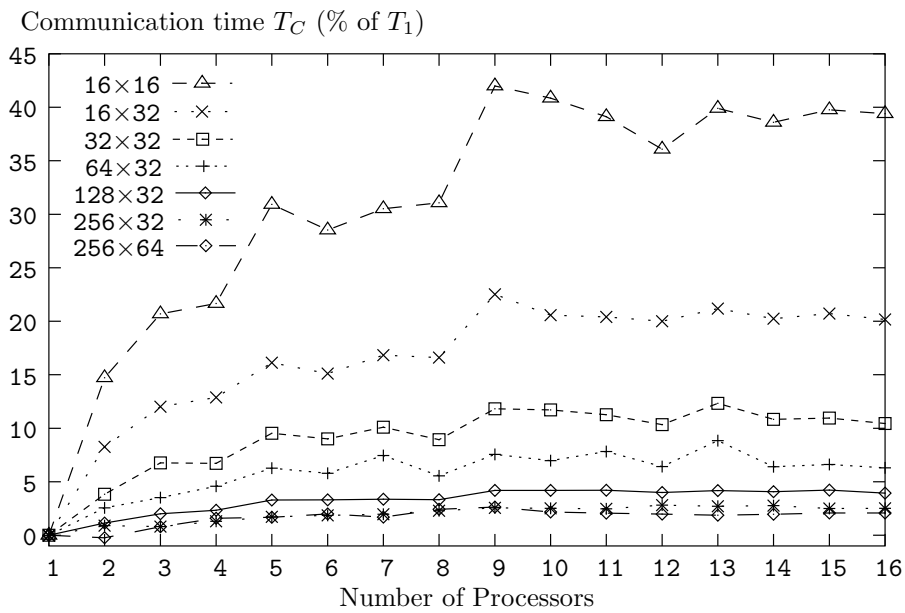


Fig. C.8: Communication time T_C (as a percentage of the process duration with a single-processor T_1) as a function of N_{procs} for the 7 test cases.

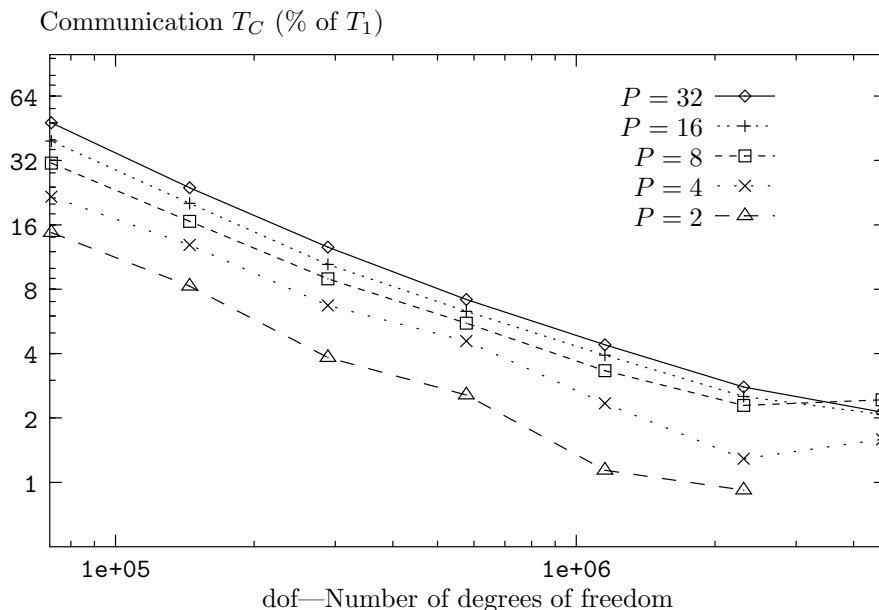


Fig. C.9: Communication time T_C (as a percentage of the process duration with a single-processor T_1) as a function of the size of the test case, for $\text{Nprocs} = 2^k$, with $k = 1, \dots, 5$.

Fig. C.8 and Fig. C.9 show that for the large cases, namely cases 6 and 7 (256×32 and 256×64 elements), the communications represent only a very small fraction 2–3% of the total computing time, for all values of Nprocs varying from 2 up to 32. For intermediate cases 4–5 (64×32 and 128×32 elements respectively), communications take less than one tenth of the total elapsed time, that is still acceptable. Finally for small cases 1–3, the communication times reach unacceptable values and can even take over the computing time, like in the smallest case studied, 16×16 with $\text{Nprocs} = 32$.

One case of ‘superlinearity’ is observed, corresponding to the largest test case 7 (256×64 elements and $\text{dof} \simeq 5.10^6$) using $\text{Nprocs} = P = 2$ processors. This phenomenon of superlinearity corresponds to a speedup $A > P$ (see Fig. C.4 and Fig. C.6), an efficiency $E > 1$ (see Fig. C.5 and Fig. C.7) and also to a negative communication time $T_C < 0$ (see Fig. C.8). This so-called superlinearity can be explained by the fact that with Speculoos, for very large cases and small number of processors, the computing effort scales with $\text{Nprocs} = P$: $T_1 \neq PT_P$.

Speculoos code running on a single processor is slightly slowed down by the useless MPI commands leading to a single-processor computing time $T_1(\text{MPI})$ greater than the real T_1 that could be measured without using any MPI commands.

For cases not too large ($\text{dof} \leq 10^6$), Fig. C.9 shows that the communications T_C/T_1 decreases linearly (in log-log scales) with the number of dof and in addition the corresponding negative slope is the same whatever the number of processors $\text{Nprocs} = P$. This observation translates into the following heuristic power-law scaling

$$\frac{T_C}{T_1} = K(P) \text{dof}^{-\alpha}, \quad (\text{C.9})$$

where $-\alpha$ is the slope measured on Fig. C.9—approximately $\alpha = 0.9$ —and K is a function of the number of processors P .

C.5 Advanced parallel benchmarking

As mentioned in Sec. C.2.4, the test case used throughout this section is the simulation of the lid-driven cubical cavity flow, detailed in Chapter 4.

C.5.1 Speculoos characteristics

Speculoos uses a small amount of main memory. Parallelization is made in order to reduce the high overall computing time. The performance measurements are made at time-step number 4, the first 3 time-steps also include initialization operations. The number of elements and the polynomial degrees in the three space directions are denoted by E_x , E_y , and E_z , and N_x , N_y , and N_z , respectively. The total number of independent variables per element is therefore $n_v \times (N_x + 1) \times (N_y + 1) \times (N_z + 1)$, where n_v is the number of vector components per Gauss-Lobatto-Legendre (GLL) quadrature point. In addition, there are $E_x \times E_y \times E_z$ elements.

C.5.2 Hardware and software used

To perform the Speculoos code benchmark, the machines presented in Table C.6 have been used.

| Name | Manufacturer | CPU type | Nodes | Cores | Interconnect |
|------------|--------------|------------|-------|-------|--------------|
| Gele | Cray | Opteron DC | 16 | 32 | SeaStar |
| Pleiades | Logics | Pentium 4 | 132 | 132 | FE |
| Pleiades2 | Dell | Xeon | 120 | 120 | GbE |
| Pleiades2+ | Dell | Xeon 5150 | 99 | 396 | GbE |

Table C.6: Characteristics of the machines used for the benchmark. DC=Dual-Core.

As mentioned previously, the Speculoos code is written in C++, uses Blas operations and implements the Message Passing Interface (MPI). The benchmarks have been performed using the compilers and libraries versions shown in Table C.7.

| Compiler | Company | Machine | Version |
|----------------|------------|------------|---------------|
| icc | Intel | Pleiades | 9.0 |
| icc | Intel | Pleiades2 | 9.1e |
| icc | Intel | Pleiades2+ | 9.1e |
| g++ | Intel | Pleiades | 4.2.0 |
| CC (pgCC) | Cray (PGI) | Gele | 6.1-4 64 bits |
| Library | Company | Machine | Version |
| MPICH | GNU | Pleiades | 1.2.7 |
| MPICH2 | GNU | Pleiades | 1.0.5 |
| MPICH | GNU | Pleiades2 | 1.2.7 |
| MPICH2 | GNU | Pleiades2 | 1.0.5 |
| MPICH | GNU | Pleiades2 | 1.2.7 |
| MPICH2 | GNU | Pleiades2+ | 1.0.5 |
| MPICH2-nemesis | GNU | Pleiades2 | 1.0.5 |
| MPICH2-nemesis | GNU | Pleiades2+ | 1.0.5 |
| MPICH2 | Cray | Gele | MPT 1.3 |
| MKL | Intel | Pleiades | 7.1 |
| MKL | Intel | Pleiades2 | 8.1e |
| MKL | Intel | Pleiades2 | 9.0e |
| MKL | Intel | Pleiades2+ | 8.1e |
| MKL | Intel | Pleiades2+ | 9.0e |
| ACML | AMD | Gele | 3.0 |
| PAPI | GNU | Gele | 3.2.1 |

Table C.7: Characteristics and versions of the software used for benchmarking. MPT stands for Message Passing Toolkit.

The PAPI (Performance API) [3] available on the Cray XT3 machine was used to measure the numbers O of operations (in GFlops) and the MFlops/s rate of Speculoos. The VAMOS service available on the three Pleiades clusters [1] maps the hardware related data from the Ganglia monitoring tool [2] with the application and user related data (from cluster RMS and Scheduler). We used the most aggressive optimization flag on all machines (-O3 flag).

C.5.3 Fixed problem size

The first measurements are done on `Pleiades2` with a fixed problem size, $E_x = E_y = E_z = 8$; $N_x = N_y = N_z = 8$; $O = 155.4$ GFlops, and varying the number P of processing elements from 1 to 60. The evolution of the runtime (for one time-step), the associated MFlops/s rate, and the efficiency E are given in Table C.8. The speedup A as a function of the number of processors is plotted in Fig. C.10. One sees that with 8 processors a speedup of 7 can be reached and a speedup of 20 with 26 processors.

| P | GFlops/s | Runtime (1 step) | E |
|-----|----------|------------------|------|
| 1 | 0.638 | 243.59 | 1.00 |
| 2 | 1.251 | 124.23 | 0.98 |
| 3 | 1.901 | 81.75 | 0.99 |
| 4 | 2.395 | 64.88 | 0.94 |
| 5 | 3.038 | 51.15 | 0.95 |
| 6 | 3.566 | 43.58 | 0.93 |
| 7 | 4.101 | 37.89 | 0.92 |
| 8 | 5.590 | 34.52 | 0.88 |
| 16 | 8.346 | 18.62 | 0.82 |
| 32 | 14.179 | 10.96 | 0.70 |

Table C.8: Evolution of GFlops/s rate and runtime for fourth time-step. E : Efficiency.

C.5.4 Increase CPU performance

In this section, the number of processors on a Cray XT3 is kept fixed at the value $P = 4$. Then, we modify the polynomial degree and measure the MFlops/s rate. The MFlops/s rate performance metric for each process element is shown on Table C.9. It increases as the problem size increases. As expected, one deduces that there is a limit on the number of processors that should be used in parallel.

| $E_x - E_y - E_z$ | $N_x - N_y - N_z$ | MFlops/s | Walltime |
|-------------------|-------------------|----------|----------|
| 8 - 8 - 8 | 6 - 6 - 6 | 1624 | 18.54 |
| 8 - 8 - 8 | 7 - 7 - 7 | 2580 | 29.79 |
| 8 - 8 - 8 | 8 - 8 - 8 | 3100 | 50.07 |
| 8 - 8 - 8 | 9 - 9 - 9 | 3700 | 83.12 |
| 8 - 8 - 8 | 10 - 10 - 10 | 4150 | 146.97 |
| 8 - 8 - 8 | 11 - 11 - 11 | 4390 | 257.36 |

Table C.9: Evolution of MFlops/s rate and runtime for one time-step on 4 Cray XT3 dual-CPU nodes as a function of the polynomial degree.

C.5.5 Varying the number of processing element P with problem size

A more common way to measure scalability, and to overcome Amdahl's law, is to fix the problem size per processor and to increase the number of processors with the overall problem size. In other words, one tries to fix Γ that measures the ratio between processor needs over communication needs. We show in Table C.10 the scalability of `Speculoos` on the `Pleiades2+` cluster. It was compiled using `MPICH2` and `icc` C++ compiler version 9.1e.

Table C.10 (A) shows results obtained when all the 4 cores are active for $P > 1$. Note that one Woodcrest node with 2 dual-core processors (Table C.10) is slightly faster than 4 dual-CPU nodes (Table C.9) of the Cray XT3. When increasing the number of nodes with the problem size, the MFlops/s rate per core remains the same for all the cases. At this point, it is legitimate to determine if `Speculoos` is memory or processor bound. To find out, all the test cases in Table C.10 have been resubmitted to the Woodcrest nodes, first (A) using all the 4 cores per node, then (B) restricting to two the maximal number of MPI threads per node. Thus, instead of 16 nodes, 32 nodes were used to run the 64-processor case (see Table C.10 (B)). One sees that the overall CPU time has been reduced by 20%, but the number of nodes was doubled. This shows that `Speculoos` includes

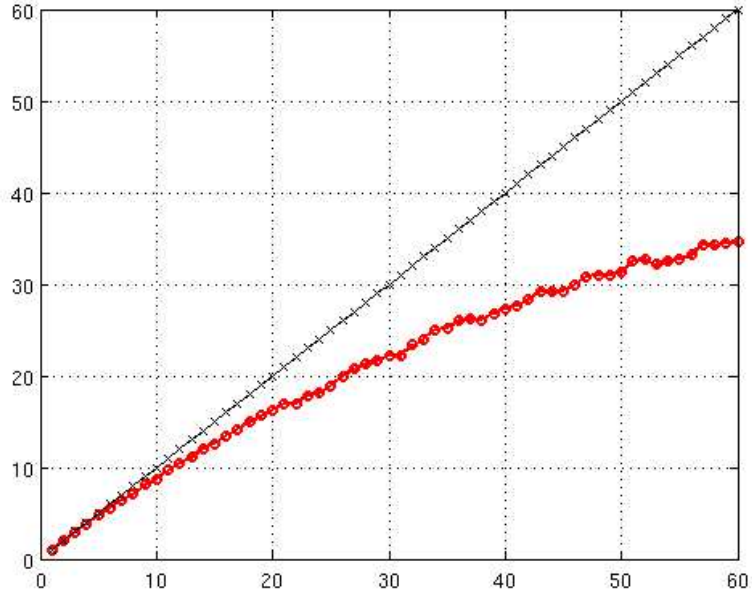


Fig. C.10: Speedup of Speculoos code on the Pleiades2 (Xeon CPU).

| $E_x - E_y - E_z$ | $N_x - N_y - N_z$ | Nodes-Cores | Elem/Core | Walltime |
|-------------------|-------------------|-------------|-----------|----------|
| 4 - 4 - 4 | 8 - 8 - 8 | 1 - 1 | 64 | 8.68 |
| 8 - 8 - 8 | 8 - 8 - 8 | 2 - 8 | 64 | 39.26 |
| 16 - 16 - 16 | 8 - 8 - 8 | 16 - 64 | 64 | 147.97 |

(A)

| $E_x - E_y - E_z$ | $N_x - N_y - N_z$ | Nodes-Cores | Elem/Core | Walltime |
|-------------------|-------------------|-------------|-----------|----------|
| 4 - 4 - 4 | 8 - 8 - 8 | 1 - 1 | 64 | 8.68 |
| 8 - 8 - 8 | 8 - 8 - 8 | 4 - 8 | 64 | 33.50 |
| 16 - 16 - 16 | 8 - 8 - 8 | 32 - 64 | 64 | 111.71 |

(B)

Table C.10: Scalability of Speculoos. Same polynomial degree, same number of elements on each compute node on Pleiades2+ (Woodcrest) cluster. (A): with 4 MPI threads per node. (B): with $n_{\text{pernode}} = 2$, two MPI threads per node.

parts that are processor bound and others that are memory bound. As a consequence, using all 4 cores does not give a two fold speedup (as one expects for a processor bound program) but neither the speedup is zero (as for a main memory bound application). Therefore, it is always more efficient to run Speculoos on all the 4 cores per node.

C.5.6 CPU usage and the Γ model

CPU usage has been monitored by the VAMOS monitoring service [1] available on the Pleiades clusters. It provides information on the application’s behavior. The higher the CPU usage is, the better the machine fits to the application. To perform that monitoring we took the same problem size ($E_x = E_y = E_z = 8$ and $N_x = N_y = N_z = 8$) during the same computing duration (10 hours = 36 000 seconds). The application is run for 10 hours and the number of iteration steps performed during this time is counted. With such a methodology, we ensure that each sample can perform a maximum of calculations in a given amount of time. It is equivalent to set the same number of iteration for each sample and to measure the walltime.

Figure C.11 shows the different behavior of Speculoos on the three different architectures. The Γ value—introduced in Eq. (C.7) and, which reflects the “fitness” of a given application on a given machine [105]—is also computed. Results are reported in Table C.11.

Using the notations introduced earlier, T , T_P , T_C , and T_L denote the total walltime, the CPU time for P processing elements, the time to communicate, and the latency time per iteration step, respectively. Then,

$$T = T_P + T_C + T_L, \quad (\text{C.10})$$

and the parameter Γ is easily expressed as

$$\Gamma = \frac{T_P}{T_C + T_L}. \quad (\text{C.11})$$

| | T [s] | Γ | b [MB/s] | S [words] | T_P [s] | T_C [s] | T_L [s] |
|------------|--------------|----------------------------|-----------------|------------------|-----------------------------|-----------------------------|-----------------------------|
| Pleiades | 23.01* | 1.44* | 12* | $180 * 10^6$ | 13.58 | 8.43 | 1 |
| Pleiades2 | 9.55* | 3.81* | 101 | $180 * 10^6$ | 7.56 | 0.98 | 1 |
| Pleiades2+ | 12.89* | 1.60* | 101 | $180 * 10^6$ | 7.93 | 3.96 | 1 |

Table C.11: Measured (*) and computed quantities using the Γ model.

It is possible to measure the total time T by means of an interpretation of the CPU usage plots (see Fig. C.11). Indeed, the middleware Ganglia determines for every time interval of 20 seconds the average CPU usage (or efficiency E) for each processing element. This information has to be put into relation to the Speculoos application. This is done via the middleware VAMOS. In the plots in Fig. C.11, are added up all the values of E that lie in between x and $x + 0.01$, where x is the percentile represented on the abscissae of the plots. The efficiency E is related to the Γ through

$$\Gamma = \frac{E}{1 - E}. \quad (\text{C.12})$$

What can also be estimated are the network bandwidths b of the GbE switch (between $b = 90$ and 100 MB/s per link), the network bandwidth of the Fast Ethernet switch (between $b = 10$ and 12 MB/s per link) and the latency ($L = 60 \mu\text{s}$ for both networks). First, a consistency test of those quantities is performed. Assuming that the Fast Ethernet switch has a fix bandwidth of $b_1 = 12$ MB/s, and for the GbE switch $b_2 = \alpha b_1$, with α unknown. Another unknown is the number of words S that is sent per node to the other nodes, and $T_C = S/b$. Based on the previous assumptions, the three Γ values for the three machines and the two networks is expressed as

$$\Gamma_1 = \frac{T_{P_1}}{S/b_1 + T_L}, \quad (\text{C.13})$$

$$\Gamma_2 = \frac{T_{P_2}}{S/b_2 + T_L}, \quad (\text{C.14})$$

$$\Gamma_3 = \frac{T_{P_3}}{S/b_2 + T_L}. \quad (\text{C.15})$$

These constitute a set of three equations for three unknown variables, namely S , α , and T_L . Solving for these variables leads to $T_L = 1$, $S = 180$ MWords, and $\alpha = 8.43$. The value of $b_2 = 101$ MB/s corresponds precisely to the one measured. This means that the model is well applicable.

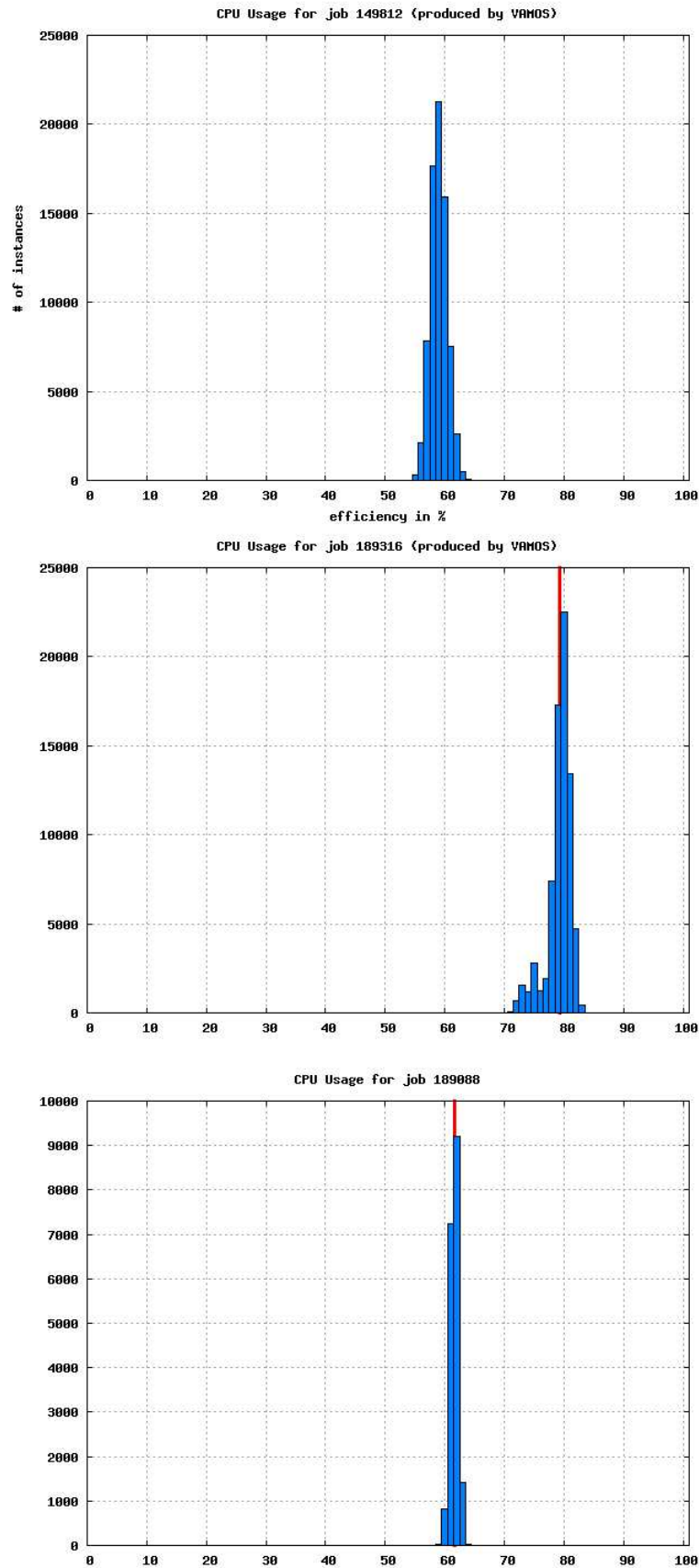


Fig. C.11: CPU Usage of Speculoos on different machines. Top: *Pleiades* cluster (CPU usage average 51.05%, $\Gamma = 1.04$). Middle: *Pleiades2* cluster (CPU usage average = 79.24%, $\Gamma = 3.81$). Bottom: *Pleiades2+* cluster (CPU usage average 61.6%, $\Gamma = 1.60$).

C.5.7 Modification of the number of running threads per SMP node

To demonstrate that Speculoos is dominated by inter-node communications, Figure C.12 shows the result of two runs of the same problem size ($E_x = E_y = E_z = 8$ and $N_x = N_y = N_z = 8$) made respectively on 4 and 8 Woodcrest nodes during the same period of time (1h = 3600 seconds) and counting the number of iteration steps. The first sample was launched forcing 2 MPI threads on each node and the second with 4 MPI threads on each node.

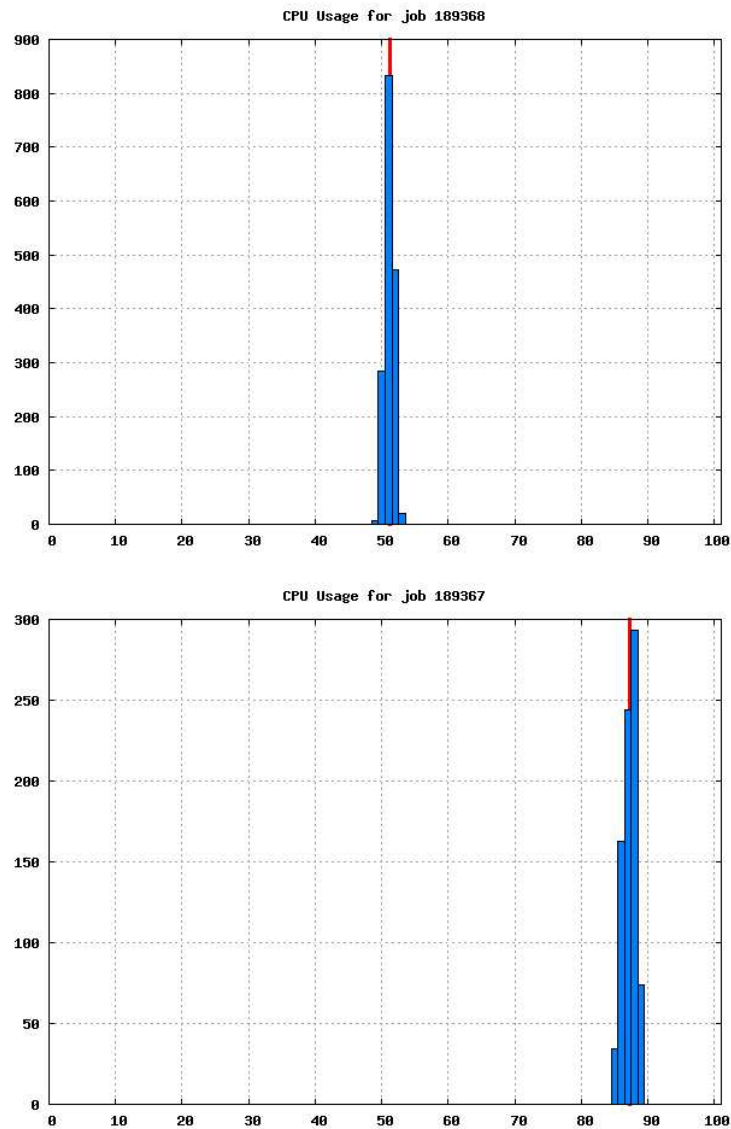


Fig. C.12: CPU Usage on the 5100-series SMP node of *Pleiades2+* cluster. 16 processing elements were required. 8 nodes/2 cores with 2 MPI threads per nodes in the upper case, 4 nodes/4 cores with 4 MPI threads per node in the lower case.

We have to note that the CPU usage (system+user+nice) monitored by Ganglia is the sum of all the process elements. For instance, for a dual-processor machine, when Ganglia measures 50% CPU usage, it means that each processor run at 100%. In Figure C.12, when 2 MPI threads are blocked per node, we get a CPU usage of 51.13% while 157 iteration loops have been performed during one hour; when 4 MPI threads run on each node, we get a CPU usage of 87.25% while only 117 iteration loops have been performed during one hour. Thus, the real CPU usage for the sample with 2 MPI threads per node is above 100% (2 cores are unused).

C.6 Conclusions

The extensive performance review presented in this appendix for the high-order spectral and mortar element method C++ toolbox, Speculoos, has shown that good performances can be achieved even with relatively common available software and hardware resources—small commodity clusters with non-proprietary compilers installed on it. However, universal and commonly employed non-proprietary libraries such as Blas and Lapack seem to require a further improvement in their optimization as compared to proprietary ones.

As a complement to the previous partial conclusions provided at each step of this performance evaluation, we can conclude that the main implementation choices made a decade ago reveal their promises. Even though those choices could have been questionable ten years ago, they are now in line with the current trend in computer architecture developments with the generalization of commodity and massively parallel clusters.

Moreover the analysis reveals some weaknesses of our C++ code. As presented in Section C.2.2, those weaknesses are inherent to C++ itself and cannot be circumvented. A proper compiler optimization and a parallel implementation could at least balance them. The trade-off between the development and implementation advantages of the object-oriented paradigm, and the computational efficiency of a lower-level programming language—Fortran 90 for instance—is not easily accessible.

The parallel implementation of Speculoos based on MPI has shown to be efficient. Reasonable scalability and efficiency can be achieved with a high loading of the cluster nodes. In addition, a smart assignment of the spectral elements to the cluster nodes leads to an additional increase in the parallel performance of Speculoos. These results support the original choices made in Speculoos parallel implementation by keeping it at a very low-level. Nevertheless, it would be interesting to further investigate and evaluate the scalability for a number of computer nodes corresponding to hundreds or even thousands. Therefore the part of this performance evaluation devoted to the parallelism of Speculoos will soon be completed by carrying out the presented benchmark test cases on the IBM eServer Blue Gene Solution, massively parallel computer comprising 8192 processors and acquired by EPFL.

C.7 Annex: Profiling information

Flat profile:

Each sample counts as 0.01 seconds.

| time | % cumulative | seconds | self seconds | calls | name |
|-------|--------------|---------|--------------|-------|--|
| 14.88 | 987.08 | 987.08 | 3461217386 | | RealVector::Multiply(RealVector*) |
| 9.86 | 1641.04 | 653.96 | 307891 | | FlatField::Multiply(Field*, int, int) |
| 8.99 | 2237.57 | 596.53 | 3603304192 | | Element::CopyAddValuesFrom(Element*, int, ...) |
| 6.02 | 2636.75 | 399.18 | 916811776 | | ElementaryField::MultiplyByWeights(int) |
| 4.14 | 2911.52 | 274.77 | 177840128 | | Edge::CopyAddValuesFromFace(Face*, int, int, ...) |
| 3.91 | 3170.74 | 259.22 | 1778679808 | | Quad::CopyAddValuesFromEdge(Edge*, int, int, ...) |
| 3.72 | 3417.45 | 246.71 | 1820727360 | | Vertex::CopyAddValuesFromEdge(Edge*, int, int, ...) |
| 3.09 | 3622.50 | 205.05 | 123303 | | FlatField::Add(Field*, double) |
| 2.63 | 3797.05 | 174.55 | 35926016 | | ElementaryField::GetWork() |
| 2.40 | 3956.46 | 159.41 | 108636 | | FlatField::SetValues(double) |
| 2.35 | 4112.24 | 155.78 | 1813419648 | | Edge::CopyAddValuesFromVertex(Vertex*, int, int, ...) |
| 2.34 | 4267.58 | 155.34 | 111474 | | FlatField::CopyFrom(Field*) |
| 2.23 | 4415.67 | 148.09 | 51311 | | FlatField::SetToWeakDivergence(FlatField*, FlatField*) |
| 1.76 | 4532.48 | 116.81 | 153676 | | FlatField::Dot(Field*) |
| 1.76 | 4649.07 | 116.59 | 1833762816 | | ElementaryField::CopyInterpolateFrom(ElementaryField*, ...) |
| 1.68 | 4760.74 | 111.67 | 51311 | | FlatField::SetToWeakGradient(FlatField*, FlatField*) |
| 1.66 | 4870.88 | 110.14 | 307981560 | | RealVector::MultiplyAndAdd(double, RealVector*, double) |
| 1.43 | 4965.67 | 94.79 | 420339712 | | RealVector::MultiplyAndSwitchSigns(RealVector*) |
| 1.33 | 5053.58 | 87.91 | 891158528 | | TensorMatrix::MatTransVec(RealVector*, RealVector*) |
| 1.29 | 5138.83 | 85.25 | 891789312 | | TensorMatrix::MatVec(RealVector*, RealVector*) |
| 1.28 | 5223.80 | 84.97 | 60070 | | FlatField::Multiply(Field*) |
| 1.28 | 5308.40 | 84.60 | 240852 | | FlatField::CopyAddValuesFrom(FlatField*, int, int, ...) |
| 1.21 | 5388.57 | 80.17 | 2311449449 | | ElementaryField::SetValues(double, int) |
| 1.09 | 5461.13 | 72.56 | 60030 | | FlatField::MultiplyAndAdd(double, Field*, double) |
| 1.06 | 5531.42 | 70.29 | 3565895681 | | ListMatrices::Search(ParentElement*) |
| 0.97 | 5595.57 | 64.15 | 2283535745 | | ElementaryField::HasSameInterpolationAs(ElementaryField*) |
| 0.96 | 5659.26 | 63.69 | 471113728 | | ElementaryField::SetToGradient(ElementaryField*, int, ...) |
| 0.90 | 5718.74 | 59.48 | 470818816 | | ElementaryField::SetToGradientT(ElementaryField*, int, ...) |
| 0.90 | 5778.22 | 59.48 | 54453 | | FlatField::Multiply(double) |
| 0.83 | 5832.98 | 54.76 | 471146496 | | ElementaryField::SetToGradientOnParents(ElementaryField*, ...) |
| 0.76 | 5883.25 | 50.27 | 3834749408 | | Vector<Edge*>::GetIndexOf(Edge*) |
| 0.71 | 5930.67 | 47.42 | 35926016 | | ElementaryField::Retrieve(ElementaryField*) |
| 0.64 | 5973.25 | 42.58 | 729517856 | | ElementaryField::CopyFrom(ElementaryField*, int, int) |
| 0.60 | 6012.88 | 39.63 | 445841408 | | ElementaryField::CopyInterpolateFrom(ElementaryField*, ...) |
| 0.60 | 6052.41 | 39.53 | 2546965353 | | RealVector::SetValuesZero() |
| 0.56 | 6089.23 | 36.82 | 356589567 | | Vector<ParentElement*>::GetIndexOf(ParentElement*) |

% the percentage of the total running time of the
time program used by this function.

cumulative a running sum of the number of seconds accounted
seconds for by this function and those listed above it.

self the number of seconds accounted for by this
seconds function alone. This is the major sort for this
 listing.

calls the number of times this function was invoked, if
 this function is profiled, else blank.

name the name of the function. This is the minor sort
 for this listing. The index shows the location of
 the function in the gprof listing. If the index is
 in parenthesis it shows where it would appear in
 the gprof listing if it were to be printed.

Bibliography

- [1] Veritable Application MONitoring Service, website, 2006. <http://pleiades.epfl.ch/~vkeller/VAMOS>.
- [2] The Ganglia Monitoring Tool, website, 2007. <http://ganglia.sourceforge.net>.
- [3] Performance API, website, 2007. <http://icl.cs.utk.edu/papi/index.html>.
- [4] Adams, N. A., Hickel, S. & Franz, S. Implicit subgrid-scale modeling by adaptive deconvolution. *J. Comput. Phys.*, **200**, 412–431, 2004.
- [5] Albensoeder, S. & Kuhlmann, H. C. Linear stability of rectangular cavity flows driven by anti-parallel motion of two facing walls. *J. Fluid Mech.*, **458**, 153–180, 2002.
- [6] Albensoeder, S. & Kuhlmann, H. C. Three-dimensional instability of two counter-rotating vortices in a rectangular cavity driven by parallel wall motion. *European J. Mechanics B-Fluids*, **21**, 307–316, 2002.
- [7] Albensoeder, S. & Kuhlmann, H. C. Accurate three-dimensional lid-driven cavity flow. *J. Comput. Phys.*, **206**, 536–558, 2005.
- [8] Albensoeder, S. & Kuhlmann, H. C. Nonlinear three-dimensional flow in the lid-driven square cavity. *J. Fluid Mech.*, **569**, 465–480, 2006.
- [9] Albensoeder, S., Kuhlmann, H. C. & Rath, H. J. Three-dimensional centrifugal-flow instabilities in the lid-driven-cavity problem. *Phys. Fluids*, **13**, 121–135, 2001.
- [10] Anagnostou, G., Maday, Y., Mavriplis, C. & Patera, A. T. On the mortar element method: Generalizations and Implementation. In T.F. Chan, R. Glowinski, J. P. & Widlund, O., editors, *Third International Symposium on Domain Decomposition Methods for Partial Differential Equations*, pages 157–173. SIAM, 1990.
- [11] Arndt, R. E. A. Cavitation in vortical flows. *Annu. Rev. Fluid Mech.*, **34**, 143–175, 2002.
- [12] Atluri, S. N. *The meshless method (MLPG) for domain & BIE discretizations*. Tech Science Press, Forsyth (GA), 2004.
- [13] Bardina, J., Ferziger, J. H. & Reynolds, W. C. Improved subgrid scale models for large eddy simulation. *AIAA J.*, **80-1357**, 1980.
- [14] Bardina, J., Ferziger, J. H. & Reynolds, W. C. Improved turbulence models based on large eddy simulation of homogeneous, incompressible, turbulent flows. Technical Report TF-19, Thermal Sciences Division, Department of Mechanical Engineering, Stanford University, Stanford, 1983.
- [15] Barragy, E. & Carey, G. F. Streamfunction-vorticity driven cavity solution using p finite elements. *Computers & Fluids*, **26**, 453–468, 1997.
- [16] Ben Belgacem, F., Bernardi, C., Chorfi, N. & Maday, Y. Inf-sup conditions for the mortar spectral element discretization of the Stokes problem. *Numer. Math.*, **85**, 257–281, 2000.
- [17] Bernardi, C., Fiétier, N. & Owens, R. G. An error indicator for mortar element solutions to the Stokes problem. *IMA J. Num. Anal.*, **21**, 857–886, 2001.
- [18] Bernardi, C., Maday, Y. & Patera, A. T. *A new nonconforming approach to domain decomposition: The mortar element method*, volume 299 of *Pitman Res. Notes Math. Ser.*, pages 13–51. Nonlinear partial differential equation and their applications, Collège de France Seminar, 11 (Paris, 1989–1991), Longman Sci. Tech., Harlow, 1994.
- [19] Bisgaard, A. V., Brøns, M. & Sørensen, J. N. Vortex breakdown generated by off-axis bifurcation in a cylinder with rotating covers. *Acta Mechanica*, **187**, 75–83, 2006.
- [20] Blackburn, H. M. Three-dimensional instability and state selection in an oscillatory axisymmetric swirling flow. *Phys. Fluids*, **14**, 3983–3996, 2002.
- [21] Blackburn, H. M. & Lopez, J. M. Symmetry breaking of the flow in a cylinder driven by a rotating end wall. *Phys. Fluids*, **12**, 2698–2701, 2000.
- [22] Blackburn, H. M. & Lopez, J. M. Modulated rotating waves in an enclosed swirling flow. *J. Fluid Mech.*, **465**, 33–58, 2002.
- [23] Blackburn, H. M. & Lopez, J. M. The onset of three-dimensional standing and modulated travelling waves in a periodically driven cavity flow. *J. Fluid Mech.*, **497**, 289–317, 2003.

- [24] Blackburn, H. M. & Schmidt, S. Spectral element filtering techniques for large eddy simulation with dynamic estimation. *J. Comput. Phys.*, **186**, 610–629, 2003.
- [25] Blazek, J. *Computational Fluid Dynamics: Principles and Applications*. Elsevier, 2001.
- [26] Blohm, C. H. & Kuhlmann, H. C. The two-sided lid-driven cavity: experiments on stationary and time-dependent flows. *J. Fluid Mech.*, **450**, 67–95, 2002.
- [27] Bodard, N. *Interaction fluide-structure par la méthode des éléments spectraux*. PhD thesis, no. 3503, École Polytechnique Fédérale de Lausanne, 2006.
- [28] Bodard, N., Bouffanais, R. & Deville, M. O. Solution of moving boundary problems by the spectral element method. *App. Num. Math.*, 2007. In Press.
- [29] Bodard, N. & Deville, M. O. Fluid-structure interaction by the spectral element method. *J. Sci. Comput.*, **27**, 123–136, 2006.
- [30] Bogatyrev, V. Y. A. & Gorin, A. V. End effects in rectangular cavities. *Fluid. Mech.-Soviet Res.*, **7**, 101–106, 1978.
- [31] Borue, V. & Orszag, S. A. Spectra in helical three-dimensional homogeneous isotropic turbulence. *Phys. Rev. E*, **55** (6), 7005–7009, 1997.
- [32] Botella, O. & Peyret, R. Benchmark spectral results on the lid-driven cavity flow. *Computers & Fluids*, **27**, 421–433, 1998.
- [33] Bouffanais, R. & Deville, M. O. Simulation of standing waves using moving-grid techniques with spectral element methods. In *Proc. Int. Conf. on Mathematical and Numerical aspects of Waves*, pages 374–375, Brown University, Providence (RI), 2005.
- [34] Bouffanais, R. & Deville, M. O. Mesh update techniques for free-surface flow solvers using spectral element method. *J. Sci. Comput.*, **27**, 137–149, 2006.
- [35] Bouffanais, R., Deville, M. O., Fischer, P. F., Leriche, E. & Weill, D. Large-eddy simulation of the lid-driven cubic cavity flow by the spectral element method. *J. Sci. Comput.*, **27**, 151–162, 2006.
- [36] Bouffanais, R., Deville, M. O., Gruber, R. & Keller, V. Computational performance analysis of a parallelized high-order spectral and mortar element toolbox. *Parallel Computing*, 2007. Submitted for publication.
- [37] Bouffanais, R., Deville, M. O. & Leriche, E. Large-eddy simulation of the flow in a lid-driven cubical cavity. *Phys. Fluids*, **19**, Art. 055108, 2007.
- [38] Boyd, J. P. Two comments on filtering (artificial viscosity) for Chebyshev and Legendre spectral and spectral element methods: Preserving boundary conditions and interpretation of the filter as a diffusion. *J. Comput. Phys.*, **143**, 283–288, 1998.
- [39] Bragg, S. L. & Hawthorne, W. R. Some exact solutions of the flow through annular cascade actuator discs. *J. Aeronaut. Sci.*, **17**, 243, 1950.
- [40] Breuer, M. Large eddy simulation of the subcritical flow past a cylinder: numerical and modeling aspects. *Int. J. Numer. Methods Fluids*, **28**, 1281–1302, 1998.
- [41] Brøns, M., Voigt, L. K. & Sørensen, J. N. Streamline topology of steady axisymmetric vortex breakdown in a cylinder with co- and counter-rotating end-covers. *J. Fluid Mech.*, **401**, 275–292, 1999.
- [42] Brøns, M., Voigt, L. K. & Sørensen, J. N. Topology of vortex breakdown bubbles in a cylinder with a rotating bottom and a free surface. *J. Fluid Mech.*, **428**, 133–148, 2001.
- [43] Brown, G. L. & Lopez, J. M. Axisymmetrical vortex breakdown. Part 2. Physical mechanisms. *J. Fluid Mech.*, **221**, 553–576, 1990.
- [44] Canuto, C., Hussaini, M. Y., Quarteroni, A. & Zang, T. A. *Spectral Methods – Fundamentals in Single Domains*. Springer Verlag, 2006.
- [45] Carati, D., Winkelmann, G. S. & Jeanmart, H. On the modelling of the subgrid-scale and filtered-scale stress tensors in large-eddy simulation. *J. Fluid Mech.*, **441**, 119–138, 2001.
- [46] Chen, C. K. & Lin, D. TIP4P potential for lid-driven cavity flow. *Acta Mechanica*, **178**, 223–237, 2005.
- [47] Chiang, T. P., Hwang, R. R. & Sheu, W. H. Finite volume analysis of spiral motion in a rectangular lid-driven cavity. *Int. J. Numer. Methods Fluids*, **23**, 325–346, 1996.
- [48] Chiang, T. P., Hwang, R. R. & Sheu, W. H. On end-wall corner vortices in a lid-driven cavity. *J. Fluids Eng.-Transactions ASME*, **119**, 201–204, 1997.
- [49] Chiang, T. P. & Sheu, W. H. Numerical prediction of eddy structure in a shear-driven cavity. *Computational Mechanics*, **20**, 379–396, 1997.

- [50] Chiang, T. P., Sheu, W. H. & Hwang, R. R. Effect of Reynolds number on the eddy structure in a lid-driven cavity. *Int. J. Numer. Methods Fluids*, **26**, 557–579, 1998.
- [51] Chung, T. J. *Computational Fluid Dynamics*. Cambridge University Press, Cambridge, 2002.
- [52] Couzy, W. *Spectral Element Discretization of the Unsteady Navier–Stokes Equations and its Iterative Solution on Parallel Computers*. PhD thesis, no. 1380, Swiss Federal Institute of Technology, Lausanne, 1995.
- [53] Couzy, W. & Deville, M. O. Spectral-element preconditioners for the Uzawa pressure operator applied to incompressible flows. *J. Sci. Comput.*, **9**, 107–112, 1994.
- [54] Couzy, W. & Deville, M. O. A fast Schur complement method for the spectral element discretization of the incompressible Navier–Stokes equations. *J. Comput. Phys.*, **116**, 135–142, 1995.
- [55] Crowley, W. P. Numerical advection experiments. *Mon. Wea. Rev.*, **96** (1), 1–11, 1968.
- [56] Daube, O. & Sørensen, J. N. Numerical-simulation of the axisymmetric periodic-flow in a cylindrical tank. *Comptes Rendus De l'Académie des Sciences Série II*, **308**, 463–469, 1989.
- [57] Day, C., Harris, J. A., Soria, J., Boger, D. V. & Welsh, M. C. Behavior of an elastic fluid in cylindrical swirling flow. *Experimental Thermal Fluid Science*, **12**, 250–255, 1996.
- [58] Deville, M. O., Fischer, P. F. & Mund, E. H. *High-order methods for incompressible fluid flow*. Cambridge University Press, Cambridge, 2002.
- [59] Dijkstra, D. & van Heijst, G. J. F. The flow between two finite rotating-disks enclosed by a cylinder. *J. Fluid Mech.*, **128**, 123–154, 1983.
- [60] Ding, Y. & Kawahara, M. Linear stability of incompressible fluid flow in a cavity using finite element method. *Int. J. Numer. Methods Fluids*, **27**, 139–157, 1998.
- [61] Ding, Y. & Kawahara, M. Three-dimensional linear stability analysis of incompressible viscous flows using the finite element method. *Int. J. Numer. Methods Fluids*, **31**, 451–479, 1999.
- [62] Domaradzki, J. A. & Adams, N. A. Direct modelling of subgrid scales of turbulence in large eddy simulations. *J. of Turbulence*, **3** (24), 2002.
- [63] Domaradzki, J. A. & Loh, K. C. The subgrid-scale estimation model in the physical space representation. *Phys. Fluids*, **11**, 2330–2342, 1999.
- [64] Donea, J. *Arbitrary Lagrangian-Eulerian finite element methods*, pages 474–516. T.B. Belytschko and T.J.R. Hugues Eds., Computational Methods for Transient Analysis. North Holland, 1983.
- [65] Donea, J., Huerta, A., Ponthot, J.-P. & Rodriguez-Ferran, A. *Arbitrary Lagrangian-Eulerian Methods*, volume 1: Fundamentals, E. Stein, R./ de Borst & T. J.R. Hugues of *Encyclopedia of Computational Mechanics*, Chapter 14. Wiley, 2004.
- [66] Dubois-Pèlerin, Y. Speculoos: an object-oriented toolbox for the numerical simulation of partial differential equations by spectral and mortar element method. Technical Report T-98-5, EPFL-LMF, 1998.
- [67] Dubois-Pèlerin, Y., Van Kemenade, V. & Deville, M. An object-oriented toolbox for spectral element analysis. *J. Sci. Comput.*, **14**, 1–29, 1999.
- [68] Dunca, A. & Epshteyn, Y. On the Stolz-Adams deconvolution model for the large-eddy simulation of turbulent flows. *SIAM J. Math. Anal.*, **37**, 1890–1902, 2006.
- [69] Escudier, M. P. Observations of the flow produced in a cylindrical container by a rotating endwall. *Experiments In Fluids*, **2**, 189–196, 1984.
- [70] Escudier, M. P. & Cullen, L. M. Flow of a shear-thinning liquid in a cylindrical container with a rotating end wall. *Experimental Thermal Fluid Science*, **12**, 381–387, 1996.
- [71] Escudier, M. P. & Keller, J. J. Recirculation in swirling flow - a manifestation of vortex breakdown. *Aiaa J.*, **23**, 111–116, 1985.
- [72] Faler, J. H. & Leibovich, S. Disrupted states of vortex flow and vortex breakdown. *Phys. Fluids*, **20**, 1385–1400, 1977.
- [73] Farhat, C. & Geuzaine, P. Design and analysis of robust ALE time-integrators for the solution of unsteady flow problems on moving grids. *Comput. Methods Appl. Mech. Engrg.*, **193**, 4073–4075, 2004.
- [74] Farhat, C., Geuzaine, P. & Grandmont, C. The discrete geometric conservation law and the nonlinear stability of ALE schemes for the solution of flow problems on moving grids. *J. Comput. Phys.*, **174**, 669–693, 2001.
- [75] Ferziger, J. H. & Perić, M. *Computational Methods for Fluid Dynamics*. Springer, 1996.

- [76] Fiétier, N. Detecting instabilities in flows of viscoelastic fluids. *Int. J. Numer. Methods Fluids*, **42**, 1345–1361, 2003.
- [77] Fiétier, N. & Deville, M. O. Linear stability analysis of time-dependent algorithms with spectral element methods for the simulation of viscoelastic flows. *J. Non-Newtonian Fluid Mech.*, **115**, 157–190, 2003.
- [78] Fiétier, N. & Deville, M. O. Time-dependent algorithms for the simulation of viscoelastic flows with spectral element methods: applications and stability. *J. Comput. Phys.*, **186**, 93–121, 2003.
- [79] Fischer, P. F., Kruse, G. W. & Loth, F. Spectral element methods for transitional flows in complex geometries. *J. Sci. Comput.*, **17**, 87–105, 2002.
- [80] Fischer, P. F. & Mullen, J. S. Filter-based stabilization of spectral element methods. *Comptes Rendus de l'Académie des Sciences Paris*, **332** (I), 265–270, 2001. Analyse Numérique.
- [81] Fischer, P. F. & Patera, A. T. Parallel spectral element solution of the Stokes problem. *J. Comput. Phys.*, **92**, 380–421, 1991.
- [82] Formaggia, L. & Nobile, F. A stability analysis for the arbitrary Lagrangian Eulerian formulation with finite elements. *East-West J. Num. Math.*, **7**, 105–132, 1999.
- [83] Formaggia, L. & Nobile, F. Stability analysis of second-order time accurate schemes for ALE–FEM. *Comput. Methods Appl. Mech. Engrg.*, **193**, 4097–4116, 2004.
- [84] Gelfgat, A. Y., Bar-Yoseph, P. Z. & Solan, A. Stability of confined swirling flow with and without vortex breakdown. *J. Fluid Mech.*, **311**, 1–36, 1996.
- [85] Gelfgat, A. Y., Bar-Yoseph, P. Z. & Solan, A. Steady states and oscillatory instability of swirling flow in a cylinder with rotating top and bottom. *Phys. Fluids*, **8**, 2614–2625, 1996.
- [86] Gelfgat, A. Y., Bar-Yoseph, P. Z. & Solan, A. Three-dimensional instability of axisymmetric flow in a rotating lid-cylinder enclosure. *J. Fluid Mech.*, **438**, 363–377, 2001.
- [87] Germano, M. A proposal for a redefinition of the turbulent stresses in the filtered Navier–Stokes equations. *Phys. Fluids*, **29**, 2323–2324, 1986.
- [88] Germano, M., Piomelli, U., Moin, P. & Cabot, W. H. A dynamic subgrid-scale eddy viscosity model. *Phys. Fluids A*, **3**, 1760–1765, 1991.
- [89] Geurts, B. J. Inverse modeling for large-eddy simulation. *Phys. Fluids*, **9**, 3585–3587, 1997.
- [90] Geurts, B. J. & Frölich, J. A framework for predicting accuracy limitations in large-eddy simulation. *Phys. Fluids*, **14**, 41–44, 2002.
- [91] Ghia, U., Ghia, K. N. & Shin, C. T. High-Re solutions for incompressible-flow using the Navier–Stokes equations and a multigrid method. *J. Comput. Phys.*, **48**, 387–411, 1982.
- [92] Ghosal, S. An analysis of numerical error in large-eddy simulation of turbulence. *J. Comput. Phys.*, **125**, 187–206, 1996.
- [93] Ghosal, S., Lund, T. S., Moin, P. & Akselvoll, K. A dynamic localization model for large-eddy simulation of turbulent flows. *J. Fluid Mech.*, **286**, 229–255, 1995.
- [94] Gingold, R. A. & Monaghan, J. J. Smoothed particle hydrodynamics: theory and application to non-spherical stars. *Mon. Not. Roy. Astron. Soc.*, **181**, 375–389, 1977.
- [95] Godunov, S. K. Finite difference method for numerical computation of discontinuous solution of the equations of fluid dynamics. *Math. Sb.*, **47**, 271, 1959. Translated from Russian by I. Bohachevsky.
- [96] Gomilko, A. M., Malyuga, V. S. & Meleshko, V. V. On steady Stokes flow in a trihedral rectangular corner. *J. Fluid Mech.*, **476**, 159–177, 2003.
- [97] Gordon, W. J. & Hall, C. A. Construction of curvilinear coordinate systems and application to mesh generation. *Int. J. Num. Meth. Eng.*, **7**, 461–477, 1973.
- [98] Gordon, W. J. & Hall, C. A. Transfinite element methods: Blending-functions interpolation over arbitrary curved element domains. *Numer. Math.*, **21**, 109–129, 1973.
- [99] Groisman, A. & Steinberg, V. Elastic turbulence in a polymer solution flow. *Nature*, **405**, 53–55, 2000.
- [100] Groisman, A. & Steinberg, V. Efficient mixing at low Reynolds numbers using polymer additives. *Nature*, **410**, 905–908, 2001.
- [101] Groisman, A. & Steinberg, V. Elastic turbulence in curvilinear flows of polymer solutions. *New J. Phys.*, **6**, 2004.
- [102] Gropp, W. D., Lusk, E. & Skjellum, A. *Using MPI: Portable Parallel Programming with the Message-Passing Interface*. MIT Press, Cambridge, Massachusetts, 1999.

- [103] Gruber, R. & Gunzinger, A. The Swiss-Tx supercomputer project. *EPFL Supercomputing Review*, **9**, 21–23, 1997.
- [104] Gruber, R. & Tran, T.-M. Scalability aspects of commodity clusters. *EPFL Supercomputing Review*, **14**, 12–17, 2004.
- [105] Gruber, R., Volgers, P., DeVita, A., Stengel, M. & Tran, T.-M. Parametrisation to tailor commodity clusters to applications. *Future Generation Computer Systems*, **19**, 111–120, 2003.
- [106] Güler, I., Behr, M. & Tezduyar, T. Parallel finite element computation of free-surface flows. *Computational Mechanics*, **23**, 117–123, 1999.
- [107] Gullbrand, J. & Chow, F. K. The effect of numerical errors and turbulence models in large-eddy simulations of channel flow, with and without explicit filtering. *J. Fluid Mech.*, **495**, 323–341, 2003.
- [108] Gustafson, K. & Halasi, K. Vortex dynamics of cavity flows. *J. Comput. Phys.*, **64**, 279–319, 1986.
- [109] Gustafson, K. & Halasi, K. Cavity flow dynamics at higher Reynolds-number and higher aspect ratio. *J. Comput. Phys.*, **70**, 271–283, 1987.
- [110] Gustafsson, B. & Sundström, A. Incompletely parabolic problems in fluid dynamics. *SIAM J. Appl. Math.*, **35**, 343–357, 1978.
- [111] Habisreutinger, M. A. Large-eddy simulation of turbulent flows by approximate deconvolution models using spectral element method. Master's thesis, École Polytechnique Fédérale de Lausanne, Section de Génie Mécanique, 2006.
- [112] Habisreutinger, M. A., Bouffanais, R., Leriche, E. & Deville, M. O. A coupled approximate deconvolution and dynamic mixed scale model for large-eddy simulation. *J. Comput. Phys.*, **224**, 241–266, 2007.
- [113] Hall, M. G. Vortex breakdown. *Annu. Rev. Fluid Mech.*, **4**, 195–218, 1972.
- [114] He, N.-Z., Wang, N.-C., Shi, B.-C. & Guo, Z.-L. A unified incompressible lattice BGK model and its application to three-dimensional lid-driven cavity flow. *Chin. Phys.*, **13**, 40–46, 2004.
- [115] Henderson, R. D. *High-order Methods for Computational Physics*, Chapter 3, pages 225–324. Springer, Berlin, T. J. Barth and H. Deconinck Eds., 1999.
- [116] Hesthaven, J., Gottlieb, D. & Gottlieb, S. *Spectral Methods for Time-Dependent Problems*. Cambridge University Press, Cambridge, 2006.
- [117] Hesthaven, J. S. & Kirby, R. M. Filtering in Legendre spectral methods. *Mathematics of Computation*, 2007. In Press.
- [118] Hickel, S., Adams, N. A. & Domaradzki, J. A. An adaptive local deconvolution method for implicit LES. *J. Comput. Phys.*, **213**, 413–436, 2006.
- [119] Hirs, A. H., Lopez, J. M. & Miraghaie, R. Symmetry breaking to a rotating wave in a lid-driven cylinder with a free surface: Experimental observation. *Phys. Fluids*, **14**, L29–L32, 2002.
- [120] Hirsch, C. *Numerical Computation of Internal and External Flows*, volume 2 of *Wiley Series in Numerical Methods*. John Wiley and Sons, 1990.
- [121] Hirt, C. W., Amsden, A. A. & Cook, J. L. An Arbitrary Lagrangian–Eulerian computing method for all flow speeds. *J. Comput. Phys.*, **14**, 227–253, 1974.
- [122] Ho, L.-W. & Patera, A. T. A Legendre spectral element method for simulation of unsteady incompressible viscous free-surface flows. *Comput. Methods Appl. Mech. Engrg.*, **80**, 355–366, 1990.
- [123] Ho, L.-W. & Patera, A. T. Variational formulation of three-dimensional viscous free-surface flows: Natural imposition of surface tension boundary conditions. *Int. J. Numer. Methods Fluids*, **13**, 691–698, 1991.
- [124] Hodges, B. R. *Numerical simulation of nonlinear free-surface waves on a turbulent open-channel flow*. PhD thesis, Department of Civil Engineering, Stanford University, 1997.
- [125] Hodges, B. R. & Street, R. L. On simulation of turbulent nonlinear free-surface flows. *J. Comput. Phys.*, **151**, 425–457, 1999.
- [126] Horiuti, K. A new dynamic two-parameter mixed model for large-eddy simulation. *Phys. Fluids*, **9**, 3443–3464, 1997.
- [127] Hourigan, K., Graham, L. J. W. & Thompson, M. C. Spiral streaklines in pre-vortex breakdown regions of axisymmetrical swirling flows. *Phys. Fluids*, **7**, 3126–3128, 1995.
- [128] Iliescu, T. & Fischer, P. F. Large eddy simulation of turbulent channel flows by the rational large eddy simulation model. *Phys. Fluids*, **15**, 3036–3047, 2003.

- [129] Ivanenko, S. A. *Handbook of grid generation*, Chapter 8: Harmonic Mappings, pages 8.1–8.41. CRC Press, Thompson & Weatherill & Soni, J. F. Thompson, N. P. Weatherill and B. K. Soni Eds., 1999.
- [130] Iwatsu, R. Analysis of flows in a cylindrical container with rotating bottom and top undeformable free surface. *JSME Int. J. Series B-Fluids Thermal Engineering*, **47**, 549–556, 2004.
- [131] Iwatsu, R. Numerical study of flows in a cylindrical container with rotating bottom and top flat free surface. *J. Phys. Soc. Japan*, **74**, 333–344, 2005.
- [132] Iwatsu, R., Ishii, K., Kawamura, T., Kuwahara, K. & Hyun, J. M. Numerical simulation of three-dimensional flow structure in a driven cavity. *Fluid. Dyn. Res.*, **5** (3), 173–189, 1989.
- [133] Jansson, T. R. N., Haspang, M. P., Jensen, K. H., Hersen, P. & Bohr, T. Polygons on a rotating fluid surface. *Phys. Rev. Lett.*, **96**, 174502, 2006.
- [134] Johnson, A. A. & Tezduyar, T. E. Mesh update strategies in parallel finite element computations of flow problems with moving boundaries and interfaces. *Comput. Methods Appl. Mech. Engrg.*, **119**, 73–94, 1994.
- [135] Jordan, S. A. & Ragab, S. A. On the unsteady and turbulent characteristics of the 3-dimensional shear-driven cavity flow. *J. Fluids Eng.-Transactions ASME*, **116**, 439–449, 1994.
- [136] Jordan, S. A. & Ragab, S. A. A large-eddy simulation of the shear-driven cavity flow using dynamic modeling. *Int. J. Computational Fluid Dynamics*, **6**, 321–335, 1996.
- [137] Joyner, I. *C++??: A Critique of C++ and Programming and Language Trends in the 1990s*. Available online at <http://www.elj.com/cppcv3/>, third Eds., 1996.
- [138] Karamanos, G. S. & Karniadakis, G. E. A spectral vanishing viscosity method for large-eddy simulations. *J. Comput. Phys.*, **163**, 22–50, 2000.
- [139] Karamanos, G. S., Sherwin, S. J. & Morrison, J. F. *Large eddy simulation using unstructured spectral/hp elements*. in Recent Advances in DNS and LES, D. Knight & L. Sakell. Kluwer Academic, Dordrecht/Norwell, MA, 1999.
- [140] Karniadakis, G. E., Israeli, M. & Orszag, S. A. High-order splitting methods for the incompressible Navier–Stokes equations. *J. Comput. Phys.*, **97**, 414–443, 1991.
- [141] Keller, J. J. A pair of stream functions for three-dimensional vortex flows. *Zeitschrift für Angewandte Mathematik und Physik*, **47**, 821–836, 1996.
- [142] Kerswell, R. R. Elliptical instability. *Annu. Rev. Fluid Mech.*, **34**, 83–113, 2002.
- [143] Kim, J. & Moin, P. Application of a fractional-step method to incompressible Navier–Stokes equations. *J. Comput. Phys.*, **59**, 308–323, 1985.
- [144] Koseff, J. R. & Street, R. L. The lid-driven cavity flow: A synthesis of qualitative and quantitative observations. *J. Fluids Eng.-Transactions ASME*, **106**, 390–398, 1984.
- [145] Koseff, J. R. & Street, R. L. Visualization studies of a shear driven 3-dimensional recirculating flow. *J. Fluids Eng.-Transactions ASME*, **106**, 21–29, 1984.
- [146] Kravchenko, A. G. & Moin, P. On the effect of numerical errors in large eddy simulations of turbulent flows. *J. Comput. Phys.*, **131**, 310–322, 1997.
- [147] Kuerten, J. G. M., Geurts, B. J., Vreman, A. W. & Germano, M. Dynamics inverse modeling and its testing in large-eddy simulation of the mixing layer. *Phys. Fluids*, **11**, 3778–3785, 1999.
- [148] Kuhlmann, H. C. & Albensoeder, S. Strained vortices in driven cavities. *Zamm-zeitschrift Für Angewandte Mathematik Und Mechanik*, **85**, 387–399, 2005.
- [149] Lamb, H. *Hydrodynamics*. Cambridge University Press, Cambridge, Sixth Eds., 1932.
- [150] Langford, J. A. & Moser, R. D. Optimal LES formulations for isotropic turbulence. *J. Fluid Mech.*, **398**, 321–346, 1999.
- [151] Lee, N. S. & Bathe, K. J. Error indicators and adaptive remeshing in large deformation finite element analysis. *Finite Elements in Analysis and Design*, **16**, 99–139, 1994.
- [152] Leibovich, S. Structure of vortex breakdown. *Annu. Rev. Fluid Mech.*, **10**, 221–246, 1978.
- [153] Leriche, E. *Direct numerical simulation of lid-driven cavity flow by a Chebyshev spectral method*. PhD thesis, no. 1932, École Polytechnique Fédérale de Lausanne, 1999.
- [154] Leriche, E. Direct numerical simulation of lid driven cavity at high Reynolds numbers. *J. Sci. Comput.*, **27**, 335–345, 2006.

- [155] Leriche, E. & Gavrilakis, S. Direct numerical simulation of the flow in the lid-driven cubical cavity. *Phys. Fluids*, **12**, 1363–1376, 2000.
- [156] Lilly, D. K. A proposed modification of the Germano-subgrid-scale closure method. *Phys. Fluids A*, **4**, 633–635, 1992.
- [157] Liu, S., Meneveau, C. & Katz, J. On the properties of similarity subgrid-scale models as deduced from measurements in a turbulent jet. *J. Fluid Mech.*, **275**, 83–119, 1994.
- [158] Lopez, J. M. Axisymmetrical vortex breakdown. Part 1. Confined swirling flow. *J. Fluid Mech.*, **221**, 533–552, 1990.
- [159] Lopez, J. M. Unsteady swirling flow in an enclosed cylinder with reflectional symmetry. *Phys. Fluids*, **7**, 2700–2714, 1995.
- [160] Lopez, J. M. Flow between a stationary and a rotating disk shrouded by a co-rotating cylinder. *Phys. Fluids*, **8**, 2605–2613, 1996.
- [161] Lopez, J. M. Characteristics of endwall and sidewall boundary layers in a rotating cylinder with a differentially rotating endwall. *J. Fluid Mech.*, **359**, 49–79, 1998.
- [162] Lopez, J. M. Rotating and modulated rotating waves in transitions of an enclosed swirling flow. *J. Fluid Mech.*, **553**, 323–346, 2006.
- [163] Lopez, J. M. & Marques, F. Mode competition between rotating waves in a swirling flow with reflection symmetry. *J. Fluid Mech.*, **507**, 265–288, 2004.
- [164] Lopez, J. M., Marques, F., Hirska, A. H. & Miraghaie, R. Symmetry breaking in free-surface cylinder flows. *J. Fluid Mech.*, **502**, 99–126, 2004.
- [165] Lopez, J. M., Marques, F. & Shen, J. An efficient spectral-projection method for the Navier–Stokes equations in cylindrical geometries II. Three-dimensional cases. *J. Comput. Phys.*, **176**, 384–401, 2002.
- [166] Lopez, J. M. & Perry, A. D. Axisymmetrical vortex breakdown. Part 3. Onset of periodic-flow and chaotic advection. *J. Fluid Mech.*, **234**, 449–471, 1992.
- [167] Lugt, H. J. & Abboud, M. Axisymmetrical vortex breakdown with and without temperature effects in a container with a rotating lid. *J. Fluid Mech.*, **179**, 179–200, 1987.
- [168] Lugt, H. J. & Haussling, H. J. Axisymmetric vortex breakdown in rotating fluid within a container. *J. Appl. Mechanics-Transactions Asme*, **49**, 921–923, 1982.
- [169] Lugt, H. J. & Hausslin, W. Development of flow circulation in a rotating tank. *Acta Mechanica*, **18**, 255–272, 1973.
- [170] Maday, Y., Mavriplis, C. & Patera, A. T. Nonconforming mortar element methods: Application to spectral discretizations. In T.F. Chan, R. Glowinski, J. P. & Widlund, O., editors, *Domain Decomposition Methods*, pages 392–418. SIAM, 1989.
- [171] Maday, Y., Meiron, D., Patera, A. T. & Rønquist, E. M. Analysis of iterative methods for the steady and unsteady Stokes problem - Application to spectral element discretizations. *SIAM J. Sci. Comput.*, **14**, 310–337, 1993.
- [172] Maday, Y. & Patera, A. T. *Spectral element methods for the incompressible Navier–Stokes equations*, pages 71–142. State-of-the-Art Survey on Computational Mechanics, A. K. Noor & J. T. Oden Eds. ASME, New-York, 1989.
- [173] Maday, Y., Patera, A. T. & Rønquist, E. M. An operator-integration-factor splitting method for time dependent problems: Application to incompressible fluid flow. *J. Sci. Comput.*, **5**, 263–292, 1990.
- [174] Maday, Y., Patera, A. T. & Rønquist, E. M. The $\mathbb{P}_N \times \mathbb{P}_{N-2}$ method for the approximation of the Stokes problem. Technical Report 92009, Department of Mechanical Engineering, MIT, Cambridge, MA, 1992.
- [175] Marcus, D. L. & Berger, S. A. The interaction between a counter-rotating vortex pair in vertical ascent and a free surface. *Phys. Fluids A*, **1** (12), 1988–2000, 1989.
- [176] Marques, F. & Lopez, J. M. Precessing vortex breakdown mode in an enclosed cylinder flow. *Phys. Fluids*, **13**, 1679–1682, 2001.
- [177] Marques, F., Lopez, J. M. & Shen, J. Mode interactions in an enclosed swirling flow: a double Hopf bifurcation between azimuthal wavenumbers 0 and 2. *J. Fluid Mech.*, **455**, 263–281, 2002.
- [178] Mathieu, J. & Scott, J. *An Introduction to Turbulent Flow*. Cambridge University Press, Cambridge, 2000.
- [179] McDonald, P. W. The combustion of transonic flow through two-dimensional gas turbine cascades. Technical report, ASME, 1971. Paper 71-GT-89.

- [180] Meneveau, C., Lund, T. S. & Cabot, W. H. A Lagrangian dynamic subgrid-scale model of turbulence. *J. Fluid Mech.*, **319**, 353–385, 1996.
- [181] Meyers, J., Geurts, B. J. & Baelmans, M. Optimality of the dynamic procedure for large-eddy simulations. *Phys. Fluids*, **17**, Art. 045108, 2005.
- [182] Miraghaie, R., Lopez, J. M. & Hirs, A. H. Flow induced patterning at the air-water interface. *Phys. Fluids*, **15**, L45–L48, 2003.
- [183] Moeng, C. H. & Wyngaard, J. C. Spectral analysis of large-eddy simulations of the convective boundary layer. *J. Atmos. Sci.*, **45**, 3573–3587, 1988.
- [184] Moffat, H. K. & Tsinober, A. Helicity in laminar and turbulent flow. *Annu. Rev. Fluid Mech.*, **24**, 281–312, 1992.
- [185] Morinishi, Y. & Vasilyev, O. V. A recommended modification to the dynamic two-parameter mixed subgrid scale model for large eddy simulation of wall bounded turbulent flow. *Phys. Fluids*, **13**, 3400–3410, 2001.
- [186] Mullin, T., Kobine, J. J., Tavener, S. J. & Cliffe, K. A. On the creation of stagnation points near straight and sloped walls. *Phys. Fluids*, **12**, 425–431, 2000.
- [187] Nayrolles, B., Touzot, G. & Villon, P. Generalizing the finite element method: diffuse approximation and diffuse elements. *Comput. Mech.*, **10**, 307–318, 1992.
- [188] Neitzel, G. P. Streak-line motion during steady and unsteady axisymmetric vortex breakdown. *Phys. Fluids*, **31**, 958–960, 1988.
- [189] Nobile, F. *Numerical approximation of fluid-structure interaction problems with application to Haemodynamics*. PhD thesis, no. 2458, Swiss Federal Institute of Technology, Lausanne, 2001.
- [190] Okulov, V. L., Sørensen, J. N. & Voigt, L. K. Alternation of the right- and left-handed helical vortices caused by increased flow swirling in a cylindrical cavity with rotating lids. *Technical Phys. Lett.*, **28**, 55–58, 2002.
- [191] Okulov, V. L., Sørensen, J. N. & Voigt, L. K. Vortex scenario and bubble generation in a cylindrical cavity with rotating top and bottom. *European J. Mechanics B-Fluids*, **24**, 137–148, 2005.
- [192] O’Neil, J. & Meneveau, C. Subgrid-scale stresses and their modelling in a turbulent plane wake. *J. Fluid Mech.*, **349**, 253–293, 1997.
- [193] Pao, H. P. A numerical computation of a confined rotating flow. *J. Appl. Mech.*, **37**, 480–487, 1970.
- [194] Patera, A. T. Spectral element method for fluid dynamics: laminar flow in a channel expansion. *J. Comput. Phys.*, **54**, 468–488, 1984.
- [195] Pereira, J. C. F. & Sousa, J. M. M. Confined vortex breakdown generated by a rotating cone. *J. Fluid Mech.*, **385**, 287–323, 1999.
- [196] Perot, J. B. An analysis of the fractional step method. *J. Comput. Phys.*, **108**, 51–58, 1993.
- [197] Perot, J. B. Comments on the fractional step method. *J. Comput. Phys.*, **121**, 190–191, 1995.
- [198] Piva, M. & Meiburg, E. Steady axisymmetric flow in an open cylindrical container with a partially rotating bottom wall. *Phys. Fluids*, **17**, Art. 063603, 2005.
- [199] Pope, S. B. *Turbulent Flows*. Cambridge University Press, Cambridge, 2000.
- [200] Prasad, A. K. Personal communication. Additional experimental data.
- [201] Prasad, A. K. & Koseff, J. R. Reynolds number and end-wall effects on a lid-driven cavity flow. *Phys. Fluids*, **1** (2), 208–218, 1989.
- [202] Prasad, A. K. & Koseff, J. R. Combined forced and natural convection heat transfer in a deep lid driven cavity flow. *Int. J. Heat Fluid Flow*, **17**, 460–467, 1996.
- [203] Pruett, C. D., Thomas, B. C., Grosch, C. E. & Gatski, T. B. A temporal approximate deconvolution model for large-eddy simulation. *Phys. Fluids*, **18**, Art. 028104, 2006.
- [204] Quarteroni, A. & Valli, A. *Numerical Approximation of Partial Differential Equations*. Springer Series in Computational Mathematics. Springer, Berlin, 1994.
- [205] Ramaswamy, B. & Kawahara, M. Arbitrary Lagrangian-Eulerian finite-element method for unsteady, convective, incompressible viscous free-surface fluid-flow. *Int. J. Numer. Methods Fluids*, **7** (10), 1053–1075, 1987.
- [206] Rembold, B. & Kleiser, L. Noise prediction of a rectangular jet using large eddy simulation. *AIAA J.*, **42**, 1823–1831, 2004.

- [207] Rhee, H. S., Koseff, J. R. & Street, R. L. Flow visualization of a recirculating flow by rheoscopic liquid and liquid-crystal techniques. *Experiments In Fluids*, **2**, 57–64, 1984.
- [208] Rodgers, S. E., Kwak, D. & Kiris, C. Paper 89-0463. AIAA, 1989.
- [209] Ronnenberg, R. Ein selbstjustierendes 3-Komponenten-Laserdoppleranemometer nach dem Vergleichsstrahlverfahren, angewandt auf Untersuchungen in einer stationären zylinder-symmetrischen Drehströmung mit einem Rückströmgebiet. Technical report, Max-Planck-Institut für Strömungsforschung, Göttingen, 1977. Bericht 19.
- [210] Rønquist, E. M. Spectral element methods for the unsteady Navier–Stokes equations. von Kármán Institute for Fluid Dynamics, February 18–22, 1991. Lecture Series 1991–01.
- [211] Rønquist, E. M. A Domain Decomposition Solver for Three-Dimensional Steady Free Surface Flows. In Bjørstad, P., Espedal, M. & Keyes, D., editors, *Domain Decomposition 9 Proceedings*, pages 792–801, Wiley, New York, 1998.
- [212] Sagaut, P. Numerical simulations of separated flows with subgrid models. *Rech. Aéro.*, **1**, 51–63, 1996.
- [213] Sagaut, P. *Large eddy simulation for incompressible flows: an introduction*. Springer, Berlin, 3rd Eds., 2005.
- [214] Sagaut, P., Comte, P. & Ducros, F. Filtered subgrid scale models. *Phys. Fluids*, **12**, 233–236, 2000.
- [215] Sahin, M. & Owens, R. G. A novel fully implicit finite volume method applied to the lid-driven cavity problem. Part I: High Reynolds number flow calculations. *Int. J. Numer. Methods Fluids*, **42**, 57–77, 2003.
- [216] Sahin, M. & Owens, R. G. A novel fully-implicit finite volume method applied to the lid-driven cavity problem. Part II. Linear stability analysis. *Int. J. Numer. Methods Fluids*, **42**, 79–88, 2003.
- [217] Salvetti, M. V. & Banerjee, S. A priori tests of a new dynamic subgrid-scale model for finite-difference large eddy simulations. *Phys. Fluids*, **9**, 2831–2847, 1997.
- [218] Sarpkaya, T. Vorticity, free surface, and surfactants. *Annu. Rev. Fluid Mech.*, **28**, 83–128, 1996.
- [219] Scardovelli, R. & Zaleski, S. Direct numerical simulation of free-surface and interfacial flow. *Annu. Rev. Fluid Mech.*, **31**, 567–603, 1999.
- [220] Schlatter, P., Stolz, S. & Kleiser, L. LES of transitional flows using the approximate deconvolution model. *Int. J. Heat Fluid Fl.*, **25**, 549–558, 2004.
- [221] Schneidesch, C. R. *Numerical simulation of incompressible flows in complex geometries by preconditioned Chebyshev collocation*. PhD thesis, Université Catholique de Louvain, Louvain-La-Neuve, 1992.
- [222] Schneidesch, C. R. & Deville, M. O. Chebyshev collocation method and multi-domain decomposition for Navier–Stokes equations in complex curved geometries. *J. Comput. Phys.*, **106**, 234–257, 1993.
- [223] Serre, E. & Bontoux, P. Vortex breakdown in a three-dimensional swirling flow. *J. Fluid Mech.*, **459**, 347–370, 2002.
- [224] Shah, K. B. & Ferziger, J. A new non-eddy viscosity subgrid-scale model and its application to channel flow. In *Annual Research Briefs*, pages 73–90. Center for Turbulence Research, NASA/ Stanford Univ., 1995.
- [225] Shankar, P. N. & Deshpande, M. D. Fluid Mechanics in the Driven Cavity. *Annu. Rev. Fluid Mech.*, **32**, 93–136, 2000.
- [226] Shen, L., Triantafyllou, G. S. & Yue, D. K. P. Turbulent diffusion near a free surface. *J. Fluid Mech.*, **407**, 145–166, 2000.
- [227] Shen, L., Zhang, X., Yue, D. K. P. & Triantafyllou, G. S. The surface layer for free-surface turbulent flows. *J. Fluid Mech.*, **386**, 167–212, 1999.
- [228] Shen, W. Z., Sørensen, J. N. & Michelsen, J. A. Numerical study of swirling flow in a cylinder with rotating top and bottom. *Phys. Fluids*, **18**, Art. 064102, 2006.
- [229] Shotorban, B. & Mashayek, F. Modeling subgrid-scale effects on particles by approximate deconvolution. *Phys. Fluids*, **17**, Art. 081701, 2005.
- [230] Shtern, V. *Core C++: A Software Engineering Approach*. Prentice Hall PTR, Upper Saddle River, New Jersey, 2000.
- [231] Shtern, V. & Hussain, F. Collapse, symmetry breaking, and hysteresis in swirling flows. *Annu. Rev. Fluid Mech.*, **31**, 537–566, 1999.
- [232] Smagorinsky, J. S. General circulation experiments with the primitive equations. I: The basic experiment. *Month. Weath. Rev.*, **91**, 99–165, 1963.

- [233] Sørensen, J. N. Visualization of rotating fluid flow in a closed cylinder. Technical report, Department of Fluid Mechanics, Technical University of Denmark, 1992. Rep. AFM 92–06.
- [234] Sørensen, J. N. & Christensen, E. A. Direct numerical-simulation of rotating fluid-flow in a closed cylinder. *Phys. Fluids*, **7**, 764–778, 1995.
- [235] Sotiropoulos, F. & Ventikos, Y. Transition from bubble-type vortex breakdown to columnar vortex in a confined swirling flow. *Int. J. Heat Fluid Flow*, **19**, 446–458, 1998.
- [236] Sotiropoulos, F. & Ventikos, Y. The three-dimensional structure of confined swirling flows with vortex breakdown. *J. Fluid Mech.*, **426**, 155–175, 2001.
- [237] Sotiropoulos, F., Ventikos, Y. & Lackey, T. C. Chaotic advection in three-dimensional stationary vortex-breakdown bubbles: Sil’nikov’s chaos and the devil’s staircase. *J. Fluid Mech.*, **444**, 257–297, 2001.
- [238] Speziale, C. G. Galilean invariance of subgrid-scale stress models in the large-eddy simulation of turbulence. *J. Fluid Mech.*, **156**, 55–62, 1985.
- [239] Spohn, A., Mory, M. & Hopfinger, E. J. Observations of vortex breakdown in an open cylindrical container with a rotating bottom. *Experiments In Fluids*, **14**, 70–77, 1993.
- [240] Spohn, A., Mory, M. & Hopfinger, E. J. Experiments on vortex breakdown in a confined flow generated by a rotating disc. *J. Fluid Mech.*, **370**, 73–99, 1998.
- [241] Stokes, J. R., Graham, L. J. W., Lawson, N. J. & Boger, D. V. Swirling flow of viscoelastic fluids. Part 1. Interaction between inertia and elasticity. *J. Fluid Mech.*, **429**, 67–115, 2001.
- [242] Stokes, J. R., Graham, L. J. W., Lawson, N. J. & Boger, D. V. Swirling flow of viscoelastic fluids. Part 2. Elastic effects. *J. Fluid Mech.*, **429**, 117–153, 2001.
- [243] Stolz, S. & Adams, N. A. An approximate deconvolution procedure for large-eddy simulation. *Phys. Fluids*, **11**, 1699–1701, 1999.
- [244] Stolz, S., Adams, N. A. & Kleiser, L. An approximate deconvolution model for large-eddy simulation with application to incompressible wall-bounded flows. *Phys. Fluids*, **13**, 997–1015, 2001.
- [245] Stolz, S., Adams, N. A. & Kleiser, L. The approximate deconvolution model for large-eddy simulations of compressible flows and its application to shock-turbulent-boundary-layer interaction. *Phys. Fluids*, **13**, 2985–3001, 2001.
- [246] Stolz, S., Schlatter, P. & Kleiser, L. High-pass filtered eddy-viscosity models for large-eddy simulations of transitional and turbulent flow. *Phys. Fluids*, **17**, Art. 065103, 2005.
- [247] Suzuki, T., Iima, M. & Hayase, Y. Surface switching of rotating fluid in a cylinder. *Phys. Fluids*, **18**, Art. 101701, 2006.
- [248] Tsai, W.-T. & Yue, D. K. P. Computation of nonlinear free-surface flows. *Annu. Rev. Fluid Mech.*, **28**, 249–278, 1996.
- [249] Tsinober, A. & Levich, E. On the helical nature of three dimensional coherent structures in turbulent flows. *Phys. Lett.*, **99**, 321–323, 1983.
- [250] Tsitverblit, N. & Kit, E. On the onset of unsteadiness in confined vortex flows. *Fluid Dyn. Res.*, **23**, 125–152, 1998.
- [251] Turner, M. J., Clough, R. W., Martin, H. C. & Topp, L. P. Stiffness and deflection analysis of complex structures. *J. Aeronautical Society*, **23**, 805, 1956.
- [252] Valentine, D. T. & Jahnke, C. C. Flows induced in a cylinder with both end walls rotating. *Phys. Fluids*, **6**, 2702–2710, 1994.
- [253] Van Kan, J. A second-order accurate pressure-correction scheme for viscous incompressible flow. *SIAM J. Sci. Stat. Comput.*, **7**, 870–891, 1986.
- [254] Van Kemenade, V. Incompressible fluid flow simulation by the spectral element method. Technical report, “Annexe technique projet FN 21-40’512.94”, IMHEF–DGM, Swiss Federal Institute of Technology, Lausanne, 1996.
- [255] Vatistas, G. H. A note on liquid vortex sloshing and Kelvin equilibria. *J. Fluid Mech.*, **217**, 241–248, 1990.
- [256] Vatistas, G. H., Wang, J. & Lin, S. Experiments on waves induced in the hollow core of vortices. *Experiments In Fluids*, **13**, 377–385, 1992.
- [257] Vatistas, G. H., Wang, J. & Lin, S. Recent findings on Kelvin’s equilibria. *Acta Mechanica*, **103**, 89–102, 1994.

- [258] Verstappen, R., Wissink, J. G., Cazemier, W. & Veldman, A. E. P. Direct numerical simulations of turbulent-flow in a driven cavity. *Future Generation Computer Systems*, **10**, 345–350, 1994.
- [259] Verstappen, R., Wissink, J. G. & Veldman, A. E. P. Direct numerical-simulation of driven cavity flows. *Appl. Scientific Research*, **51**, 377–381, 1993.
- [260] Vogel, H. U. Experimentelle Ergebnisse über die laminare Strömung in einem zylindrischen Gehäuse mit darin rotierender scheibe. Technical report, Max-Planck-Institut für Strömungsforschung, Göttingen, 1968. Bericht 6.
- [261] von Kaenel, R., Kleiser, L., Adams, N. A. & Vos, J. B. Large eddy simulation of shock-turbulence interaction. *AIAA J.*, **42**, 2516–2528, 2004.
- [262] von Kaenel, R. *Large-eddy simulation of compressible flow using the finite-volume method*. PhD thesis, no. 15255, Swiss Federal Institute of Technology, ETH Zürich, 2003.
- [263] Vreman, B., Geurts, B. & Kuerten, H. On the formulation of the dynamic mixed subgrid-scale model. *Phys. Fluids*, **6**, 4057–4059, 1994.
- [264] Vreman, B., Geurts, B. & Kuerten, H. Large-eddy simulation of the turbulent mixing layer. *J. Fluid Mech.*, **339**, 357–390, 1997.
- [265] Watson, J. P. & Neitzel, G. P. Numerical evaluation of a vortex-breakdown criterion. *Phys. Fluids*, **8**, 3063–3071, 1996.
- [266] Winckelmans, G. S. & Jeanmart, H. *Assessment of some models for LES without/with explicit filtering*, pages 55–66. Direct and large-eddy simulation IV. Kluwer, Geurts, Friedrich and Métais Eds., 2001.
- [267] Winckelmans, G. S., Wray, A. A., Vasilyev, O. V. & Jeanmart, H. Explicit-filtering large-eddy simulation using the tensor-diffusivity model supplemented by a dynamic Smagorinsky term. *Phys. Fluids*, **13**, 1385–1403, 2001.
- [268] Xue, S. C., Phan-Thien, N. & Tanner, R. I. Fully three-dimensional, time-dependent numerical simulations of Newtonian and viscoelastic swirling flows in a confined cylinder - Part I. Method and steady flows. *J. Non-Newtonian Fluid Mech.*, **87**, 337–367, 1999.
- [269] Young, D. L., Sheen, H. J. & Hwu, T. Y. Period-doubling route to chaos for a swirling flow in an open cylindrical container with a rotating-disk. *Experiments In Fluids*, **18**, 389–392, 1995.
- [270] Zandbergen, P. J. & Dijkstra, D. von Kármán swirling flows. *Annu. Rev. Fluid Mech.*, **19**, 465–491, 1987.
- [271] Zang, Y., Street, R. L. & Koseff, J. R. Application of a dynamic subgrid-scale model to turbulent recirculating flows. In *Annual Research Briefs*, volume 85. Center for Turbulence Research, Stanford University/NASA-Ames, 1992.
- [272] Zang, Y., Street, R. L. & Koseff, J. R. A dynamic mixed subgrid-scale model and its application to turbulent recirculating flows. *Phys. Fluids A*, **5**, 3186–3193, 1993.
- [273] Zang, Y., Street, R. L. & Koseff, J. R. A non-staggered grid, fractional step method for time-dependent incompressible Navier–Stokes equations in curvilinear coordinates. *J. Comput. Phys.*, **114**, 18–33, 1994.
- [274] Zhou, Y., Hossain, M. & Vahala, G. A critical-look at the use of filters in large eddy simulation. *Phys. Lett. A*, **139**, 330–332, 1989.

Curriculum vitae

Roland Bouffanais

French citizen

Born on August 1st, 1974 (France)

Education

- École Polytechnique Fédérale de Lausanne**, (EPFL) Lausanne, Switzerland
Ph.D., Science July 2007
Dissertation Topic: “Simulation of shear-driven flows: transition with a free surface & confined turbulence”
Supervisors: Prof. Michel O. Deville & Prof. Emmanuel Leriche
- National University of Singapore**, (NUS) Singapore 2002
Graduate Student, Faculty of Science, Department of Computational Science
Research Project: “Solution of nonlinear PDEs using discrete singular convolution kernels”
Supervisors: Prof. Lai Choy Heng & Prof. Wei Guo-Wei
- École Normale Supérieure**, (ENS) Lyon, France 1999
M.Sc., Fundamental Physics
Research Project: “Numerical modeling of the ultrafast electron relaxation in metal films”
Supervisor: Dr. Fabrice Vallée
- Université Pierre & Marie Curie, Paris 6**, (UPMC) Paris, France 1999
M.Sc., Physics of liquids
Research Project: “Viscous fingering and the Saffman–Taylor instability in a Hele–Shaw cell”
Supervisor: Prof. Martine Ben Amar
- French Ministry of Education**, Paris, France 1998
‘Agrégation’, Physics

Academic Experience

- École Polytechnique Fédérale de Lausanne**, (EPFL) Lausanne, Switzerland
Research Assistant October 2003–September 2007
Teaching Assistant October 2003–September 2007
- Johns Hopkins University**, (JHU) Baltimore MD, USA July 2006
Visiting Scholar
- National University of Singapore**, (NUS) Singapore
Research and Teaching Assistant September 2001–August 2003
Program Manager and Advisor September 2001–August 2003
- École Centrale Paris, École Supérieure d’Électricité**, (ECP) and (Supélec), France June 2001
Member of the Admission Board
- Preparatory Classes for Engineering Schools**, Cluny, France September 1999–August 2001
Physics Instructor

Reviewing Activities

- Manuscript reviews for *J. Comput. Phys.*
Manuscript reviews for *Computers and Fluids*.
Manuscript reviews for *App. Num. Math.*

Journal Publications

1. Habisreutinger, M. A., Bouffanais, R., Leriche, E. & Deville, M. O. A coupled approximate deconvolution and dynamic mixed scale model for large-eddy simulation. *J. Comput. Phys.*, **224**, 241–266, 2007.
2. Bouffanais, R., Deville, M. O., Gruber, R. & Keller, V. Computational performance analysis of a high-order spectral and mortar element toolbox. *Parallel Computing*, 2007. Submitted for publication.
3. Bouffanais, R., Deville, M. O. & Leriche, E. Large-eddy simulation of the flow in a lid-driven cubical cavity. *Phys. Fluids*, **19**, Art. 055108, 2007.
4. Bodard, N., Bouffanais, R. & Deville, M. O. Solution of moving boundary problems by the spectral element method. *App. Num. Math.*, 2007. In Press.
5. Bouffanais, R. & Deville, M. O. Mesh update techniques for free-surface flow solvers using spectral element method. *J. Sci. Comput.*, **27**, 137–149, 2006.
6. Bouffanais, R., Deville, M. O., Fischer, P. F., Leriche, E. & Weill, D. Large-eddy simulation of the lid-driven cubic cavity flow by the spectral element method. *J. Sci. Comput.*, **27**, 151–162, 2006.
7. Bouffanais, R. Résolution des systèmes optiques et Maple. *Bulletin de l'Union des Physiciens*, **831**, 1003–1013, 2001.
8. Del Fatti, N., Bouffanais, R., Vallée, F. & Flytzanis, C. Nonequilibrium electron interactions in metal films. *Phys. Rev. Lett.*, **81**, 922–925, 1998.

Book Publication

9. Bouffanais, R. *Thermodynamique Sup & Spé*. Number ISBN 2–910350–30–4, 192 pages. Prepamath, 1999.

Conference Proceedings Publication

10. Bouffanais, R. & Deville, M. O. Simulation of standing waves using moving-grid techniques with spectral element methods. In *Proc. Int. Conf. on Mathematical and Numerical aspects of Waves*, pages 374–375, Brown University, Providence (RI), 2005.

